Geochemical Modelling of Shallow Fractionation and Deep Mantle Melting Below Mauna Loa Volcano, Hawaii

Jennifer Clare Prichard

A thesis submitted for the degree of Doctor of Philosophy from the Australian National University

Declaration

The work herein is an account of the research performed during the academic programme towards the degree of Doctor of Philosophy at the Australian National University.

I certify that this thesis does not contain any materials previously submitted for a degree or diploma at a university, nor does it contain any material previously published or written by another person, except where due reference is made in the text.

Jennifer Prichard

Australian National University

Digitally signed by Jennifer Prichard
DN: cn=Jennifer Prichard, o=Australian NAtional University, ou=Research School of Earth Sciences, email=jenniferprichard1@gmail.com, c=AU
Date: 2020.04.06 15:10:56 +10'00'

Acknowledgements

This thesis would not have been possible without the massive efforts of Marc Norman and Victoria Bennett who devoted a large amount of time and effort into what was a difficult project. Thank you for the thorough reviewing and advice and thanks to Vickie Bennett for taking over as my supervisor half-way through the project, although she did not have to. Thank you to Greg and Hugh who's advice was invaluable and greatly appreciated throughout the project.

I would like to thank Mr. Les Kinley for his expert help with conducting my solution ICP MS work and for advising me on how to get the best from my samples and the machine.

Thank you to Linda McMorrow for her guidance in teaching me how to use the clean lab, and making sure I always had all the acids and equipment I needed to get the bulk rock dissolution complete. She ensured I was safe and knew how to effectively operate in the clean lab when using dangerous chemicals.

Thanks to Sonja Zrink for her contribution to the project through her guidance of me in the ultra-clean lab. She taught me the procedures for Sr and Nd isotope column chemistry and ensured I was able to operate safely and effectively in an ultra-clean laboratory.

I would like to thank our collaborators at the University of Massachusetts Michael Rhodes and Michael Vollinger. They have performed all of our major element XRF analysis using their XRF laboratory. In addition they provided many crushed sample powders for us to add to our collection. They have also provided thin sections, and their interpretations and suggestions are greatly appreciated. The suggestions and guidance from Michael Garcia is also very much appreciated.

The help of Paula Smith, Paul Asimov, Eleanor Green, and Mark Ghiorso is also very much appreciated. This study required the extensive use of multiple magma melting programs and their advice allowed me to get the best out of these programs as well as technical advice on how to fix things that went wrong.

I would also like to thanks Richard Skelton and Oscar Branson for their help when I have required the use of a coding language or to get a program up and running. They have also helped me out with amazing discussions on the science of the project, and been great sounding boards for some of my thoughts. Thanks also to Charles and Guil for great discussions.

Thanks to Brian Harold and Maree Coldrick for all their help in with the technical side of getting a PhD done. Brian is always there if I need a specific program or computer or any other

kind of help. Maree has helped me through some really tough time and has ensured that I do not quit my PhD and helped me get access to all the resources I need to complete a PhD.

I would also like to thank Penny King for her help during my second year of my PhD. This was a tough time for me and she ensured I had the resources I needed, helped me with my supervision, and was there for me at several times during my PhD to help iron out kinks in the project, and has provided me with invaluable teaching experience. She checked up on me and made sure I was feeling like I could somewhat handle my project. Thanks also to Andrew Berry who has provided we with some amazing teaching opportunities and the chance to go on the Earth field trip.

I would like to thank my PhD friends who have made the whole experience worthwhile. During my PhD I have met some of the most amazing people and I know they will be life-long friends. In particular I would like to thank my partner in crime, Jessica Lowczak for her constant and unwavering support throughout our turbulent PhD journey. She has been the rock that I turn to in good times as well as bad times and I could not have gotten through this experience without her. Aside from her friendship in this time, she has engaged me in scientific discussion and allowed me to think through with her my scientific questions and dilemmas. At times she has convinced me not to give up and to keep going despite the difficulties I have had during this experience.

Thank you to my housemates past and present including Laura Crisp, Nicholas farmer, and Brendan Hanger who ensured our humble abode was always a place for fun chats and tasty food. It was always great to be able to go home and watch TV with them or just vent and chat. To all the wonderful ladies who made my PhD journey worthwhile especially Mimi, Kate, Jo, and Laura who are such amazing women who I have loved spending four years with. To the RSES soccer team, the trivia team, and the morning tea dwellers that really make RSES the wonderful place to be that it is.

Finally, I would like to thank my family for all of their help during this seemingly insurmountable task: Mum, Dad, David, Juanita, and Ross. They have always been a place to turn to when things got tough. I am very lucky to have had them so close by during my PhD so that I could go home on weekends, or spend time with them at the coast or just chilling out, and for housing me towards the end of my program. There is zero chance I would have finished this without such a supportive family.

Abstract

Hawaii is the archetypal example of intra-plate 'hotspot' volcanism, yet the mechanisms of plume formation, hotspot volcano formation, and the nature of chemical heterogeneity in hotspot lavas such as those at Hawaii remains in question. This study aims to disentangle the nature of peridotite melting and melt evolution below Mauna Loa Volcano, Hawaii, in order to determine the source-rock composition and mechanical processes which give rise to the Hawaiian Islands. Of particular interest is understanding what physical and chemical processes lead to the distinctive 'double-track' geochemical trend, whereby the volcanoes on the south-west side of the Hawaiian volcanic chain ('Loa' track) vary systematically compared with those on the north-east side ('Kea' track) with respect to major elements, trace elements, and isotopic ratios. In order to make meaningful inferences about how the parallel distinction may arise, it is necessary to understand how the chemistry of magma evolves at Hawaii starting with the composition and melting of the mantle source, followed by emplacement of the magma into the crust with associated residence times and mixing, the progression of the crystallisation process as the magma cools, and finally the eventual eruption through the volcanic edifice. Here, major element, trace element, and Sr and Nd isotopic analyses of tholeiites from submarine Mauna Loa volcano are used alongside compiled literature data of Mauna Loa and Kilauea Volcanoes to investigate both shallow magmatic processes in the crust and deep mantle melting in the upwelling plume. Evidence from modal olivine, olivine forsterite content, glass compositions, and whole rock Ni suggest that none of the whole rock samples are direct parental magmas, but instead reflect an evolved magma in which olivine has remained entrained or become subsequently entrained to varying degrees. Computational geochemical modelling suggests the occurrence of two distinct fractionation sequences: ol + sp + opx + cpx + plag and another with ol + sp + cpx, which could be achieved with minor variations in water content (0 – 0.5 wt. %). Furthermore, a compilation of experimental melt studies and trace element models are presented, showing that the source of Hawaii's lava is most probably a garnet-bearing peridotite from ~4 GPa with a major element composition similar to that of primitive mantle or Hawaiian pyrolite, contradicting some current hypotheses which argue for a pyroxenitic source. Trace element modelling reveals the differences between Mauna Loa and Kilauea can broadly be explained by variable degrees of melting of a fertile, garnet peridotite, with Mauna Loa resulting from ~12% melting and Kilauea resulting from ~6%. It was shown that low-olivine pyroxenites cannot produce the required high Ni content of Mauna Loa lavas, and that Ni concentrations may be better explained by the high temperatures and high MgO contents associated with the Hawaiian plume which cause an associated decrease in the bulk D_{Ni}. This negates the need for a low-olivine pyroxenite as the source. Despite this, a component with high radiogenic lead and

$^{143}Nd/^{144}Nd$ with low $^{87}Sr/^{86}Sr$ is required in the Kilauea source, while the Mauna Loa source lies isotopically between Bulk Silicate Earth and Depleted MORB mantle.

Table of Contents

1 Background

This chapter will cover some of the broad background material relevant to Hawaii in order to show where Hawaii fits into the global setting, and to show the progression of discovery that was necessary for the science to get to where it is today.

1.1 Ocean Island Basalts (OIB)

Basaltic crust covers 70% of the Earth's surface, and can be generated in two fundamentally different types of tectonic setting: from mid-ocean ridges at the margins of two tectonic plates, and from ocean island hotspot settings where intra-plate magmatism occurs independently of plate movement. These two basalt types are significantly different in their trace-element and isotopic compositions, and to a lesser extent, in their major element compositions. Mid-Ocean Ridge Basalts (MORB) are produced when adjacent tectonic plates diverge causing the mantle to undergo passive adiabatic decompression until the solidus temperature is reached and partial melting occurs. The magmatism that occurs is the result of tectonic plate processes and as such a relatively shallow part of the upper mantle is sampled each time, leading to the depletion of incompatible elements and isotopic signatures in this frequently tapped portion of the mantle. The resulting MORB are tholeiitic and remarkably restricted in chemical composition (Winter, 2010). The second method of producing oceanic crust involves the active upwelling of mantle material, which can be expressed at the surface far from tectonic boundaries. These volcanic provinces have been allocated many names including hotspots, OIB, mantle plumes, wetspots, or simply 'melting anomalies'. On the modern Earth, they tend to cluster either in the mid-Pacific or underneath Africa, at antipodal points of the globe, which may be the result of two slow seismic areas located below these locations known as 'superplumes' e.g. (Courtillot et al., 2003). These superplumes are large, seismically slow areas that are associated with most of the hotspots globally. It is thought that the position of a plume or hotspot in relation to the superplume may have consequences for the chemical composition of the hotspot volcano (Romanowicz and Gung, 2002). One study suggested that for these superplumes to form isolated, rounded formations, some element of compositional difference is required to obtain the necessary viscosity contrast (McNamara and Zhong, 2004).

1.2 Mantle Plumes

The idea that particular types of volcanism may be the result of active mantle upwelling, first came to light in the late 60's, when Wilson and later Morgan (Wilson, 1963, Morgan, 1971) argued that plumes and the movement of the plates above them, were the result of mantle convection. Morgan first proposed a 'mantle plume theory' where the entire mantle was a single,

chemically homogeneous reservoir, in which plumes rise from a deeper boundary layer (Figure 1.1). Geochemists later noted the large amount of chemical heterogeneity within these 'plumes' and suggested that they may come from a place in the mantle that was more primitive than a MORB source.

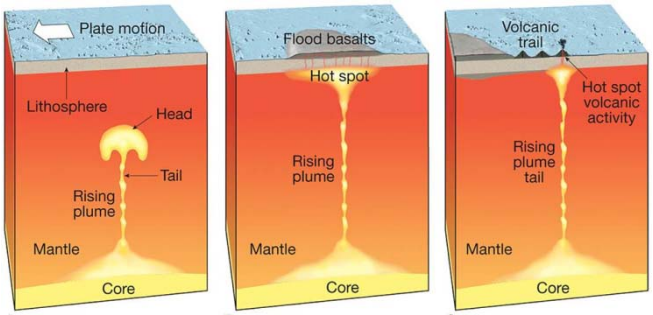

Figure 1.1 An impression of a mantle plume envisaged as the source of Hawaii. Coloured to look like the lava, this sketch gives the false impression that plumes are molten as they rise through the mantle (Image by Tasa Graphic arts Inc., 2010).

There have been attempts to model the shape and movement of mantle plumes using dynamic models of fluids with variable viscosity. Campbell and Griffiths used these experiments to show that a mantle plume is initially 'mushroom' shaped, with a large bulbous head producing the majority of lava (Figure 1.2) – seen at the surface as flood basalts or large igneous provinces, followed by a thin tail that forms a time-transgressive chain of volcanoes such as the Hawaiian-Emperor chain of seamounts and ocean islands (Campbell and Griffiths, 1990).

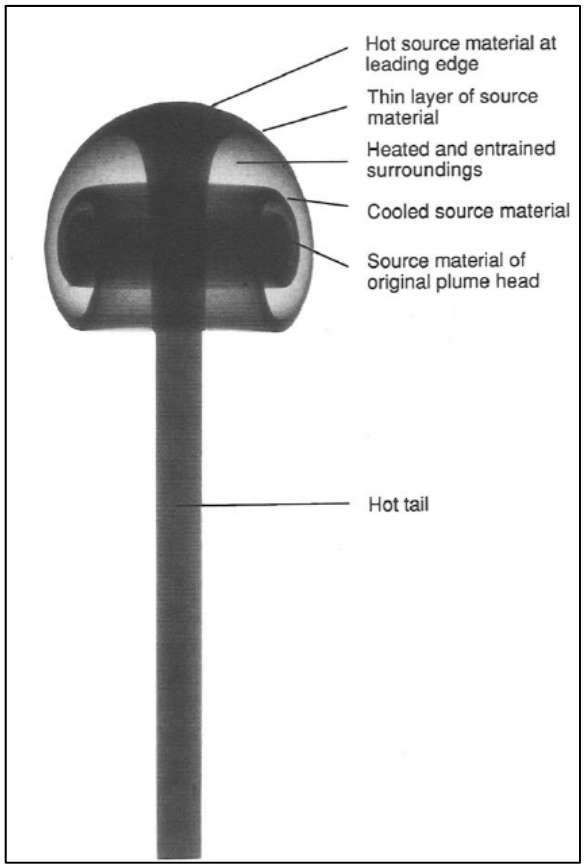

Figure 1.2 Early fluid dynamic experiments where glucose syrup was dyed, heated, and allowed to rise through cool, uncoloured glucose syrup, forming the 'mushroom' shaped head and narrow tail from (Campbell and Griffiths, 1990).

Whitehead and Luther have shown using fluids of variable viscosities that the quantitative shape that a plume will take depends on the viscosity contrast between the fluids (Whitehead and Luther, 1975). A plume that is far less viscous than the surrounding material will form rounding of the head of the plume, overhang, and 'necking off', whereas a plume in which the rising material is far more viscous than the surrounding material will form straight, vertical columns in which there is no visible 'head' and where the radius decreases with height above the source. It has been suggested by Montelli and co-authors that for a reasonable heat-flux and mass to be calculated, the plume velocity must be slowed by increased viscosity or a chemical anomaly involving a heavy element such as Fe (Montelli et al., 2006, Nolet et al., 2006).

Further experiments were conducted using fluids in which the buoyancy flux was variable. The study found that the amount of entrainment of ambient mantle into the rising plume may be significant, ranging from 5 to 90% and is negatively correlated to buoyancy flux. It also showed that the lower mantle is the region most likely to be entrained. The study has suggested that the 'FOZO' component ('Focal Zone' isotopic signature – discussed further below) that is common

to most OIB may come from entrainment of the lower mantle. This lower mantle component is not completely primitive and may have been affected by melting and differentiation events in the past (Hauri et al., 1994).

1.3 Plume source depth

The debate surrounding the source depth of mantle plumes, and the type of anomalous conditions which may cause plumes to exist remains ongoing. Many techniques have been used to try to provide some answers, including seismic geophysics, computational modelling, petrological experiments, and geochemical analysis comprising major elements, trace elements and isotopes.

There have been many possibilities for source depth put forward since the proposal of mantle plumes, including core-mantle boundary origins, shallow asthenospheric mantle origins, transition zone origins, as well as the complete non-existence of plume all together (although this view is no longer common and the research has progressed beyond arguing the existence of mantle plumes). Anderson has argued that the source of Hawaii and other hotspots is shallower than that of mid-ocean ridges, and that due to the complementary nature of MORB and OIB geochemistry, OIB must be the result of metasomatism of upper mantle with residual large ion lithophile (LIL) and incompatible element-rich material after the subtraction of MORB (Anderson, 1981). Fitton has described Anderson's model where OIB are the product of melting of a global, weak, enriched layer that lies immediately beneath the lithosphere, while this layer is pulled aside by diverging plates to make way for the melting of depleted mantle at mid-ocean ridges (Fitton, 2007, Anderson, 1995). Others have suggested that the source probably originates at the 660 km discontinuity as a result of subducted slab becoming neutrally buoyant due to mineral phase change e.g. (Ringwood, 1994). In this model, subducted oceanic slab is mostly unable to penetrate the lower mantle due to the mineral phase change of silicate spinel into Mg perovskite + magnesiowustite, as well as the formation of a gravitationally stable layer of garnetite just above the transition zone. More recently, there has been growing evidence that the source of mantle plumes may, in many cases, be the lower mantle or even close to the core-mantle boundary e.g. (Courtillot et al., 2003).

In recent times, geophysical techniques for mapping the internal structure of the Earth, such as seismic tomography have improved, and several studies have investigated the mantle underneath multiple proposed-to-be plume-origin volcanoes e.g. (Ji and Nataf, 1998, Montelli et al., 2004, Montelli et al., 2006, Zhao, 2009). Seismic tomography is an imaging technique that uses earthquake-generated seismic waves to create three-dimensional images of Earth's interior. Strong, slow anomalies to the core-mantle boundary (CMB) at 2800 km depth were revealed

below Hawaii (Figure 1.3), Kerguellen, Ascension, Samoa, Canary Islands, and Easter Island (Montelli et al., 2006). Many other hotspots such as Reunion, Cocos, and Louisville have been tracked to the lower mantle, but Eiffel, Seychelles, East Australia, Juan Fernandez were found to have only shallow slow anomalies. In a useful summary, Zhao compiled seismic data for 60 hotspots globally and found that 12 had lower mantle low velocity zones beneath them, which indicate a source close to the core-mantle boundary (CMB) (Zhao, 2007). The previously mentioned study by Courtillot and co-authors had documented 49 hotspots, including flood basalts and oceanic plateaus, comparing them against a set of criteria for a deep mantle source (Courtillot et al., 2003). These criteria included whether the hotspot left a long-lived track, if it produced flood basalts early in the life of the plume, how buoyant it was, the $^{3}He/^{4}He$ ratio of magmas, and the evidence of low velocity zones beneath the hotspot. Only nine of the 49 hotspots including Hawaii were determined to have a deep mantle source. As an approximate estimate from these studies, the number of plumes which have origins at the CMB range from between 5-12.

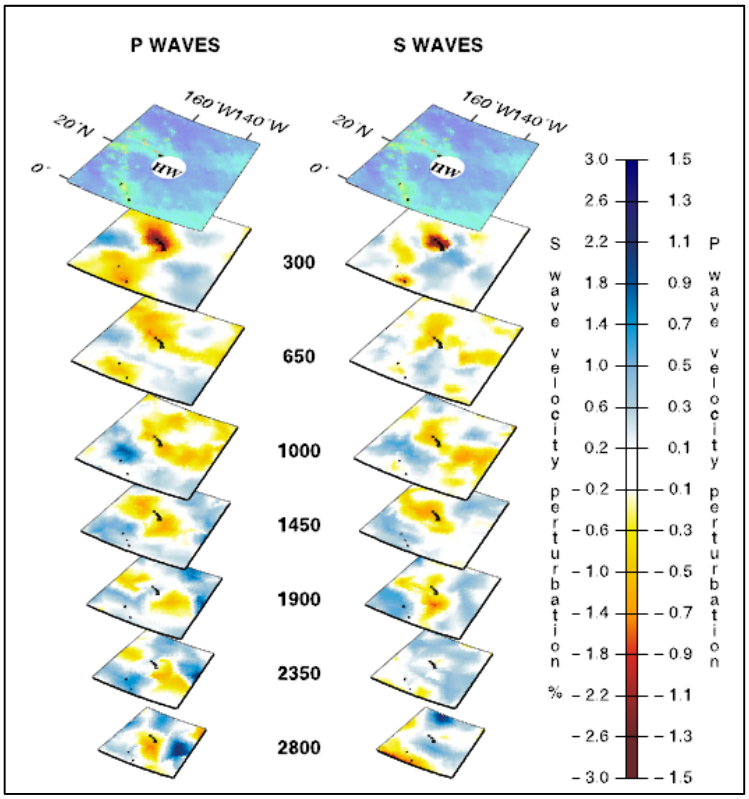

Figure 1.3 Finite frequency tomographic image of the mantle below Hawaii (Montelli et al., 2006). Slow seismic velocity regions (yellow) are seen down to the core-mantle boundary

1.4 Opposition to the plume hypothesis

Despite the ongoing quest for an explanation to mantle plumes, the pursuit of a single plume model to fit all hotspots (here meaning a localized melting anomaly) has been flagged as inappropriate by some authors. Each hotspot documented globally is unique in terms of volume flux, uplift and subsidence rates, presence (or not) of volcano tracks and flood basalts, isotopic and trace element composition, source depth, and many plume-like systems have features that remain unexplained (Sleep, 1990). These issues have been outlined by Foulger, who suggested that the large magma flux of most Large Igneous Provinces (LIPs) thought to be plume related cannot be accounted for with a compositional or thermal anomaly, and that the timing of LIPs associated with volcanic chains does not align with the Campbell model of plume structure, as LIPs have been known to occur during or even after the formation of the chain (Foulger, 2007). Similarly, if such a LIP formed during the initial stages of the plume, evidence of the material should be found at accretionary zones at plate boundaries. Foulger states that there is no systematic evidence for differential vertical motion, either rise or subsidence, of plates surrounding most hotspots that would be consistent with the presence of an underlying thermally buoyant plume. Foulger's preferred model is that melting anomalies can be attributed to shallow processes related to plate tectonics (Anderson, 2001). In this model, volcanic chains are the result of decompression near to cracks, fissures, or faults. Anderson concedes that neither the plate nor the plume models can account for Hawaii, however, which appears to be unique when compared to other global phenomena, especially in its high buoyancy flux and long-lived persistence of active volcanism e.g. Sleep (1990).

It must be noted that 'plume deniers' are few and far between, and the presence of plumes is now generally accepted.

1.5 The thermal versus chemical plume

In addition to the uncertainty in the source depth is the question of whether the buoyant upwelling of lower mantle material is the result of thermal or chemical heterogeneity. Seismic data can only reveal the speed that a seismic wave is travelling through a medium; however there are many factors that can affect the velocity of a seismic wave including temperature, chemical composition, phase assemblage, and crystal orientation. Questions still remain over the extent to which buoyancy is the result of a thermal anomaly at the source of the plume, or the result of compositional heterogeneity at the CMB, upper mantle, or crust. It is important to note that the CMB, where the Hawaiian plume is thought to originate, is located 2800-2900 km below the surface of the Earth, while the region where the magma melts is significantly shallower, with estimates ranging from 200-400 km depth in the Earth for example from pressure sensitive mineral/melt partition coefficients (Putirka, 1999), or 150-90 km from seismic observations (Li

et al., 2000). This is a large range in potential pressures of melting that could have a significant impact on phase stability where melting is occurring, and therefore an impact on the chemistry of the parental magmas that feed Hawaii.

As previously stated, seismic studies have concluded that shear wave velocities are highly likely the result of positive thermal anomalies. Multiple studies have found excess mantle potential temperatures for hotspots when compared with ambient mantle conditions. For example, (Mckenzie and Bickle, 1988) calculated a potential temperature for MORB of 1280 °C and found that the composition of parental MOR magmas therefore have an MgO content of no more than 11 wt. %, whereas the MgO content of OIB was likely to be 17 wt. % as a result of an excess potential temperature of 1480 °C. Multiple authors (Mckenzie and Bickle, 1988, Putirka, 2005, Putirka et al., 2007) using flux calculations have also suggested mantle excess temperatures for plumes (Schilling, 1991). The heat source in this hypothesis is residual heat from the Earth's core. The melting point of iron-nickel alloy (Campbell, 2007), and the presence of the Earth's geodynamo indicates that the core must be hotter than surrounding mantle, and that it must have lost significant heat for a sustained period of time (Gubbins et al., 2003) in order to maintain core convection. The heat is transferred to the mantle via convection, forming a thermal boundary layer at the bottom of the mantle. This layer then becomes unstable and rises due to buoyancy (Davies, 2005), causing the upwelling of the material known as a plume.

The reduction in the shear wave velocity (by about 1.7%) and compressional wave velocity (by about 1%) observed for Hawaii using seismic tomography would require excess temperatures of more than 100 K in the upper mantle and more than 200 K in the lower mantle (Julian, 2004) Alternatively, if the effect is chemical in nature then anomalous material must be more buoyant in nature than the surrounding mantle to reproduce the slow seismic velocities.

1.6 LLSVP

LLSVP are Large, Low Seismic Velocity Provinces that sit above the CMB and have been suggested as a possible source for mantle plumes. Mineral physics experiments imply that variations in temperature, composition, and phase may be required to explain the presence of these provinces in the deep mantle, however it remains unclear the extent to which each of these variables plays a part in the formation of LLSVP and mantle plumes. Various mantle models have suggested that they may be thermal, chemical, or thermochemical in nature (Mulyukova et al., 2015).

Numerous seismic studies have noted the presence of LLSVP in the Earth's mantle beneath Africa and the Pacific Ocean at antipodal points of the globe (McNamara and Zhong, 2004, McNamara and Zhong, 2005, McNamara et al., 2010, Garnero and McNamara, 2008, Davies et

al., 2015), with the Pacific anomaly extending from the CMB up to approximately 400-500 km in the mantle, and the African anomaly extending up to 1000 km into the mantle. (McNamara and Zhong, 2005) have shown that Earth's subduction history has caused a NW-SE-trending pile of dense material to accumulate below the African plate, and a rounded pile to accumulate beneath the Pacific plate. Each anomaly is around 15,000 km across with sharp boundaries, and together they cover almost half of the CMB (Garnero and McNamara, 2008).

LLSVP are dense, long-lived, stable in their position, and may affect the location and geometry of flow in the deep mantle (Mulyukova et al., 2015). They may be the result of dense material being swept and accumulated into dune-like structures, where convecting mantle may flow from pile-tops, peaks or ridges of the LLSVP structure (McNamara and Zhong, 2005). If the dense LLSVP material is made up of ancient, subducted oceanic slab, then these structures are chemically very different to the surrounding mantle, and therefore the cause of LLSVP, and by association mantle plumes, may be chemical in nature.

A causal relationship between LLSVP structures and mantle plumes has been suggested, because plumes are found to disproportionately appear on the same two sides of the globe as the LLSVP, and OIB tend to be located above LLSVP edges after plume drift is accounted for. This may indicate that plumes are the result of edge-driven flow of mantle material that is directed upwards when it comes into contact with the LLSVP wall, where primordial mantle and subducted material may then be entrained into the upwelling plume (Thorne et al., 2004, Torsvik et al., 2006, Garnero and McNamara, 2008).

Further evidence for compositionally-driven mantle plumes is the presence of Ultra Low Velocity Zones (ULVZ) which sit at the CMB and have much smaller length scales (10 km thick to 100 km across) compared to LLSVP. The CMB is thought to be isothermal, which means that if ULVZ were caused by partial melting, they should occur globally, and not be sporadically distributed. Many CMB regions do not show any evidence of ULVZ which indicates a chemically different component, regardless of whether or not the ULVZ is partially molten (McNamara et al., 2010). These ULVZ may be a bi-product of core-mantle interactions, or dense remnants of ancient subducted material. ULVZ are correlated to the edges of LLSVP in terms of location, and so it is suggested that subduction-driven currents may sweep dense subducted oceanic crust towards upwelling regions at the perimeters of LLSVP below Africa and the Pacific (McNamara et al., 2010). A heterogeneous lower mantle was again suggested by (Ballmer et al., 2016) who have stated that secondary 'plumelets' may rise from the LLSVP roof and entrain basaltic material, while more long-lived primary plumes may originate from LLSVP margins and entrain small fractions of primordial material.

Van der Hilst and co-authors have further suggested that the CMB and D" layer are not isothermal, and that the regions below subducted slab may be much cooler (~3250° K) compared to the estimated temperature of the rest of the CMB (3950° K) (van der Hilst et al., 2007). The variation in temperatures may indicate a significantly thermally heterogeneous CMB, which may favour the formation of mantle plumes above only selected parts of the CMB.

In opposition to the theory that LLSVP may be chemical in origin, some observations suggest that they may be predominantly thermal in nature. One study has calculated that a thermal anomaly could account for the differences in shear wave velocity seen in these piles, and that statistically there is no correlation between the margins of LLSVP and the location of plume hotspots. In addition, it was concluded that plate tectonics and mantle convections can cause the arrangement of dense material in the mantle to form LLSVP. The authors do not advocate an isochemcial mantle; rather they suggest that the effect of chemical heterogeneity may be small, and that only ~3% of heterogeneous material can be accommodated in the lower mantle (Davies et al., 2012). Further to this, (Davies et al., 2015) found that a CMB estimated temperature of 4000 K combined with anelastic seismic sensitivity to temperature, means that purely thermal LLSVP can reconcile observed shear wave velocity anomalies and gradients. It has been suggested that chemical piles are not needed to reconcile seismic observations, and that if chemical piles were involved in deep mantle processes, the resulting seismic observations would over-predict deep-mantle anomaly amplitudes.

A number of geochemical studies have used the composition of olivine in OIB and MORB to infer that higher forsterite olivines found in OIB require higher mantle potential temperatures when compared to the lower forsterite MORB olivines. Putirka used olivine-liquid equilibria to infer excess mantle temperatures of Hawaii and Iceland of 250 °C and 165 °C respectively relative to MORB (Putirka, 2005).

An early study by (Schilling, 1991) calculated excess temperatures of mantle plumes compared to ambient mantle of 200 – 250 K, and up to 300 K for Hawaii. The difference is large because the model assumed that the entire buoyancy flux of the plume was thermal in origin, and therefore the excess T was directly proportional to the excess elevation of the overlying ridge. A later study by Farnetani used advection-diffusion equations to model mantle plume temperatures and has assumed that there is a chemically heterogeneous boundary layer at the CMB, which produces excess mantle temperatures of 300-350 °C (Farnetani, 1997). This was still much lower than the temperature calculated in the same study assuming no chemical boundary layer (~800 °C).

Olivine addition calculations have also been used to infer plume temperatures. Green and Falloon estimated parental magma compositions for MOR to be 13-16 wt. % MgO and >13 wt. % MgO for Hawaii (Green and Falloon, 2005). This resulted in estimated mantle potential temperatures of 1430 ºC and 1400 ºC for MORB and Hawaii respectively, suggesting that there is very little difference in the potential temperatures of MORB and Hawaiian lavas. This study also states that all intra-plate and hotspot magmatism is the result of subduction-driven mantle convection, and that there is no need to invoke an additional, independent convective process such as a thermal plume.

1.7 Compositional heterogeneity in mantle plumes

Despite the evidence for thermal and chemical heterogeneity at the CMB where the Hawaiian mantle plume is thought to originate, the fact remains that Hawaiian lavas and other OIB are very chemically heterogeneous over a wide range of scales compared to MORB. The preceding evidence has been mostly physical and structural, and while it is impossible to directly sample the deep mantle, plume material is able to be sampled through the chemical analysis of erupted basalts, glasses, phenocrysts, and xenoliths. The material erupted from plumes has been shown to differ in major element, trace element and isotopic compositions relative to MORB, and can also display large heterogeneities within a single volcano.

OIB are less depleted in incompatible elements than MORB, because they either originate from a less depleted lower part of the mantle, or they reflect a lesser degree of melting of the source material. OIB are more enriched in the high field strength elements, have a lower K/Ba ratio and are generally less enriched in Cr and Ni. Despite being more enriched than MORB in the highly incompatible trace elements, elements such as Al, Yb and Sc tend to be more depleted in OIB, possibly due to the presence of residual garnet in the mantle source (Hofmann, 2014). Relative to MORB, variation in OIB geochemistry is large, with a wide range in major elements, trace elements and isotopic signatures suggesting OIB tap into chemically heterogeneous parts of the mantle (Hofmann, 1997). The scale of this chemical heterogeneity remains unresolved, and many hypotheses exist. One states that the mantle is layered into a depleted, convecting upper mantle and a primitive, untapped lower mantle e.g. (Wasserburg and Depaolo, 1979). Others suggest there to be small scale 'plums' composed of subducted oceanic crust and sediments floating around in a 'pudding' mantle made up of residual material (Phipps Morgan and Morgan, 1999). More recently, isotopic studies have suggested that the lower mantle may be significantly more depleted than initially thought, consisting of the 'FOZO' isotopic signature, which is very similar to depleted MORB mantle (DMM) but with slightly more radiogenic strontium, lower radiogenic neodymium, significantly more radiogenic lead, and higher in ^{3}He. This signature is thought to be present in all deep mantle-sourced basalts (Hofmann, 2014).

Studies by Green and co-authors and Sobolev and co-authors have investigated the nature of chemical differences in plume material, and have suggested that mantle plumes are the result of compositional, buoyancy driven upwelling (Green et al., 2001, Sobolev et al., 2000). It was observed that many OIB have residual garnet trace element signatures, which has been used along with isotopic heterogeneity, as evidence of compositional heterogeneity at the source. In this model it is suggested that oceanic crust is subducted and transformed to eclogite at depth, which can be heated, become positively buoyant, and rise inside a plume conduit. The material will partially melt at low enough pressures due to the low melting point of eclogite relative to pyroxenite, and those melts will then react with surrounding mantle peridotite to form pyroxenite (Yaxley and Green, 1998, Rosenthal et al., 2014). Peridotite and pyroxenite may then be sampled in different proportions by the different Hawaiian volcanoes. The accumulation and entrainment of subducted oceanic sediments/crust/gabbro/lithosphere is the basis of many, if not most, geochemical studies which seek to investigate the source chemistry of Hawaiian volcanoes e.g. (Hofmann and White, 1982, Christensen and Hofmann, 1994, Bennett et al., 1996, Lassiter and Hauri, 1998, Norman and Garcia, 1999, Blichert-Toft et al., 1999, Sobolev et al., 2000, Huang and Frey, 2005, Herzberg, 2006, Pietruszka et al., 2012). These studies all suggest enrichment of the Hawaiian source with some subducted material, however the specifics pertaining to proportions of sediments, crust/metasomatized crust, or lower lithosphere vary from paper to paper depending on if the study is trying to reconcile the major element, trace element, or isotopic components of the samples analysed. Pb isotopes often suggest a sediment component, Sr, Nd, and Os isotopes suggest a crustal component, He isotopes imply a lower mantle signature, trace elements suggest the presence of garnet at the source, Sr suggests the involvement of subducted plagioclase in the form of gabbro, while Ni and major elements imply a pyroxene-rich source. Further detail on the presence, or absence, of recycled, subducted material will be presented in chapter 8.

As well as reaction of subducted material with ambient mantle to create a pyroxenite source, the higher volatile contents of subducted slabs may play an important role by inducing melting in the upper mantle. Examination of hotspot glasses in comparison to MORB suggests that some OIB, in particular Hawaii, may have greater dissolved volatile H_2O + CO_2 contents (Green, 2015). The interface of the upwelled eclogitic crust with surrounding mantle may provide a f_{H2O} redox contrast, and the higher concentrations of H, C, and O may reduce the liquidus temperature and induce melting and diapirism. This model does not require a deep source, and suggests that increased volatile contents of OIB basalts may be the cause of 'wetspot'-type magmatism (Green, 2015).

Hirschmann and co-authors have summarised H_2O contents in the upper mantle and found that MORB contain between 50-200 ppm, while the source of OIB may contain 300-1000 ppm (Hirschmann, 2006). Wallace has also confirmed that the source of Hawaii contains up to three times the amount of H_2O compared to MORB from analysis of basaltic glasses and melt inclusions from Kilauea (Wallace, 1998). The increased volatile contents of OIB must have implications for melting at the source, and may help to explain Hawaii's large magma volumes which are observed despite the large overburden pressures above the deep melt-zone compared to MORB.

As discussed by Dixon and Clague, the fact that OIB are more hydrous that MORB does not necessarily mean that the OIB source is more enriched in H_2O than the MORB source (Dixon and Clague, 2001). Because water is thought to behave as an incompatible element with D similar to that of the Ce ($La>H_2O\approx Ce>Nd$) (Michael, 1995), variation in water content between OIB and MORB or between the Kea and Loa trends within Hawaii may be the result of variations in degree of melting. Dixon and Clague suggest that if the ratio of H_2O/Ce remains constant between volcanoes, the variation in water is likely due to variable degrees of melting of the mantle, whereas if the ratio varies this could be the result of migration of a C+H+O fluid phase, mixing of source regions with different volatile contents, or shallow assimilation or degassing (Dixon and Clague, 2001). In their study, they conclude that Hawaii is wetter than MORB, but not more so relative to the other incompatible elements, indicating that general differences between MORB and Hawaii could be explained by degree of melting. They also vie in favour of the 'thermally zoned plume' hypothesis for Hawaii by demonstrating that the volcanoes nearest the plume centre contain the lowest amounts of water. In addition, they use the correlation of H_2O/Ce with radiogenic isotopes such as $^{206}Pb/^{204}Pb$ to infer that the Koolau component must contain well-dehydrated subducted oceanic crust + sedimentary cover.

Kovalenko and co-authors have compiled estimations of volatile content in various mantle sources including primitive mantle, depleted mantle, N-MORB, E-MORB, and an ultra-depleted source (Kovalenko et al., 2006). They show that the various mantle minerals contain increasing amounts of water in the order olivine (4ppm), opx and cpx (20 ppm), and garnet (44ppm). They also state that the average MORB composition cannot be formed through depletion of a primitive mantle composition via mantle melting, and that an enriched component must be added to account for the range in MORB composition. Kovalenko and co-authors suggest one such

They found that 75% of the lavas from Mauna Loa have H_2O/K_2O less than Kilauea's proposed parental magma (H_2O/K_2O = 1.3), and an estimate of 0.7 wt. % H_2O in

differentiated Kilauean magmas after the effects of degassing were taken into account according to the parental magma estimates by (Wallace and Anderson, 1998).

1.8 Crystallization and melting - effects on OIB chemistry

Significant chemical heterogeneity may exist in OIB due to shallow fractionation processes such as degree of melting, crystal fractionation, crystal accumulation, and chamber replenishment. In order to account for chemical variation in OIB as a result of source heterogeneity, it is first necessary to identify and quantify these other processes. A major controlling factor of the geochemistry of OIB is the cyclic patterns of a volcano's evolution; which may move through pre-shield, shield-building, post-shield, and rejuvenated stages e.g. (Moore and Clague, 1992). Each stage produces characteristic volcanism with differing melt fractions, lava chemistry, and physical properties. In the case of Hawaii, the major element composition changes so dramatically during the lifecycle of the volcano building that the basalts can cycle from alkalic to tholeiitic in composition, and back again. The pre-shield stage has yielded predominantly alkalic lavas, followed by voluminous amounts of tholeiitic lava during the shield-building stage, and then highly chemically variable, sporadic eruptions during the post-shield stage. Lavas from Iceland and Reunion are typically tholeiitic, whereas Tahiti and Tristan da Cunha are predominantly alkalic. Tholeiitic lavas are the less prevalent type in OIB globally (though constitute the volumetric majority of Hawaiian magmas) and are more similar to MORB in composition except that they have higher K_2O, TiO_2 and P_2O and lower Al_2O_3. They have higher silica, lower $Na_2O + K_2O$, and have a relatively narrow range of forsterite compositions (Fo_{70-90}) (Winter, 2010). Alkali lavas are more common at ocean islands because the melted material has encountered a thicker, colder lithospheric lid and melted at deeper levels, leading to lower degrees of melting compared to MORB (Hofmann, 2014). These alkalic lavas have higher $Na_2O + K_2O$ and are more heterogeneous with a broader range of major element and forsterite compositions (Fo_{35-90}). They have a similar REE trend to tholeiitic OIB only shifted towards being relatively more enriched (higher concentrations of the REE).

The degree of melting can affect the ratios of the incompatible and rare earth elements (REE) by fractionating the heavy REE (HREE) and moderately incompatibles from the light REE (LREE) and highly incompatible elements. In addition, the processes of crystal fractionation and crystal accumulation can have a dramatic impact on the major and trace element budget of tholeiitic OIB through the addition and subtraction of olivine. These processes will therefore be explored in more detail in the discussion section of this thesis.

Aside from the natural variation in lavas as a result of eruption cyclicity and shallow fractionation processes, there is chemical heterogeneity between ocean islands globally. Some alkali lavas from different ocean islands differ beyond fractional crystallization when compared to one another, for example tephritic alkali OIB will have much greater alkali/silica ratios; others will be trachytic and rhyolitic in composition due to differences in the silica and alkali content of the respective source (Winter, 2010). Further to this, radiogenic isotopes which remain unfractionated by shallow processes show a wide range of signatures in Hawaiian lavas e.g. (Weis et al., 2011).

1.9 Radiogenic isotopic signatures in OIB and MORB

Radiogenic isotopes are used to infer differences in the source of oceanic basalts because they are not fractionated in shallow magma chamber processes. Significant correlations between isotopic ratios and major element concentrations have been observed at Hawaii, e.g. (Jackson et al., 2012), implying that some major element variation may be the result of source heterogeneity or coupled variations in source composition and conditions of melting.

Radiogenic isotope pairs are almost identical in mass (for example ^{143}Nd and ^{144}Nd) and as such their ratios are not fractionated by melting or crystallization processes, and are proposed to reflect source composition (Rollinson, 1993). Four isotopic end members (enriched mantle 1 (EM1), enriched mantle 2 (EM2), depleted MORB mantle (DMM), and high ^{238}U/^{204}Pb (HIMU)) have been determined to account for 97.5% of the variance in 570 oceanic basalts (Zindler et al., 1982, Hart and Dunn, 1992) (Figure 1.4). Later, additional isotopic systems He and Hf became increasingly used and this information was added to the global Ocean Floor Basalt (OFB) data set. The original four end-member model was then revised to include at least five mantle 'types' to account for variation in OFB globally. The fifth was called 'PREMA' (Prevalent Mantle) composition, which was an intermediary, or 'common component' between DMM, EM and HIMU. This type was used to describe the compositions of many ocean islands including Hawaii and Iceland, which are both characterized by relatively high ^{3}He/^{4}He ratios (Zindler and Hart, 1986). A similar intermediary was coined 'FOZO' (Focal Zone) by Hart and co-authors (Hart et al., 1992), where it is noted that FOZO is rarely sampled in its pure form, but is thought to represent entrained material from the CMB.

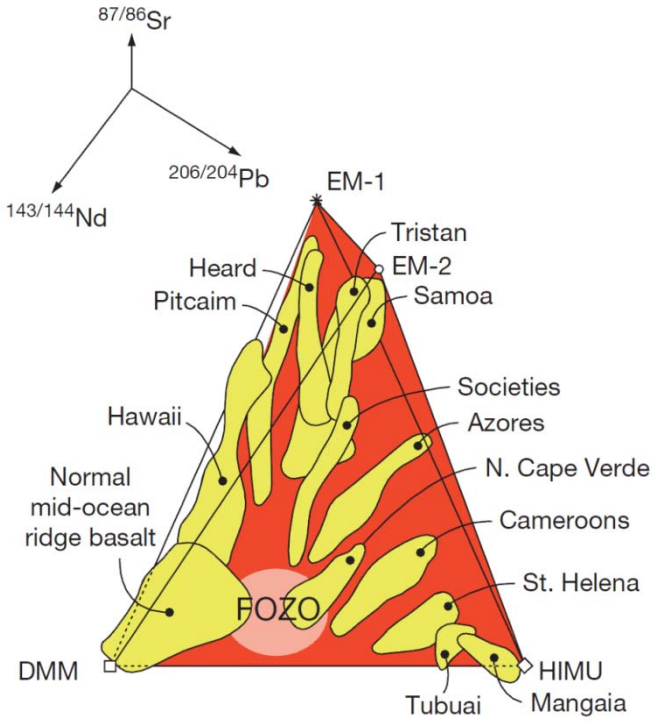

Figure 1.4 3D representation of the five isotopic components that account for isotopic heterogeneity in ocean floor basalts. FOZO appears to be a common component in many (Hart et al., 1992;Hofmann, 2014;Hofmann, 2014).

These end members represent specific isotopic ratios of $^{143}Nd/^{144}Nd$, $^{87}Sr/^{86}Sr$ and $^{206}Pb/^{204}Pb$ which change with time as a result of the decay of ^{147}Sm, ^{87}Rb, and ^{238}U respectively. As the decay rate of these systems is very well constrained, if the age of the sample is known then the isotopic ratios can be used as an indicator of source composition. The mantle ratios are altered as a result of removal of crust from the mantle, and the recycling of crust and sediments back into the mantle. For example, the rate of increase of $^{87}Sr/^{86}Sr$ in the mantle will be slowed by the extraction of crust due to the highly incompatible nature of Rb compared to Sr leading to a decrease in the $^{87}Rb/^{86}Sr$ ratio. Conversely, the growth of ^{143}Nd to ^{144}Nd will be accelerated in the mantle due to the incompatibility of Nd compared to Sm, resulting in a higher $^{147}Sm/^{144}Nd$ ratio in the depleted mantle. When geologically interpreted, this allows us to determine the time integrated degree of depletion of the source, or the amount and type of recycled material in the source. The EM1, EM2, DMM and HIMU endmembers may represent recycled metasomatized mantle or mantle with recycled lower oceanic crust, recycled upper continental crust, depleted MORB mantle, and recycled oceanic crust respectively.

1.10 He, Re, and Os isotope evidence for deep mantle plumes

The $^{3}He/^{4}He$ isotopic system has been used to support the deep-sourced mantle plume theory, as some lavas have He ratios that suggest input from the lower mantle (Hahm et al., 2009). It is thought that the D" layer contains elevated $^{3}He/^{4}He$ which is imparted from the core or from primitive, un-degassed mantle. It has been suggested that small additions of liquid are infiltrating the mantle via capillary action at the CMB (Brandon and Walker, 2005) and injecting it with a distinct isotopic signature. This is consistent with $^{187}Os/^{186}Os$ isotope systematics and high nickel concentrations in olivine (Macpherson et al., 1998), but is contradicted by the PGE, copper, and cobalt concentrations of olivine (Sobolev et al., 2007) and lead ratios (Shirey and Walker, 1998), which do not appear to reflect any significant core input. He isotopic ratios are not consistent with a simple four end-member system because none of the end-members have the high $^{3}He/^{4}He$ ratios that are present in some OIB such as Hawaii, Reunion and Iceland (Hart et al., 1992). This isotope system is not yet routinely used due to concerns that other processes such as crush release of radiogenic ^{4}He in the olivine lattice and melt inclusions or crustal contamination by amphibolite and granulite facies basement rocks may affect the ratios (Stuart et al., 2003).

Re-Os isotopes have also been applied to oceanic basalts as a method of investigating source e.g. (Hauri and Kurz, 1997, Bennett et al., 2002, Alard et al., 2005, Harvey et al., 2006, Ireland et al., 2011), and the uses of the system are broadening. Both elements are chalcophile, however Re is a transition metal, while Os is a Platinum Group Element (PGE). Both behave relatively compatibly in the mantle, however Re is less compatible than Os and as such the two are fractionated during processes such as mantle melting. OIB have higher $^{187}Os/^{188}Os$ than MORB (Shirey and Walker, 1998). This cannot be explained by simply adding a recycled component to DMM, and as such is further evidence of a deep, radiogenic Os-rich source for mantle plumes. The radiogenic Os may come from the infiltration of core into the lower mantle with which it reacts and is entrained into an upwelling plume (Humayun et al., 2004). Although Re is generally less compatible than Os, it does not behave consistently in the same way that Os does, meaning there is no consistent gradation of Re contents as you move from high degree tholeiitic melts to low degree alkali melts. There is evidently still much to learn about the way Re and Os partition during mantle melting, and what controls sulphides, garnet, and clinopyroxene might have on partition coefficients (Shirey and Walker, 1998). In addition, Re can be lost as a volatile species during eruption of subaerial lavas, which can further complicate attempts to evaluate source compositions e.g., (Norman et al., 2004).

1.11 Hawaii – a double-tracked volcanic chain

Hawaii is an OIB of particular interest in trying to explain the origins of mantle plumes because any plume model will have to account for the two parallel geochemical trends known as the Kea and Loa trends, which separate the northeast and southwest volcanoes in terms of major elements, trace elements, and isotopic signatures. There have been many hypotheses about why this bilateral symmetry exists and many attempts to resolve it in the context of mantle plume theory e.g. (Weis et al., 2011, Ballmer et al., 2011, Hofmann and Farnetani, 2013, Frey et al., 2016). As discussed further in the Geological Context section of this thesis, the most prominent theories involve either a concentrically zoned plume in which a thermal gradient exists between the centre and periphery of the conduit, or a bilaterally zoned plume where two distinct chemical sides of the conduit are preserved form the CMB to the erupting volcanoes at the surface. (Jones et al., 2016) have determined using computational models that it is not possible to preserve this chemical differentiation during the plume's ascent through the mantle if LLSVP structures are thermo-chemical in nature. Instead, they have shown it is only possible to preserve the spatial distribution of chemical heterogeneity in the plume if LLSVP are thermal in nature and chemical heterogeneities behave passively. The authors note it is most likely to be recycled oceanic crust which causes the chemical signature of the Hawaiian plume, and that the dense recycled material is most likely to be sampled by the centre of the conduit due to the higher temperatures in the centre. A follow-up study (Jones et al., 2017) has determined that the likely cause of the parallel trends is a combination of plate tectonic motion and variable depths of melting at the plume source. In this model, the tilting of the plume beneath Hawaii causes lateral separation of high- and low-pressure melt regions, which are separated during the azimuthal change of plate motion. Jones and co-authors suggest that over the last 10 Ma there has been a progressively larger northward component in the direction of the plate motion above Hawaii, with the most rapid migration occurring over the last 4.2 Ma – a period of time coinciding with the emergence of double-track volcanoes across the Pacific plate. The Loa side of this track is formed via shallow pyroxenite melts which are the product of eclogite reacting with mantle peridotite, while the Kea side is the product of deep peridotite melting. This model does not require the preservation of a bilaterally zoned plume conduit from the CMB, and is supported by observations of multiple double track volcanoes elsewhere on the Pacific plate, an observation which few other studies - aside from Hieronymus and Bercovici (Hieronymus and Bercovici, 1999) - have addressed. The chemical assumptions made by Jones and co-authors however, are difficult to reconcile with major and trace element evidence, which will be later discussed in this thesis.

1.12 Pyroxenite or peridotite source for Hawaii?

Hawaii has long been recognised to contain a residual garnet signature due to the buffering of the HREE relative to the highly variable and high-overall concentrations of LREE e.g. (Rhodes, 2016). This signature has been found in volcanoes on both sides of the Kea and Loa trends. The same study has determined that the chemistry of Hawaiian shield lavas can be explained if garnet peridotite melt is then reacted with harzburgite. This would explain the buffering of Al_2O_3 and HREE and simultaneously high silica contents of lavas erupted from Hawaii. The trace elements and Al content of Hawaiian lavas has been used as evidence for garnet in the source, but the debate as to the extent to which pyroxene in the source plays a part remains ongoing. It is clear that the chemistry of OIB is very different to MORB (thought to be derived from passive melting of peridotite), and so the source chemistry must be different as well as the conditions and extent of melting and residual mineralogy. Many have used the major element chemistry of Hawaii to invoke pyroxenite in the source of many of the Hawaiian volcanoes because of the high SiO_2, Al_2O_3, Na_2O, and low FeO and CaO. The high silica content particularly has been used to infer that the melt must be produced by an olivine-free source (Sobolev et al., 2005). This high silica component is seen most strongly in Ko'olau but also to a lesser extent in Mauna Loa and Kahoolawe. It is noted that variations in major elements in MORB have been explained by invoking variable pressure of melting, however this explanation is has been cast as unsatisfactory for OIB because of the correlation between major elements and isotopes (Hauri, 1996). Hauri has also suggested that only the low Si end of the Hawaiian spectrum (Loihi) and the Kea-trend volcanoes could be explained by the partial melting of mantle peridotite. In that study, three end-members were identified; these were the Ko'olau component, Loihi component, and the Kea component. The Ko'olau component is characterised by high Si, Na, and K, low Fe, Mg, Ca, and Ti, while having high Sr and low Nd isotopic compositions. The Kea and Loihi trends are the opposite of this, though they differ from one another mostly in terms of He isotopes and somewhat in terms of Sr isotopes.

The high Ni and Si content has been used to infer the presence of eclogite and therefore subsequent pyroxenite in the Hawaiian mantle source e.g. (Wang and Gaetani, 2008), with Sobolev and co-authors proposing a completely olivine-free source for Hawaii (Sobolev et al., 2007). Meanwhile, Lambart and co-authors have stated that low Si and high Fe and CaO/Al_2O_3 ratios may be evidence of pyroxenite in the source, while the high Si and low Ti contents of some lithologies cannot distinguish peridotite sources from pyroxenite sources, and rather that they are determined by carbonate or amphibole in the source (Lambart et al., 2013).

Hawaii has also been shown to contain elevated iron compared to other OIB, which has been suggested as further evidence for a pyroxenite source of Hawaii. Humayun and co-authors

suggest that Fe from the core may explain the high Fe/Mn ratios in Hawaii, suggesting that the most tenable explanation for increased Fe content in Hawaiian lavas is FeO metasomatism at the CMB (Humayun et al., 2004). This would explain the ultra-dense ULVZ parts of the lower mantle, and is consistent with Os isotope evidence.

Herzberg and Asimow (Herzberg and Asimow, 2008), and later Rhodes and co-authors (Rhodes et al., 2012) have used the Ca content at a given MgO content to distinguish peridotite-source from pyroxenite-source lavas, and have shown that many Hawaiian lavas fall into the pyroxenite-source field. Rhodes however, has used lavas from Mauna Kea to show that not all lavas with high Ni contents necessarily have correspondingly high Si and low Ca contents, as this pyroxenite-source model predicts.

The major element contents of Mauna Loa and Kilauea are compared using data from this study as well as Kilauea + Mauna Loa literature data, and discussed in light of the preceding information in the discussion section of this thesis. Any model proposed must account for the chemical differences between OIB and MORB, and must account for Hawaii's distinct isotopic signature and the isotopic differences in the Kea and Loa trends.

It is evident that there are many dichotomies and uncertainties that exist relating to the nature of Hawaii's geochemistry. One of these is whether the Hawaiian mantle plume is thermal or chemical in nature. This is often discussed from either a deep-mantle seismic point of view or a shallow basaltic geochemical view point. It is often not explicitly explained that the dense seismic structures at the CMB are ~2800 km away from where the material actually melts to produce the lava which is eventually erupted at the surface. It seems likely that the CMB is not isothermal, but it also seems possible that it is not isochemical either. Certainly, there must be significant chemical heterogeneity where the material is melting to produce the array of isotopic signatures in the eventual lava, but it also seems likely that there is a potential temperature difference between OIB and MORB mantle sources given the differences in pressure at which melting occurs between these two regimes. Other interesting dichotomies which exist are the peridotite source versus the pyroxenite source question and the bilaterally versus concentrically zoned plume question. The results from this thesis will be discussed in relation to some of these interesting conundrums, with the ultimate aim of determining the extent to which whole-rock geochemistry can be used to infer melting and crystallization mechanisms, and source lithology of Mauna Loa volcano, Hawaii.

2 Geological Context

The samples analysed in this study are loose material dredged from the submarine southwestern flank of Mauna Loa volcano on the Big Island of Hawaii. This chapter will explain the sample dredge localities and the geological setting of the samples, as well as cover some of the broader geology of the island of Hawaii, and discuss the sampling strategy. It will briefly cover some of the eruption history, structures, and geochemistry of the volcanoes on the island, as well as the history, structures, and geochemistry more specifically of Mauna Loa, and then briefly cover previous work conducted on samples from this study.

2.1 Hawaiian-Emperor Seamount Chain

The Hawaiian-Emperor chain is composed of a line of volcanic seamounts situated in the centre of the Pacific plate. The Hawaiian Island Chain, along with the Emperor Chain, is thought to be the surface expression of a dynamic reservoir of low density material erupting at the surface of the Earth due to buoyancy (Sleep, 1990). It has been proposed that this material is the tail of a large, long-lived mantle plume that may have a deep source close to the core-mantle boundary (CMB) (Campbell and Griffiths, 1990). Considering the volume of magma the tail has produced, the head of such a plume would have been immense in volume when it erupted, perhaps producing an oceanic plateau, although the surface expression of this has not yet been recognised.

The Hawaiian and Emperor chains contain more than 129 individual volcanoes with calculated volume estimates of 336.3 x 10^3 km^3 for the Emperor chain and 744.9 x 10^3 km^3 for the Hawaiian chain resulting in a combined volume of over 1 000 000 km^3 (Bargar and Jackson, 1974), and a total area of 1 200 000 km^2 (Clague and Dalrymple, 1987). The chain is the archetypal example of a hotspot track, formed as the Pacific plate moves over the plume below it. The chain ends just past the Big Island of Hawaii at Loihi (the youngest seamount) and tracks northwest until it reaches the Kure Atoll, where it sharply changes to a northerly direction, and stretches back to the Aleutian Trench off Alaska. The Kure Atoll separates the 'Hawaiian' from the 'Emperor' segments of the volcanic chain. The chain is age progressive, ranging from age zero at the most southerly volcanoes, to 75-85 Ma at the most northerly and the combined distance of the Hawaiian-Emperor seamount chain is over 6,000 km (Clague and Dalrymple, 1989).

2.1.1 Emperor seamounts

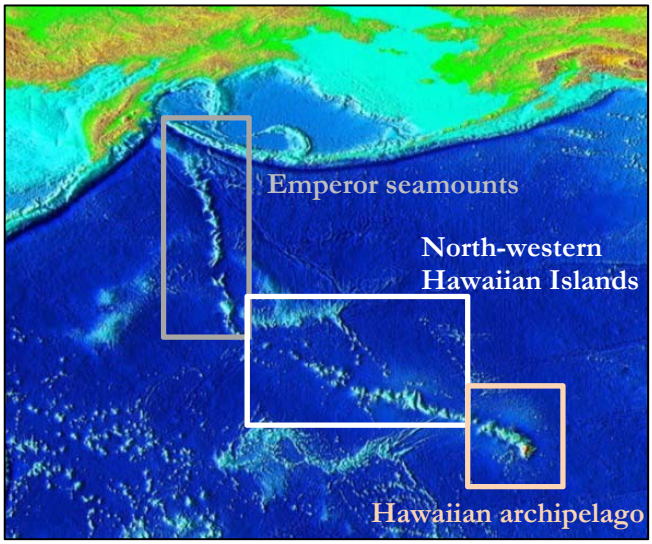

Figure 2.1 Bathymetry of the Hawaiian-Emperor chain in the context of the northern Pacific. The Emperor Chain (the northern-most segment of the chain) enclosed in the in red box (image courtesy of NOAA (NOAA, 2004)).

The Emperor Seamount chain is the oldest part of the hotspot track (Figure 2.1), with its youngest seamount being (Abbott Seamount) being 42 million years old. The Abbott seamount is located near the bend, which denotes the cut-off between the Hawaiian chain and the Emperor chain, and progressively increases in age in a northerly direction up to the Meiji seamount (85 Ma) near the Aleutian Trench. All of the older (>85 Ma) volcanoes extending beyond the Kure Atoll are now subducted. The wide variety of rock types in the Emperor volcanoes ranging from tholeiitic and alkalic basalts to silica-undersaturated lavas such as basanite, and nephelinite, suggests that these volcanoes cycled through similar evolutionary stages as the younger Hawaiian volcanoes (as discussed in geological background section of this thesis), producing both tholeiitic and alkali lavas with large temporal ranges in trace element and isotopic composition (Regelous et al., 2003). Regelous and co-authors suggest that the Emperor Seamount volcanoes have lower $^{87}Sr/^{86}Sr$ and higher $^{143}Nd/^{144}Nd$ compared with the Hawaiian Chain volcanoes. The oldest of the Emperor Seamount volcanoes Meiji, and Detroit, have low concentrations of incompatible elements and depleted trace element and Sr isotope ratios. This is particularly true of Detroit which has compositions similar to that of Pacific N-MORB (Regelous et al., 2003). After this time there appears to be a systematic increase in the $^{87}Sr/^{86}Sr$, up until 42 Ma where the ratio appears to stabilize again.

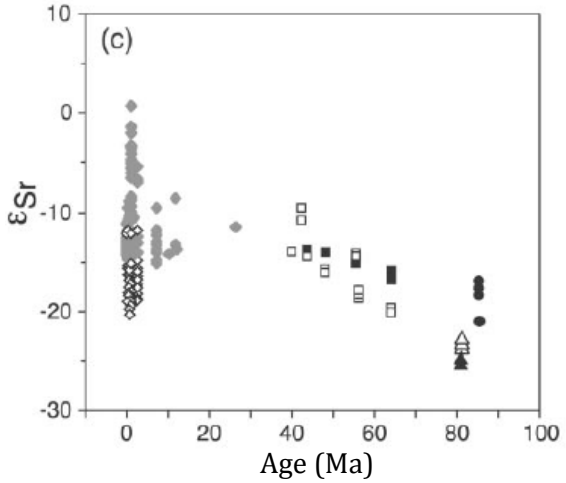

Figure 2.2 Progression of Sr isotopic signature versus age of seamounts (from Regelous *et al.*, 2003).

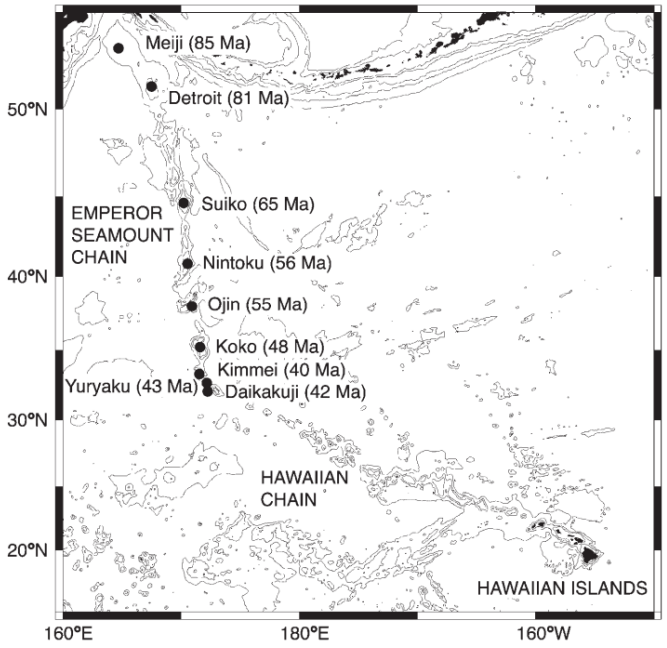

Figure 2.3 Emperor Seamount chain with age progression of seamounts (from Regelous *et al.*, 2003).

2.1.2 North-western Hawaiian Islands

The next part of the Hawaiian chain contains the north western Hawaiian Islands. These range in age from Nihoa (approximately 7 million years old) and extend up to Kure Atoll at the bend (approximately 40 million years old). Most of these volcanoes are now seamount coral atolls, as the processes of erosion have reduced the volcanic edifices to submarine elevations, and those above sea level are islands only because the coral atolls are emergent. The bend demarking the

start of the Hawaiian Island Chain at the Kure Atoll is commonly thought to reflect a change in the motion of the Pacific plate from a northerly to north-westerly direction approximately 50 million years ago. The change in motion was explained by Sharp and Clague by the collision of the Indian subcontinent into Eurasia, which caused the initiation of subduction and consequent arc-magmatism in the Izu-Bonin-Mariana arc system to the west of Hawaii (Sharp and Clague, 2006).

2.1.3 Hawaiian Archipelago

The youngest segment of the chain (Figure 2.1), making up the US state of Hawaii, currently contains the most active and productive volcanoes on Earth. These are Loihi, which is currently situated over the plume (last major seismic activity 1996), Kilauea (currently erupting), Mauna Loa (last erupted 1984), and Hualalai (last erupted 1801) (USGS, 2015), as well as the dormant Mauna Kea and extinct Kohala volcanoes. The other islands of the Hawaiian Archipelago are Maui, Lana'i, Moloka'i, O'ahu, Ka'ula, Ni'ihau, and Kaua'i, which contain the few volcanoes that still remain above sea level. The youngest of the volcanoes in this first segment of the chain (Lō'ihi) dates back approximately 400 000 years (Garcia et al., 2006) and has not yet breached the ocean surface, while the oldest (Kaua'i) may be up to 5.14 million years old (McDougall, 1979). In this segment of the Hawaiian-Emperor chain, the volcanoes begin to separate into the 'Kea' and 'Loa' geochemical trends (discussed briefly in chapter 1) around 3 million years ago (Jones et al., 2017). The volcanoes diverge from Penguin bank and West Moloka'i and continue in two geographically distinct chains including the youngest volcanoes in the chain.

2.2 The Big Island

The largest island in the Hawaiian Archipelago, aptly named the 'Big Island', contains the five volcanoes Kilauea, Mauna Loa, Hualalai, Mauna Kea, and Kohala, in order of youngest to oldest (Figure 2.5). It is the newest part of the Hawaiian-Emperor chain, and the youngest volcano Kilauea, has been erupting almost continuously since 1983.

2.2.1 Kilauea

The majority of Kilauea's erupted volume has come from the volcano's east and south-west rift zone, however in 2008 the Halema'uma'u vent opened on the volcano's summit. The majority of the surface area is covered in lavas erupted between 250 000 - 500 000 years ago. Approximately 90% of Kilauea's surface is younger than 1,100 years old, and consists of mostly tube- and surface-fed pahoehoe, with small amounts of a'a (Holcomb, 1987). Kilauea is located on the south-east side of the island of Hawaii and is part of the Kea trend, resulting in an overall more depleted signature in terms of Sr and Nd isotopes, less range in Sr and Nd isotopic composition, and a wider range in the lead isotopic signature (Weis et al., 2011).

2.2.2 Mauna Kea and Kohala

The other two volcanoes in the Kea track are Mauna Kea and Kohala. Mauna Kea (meaning 'White Mountain') is the highest volcano on the island of Hawaii (4,205 m elevation), and as a result is capped in snow. Although it is in the 'advanced post-shield stage' of its eruptive life, Mauna Kea last erupted about 4 500 years ago (USGS, 2018). It is thought that the volcano's shield stage lasted about 400 000 years, where it erupted 90% of its total mass, whilst the oldest parts of the volcano are thought to be over 700 000 years old in total (Frey et al., 1990). Kohala, the oldest Kea-trend volcano on the island, consists of two main flow types: shield-stage tholeiitic basalts known as the Pololu Volcanics, and the overlying alkalic lavas known as the Hawi Volcanics. The oldest Kohala lavas found are over 700 000 years old (Clague and Dalrymple, 1987); however the volcano itself is thought to be at least 1 million years old.

2.2.3 Hualālai

Aside from Mauna Loa, the only other Loa-track volcano on the Big Island is Hualalai, which most recently erupted in 1801 while 95% of its surface is Holocene in age (Moore et al., 1987). It is the Big Islands third-most active volcano after Mauna Loa and Kilauea, and has a calculated total erupted volume of 12.4 x 10^3 km^3 (Bargar and Jackson, 1974). The volcano has passed its main shield-building stage, and associated tholeiitic basalts are no longer exposed subaerially, but have been dredged from the sea-floor (Ruben, 2018a). The only currently exposed lavas are post-shield alkalic basalts, with rare occurrences of trachyte present, continuing the trend of Hawaiian volcanoes that are predominantly composed of tholeiitic basalt, with a thin cap of alkalic lava (Moore et al., 1987).

2.2.4 Geochemical context of the Hawaiian Islands

The Hawaiian volcanoes produce Ocean Island Basalts (OIB), which are known to be more heterogeneous in composition compared to mid-ocean ridge basalts (MORB) in terms of major and trace elements. Hawaiian volcanoes are geochemically heterogeneous, and the chemistry may be controlled by multiple, complex processes and factors. The chemistry is dependent on the life-cycle of the volcano, which is determined by the volume of magma being delivered to the magma chamber. Eaton and Murata (Eaton and Murata, 1960) speculated that during the tholeiitic eruption phase, only olivine had the chance to crystallise before melts were erupted, producing high-silica melts. However when the eruption volumes begin to wane late in the volcano's lifetime the magma can sit in magma chambers for a longer period of time and crystallize cpx, changing the chemical composition of the magma. More recently it has been suggested that the change in chemistry during the alkali phase is the result of a decrease in the degree of partial melting of the mantle source during late stages of the volcano's life (Frey et al., 1990). Stages range from pre- shield and shield building, to post-shield and rejuvenated

magmatism. Each type is represented in the variably-aged volcanoes in the Hawaiian Chain, with some volcanoes demonstrating the indicative chemistry of multiple stages throughout its lifetime e.g. (Macdonald et al., 1970, Peterson and Moore, 1987).

The major, trace, and isotopic chemistry of the lava reflects the stage of life the volcano is in. The pre-shield stage is dominated by submarine eruptions of alkali basalts and basanites, followed by more tholeiitic lavas. The youngest volcano (still submarine) in the Hawaiian chain, Loihi, is currently in this stage. The shield-building stage is dominated by large volumes (up to 99% of the total volume) of tholeiitic basalt, which travel down slope of the growing volcano to form a very gradual gradient in the slope, and the characteristic 'shield' shaped topography of volcanoes such as Kilauea and Mauna Loa. This could be because the plume is directly underneath the volcano where the highest degrees of melting can occur, it may be sampling the hottest part of the plume, or it may be sampling the part with the greatest buoyancy flux. The third stage is called the post-shield stage. Eruptions become less frequent, more violent, and basalts can have a wider range of composition, from hawaiite to trachyte (Winter, 2010). Kohala, Mauna Kea and Hualalai are all in the post-shield stage. After this the volcano will become mostly dormant erupting only rejuvenated stage lavas occasionally, and will eventually succumb to erosion in the post-erosional stage e.g. Diamond Head on Ko'olau. It is thought that most of the chemical variation throughout the lifecycle of the volcano is the result of variation in the rate at which heat is supplied to the mantle and therefore the degree of melting due to the position of the volcano above the plume (Clague and Sherrod, 2014).

Kilauea Volcano displays a wider range in Pb isotopic systematics compared to Mauna Loa and other Loa-track volcanoes, and has been suggested to contain lower SiO_2 and Na_2O contents, and higher TiO_2, FeO, CaO, K_2O, and P_2O_5 contents for a given value of MgO compared to Loa-track volcanoes e.g. (Frey et al., 2016, Wilkinson and Hensel, 1988). Rhodes and co-authors have also documented the trace element differences between Kilauea and Mauna Loa. They demonstrate that Kilauea has lower Zr/Nb and Zr/Y, and higher La/Yb than Mauna Loa volcano at a given MgO content (Rhodes et al., 1989). The trace element differences have also been outlined by Frey and co-authors who have shown that Kea trend volcanoes have higher HREE relative to LREE compared to Loa trend volcanoes, higher Th/La, and lower La/Nb, Sr/Nd, and Zr/Nb (Frey et al., 2016).

The lavas of Mauna Kea display chemical characteristics similar to Kilauea, in that they have a higher $^{143}Nd/^{144}Nd$ and $^{206}Pb/^{204}Pb$ and lower $^{87}Sr/^{86}Sr$ isotopic signatures, higher La/Nb, and lower Th/La and Zr/Nb when compared to Loa trend volcanoes (Frey et al., 2016).

Hualalai volcano displays higher $^{87}Sr/^{86}Sr$ and lower $^{206}Pb/^{204}Pb$ than Mauna Loa volcano (both are Loa-trend volcanoes), though both display significant temporal and spatial isotopic variation throughout their eruption history (Yamasaki et al., 2009). The comparison has been used by Yamasaki and co-authors to suggest that the Hualalai source may contain heterogeneous 'streaks' which present themselves in a cyclic fashion, similar to Mauna Loa.

As alluded to above, the Hawaiian-Emperor chain displays significant variability in a number of the key isotopic systems, which vary both spatially and temporally. The isotopic variability can also be looked at through the lens of the 'mantle zoo' (Stracke et al., 2005), where OIB have been categorized in terms of the mantle end members PREMA/FOZO, EM1, EM2, DMM, and HIMU. The Hawaiian isotopic composition is closest to 'PREMA', or Prevalent Mantle' composition, which is a mixture of DMM, HIMU, and EM mantle compositions with or without BSE (Bulk Silicate Earth) (Zindler and Hart, 1986). The PREMA field coincides with many ocean islands, depleted continental basalts, and many intra-oceanic island arcs. The Hawaiian OIB isotopic composition has also been called the Focal Zone aka 'FOZO' (Hart and Dunn, 1992) because it is thought that this signature is a mixing component which is present in all deep mantle reservoirs.

The isotopic range within the Hawaiian system is large, with studies recording samples that range between DMM and Bulk Silicate Earth (and EM1) in terms of Sr and Nd isotopes, but that stretch towards higher $^{206}Pb/^{204}Pb$, bringing them out of line with a purely DMM and BSE signature (Roden et al., 1994). The cause of this isotopic composition may be the result of varying levels of input from a DMM component, a BSE component, and a component with more radiogenic lead: potentially from recycled oceanic crust which has lost alkalis and lead during subduction, or has been infiltrated with low degree partial melts (Hofmann and White, 1982, Sun and McDonough, 1989). Hawaii also fits between the EM1 component, which is said to come from either recycled delaminated sub-continental lithosphere e.g. (Frey et al., 2016) and pelagic sediment or lower continental crust e.g. (Pietruszka et al., 2012); however in plots by Zindler and Hart it can be seen that having BSE as one end-member better fits the majority of OIB including Hawaii (Zindler and Hart, 1986). Although BSE is an appropriate end-member, Hofmann has noted that the constant but non-primitive ratios of Nb/U and Ce/Pb in OIB and MORB preclude BSE as a direct source component and suggest a slightly more depleted signature (Hofmann, 1988).

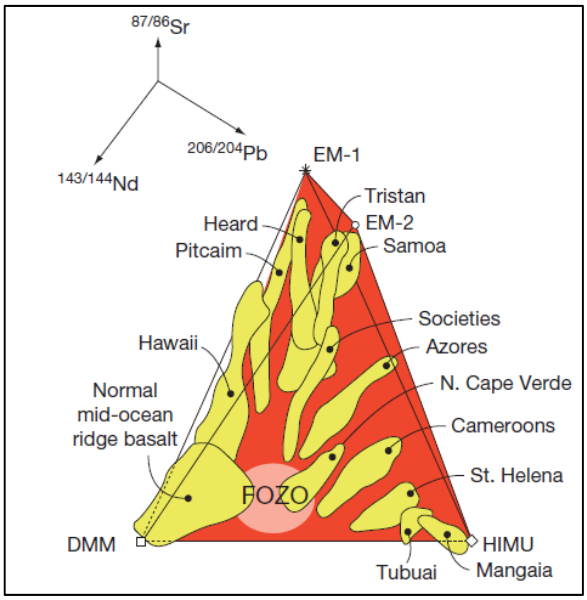

Figure 2.4 Isotopic compositions of some OIB (Hofmann, 2014).

The nature of how these significant heterogeneities are formed remains a topic of debate. In short, it is clear that the isotopic heterogeneities within the plume occur across the very large scale as well as the very small scale spatially, and they also vary greatly vertically within the plume, meaning that the isotopic signature changes with time in both the short- and long-term. Some studies have concluded that the plume may be concentrically zoned, which could imply that a melting gradient exists going from highest degree of melting in the centre to lowest degree of melting in the periphery e.g. (DePaolo et al., 2001, Hauri, 1996). Such a model assumes that the compositions of erupted lavas are determined by the position of individual volcanoes over a zoned plume. In this scenario the heterogeneities within the plume would be preferentially sampled based on melting point. The packages of the plume with the highest melting point would only be sampled at the very centre of the plume. In addition to this it is possible that ambient mantle might become entrained into the periphery of the plume conduit, adding to the concentric geochemical gradient.

In contrast, there is also substantial evidence that the plume might be bilaterally zoned because of the emergence of two parallel isotopic trends that separate the volcanoes in the north-east from the volcanoes in the south-west (Hofmann and Farnetani, 2013, Weis et al., 2011, Xu et al., 2014). These two distinct trends are known as the Kea and Loa trends respectively, and vary particularly in their lead and neodymium isotopic ratios (Abouchami et al., 2005). Why the isotopic chemistry differs so much in a chain of volcanoes thought to be sourced from a single plume remains unclear, as does how such a plume may be physically separated into two such distinct trends. The Kea trend appears to display an overall more depleted signature in Nd and

Sr isotopic compositions (reflecting time integrated low Rb/Sr and high Sm/Nd), indicating it is closer to the DMM end-member. The Loa trend appears more enriched in Nd and Sr isotopic signatures and trends towards the EM1 end-member. Loa also has significantly higher $^{208}Pb/^{206}Pb$ when compared to the Kea trend, a signature which is postulated to be the result of pelagic sediment addition containing high Th/U (Roden et al., 1994).

It is important to note that the discussion relating to the Kea and Loa trends refers only to the emergent Hawaiian island volcanoes. Further back in time at East and West Molokai, this dichotomy breaks down and no bilateral distinctions can be seen (Frey et al., 2016).

2.3 Mauna Loa

Mauna Loa is the largest and most productive volcano on the island of Hawaii, as well as the most productive volcano on Earth, with a total volume of over 40 000 km^3 e.g. (Bargar and Jackson, 1974, Lockwood and Lipman, 1987). It is also Earth's tallest mountain, rising 9 km from the sea floor (Rhodes and Lockwood, 1995). Most of the sampled basalts that have erupted from Mauna Loa are younger than 30,000 years old, with the most recent, eruption occurring in 1984. The lava from the giant volcano covers more than 50% of the Big Island, and 90% of this material is lava that is younger than 4,000 years old (Moore and Clague, 1992). K-Ar ages suggest the oldest lavas analysed are up to 200,000 years old, however it is thought the volcano may have emerged above sea level approximately 300,000 years ago (Moore and Clague, 1992). Rhodes has emphasized that the ages for Mauna Loa submarine lavas are poorly constrained, though the samples on the western flank are probably contemporary with subaerial lavas and quite young (<36 ka) (Rhodes, 2015). Similarly, those from the submarine radial vents are estimated to be quite young (<47 ka) based on flow morphology and Mn coatings on lavas (Wanless et al., 2006).

2.3.1 Mauna Loa Eruptive History

The eruptive history of Mauna Loa has been well recorded back to the year 1843, however before this, historical accounts are sparse because early Polynesian settlers who arrived at Hawaii 1500 years ago preserved no known record of Mauna Loa's eruptive history, and neither did European settlers between 1778 and 1843 (Lockwood and Lipman, 1987). The eruptions since 1843 comprise 13% of the total area of Mauna Loa, and originate at various points along the linear rift-zones, flowing downhill on both the north-west and south-east flanks of the volcano (Lockwood and Lipman, 1987).

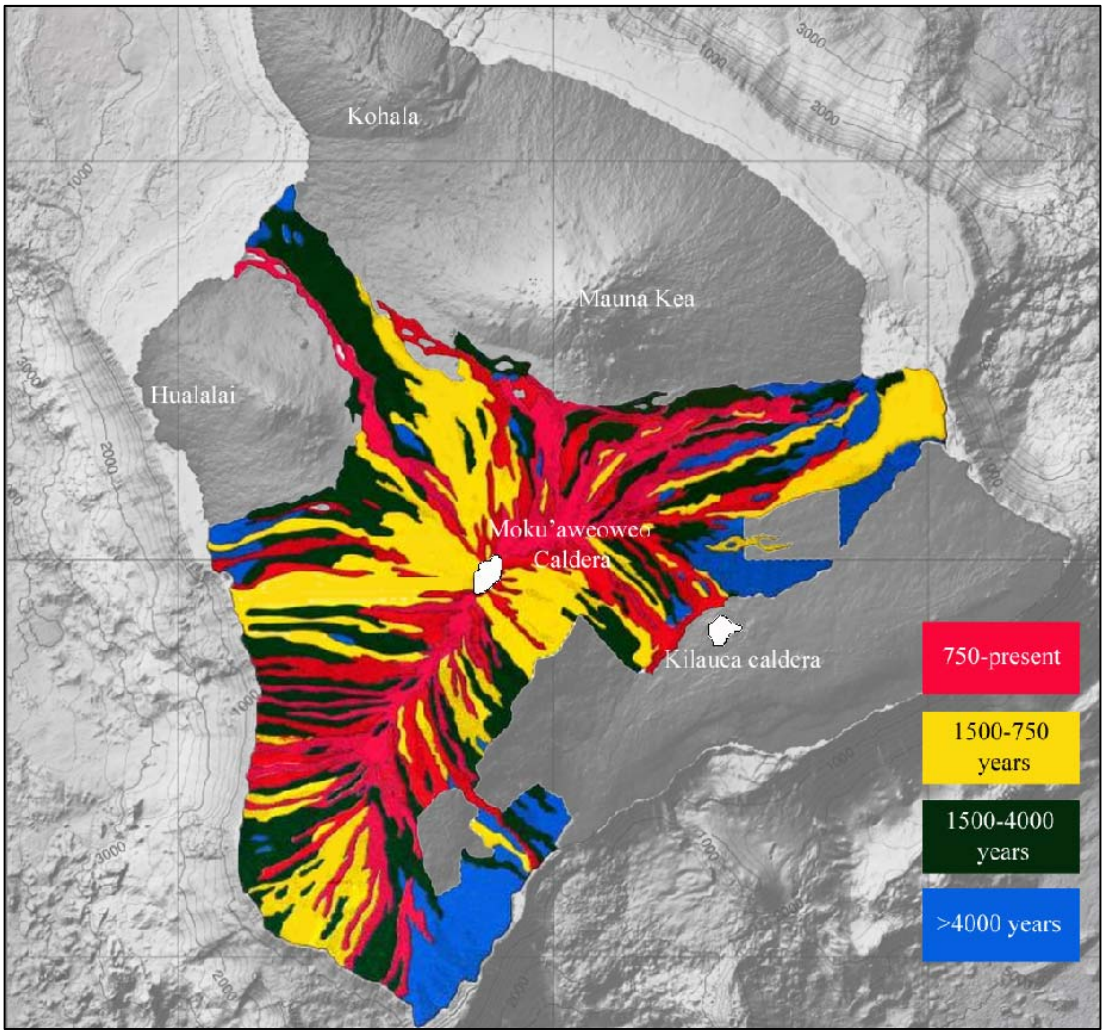

Figure 2.5 Historical lava flow on Mauna Loa volcano, in years before present (modified from Lockwood and Lipman, 1987 and U.S.G.S. bathymetric data, 2006.)

Since 1832 there have been 39 eruptions occurring every 3.6 years on average (Barnard, 1995), with majority originating at the Moku'aweoweo summit caldera and progressing down the flanks of the volcano via lateral rift-zone propagation. The oldest eruption of Mauna Loa in written history occurred in 1780, not long after Captain Cook's visit to the islands. The 1868 eruption caused one of the largest earthquakes in Hawaii's recorded history, and one of the largest flows ever seen. The 1868 eruption is one of two historical eruptions to produce 'picritic' lava, the other occurring in 1852. Rhodes has documented that these picritic eruptions contain high MgO (over 22 wt. %), though he notes that the picrites do not reflect melt compositions and that they have accumulated varying amounts of olivine which is too low in Mg to be in equilibrium with the whole-rock (Rhodes, 1995). Since 1877, the eruption rate per year has more than halved (Lockwood and Lipman, 1987).

Two large eruptions occurred in 1855 and 1881 which threatened the city of Hilo on the eastern side of the island. During these eruptions lobes of lava reached within a few kilometres and 70m of the town respectively. The 1950's brought further activity, this time predominately originating from the south-west rift-zone. In a summary by Prof. Michael Rhodes, there were seven large flows recorded pouring down the south-west side of the mountain, with three of them reaching the sea (Ruben, 2018b). During the 1950 eruption historical accounts are hazy because of the low lying cloud that obscured the view of the summit, and the fact that helicopters were not in use for observation. Of note is the fact that the chemistry of this 1950 eruption is compositionally heterogeneous, however the MgO contents of the erupted lava lies within a relatively narrow range of 7-10 wt. %. It was also noted that the MgO contents appeared to be higher in lavas the further down-rift they were. Following the 1950 eruption, Mauna Loa remained quiet for 24 years until it next erupted (Lockwood and Lipman, 1987).

The most recent eruption of Mauna Loa volcano occurred in 1984 and lasted 22 days, producing remarkably chemically homogeneous lava (Rhodes, 1988). The eruption started at the summit in Moku'aweoweo crater and then extended to the south-west rift zone. It then migrated to the north-east rift, where it remained for 21 days (Ruben, 2018b).

2.3.2 Structure of Mauna Loa

Mauna Loa means 'Long Mountain', a fitting name that was given due to the linear arrangement of the subaerial eruptions from the north-east to the south-west rift zones. The subaerially exposed combined length of these rift zones is 120 km (USGS Mauna Loa), however they are separated by the Moku'aweoweo Summit Caldera, a 3 x 5 km collapsed caldera which is situated in the centre of the volcano (Lockwood and Lipman, 1987) (Figure 2.6). The historical eruptions are either summit eruptions, where activity is restricted to the immediate vicinity of Moku'aweoweo, or flank eruptions, which invariably begin at the summit but then the majority of the erupted material comes from lower altitude vents (Lockwood and Lipman, 1987). Almost half of summit-based historical eruptions have been followed by voluminous flank eruptions.

Submarine Mauna Loa and Kilauea lavas are generally draped in younger lavas, though it has been noted that those erupted from Mauna Loa's south-west rift zone are relatively free of young lavas, and it is thought that the age of lavas there must be older than the oldest exposed subaerial lavas (greater than 100,000-200,000 years) (Garcia et al., 1995). Garcia and co-authors note that attempts to date submarine lavas have been unsuccessful because of their relatively low radiogenic argon content, but they estimate an approximate age of 100,000 to 300,000 years based on extrapolation of the subaerial lava ages.

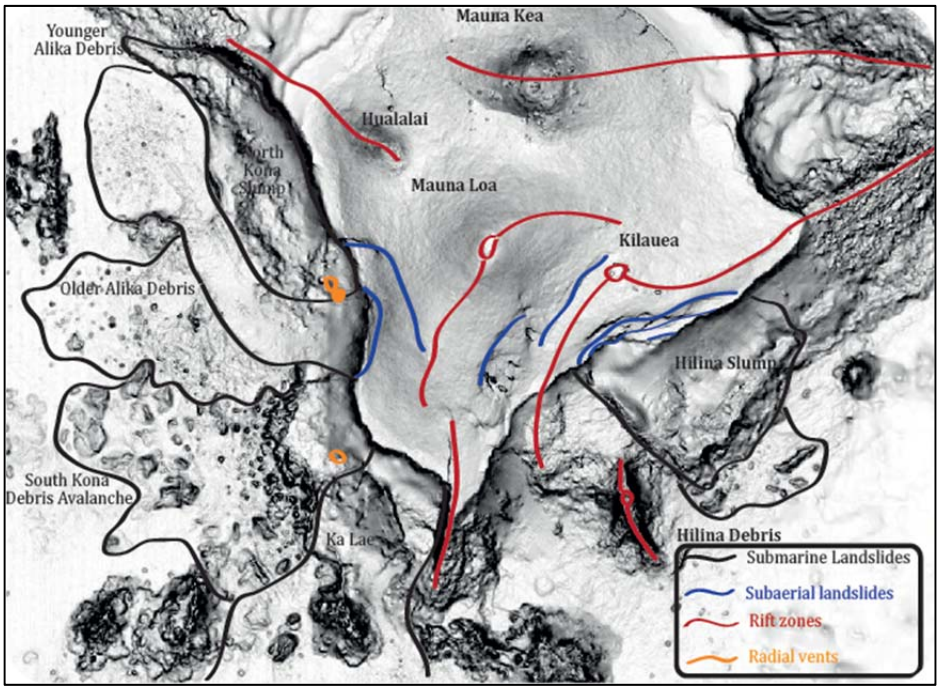

Figure 2.6 Rift zones on the island of Hawaii highlighted in red, with circular calderas marked, in addition to landslides (blue) and vents (yellow). Modified from (Lipman and Coombs, 2006) and (Moore and Chadwick, 1995).

The samples in this study were collected in 1999 during the final voyage of the *Moana Wave,* a specialised research vessel owned and operated by the University of Hawaii. The voyage dredged samples from approximately 30 locations (Figure 2.7) on the south-west flank of submarine Mauna Loa. The aim was to collect pristine picritic tholeiites which were minimally weathered or altered by sea water. It was intended that submarine lavas may sample a deeper and more primitive part of Mauna Loa's magma chamber (Garcia and Hulsebosch, 1995) because picritic eruptions have been found in higher abundance on the volcano's flanks (44 % of the suite from Garcia and co-authors contain >15% total olivine), and the forsterite contents of olivine from submarine lavas was found to be higher than in olivines from those that were erupted subaerially. For these reasons, it was speculated that extensive sampling of these submarine lavas would be ideal for investigating primitive magmas which have undergone minimal olivine fractionation.

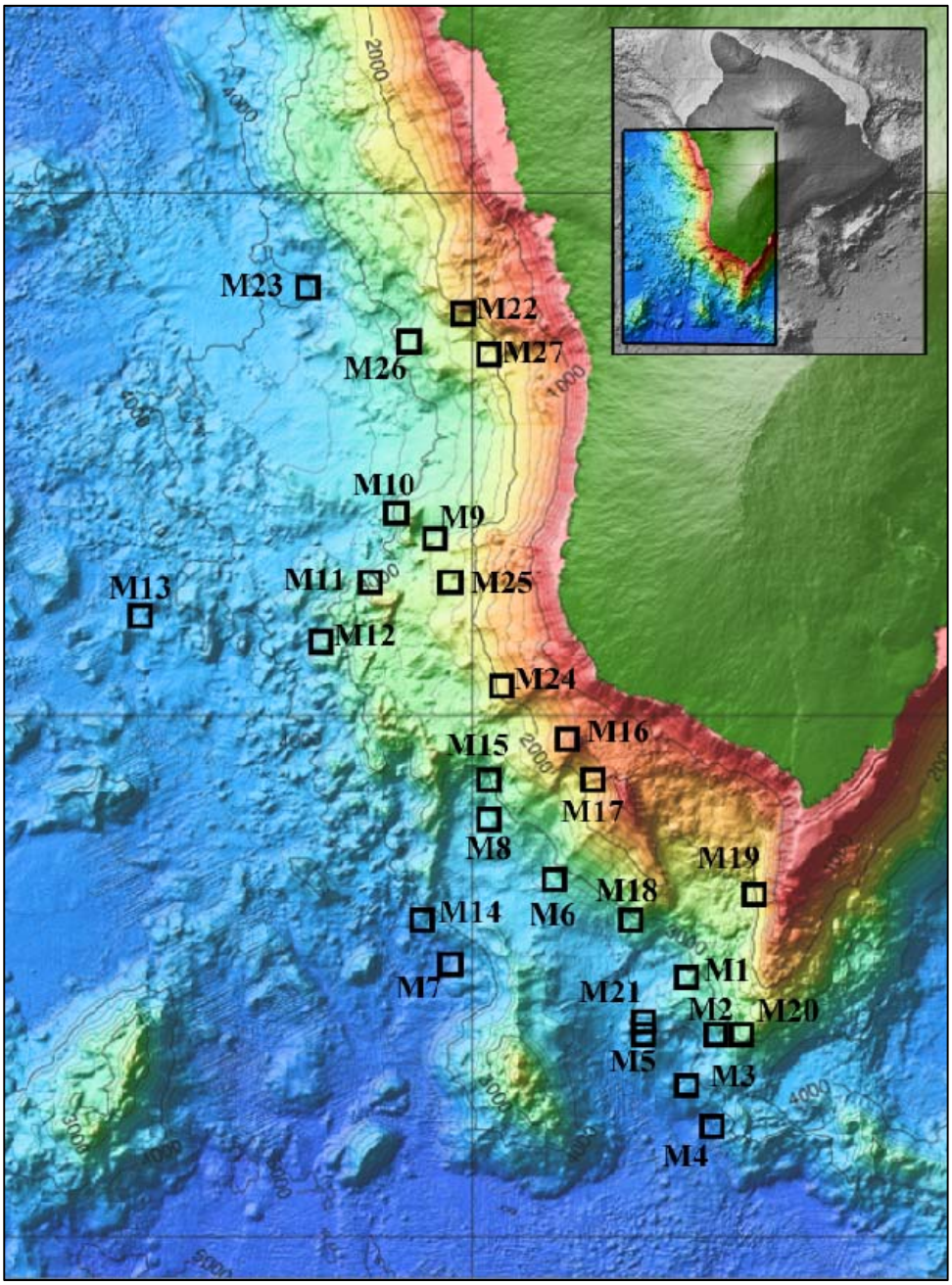

Figure 2.7 Sample dredge site locations (image modified from U.S.G.S. bathymetric image, 2006).

The samples were further divided into four dredge-type localities (radial vents, rift zone, slope, and landslide) (Figure 2.8). It must be noted that although a sample may have been dredged from near a radial vent or the rift zone, we cannot be sure if the lavas were erupted locally or have been carried to their dredge location. The origins of landslide and slope samples may be even less well constrained, and may include lavas from the underlying Hualalai or overlying Kilauea.

Radial vents are young cones that post-date the large landslides that occurred in the same region (Davis et al 2003- volatiles in glasses). Lockwood and Lipman recorded 66 vents (Lockwood and Lipman 1897), though Wanless and co-authors suggest that the number is closer to 44 because some are not oriented radially to the summit caldera (Wanless et al 2006- submarine radial vents). Wanless and co-authors subsequently discovered 9 new vents during their research, bringing their estimated total to 54. These vents may be related to faults, such as the Kealakekuka fault and slump structures (Davis et al., 2003), while Rubin has suggested that radial dykes may propagate when no further magma can be injected into the rift zones, leading to pressure build up (Rubin 1990- a comparison of rift zone tectonics). Wanless and co-authors further determined that the radial vent lavas span a wide range of ages, with some erupting in 1877, while others are estimated to be ~47,000 years old.

The southwest rift zone extends 65 km subaerially and 35 km below the sea level to a depth of ~500m. At the Kahuku scarp, the rift zone begins to bend and is submerged from that point on. The lavas from the Kahuku scarp are not draped in younger lavas, making lavas from this rift-zone ideal for studying a wide range in lava ages (Garcia et al., 1995). Garcia and co-authors note that the lavas from the southwest rift vary dramatically in modal olivine (<2 to ~47 vol. %), and some contain between 1 – 4 % modal plagioclase and augite. Garcia and co-authors speculated that only dense, olivine rich magmas would enter the rift zones, and would bypass the summit magma chamber, while more buoyant, evolved magma would continue to the summit. Davis and co-authors found that unlike the radial vent lavas of Mauna Loa, many rift zone glasses are un-degassed or only partially degassed, with a positive correlation of S concentration with increasing depth (Davis et al., 2003).

Davis and co-authors have outlined that the landslide samples are from two landslide events; the South Kona landslide (Moore et al., 1989) and a younger Ka Lae landslide (Moore et al., 1995) which contained up to 20 different lithologies. These included vesicular and oxidized lavas, sedimentary breccias, and rare pillow lavas.

The 'slope' samples are from various locations on the submarine flanks of Mauna Loa. All of the sample dredge localities have been marked in Figure 2.8.

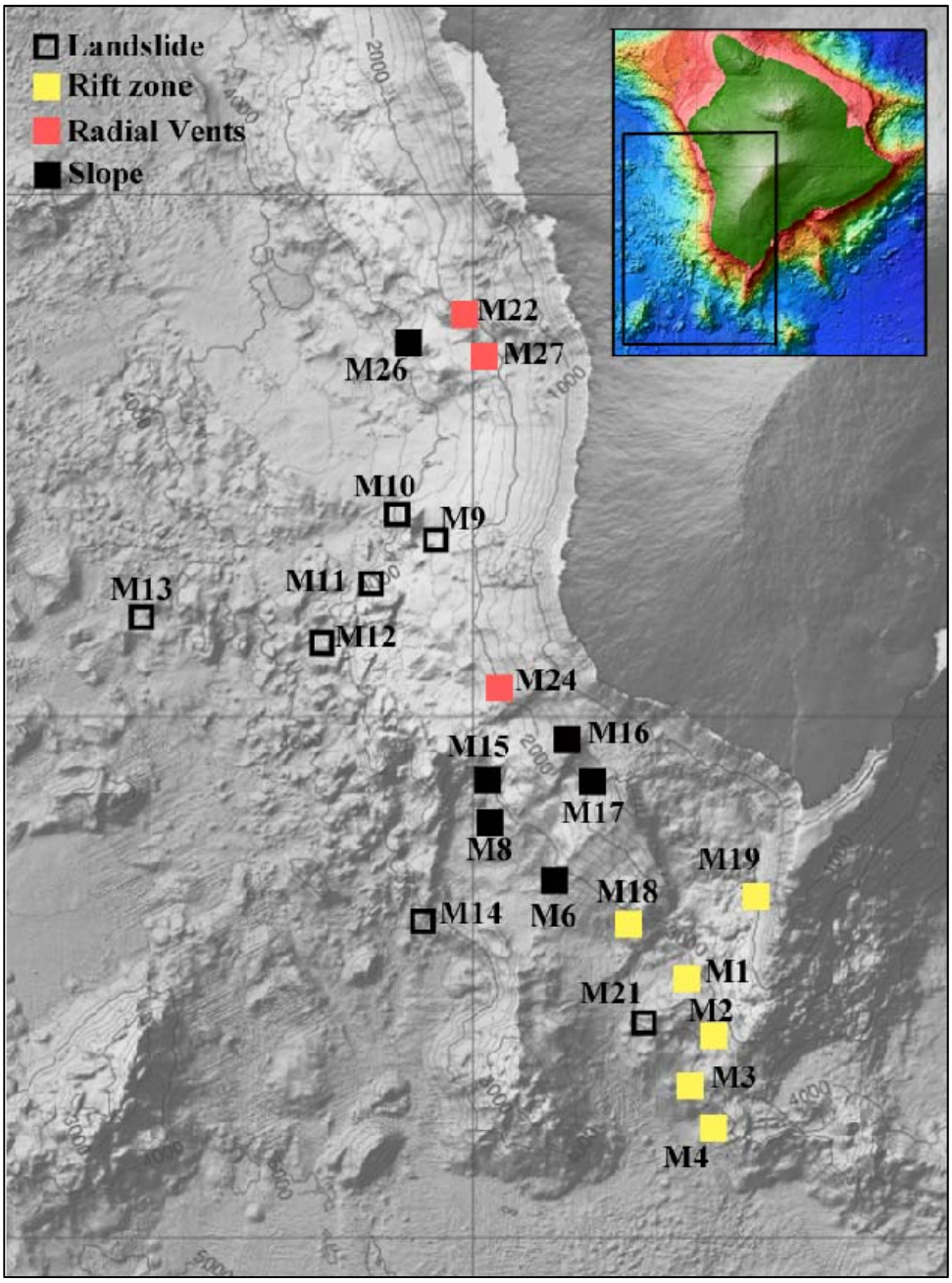

Figure 2.8 Locations of sample types: radial vents, rift zone, slope, and landslide (modified from U.S.G.S. bathymetric image, 2006).

2.3.3 Geochemistry of Mauna Loa

Detailed investigation into the geochemistry of Mauna Loa increased in the late 80's after the volcano's most recent eruption, with studies aiming to characterize the volcano spatially and temporally in terms of major elements, trace elements and isotopic signatures. Mauna Loa volcano displays an overall enriched trace element signature when compared to primitive mantle, with the highly incompatible and LREE reaching 10-fold enrichment (Hofmann and

Jochum, 1996). Conversely, they display a significantly depleted HREE signature, thought to be due to the presence of residual garnet in the source e.g. (Hofmann and Jochum, 1996). The possible suggestions for the source of Mauna Loa magmas are vast and variable, many involving a recycled crustal component with variable contributions of gabbro, plagioclase, oceanic crustal basalt, pelagic sediment, water, and CO_2 e.g. (Sobolev et al., 2000, Farnetani and Hofmann, 2010, Blichert-Toft et al., 1999, Green, 2015). In addition to this the contribution of ambient mantle is debated, with the amount, level of depletion, and pyroxenite/garnet content widely debated e.g. (Rhodes, 2016, Matzen et al., 2017, Sobolev et al., 2005).

The geochemistry of Mauna Loa differs significantly from the other volcanoes in the chain, even from the very proximal Kilauea. This is significant because Mauna Loa and Kilauea are analogous volcanoes in that they are both in the shield building stage of their volcanic lives, they are very similar in age, and they are spatially very close. In fact, Kilauea sits on top of Mauna Loa's south-east flank. Because Kilauea is a Kea-track volcano, whereas Mauna Loa is a Loa-track volcano, comparisons between the two are useful because they can reveal detailed differences in the chemistry of the Kea and Loa trends which control much of the chemistry of the Hawaiian Islands.

There has been continued debate pertaining to whether the conduits suppling magma to Kilauea and Mauna Loa are interconnected, or if the two volcanoes are supplied by separate parental magmas. It seems that the periodicity of eruptions from Kilauea and Mauna Loa do not appear to be random, with periods of activity in one corresponding to periods of quiescence in the other (Klein, 1982, Miklius and Cervelli, 2003), which might suggest that the volcanoes are competing for magma from a common source. More recent studies have backed this up: lavas dated between 250-1400 AD were found to bridge the 'chemical divide' between Mauna Loa and Kilauea, most notably in terms of Pb isotopes (Marske et al., 2007).

Distinct differences in trace and major elements, and isotopes, however, suggest the existence of two separate mantle sources for Kilauea and Mauna Loa, which produced magmas that may have been mixed subsequently during invasion of Kilauea by Mauna Loa's shallow plumbing system (Rhodes et al., 1989). Mauna Loa is more enriched isotopically than Kilauea, with higher $^{87}Sr/^{86}Sr$, lower $^{143}Nd/^{144}Nd$, and more variability in both ratios e.g. (Weis et al., 2011). Conversely Mauna Loa has less variability in Pb isotope ratios compared to Kilauea, with higher overall $^{206}Pb/^{204}Pb$, and lower $^{208}Pb/^{204}Pb$. Mauna Loa is also documented to have higher SiO_2 than Kilauea, but lower TiO_2, CaO, and K_2O (Frey and Rhodes, 1993), and lower LREE at a given MgO content compared to Kilauea e.g. (Frey et al., 2016).

As is evident from this brief summary, however, the majority of our knowledge of Hawaiian volcanism comes from observations made on subaerially erupted lava (Rhodes and Vollinger, 2005, Rhodes et al., 1989, Davis et al., 2003, Rhodes and Vollinger, 2004). Much of this extensive subaerial sampling occurred during the Hawaii Scientific Drilling Project (HSDP), where over 4600m of core was drilled out over 15 years, and was then geochemically analysed by an international team of more than 40 scientists (DePaolo et al., 2003). This sampling bias is potentially significant, because for every eruption that occurs subaerially there is thought to be equivalent volumes of submarine volcanic activity (Lockwood and Lipman, 1987) which have been largely overlooked, and the better exposure of the north-west flank relative to the south-east has also precluded representative sampling. The sampling bias means that a large fraction of Mauna Loa's eruptions remain chemically uncharacterised, and it is therefore unclear if there are any systematic differences in the chemistry and therefore differences in subaerial versus submarine plumbing systems.

Two studies were conducted in 2005/06 on submarine samples from the south-west flank of Mauna Loa, collected by the ROV Jason 2 – a robotic vehicle tethered to a ship which can collect images and samples from the sea floor. The first (Wanless et al., 2005) presented major and trace element analyses of 26 whole rock samples, and 15 glasses taken from two radial vent sites. Wanless and co-authors were the first to document alkali basalts at Mauna Loa, an occurrence which is a key distinguishing feature between the subaerial and submarine lavas. The presence of these alkali basalts near submarine radial vents may indicate that these magmas have bypassed the primary conduit that supplies the tholeiitic Mauna Loa basalts. In a model by Garcia and co-authors, submarine-erupted lavas from distal parts of the rift-zone or vents may bypass the primary volcanic conduits which supply the subaerial caldera due to density stratification of olivine-rich magmas (Garcia et al., 1995).

It was concluded by Wanless and co-authors that the lavas coming from both vents were alkalic and therefore could signify the transition of Mauna Loa from shield-building to post-shield volcano. Wanless and co-authors neatly summarised the current hypotheses which explains the transition from alkalic lava production during pre-shield, to tholeiitic lavas during the shield-building stage, and then back to alkalic lavas during the post-shield stage. The hypothesis states that variation in degree of melting will cause tholeiitic lavas to have a different concentration of Si, Ti, alkalis, and a lower proportion of LREE to HREE (e.g. La/Yb) because they are produced by a higher degree of melting in comparison to alkalic lavas. Alkalic lavas lie on the opposite side of a thermal divide in the cpx-olivine-nepheline field, compared to tholeiites which are typically silica-oversaturated and lie within the cpx-olivine-quartz field. In addition to this, the Sc/Zr and CaO/Al_2O_3 ratios of the alkalic lavas were found to be lower in the alkalic lavas

in comparison to the tholeiitic at a given MgO contents due to clinopyroxene fractionation (Wanless et al., 2005). MELTS modelling of the alkalic samples presented by Wanless and co-authors confirms pyroxene fractionation, with orthopyroxene followed by clinopyroxene being the dominant liquidus phases at pressures >0.4 GPa. A further distinction between the subaerially- versus submarine-erupted lavas is the concentration of volatiles that remain after eruption. It has been documented that subaerial lavas may be more degassed than submarine samples (Davis et al., 2003) due to the increased pressures that occur with increasing water depth. This was somewhat confirmed by Dixon and co-authors who compared volatile element concentrations of submarine lavas from Kilauea's Puna Ridge to subaerially erupted lavas from the same volcano (Dixon et al., 1991). Dixon and co-authors showed that submarine lavas from Kilauea were likely the result of mixing of degassed magmas with less degassed magmas, followed by further degassing upon eruption on the sea floor. They found a correlation between dissolved CO_2 and eruption depths, but not with H_2O, and concluded that only wholly submerged volcanoes (like Loihi) will retain the un-degassed end-member while volcanoes that have breached sea level will become relatively depleted in volatiles.

The samples we present in this study are an important addition to previously existing data sets because they add to the lesser investigated set of submarine samples which will enable chemical differences between submarine and subaerial lavas to be compared in greater detail. In addition, they cover a wide range of MgO contents from 5-28 wt. % MgO and appear to be genetically related by fractionation processes.

2.4 Previous work on samples from this study

Some previous work has been conducted on a sub-sample of the lavas from this study, which have investigated the major elements, trace elements, and volatile content of glasses, as well as isotopic chemistry of the whole rock samples. These studies are summarised below.

Davis and co-authors analysed 114 glasses from submarine pillow lavas, 23 subaerial basalts, and some olivine-hosted glass inclusions from the south-west rift zone and western flank of Mauna Loa (Davis et al., 2003). The study analysed major elements and volatile contents including sulphur, chlorine, fluorine, water, and carbon dioxide. A main conclusion of this study was that most of the vent and submarine pillows lavas have relatively low S and Cl concentrations, despite being erupted at great depths. This is not what would be expected according to a previous study which has shown that the depth of water for volatiles to remain in the lava upon eruption at Hawaii is 1000m below sea level (Moore, 1970). It was concluded that these lavas must be subaerially erupted lavas that were transported to great ocean depths via landslides. Conversely, unlike the radial vent lavas of Mauna Loa, many rift zone glasses are un-degassed or

only partially degassed, with a positive correlation of S concentration with increasing depth (Davis et al., 2003).

In addition to this, Davis and Co-authors found that the MgO-normalized H_2O concentrations for Mauna Loa were shown to be significantly lower when compared to Kilauea. This may mean that Kilauea has a source composition that is higher in H_2O compared to Mauna Loa which may contain dehydrated recycled crust, or that Kilauea lavas formed by lower degrees of melting than Mauna Loa as H_2O behaves like an incompatible element (Dixon et al., 1991, Dixon and Clague, 2001).

Davis and co-authors also analysed the major element compositions of olivine-hosted glass inclusions in addition to the volatile composition (Davis et al., 2003). Basaltic glasses are considered representative of melt composition because they remain unfractionated by crystallization after eruption due to rapid quenching (though fractional crystallization can occur before eruption). The melt inclusions with the highest MgO contained up to 11.4 wt. %, however it was determined that these may have been affected by re-equilibration of the glass inclusion with the host olivine. The samples that did not appear to be affected by re-equilibration had MgO contents of up to 9.8 wt. % MgO. Davis and co-authors then modelled a potential chemical fractionating path using the MELTS program and concluded that the highest MgO glasses (7-10 wt. %) were suitable parental magmas for the majority of glasses examined, and that crystal fractionation is the dominant process affecting Mauna Loa magmas.

3 Methods

This chapter summarises the analytical methods used for this study to measure trace element concentrations by solution aspiration ICP-MS and Sr-Nd isotopic compositions by thermal ionisation mass spectrometry.

3.1 XRF analysis of major and trace elements

All major and trace element XRF analysis was conducted courtesy of Prof. J. Michael Rhodes and Mr. Michael Vollinger at the University of Massachusetts, and kindly provided by them for this study on a collaborative basis. Details of the XRF major element and trace element analytical procedures are described in Rhodes (1996), while the typical reproducibility of major and trace element concentrations during repeat analysis of a Hawaiian basalt reference material was published by Rhodes and Vollinger (Rhodes, 1996, Rhodes and Vollinger, 2004). Variation in trace element concentrations analysed by XRF versus ICP-MS can be seen in Figure 3.2, XRF major element concentrations are provided in Chapter 4, and the trace element concentrations can be found in the appendix to this thesis. The rock crushing method used by Rhodes used a tungsten carbide (WC) mill which has resulted in Ta contamination in some samples. WC milling has been associated with the possible contamination of the HFSE Nb, Ta, Zr, Hf, and Ti, though it has been found that only Ta is affected by contamination to a significant degree (Roser et al., 2003).

3.2 Procedure for solution ICPMS (Inductively Coupled Plasma Mass Spectrometry) and determination of trace element concentrations.

All work was carried out in HEPA filtered clean laboratories at the Australian National University in laminar flow work stations. All reagents used were distilled in Savillex brand Teflon sub-boiling stills. MQ= milliQ 18.2 megaohm H_2O.

3.2.1 Procedure for cleaning Savillex screw-cap vials

1. Old labels were removed with ethanol/acetone and Kimwipe and the interior of the vial was cleaned by running a gloved finger around the inside.
2. Vials were then rinsed under the tap.
3. Vials were then boiled in a beaker with tap water and Decon-90 for ~2 hours with watch glass on top, and then rinsed with MQ.
4. Vials were then boiled in beaker again in 20% HCl for a further two hours, rinsed, and the same step was repeated with 20% HNO_3 and rinsed again in MQ.
5. After boiling in acid solution, the acids were reclaimed for further use.

6. The vials were then boiled a fourth time in MQ.
7. The vials were removed from beaker, and the bottoms were covered with concentrated HCl and left to reflux overnight with lids on at ~65° C.
8. The HCl was emptied into waste, and the same amount of concentrated HNO_3 was added, followed by 6-7 drops of concentrated HF and again left to reflux overnight.
9. The conc. HNO_3+HF solution was emptied to the waste, and replaced with enough MQ to cover the bottom of the vials. This was again left to reflux overnight.
10. MQ was emptied and lids replaced.

3.2.2 Procedure for cleaning 100 ml jars and auto-sampler tubes

1. Jars were washed in tap water + Decon90 and then rinsed under the tap.
2. Jars were then rinsed in MQ and filled to the brim with ~2% HNO_3 such that the solution was in contact with the lid, and left to leach for ~2 days.
3. The acid was reclaimed for future use, and the jars were filled with MQ and left for a further 1-2 days.
4. Jars and lids were then rinsed again in MQ and left to dry under a fume hood.

3.2.3 Sample digestion

1. 0.05g (±0.0005) of sample was weighed out into aluminium foil weigh boat using small spatula, and transferred to clean (see above) Teflon vial after antistatic gun applied to vial.
2. Five drops of 2% HNO_3 was added to sample.
3. Using pipette, 1 ml of concentrated HNO_3 was added to each vial, followed by 1 ml of concentrated HF.
4. Vials were placed on a hotplate and left to reflux overnight at ~65° C.
5. If significant solid residue was present, they were placed into an ultrasonic bath for ~5 mins.
6. Samples were then left to dry down on the hotplate for ~2 hours (until dry but not baked) at ~90° C.
7. Steps 2-5 were repeated, ensuring the vials with dry sample were not picked up from the hotplate in order to prevent loss of material.
8. 2 ml of concentrated HNO_3 was added to dried material, left to reflux overnight at ~65° C.
9. Sample was dried down again on hotplate at ~90 °C.
10. 4 ml of 50% HNO_3 was added to dried samples (made by pipetting 2 ml concentrated HNO_3 then 2ml milliQ to vials). Left to reflux at ~65 °C.

3.2.4 Dilution of digested samples

1. 125 ml polycarbonate jars were cleaned via method above.
2. Jar and lid were labelled with individual sample name.
3. Jar was placed on scale without lid and tared.
4. 1 ml of internal standard (IS) solution containing Be, In, Re, and Bi was pipetted into the jar, weighed, and the mass of IS was recorded.
5. Sample solutions were transferred to the jar, and the Savillex vials and lids were rinsed out twice into the jars using 2% HNO_3.
6. The jars were then filled to the 100 ml marker with 2% HNO_3, weighed without lid, and the final mass recorded. Dilution factor = final solution weight/initial weight of sample powder.
7. Lid was replaced.
8. One of the blanks did not have IS added, and the remaining volume was replaced with 2% HNO_3 to bring it up to 100 ml.

3.2.5 Analytical procedure – trace elements

Sample solutions were analysed on the Varian 820 quadrupole ICP-MS with the help of Mr. Les Kinsley. 46 masses were analysed including four internal standard masses (^{9}Be, ^{115}In, ^{185}Re, and ^{209}Bi). Unknowns were analysed in sets of six, bracketed by analysis of a BHVO-2 solution used for calibration of element sensitivities and a procedural blank. Intensities of internal standard masses in the unknowns were normalised to those in the preceding BHVO-2 solution to correct for instrument drift. Five additional basaltic reference materials (W-2, BIR-1, DNC-1, KIL-93, and KIL-1919) were analysed as unknowns for quality control. The raw counts were corrected by a dilution factor of approximately 2000, as calculated for each solution. Corrections for Pr oxide formation affecting mass ^{157}Gd, Ba oxide formation affecting mass ^{153}Eu and ^{151}Eu, and the isobaric interference of ^{160}Dy affecting ^{160}Gd. Instrument precision was good, with reproducibility within the run was good, with Relative Standard Deviations (RSD%) of <1% for most elements during repeat analyses of reference material BHVO-2 as an unknown (n = 4), and RSD% 1-2% for Y, Zr, Cd, Ce, Tm, and U, while elements Sb, Mo, Eu, and Pb have large RSD (%) (Table 3.1). When Kil-93 is analysed as an unknown (n = 6), most elements have RSD <1%, Ni, Co, Ga, Y, Cs, Ce, Gd, Ho, Tm, Yb, Hf, Th, and U have RSD <2%, and Mo, Cd, Eu, and Pb have high RSD between 5-15%. Accuracy was good for most elements when BHVO-2 was run as an unknown. When compared to literature values and preferred values (Norman et al., 2004, Norman et al., 1996, Jenner et al., 1990, Eggins et al., 1997, Strnad et al., 2005) some differences in values can be found, mostly for elements with very low concentrations (<1ppm). Elements that have the largest average deviation from preferred values are Cd and Mo

(underestimated by an average of ~60%), Ti and V (underestimated by an average of ~12%), Zn (overestimated by an average of ~12%), Sb, Pb, and Ta (overestimated by an average of ~20%). For elements Sb, Ta, Cd, and Mo, this may be a result of low concentrations, with average concentrations less than 1 ppm. Ti, V, Zn, and Pb however, are present in much higher concentrations. Most elements were accurate within 5%. Li, Sn, Eu, Y, Cs, Lu, and Rb were accurate within 10% and Zn, V, Ti, Pb, Sb, Ta, Mo, and Cd were moderately inaccurate (greater than 10% average difference from this study to reference value). Preferred values from Marc Norman pers. comm., (Eggins et al., 1997) of the reference materials analysed are compared to values collected in two analytical sessions in 2015 and 2016 (Figure 3.1).

Table 3.1 Replicate analyses of reference materials analysed during 2015 and 2016.

		W-2 (n = 6)			DNC-1 (n = 6)			BHVO-2 (n = 4)			BIR-1 (n = 6)			KIL-93 (n = 6)		
	Mass	*Average*	*σ*	*%RSD*	*Average*	*σ*	*%RSD*	*Average*	*σ*	*%RSD*	*Average*	*σ*	*%RSD*	*Average*	*σ*	*%RSD*
Li	7	10.2	0.1	1.16	5.5	0.1	1.12	5.0	0.0	0.75	3.6	0.1	1.85	5.1	0.0	0.73
Sc	45	36.2	0.4	1.23	32.4	0.4	1.26	32.4	0.2	0.71	45.4	0.9	2.09	31.7	0.2	0.76
Ti	49	6444	58	0.90	2985	35	1.17	16908	77	0.46	6048	75	1.25	14610	131	0.89
V	51	273	1	0.42	156	1	0.69	329	1	0.32	343	5	1.32	308	3	0.83
Cr	53	87	0	0.51	279	3	0.92	282	1	0.27	388	5	1.20	415	40	9.71
Co	59	45	0	0.83	59	1	1.22	46	0	0.75	55	1	1.64	53	1	1.04
Ni	60	73	1	1.21	272	3	1.04	123	1	0.77	180	3	1.63	159	2	1.26
Cu	65	104	1	1.15	94	1	1.44	129	1	0.56	120	2	1.52	124	1	0.75
Zn	66	74	2	2.66	62	3	5.05	105	1	0.54	70	1	1.49	105	1	0.70
Ga	71	17.2	0.1	0.80	13.5	0.2	1.38	20.9	0.2	0.81	15.3	0.2	1.16	19.1	0.2	1.05
Rb	85	20.2	0.1	0.48	3.7	0.0	0.77	9.4	0.0	0.53	0.2	0.0	0.38	7.1	0.0	0.59
Sr	86	192	1	0.27	142	1	0.80	390	1	0.28	109	1	1.20	318	2	0.59
Y	89	21.1	0.4	1.69	17.2	0.2	1.35	25.3	0.4	1.44	15.6	0.2	1.13	25.0	0.4	1.73
Zr	90	91	1	1.18	37	0	0.66	175	2	1.42	15	0	2.76	147	3	2.17
Nb	93	7.5	0.1	0.77	1.6	0.0	0.91	19.1	0.1	0.65	0.6	0.0	1.38	13.1	0.1	0.58
Mo	95	0.5	0.0	2.09	0.1	0.0	19.89	3.2	0.5	15.57	0.1	0.0	28.66	0.6	0.1	12.29
Cd	111	0.05	0.00	8.67	0.04	0.00	13.49	0.07	0.00	2.90	0.04	0.01	31.11	0.07	0.00	5.99
Sn	118	2.05	0.02	0.73	1.82	0.28	15.34	2.11	0.02	0.84	0.89	0.01	0.99	1.66	0.01	0.63
Sb	121	1.008	0.057	5.68	1.145	0.036	3.15	0.179	0.036	20.30	0.611	0.016	2.64	0.037	0.001	3.90
Cs	133	0.934	0.008	0.86	0.217	0.002	0.77	0.102	0.001	0.51	0.005	0.000	4.81	0.073	0.001	1.10
Ba	137	170	1	0.41	103	1	1.00	131	1	0.66	7	0	1.33	100	1	0.83
La	139	10.5	0.0	0.36	3.6	0.0	0.78	15.1	0.0	0.28	0.6	0.0	1.25	11.2	0.1	0.80
Ce	140	23	0	0.86	8	0	1.70	38	0	1.22	2	0	2.15	28	0	1.46
Pr	141	3.04	0.01	0.35	1.11	0.01	1.09	5.39	0.00	0.05	0.38	0.00	1.17	4.14	0.02	0.47
Nd	146	13.3	0.1	0.51	5.1	0.0	0.67	25.1	0.1	0.44	2.5	0.0	1.49	19.9	0.1	0.35
Sm	147	3.28	0.03	0.90	1.43	0.02	1.18	6.07	0.04	0.72	1.11	0.02	2.22	5.20	0.03	0.65
Eu	151	1.07	0.14	13.38	0.58	0.08	13.24	1.91	0.32	16.58	0.51	0.07	13.55	1.74	0.24	13.82
Eu	153	1.15	0.01	0.88	0.62	0.01	1.43	2.10	0.01	0.39	0.54	0.01	1.79	1.85	0.02	0.86
Gd	157	3.79	0.04	1.01	2.06	0.04	2.00	6.36	0.05	0.84	1.85	0.07	3.81	5.73	0.10	1.67
Gd	160	3.78	0.04	1.04	2.08	0.04	2.05	6.32	0.05	0.87	1.90	0.04	2.30	5.74	0.04	0.75
Tb	159	0.61	0.00	0.69	0.38	0.00	0.73	0.93	0.01	0.84	0.36	0.00	0.62	0.87	0.00	0.45
Dy	163	3.93	0.04	0.94	2.82	0.03	0.98	5.39	0.04	0.74	2.66	0.04	1.57	5.17	0.03	0.66
Ho	165	0.79	0.01	0.79	0.63	0.01	1.38	0.99	0.00	0.34	0.58	0.01	1.53	0.96	0.01	1.17
Er	166	2.25	0.02	0.67	1.92	0.01	0.50	2.57	0.02	0.83	1.72	0.01	0.78	2.54	0.02	0.80
Tm	169	0.32	0.00	1.06	0.29	0.00	1.26	0.33	0.01	1.67	0.26	0.01	1.96	0.33	0.01	1.54
Yb	174	2.05	0.02	0.77	1.93	0.02	1.21	2.00	0.02	0.96	1.66	0.02	1.28	2.01	0.02	1.06
Lu	175	0.30	0.00	0.94	0.29	0.00	1.01	0.27	0.00	0.59	0.25	0.00	1.51	0.28	0.00	0.55
Hf	177	2.31	0.04	1.58	0.98	0.03	2.58	4.29	0.04	0.96	0.57	0.01	2.21	3.61	0.04	1.21
Ta	181	0.48	0.03	5.62	0.11	0.04	38.21	1.19	0.01	0.81	0.07	0.03	47.16	0.83	0.03	3.18
Pb	208	7.91	0.96	12.12	7.00	1.10	15.79	3.15	1.07	34.02	3.20	0.47	14.59	0.87	0.05	6.03
Th	232	2.11	0.03	1.62	0.24	0.00	1.97	1.23	0.00	0.38	0.03	0.00	1.62	0.83	0.01	1.51
U	238	0.48	0.01	2.45	0.06	0.00	2.98	0.41	0.01	1.99	0.01	0.00	4.99	0.27	0.01	1.93

The preferred values of the reference materials BHVO-2, W-2, DNC-1, and KIL-93 from various literature are displayed below (Table 3.2 - Table 3.5).

Table 3.2 Average values of reference material BHVO-2 from this study compared to other studies (Eggins et al., 1997, Gao et al., 2002, Weis et al., 2005, Norman et al., 2004, Strnad et al., 2005) and Norman-preferred values (MN). Dash = no value.

		BHVO-2						
Element	**Mass**	**This study**	**Eggins 1997**	**Gao et al. 2002**	**Weis et al. 2005**	**MN**	**Norman et al. 2004**	**Strnad et al. 2005**
Li	7	5.0	4.9	5.0	5.9	4.4	-	-
Sc	45	32.4	31.8	31.0	28.6	32.4	31.9	-
Ti	49	16908	16610	15621	-	16864	16841	-
V	51	329	321	329	310	330	286	-
Cr	53	282	289	285	-	-	307	-
Co	59	46	45	47	47	46	-	-
Ni	60	123	120	112	121	122	128	-
Cu	65	129	136	142	117	129	114	-
Zn	66	105	105	107	95	105	103	-
Ga	71	21	21	21	21	21	-	-
Rb	85	9.4	9.5	10.1	9.6	9.4	9.1	-
Sr	86	390	390	382	381	389	390	-
Y	89	25	28	23	23	28	25	-
Zr	90	175	180	160	174	180	173	-
Nb	93	19.1	19.5	16.4	17.2	19.4	19.0	-
Mo	95	3.22	1.00	-	4.15	3.67	-	-
Cd	111	0.074	0.069	-	0.060	0.076	0.091	-
Sn	118	2.1	2.3	2.6	1.7	2.1	-	-
Sb	121	0.18	0.17	0.21	0.10	0.13	-	-
Cs	133	0.1	0.1	0.1	0.0	0.1	0.1	-
Ba	137	131	133	128	133	131	131	-
La	139	15.1	15.5	15.6	-	15.1	15.2	15.8
Ce	140	38	38	37	-	38	37	37
Pr	141	5.39	5.45	5.00	-	5.39	5.20	5.77
Nd	146	25.1	24.7	24.0	-	25.1	24.5	25.3
Sm	147	6.07	6.17	5.80	-	6.09	6.00	6.56
Eu	151	1.91	-	2.00	-	-	-	-
Eu	153	2.10	2.06	-	-	2.10	2.05	2.09
Gd	157	6.36	6.22	-	-	-	6.08	-
Gd	160	6.32	-	-	-	6.32	-	5.80
Tb	159	0.93	0.95	0.86	-	0.94	-	0.95
Dy	163	5.39	5.25	4.90	-	5.39	5.21	5.23
Ho	165	0.99	1.00	0.91	-	0.98	0.97	1.01
Er	166	2.57	2.56	2.30	-	2.56	2.51	2.61
Tm	169	0.33	-	0.30	-	0.33	-	0.34
Yb	174	2.00	1.98	2.00	-	2.00	1.98	2.09
Lu	175	0.270	0.278	0.260	-	0.270	0.275	0.280
Hf	177	4.3	4.3	4.1	4.3	4.3	4.2	-
Ta	181	1.2	1.2	0.9	1.1	1.2	1.2	-
Pb	208	3.2	2.1	1.4	1.3	1.7	2.1	-
Th	232	1.23	1.26	1.18	1.03	1.23	1.24	-
U	238	0.41	0.42	0.44	0.38	0.40	0.40	-

Table 3.3 Average values of reference material W-2 from this study compared to other studies (Jenner et al., 1990, Eggins et al., 1997, Norman et al., 1996) and Norman-preferred values (MN). Dash = no value.

		W-2				
Element	**Mass**	**This study**	**MN**	**Jenner et al. 1990**	**Eggins 1997**	**Norman et al. 1996**
Li	7	10.2	9.9	9.3	9.6	10.2
Sc	45	36.2	32.2	35.0	36.2	36.0
Ti	49	6444	5892	-	6700	-
V	51	273	249	-	270	278
Cr	53	87	-	-	92	-
Co	59	45	41	-	46	46
Ni	60	73	67	-	74	77
Cu	65	104	90	-	104	-
Zn	66	74	64	-	76	-
Ga	71	17	16	-	17	-
Rb	85	20.2	18.9	21.0	20.1	24.0
Sr	86	192	180	196	192	189
Y	89	21	23	21	23	21
Zr	90	91	90	97	92	84
Nb	93	7.5	7.7	7.3	7.8	6.6
Mo	95	0.49	0.53	-	0.43	-
Cd	111	0.046	-	-	0.057	-
Sn	118	2.0	-	-	2.0	-
Sb	121	1.01	-	-	0.79	-
Cs	133	0.9	0.9	0.9	0.9	1.1
Ba	137	170	173	168	171	170
La	139	10.5	10.6	10.2	10.6	10.7
Ce	140	23	24	23	23	24
Pr	141	3.04	2.94	2.87	3.03	3.10
Nd	146	13.3	13.2	12.4	13.0	13.5
Sm	147	3.28	3.38	3.22	3.31	3.50
Eu	151	1.07	-	1.12		1.04
Eu	153	1.15	1.12	-	1.09	-
Gd	157	3.79	3.68	-	3.69	-
Gd	160	3.78	-	3.60		3.50
Tb	159	0.61	0.62	0.63	0.62	-
Dy	163	3.93	3.75	4.00	3.79	3.90
Ho	165	0.79	0.80	0.86	0.80	0.76
Er	166	2.25	2.25	2.25	2.26	2.00
Tm	169	0.32	-	0.31		-
Yb	174	2.05	2.01	2.05	2.03	2.00
Lu	175	0.296	0.295	0.300	0.299	0.310
Hf	177	2.3	2.3	2.4	2.3	2.1
Ta	181	0.5	0.5	0.5	0.5	0.4
Pb	208	7.9	7.7	7.7	7.8	-
Th	232	2.11	2.19	2.10	2.21	2.00
U	238	0.48	0.49	0.49	0.50	0.53

Table 3.4 Average values of reference material DNC-1 from this study compared to other studies (Jenner et al., 1990, Eggins et al., 1997, Norman et al., 1996) and Norman-preferred values (MN). Dash = no value.

		DNC-1				
Element	**Mass**	**This study**	**MN**	**Jenner et al. 1990**	**Eggins 1997**	**Norman et al. 1996**
Li	7	5.5	5.2	4.9	5.1	5.3
Sc	45	32.4	30.7	31.0	31.1	35.0
Ti	49	2985	2900	-	3141	-
V	51	156	151	-	157	204
Cr	53	279	-	-	291	-
Co	59	59	56	-	57	59
Ni	60	272	260	-	264	256
Cu	65	94	88	-	86	-
Zn	66	62	56	-	57	-
Ga	71	13	14	-	14	-
Rb	85	3.7	3.7	3.9	3.6	3.2
Sr	86	142	143	145	141	128
Y	89	17	19	17	18	17
Zr	90	37	38	40	36	33
Nb	93	1.6	1.6	16.0	1.6	1.4
Mo	95	0.13	0.36	-	0.12	-
Cd	111	0.037	-	-	0.064	-
Sn	118	1.8	-	-	2.5	-
Sb	121	1.15	-	-	0.87	-
Cs	133	0.2	0.2	0.2	0.2	0.3
Ba	137	103	105	102	105	88
La	139	3.6	3.7	3.6	3.7	3.6
Ce	140	8	8	8	8	8
Pr	141	1.11	1.08	1.07	1.11	1.07
Nd	146	5.1	5.1	4.8	5.0	4.9
Sm	147	1.43	1.47	1.38	1.44	1.40
Eu	151	0.58	-	0.61	-	0.56
Eu	153	0.62	0.61	-	0.59	-
Gd	157	2.06	1.97	-	2.02	-
Gd	160	2.08	-	1.96	-	1.80
Tb	159	0.38	0.38	0.40	0.39	-
Dy	163	2.82	2.65	2.86	2.71	2.50
Ho	165	0.63	0.63	0.67	0.64	0.62
Er	166	1.92	1.92	1.92	1.95	1.70
Tm	169	0.29	-	0.28	-	-
Yb	174	1.93	1.88	1.97	1.92	1.80
Lu	175	0.291	0.288	0.300	0.292	0.280
Hf	177	1.0	1.0	1.1	1.0	0.9
Ta	181	0.1	0.1	0.2	0.1	0.1
Pb	208	7.0	5.9	6.2	6.5	-
Th	232	0.24	0.25	0.24	0.24	0.19
U	238	0.06	0.09	0.05	0.05	0.06

Table 3.5 Average values of reference material KIL-93 from this study compared to other studies (Norman et al., 2004) and Norman-preferred values (MN). Dash = no value.

		KIL-93		
Element	**Mass**	**This study**	**MN**	**Norman et al. 2004**
Li	7	5.1	4.9	-
Sc	45	31.7	33.5	-
Ti	49	14610	15275	-
V	51	308	322	-
Cr	53	415	-	-
Co	59	53	54	-
Ni	60	159	164	-
Cu	65	124	126	124
Zn	66	105	108	103
Ga	71	19	20	-
Rb	85	7.1	7.3	-
Sr	86	318	321	-
Y	89	25	28	24
Zr	90	147	151	-
Nb	93	13.1	13.5	-
Mo	95	0.62	0.77	-
Cd	111	0.066	0.065	0.112
Sn	118	1.7	1.6	-
Sb	121	0.04	0.04	-
Cs	133	0.1	0.1	-
Ba	137	100	100	-
La	139	11.2	11.1	-
Ce	140	28	28	-
Pr	141	4.14	3.94	-
Nd	146	19.9	19.3	-
Sm	147	5.20	5.22	-
Eu	151	1.74	-	-
Eu	153	1.85	1.78	-
Gd	157	5.73	5.55	-
Gd	160	5.74	-	-
Tb	159	0.87	0.86	-
Dy	163	5.17	4.93	-
Ho	165	0.96	0.96	-
Er	166	2.54	2.51	-
Tm	169	0.33	-	-
Yb	174	2.01	1.97	2.05
Lu	175	0.276	0.278	-
Hf	177	3.6	3.6	3.8
Ta	181	0.8	0.8	-
Pb	208	0.9	0.9	-
Th	232	0.83	0.86	-
U	238	0.27	0.27	-

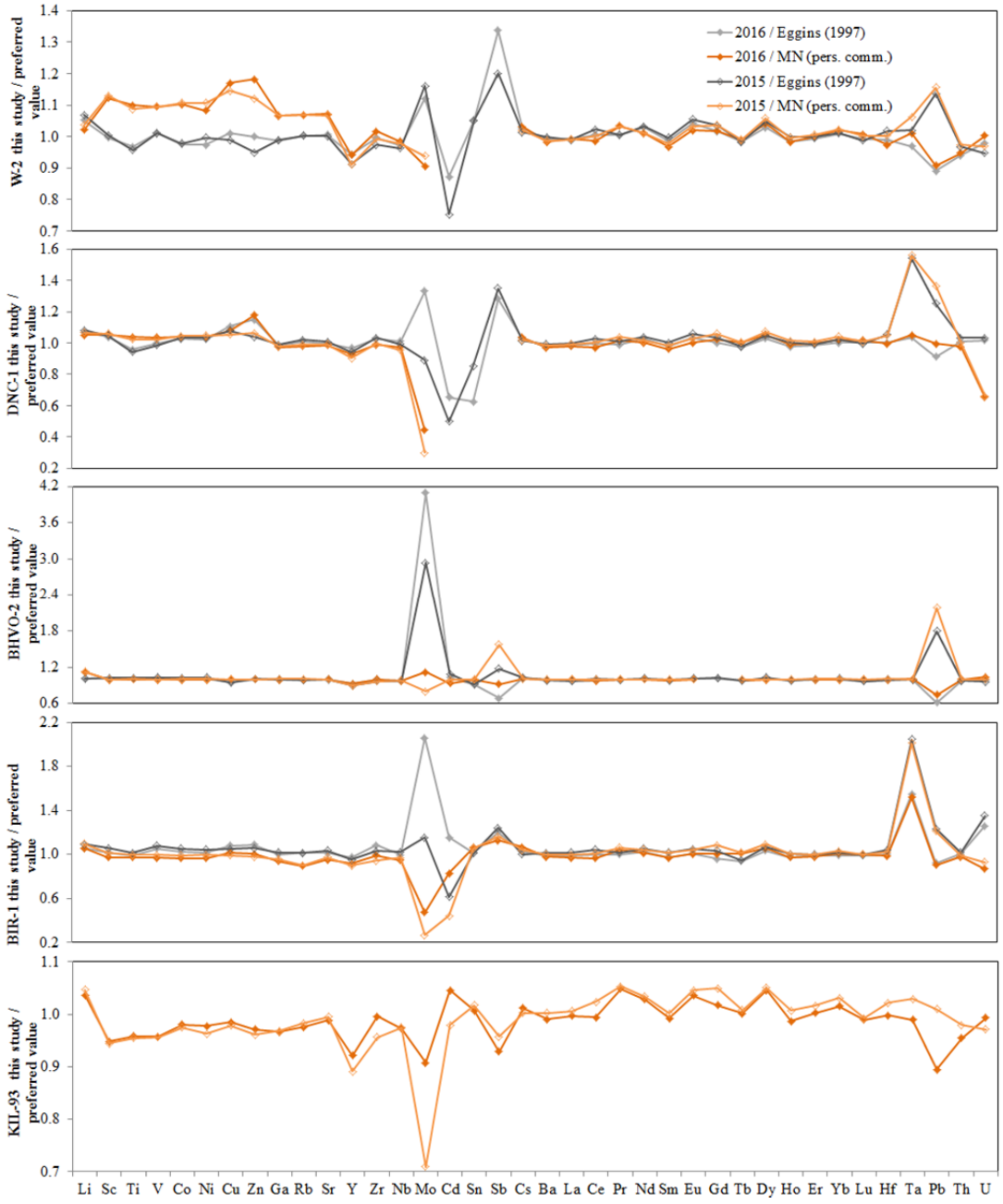

Figure 3.1 Analyses of reference materials from this study analysed in 2015/16 relative to those of Eggins (1997) and preferred values of Marc Norman (Pers. Comm.).

The percentage difference for those elements analysed via both ICP-MS and XRF are shown in Figure 3.2, with % difference representing the value 1- (ICP-MS element conc./XRF element conc.) x 100. The largest differences were for Th (>60%), Pb (>100%), Ni (>20%), Cr (>40%), and La (~70%). Nb, Zr, Y, Sr, and Ga were within 20% difference.

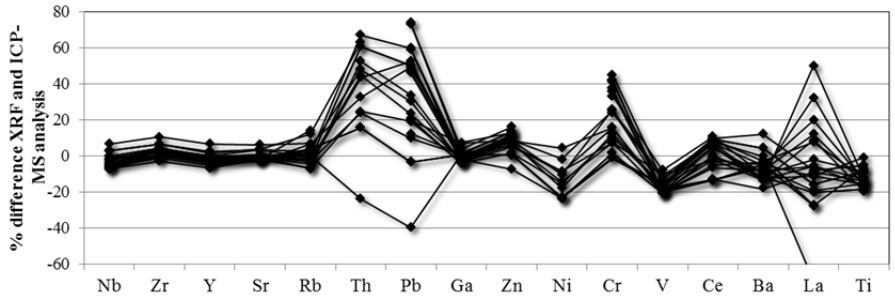

Figure 3.2 Percentage difference in element concentration between XRF and ICP-MS analyses.

3.3 Determination of Sr and Nd isotopic compositions by Thermal Ionisation Mass Spectrometry (TIMS)

All work was carried out in the ANU SPID²ER clean laboratory in HEPA filtered work stations. All acids used were purified using Savillex Teflon sub-boiling stills. For the initial experiments the samples were weighed into pre-cleaned 15 ml Savillex Teflon beakers. Isotopic measurements were made on the ANU Triton-plus multi-collector mass spectrometer.

3.3.1 Sample preparation

1. 20-40 mg of sample powder were weighed and added to screw-cap Teflon beakers with 0.2 ml of 0.5 M HNO_3.
2. 1.5 ml HF + 1 ml HNO_3 (conc.) was added to each sample and the sealed samples were refluxed at 110˚c for 2-3 days, until sample was dissolved.
3. Next, the samples were dried down and then 2 ml of 6 M HCl was added and left to reflux overnight.
4. The samples were dried down and 1 ml conc. HNO_3 was added and left to reflux overnight.
5. Samples were dried down again and 1 ml 2 M HNO_3 was added and left to reflux overnight.
6. The REE containing fraction was separated using Eichrom TRU-spec column chemistry.
7. The non-REE fraction was loaded onto to Eichrom Sr-spec columns to isolate Sr.
8. The REE fraction (left over from the TRU-Spec separation) was loaded onto Eichrom Ln-Spec columns and the Nd fraction was collected.
9. For each fraction a small drop of dilute H_3PO_4 acid was added and the samples dried at at 70˚c.

3.3.2 Isotopic Analysis

1. For a typical Sr analysis 100 mg Sr was used. For loading, the Sr fraction was mixed with 3 μl of TaF activator and then 1 μl was loaded onto outgassed zone-refined Re H-Cross single filament.
2. After loading, the samples were dried down by increasing the current on the filament.
3. The Sr fractions were analysed on the Triton-plus TIMS using single filament measurements and faraday cups in static collection mode.
4. The quality control standard NBS987 was measured throughout the sessions and throughout the multiple analysis days yielding an average value of 0.710257 with a standard deviation on the mean of 7.1×10^{-6} (n = 7) (Figure 3.3). This is within error of the NBS987 28 year analysis average of $0.710263 \pm 3.6 \times 10^{-6}$.
5. Nd fractions + H_3PO_4 were mixed with 1 μl of 1M HNO_3, and loaded onto outgassed zone refined Re filaments.
6. Quality control in house standard Nd-1 (an AMES metal) was used throughout sessions and over the multiple analysis days (Figure 3.4) yielding an average value of 0.512141 with a standard deviation on the mean of $3.2 \times 10^{-6.}$ (n = 4).

Isotopic ratios were determined by static collection on Faraday cups and corrected for mass fractionation using the following stable isotopic ratios in each analysis; $^{146}Nd/^{144}Nd = 0.7219$ (O'nions et al., 1979), and $^{86}Sr/^{88}Sr = 0.1194$ (Steiger and Jager, 1977). Each analysis of Sr and Nd consisted of 15 blocks of 12 scans consisting of 8 second integration periods. A 30 second baseline was measured every 3 blocks and a peak centre and focus at the beginning of the run and after 8 blocks.

Total procedural blanks were run with every batch of samples during the period of this study and were for Nd <30 pg, Sr between 50–300 pg and for all samples of this study were negligible.

Over the period of this study the external precision of Triton multi-collector TIMS was monitored with the in-house Nd-1 (Nd) standard (originally prepared from an AMES metal) and NBS987 (Sr) standards. Fifteen analyses using similar running conditions of Nd-1 over 3 years yield an average value of 0.512142 ± 0.0000036 (2SE). International reference materials La Jolla (0.5118503 ± 0.0000051; 2SE) and JNd1 (0.5120986 ± 0.0000047) were also analysed over this time period. Twenty-eight analyses of NBS987 yielded an average $^{87}Sr/^{86}Sr$ of 0.710263 ± 0.0000036 (2SE).

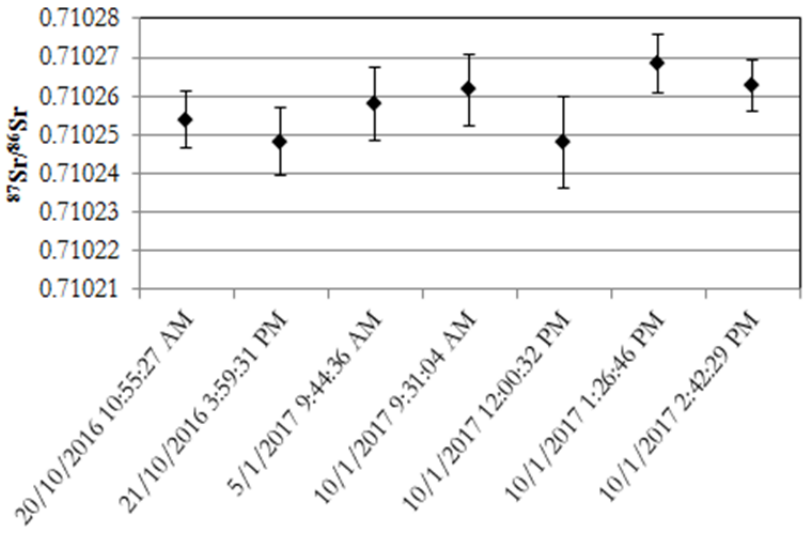

Figure 3.3 Repeat $^{87}Sr/^{86}Sr$ analyses of quality control standard NBS987. Error bars are ± 2 standard errors.

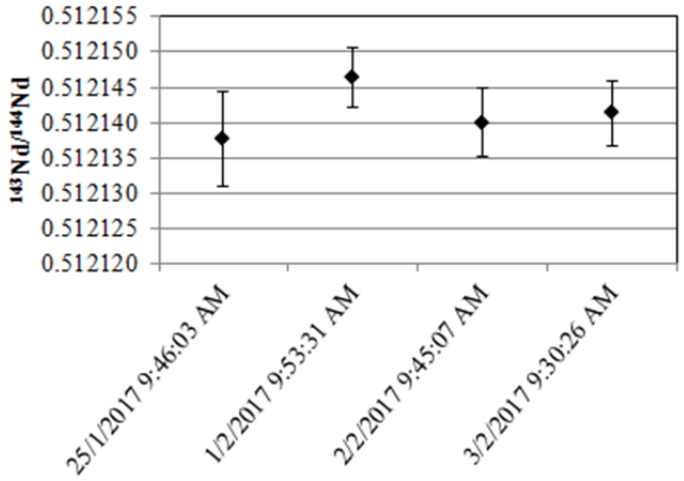

Figure 3.4 Repeat $^{143}Nd/^{144}Nd$ analyses of quality control standard Nd AMES. Error bars are ± 2 standard errors.

4 Results – Major elements and modal mineralogy

4.1 Major elements

XRF analyses of submarine dredge samples from Mauna Loa (n=170) reveal that they span a wide range of MgO contents and are basalts based on the geochemical classification scheme of Le Maitre (International Union of Geological Sciences, 1989). Le Maitre based their classification on the total silica and alkali contents of extrusive igneous rocks, which has been used here to categorise the samples from this study (Figure 4.1). All samples fall into the 'basalt' field, as they contain relatively low SiO_2 and low alkalis, although some samples with higher or lower SiO_2 come close to the categories of basaltic andesite or picro-basalt respectively, highlighting the wide range in SiO_2 contents. The samples with the highest SiO_2 also have higher relative $Na_2O + K_2O$ than the lower SiO_2 samples.

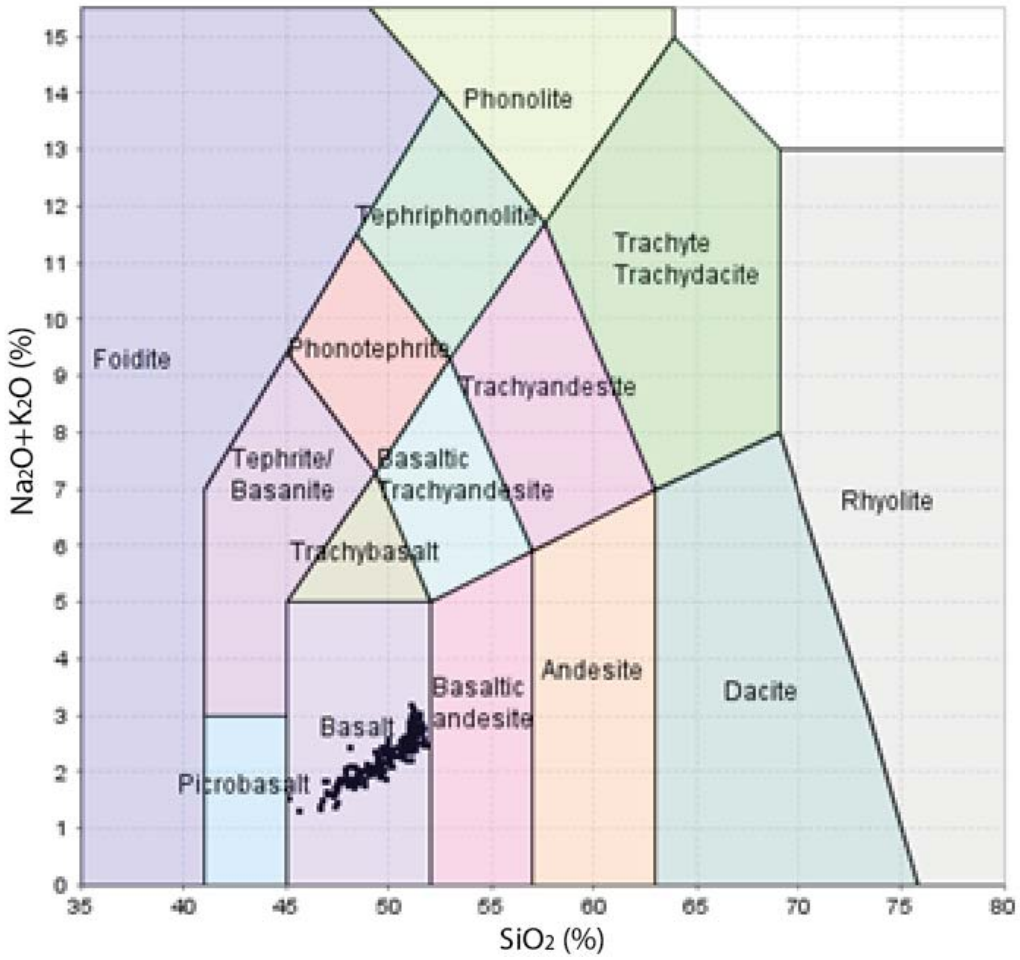

Figure 4.1 Total Silica vs. Total Alkalis diagram (wt. %) (International Union of Geological Sciences, 1989), produced using ioGAS™, with Mauna Loa samples (black points) falling in the basaltic range in terms of silica and alkali content.

According to the Irvine and Baragar definition (Irvine and Baragar, 1971), which classifies basalts into either the calc-alkali or tholeiitic sub-groups depending on alkali, iron, and magnesium contents, the basalts are tholeiitic in nature. As shown in Figure 4.2, the Mauna Loa samples fall in a linear arrangement, varying mostly in terms of Mg or Fe content which comprise the majority of the composition, with a much smaller range and proportion of alkalis.

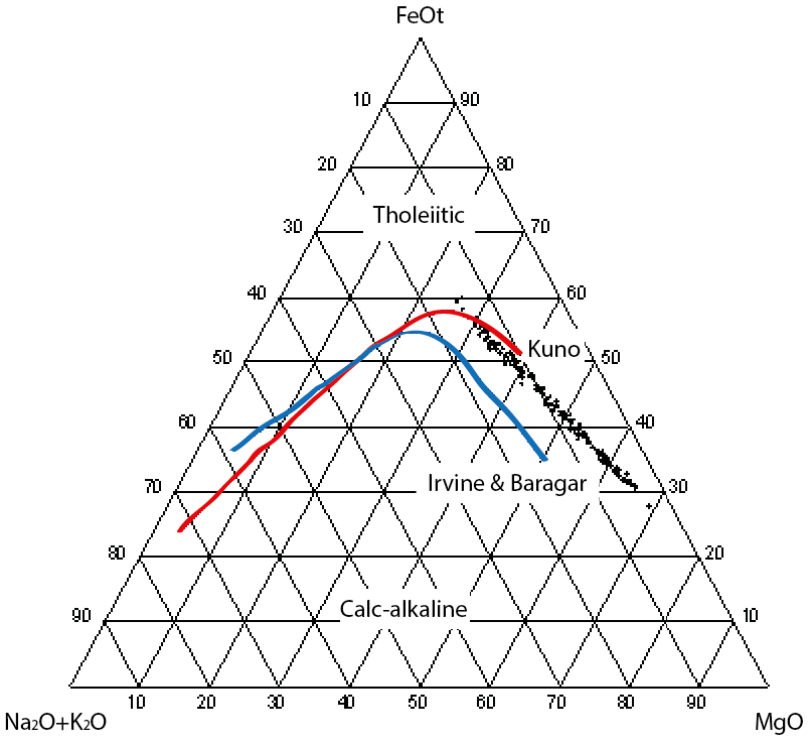

Figure 4.2 Alkalis (Na_2O + K_2O), iron (FeO_t), and magnesium (MgO) ternary diagram of samples showing Mauna Loa basalts (black points) lie in the tholeiitic range according to Irvine and Baragar (1971).

The MgO contents of these lavas span a wide range in MgO (5.45 – 27.04 wt. %), with some containing up to 27 wt. %; a higher MgO content than some previously investigated Mauna Loa basalt suites e.g. (Moore and Clague, 1987, Davis et al., 2003). The other major elements range from 45.15 – 51.84 wt. % SiO_2, 5.61 – 11.28 wt. % CaO, 7.01 – 14.57 wt. % Al_2O_3, 10.18 – 12.97 wt. % FeO* (total iron as FeO), 1.11 – 3.23 wt. % TiO_2, 1.15 – 2.59 wt. % Na_2O, 0.15 – 0.60 wt. % K_2O, 0.11 – 0.37 wt % P_2O_5, and 0.161 – 0.201 wt. % MnO. It is expected that ~90% of the iron in these samples is present as Fe^{2+} (e.g. Fe^{3+}/Fe^{2+} = 0.12 - (Brounce et al., 2017)).

Table 4.1 Major element compositions of whole rock Mauna Loa tholeiites in weight %.

Sample	SiO_2	TiO_2	Al_2O_3	FeO*	MnO	MgO	CaO	Na_2O	K_2O	P_2O_5	Sum
M1-1	46.70	1.14	7.77	11.20	0.17	23.77	6.30	1.16	0.20	0.11	98.51
M1-2	50.67	1.83	12.87	10.54	0.17	8.83	10.95	2.00	0.35	0.20	98.42
M1-6	49.66	1.62	11.47	10.70	0.18	12.93	9.93	1.65	0.30	0.18	98.62
M1-8	49.57	1.68	10.87	10.77	0.17	15.08	8.72	1.60	0.29	0.16	98.91
M1-9	50.90	1.85	12.95	10.54	0.17	8.58	11.07	1.96	0.40	0.21	98.63
M1-13	47.42	1.18	8.86	10.68	0.17	21.66	7.10	1.20	0.19	0.11	98.56
M1-14	49.11	1.54	10.90	10.71	0.17	14.35	9.51	1.66	0.29	0.17	98.41
M1-16	48.83	1.47	10.57	10.41	0.16	16.71	8.43	1.52	0.23	0.14	98.48
M1-20	49.44	1.58	11.23	10.32	0.16	15.18	8.80	1.71	0.27	0.15	98.85
M1-26	47.55	1.22	8.65	10.69	0.16	22.14	6.89	1.24	0.20	0.12	98.87
M1-27	50.72	1.84	12.74	10.41	0.17	10.42	9.97	1.93	0.30	0.18	98.68
M1-30	51.76	2.03	13.81	10.32	0.17	7.41	10.73	2.12	0.34	0.19	98.89
M2-2	47.48	1.44	9.18	10.91	0.17	20.01	7.16	1.44	0.29	0.15	98.23
M2-3	48.46	1.65	10.12	10.86	0.17	17.21	7.97	1.61	0.30	0.17	98.52
M2-4	47.95	1.54	9.58	10.95	0.17	18.76	7.48	1.56	0.25	0.16	98.40
M2-10	50.23	1.78	12.06	10.83	0.17	11.71	9.30	1.81	0.28	0.18	98.33
M2-12	49.77	1.79	11.57	10.62	0.17	13.31	9.01	1.75	0.28	0.18	98.46
M2-18	50.09	1.84	11.81	10.67	0.17	12.48	9.21	1.82	0.29	0.19	98.56
M2-19	47.04	1.34	8.55	10.88	0.17	21.91	6.72	1.45	0.20	0.15	98.41
M2-20	46.65	1.27	8.15	11.06	0.18	23.35	6.43	1.18	0.21	0.14	98.62
M2-21	47.33	1.33	8.67	10.59	0.16	21.61	6.89	1.38	0.22	0.14	98.32
M2-23	47.90	1.48	9.60	10.77	0.17	19.05	7.55	1.61	0.24	0.15	98.53
M2-24	48.35	1.50	10.01	10.68	0.17	18.42	7.66	1.53	0.23	0.15	98.70
M2-26	49.06	1.74	10.71	10.83	0.17	15.65	8.39	1.63	0.32	0.18	98.67
M2-27	47.90	1.48	9.60	10.77	0.17	19.05	7.55	1.61	0.24	0.14	98.52
M3-1	49.45	1.80	11.05	10.94	0.18	14.65	8.56	1.76	0.32	0.20	98.91
M3-2	49.35	1.82	11.08	10.76	0.17	14.09	8.62	1.92	0.43	0.19	98.43
M3-3	49.43	1.82	11.11	10.78	0.17	14.27	8.66	1.86	0.36	0.19	98.66
M3-4	49.67	1.85	11.20	10.90	0.17	13.83	8.66	1.79	0.34	0.19	98.60
M3-5	49.49	1.85	11.50	10.84	0.17	13.61	8.69	1.77	0.35	0.19	98.46
M3-6	48.47	1.58	10.00	11.04	0.18	18.00	7.70	1.62	0.24	0.18	99.01
M3-7	49.63	1.81	11.00	10.86	0.17	14.58	8.58	1.65	0.40	0.19	98.86
M3-12	46.97	1.31	8.52	10.92	0.16	22.01	6.72	1.38	0.21	0.13	98.33
M3-13	47.32	1.34	8.69	10.91	0.16	21.72	6.82	1.38	0.20	0.14	98.68
M4-3	49.63	1.88	11.42	10.79	0.17	13.68	8.95	1.80	0.32	0.19	98.83
M4-7	47.47	1.48	9.15	10.81	0.17	20.32	7.10	1.54	0.24	0.16	98.44
M4-8	47.91	1.59	9.71	10.85	0.16	18.45	7.63	1.78	0.26	0.16	98.50
M4-9	47.45	1.44	8.76	10.81	0.16	21.42	6.93	1.47	0.23	0.15	98.82
M4-13	49.72	1.93	11.56	10.88	0.17	13.09	9.03	1.99	0.32	0.20	98.89
M4-14	50.07	1.89	11.57	10.81	0.17	13.02	9.01	1.78	0.41	0.19	98.92
M4-15	49.35	1.87	11.23	10.88	0.17	14.02	8.77	2.02	0.32	0.19	98.81
M4-17	48.32	1.63	9.91	10.78	0.16	18.23	7.78	1.82	0.25	0.17	99.05
M4-21	46.77	1.26	8.40	11.16	0.18	23.04	6.65	1.32	0.18	0.13	99.09

Table 4.2 Major element compositions of whole rock Mauna Loa tholeiites in weight %.

Sample	SiO_2	TiO_2	Al_2O_3	FeO*	MnO	MgO	CaO	Na_2O	K_2O	P_2O_5	Sum
M6-1	50.81	2.10	12.87	10.77	0.17	9.22	10.07	2.24	0.35	0.21	98.81
M6-5	50.67	2.08	12.87	10.77	0.17	9.27	9.94	2.23	0.33	0.22	98.55
M6-6	51.15	2.38	13.48	11.54	0.19	6.79	10.23	2.25	0.41	0.26	98.68
M6-13	48.08	1.51	10.11	10.69	0.16	17.80	7.83	1.84	0.25	0.15	98.42
M6-14	48.50	1.56	9.87	11.01	0.18	17.83	7.74	1.58	0.23	0.16	98.66
M6-26	51.27	2.39	13.32	11.42	0.18	6.78	10.07	2.33	0.40	0.27	98.43
M6-27	51.47	2.40	13.29	11.39	0.18	6.60	10.30	2.59	0.43	0.25	98.89
M6-28	51.54	2.39	13.36	11.34	0.18	6.87	10.25	2.37	0.42	0.26	98.98
M6-32	49.97	2.02	11.12	11.15	0.17	13.55	8.62	2.00	0.32	0.21	99.13
M8-1	51.15	2.29	13.46	11.16	0.17	7.26	10.42	2.39	0.38	0.23	98.91
M8-5	51.13	2.19	13.31	11.01	0.17	7.98	10.30	2.33	0.36	0.22	99.00
M8-8	51.04	2.25	13.32	11.14	0.17	7.14	10.26	2.34	0.36	0.23	98.26
M9-15	51.26	2.01	13.99	10.36	0.17	7.59	10.84	2.17	0.30	0.19	98.87
M9-16	51.44	2.19	14.13	10.72	0.17	6.77	10.75	2.38	0.34	0.21	99.10
M10-9	51.26	2.32	14.13	11.41	0.18	6.20	10.26	2.59	0.32	0.23	98.91
M10-13	50.99	2.00	12.79	10.80	0.17	8.92	10.18	2.17	0.31	0.20	98.52
M11-5	51.14	3.23	13.07	12.59	0.20	5.45	9.09	2.59	0.60	0.37	98.33
M11-11	50.49	1.86	12.31	10.68	0.17	11.04	10.17	2.10	0.19	0.18	99.19
M11-13	49.51	1.85	11.66	10.85	0.17	12.51	9.52	1.95	0.31	0.17	98.48
M12-2	47.56	1.48	9.65	11.35	0.17	18.81	7.98	1.65	0.21	0.14	99.00
M12-3	50.91	2.10	12.89	10.49	0.17	9.39	10.57	1.89	0.32	0.20	98.92
M12-4	51.43	2.47	14.11	11.29	0.18	6.28	10.32	2.28	0.38	0.24	98.97
M12-12	46.73	1.41	8.47	11.31	0.17	21.91	7.18	1.21	0.16	0.14	98.70
M12-14	51.14	2.42	14.29	11.12	0.18	6.39	10.39	2.25	0.38	0.24	98.80
M12-15	50.61	1.98	12.58	10.96	0.17	9.56	10.12	2.09	0.30	0.19	98.56
M12-17	51.75	2.17	13.63	10.50	0.17	6.89	10.91	2.22	0.32	0.21	98.77
M12-18	49.36	1.78	11.24	11.03	0.17	13.81	9.26	1.78	0.25	0.17	98.84
M12-19	51.15	2.04	13.55	10.69	0.18	7.89	11.08	2.01	0.32	0.19	99.10
M12-27	50.86	1.91	13.09	10.76	0.17	9.07	10.34	2.26	0.26	0.18	98.90
M12-29	50.64	2.01	13.15	10.92	0.17	8.83	10.37	2.23	0.32	0.19	98.84
M12-34	50.43	1.97	12.45	11.02	0.18	10.34	9.96	2.09	0.32	0.19	98.94
M12-42	51.09	2.10	13.47	10.83	0.18	7.79	10.96	1.89	0.32	0.20	98.83
M13-2	51.35	2.36	14.57	11.11	0.18	5.79	10.66	2.31	0.34	0.23	98.90
M13-4	50.97	2.11	12.80	10.69	0.17	9.43	9.73	2.38	0.39	0.24	98.91
M13-5	51.07	2.20	13.71	10.86	0.18	7.17	10.67	2.14	0.37	0.22	98.59
M13-9	51.38	1.94	13.25	10.50	0.17	8.29	10.49	2.19	0.29	0.18	98.69
M13-12	47.61	1.48	9.36	10.70	0.17	19.66	7.70	1.51	0.26	0.16	98.60
M13-14	49.89	1.54	11.30	10.85	0.17	14.15	8.97	1.60	0.27	0.15	98.89
M13-15	51.30	2.18	13.76	10.84	0.18	7.43	10.70	2.13	0.39	0.22	99.12
M13-21	46.96	1.56	9.16	10.90	0.17	20.00	7.76	1.52	0.32	0.17	98.53
M13-25	45.15	1.43	7.30	11.76	0.19	25.32	6.20	1.26	0.26	0.18	99.05
M13-27	49.70	1.99	12.27	10.67	0.16	11.06	10.03	2.05	0.36	0.19	98.49
M13-29	49.97	1.88	12.04	10.80	0.18	11.21	9.85	1.85	0.36	0.18	98.32

Table 4.3 Major element compositions of whole rock Mauna Loa tholeiites in weight %.

Sample	SiO_2	TiO_2	Al_2O_3	FeO*	MnO	MgO	CaO	Na_2O	K_2O	P_2O_5	Sum
M13-33	45.60	1.11	7.01	10.90	0.18	27.04	5.61	1.15	0.15	0.12	98.87
M13-35	51.12	2.49	14.29	10.89	0.17	6.10	10.45	2.30	0.42	0.27	98.51
M13-38	46.92	1.51	8.89	10.99	0.18	21.11	7.51	1.53	0.29	0.17	99.10
M13-39	50.82	1.99	13.07	10.82	0.17	8.45	10.44	2.11	0.33	0.18	98.38
M13-40	48.91	1.83	10.53	11.12	0.17	15.42	8.31	1.85	0.29	0.18	98.60
M14-3	48.50	1.51	9.89	10.84	0.17	17.92	7.97	1.57	0.23	0.15	98.75
M14-4	49.44	1.82	11.36	10.66	0.17	13.36	9.23	1.79	0.26	0.18	98.26
M14-5	50.74	2.01	12.93	10.82	0.17	8.82	10.32	2.15	0.30	0.20	98.46
M14-20	51.08	2.04	13.12	10.77	0.17	8.30	10.62	2.13	0.32	0.21	98.76
M14-21	47.39	1.39	9.15	10.95	0.17	20.32	7.33	1.39	0.20	0.14	98.43
M14-27	47.46	1.43	9.39	11.05	0.17	20.06	7.57	1.48	0.19	0.15	98.95
M14-28	49.35	1.76	11.07	10.80	0.17	14.51	8.94	1.79	0.26	0.17	98.82
M14-31	51.75	2.04	13.75	10.27	0.17	7.17	10.80	2.25	0.31	0.20	98.71
M14-32	49.57	1.68	10.59	10.86	0.17	15.47	8.40	1.80	0.19	0.16	98.88
M17-1	48.06	1.39	9.94	10.50	0.16	18.46	7.98	1.65	0.22	0.14	98.51
M17-2	51.25	2.41	13.25	10.90	0.17	7.06	10.05	2.54	0.41	0.27	98.30
M17-6	51.31	2.16	13.14	10.75	0.17	8.25	10.17	2.29	0.34	0.22	98.80
M17-7	47.94	1.51	9.57	10.91	0.17	18.91	7.54	1.72	0.24	0.15	98.66
M17-8	51.25	2.84	13.02	12.22	0.19	5.68	9.73	2.59	0.51	0.32	98.34
M17-11	49.97	1.81	11.76	10.54	0.17	12.85	9.20	1.86	0.30	0.18	98.64
M17-15	49.77	1.60	11.60	10.32	0.16	14.04	9.15	1.91	0.26	0.17	98.98
M17-16	47.98	1.51	9.45	10.86	0.17	19.26	7.51	1.58	0.25	0.16	98.72
M17-17	49.70	1.89	11.59	10.87	0.17	12.77	9.07	2.06	0.32	0.20	98.64
M17-18	50.67	2.24	12.37	11.35	0.17	9.97	9.50	1.95	0.37	0.24	98.83
M17-32	51.59	2.42	13.33	10.99	0.17	7.02	10.20	2.42	0.41	0.27	98.82
M17-33	51.29	2.35	13.55	10.83	0.17	7.11	10.44	2.54	0.36	0.27	98.91
M17-38	50.07	1.65	11.70	10.18	0.16	13.46	9.27	1.83	0.27	0.18	98.77
M17-40	51.38	2.42	12.97	10.87	0.17	8.03	9.94	2.38	0.42	0.26	98.84
M17-41	51.12	2.78	12.62	12.53	0.19	6.73	9.56	2.51	0.46	0.30	98.79
M17-43	51.22	3.01	12.49	12.97	0.19	5.64	9.44	2.56	0.50	0.32	98.35
M17-44	51.60	2.15	13.57	10.81	0.17	7.28	10.50	2.37	0.35	0.22	99.02
M18-2	50.19	1.93	12.08	10.90	0.17	11.33	9.49	2.05	0.32	0.19	98.65
M18-9	50.14	1.96	12.27	10.87	0.17	10.41	9.69	2.03	0.33	0.20	98.08
M18-12	49.94	1.90	11.92	11.01	0.17	11.88	9.37	2.19	0.33	0.19	98.89
M18-16	48.51	1.59	10.04	10.86	0.17	17.30	7.92	1.77	0.25	0.16	98.56
M18-17	50.97	2.10	13.13	10.94	0.17	8.56	10.25	2.18	0.34	0.21	98.85
M18-19	47.99	1.50	9.67	10.80	0.17	18.72	7.71	1.52	0.23	0.15	98.46
M18-21	50.76	2.08	13.13	10.80	0.17	8.46	10.25	2.15	0.34	0.21	98.35
M18-25	49.97	1.89	11.82	11.00	0.17	11.92	9.35	2.05	0.32	0.19	98.68
M18-28	50.67	2.06	12.62	10.62	0.17	10.15	9.83	2.11	0.32	0.20	98.75
M18-29	50.93	2.05	13.15	10.71	0.17	8.81	10.31	2.12	0.31	0.20	98.75
M18-31	48.10	1.49	10.02	10.90	0.18	18.27	7.73	1.61	0.24	0.16	98.70
M18-32	48.79	1.75	10.35	10.84	0.17	16.53	8.07	1.73	0.30	0.18	98.70

Table 4.4 Major element compositions of whole rock Mauna Loa tholeiites in weight %

Sample	SiO_2	TiO_2	Al_2O_3	FeO*	MnO	MgO	CaO	Na_2O	K_2O	P_2O_5	Sum
M18-33	48.55	1.61	9.94	10.73	0.17	17.42	7.81	1.65	0.27	0.17	98.31
M18-34	47.95	1.52	9.98	10.88	0.18	18.01	7.83	1.57	0.24	0.15	98.31
M18-35	50.99	2.47	13.84	11.57	0.19	6.73	9.88	2.44	0.43	0.27	98.81
M18-36	51.03	2.13	13.46	11.15	0.19	8.04	10.35	2.13	0.34	0.22	99.04
M19-1	48.84	1.57	10.43	10.47	0.16	16.99	8.19	1.60	0.27	0.16	98.69
M19-2	49.92	1.90	11.87	10.70	0.17	12.04	9.47	2.07	0.34	0.19	98.67
M19-4	48.11	1.50	10.09	10.58	0.16	17.84	8.00	1.58	0.23	0.15	98.24
M19-5	48.38	1.52	10.06	10.59	0.16	18.07	7.92	1.76	0.27	0.15	98.89
M19-11	49.51	1.71	11.33	10.45	0.16	14.28	8.93	1.83	0.29	0.17	98.67
M19-17	51.13	2.20	12.94	10.91	0.17	8.53	10.23	2.23	0.39	0.22	98.95
M19-18	49.17	1.70	10.96	10.83	0.17	15.18	8.50	1.81	0.27	0.17	98.75
M19-20	51.60	2.22	13.70	10.89	0.17	6.64	10.53	2.34	0.35	0.22	98.67
M19-21	50.07	1.87	11.93	10.82	0.17	11.90	9.33	1.99	0.30	0.19	98.57
M19-22	51.45	2.37	13.46	11.15	0.18	6.56	10.39	2.28	0.39	0.23	98.45
M19-23	50.56	1.92	12.56	10.67	0.17	10.46	9.78	2.03	0.30	0.20	98.65
M19-24	49.61	1.82	11.64	10.80	0.17	12.88	9.08	1.94	0.28	0.18	98.40
M19-28	48.15	2.01	10.49	11.08	0.17	15.58	8.17	2.06	0.36	0.23	98.28
M21-1	49.41	1.73	11.13	11.26	0.17	13.95	8.86	1.94	0.25	0.16	98.87
M21-11	50.11	1.78	11.61	10.78	0.17	12.97	9.21	1.84	0.29	0.17	98.93
M21-15	51.81	2.10	13.65	10.59	0.17	7.29	10.62	2.17	0.28	0.20	98.88
M22-4	48.47	1.65	9.85	10.87	0.17	17.98	7.69	1.61	0.28	0.18	98.75
M22-11	48.67	1.72	10.20	10.90	0.17	16.91	7.95	1.69	0.29	0.18	98.68
M22-17	48.56	1.76	10.14	10.96	0.17	16.79	7.78	1.74	0.28	0.20	98.38
M22-20	48.95	1.81	10.48	10.97	0.17	16.10	8.01	1.80	0.29	0.20	98.78
M22-21	48.94	1.81	10.58	10.81	0.17	15.72	8.12	1.77	0.28	0.20	98.40
M24-1	51.32	2.14	13.13	10.83	0.17	8.21	10.10	1.93	0.45	0.26	98.53
M24-3	51.20	2.12	13.15	10.79	0.17	8.12	10.09	2.39	0.44	0.25	98.72
M24-5	51.84	2.06	13.77	10.52	0.17	6.96	10.65	2.03	0.42	0.25	98.67
M24-8	51.21	2.14	13.15	10.75	0.17	8.15	10.13	2.08	0.44	0.26	98.48
M26-1	49.17	1.61	10.79	11.05	0.17	15.36	8.35	1.75	0.27	0.17	98.69
M26-10	51.69	2.18	14.18	10.69	0.17	6.53	10.55	2.32	0.45	0.26	99.02
M26-14	48.29	1.48	9.89	11.19	0.17	17.90	7.68	1.54	0.25	0.15	98.54
M26-16	48.83	1.56	10.44	11.11	0.17	16.37	8.09	1.77	0.26	0.16	98.76
M26-18	49.99	1.75	11.77	11.13	0.18	12.43	9.08	1.95	0.30	0.18	98.76
M26-43	49.44	1.65	11.01	11.16	0.18	14.81	8.53	1.89	0.27	0.17	99.11
M26-44	48.77	1.60	10.70	11.17	0.18	15.44	8.18	1.76	0.25	0.17	98.22
M27-2	50.97	2.13	14.05	10.76	0.17	6.97	11.28	2.28	0.38	0.24	99.22
M27-11	50.80	2.10	14.06	10.64	0.17	6.93	11.28	2.24	0.38	0.23	98.83
M27-32	50.25	1.98	12.27	11.17	0.18	10.87	9.69	1.95	0.31	0.20	98.86
M28-2	51.53	2.28	13.57	11.62	0.19	6.21	10.33	2.48	0.47	0.27	98.95
M29-4	50.42	2.04	12.38	10.87	0.17	10.45	9.74	1.93	0.33	0.20	98.53
M29-5	50.01	1.98	11.98	10.87	0.17	11.57	9.31	2.25	0.32	0.20	98.66
M30-1	48.34	1.37	9.71	10.79	0.17	18.19	7.78	1.48	0.23	0.13	98.19

All major element oxides are strongly negatively correlated with MgO contents in the MgO range 8-27 wt. %, with the exception of iron which remains relatively constant over this range (Figure 4.3a-h). Below 8 wt. % MgO, the TiO_2, FeO*, K_2O, and P_2O_5 concentrations increase sharply while MgO remains more constant. In contrast, CaO, and Al_2O_3 contents decrease below 8 wt. % MgO, and SiO_2 decreases only slightly or remains relatively constant below 8 wt. % MgO. The element oxides SiO_2, CaO, and Al_2O_3 display a steep slope against MgO at >8 wt. %, while the slope of other element oxides is shallower.

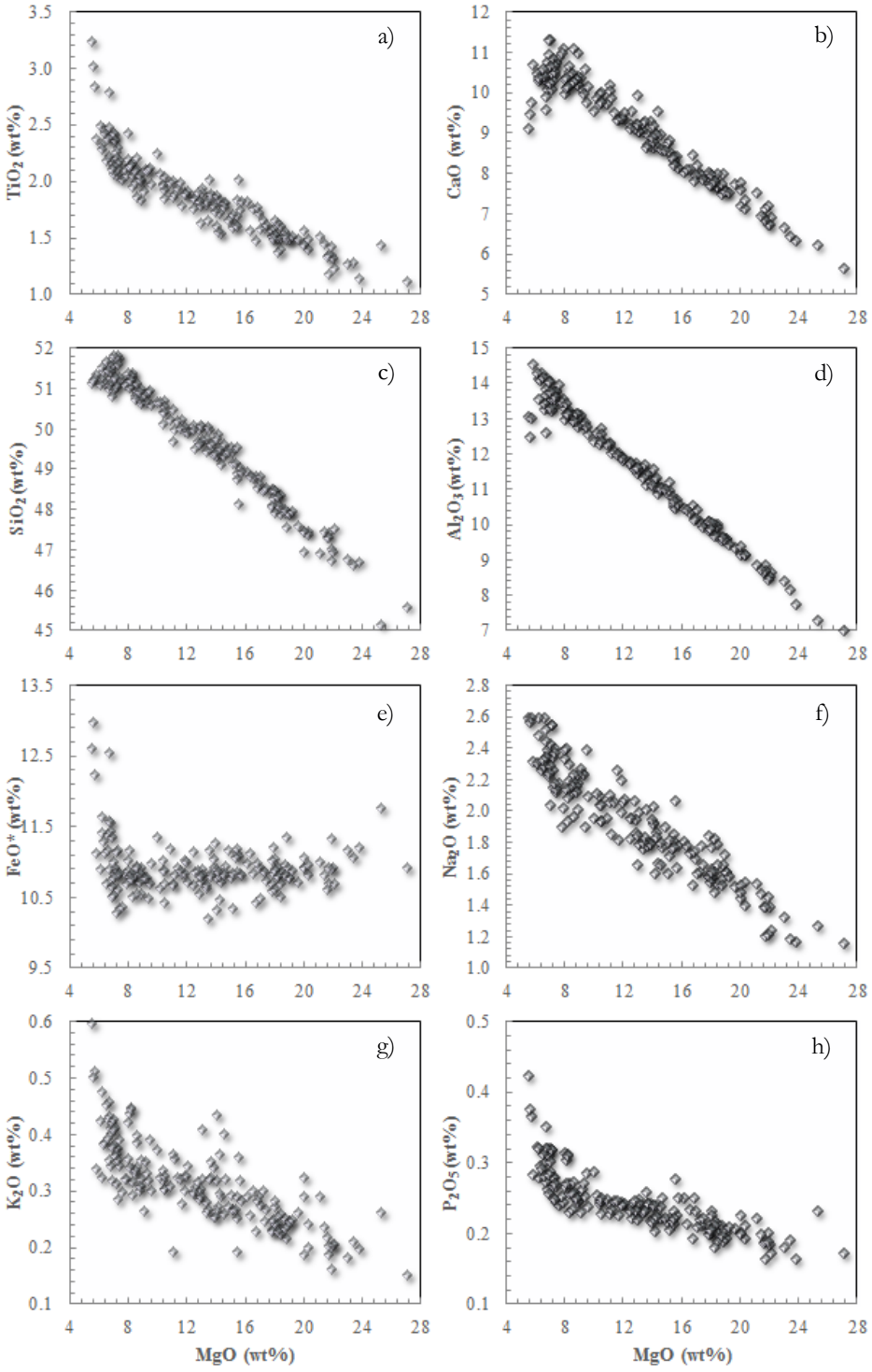

Figure 4.3 Major element oxides versus MgO content (weight %). FeO* is total iron expressed as FeO.

SiO_2 decreases relative to CaO with decreasing MgO content up until 8 wt. % MgO and then CaO decreases relative to SiO_2 (Figure 4.4). The same is seen with SiO_2 relative to Al_2O_3. SiO_2/TiO_2 behaves similarly down to 8 wt. % MgO, where SiO_2 begins to decrease more rapidly

relative to TiO_2. CaO/Al_2O_3 remains relatively constant at high MgO, and then decreases significantly below 8 wt. % MgO, although there may be a slight uptick in CaO/Al_2O_3 at >15 wt. % MgO.

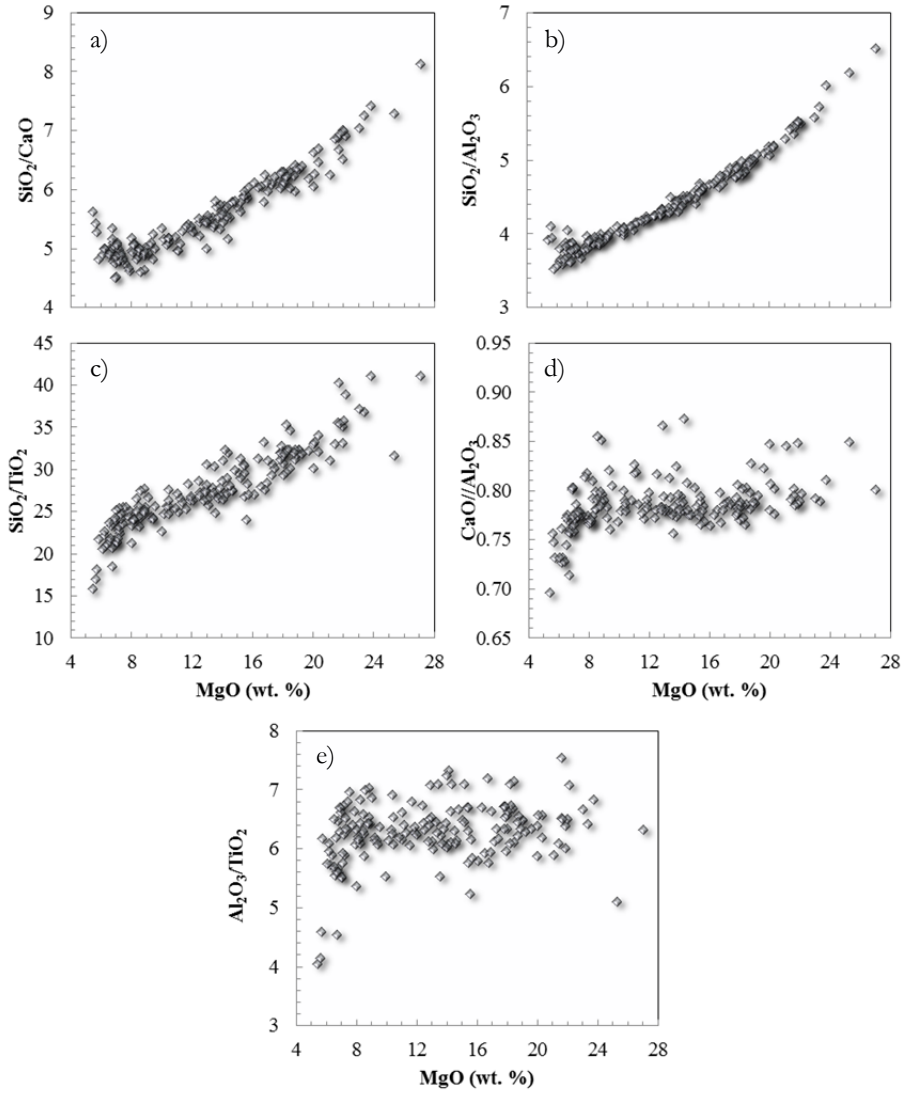

Figure 4.4 major element oxide ratios versus MgO (wt. %).

The major element oxide ratios K_2O/TiO_2 and K_2O/P_2O_5 remain constant with increasing MgO contents, although there is slightly more scatter in the K_2O/P_2O_5 ratio with increasing values of MgO (Figure 4.5).

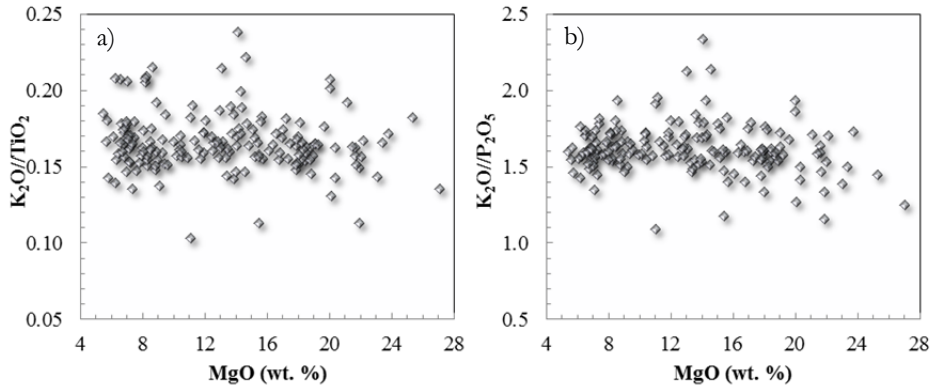

Figure 4.5 Major element oxide ratios against MgO (wt. %).

Box-and-whisker plots (Figure 4.6a-h) show the variation in major elements of samples when broken into dredge locality types (rift zone, landslide, slope, and radial vent). The box-and-whisker plots represent the minimum and maximum value, the values at the 1st and 3rd quartiles, and the median value of the major element oxides. The rift-zone and landslide samples show the greatest range in SiO_2, MgO, CaO, and Al_2O_3, while the landslide and slope samples show the greatest range in $Fe_2O_{3(t)}$, TiO_2, K_2O, and Na_2O. Overall the landslide samples display the greatest variance from the median value. In general the four dredge locality types are very similar in major element-oxide compositions, although the rift-zone samples appear to be slightly higher in MgO and lower in the other oxides compared to the other dredge locality types. Overall, the median MgO value is closer to Q1 than Q3 while the median value for the other oxides is closer to Q3 than Q1. This indicates that the majority of samples have low MgO contents while being high in the other major elements.

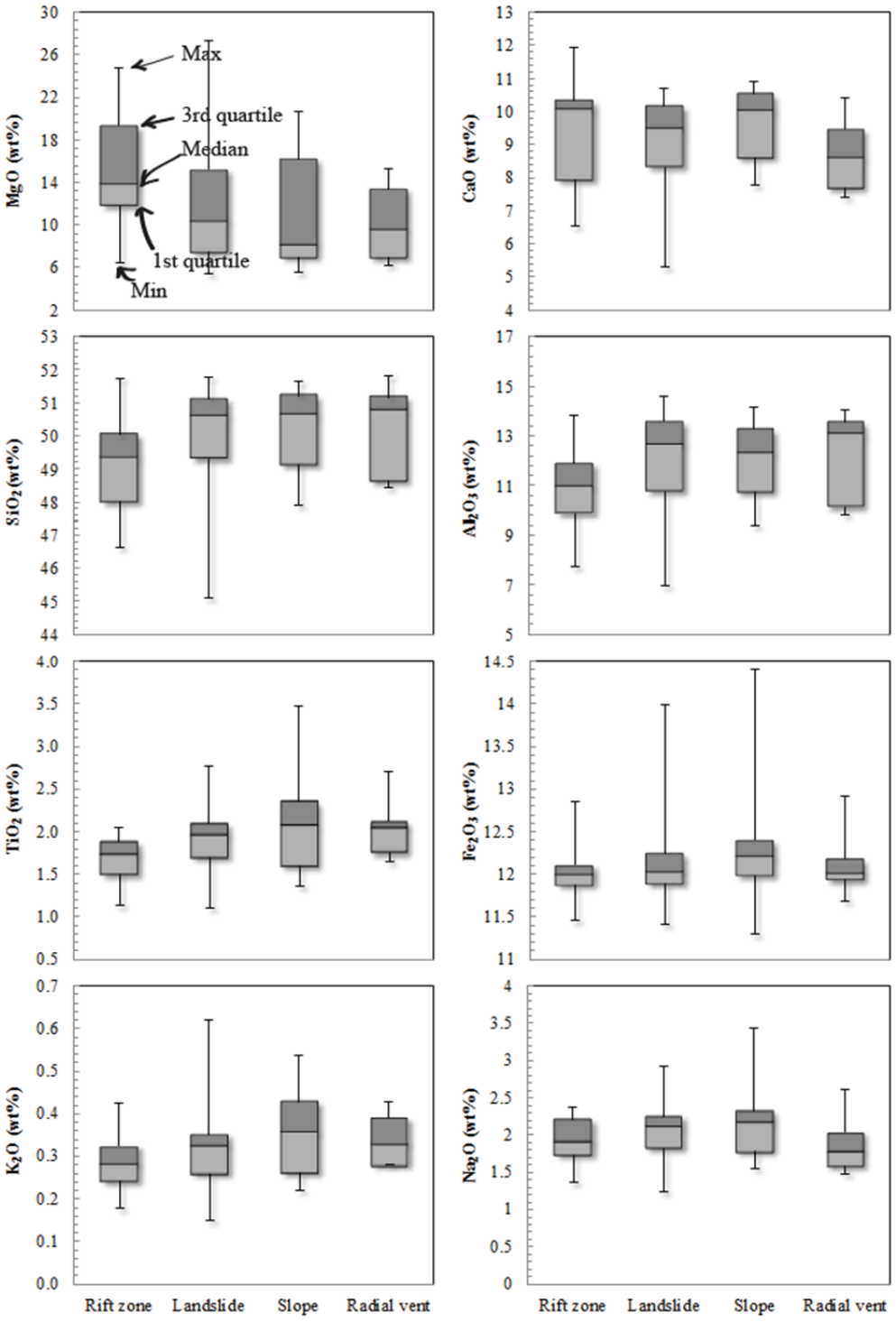

Figure 4.6 Five number summary of Mauna Loa major element data broken out into dredge locality type. Each box-and-whisker shows maximum value, first quartile, median, third quartile, and maximum value.

The same data were then normalized to 15 wt. % MgO and the major element oxides of the samples were plotted, subdivided into dredge locality type (Figure 4.7). The range between the 1st and 3rd quartiles is reduced significantly, while the outliers remain far from the mean. The samples are very similar to one-another in terms of normalised major element oxide composition, with the exception of K_2O and P_2O_5. The slope and vent sample have slightly higher relative K_2O and P_2O_5 concentrations than the rift and landslide samples.

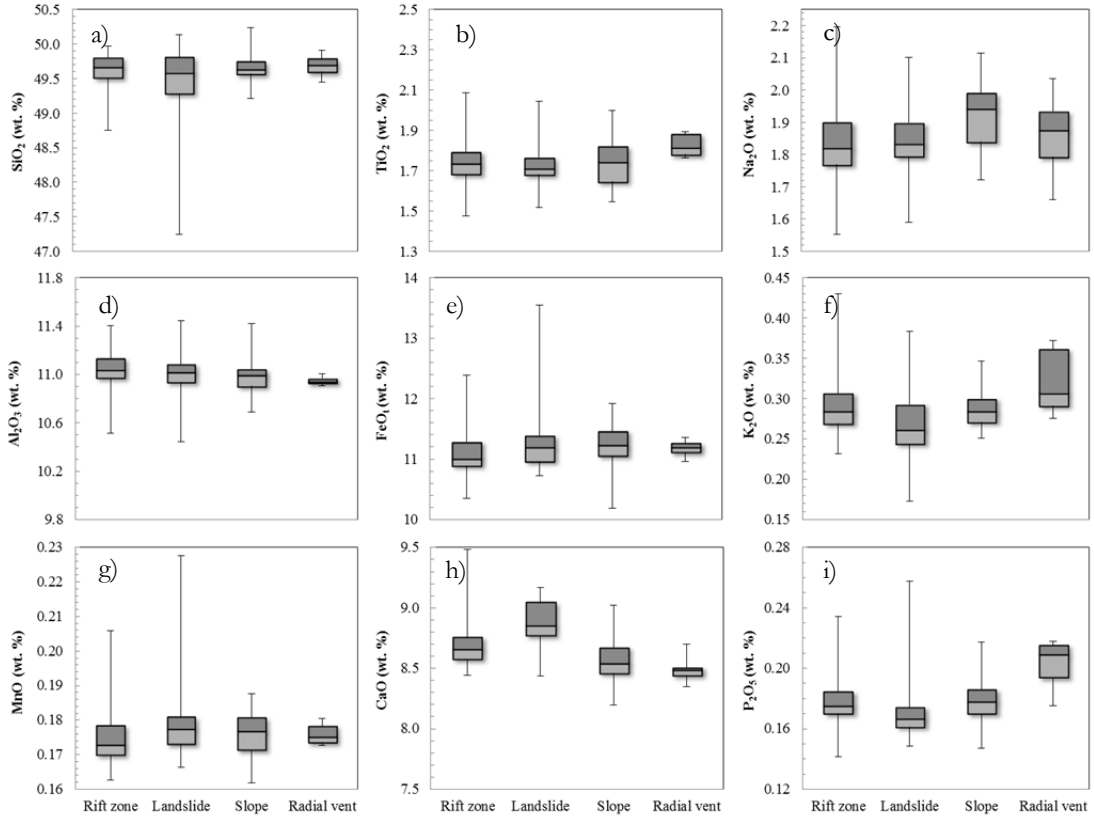

Figure 4.7 Five number summaries (minimum, maximum, median, 1st quartile, and 3rd quartile) of MgO normalised compositions (samples with <7 wt. % MgO excluded as these lie beyond olivine control).

The landslide samples with >8 wt. % MgO have higher CaO/Al_2O_3 ratios compared to the other dredge location types (Figure 4.8). The CaO contents relative to Al_2O_3 contents appears to be what sets the landslide samples apart from the others to the greatest degree, which is mainly due to higher CaO in the landslide samples (Figure 4.7h).

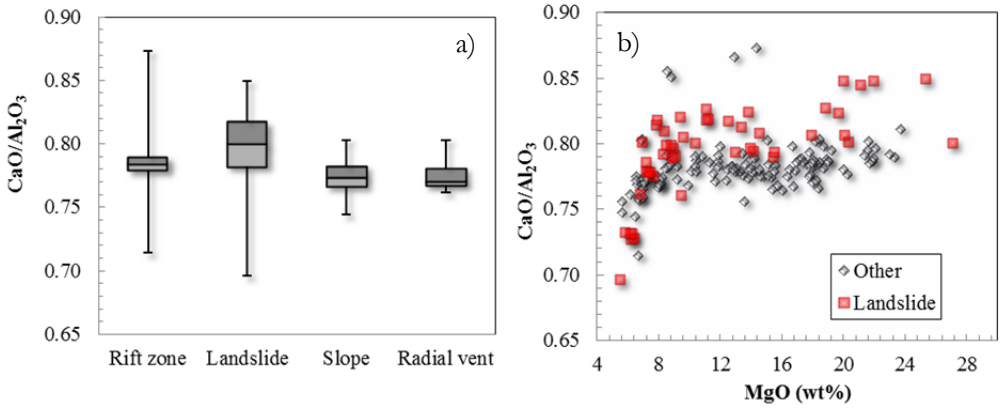

Figure 4.8 CaO/Al_2O_3 versus MgO for landslide samples compared to all other sample location types.

The other major element oxides were normalised to 15 wt. % MgO (an arbitrary value close to the inferred parental magma composition in chapter 7) in order to correct for olivine control, and then plotted to distinguish the landslide samples from the other dredge type localities (Figure 4.9). The correction was performed using Petrolog software which enables the user to add or subtract olivine from a given composition in order to control for olivine accumulation or fractionation. While there is no correlation between most of the olivine-corrected major elements and SiO_2, there is a negative correlation (R^2 = 0.62) in normalised FeO_t with normalised SiO_2.

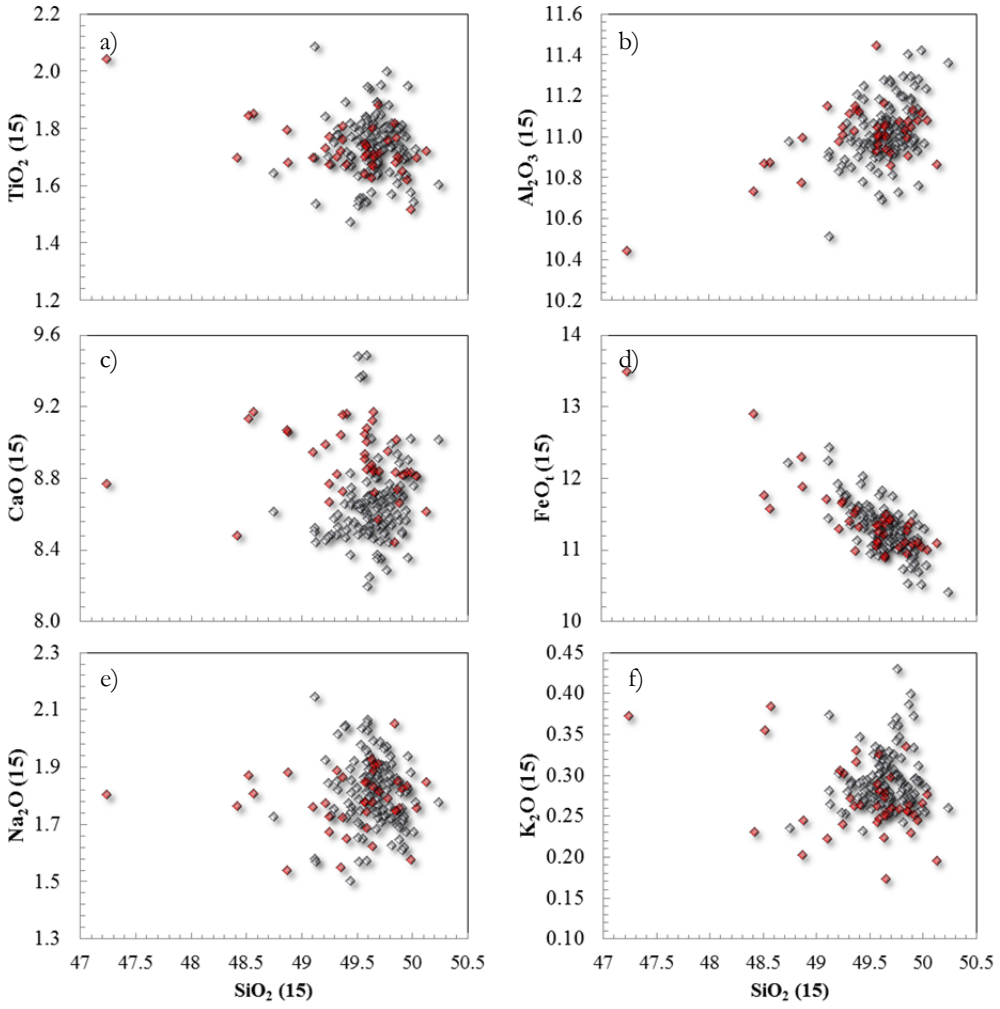

Figure 4.9 Major elements normalized to 15 wt. % MgO with samples containing <7 wt. % MgO removed. Mauna Loa in grey, landslide in red.

An ANOVA (analysis of variance) test was performed to determine if the differences in major element oxide compositions between the four dredge type localities were significant. Results suggest that for MgO, $p<0.05$ meaning the null hypothesis is rejected and two or more means (of the four dredge locality types: slope, landslide, radial vent, or rift zone) are significantly different from one another at the 0.05 level. Given that this variation could be due to olivine control, the same test was applied to the major element oxides after they were normalised for MgO. It was found that there were significant differences between two or more of the means for the oxides SiO_2, TiO_2, CaO, Na_2O, K_2O, and P_2O_5, while there were not significant differences between two or more of the dredge type localities for Al_2O_3 or FeO_t. In order to find out which dredge locality types had means significantly different from each other, a Tukey HSD test was performed for all major element oxides (Table 4.5). A Tukey HSD (honestly

significant data) test is a way of reporting ANOVA results, and determines whether the relationship between two sets of data is statistically significant.

The Tukey test revealed that CaO was the most statistically significant differentiator between the dredge type localities, with significant differences between the slope and rift, slope and landslide, vent and rift, vent and landslide, and rift and landslide. Al_2O_3 and FeO_t were not statistically significant differentiators of the dredge type localities. In terms of dredge localities, the landslide samples were the most different from the other localities, with 10 occasions where they were different from other localities. The next most different were the radial vents, with 8 occasions.

Table 4.5 Tukey HSD test results where sample symbols are S = slope, V = radial vent, R = rift zone, and L = landslide. 'Insignificant' means that the p value was greater than 0.05.

Treatment pairs	Tukey HSD Q statistic	Tukey HSD p-value	Tukey HSD inference	Tukey HSD Q statistic	Tukey HSD p-value	Tukey HSD inference
		SiO_2			**TiO_2**	
S vs V	0.102	0.900	Insignificant	2.573	0.268	Insignificant
S vs R	0.908	0.900	Insignificant	2.162	0.424	Insignificant
S vs L	3.871	0.035	* p<0.05	1.673	0.622	Insignificant
V vs R	0.663	0.900	Insignificant	4.068	0.024	* p<0.05
V vs L	2.615	0.255	Insignificant	3.726	0.046	* p<0.05
R vs L	3.672	0.050	Insignificant	0.338	0.900	Insignificant
		Al_2O_3			**FeO_t**	
S vs V	1.126	0.839	Insignificant	0.348	0.900	Insignificant
S vs R	2.602	0.259	Insignificant	1.930	0.521	Insignificant
S vs L	0.650	0.900	Insignificant	0.883	0.900	Insignificant
V vs R	2.790	0.203	Insignificant	0.806	0.900	Insignificant
V vs L	1.577	0.660	Insignificant	0.929	0.900	Insignificant
R vs L	2.048	0.473	Insignificant	3.162	0.119	Insignificant
		CaO			**Na_2O**	
S vs V	1.800	0.572	Insignificant	2.402	0.328	Insignificant
S vs R	4.286	0.015	* p<0.05	5.525	0.001	** p<0.01
S vs L	9.010	0.001	** p<0.01	4.976	0.003	** p<0.01
V vs R	4.538	0.009	** p<0.01	0.805	0.900	Insignificant
V vs L	7.691	0.001	** p<0.01	0.762	0.900	Insignificant
R vs L	6.185	0.001	** p<0.01	0.021	0.900	Insignificant
		K_2O			**P_2O_5**	
S vs V	3.557	0.062	Insignificant	5.184	0.002	** p<0.01
S vs R	1.227	0.799	Insignificant	2.257	0.385	Insignificant
S vs L	2.657	0.242	Insignificant	3.973	0.029	**p<0.05
V vs R	3.052	0.140	Insignificant	6.916	0.001	** p<0.01
V vs L	5.375	0.001	** p<0.01	7.898	0.001	** p<0.01
R vs L	4.534	0.009	** p<0.01	2.328	0.357	Insignificant

4.2 Modal mineralogy

Modal mineralogy and petrographic descriptions were collected by Michael Garcia at the University of Hawaii on a collaborative basis. The descriptions in the tables below contain the verbatim petrographic descriptions of Garcia, so some abbreviations were used. These include: points = the number of points in each sample analysed, mph = microphenocrysts, ol = olivine, plag = plagioclase, med = medium, and phenos = phenocrysts (crystals >1mm).

Table 4.6 Petrographic descriptions and EMP points (Garcia, unpublished data) of samples. Modal abundances are in vol. % and % olivine and plagioclase are phenocrysts only.

Sample #	Olivine	% Plag	% Vesicles	Points	Notes
M1-1	30.0	-	2	100	rare plag mph; vesicular
M1-2	5.5	-	-	73	plag mph; many small olivines
M1-3	4.0	-	-	100	
M1-4	3.1	-	-	65	
M1-5	6.7	-	-	30	
M1-6	20.0	-	-	80	plag mph
M1-7	20.0	-	-	100	tiny matrix plag
M1-8	16.0	-	-	100	elongate ol
M1-9	5.0	-	-	100	
M1-10	22.9	-	-	35	many small ol
M1-11	20.5	-	-	88	elongate ol
M1-12	16.0	-	-	100	elongate ol
M1-13	19.0	-	-	100	many small vesicles
M1-14	10.0	-	-	100	
M1-15	6.7	-	-	30	
M1-16	20.0	-	-	100	many small ol; many small vesicles
M1-17	13+	-	-	100	many small ol; small vesicles; elongate ol
M1-18	12.9	-	-	70	
M1-19	13.0	-	-	100	
M1-20	11.0	-	-	100	many small vesicles
M1-21	18.9+	-	-	90	some small vesicles; many small ol
M1-22	23.0	-	-	100	few small vesicles
M1-23	16.3	-	-	80	few small vesicles; many small ol
M1-24	11.1(+?)	-	-	36	non vesicular
M1-25	13.3	-	-	15	Gabbroic
M1-26	17+	-	-	100	Dunite xenolith; many small ol
M1-27	7.5	-	-	80	small ol
M1-28	7.0	-	18	100	large vesicles; altered (red) ol
M1-29	21.0	-	-	100	some small vesicles
M1-30	1.0	<1	-	-	dike rock
M2-1	25.0	-	-	100	elongate ol; small vesicles
M2-2	22.0	-	-	100	small vesicles; ol altered (red)
M2-3	18.0	-	-	100	many small vesicles; elongate ol
M2-4	24.0	-	-	100	many small vesicles; few elongate ol
M2-5	14.0	-	-	100	some small vesicles
M2-6	22.5	-	-	80	elongate ol; some small vesicles
M2-7	14.4	-	-	90	some very small vesicles; elongate ol
M2-8	20.0	-	-	90	some small vesicles
M2-9	9.0	-	-	100	some small vesicles
M2-10	11.0	-	-	100	many elongate ol
M2-11	18.0	-	-	100	few small vesicles

Table 4.7 Petrographic descriptions and EMP points (Garcia, unpublished data) of samples. Modal abundances are in vol. % and % olivine and plagioclase are phenocrysts only.

Sample #	Olivine	% Plag	Vesicles	Points	Notes
M2-12	17.9	-	-	95	
M2-13	18.0	-	-	100	
M2-14	13.3	-	-	60	small vesicles
M2-15	15.0	-	-	100	
M2-16	24.7	-	-	73	few small vesicles
M2-17	10.0	-	-	90	
M2-18	10.0	-	2	100	some med. vesicles; diktytaxitic
M2-19	33.0	-	-	100	small vesicles; large ol
M2-20	30.0	-	-	100	small vesicles; large ol
M2-21	27.0	-	-	100	small vesicles; large ol
M2-22	30.0	-	-	40	many small vesicles; med. ol
M2-23	23.0	-	-	100	many small vesicles; plag in matrix
M2-24	28.4	-	-	95	some small vesicles; med. ol
M2-25	33.3	-	-	70	
M2-26	23.0	-	-	100	some small vesicles
M2-27	29.0	-	-	100	
M3-1	17.0	-	-	100	small vesicles; few elongate ol;
M3-2	18.0	-	-	100	few small vesicles; elongate ol
M3-3	20.0	-	-	100	small vesicles; elongate ol
M3-4	17.0	-	-	100	few small vesicles; elongate ol;
M3-5	17.0	-	-	100	many small vesicles (diktytaxitic); elong ol
M3-6	24.0	-	-	75	small vesicles (diktytaxitic); elongate ol
M3-7	17.0	-	-	100	many small vesicles; elongate ol; plag
M3-8	15.0	-	-	100	many small vesicles; elongate ol
M3-9	14.0	-	-	100	many small vesicles; elongate ol; plag
M3-10	13.7	-	-	95	some small vesicles; elongate ol
M3-11	15.0	-	-	40	v. few small vesicles; elongate ol
M3-12	25.0	-	-	100	elongate ol
M3-13	21.0	-	-	100	few (if any) elongate ol; plag in matrix
M3-14	11.0	-	-	100	some small vesicles; some elongate ol; plag
M4-1	19.0	-	-	100	elongate ol; many small vesicles; plag
M4-2	20.0	-	-	100	some small vesicles; plag
M4-3	20.0	-	-	100	elongate ol; few small vesicles
M4-4	20.0	-	3	60	v. large ol; large vesicles
M4-5	15.3	-	-	85	many small vesicles
M4-6	18.9	-	-	90	some elongate ol
M4-7	33.0	-	-	100	picrite
M4-8	15.0	-	-	100	elongate ol; some small vesicles
M4-9	25.0	-	-	100	big ol; small vesicles
M4-10	9.0	-	-	100	elongate ol; many tiny vesicles
M4-11	12.0	-	-	100	some elongate ol; some tiny vesicles

Table 4.8 Petrographic descriptions and EMP points (Garcia, unpublished data) of samples. Modal abundances are in vol. % and % olivine and plagioclase are phenocrysts only.

Sample #	Olivine	% Plag	Vesicles	Points	Notes
M4-12	9.2	-	-	65	many small vesicles; plag rich matrix
M4-13	6.0	-	-	100	many tiny vesicles; many elongate ol
M4-14	11.0	-	-	100	plag matrix; some small vesicles
M4-15	7.0	-	-	100	Pyroxene; many tiny vesicles
M4-16	7.0	-	-	100	some small vesicles; small elongate ol
M4-17	12.0	-	-	100	small vesicles diktytaxitic; small elong ol
M4-18	11.0	-	-	100	some small vesicles; elongate ol
M4-19	22.0	-	-	50	small vesicles
M4-20	7.8	-	-	90	some small diktytaxitic vesicles
M4-21	4.4	-	-	90	small vesicles; elongate ol
M4-22	11.4	-	-	70	some tiny vesicles; some tiny elongate ol
M6-1	7.0	-	-	100	elongate ol; plag mph
M6-2	5.0	2	-	100	elongate ol; plag and plag mph
M6-3	5.0	1	-	100	elongate ol; plag and plag mph
M6-4	7.0	2	-	100	elongate ol; plag and plag mph
M6-5	8.0	3	-	100	elongate ol; plag and plag mph
M6-6	4.0	-	-	100	plag and plag mph
M6-7	3.0	1	-	100	elongate ol; plag and plag mph
M6-8	3.0	1	-	100	plag
M6-9	4.4	1.1	-	90	elongate ol; plag
M6-10	4.0	1	-	100	plag
M6-11	5.0	-	-	100	elongate ol; plag
M6-12	-	-	9	100	highly vesicular (3 sizes); ol
M6-13	18.0	-	-	100	elongate ol
M6-14	17.0	-	-	100	elongate ol
M6-15	15.0	-	-	100	elongate ol; tiny vesicles
M6-16	2.0	-	-	100	plag mph
M6-17	3.2	1.6	-	63	plag mph
M6-18	1.3	-	-	80	plag
M6-19	2.9	-	-	70	plag
M6-20	1.1	-	-	95	plag and plag mph; elongate ol
M6-21	2.5	-	-	80	elongate ol; plag mph
M6-22	3.2	-	-	94	elongate ol; plag and plag mph
M6-23	2.0	-	-	100	plag and plag mph
M6-24	4.0	2	-	50	plag
M6-25	1.1	-	-	95	elongate ol; plag mph
M6-26	3.0	-	-	100	elongate ol; plag mph
M6-27	3.0	1	-	100	elongate ol; plag and plag mph
M6-28	1.0	1	-	100	plag; elongate ol
M6-29	3.0	2	-	100	plag and plag mph
M6-30	4.2	2.1	-	95	plag

Table 4.9 Petrographic descriptions and EMP points (Garcia, unpublished data) of samples. Modal abundances are in vol. % and % olivine and plagioclase are phenocrysts only.

Sample #	Olivine	% Plag	Vesicles	Points	Notes
M6-31	2	-	-	100	plag mph
M6-32	10	-	-	90	
M6-33	6	1	-	100	elongate ol; plag mph
M8-1	2.0	-	-	100	plag mph in matrix
M8-2	5.0	-	-	100	plag mph in matrix
M8-3	5.0	-	-	100	plag mph in matrix
M8-4	9.0	-	2	100	elongate ol; diktytaxitic vesicles
M8-5	8.0	-	1	100	plag; small diktytaxitic vesicles
M8-6	8.0	-	1	50	small diktytaxitic vesicles
M8-7	1?	-	-	75	plag mph; ol mph
M8-8	2.0	-	-	100	plag mph; ol mph
M9-1		-		-	Not cut
M9-2	2.5	-	22.5	40	large and small vesicles; small ol
M9-3	-	-	15	80	partially oxidized; mph of ol and plag
M9-4	1?	-	17.1	70	vesicles are layered by size; ol mph
M9-5	-	-	14.3	70	vesicles all the same size
M9-6	-	-	20	100	vesicles of similar size; ol mph
M9-7	-	-	22.2	63	like #2
M9-8	2.9	-	15.7	70	like #6
M9-9	-	-	6.67	75	similar to #3
M9-10	-	-	13.3	90	vesicles layered by size (like #4)
M9-11	1.4	-	20	70	ol mph
M9-12	1.5?	-	8.33	60	oxidized; ol mph
M9-13	2.0	-	15	100	ol mph
M9-14	-	-	19	100	ol mph; large vesicles
M9-15	1.0	-	12	100	small and large vesicles; ol mph
M9-16	1.0	-	12	100	small and large vesicles; ol mph
M10-1	-	-	-	-	Breccia: various basalt clasts and matrix
M10-2	-	-	-	-	Breccia: poorly sorted clasts fine matrix
M10-3	-	-	-	-	Breccia: poorly sorted large basalt clasts
M10-4	8.3	1.67	-	60	plag rich matrix; plag phenos
M10-5	11.4	1.43	-	70	plag rich matrix; plag; chrome-diopside
M10-6	-	-	15	100	weathered; two populations of vesicles
M10-7	3.0	-	12	100	many medium/small vesicles; oxidized ol
M10-8	-	-	18	100	highly vesicular; slightly diktytaxitic
M10-9	-	-	1.1	90	weakly phyric; small diktytaxitic vesicles
M10-10	-	-	2	100	weakly phyric; large diktytaxitic vesicles
M10-11	2.0	-	4	100	weakly phyric; small diktytaxitic vesicles
M10-12	-	-	-	100	weakly phyric; diktytaxitic; plag-rich matrix
M10-13	-	-	-	100	weakly phyric; plag rich matrix
-	-	-	-	-	-

Olivine: The petrography of 145 representative samples reveals the majority contain 0-5% olivine (n=44), 24 samples contain 5-10%, 24 samples contain 10-15%, 28 contain 15-20%, 16 contain 20-25% and nine samples contain greater than 25% olivine with the maximum amount of modal olivine at 33.3% (Figure 4.10).

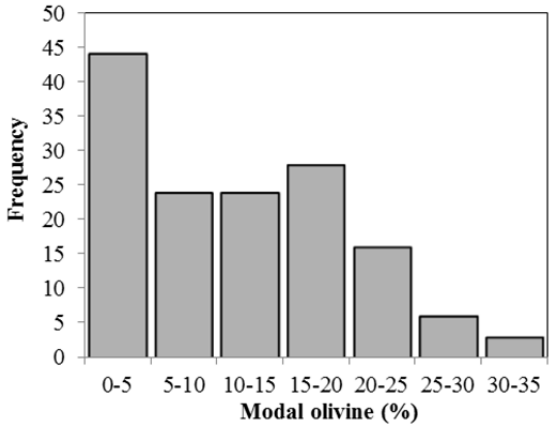

Figure 4.10 Modal olivine from petrographic observations, courtesy of M. O. Garcia at the University of Hawaii.

Plagioclase: 18 samples contain up to 3% modal plagioclase (e.g. M6-5 contains 3%), while most contain no identifiable plagioclase (Table 4.8).

Spinel: 'minor' spinel was observed in most samples (pers. comm. M. O. Garcia, 2017).

4.3 CIPW normative mineralogy

Normative olivine: The CIPW normative mineralogy was calculated for samples which have major element and trace element analyses using the Excel-macro of Kurt Hollocher which is based on the pioneering work by Cross, Iddings, Pirsson, and Washington (Cross et al., 1902) (Figure 4.11). The assumed ratio of Fe^{3+}/Fe_{total} was 0.1.

Table 4.10 Calculated CIPW normative mineralogy with mineral proportions in vol. %. Not shown are minor amounts of chromite, zircon, and apatite (<1% total).

	Olivine	Plag (Al+An)	Opx	Quartz	Cpx	K-feld	Ilmenite	Magnetite
M1-1	30	29	20	0.00	12	1.42	1.42	1.08
M1-2	0	49	23	1.60	22	2.55	2.30	1.02
M1-6	5	43	26	0.00	19	2.20	2.02	1.03
M1-8	8	40	28	0.00	16	2.06	2.09	1.04
M1-9	0	48	22	2.24	22	2.84	2.32	1.02
M1-13	25	33	23	0.00	12	1.35	1.47	1.03
M1-14	10	41	24	0.00	19	2.06	1.93	1.04
M1-16	13	39	26	0.00	15	1.63	1.84	1.00
M1-20	10	42	25	0.00	16	1.91	1.98	0.99
M1-26	25	32	22	0.00	12	1.49	1.53	1.03
M1-27	0	48	28	0.88	18	2.20	2.31	1.00
M1-30	0	52	20	4.67	19	2.48	2.53	0.99
M2-2	23	35	21	0.00	13	2.06	1.80	1.05
M2-3	16	38	24	0.00	15	2.13	2.07	1.04
M2-4	20	37	22	0.00	14	1.77	1.93	1.06
M2-10	1	45	32	0.00	16	1.99	2.22	1.04
M2-12	5	44	29	0.00	16	1.99	2.25	1.03
M2-18	3	44	30	0.00	16	2.13	2.30	1.03
M2-19	28	33	19	0.00	12	1.42	1.68	1.05
M2-20	29	30	20	0.00	11	1.49	1.59	1.06
M2-21	25	33	21	0.00	13	1.56	1.67	1.03
M2-23	21	37	21	0.00	14	1.77	1.85	1.04
M2-24	18	38	24	0.00	13	1.63	1.88	1.03
M2-26	11	40	26	0.00	15	2.27	2.17	1.04
M2-27	21	37	20	0.00	14	1.77	1.85	1.04
M3-1	9	42	27	0.00	15	2.27	2.25	1.05
M3-2	10	42	23	0.00	16	3.12	2.28	1.04
M3-3	9	42	25	0.00	16	2.62	2.28	1.04
M3-4	7	42	28	0.00	16	2.41	2.31	1.05
M3-5	7	43	28	0.00	15	2.55	2.32	1.04
M3-6	17	38	24	0.00	14	1.70	1.96	1.06
M3-7	8	41	28	0.00	15	2.84	2.26	1.04
M3-12	27	33	20	0.00	12	1.49	1.64	1.05
M3-13	26	33	21	0.00	12	1.42	1.67	1.05
M4-3	7	43	27	0.00	16	2.34	2.33	1.04
M4-7	24	35	20	0.00	13	1.70	1.85	1.04
M4-8	22	38	18	0.00	15	1.84	1.99	1.04
M4-9	26	33	19	0.00	13	1.70	1.79	1.04
M4-13	7	44	25	0.00	17	2.27	2.41	1.04
M4-14	5	43	29	0.00	16	2.91	2.36	1.04
M4-15	11	44	22	0.00	17	2.27	2.33	1.04
M4-21	31	32	17	0.00	12	1.28	1.57	1.07
M6-1	0	50	25	0.89	19	2.48	2.62	1.04

Table 4.11 Calculated CIPW normative mineralogy with mineral proportions in vol. %. Not shown are minor amounts of chromite, zircon, and apatite (<1% total).

	Olivine	Plag (Al+An)	Opx	Quartz	Cpx	K-feld	Ilmenite	Magnetite
M6-5	0	50	25	0.92	18	2.34	2.60	1.04
M6-6	0	51	20	4.31	19	2.91	2.98	1.11
M6-13	21	40	18	0.00	15	1.77	1.89	1.04
M6-14	17	38	25	0.00	14	1.63	1.95	1.06
M6-26	0	51	20	4.49	19	2.91	2.99	1.10
M6-27	0	52	18	3.15	20	3.05	2.99	1.09
M6-28	0	51	20	4.20	19	2.98	2.98	1.09
M6-32	7	43	27	0.00	16	2.27	2.51	1.07
M8-1	0	52	20	2.77	20	2.69	2.85	1.07
M8-5	0	51	22	2.25	19	2.55	2.73	1.05
M8-8	0	52	20	3.52	19	2.62	2.83	1.08
M9-15	0	53	20	3.40	19	2.13	2.51	0.99
M9-16	0	54	18	3.59	20	2.41	2.73	1.03
M10-9	0	55	19	3.37	18	2.34	2.89	1.09
M10-13	0	49	24	2.02	19	2.20	2.49	1.04
M11-5	0	51	18	5.81	16	4.25	4.05	1.21
M11-11	2	47	25	0.00	20	1.35	2.31	1.03
M11-13	7	45	24	0.00	18	2.20	2.31	1.04
M12-2	23	37	17	0.00	15	1.56	1.84	1.09
M12-3	0	48	24	2.40	20	2.27	2.62	1.01
M12-4	0	53	19	5.19	18	2.69	3.07	1.09
M12-12	27	32	20	0.00	13	1.13	1.77	1.09
M12-14	0	54	19	4.70	17	2.77	3.02	1.07
M12-15	0	48	26	0.96	19	2.13	2.47	1.05
M12-17	0	52	18	4.97	21	2.27	2.70	1.01
M12-18	8	43	25	0.00	18	1.77	2.21	1.06
M12-19	0	51	21	3.30	21	2.27	2.54	1.03
M12-27	0	51	24	0.81	20	1.84	2.38	1.04
M12-29	0	50	24	0.77	20	2.27	2.52	1.05
M12-34	1	48	27	0.00	19	2.27	2.46	1.06
M12-42	0	50	21	4.23	20	2.27	2.63	1.04
M13-2	0	55	17	5.24	18	2.41	2.95	1.07
M13-4	0	50	25	0.43	18	2.77	2.63	1.03
M13-5	0	52	20	3.95	19	2.69	2.75	1.04
M13-9	0	51	22	2.92	20	2.13	2.42	1.01
M13-12	23	36	19	0.00	15	1.84	1.85	1.03
M13-14	6	42	30	0.00	16	1.91	1.93	1.04
M13-15	0	52	20	3.70	19	2.77	2.70	1.04
M13-21	26	35	15	0.00	15	2.34	1.95	1.05
M13-25	39	28	10	0.00	12	1.84	1.78	1.13
M13-27	4	47	23	0.00	20	2.62	2.49	1.03
M13-29	2	45	28	0.00	19	2.55	2.36	1.04

Table 4.12 Calculated CIPW normative mineralogy with mineral proportions in vol. %. Not shown are minor amounts of chromite, zircon, and apatite (<1% total).

	Olivine	Plag (Al+An)	Opx	Quartz	Cpx	K-feld	Ilmenite	Magnetite
M13-33	40	27	14	0.00	10	1.06	1.38	1.04
M13-35	0	54	18	4.99	18	3.05	3.11	1.05
M13-38	29	34	14	0.00	15	2.06	1.88	1.05
M13-39	0	50	23	2.33	20	2.41	2.49	1.04
M13-40	13	41	24	0.00	16	2.06	2.28	1.07
M14-3	17	38	24	0.00	15	1.63	1.89	1.04
M14-4	6	43	27	0.00	17	1.91	2.27	1.03
M14-5	0	50	24	1.77	20	2.13	2.52	1.04
M14-16	0	50	22	2.65	20	2.27	2.56	1.04
M14-21	23	35	21	0.00	13	1.42	1.74	1.05
M14-27	24	36	19	0.00	14	1.35	1.78	1.06
M14-28	10	42	25	0.00	17	1.84	2.20	1.04
M14-31	0	53	19	4.53	20	2.20	2.56	0.98
M14-32	10	41	27	0.00	16	1.35	2.10	1.04
M17-1	20	38	20	0.00	15	1.56	1.74	1.01
M17-2	0	52	19	3.33	19	2.98	3.02	1.05
M17-6	0	51	22	2.73	19	2.41	2.70	1.04
M17-7	22	37	19	0.00	14	1.70	1.89	1.05
M17-8	0	51	18	4.98	19	3.69	3.56	1.18
M17-11	4	45	28	0.00	17	2.13	2.26	1.02
M17-15	9	44	24	0.00	17	1.84	2.00	0.99
M17-16	21	36	21	0.00	14	1.77	1.88	1.04
M17-17	7	45	24	0.00	17	2.27	2.37	1.04
M17-18	0	46	28	1.75	17	2.69	2.79	1.09
M17-32	0	52	19	4.14	19	2.91	3.02	1.05
M17-33	0	53	19	2.82	20	2.55	2.94	1.04
M17-38	6	44	27	0.00	17	1.91	2.06	0.98
M17-40	0	50	22	3.06	19	2.98	3.01	1.04
M17-41	0	50	21	3.78	19	3.26	3.47	1.21
M17-43	0	50	18	5.50	19	3.62	3.78	1.25
M17-44	0	52	20	3.48	20	2.55	2.67	1.04
M18-2	3	46	27	0.00	18	2.34	2.41	1.05
M18-9	0	47	28	0.00	18	2.41	2.47	1.05
M18-12	6	46	23	0.00	18	2.34	2.36	1.06
M18-16	17	39	22	0.00	15	1.77	1.99	1.04
M18-17	0	50	23	2.05	19	2.41	2.62	1.05
M18-19	19	37	22	0.00	14	1.70	1.88	1.04
M18-21	0	50	23	2.35	19	2.41	2.60	1.04
M18-25	5	46	26	0.00	18	2.34	2.36	1.06
M18-28	0	48	27	0.55	18	2.34	2.57	1.02
M18-29	0	50	24	2.14	19	2.20	2.56	1.03
M18-31	19	38	22	0.00	14	1.70	1.86	1.05
M18-32	14	39	24	0.00	15	2.13	2.19	1.04

Table 4.13 Calculated CIPW normative mineralogy with mineral proportions in vol. %. Not shown are minor amounts of chromite, zircon, and apatite (<1% total).

	Olivine	Plag (Al+An)	Opx	Quartz	Cpx	K-feld	Ilmenite	Magnetite
M18-33	16	38	24	0.00	14	1.91	2.02	1.04
M18-34	19	38	22	0.00	14	1.70	1.90	1.05
M18-35	0	53	20	3.28	17	3.05	3.09	1.11
M18-36	0	51	23	2.78	19	2.41	2.65	1.07
M19-1	14	39	25	0.00	15	1.99	1.96	1.01
M19-2	0	46	24	0.00	18	2.48	2.38	1.03
M19-4	18	38	22	0.00	14	1.63	1.89	1.02
M19-5	20	39	19	0.00	15	1.91	1.89	1.02
M19-11	9	43	25	0.00	16	2.13	2.14	1.01
M19-17	0	50	23	2.08	20	2.77	2.74	1.04
M19-18	11	42	25	0.00	15	1.91	2.12	1.04
M19-20	0	53	18	4.65	20	2.55	2.78	1.05
M19-21	3	46	27	0.00	17	2.13	2.35	1.04
M19-22	0	52	19	5.11	19	2.84	2.96	1.08
M19-23	0	48	28	0.32	18	2.13	2.41	1.03
M19-24	6	45	26	0.00	17	2.06	2.28	1.04
M19-28	17	42	18	0.00	16	2.55	2.52	1.07
M21-1	10	43	24	0.00	17	1.84	2.16	1.08
M21-11	5	44	28	0.00	17	2.06	2.22	1.04
M21-15	0	52	20	5.03	19	2.06	2.62	1.02
M22-4	17	37	24	0.00	14	1.99	2.06	1.04
M22-11	15	39	24	0.00	14	2.06	2.15	1.05
M22-17	15	39	24	0.00	14	1.99	2.21	1.06
M22-20	13	40	24	0.00	14	2.06	2.26	1.05
M22-21	12	41	26	0.00	15	1.99	2.27	1.04
M24-1	0	49	23	4.54	18	3.19	2.67	1.04
M24-3	0	51	22	1.98	19	3.12	2.65	1.04
M24-5	0	51	19	5.92	19	3.05	2.58	1.01
M24-8	0	50	23	3.63	18	3.19	2.68	1.04
M26-1	11	41	26	0.00	15	1.91	2.01	1.06
M26-10	0	54	18	4.50	19	3.19	2.72	1.03
M26-14	17	37	24	0.00	14	1.77	1.85	1.08
M26-16	15	40	23	0.00	15	1.84	1.95	1.07
M26-18	5	45	27	0.00	17	2.13	2.19	1.07
M26-43	11	42	24	0.00	16	1.91	2.06	1.07
M26-44	12	41	25	0.00	15	1.77	2.01	1.08
M27-2	0	53	18	2.38	21	2.69	2.64	1.03
M27-11	0	53	18	2.61	21	2.69	2.62	1.02
M27-32	1	46	29	0.00	18	2.20	2.47	1.07
M28-2	0	52	18	3.86	20	3.40	2.84	1.11
M29-4	0	47	29	0.76	18	2.34	2.56	1.04
M29-5	6	47	23	0.00	18	2.27	2.47	1.04
M30-1	17	37	25	0.00	14	1.63	1.72	1.04

CIPW normative calculations reveal a large range in normative olivine from 0-39.6 vol. %. 68 out of the 172 samples are silica-oversaturated with no normative olivine and up to 5.9 vol. % normative quartz, while 104 samples are silica-saturated with no normative quartz and up to 39.6 vol. % olivine. Only four samples have normative olivine over 30 vol. %, while the majority of those with olivine contain between 5-10 vol. % (n = 24) (Figure 4.11a).

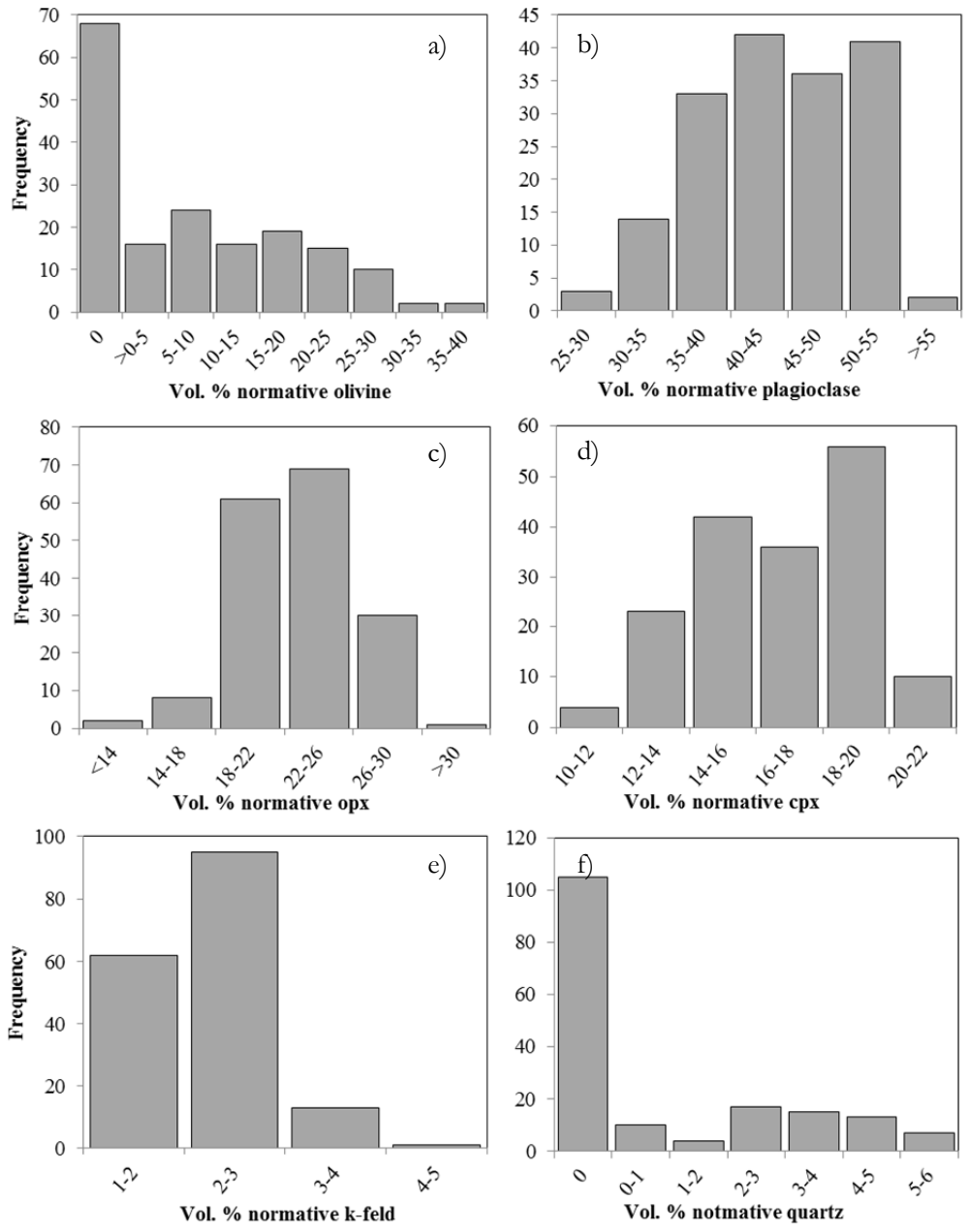

Figure 4.11 CIPW normative proportions (vol. %) of a) olivine, b) plagioclase (albite + anorthite), c) orthopyroxene (hypersthene), d) clinopyroxene (diopside), e) potassium feldspar (orthoclase), and f) quartz.

Feldspar: plagioclase feldspars (albite + anorthite) have the highest normative abundance of any mineral within these samples, comprising up to 55.2 vol. %. The percentage of plagioclase ranges from 26.8 – 55.2 vol. %, with the majority of samples containing 40-45 vol. %. The Ab/An ratio ranges from 0.56 - 1.03. Orthoclase feldspar makes up a much smaller proportion of the normative mineralogy, ranging from 1.1 – 4.3 vol. %.

Pyroxene: CIPW calculations show a significant proportion of hypersthene (10-32 vol. %) and diopside (10-22 vol. %), showing that melts vary in their relative proportions of Ca to Mg. The majority of samples contain between 22-26 vol. % hypersthene and between 18-20 vol. % diopside.

Quartz: normative quartz is absent from 105 out of the 172 samples, suggesting most are silica-saturated, rather than silica-oversaturated. The rest of the samples which contain normative quartz most frequently contain 2-3 vol. %, however some contain up to 5.9 vol. %.

There is a positive correlation between CIPW normative olivine abundance and whole rock MgO contents (Figure 12c) and a positive correlation between modal olivine proportion and whole rock MgO content (Figure 12b). The normative olivine is positively correlated ($R^2 = 0.54$) to modal olivine (Figure 12a).

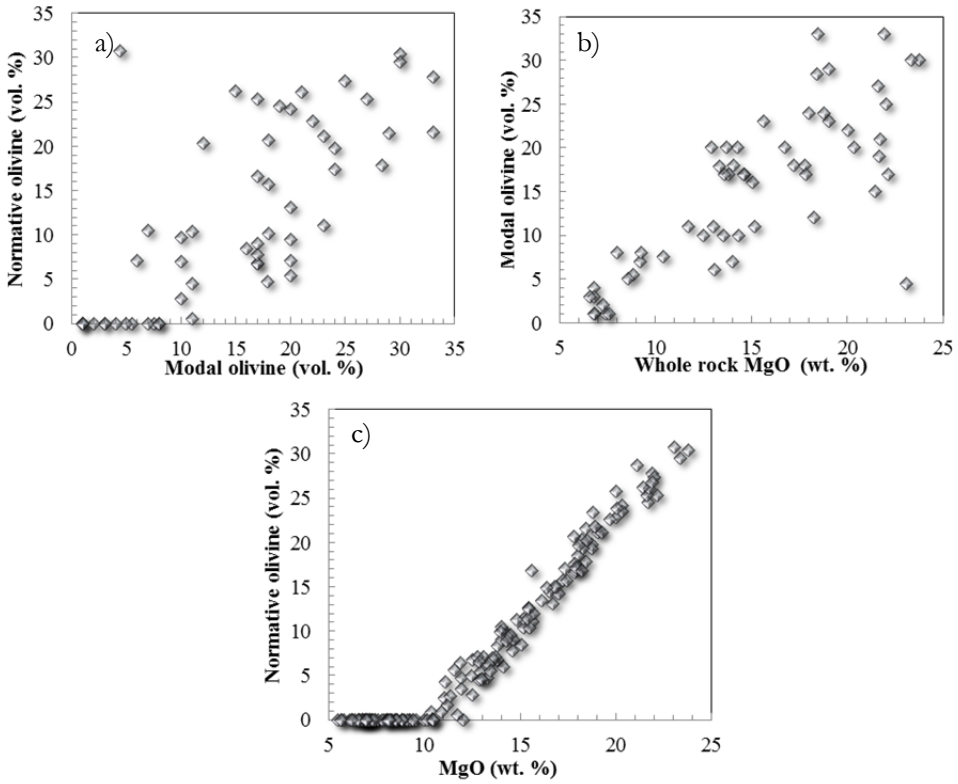

Figure 4.12 a) Normative olivine versus modal olivine content, b) modal olivine versus whole rock MgO content, c) normative olivine versus whole rock MgO content.

4.4 Olivine compositions

The composition of phenocrystic olivine ranges in forsterite content from Fo_{80} to Fo_{91} (M.O. Garcia and M. D. Norman – unpublished data). The average forsterite content across all measurements is Fo_{88} while $Fo_{89\text{-}90}$ olivines (categorized below in the Fo_{90} bin) are the most abundant. Two populations of olivine may be present, as the next most abundant type of olivine is $Fo_{84\text{-}85}$ (categorized below in the Fo_{85} bin) (Figure 4.13a).

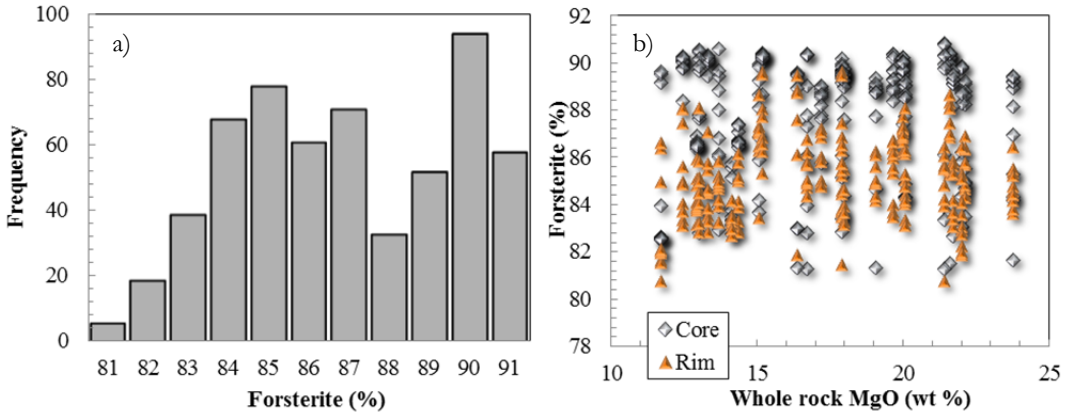

Figure 4.13 a) forsterite content frequency from measured compositions, and b) forsterite content versus whole rock MgO content.

The olivine forsterite contents are plotted in Figure 4.13, illustrating that there is no correlation between whole rock MgO content and Fo content of the olivines present. Represented are 15-20 olivines from each sample, and there are ~30 different samples represented from a range of the different dredge types (M1, 2, 3, 4, 13, 14, 16, 22, 26). The whole range of forsterite (80-91) can be seen in samples regardless of overall MgO content (Figure 4.13b).

5 Trace element Results

This section will present the trace element ICP-MS analysis results of 99 samples (Table 5.1 - Table 5.6), including element concentrations for 35 masses. Each analysis is labelled along sides its dredge-type locality. For details of the ICP-MS method, see chapter 3 – 'Methods', and for the results of 47 trace element analyses by XRF see the appendix to this thesis. Note that although Ta concentrations are tabulated below, an unknown number of samples were contaminated with Ta during the preparation process with a tungsten carbide mill, and therefore Ta results should be disregarded.

Table 5.1 ICP MS trace element results (in ppm). Dash = no value, RZ = rift zone, S = slope, L = landslide, and RV = radial vent. Ni was above the detection limit for some analyses.

Sample #	Dredge type	Li	Sc	V	Co	Ni	Cu	Zn	Ga	Rb	Sr	Y	Zr	Nb	Mo	Sn	Sb	Cs
M1-1	RZ	3.9	21.6	177	97	1327	75	99	11.0	2.9	153	14.1	67	4.7	0.4	0.78	0.016	0.029
M1-2	RZ	5.0	32.4	268	58	188	116	96	17.6	5.5	275	23.4	123	8.6	0.7	1.41	0.026	0.063
M1-6	RZ	4.6	29.5	237	71	400	105	93	15.6	4.8	248	20.7	107	7.6	0.7	1.28	0.024	0.055
M1-8	RZ	4.2	27.6	239	61	530	108	92	15.8	4.2	230	21.6	104	7.8	0.4	1.23	0.033	0.042
M1-9	RZ	3.2	32.5	272	55	156	120	96	17.9	5.8	286	23.8	125	8.7	0.7	1.46	0.032	0.102
M1-13	RZ	4.2	23.1	183	90	1162	80	93	11.9	2.7	166	14.7	67	4.7	0.3	0.78	0.018	0.026
M1-14	RZ	4.3	27.8	220	78	538	99	92	14.3	4.4	227	19.0	99	6.9	0.6	1.13	0.021	0.052
M1-16	RZ	4.5	26.5	234	72	807	105	95	15.3	3.7	214	19.2	89	6.5	0.7	0.97	0.018	0.038
M1-20	RZ	4.5	26.5	241	69	675	108	92	15.3	3.9	224	19.2	95	6.8	0.5	1.11	0.032	0.050
M1-26	RZ	3.3	19.7	153	75	1003	88	86	11.3	2.8	174	15.3	71	5.5	0.3	0.87	0.029	0.031
M1-27	RZ	4.9	29.4	273	60	322	119	94	17.3	4.5	250	21.7	110	7.8	0.6	1.26	0.036	0.058
M1-30	RZ	5.4	31.3	300	53	140	134	97	19.0	5.2	274	24.1	122	8.6	0.7	1.40	0.050	0.076
M2-2	RZ	3.9	22.7	200	82	1083	83	94	12.9	4.5	192	18.2	88	6.3	0.4	0.93	0.024	0.054
M2-3	RZ	4.6	25.6	234	72	818	98	97	15.0	4.4	220	21.5	105	7.5	0.6	1.07	0.024	0.046
M2-4	RZ	4.1	23.6	201	77	1002	97	99	14.2	4.0	207	20.1	99	7.1	0.4	1.18	0.025	0.042
M2-10	RZ	5.3	29.2	268	58	374	116	100	17.4	4.1	243	23.4	108	7.3	0.5	1.17	0.022	0.040
M2-12	RZ	4.8	26.4	249	72	597	110	95	15.9	4.1	232	20.8	107	7.3	0.7	1.23	0.026	0.044
M2-18	RZ	4.9	29.3	275	58	429	116	98	17.4	4.3	252	23.9	114	7.9	0.6	1.24	0.030	0.049
M2-19	RZ	4.0	21.9	186	88	1272	84	94	12.2	2.8	183	16.9	79	6.1	0.3	0.97	0.026	0.073
M2-20	RZ	4.4	20.3	177	90	-	78	87	11.5	2.9	171	14.4	72	5.5	0.3	0.92	0.024	0.052
M2-21	RZ	4.1	21.9	195	83	-	86	87	12.4	3.1	180	15.4	79	5.5	0.6	0.99	0.025	0.035
M2-24	RZ	5.3	25.3	229	78	984	99	97	14.3	3.6	204	19.4	92	6.4	0.5	0.98	0.020	0.039
M2-26	RZ	5.4	26.8	246	72	797	106	100	15.6	4.6	226	22.0	108	7.7	0.7	1.29	0.026	0.044
M2-27	RZ	5.1	24.4	218	82	1135	95	95	13.5	3.4	195	18.4	87	6.0	0.6	0.90	0.019	0.040
M3-1	RZ	4.0	25.9	252	64	-	98	95	16.0	4.6	228	20.9	110	7.7	0.5	1.32	0.027	0.047
M3-2	RZ	3.1	26.7	253	63	628	113	99	16.2	4.9	233	23.6	116	8.1	0.5	1.33	0.037	0.052
M3-3	RZ	3.3	26.6	253	60	609	98	96	16.3	4.9	233	23.6	116	8.1	0.6	1.31	0.023	0.050
M3-4	RZ	3.7	26.2	247	60	606	98	96	16.0	4.7	233	23.7	117	8.1	0.6	1.29	0.027	0.048
M3-5	RZ	3.5	26.5	252	60	604	96	96	16.1	4.7	232	23.7	116	8.1	0.6	1.30	0.024	0.048
M3-6	RZ	4.5	23.8	226	76	-	101	93	14.3	4.0	206	18.3	97	6.8	0.5	1.16	0.026	0.042
M3-7	RZ	3.6	26.1	254	73	688	110	98	16.0	4.8	230	22.0	115	7.9	0.6	1.30	0.029	0.054
M3-13	RZ	3.7	21.1	187	98	1212	72	87	12.0	2.5	174	15.8	80	5.6	0.5	0.97	0.019	0.032
M4-3	RZ	4.7	26.5	249	74	638	108	96	16.1	4.8	239	21.6	114	8.0	0.8	1.31	0.030	0.064

Table 5.2 ICP MS trace element results (in ppm) cont. Dash = no value, RZ = rift zone, S = slope, L = landslide, and RV = radial vent. *Ta concentrations are unreliable as an unknown quantity have been contaminated during the milling process.

Sample #	Dredge type	Ba	La	Ce	Pr	Nd	Sm	Eu	Gd	Dy	Ho	Er	Yb	Lu	Hf	Ta*	Pb	Th	U
M1-1	RZ	35	4.3	11	1.61	8.2	2.35	0.85	2.65	2.48	0.50	1.30	1.09	0.16	1.62	0.30	0.39	0.30	0.10
M1-2	RZ	76	8.3	21	3.22	15.8	4.40	1.57	4.92	4.66	0.88	2.33	1.89	0.26	2.96	0.71	0.75	0.54	0.19
M1-6	RZ	67	7.3	19	2.84	14.0	3.86	1.39	4.39	4.13	0.78	2.06	1.68	0.24	2.59	0.75	0.72	0.48	0.16
M1-8	RZ	53	7.0	18	2.53	12.7	3.62	1.29	4.12	3.90	0.76	2.00	1.65	0.23	2.53	0.49	0.64	0.47	0.14
M1-9	RZ	76	8.4	22	3.27	16.0	4.45	1.61	4.99	4.72	0.89	2.35	1.92	0.27	3.00	0.75	0.73	0.55	0.21
M1-13	RZ	34	4.2	11	1.60	8.1	2.39	0.85	2.80	2.57	0.52	1.35	1.10	0.17	1.65	0.30	0.38	0.30	0.10
M1-14	RZ	62	6.7	17	2.59	12.8	3.55	1.29	4.01	3.82	0.71	1.89	1.55	0.22	2.40	0.68	0.68	0.44	0.15
M1-16	RZ	47	5.9	15	2.21	11.4	3.27	1.16	3.69	3.51	0.69	1.84	1.48	0.21	2.25	0.41	0.56	0.40	0.13
M1-20	RZ	52	6.3	16	2.47	12.2	3.43	1.26	3.94	3.79	0.72	1.92	1.57	0.22	2.33	0.62	0.61	0.41	0.28
M1-26	RZ	40	4.8	12	1.77	9.0	2.60	0.93	2.98	2.85	0.55	1.45	1.18	0.17	1.81	0.35	0.46	0.32	0.22
M1-27	RZ	57	7.0	18	2.80	13.8	3.89	1.42	4.45	4.32	0.81	2.17	1.77	0.25	2.62	0.69	0.65	0.47	0.27
M1-30	RZ	63	7.9	21	3.11	15.4	4.36	1.58	4.96	4.78	0.91	2.42	1.96	0.27	2.91	0.80	0.72	0.52	0.27
M2-2	RZ	48	5.5	15	2.12	10.8	3.16	1.13	3.59	3.22	0.63	1.72	1.32	0.19	2.12	0.40	0.45	0.39	0.13
M2-3	RZ	59	6.6	17	2.51	12.7	3.73	1.33	4.19	3.76	0.75	1.97	1.54	0.22	2.52	0.47	0.55	0.47	0.15
M2-4	RZ	54	6.1	16	2.27	11.6	3.35	1.17	3.80	3.54	0.68	1.77	1.44	0.20	2.36	0.43	0.56	0.43	0.13
M2-10	RZ	54	6.7	18	2.59	13.1	3.89	1.40	4.46	4.06	0.81	2.20	1.70	0.25	2.60	0.46	0.63	0.44	0.14
M2-12	RZ	53	6.7	18	2.70	13.5	3.78	1.35	4.25	4.11	0.77	2.07	1.69	0.24	2.58	0.72	0.60	0.45	0.15
M2-18	RZ	54	7.1	19	2.74	13.8	4.05	1.44	4.61	4.18	0.81	2.23	1.71	0.25	2.70	0.48	0.68	0.48	0.16
M2-19	RZ	47	5.3	14	2.03	10.3	2.95	1.04	3.35	3.12	0.61	1.59	1.24	0.19	2.01	0.38	0.46	0.35	0.40
M2-20	RZ	44	5.0	13	1.98	9.9	2.82	1.02	3.17	2.98	0.55	1.47	1.19	0.16	1.86	0.36	0.37	0.34	0.17
M2-21	RZ	39	5.1	14	2.06	10.4	2.91	1.05	3.33	3.19	0.60	1.59	1.32	0.18	2.02	0.40	0.41	0.34	0.12
M2-24	RZ	45	5.7	15	2.21	11.1	3.26	1.20	3.71	3.40	0.68	1.85	1.39	0.21	2.19	0.40	0.50	0.39	0.13
M2-26	RZ	60	6.8	18	2.56	13.0	3.81	1.33	4.31	3.87	0.76	2.03	1.57	0.23	2.54	0.47	0.59	0.48	0.15
M2-27	RZ	42	5.4	14	2.08	10.5	3.05	1.09	3.52	3.21	0.63	1.71	1.35	0.19	2.07	0.37	0.47	0.37	0.16
M3-1	RZ	57	7.1	19	2.82	14.1	3.96	1.42	4.52	4.33	0.81	2.16	1.79	0.24	2.79	0.49	0.68	0.48	0.15
M3-2	RZ	58	7.3	19	2.79	14.2	4.10	1.42	4.59	4.32	0.85	2.22	1.78	0.26	2.87	0.50	0.95	0.50	0.17
M3-3	RZ	58	7.3	19	2.79	14.1	4.03	1.40	4.57	4.34	0.85	2.21	1.79	0.26	2.88	0.51	0.71	0.50	0.16
M3-4	RZ	58	7.2	19	2.74	14.1	4.00	1.40	4.56	4.27	0.85	2.20	1.78	0.26	2.88	0.50	0.69	0.48	0.16
M3-5	RZ	58	7.2	19	2.77	14.2	4.02	1.41	4.54	4.26	0.85	2.22	1.78	0.26	2.87	0.50	0.70	0.49	0.16
M3-6	RZ	50	6.3	17	2.51	12.6	3.50	1.25	4.00	3.79	0.71	1.91	1.56	0.21	2.42	0.43	0.59	0.43	0.13
M3-7	RZ	58	7.2	19	2.86	14.3	4.01	1.43	4.48	4.35	0.82	2.19	1.77	0.25	2.74	0.77	0.64	0.49	0.15
M3-13	RZ	37	5.2	13	2.06	10.3	2.91	1.06	3.29	3.16	0.60	1.57	1.28	0.18	1.95	0.57	0.45	0.33	0.11
M4-3	RZ	62	7.2	19	2.86	14.4	4.01	1.46	4.51	4.28	0.81	2.15	1.73	0.24	2.74	0.75	0.64	0.50	0.17

Table 5.3 ICP MS trace element results (in ppm) cont. Dash = no value, RZ = rift zone, S = slope, L = landslide, and RV = radial vent. Ni was above the detection limit for some analyses.

Sample #	Dredge type	Li	Sc	V	Co	Ni	Cu	Zn	Ga	Rb	Sr	Y	Zr	Nb	Mo	Sn	Sb	Cs
M4-7	RZ	4.1	24.0	219	84	1200	92	101	14.0	3.7	201	19.1	94	6.6	0.4	1.05	0.037	0.040
M4-8	RZ	4.6	26.2	241	69	783	102	100	15.7	4.2	227	22.1	108	7.6	0.5	1.10	0.024	0.048
M4-9	RZ	4.1	22.1	194	89	1428	82	99	12.4	3.4	179	17.3	85	5.9	0.5	0.89	0.022	0.037
M4-10	RZ	4.3	25.2	226	77	843	97	103	14.0	3.9	197	19.1	90	7.1	0.6	0.97	0.025	0.040
M4-14	RZ	4.2	27.6	268	69	547	117	99	16.7	5.4	242	22.6	117	8.0	0.6	1.34	0.035	0.069
M4-21	RZ	4.9	20.9	187	90	1333	82	93	11.7	2.7	175	14.7	77	5.3	0.6	0.89	0.019	0.027
M6-1	S	5.0	30.9	305	50	244	134	105	19.3	5.4	271	27.2	130	9.4	0.6	1.45	0.027	0.056
M6-5	S	5.2	31.1	303	51	264	132	104	19.0	4.8	268	26.8	128	9.3	0.6	1.44	0.027	0.055
M6-6	S	5.5	31.6	323	46	101	139	110	20.1	6.4	290	28.9	154	10.8	0.8	1.74	0.034	0.066
M6-13	S	4.5	25.6	235	76	941	96	99	15.0	4.1	213	20.3	97	6.8	0.5	1.03	0.017	0.042
M6-14	S	4.1	24.8	233	77	923	100	99	14.8	3.8	202	20.3	96	6.5	0.5	1.06	0.015	0.040
M6-26	S	5.3	31.6	323	46	104	138	113	20.5	6.6	295	31.9	159	11.5	0.7	1.75	0.031	0.067
M6-27	S	5.4	32.1	325	46	103	142	112	20.4	6.6	295	31.7	157	11.4	0.7	1.74	0.029	0.064
M8-1	S	5.4	32.0	323	53	141	147	111	19.8	5.6	281	27.5	139	9.5	0.7	1.61	0.031	0.058
M11-5	L	5.6	31.0	393	47	64	132	129	22.8	8.4	327	34.3	203	18.9	0.9	2.30	0.049	0.025
M11-11	L	8.0	30.0	274	61	370	47	99	17.0	2.8	250	21.3	105	7.6	0.5	1.87	0.021	0.047
M12-3	L	6.1	29.8	279	54	249	112	93	17.7	4.3	286	20.7	114	10.5	0.5	1.33	0.030	0.051
M12-4	L	5.6	31.2	321	53	75	105	107	20.8	6.0	307	26.4	144	12.7	0.6	1.65	0.031	0.063
M12-14	L	5.8	31.4	326	51	74	66	107	20.9	6.4	314	26.5	143	12.8	0.6	1.70	0.030	0.070
M12-17	L	4.4	32.5	307	43	83	105	107	19.3	4.8	282	23.2	119	9.5	0.7	1.45	0.026	0.047
M12-29	L	5.1	30.7	290	58	196	107	100	18.6	5.0	280	22.9	119	8.7	0.6	1.38	0.025	0.049
M12-42	L	5.5	32.7	304	54	118	101	98	19.2	4.9	283	23.5	123	9.8	0.5	1.50	0.035	0.058
M13-2	L	6.2	33.7	343	40	78	105	110	20.8	4.9	261	31.4	135	8.9	0.9	1.66	0.028	0.053
M13-5	L	6.3	34.1	336	52	116	117	106	19.4	6.0	259	29.9	136	9.3	1.0	1.59	0.040	0.081
M13-12	L	4.2	22.3	201	82	-	88	88	12.6	4.2	204	14.9	82	8.4	0.6	0.95	0.022	0.041
M13-14	L	4.7	27.4	251	75	495	118	94	15.4	4.3	219	18.8	90	6.4	0.7	1.11	0.021	0.046
M13-21	L	4.4	23.3	219	88	-	91	92	13.6	6.0	246	16.0	98	12.0	0.5	1.16	0.031	0.059
M13-25	L	3.8	19.8	188	103	-	70	97	11.8	4.3	223	14.1	91	10.2	0.4	1.11	0.029	0.088
M13-29	L	6.0	31.7	290	64	287	101	98	17.1	5.6	232	25.0	118	8.4	0.7	1.36	0.040	0.087
M13-33	L	4.3	17.9	160	97	-	70	84	9.9	2.4	143	12.0	62	4.6	0.4	0.84	0.014	0.031
M13-35	L	6.0	31.4	327	50	98	122	109	21.1	6.6	323	28.3	151	13.2	0.6	1.73	0.039	0.072
M13-38	L	4.3	22.7	215	84	-	89	93	13.3	5.8	238	15.4	94	11.4	0.5	1.09	0.029	0.055
M14-20	L	5.4	31.8	298	61	160	132	101	18.6	5.1	278	23.8	121	10.4	0.7	1.42	0.030	0.051

Table 5.4 ICP MS trace element results (in ppm) cont. Dash = no value, RZ = rift zone, S = slope, L = landslide, and RV = radial vent. *Ta concentrations are unreliable as an unknown quantity have been contaminated during the milling process.

Sample #	Dredge type	Ba	La	Ce	Pr	Nd	Sm	Eu	Gd	Dy	Ho	Er	Yb	Lu	Hf	Ta*	Pb	Th	U
M4-7	RZ	47	6.1	16	2.30	11.7	3.36	1.20	3.82	3.48	0.70	1.82	1.46	0.20	2.34	0.41	0.52	0.41	0.14
M4-8	RZ	56	6.7	18	2.62	13.0	3.84	1.34	4.27	3.85	0.78	2.06	1.62	0.23	2.71	0.48	0.58	0.47	0.16
M4-9	RZ	42	5.3	14	2.04	10.1	2.93	1.05	3.35	3.02	0.61	1.60	1.25	0.18	2.09	0.37	0.46	0.36	0.13
M4-10	RZ	49	6.1	16	2.27	11.2	3.21	1.16	3.65	3.36	0.66	1.82	1.44	0.20	2.28	0.45	0.50	0.43	0.14
M4-14	RZ	60	7.4	19	2.93	14.8	4.14	1.49	4.70	4.51	0.86	2.27	1.84	0.26	2.83	0.73	0.66	0.50	0.16
M4-21	RZ	35	5.2	13	2.00	9.8	2.72	0.99	3.04	2.91	0.55	1.46	1.18	0.17	1.85	0.35	0.45	0.35	0.12
M6-1	S	69	8.4	22	3.23	16.3	4.70	1.67	5.29	4.89	1.00	2.61	2.08	0.30	3.23	0.59	0.81	0.58	0.19
M6-5	S	69	8.3	22	3.14	16.0	4.57	1.62	5.26	4.84	0.97	2.56	2.04	0.29	3.15	0.58	0.81	0.57	0.18
M6-6	S	81	9.8	26	3.88	19.4	5.40	1.92	6.04	5.76	1.09	2.89	2.32	0.33	3.75	0.68	0.85	0.68	0.22
M6-13	S	50	6.2	16	2.36	12.2	3.44	1.22	3.92	3.65	0.73	1.94	1.55	0.22	2.38	0.42	0.60	0.42	0.13
M6-14	S	49	6.1	16	2.37	11.9	3.48	1.23	3.98	3.67	0.74	1.96	1.58	0.22	2.41	0.41	0.58	0.41	0.13
M6-26	S	85	10.4	27	3.92	19.6	5.74	1.96	6.27	5.67	1.13	3.01	2.44	0.33	3.94	0.71	0.95	0.72	0.23
M6-27	S	83	10.2	26	3.84	19.3	5.67	1.94	6.29	5.60	1.11	2.96	2.38	0.33	3.80	0.69	0.94	0.71	0.22
M8-1	S	70	8.6	23	3.45	17.5	4.94	1.78	5.61	5.43	1.02	2.72	2.20	0.31	3.34	0.74	0.77	0.57	0.19
M11-5	L	123	16.7	43	6.14	29.4	7.52	2.55	8.21	7.28	1.34	3.53	2.83	0.38	5.11	1.24	1.40	1.24	0.39
M11-11	L	52	6.6	17	2.67	13.4	3.85	1.41	4.31	4.19	0.80	2.12	1.71	0.25	2.55	0.55	0.59	0.45	0.13
M12-3	L	75	8.9	23	3.30	16.0	4.22	1.54	4.71	4.38	0.81	2.15	1.72	0.24	2.90	0.82	0.80	0.64	0.20
M12-4	L	88	10.6	27	4.01	19.4	5.28	1.89	5.85	5.48	1.03	2.74	2.25	0.31	3.64	0.99	0.81	0.75	0.25
M12-14	L	87	10.4	27	3.93	19.2	5.17	1.86	5.76	5.42	1.02	2.68	2.22	0.31	3.54	0.95	0.90	0.76	0.24
M12-17	L	62	8.3	22	3.24	16.0	4.46	1.64	5.01	4.77	0.90	2.38	1.96	0.27	3.00	0.60	0.77	0.55	0.17
M12-29	L	68	8.0	21	3.14	15.5	4.32	1.56	4.80	4.53	0.86	2.27	1.82	0.26	2.88	0.67	0.67	0.54	0.16
M12-42	L	70	8.6	22	3.34	16.4	4.57	1.66	5.11	4.85	0.91	2.41	1.99	0.27	3.07	0.74	0.76	0.60	0.18
M13-2	L	60	8.1	22	3.40	17.2	5.04	1.80	5.91	6.04	1.20	3.26	2.87	0.40	3.45	0.58	0.88	0.55	0.19
M13-5	L	67	8.2	22	3.33	16.9	4.79	1.73	5.60	5.69	1.11	3.04	2.58	0.37	3.27	0.80	0.78	0.57	0.24
M13-12	L	57	7.3	18	2.56	12.0	3.11	1.11	3.37	3.08	0.58	1.52	1.24	0.17	2.05	0.52	0.53	0.52	0.15
M13-14	L	54	6.1	16	2.36	11.7	3.28	1.21	3.76	3.68	0.70	1.87	1.55	0.22	2.21	0.68	0.65	0.40	0.12
M13-21	L	82	10.0	25	3.32	15.0	3.61	1.27	3.89	3.35	0.62	1.65	1.31	0.18	2.41	0.92	0.79	0.71	0.21
M13-25	L	72	8.7	22	2.98	13.8	3.36	1.16	3.50	3.02	0.55	1.44	1.13	0.15	2.24	0.62	0.54	0.65	0.20
M13-29	L	71	7.7	20	2.99	15.0	4.19	1.50	4.83	4.82	0.94	2.56	2.15	0.30	2.86	0.76	0.79	0.55	0.18
M13-33	L	32	4.2	11	1.64	8.1	2.30	0.83	2.59	2.47	0.46	1.23	1.01	0.14	1.56	0.30	0.30	0.27	0.09
M13-35	L	89	11.2	29	4.18	20.3	5.48	1.95	6.09	5.70	1.08	2.87	2.34	0.32	3.80	1.05	0.96	0.76	0.32
M13-38	L	78	9.7	24	3.24	14.8	3.52	1.24	3.81	3.27	0.61	1.60	1.26	0.18	2.37	0.69	0.70	0.70	0.21
M14-20	L	70	9.0	23	3.34	16.2	4.34	1.57	4.90	4.69	0.88	2.39	1.93	0.27	2.95	0.88	0.70	0.60	0.19

Table 5.5 ICP MS trace element results (in ppm) cont. Dash = no value, RZ = rift zone, S = slope, L = landslide, and RV = radial vent. Ni was above the detection limit for some analyses.

Sample #	Dredge type	Li	Sc	V	Co	Ni	Cu	Zn	Ga	Rb	Sr	Y	Zr	Nb	Mo	Sn	Sb	Cs
M14-21	L	4.8	21.8	197	94	1222	85	92	12.3	2.9	185	15.6	81	5.8	0.5	0.93	0.020	0.030
M14-32	L	8.1	26.4	245	72	595	85	71	15.1	3.6	205	17.4	45	6.8	0.3	1.07	0.018	0.120
M18-17	RZ	5.0	30.9	301	61	188	133	103	18.9	5.0	260	25.5	129	8.7	0.8	1.51	0.029	0.054
M18-31	RZ	4.0	24.0	219	78	-	93	92	14.1	3.5	204	17.5	89	6.2	0.4	1.13	0.025	0.042
M18-32	RZ	4.9	25.2	244	77	800	104	97	15.4	4.6	233	20.5	112	7.9	0.6	1.29	0.025	0.046
M18-33	RZ	4.6	24.6	229	75	-	97	93	14.3	4.0	205	19.0	97	6.9	0.6	1.20	0.022	0.042
M18-34	RZ	4.2	24.2	222	76	-	95	91	14.1	3.6	199	17.4	88	6.4	0.4	1.12	0.022	0.038
M18-35	RZ	5.7	29.9	336	46	143	150	112	20.5	6.5	290	28.9	152	11.1	0.8	1.87	0.035	0.067
M18-36	RZ	5.2	31.4	306	49	159	129	106	19.1	5.1	263	26.0	132	8.8	0.6	1.54	0.028	0.054
M19-1	RZ	4.1	23.9	216	74	-	89	87	13.8	4.1	202	17.3	87	6.3	0.4	1.21	0.030	0.055
M19-2	RZ	4.9	28.9	272	66	470	114	96	16.8	6.2	278	22.0	123	11.6	0.7	1.34	0.044	0.058
M19-5	RZ	4.0	22.9	203	81	-	85	86	13.0	3.8	188	16.1	81	6.0	0.4	1.05	0.029	0.049
M19-17	RZ	5.4	31.3	306	49	232	117	102	18.9	6.7	306	24.5	133	12.4	0.7	1.58	0.041	0.059
M19-24	RZ	4.9	27.1	258	64	524	113	99	16.5	4.5	243	21.8	111	7.6	0.5	1.36	0.028	0.048
M22-4	RV	4.5	24.6	240	92	922	103	102	15.1	4.4	220	22.4	112	7.9	0.7	1.26	0.021	0.046
M22-11	RV	4.7	26.1	257	83	826	108	104	15.9	4.7	232	24.0	119	8.3	0.6	1.32	0.025	0.051
M22-17	RV	5.0	25.8	255	74	844	107	106	15.6	4.8	223	23.6	118	8.2	0.6	1.27	0.023	0.049
M22-20	RV	4.9	26.3	258	72	791	108	104	16.1	4.8	227	23.9	119	8.2	0.5	1.32	0.025	0.049
M22-21	RV	4.9	26.4	259	70	773	109	103	16.2	4.9	231	24.4	120	8.4	0.6	1.32	0.025	0.051
M24-8	RV	5.7	30.1	299	59	156	117	101	19.1	7.2	325	25.1	141	10.3	0.7	1.80	0.040	0.072
M26-1	S	4.7	27.3	258	84	701	106	107	16.2	4.1	240	22.1	104	7.2	0.5	1.18	0.021	0.045
M26-10	S	5.3	30.8	300	53	105	122	108	20.3	7.1	353	28.2	147	10.8	0.8	1.61	0.028	0.076
M26-14	S	4.5	25.0	233	95	921	97	107	14.7	3.8	217	20.1	95	6.6	0.6	1.09	0.017	0.039
M26-16	S	4.6	26.2	242	86	773	101	106	15.2	3.9	227	20.9	99	6.9	0.6	1.09	0.022	0.042
M26-18	S	5.0	28.6	268	68	475	113	108	17.2	4.5	256	23.4	110	7.5	0.6	1.27	0.020	0.047
M26-43	S	4.7	27.4	256	67	554	106	107	16.5	4.2	242	22.3	104	7.0	0.5	1.17	0.018	0.044
M26-44	S	4.6	26.1	246	73	683	101	104	15.9	4.1	230	21.2	99	6.6	0.5	1.11	0.016	0.039
M27-2	RV	5.4	32.5	303	56	112	122	100	19.5	5.7	305	25.3	131	9.1	0.6	1.55	0.032	0.065
M27-11	RV	5.3	32.8	304	46	113	125	104	20.1	5.9	311	28.6	138	9.2	0.7	1.55	0.025	0.063
M27-32	RV	5.1	30.9	284	72	348	124	109	18.5	4.8	271	26.1	127	8.6	0.6	1.47	0.028	0.050
M28-2	RV	6.0	34.4	340	56	79	130	119	21.2	7.5	339	31.0	158	11.3	0.8	1.77	0.031	0.082
M29-5	S	4.9	28.5	283	56	411	124	96	17.6	4.3	252	22.9	118	8.7	0.5	1.39	0.031	0.044
M30-1	S	3.9	23.6	204	78	-	88	87	13.0	3.3	184	15.3	76	5.5	0.4	0.94	0.029	0.036

Table 5.6 ICP MS trace element results (in ppm) cont. Dash = no value, RZ = rift zone, S = slope, L = landslide, and RV = radial vent. *Ta concentrations are unreliable as an unknown quantity have been contaminated during the milling process.

Sample #	Dredge type	Ba	La	Ce	Pr	Nd	Sm	Eu	Gd	Dy	Ho	Er	Yb	Lu	Hf	Ta*	Pb	Th	U
M14-21	L	41	5.6	14	2.15	10.6	2.91	1.05	3.25	3.09	0.59	1.57	1.28	0.18	1.96	0.51	0.49	0.38	0.14
M14-32	L	42	6.2	16	2.46	12.3	3.44	1.25	3.87	3.61	0.66	1.71	1.33	0.18	1.33	0.51	0.21	0.15	0.06
M18-17	RZ	65	7.9	21	3.21	16.2	4.60	1.65	5.21	5.06	0.96	2.57	2.07	0.29	3.15	0.74	0.68	0.53	0.17
M18-31	RZ	47	5.9	16	2.34	11.8	3.31	1.20	3.75	3.56	0.68	1.80	1.44	0.21	2.25	0.39	0.49	0.38	0.18
M18-32	RZ	63	7.3	19	2.86	14.1	3.91	1.39	4.32	4.09	0.76	2.04	1.65	0.23	2.67	0.61	0.67	0.49	0.16
M18-33	RZ	51	6.4	17	2.54	12.7	3.58	1.29	4.10	3.85	0.73	1.95	1.56	0.22	2.45	0.43	0.54	0.42	0.13
M18-34	RZ	45	5.7	15	2.29	11.5	3.23	1.18	3.72	3.55	0.67	1.79	1.45	0.20	2.23	0.41	0.48	0.38	0.12
M18-35	RZ	83	10.1	27	3.97	19.9	5.41	1.96	6.21	5.91	1.12	2.98	2.42	0.33	3.85	0.71	0.96	0.69	0.22
M18-36	RZ	63	8.0	21	3.24	16.3	4.64	1.66	5.30	5.11	0.96	2.56	2.08	0.29	3.21	0.56	0.69	0.54	0.18
M19-1	RZ	46	5.8	15	2.31	11.5	3.21	1.17	3.70	3.58	0.67	1.80	1.46	0.20	2.22	0.41	0.50	0.39	0.15
M19-2	RZ	85	11.3	27	3.71	17.0	4.22	1.49	4.67	4.36	0.81	2.17	1.77	0.25	2.93	0.88	0.85	0.80	0.26
M19-5	RZ	43	5.4	14	2.14	10.7	2.99	1.10	3.39	3.31	0.62	1.65	1.35	0.19	2.08	0.39	0.48	0.37	0.15
M19-17	RZ	89	12.0	30	4.11	19.1	4.82	1.72	5.35	5.01	0.94	2.54	2.04	0.28	3.38	0.77	1.03	0.84	0.24
M19-24	RZ	58	7.1	19	2.91	14.5	4.08	1.49	4.70	4.49	0.84	2.24	1.81	0.25	2.81	0.49	0.66	0.47	0.15
M22-4	RV	57	7.1	18	2.68	13.7	3.94	1.36	4.47	4.22	0.80	2.10	1.71	0.24	2.76	-	0.75	0.48	0.16
M22-11	RV	61	7.5	20	2.83	14.6	4.27	1.45	4.85	4.43	0.86	2.24	1.82	0.26	2.90	-	0.80	0.52	0.16
M22-17	RV	59	7.5	20	2.86	14.2	4.18	1.43	4.62	4.22	0.83	2.19	1.79	0.25	2.87	0.50	0.70	0.52	0.16
M22-20	RV	60	7.6	20	2.89	14.5	4.22	1.43	4.65	4.30	0.85	2.23	1.79	0.25	2.92	0.51	0.71	0.53	0.16
M22-21	RV	61	7.6	20	2.84	14.6	4.18	1.43	4.68	4.43	0.86	2.25	1.81	0.26	2.95	0.52	0.71	0.53	0.16
M24-8	RV	95	10.9	28	4.05	19.5	5.11	1.80	5.57	5.23	0.97	2.57	2.08	0.29	3.48	0.88	1.02	0.68	0.21
M26-1	S	56	6.6	17	2.52	13.0	3.82	1.33	4.38	4.08	0.80	2.13	1.70	0.24	2.54	-	0.70	0.42	0.14
M26-10	S	98	10.4	27	3.76	18.8	5.20	1.82	5.66	5.15	1.00	2.64	2.12	0.30	3.51	-	1.06	0.66	0.22
M26-14	S	51	6.1	16	2.29	11.8	3.40	1.22	3.94	3.79	0.72	1.85	1.53	0.22	2.29	-	0.70	0.38	0.13
M26-16	S	53	6.3	17	2.39	12.4	3.62	1.27	4.11	3.86	0.76	1.91	1.60	0.23	2.41	-	0.69	0.41	0.14
M26-18	S	58	7.0	18	2.65	13.6	4.02	1.41	4.51	4.25	0.84	2.18	1.76	0.25	2.71	0.46	0.69	0.45	0.15
M26-43	S	55	6.6	17	2.49	12.8	3.71	1.32	4.25	3.99	0.79	2.06	1.66	0.24	2.55	0.44	0.65	0.43	0.14
M26-44	S	52	6.3	16	2.40	12.1	3.60	1.28	4.10	3.77	0.74	1.94	1.58	0.23	2.43	0.42	0.61	0.40	0.13
M27-2	RV	77	8.8	23	3.51	17.4	4.86	1.75	5.48	5.23	0.98	2.59	2.11	0.29	3.28	0.82	0.95	0.57	0.18
M27-11	RV	77	9.1	24	3.44	17.3	4.88	1.75	5.58	5.04	1.00	2.66	2.07	0.30	3.31	0.57	0.86	0.59	0.19
M27-32	RV	66	7.8	21	3.02	15.4	4.64	1.63	5.17	4.79	0.93	2.47	1.94	0.28	3.07	-	0.69	0.52	0.17
M28-2	RV	102	11.1	28	3.98	19.8	5.61	1.96	6.15	5.55	1.08	2.86	2.26	0.33	3.73	-	1.09	0.70	0.23
M29-5	S	62	7.8	21	3.12	15.6	4.37	1.57	4.92	4.77	0.89	2.37	1.95	0.27	3.01	0.55	0.70	0.52	0.17
M30-1	S	40	5.0	13	2.00	10.0	2.81	1.03	3.19	3.13	0.60	1.57	1.30	0.18	1.95	0.35	0.40	0.33	0.14

5.1 Trace element variation

5.1.1 Variation with MgO

All trace elements except Ni and Co increase with decreasing MgO in a linear trend above approximately 8 wt. % MgO. Below 8 wt. % MgO the slopes of the trends change and many trace elements continue to increase in concentration while MgO ceases to decrease (Figure 5.1, Figure 5.2, Figure 5.3). Ni and Co are positively correlated with MgO (Figure 5.1b, j). Cu and Sc are negatively correlated with MgO, though decrease in concentration at MgO <8 wt. % (Figure 5.1d, e).

When Ni is plotted against MgO a linear trend is created for samples with >8 wt. % MgO (116.3 – 1327.5 ppm Ni) (Figure 5.1b). Below 8 wt. % the trend begins to flatten out and there is less of a decrease in Ni with decreasing MgO (64.1 – 111.9 ppm Ni).

Co shows a similar relationship to MgO as Ni, though with slightly more spread in the day (R^2 = 0.82) (Figure 5.1j).

The highly incompatible elements e.g. Pb, U, Th, Y, Rb, and Mo are highly scattered, other incompatible elements Ho, Lu, Eu, Zr, and Yb are linear, while Ni can be fitted tightly to a linear trend line with an R^2 value of 0.96 (Figure 5.1b). Elements with the lowest concentrations tend to display the most scatter e.g. Mo, and Sb.

It can also be seen that there are more samples with lower MgO, as the mean MgO value of 13.01 wt. % is closer to the min (5.45 wt. %) than the max (27.04 wt. %), i.e. the data are not normally distributed.

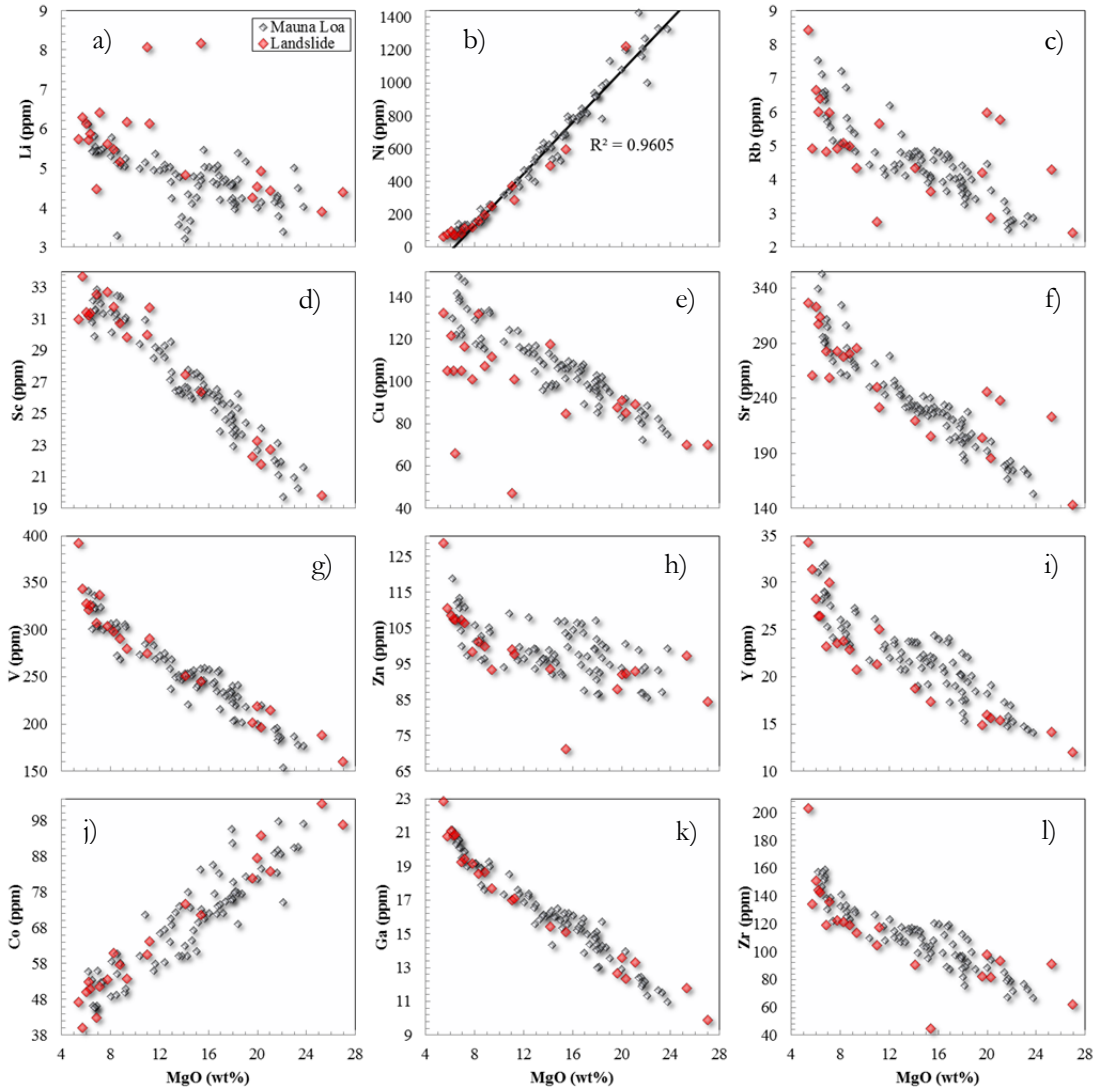

Figure 5.1 ICP MS trace elements showing slops, vent, and ridge samples (grey) and landslide samples (red). All 1σ SD errors are smaller than the data points. Window b) contains a linear trend to Ni data with >7 wt. % MgO with R^2 value to the fit.

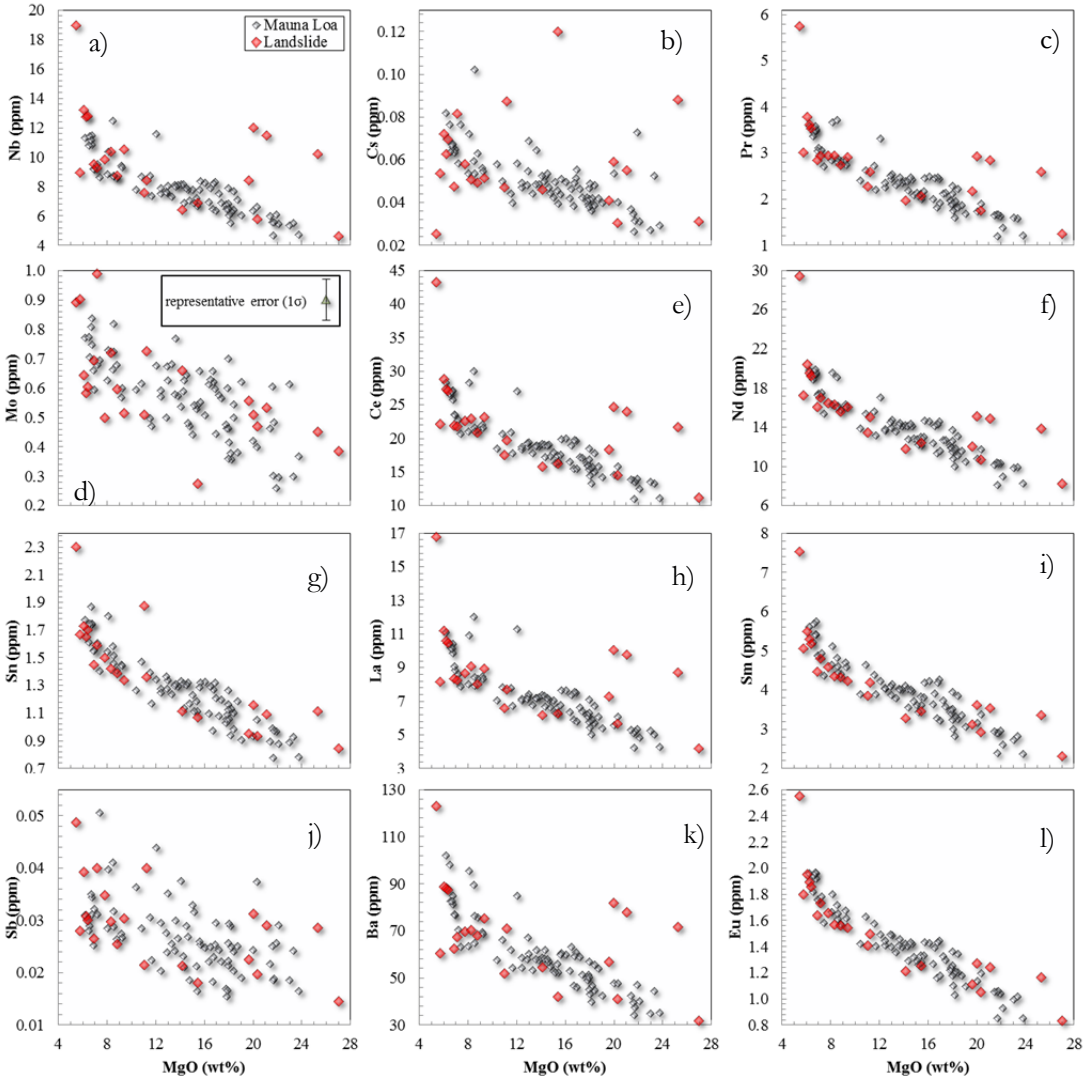

Figure 5.2 ICP MS trace elements showing slops, vent, and ridge samples (grey) and landslide samples (red). 1σ errors are smaller than data points unless otherwise indicated. All 1σ SD errors are smaller than the data points.

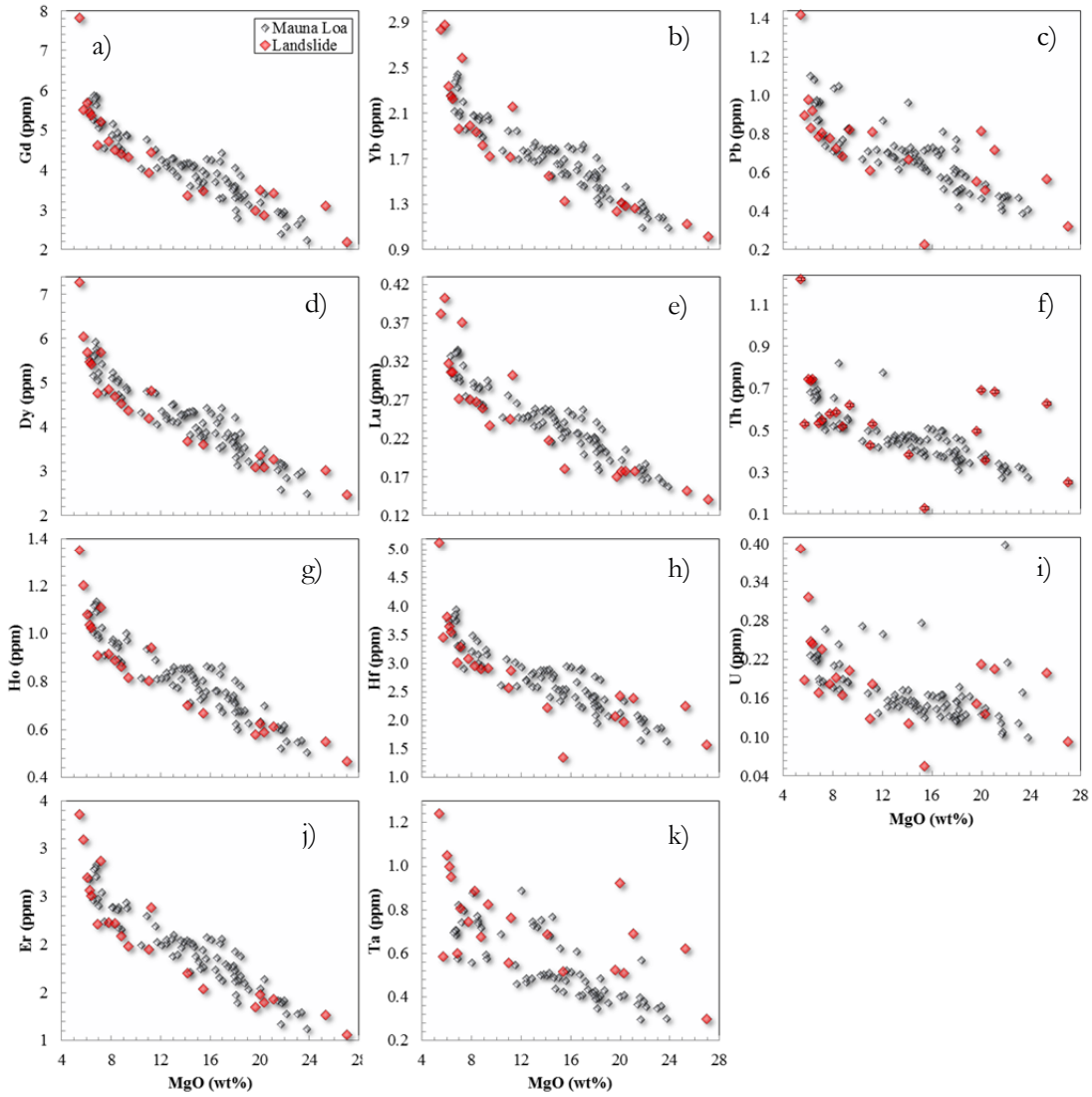

Figure 5.3 ICP MS trace elements showing slops, vent, and ridge samples (grey) and landslide samples (red). All 1σ errors are smaller than the data points. All 1σ SD errors are smaller than the data points.

5.1.2 Trace element variation with CaO

The change in slope of trace element concentrations in the more evolved lavas can be seen clearly when plotted against CaO (e.g. Figure 5.4- Figure 5.6). All trace elements increase with increasing CaO at low values of CaO, except Ni and Co which decrease. Between 10-12 wt. % CaO the concentrations of the trace elements continue to increase while the concentration of CaO begins to decrease. This can be seen clearly when La, Ce, Sn, and Sm are plotted against CaO at 10-11 wt. % CaO (Figure 5.5e, g, h, i). The effect is less clear when a moderately incompatible element such as Ho is plotted against CaO (Figure 5.6g).

Some elements such as Y, Ga, and Zr display a bump in the linear trend line at ~ 8 wt. % CaO, where data are more spread out (Figure 5.4i, k, l).

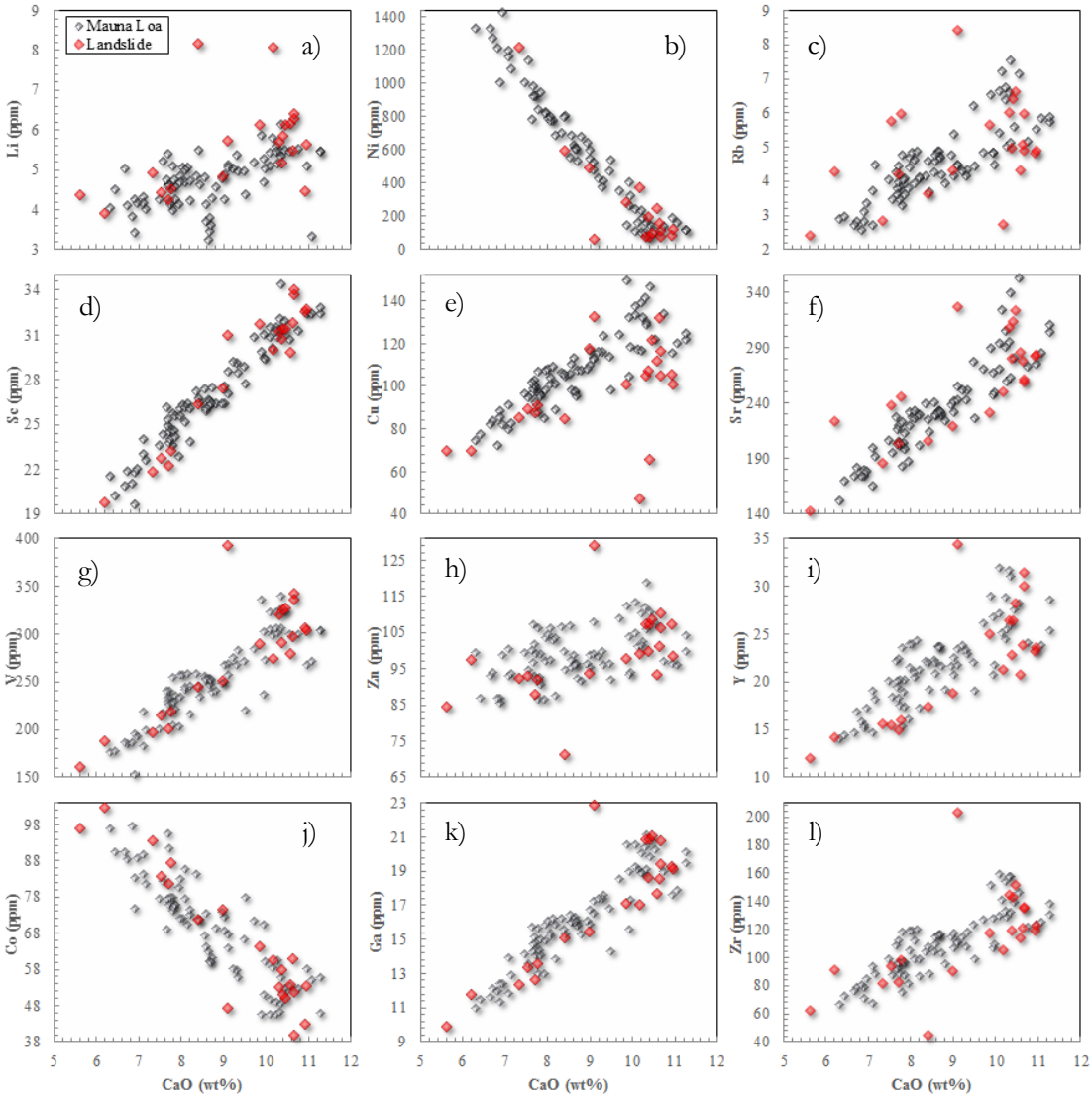

Figure 5.4 ICP MS trace elements showing slops, vent, and ridge samples (grey) and landslide samples (red). All 1σ errors are smaller than the data points.

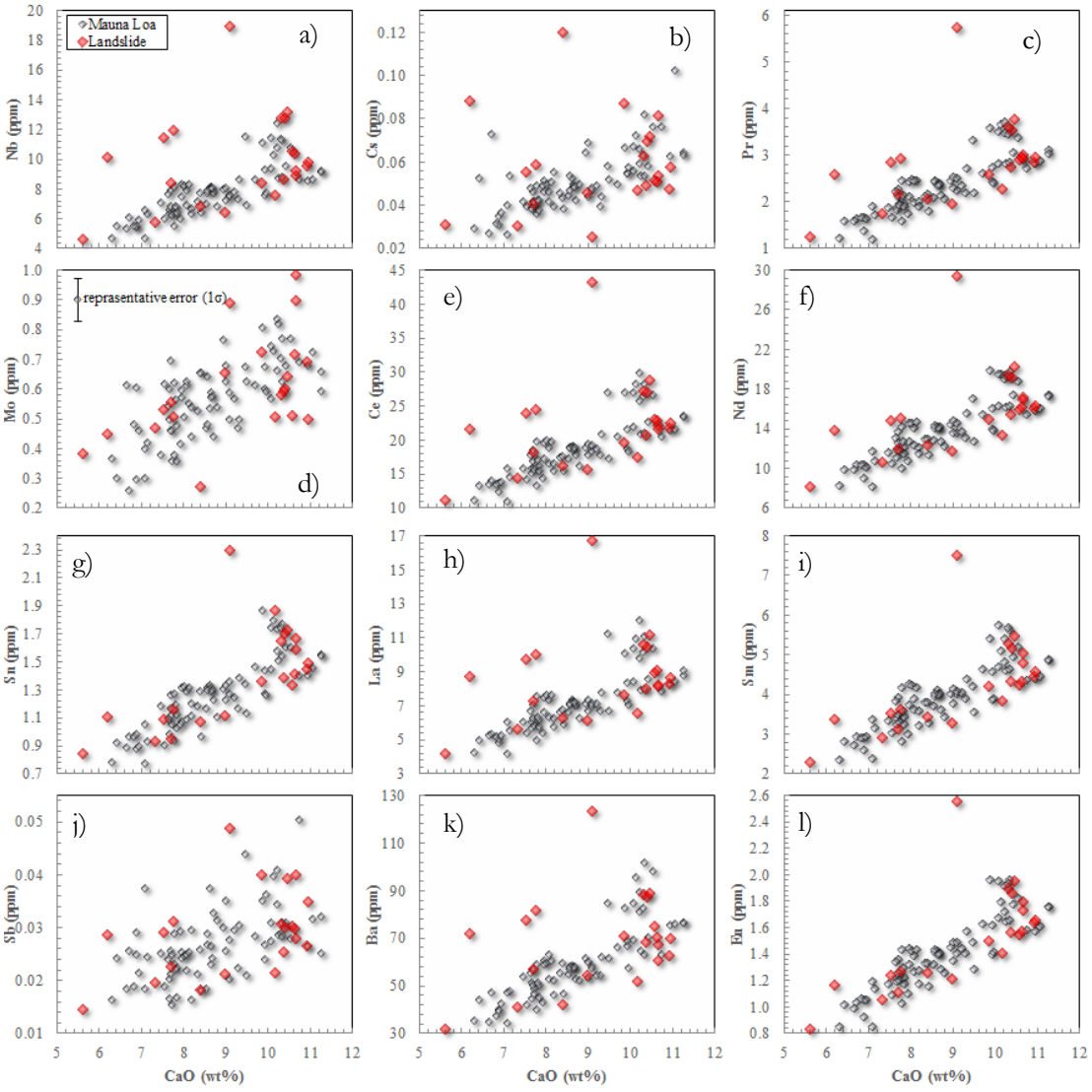

Figure 5.5 ICP MS trace elements showing slops, vent, and ridge samples (grey) and landslide samples (red). 1σ errors are smaller than data points unless otherwise indicated.

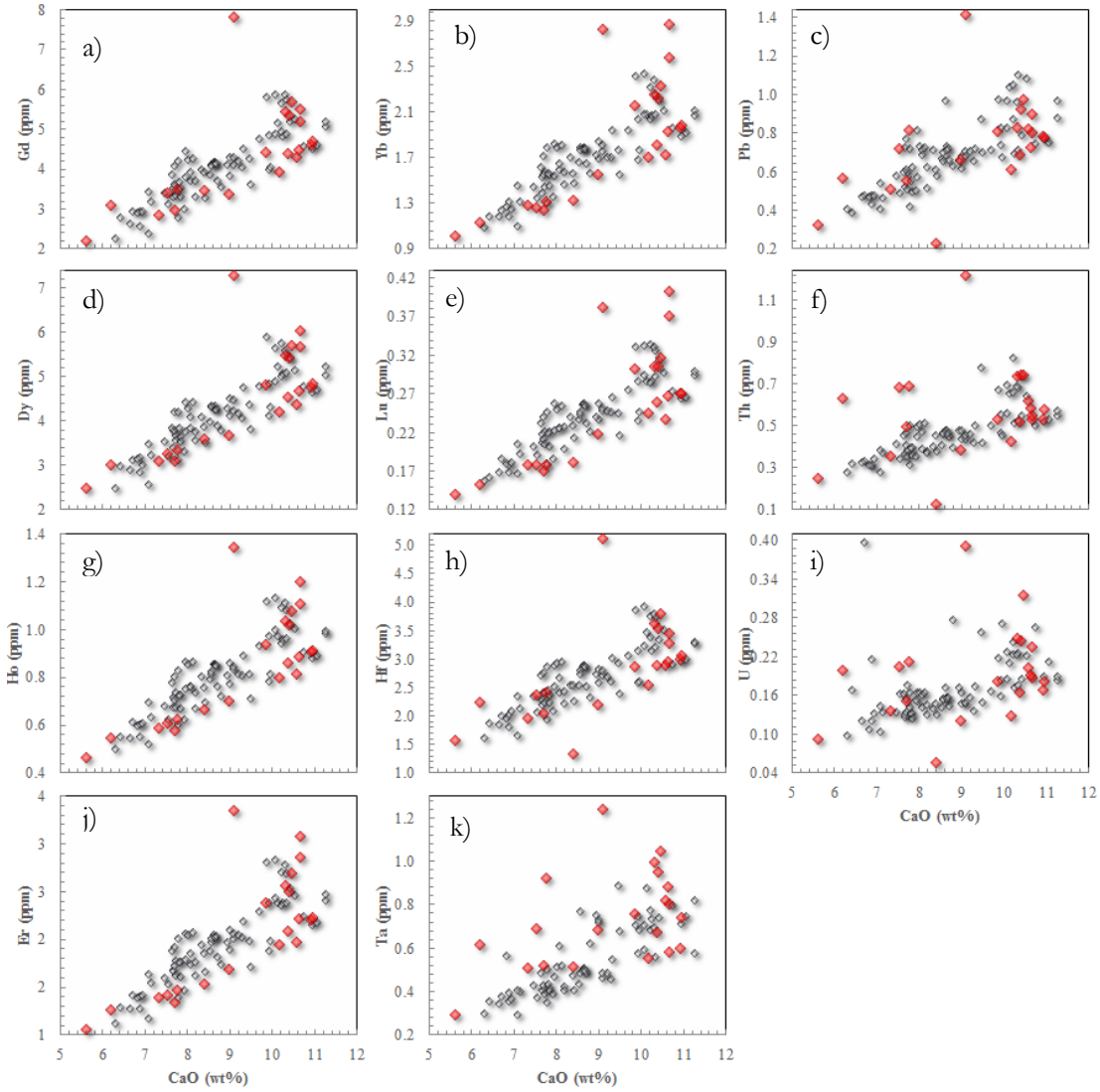

Figure 5.6 ICP MS trace elements showing slops, vent, and ridge samples (grey) and landslide samples (red). All 1σ errors are smaller than the data points.

5.2 Sample dredge types

The trace element concentrations of the four dredge types (rift zone, landslide, slope, and radial vent) are plotted in Figure 5.7, Figure 5.8,Figure 5.9. It can be seen that the landslide samples display the widest range in most trace element concentrations of the four locality types e.g. Li, Sc, V, Co, Zn, Rb, Y etc. (Figure 5.7a, b, c, d, g, i, k) and the lowest median concentration of Ni (Figure 5.7e). To the eye the trace element concentrations for the other dredge types are fairly similar, in particular Co (Figure 5.7d), Mo (Figure 5.8b), Cs (Figure 5.8e), and U (Figure 5.9f). The radial vent samples appear to have higher minimum values than the other types, and the rift zone lavas appear to have lower median concentrations of most trace elements. When the samples are broken into landslide versus non-landslide, it can be seen that the landslide samples

are more scattered and display a wider range in trace element compositions. This is particularly the case for a few samples with the highly incompatible elements La, Nb, Ba, and Ce (Figure 5.5a, e, h, k). The landslide samples have high Nb for a given value of La, higher La for a given Zr, and also high Nb for a given value of Zr (Figure 5.16). The composition of the landslide samples differs from those of the other suites based on their geological setting, in particular for the trace element ratios in Figure 5.12 and Figure 5.13.

A more quantitative ANOVA (analysis of variance) test was performed and is discussed later to determine if these variations are significant, and if they remain when the effect of olivine accumulation/fractionation is removed.

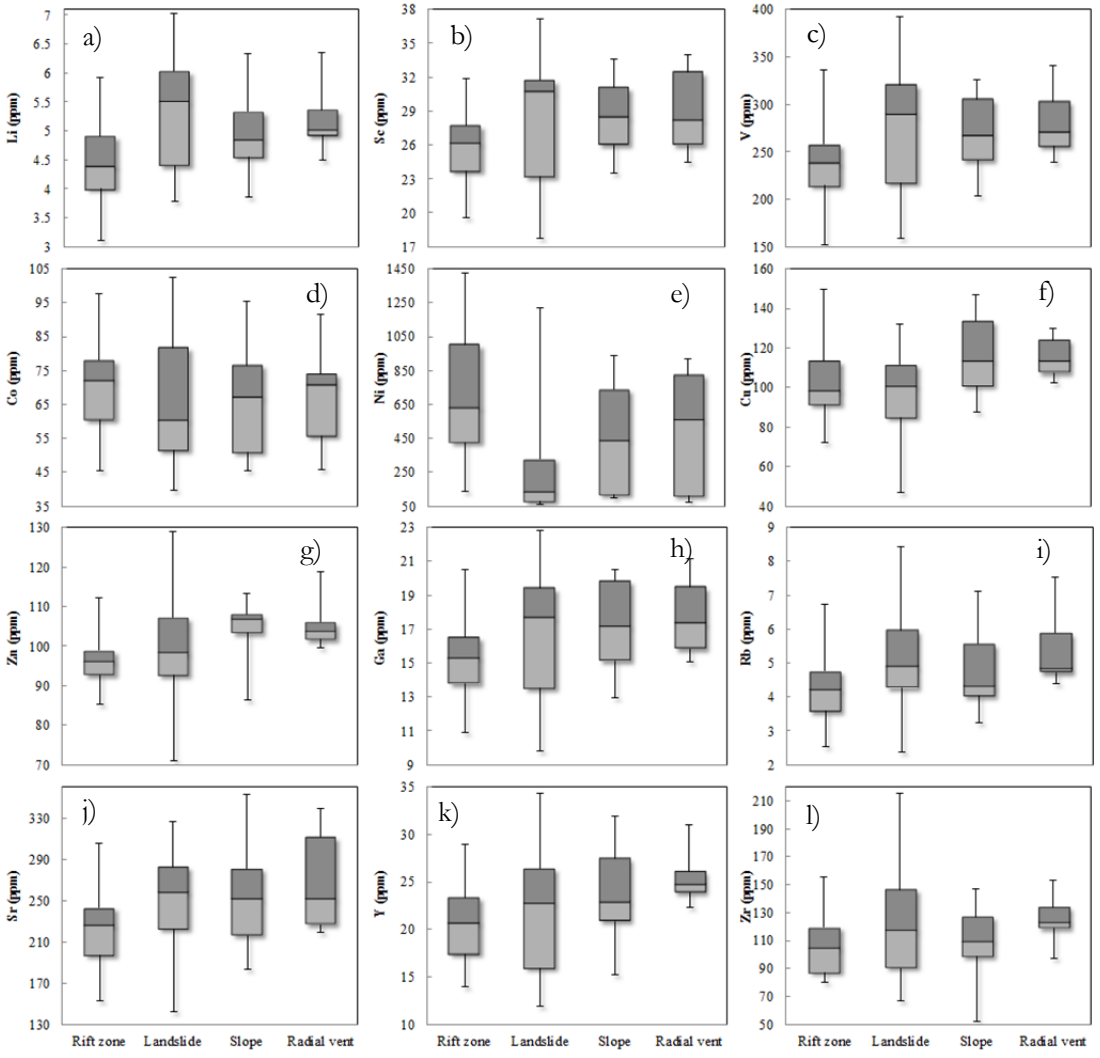

Figure 5.7 Five figure summaries (minimum, maximum, median, 1st quartile, and 3rd quartile) of trace element concentrations for rift zone, landslide, slope, and radial vent sample types. Whiskers display minimum and maximum range, while boxes display 1st quartile, median, and 3rd quartile values.

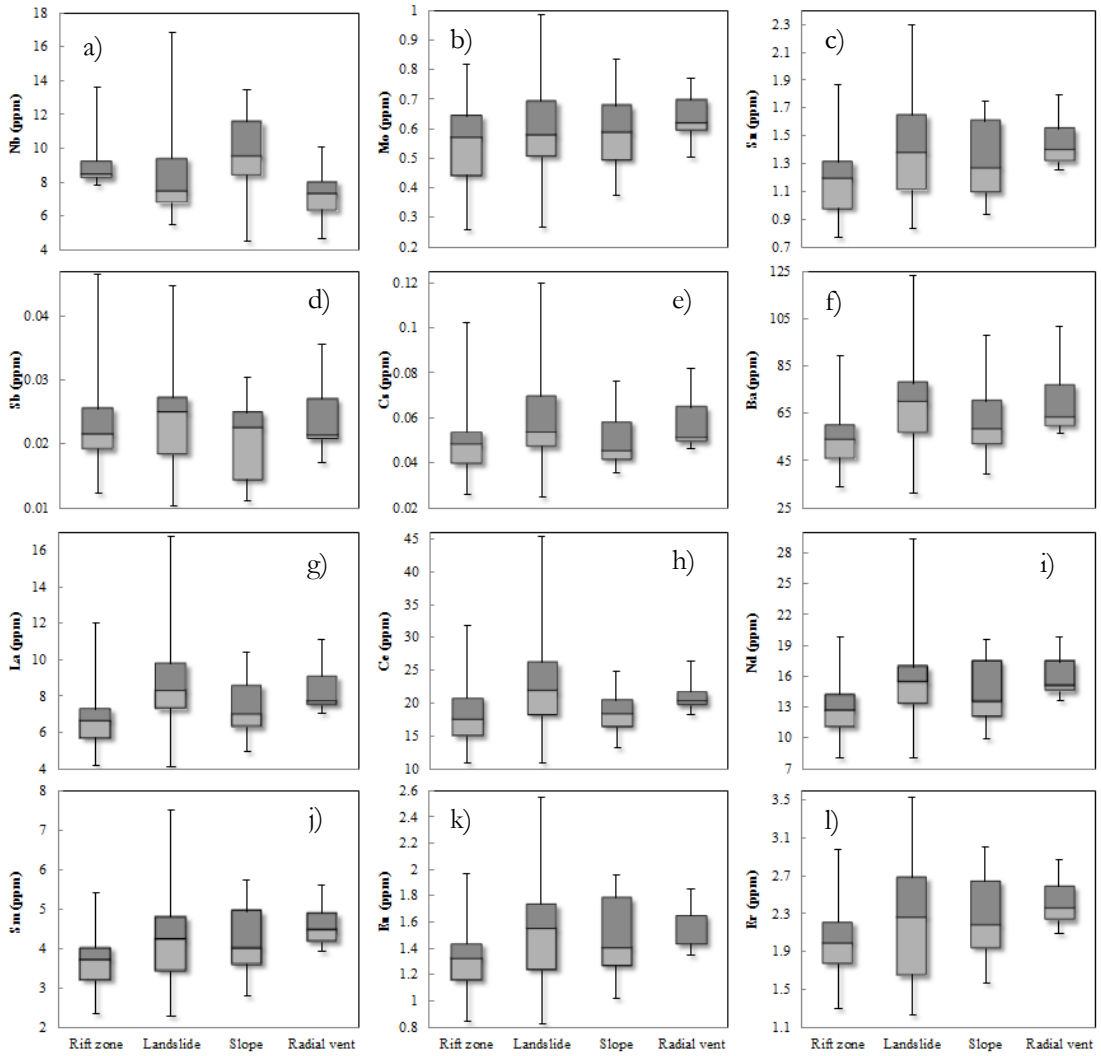

Figure 5.8 Five figure summaries (minimum, maximum, median, 1st quartile, and 3rd quartile) of trace element concentrations for rift zone, landslide, slope, and radial vent sample types. Whiskers display minimum and maximum range, while boxes display 1st quartile, median, and 3rd quartile values.

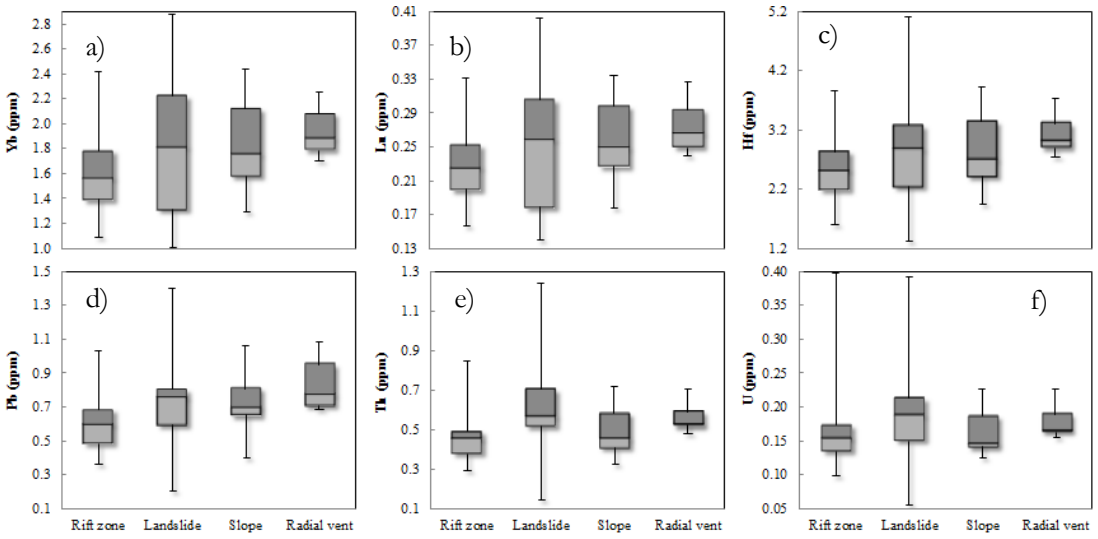

Figure 5.9 Five figure summaries (minimum, maximum, median, 1st quartile, and 3rd quartile) of trace elements ratios for rift zone, landslide, slope, and radial vent sample types. Whiskers display minimum and maximum range, while boxes display 1st quartile, median, and 3rd quartile values.

In order to establish if trace element variations between dredge localities remain when the effect of olivine accumulation/fractionation is removed, samples with <7 wt. % MgO were filtered out and the remaining samples were normalised to 15 wt. % MgO (an arbitrary value close to the inferred parental magma composition in chapter 7). The MgO normalisation was performed using the olivine addition/subtraction function in Petrolog, where progressive amounts of olivine can be added or subtracted to a sample composition that the user inputs. Results are shown below in Figure 5.10Figure 5.11.

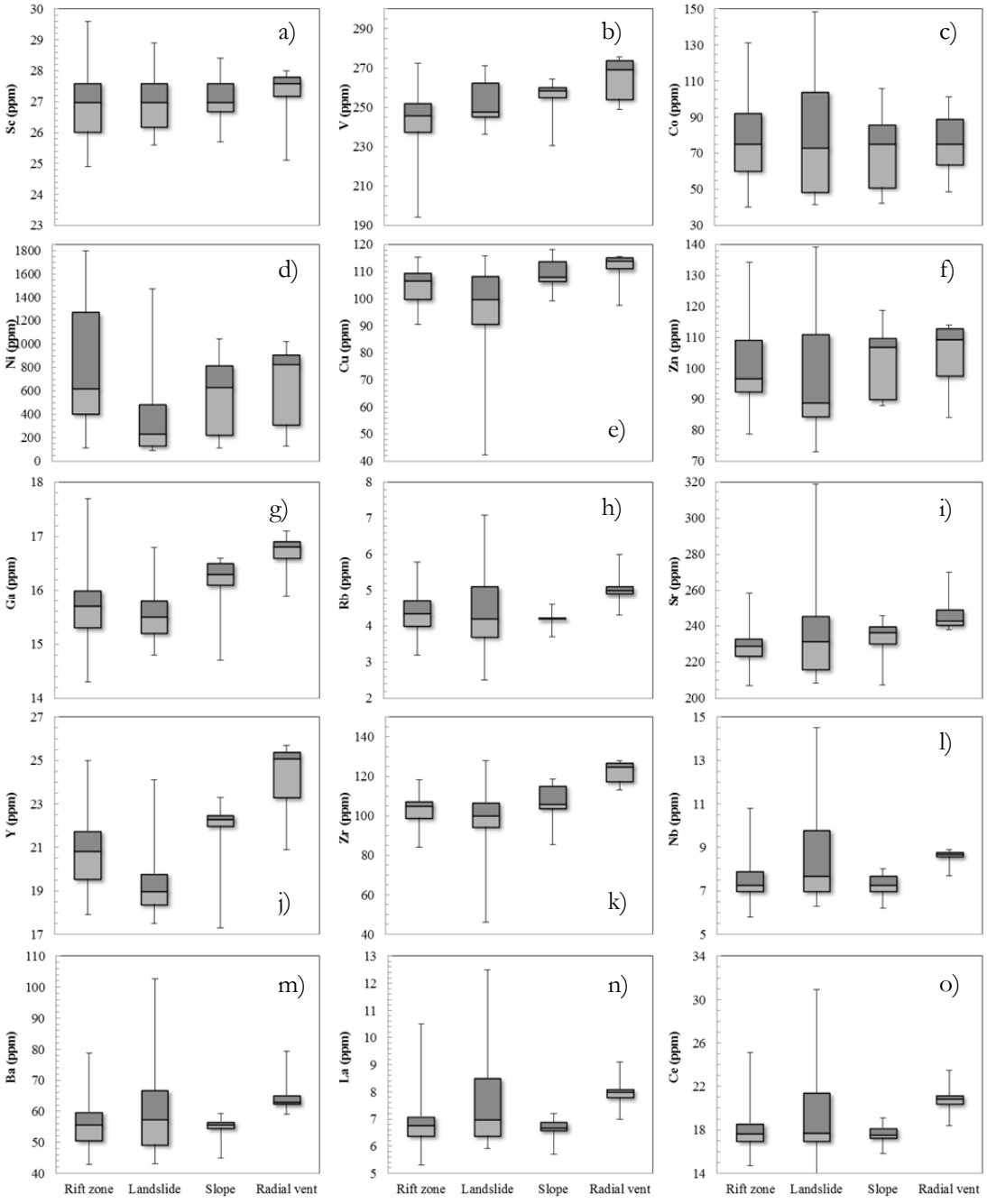

Figure 5.10 Trace element concentrations normalized to 15 wt. % MgO for samples with >7 wt. % MgO.

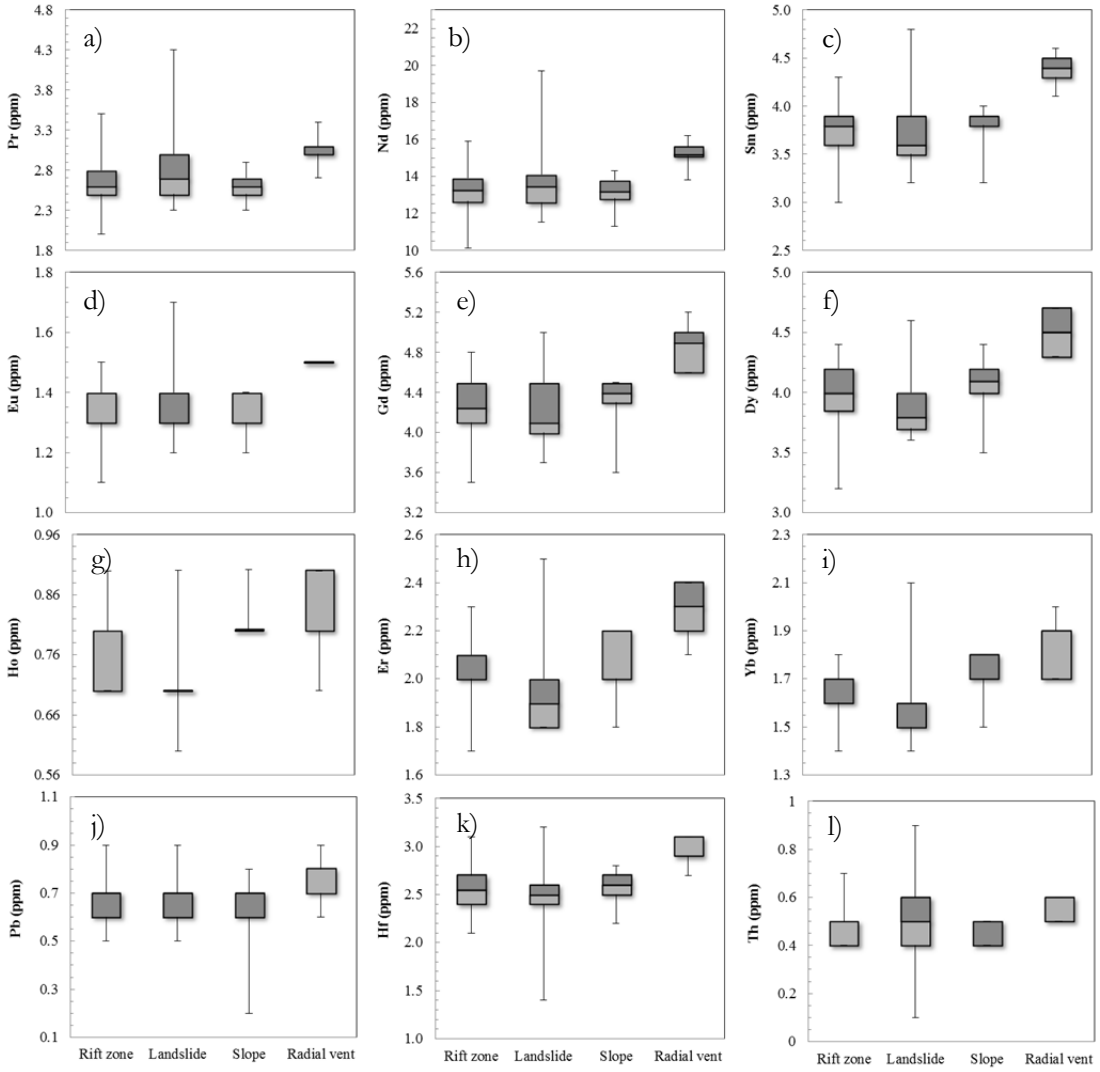

Figure 5.11 Trace element concentrations normalized to 15 wt. % MgO for samples with >7 wt. % MgO cont.

An ANOVA (analysis of variance) test was performed to determine if the differences in normalised trace element compositions of the four dredge type localities were significant. Results show that at the significance level of $p<0.05$ the null hypothesis is rejected and two or more means (of the four dredge locality types: slope, landslide, radial vent, or rift zone) are significantly different from one another in 21 of the 27 trace elements shown in Table 5.7Table 5.8Table 5.9. In order to establish which dredge locality types have means significantly different from each other, a Tukey HSD test was also performed on trace element concentrations. A Tukey HSD (honestly significant data) test is a way of reporting ANOVA results, and determines whether the relationship between pairs of data is statistically significant.

Table 5.7 Tukey HSD test results where sample symbols are S = slope, V = radial vent, R = rift zone, and L = landslide. 'Insignificant' means that the p value was greater than 0.05.

Pair	Tukey HSD Q statistic	Tukey HSD p-value	Tukey HSD inference	Tukey HSD Q statistic	Tukey HSD p-value	Tukey HSD inference	Tukey HSD Q statistic	Tukey HSD p-	Tukey HSD inference
	Sc			**V**			**Co**		
R vs L	0.461	0.900	insignificant	3.052	0.144	insignificant	0.460	0.900	insignificant
R vs S	0.704	0.900	insignificant	4.739	0.007	** p<0.01	1.150	0.829	insignificant
R vs V	1.123	0.839	insignificant	6.336	0.001	** p<0.01	0.234	0.900	insignificant
L vs S	0.221	0.900	insignificant	1.527	0.681	insignificant	1.308	0.767	insignificant
L vs V	0.695	0.900	insignificant	3.628	0.058	insignificant	0.504	0.900	insignificant
S vs V	0.500	0.900	insignificant	2.308	0.368	insignificant	0.566	0.900	insignificant
	Ni			**Cu**			**Zn**		
R vs L	3.465	0.078	insignificant	4.739	0.007	** p<0.01	0.960	0.900	insignificant
R vs S	1.672	0.624	insignificant	1.988	0.499	insignificant	0.647	0.900	insignificant
R vs V	0.631	0.900	insignificant	2.509	0.294	insignificant	1.253	0.788	insignificant
L vs S	1.580	0.660	insignificant	5.340	0.002	** p<0.01	1.283	0.777	insignificant
L vs V	1.967	0.509	insignificant	5.280	0.002	** p<0.01	1.728	0.602	insignificant
S vs V	0.615	0.900	insignificant	0.840	0.900	insignificant	0.650	0.900	insignificant
	Ga			**Rb**			**Sr**		
R vs L	0.620	0.900	insignificant	1.633	0.639	insignificant	2.918	0.174	insignificant
R vs S	4.390	0.014	* p<0.05	0.768	0.900	insignificant	0.983	0.895	insignificant
R vs V	6.311	0.001	** p<0.01	3.506	0.071	insignificant	3.432	0.080	insignificant
L vs S	4.106	0.024	* p<0.05	1.908	0.531	insignificant	1.467	0.705	insignificant
L vs V	5.979	0.001	** p<0.01	2.044	0.476	insignificant	1.148	0.830	insignificant
S vs V	2.519	0.290	insignificant	3.538	0.067	insignificant	2.306	0.368	insignificant

Table 5.8 Tukey HSD test results where sample symbols are S = slope, V = radial vent, R = rift zone, and L = landslide. 'Insignificant' means that the p value was greater than 0.05.

Pair	Tukey HSD Q statistic	Tukey HSD p-value	Tukey HSD inference	Tukey HSD Q statistic	Tukey HSD p-value	Tukey HSD inference	Tukey HSD Q statistic	Tukey HSD p-	Tukey HSD inference
	Y			**Zr**			**Nb**		
R vs L	4.325	0.016	* p<0.05	2.309	0.367	insignificant	5.023	0.004	** p<0.01
R vs S	2.883	0.183	insignificant	0.094	0.900	insignificant	0.576	0.900	insignificant
R vs V	7.518	0.001	** p<0.01	6.025	0.001	** p<0.01	2.665	0.243	insignificant
L vs S	5.755	0.001	** p<0.01	1.880	0.542	insignificant	4.396	0.014	* p<0.05
L vs V	9.440	0.001	** p<0.01	6.818	0.001	** p<0.01	0.890	0.900	insignificant
S vs V	4.566	0.010	** p<0.01	5.137	0.003	** p<0.01	2.684	0.237	insignificant
	Ba			**La**			**Ce**		
R vs L	3.819	0.041	* p<0.05	4.309	0.016	* p<0.05	3.957	0.032	* p<0.05
R vs S	0.281	0.900	insignificant	0.499	0.900	insignificant	0.434	0.900	insignificant
R vs V	3.191	0.118	insignificant	3.390	0.086	insignificant	3.787	0.044	* p<0.05
L vs S	3.213	0.114	insignificant	3.775	0.045	* p<0.05	3.447	0.079	insignificant
L vs V	0.352	0.900	insignificant	0.212	0.900	insignificant	0.791	0.900	insignificant
S vs V	2.941	0.169	insignificant	3.258	0.106	insignificant	3.558	0.065	insignificant
	Pr			**Nd**			**Sm**		
R vs L	3.797	0.043	* p<0.05	3.077	0.139	insignificant	0.387	0.900	insignificant
R vs S	0.781	0.900	insignificant	0.192	0.900	insignificant	1.142	0.832	insignificant
R vs V	3.830	0.041	* p<0.05	5.003	0.004	** p<0.01	8.150	0.001	** p<0.01
L vs S	3.608	0.060	insignificant	2.560	0.277	insignificant	0.640	0.900	insignificant
L vs V	0.932	0.900	insignificant	2.434	0.320	insignificant	6.953	0.001	** p<0.01
S vs V	3.826	0.041	* p<0.05	4.446	0.012	* p<0.05	6.272	0.001	** p<0.01

Table 5.9 Tukey HSD test results where sample symbols are S = slope, V = radial vent, R = rift zone, and L = landslide. 'Insignificant' means that the p value was greater than 0.05.

Pair	Tukey HSD Q statistic	Tukey HSD p-value	Tukey HSD inference	Tukey HSD Q statistic	Tukey HSD p-value	Tukey HSD inference	Tukey HSD Q statistic	Tukey HSD p-value	Tukey HSD inference
	Eu			**Gd**			**Dy**		
R vs L	1.369	0.743	insignificant	0.596	0.900	insignificant	1.230	0.798	insignificant
R vs S	0.631	0.900	insignificant	1.311	0.766	insignificant	1.700	0.613	insignificant
R vs V	6.338	0.001	** p<0.01	8.012	0.001	** p<0.01	7.188	0.001	** p<0.01
L vs S	0.548	0.900	insignificant	1.546	0.673	insignificant	2.363	0.346	insignificant
L vs V	4.718	0.007	** p<0.01	7.466	0.001	** p<0.01	7.148	0.001	** p<0.01
S vs V	5.049	0.003	** p<0.01	6.040	0.001	** p<0.01	5.070	0.003	** p<0.01
	Ho			**Er**			**Yb**		
R vs L	2.430	0.321	insignificant	2.099	0.453	insignificant	2.080	0.461	insignificant
R vs S	2.956	0.165	insignificant	2.126	0.442	insignificant	2.246	0.392	insignificant
R vs V	6.636	0.001	** p<0.01	6.074	0.001	** p<0.01	6.251	0.001	** p<0.01
L vs S	4.336	0.015	* p<0.05	3.393	0.086	insignificant	3.477	0.075	insignificant
L vs V	7.435	0.001	** p<0.01	6.725	0.001	** p<0.01	6.869	0.001	** p<0.01
S vs V	3.755	0.046	* p<0.05	3.824	0.041	* p<0.05	3.897	0.036	* p<0.05
	Hf			**Pb**			**Th**		
R vs L	1.783	0.580	insignificant	0.349	0.900	insignificant	3.434	0.080	insignificant
R vs S	0.302	0.900	insignificant	1.141	0.832	insignificant	1.125	0.839	insignificant
R vs V	6.545	0.001	** p<0.01	4.454	0.012	* p<0.05	3.557	0.065	insignificant
L vs S	1.641	0.636	insignificant	0.670	0.900	insignificant	3.609	0.060	insignificant
L vs V	6.938	0.001	** p<0.01	3.712	0.050	insignificant	0.925	0.900	insignificant
S vs V	5.447	0.001	** p<0.01	3.083	0.138	insignificant	3.820	0.041	* p<0.05

Ga, Y, and Ho were the trace elements which differentiated the dredge type localities the most, with concentrations of Y being significantly different between 5 of 6 dredge locality pairs. Ho and Ga concentrations were significantly different in 4 of 6 dredge locality pairs. Sc, Co, Ni, Zn, Rb, and Sr all had insignificant differences between the 6 dredge locality pairs, meaning that all four dredge localities were fairly homogeneous in terms of these elements. The radial vent and

rift zone pair was the most different pair, with significant differences across 16 of 27 trace elements, followed by the radial vent and slope pair (13), and then radial vent and landslide (12). The radial vent samples were therefore the most statistically different locality type for trace elements, thought these were the fewest in number (n = 7) and often not normally distributed; a requirement of the Tukey and ANOVA tests.

5.3 Trace element ratios

Trace element ratios that are commonly used to show variation in source or degree of melting are plotted in Figure 5.12 -Figure 5.15. All ratios e.g. La/Yb, Zr/Nb, Zr/Hf, Ce/Pb, K/U, Nb/U, Ba/Rb, Nb/Y, Nb/Ta, Sc/Y, and Sr/Nd should remain constant during olivine fractionation/accumulation except Ni/Co and Cu/Zn (Figure 5.12l and Figure 5.13f).. The data for these Mauna Loa lavas show that the ratios K/Cs, Zr/Hf, Nb/U, and Cs/Rb remain constant when plotted against MgO (Figure 5.12c,g,l, and Figure 5.13c) and CaO (Figure 5.14c,g,l, and Figure 5.15c). The average Nb/U and Ce/Pb ratios in these samples are 48.6 and 29.4 respectively, which are significantly elevated relative to the primitive mantle values of 30 and 9 (Hofmann et al., 1986). La/Yb, Zr/Nb, La/Sm, Nb/Y, and Th/U are constant for the majority of the data; however a second group of data can be differentiated using these ratios (La/Yb >5, Zr/Nb <10, La/Sm >2, Nb/Y >0.5 - Figure 5.12a, b, d, e and Th/U <2.5 - Figure 5.13g). Some of the evolved samples (MgO < 10 wt. %) have higher La/Yb, La/Sm, Nb/Y, and lower Zr/Nb, while the higher MgO samples (MgO >10 wt. %) have lower La/Yb, La/Sm, Nb/Y, and Zr/Nb (Figure 5.12a, b, d, e, h). In addition, 6 rift zone samples (M2-19, M2-20, M1-20, M1-26, M1-27, M1-30) have low Nb/U (<35) (Figure 5.12i).

Sample M14-32 has an anomalously high Ce/Pb of 77.8 and Nb/U of 123.2 due to low Pb and U (0.21 and 0.06 ppm respectively) (Figure 5.12i, j), and sample M11-5 has anomalously low K/Cs (19.5) due to high K (0.5 wt. %) (Figure 5.12c).

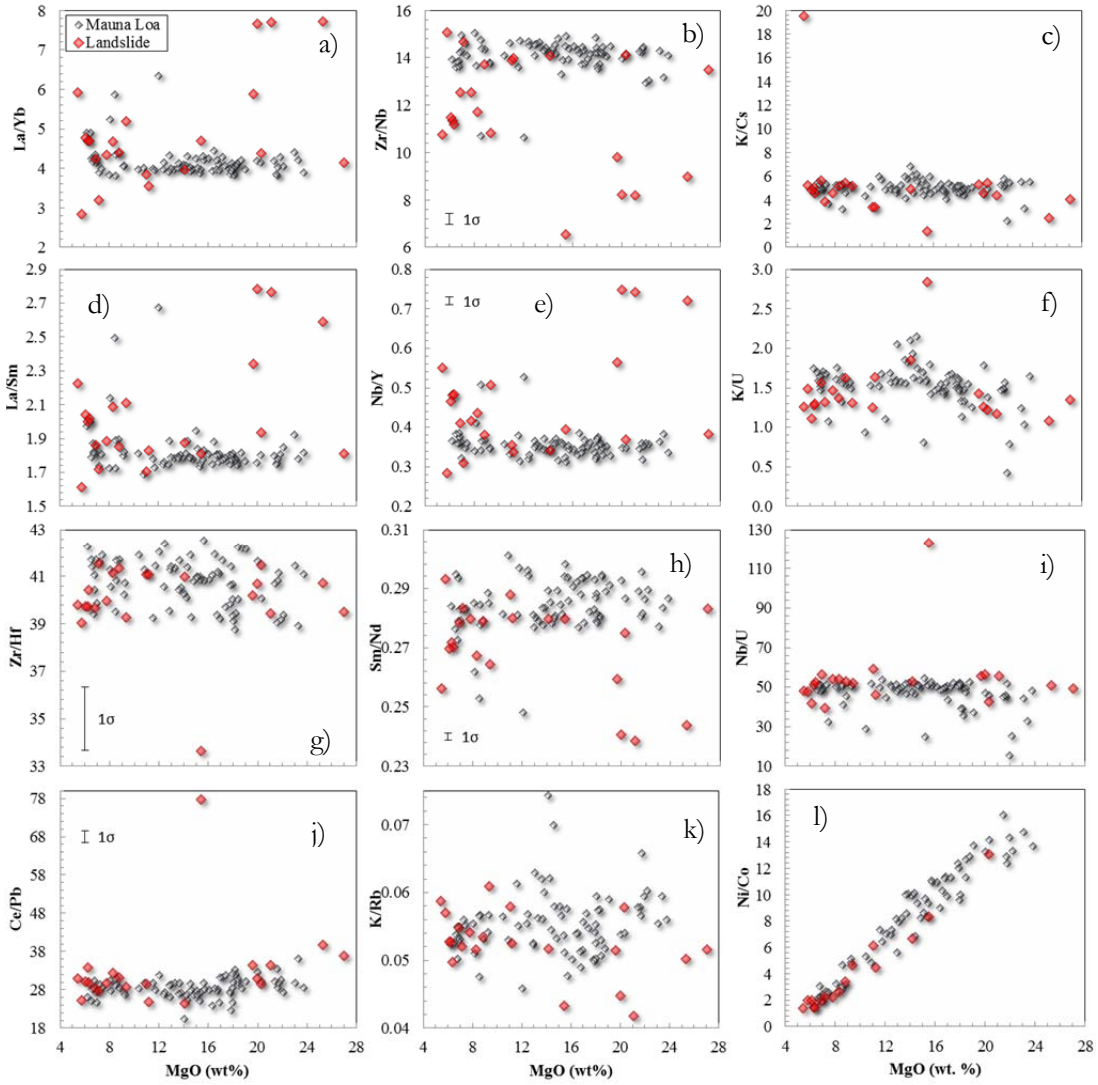

Figure 5.12 Trace element ratios versus MgO (wt. %). Here, K (element) is in weight %.

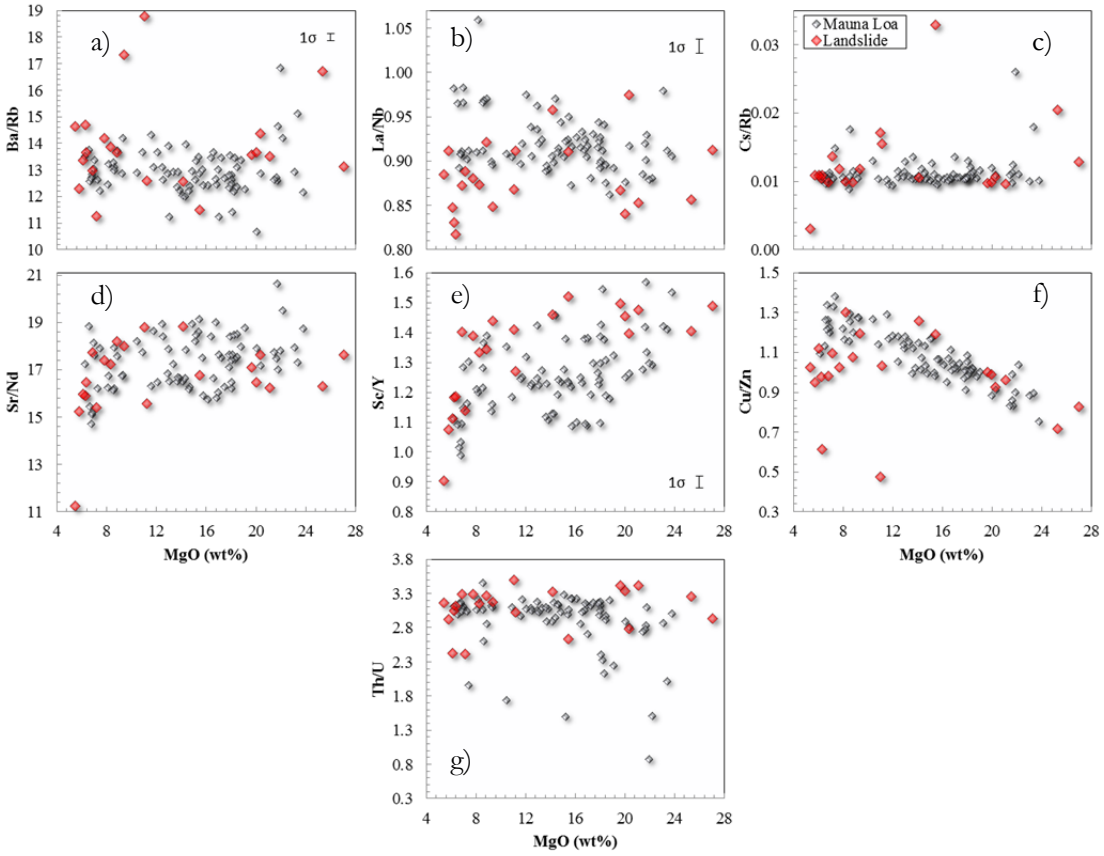

Figure 5.13 Trace element ratios versus MgO (wt. %) cont.

Some ratios display an apparent break in slope at approximately 15 wt. % MgO e.g. K/U (Figure 5.12f) and Ce/Pb (Figure 5.12j) while others such as Sc/Y and Cu/Zn show a break in slope at around 8 wt. % MgO (Figure 5.13e,f). Ba/Rb may show a slight break in slope at around 18 wt. % MgO (Figure 5.13a).

As with the trace element concentrations, the landslide samples are more scattered in their ratio values, most noticeably in La/Yb, Zr/Nb, La/Sm, and Nb/Y (Figure 5.12a,b,d,e).

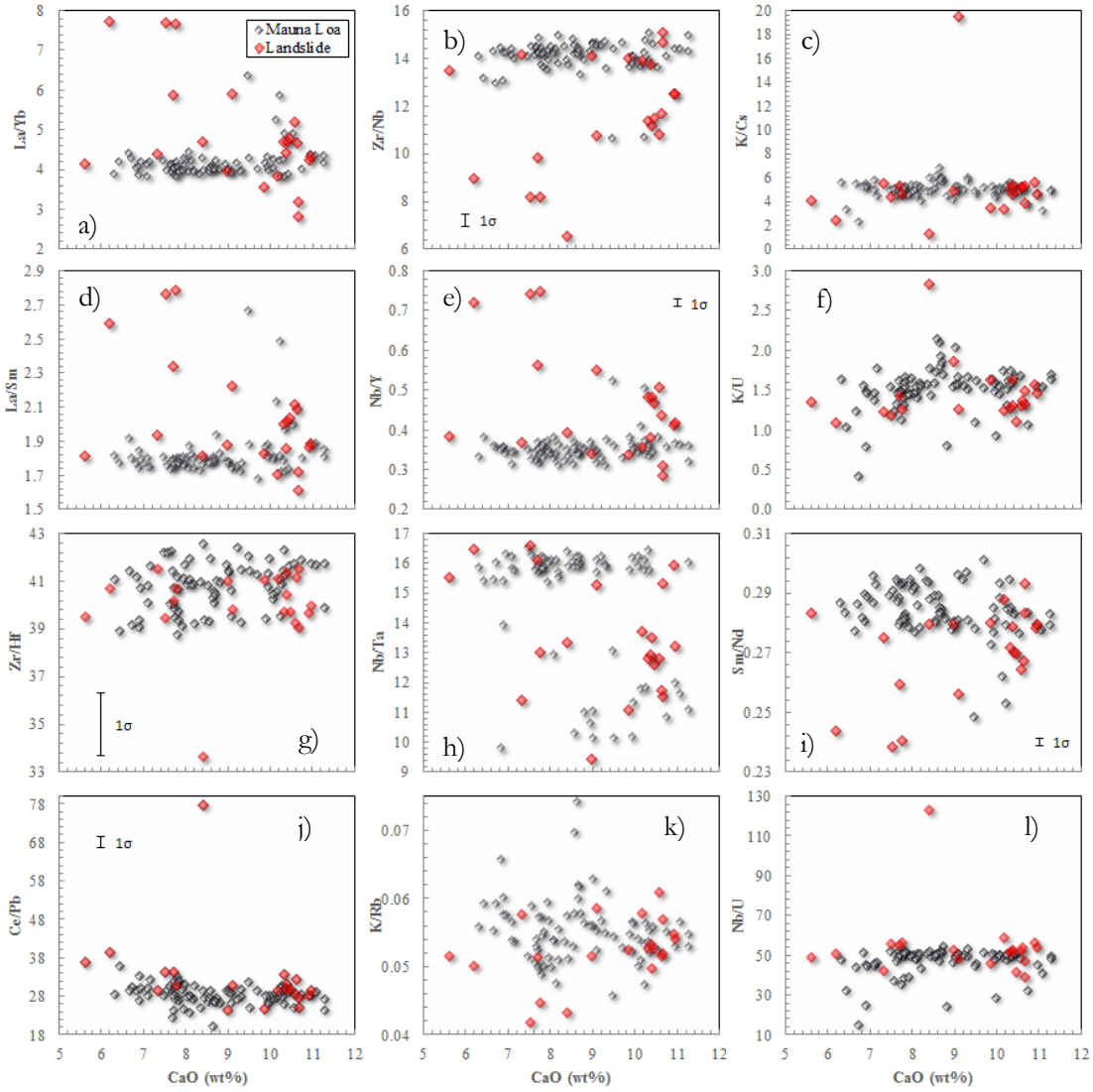

Figure 5.14 Trace element ratios versus CaO (wt. %). Here, K is in weight %.

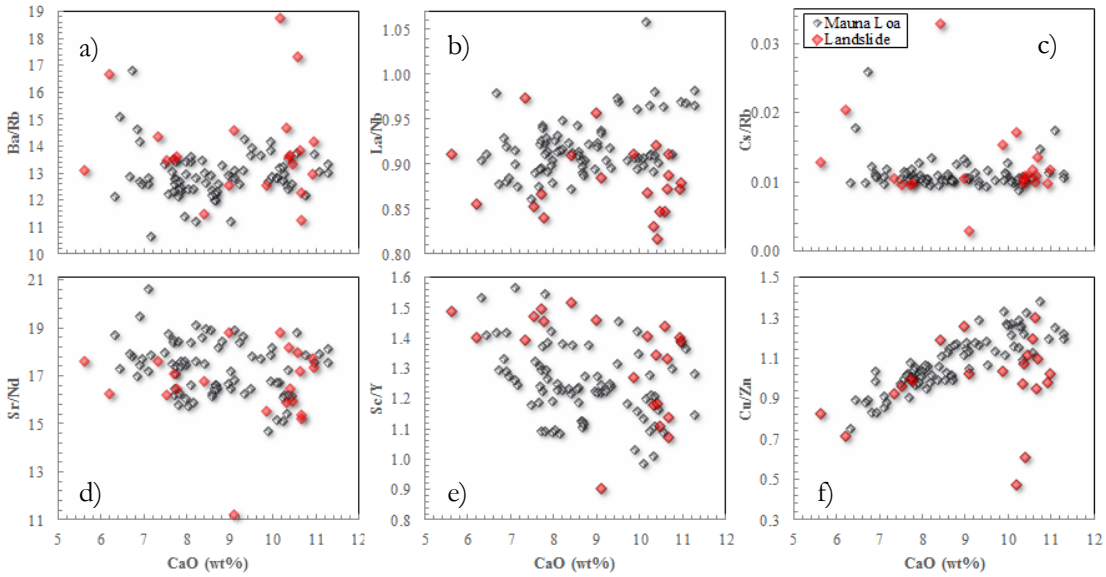

Figure 5.15 Trace element ratios versus CaO (wt. %) cont.

5.3.1 Zr, Nb, and La

The plots shown in Figure 5.16 a, b, and c show that the concentrations of Zr, Nb, and La clearly distinguish the landslide samples from the rest of the Mauna Loa dredge samples. Some landslide samples have a higher Nb and La concentration for a given Zr concentration, and a higher Nb for a given value of La at high concentrations of La and Nb. There is also a break in the data separating the high La and Nb samples (4.2-8.9 and 4.6-10.5 respectively) from the low La and Nb samples (9.8-16.7 and 10.8-18.9 respectively).

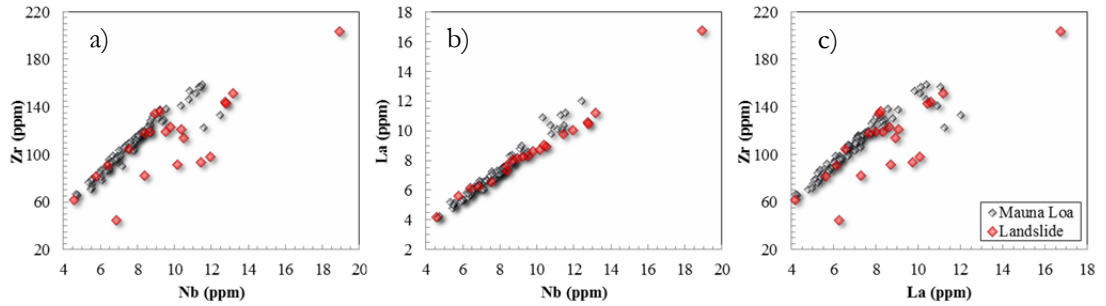

Figure 5.16 a) Zr versus Nb, b) La versus Nb, and c) Zr versus La.

The trace element ratio Zr/Nb has been observed to correlate with isotopic signatures in observations across multiple Hawaiian volcanoes e.g. (Roden et al., 1994, Norman and Garcia, 1999) (Frey et al., 2016). The Zr/Nb ratios for these samples mostly do not correlate with MgO or CaO, and display a horizontal trend confirming they are unaffected by olivine fractionation (Figure 5.12b and Figure 5.14b).

The ratio of Zr/Nb versus CaO distinguishes two groups very clearly, separating them into low Zr/Nb (6.6-12.5) and high Zr/Nb (13.1-15.1) groups (Figure 5.14b). The variation in this ratio is mostly the result of variation in Nb concentration, while Zr remains fairly constant.

The samples with Zr/Nb average of 14.5 have relatively constant Zr/Nb regardless of CaO contents; however the samples with low Zr/Nb (6-12) are mostly landslide samples plus M26-43 and M17-6, and appear to be slightly positively correlated with CaO. Other TE ratios also show similar trends, e.g. La/Sm, La/Yb, Nb/Y (Figure 5.14a, d, e).

A plot of Zr/Nb versus SiO_2 normalized to 13 wt. % MgO was used by (Rhodes et al., 2012) to distinguish various types of tholeiitic Mauna Kea lavas from one-another. It was inferred in the Rhodes study that MgO normalised SiO_2 and Zr/Nb would reflect changes in melt production, depth of melt segregation, and differences in plume source components (Rhodes and Vollinger, 2004). Data from this study are plotted in Figure 5.17, where Zr/Nb is plotted against SiO_2 normalized to 15 wt. % MgO, because 15 wt. % is thought to be closer to the estimated Mauna Loa parental Magma composition (see background section of this thesis). There is a clustering of the majority of the data between 49.2 and 50 wt. % SiO_2 and Zr/Nb of 13.9 to 15.1. Many of the landslide samples vary in Zr/Nb (6.6-14.7) and somewhat in SiO_2 (15) (47.2-50.1). The same study plotted Y (13) against Nb (13) to distinguish samples that may have formed from a lower degree of melting in the presence of garnet, forming a negative slope. Figure 5.17b shows a plot of Y (15) versus Nb (15) for the data in this study. The majority of the samples form a steep positive slope, while many of the landslide samples are scattered toward higher values of Nb as well as M19-2 and M19-17. Again, it appears to be the Nb which is causing the differentiation between the two sample types.

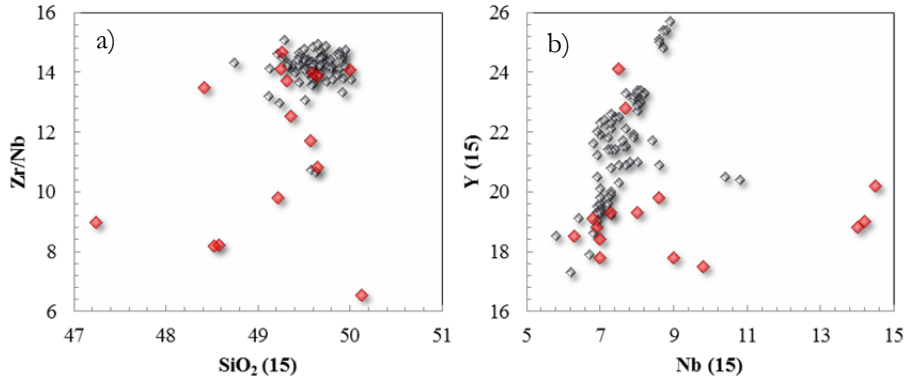

Figure 5.17 a) SiO_2 normalized to 15 wt. % MgO versus Zr/Nb, b) Y versus Nb normalized to 15 wt. % MgO. All samples off olivine control line (<7 wt. % MgO) removed.

5.3.2 La/Yb, La/Sm, and Nb/Y

Like with the Zr/Nb ratio, two main groups can also be seen when La/Yb, La/Sm, and Nb/Y are plotted against CaO (Figure 5.14a, d, e), or two trends that intersect at high CaO. The two groups are visibly separated from one another, and the high La/Yb, La/Sm, and Nb/Y group is negatively correlated with CaO.

La/Yb, La/Sm, and Nb/Y are thought to remain constant during olivine frationation, and may be able to distinguish variable degrees of partial melting e.g. (West et al., 1992, Norman and Garcia, 1999). The samples have La/Yb values from 2.5 through to 7.7 and La/Sm ratios ranging from 1.5 to 2.8. La/Sm, and La/Yb are moderately negatively correlated with Zr/Nb with R^2 values of 0.62-0.64 (Figure 5.18b,c).

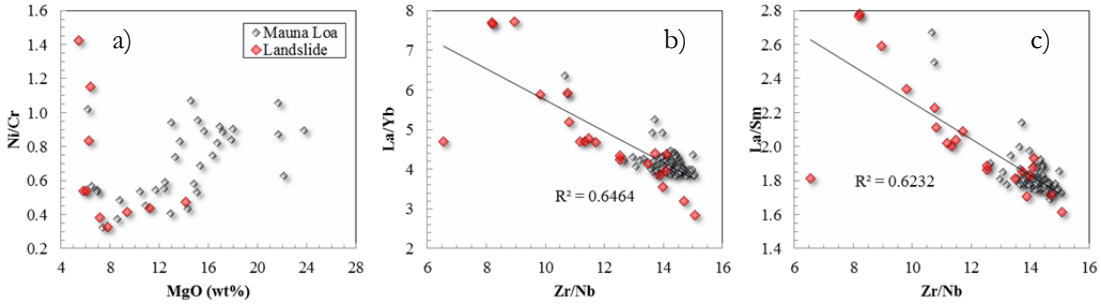

Figure 5.18 Trace element ratios a) Ni/Cr versus MgO (wt. %), b) La/Yb versus Zr/Nb, and c) La/Sm versus Zr/Nb.

5.3.3 Sr/Nd, Sc/Y

The ratios Sr/Nd and Sc/Y (Figure 5.13d, e) may be able to distinguish the effects of plagioclase and pyroxene fractionation, respectively. For the samples studied here, Sc/Y decreases slightly with decreasing values of MgO, and appears to decrease further below ~8 wt.

% although the data points are highly scattered. It can also be seen that the landslide samples have higher Sc/Y on average than the other samples. There is also a cluster of data at around 15 wt. % MgO which has low Sc/Y. Sr/Nd remains constant at most values of MgO, with the exception of 4 evolved samples which have slightly lower Sr/Nd (M11-5, M18-35, M6-6, and M6-26).

5.3.4 K, Th, U

K/U can be fractionated by alkali feldspar however the data from this study show little variation in K/U (Figure 5.14f). The ratio of K (ppm)/U (ppm) for the bulk silicate Earth is 1.27 x 10^{-4} (Jochum et al., 1983) (K (wt. %)/U = 1.27) and in this study it is closer to 1.5 for most samples. The concentrations of Th and U may be affected by sea water contamination (Jochum et al., 1983) and U is known to be affected by low-T alteration in Hawaiian basalts (Hofmann and White, 1982). The primitive mantle has a Th/U ratio of 3.6-4 while most of the samples in this study have a ratio of 3.1-3.2, although some have very low Th/U (0.8-1.8) (Figure 5.13g), and there is no correlation with MgO. A plot of La/Yb versus Th/U distinguishes a group with a wide range in La/Yb (3-7.8) and narrow range in Th/U from and a group with a wide range of Th/U (0.8-3.4) and narrow range in La/Yb (Figure 5.19).

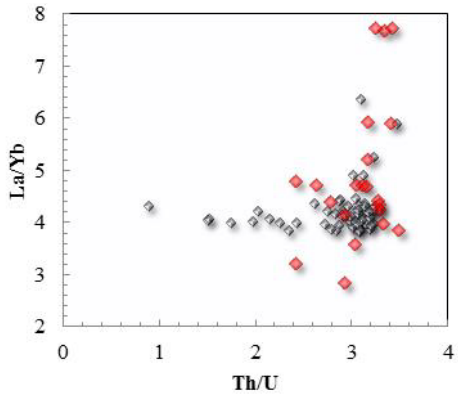

Figure 5.19 La/Yb versus Th/U.

The lavas with anomalously low Th/U tend to have unusually high U (e.g. 0.215-0.397) corresponding to samples M1-20, M1-26, M1-27, M1-30, and M2-19.

5.3.5 Ni/Cr

Figure 5.18a shows the ratio of Ni/Cr changing with MgO. The ratio decreases with decreasing MgO until below 8 wt. % it increases sharply. Ni and Cr ratios may be able to distinguish between olivine and clinopyroxene fractionation because of the strong compatibility of Ni into olivine and Cr into cpx. As the proportion of olivine increases with increasing MgO, Ni

increases relative to Cr, while a jump in Ni/Cr at low MgO may indicate that Cr is being removed by a fractionating cpx phase.

5.3.6 Redox indicators

The ratios of Sc/V, Zr/V, and Ti/100V have been used by (Canil, 1999) to determine the fO_2 of silicic melts using the variable valence state of V in the fO_2 range NNO-3 to NNO+2 (within the range of Hawaiian magma chambers ~QFM). The partition coefficients of V between a phase such as opx or olivine (and therefore the bulk rock) and the melt will change due to the variable valence state of V with varying fO_2. Data from this study are plotted (Figure 5.20a, b, c) showing that the ratios differ greatly from primitive mantle values. The data are significantly lower in Sc/V, and higher in Zr/V and Ti/100V than primitive mantle. The Sc/V vs. V data appears to suggest slightly different slopes for the landslide vs. other samples (Figure 5.20a).

The evaluation of redox through this method however, requires a good understanding of mineralogy during melting as these elements can be strongly fractionated by garnet and pyroxene. The large difference seen in these ratios vs. PM is unlikely the results of redox effects alone.

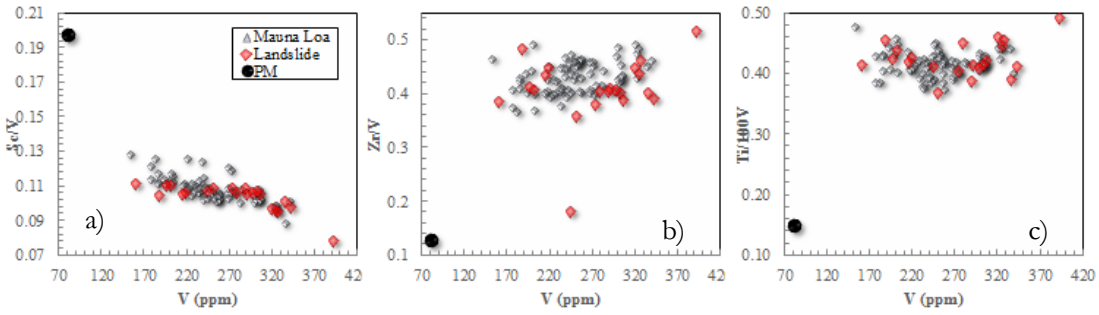

Figure 5.20 a) Sc/V, b)Zr/V, and c)Ti/100V versus V. Black marker shows primitive mantle values.

5.4 Comparison to primitive mantle and MORB

When the trace elements are normalised against primitive mantle, they display an overall enriched signature, with most trace elements enriched 5-10 times relative to primitive mantle (PM) (Figure 5.21). The large ion lithophile elements (LILE), light rare earth elements (LREE), and high field strength elements (HFSE) are more enriched relative to the heavy rare earth elements (HREE) and display a wider range in composition, in particular Rb, Ba, Nb, La, and Ce. Cs, Rb, Ba, Th, U, Nb, La, Ce, Pb, Pr, Nd, Sr, Sm, Zr, Hf, Eu, Sn, Sb, Gd, and Li are also enriched relative to MORB while the mid-heavy REE (Dy, Ho, Y, Er, Yb, and Lu) are depleted with respect to MORB. Elements Th, Pb, Sb, and Li all show significant negative anomalies,

with Pb, Sb, and Li anomalies also appearing in MORB. Sr shows a slight positive anomaly in contrast to MORB which displays a slight negative anomaly. The elements displaying the widest range in concentration are Nb, Ce, La, Nd, Sr, and Ba while elements such as Th, Pb, Li, Cs, and Lu have the narrowest range in normalised value.

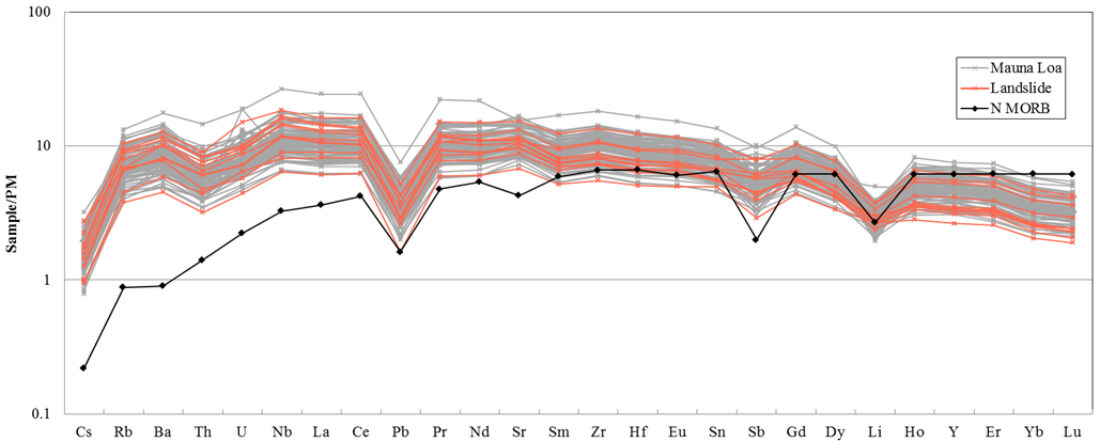

Figure 5.21 Sample trace element concentrations normalized to primitive mantle (McDonough and Sun, 1995). N-MORB normalized to 8 wt. % MgO (Sun and McDonough, 1989) is also shown in black.

The elements which are compatible in olivine Co, Cr, and Ni are below primitive mantle values. PM-normalised Ni ranges are wide from 0.03 to 0.73, as are PM-normalised Cr ranging from 0.02 to 0.61. Sc, Zn, Ga, Cu, and V are enriched relative to PM (1.1-5.3 times) and have a smaller range in normalized values (Figure 5.22). Co is slightly depleted relative to PM (0.38 to 0.98). There is a twist in the data in Figure 5.22 between V and Cr, and Ni and Cu indicating that those samples which are high in Ga, Cu, V, Zn, and Sc are low in Cr, Co, and Ni.

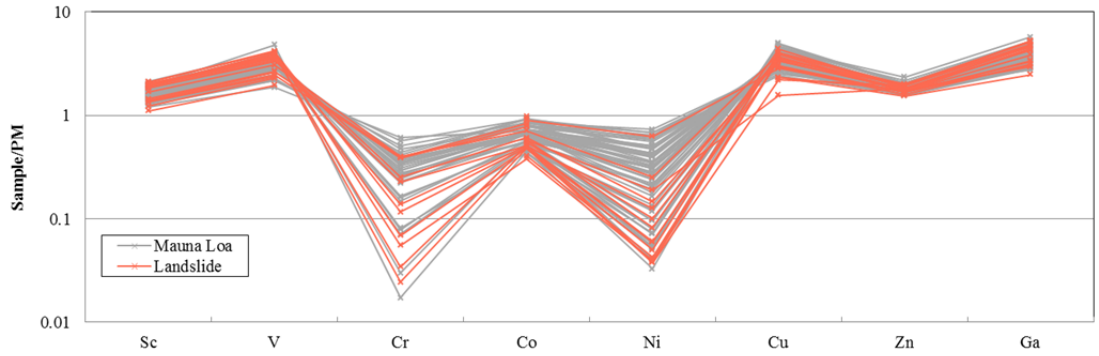

Figure 5.22 Sample compatible and moderately incompatible trace element concentrations normalized to primitive mantle (McDonough and Sun, 1995).

The range in variation from PM is reduced slightly when the trace element concentrations are normalized to 15 wt. % MgO (Figure 5.23). This was achieved by adding/subtracting olivine. Some concentrations appear to step in integers however this is simply an artefact of Petrolog, because of the limited number of decimal places allowed in the input.

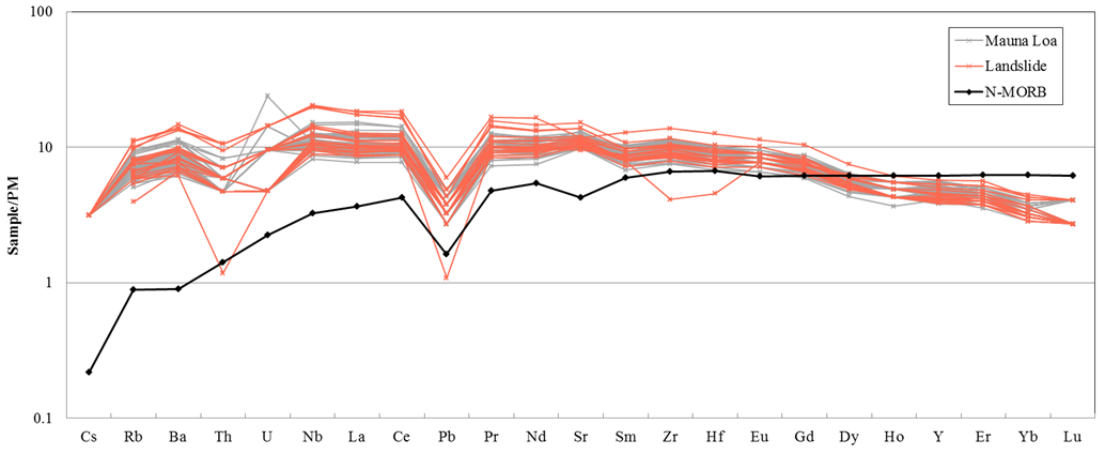

Figure 5.23 Sample trace element concentrations normalized to primitive mantle (McDonough and Sun, 1995) and to 15 wt. % MgO. N-MORB normalized to 8 wt. % MgO (Sun and McDonough, 1989) is also shown in black.

This range is again slightly reduced for Nb, Pr, Sm, Zr, Hf and some of the HREE when samples with less than 7 wt. % MgO (which may be affected by cpx or plagioclase fractionation) are removed (Figure 5.24).

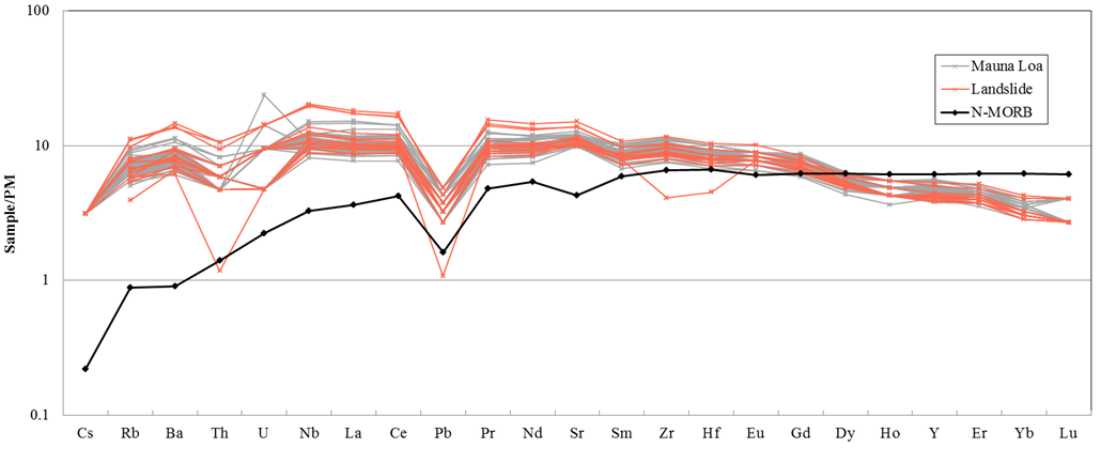

Figure 5.24 Sample trace element concentrations normalized to primitive mantle (McDonough and Sun, 1995) and to 15 wt. % MgO, with samples with less than 7 wt. % MgO removed. N-MORB normalized to 8 wt. % MgO (Sun and McDonough, 1989) is also shown in black.

6 Isotope results

The $^{143}Nd/^{144}Nd$ and $^{87}Sr/^{86}Sr$ isotopic composition was obtained for 20 Mauna Loa submarine samples. These samples were chosen so as to represent a wide range in major element and trace element compositions; in particular the ratio Zr/Nb which is often used as a proxy for isotopic source composition as it should remain constant during magmatic fractionation processes and remain unaltered by seawater (Table 6.1). Details of laboratory and analytical procedures can be found in 'Methods' section in the appendices.

The Mauna Loa submarine south west rift samples from this study range from 0.703697 – 0.704184 $^{87}Sr/^{86}Sr$ and 0.512862 – 0.512943 $^{143}Nd/^{144}Nd$.

Table 6.1 $^{143}Nd/^{144}Nd$ and $^{87}Sr/^{86}Sr$ of Mauna Loa submarine south west rift zone samples. 2 S.E is two times the absolute error value of the individual sample analysis (internal error) multiplied by 10^6. *Data in light grey is the Weis et al. (2011) result for two samples which were analysed in both labs. 1σ for standard analysis is the standard deviation of seven replicate analyses of the standard NBS 987.

Sample #	Dredge type	$^{87}Sr/^{86}Sr$	2 S.E.	$^{143}Nd/^{144}Nd$	2 S.E.	εnd
M1-1	Rift zone	0.703749	11	0.512919	5	5.5
M1-16	Rift zone	0.703699	10	0.512916	4	5.4
M2-10	Rift zone	0.703772	8	0.512923	4	5.6
M2-18	Rift zone	0.703743	15	0.512930	4	5.7
M2-19-a	Rift zone	0.703768	9	0.512941	4	5.9
M2-19-b	Rift zone	0.703774	9	0.512939	6	5.9
M2-26	Rift zone	0.703719	11	0.512942	6	5.9
M4-7	Rift zone	0.703742	11	0.512943	5	5.9
M4-21	Rift zone	0.703955	116	0.512890	6	4.9
M19-17	Rift zone	0.703847	10	0.512862	4	4.4
M19-17*	Rift zone	0.703812	5	0.512880	20	4.7
M26-43	Slope	0.703814	11	0.512916	4	5.4
M26-44	Slope	0.703821	20	0.512916	5	5.4
M29-5	Slope	0.703708	11	0.512935	4	5.8
M11-5	Landslide	0.704184	10	0.512914	4	5.4
M12-4	Landslide	0.70377	8	0.512917	3	5.4
M12-17	Landslide	0.703776	11	0.512921	6	5.5
M12-42	Landslide	0.703744	10	0.512934	8	5.8
M13-12	Landslide	0.703712	8	0.512905	6	5.2
M13-12*	Landslide	0.703659	4	0.512916	4	5.4
M13-25	Landslide	0.703736	18	0.512934	5	5.8
M13-38	Landslide	0.703697	7	0.512903	4	5.2
Standard	-	**average**	**1σ**	**n**	-	-
NBS 987	-	0.710257	7.1E-06	7	-	-

The standard NSB 987 was analysed seven times over two analytical sessions separated by three months, and had an average value of 0.710257 and a standard deviation of 7.1 x 10^{-6}.

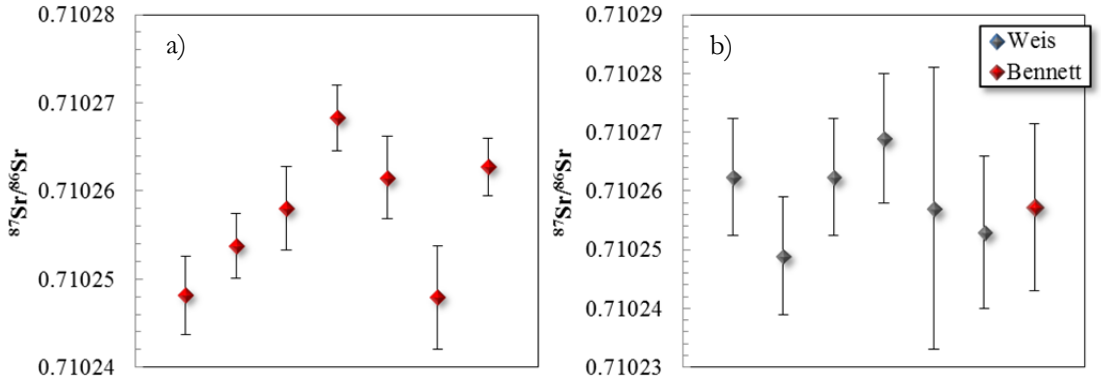

Figure 6.1 a) individual analyses of standard NSB 987 from this study where errors are two times the absolute error value of the individual sample analysis, b) repeat analyses of standard NSB 987 by Weis (grey) where points are averages of 19, 19, 19, 11, 3, and 7 analyses respectively, and this study (red) where n = 7. In (b) error bars represent two times the standard deviation of the average of repeat analyses in each session.

A further criteria for sample selection was that the samples compliment the suite of isotopic data already collected by Weis et al. (2011). Samples were compiled and plotted by lab and by dredge type (Figure 6.2). The Weis data plot in a similar isotopic range, but reach to sligthly lower values of $^{87}Sr/^{86}Sr$ and higher values of $^{143}Nd/^{144}Nd$. This trend is seen in the replicate analysis of samples M13-12 and M19-17 from both the Weis and Bennett labs, where the Weis lab analyses are lower in $^{87}Sr/^{86}Sr$ by 5.3 x 10^{-5} and 3.5 x 10^{-5} respectively, and higher in $^{143}Nd/^{144}Nd$ by 2.9 x 10^{-5} and 1.8 x 10^{-5} respectively. This may not be significant for Sr given that repeat analyses of one sample (M2-19) in our lab revealed a difference in $^{87}Sr/^{86}Sr$ of 3.1 x 10^{-5}. The sample was separated into two aliquots (a and b) after the acid digestion process, and therefore the variation is the result of the isotope column separation procedure. A difference in $^{143}Nd/^{144}Nd$ of 2.0 x 10^{-6} was found for the M2-19 repeat, which is the same order of magnitude as internal reproducibility.

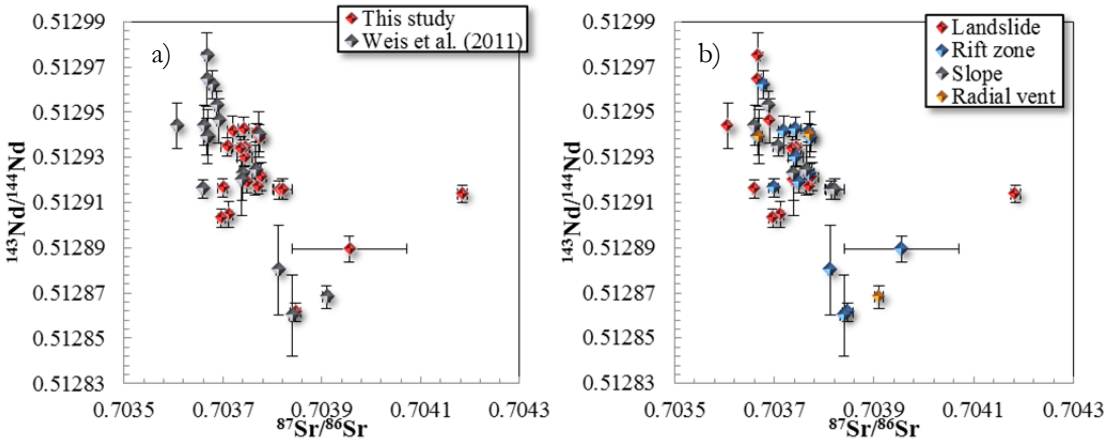

Figure 6.2 $^{143}Nd/^{144}Nd$ versus $^{87}Sr/^{86}Sr$ of Mauna Loa submarine south west rift zone samples. a) $^{143}Nd/^{144}Nd$ versus $^{87}Sr/^{86}Sr$ from this study (red) and Weis et al. (2011) (grey), b) the same results by dredge type locality. Error bars are 2 x the absolute error value of the individual sample analysis (internal error).

A weak negative relationship (R^2 = 0.31) can be seen when $^{143}Nd/^{144}Nd$ is plotted against $^{87}Sr/^{86}Sr$ (Figure 6.1) and two main groupings can be seen, one at higher $^{87}Sr/^{86}Sr$ and lower $^{143}Nd/^{144}Nd$ and one at lower $^{87}Sr/^{86}Sr$ and higher $^{143}Nd/^{144}Nd$. There is no obvious isotopic grouping of the samples by dredge locality type (landslide, rift zone, slope, or radial vent). One sample displays anomalously high $^{87}Sr/^{86}Sr$ (M11-5).

6.1 Isotopic composition with major element variation

Analyses of Sr and Nd isotopes were plotted by dredge type by major element oxides (Figure 6.3, Figure 6.4). No correlation was observed between $^{87}Sr/^{86}Sr$ and $^{143}Nd/^{144}Nd$ and the major element oxides (e.g. R^2 for MgO versus $^{87}Sr/^{86}Sr$ = 0.0098, R^2 for MgO versus $^{143}Nd/^{144}Nd$ = 0.0124). The array remains uncorrelated when the high $^{87}Sr/^{86}Sr$, low $^{143}Nd/^{144}Nd$ group is removed.

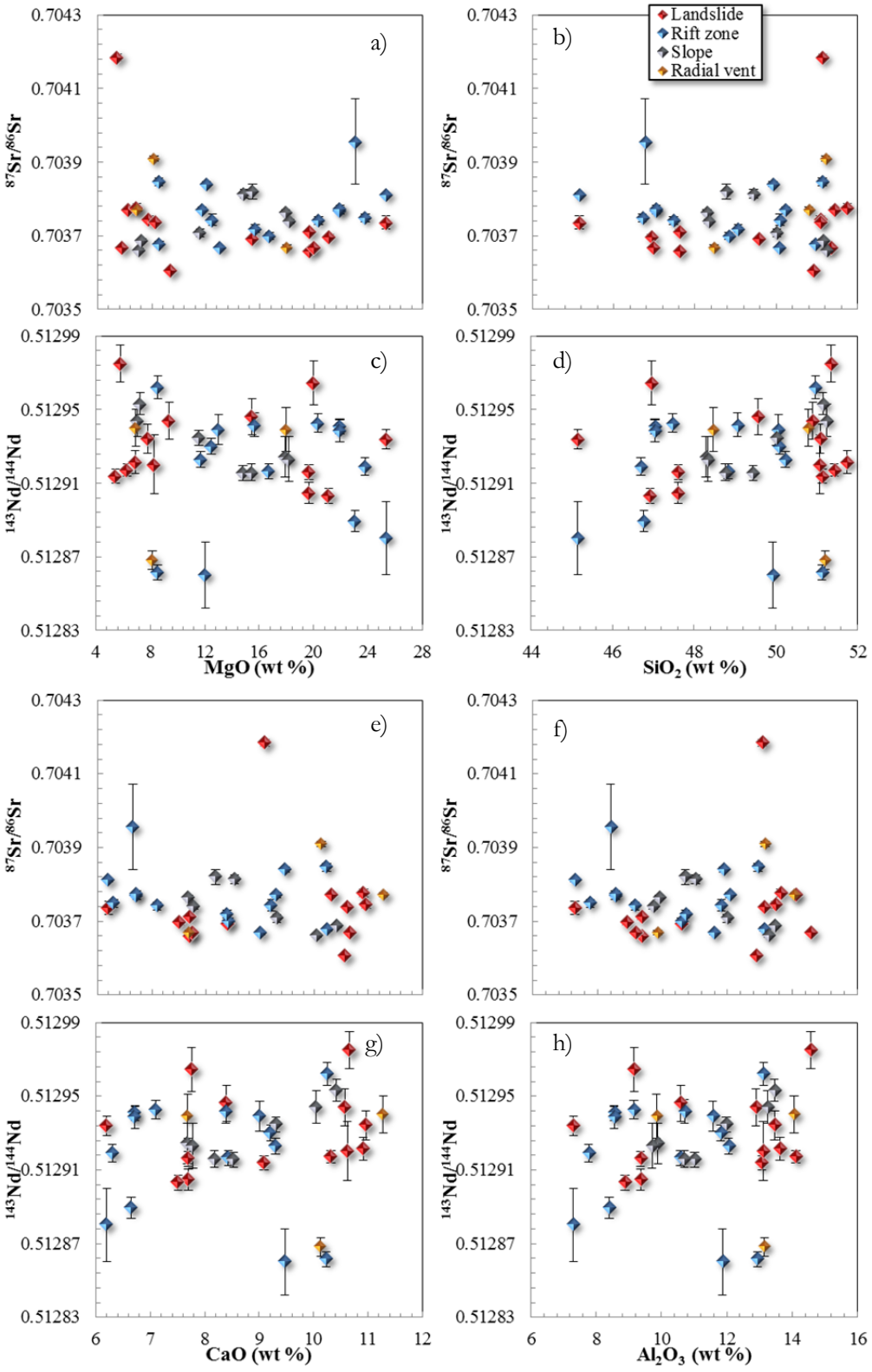

Figure 6.3 $^{87}Sr/^{86}Sr$ and $^{143}Nd/^{144}Nd$ versus major element oxides.

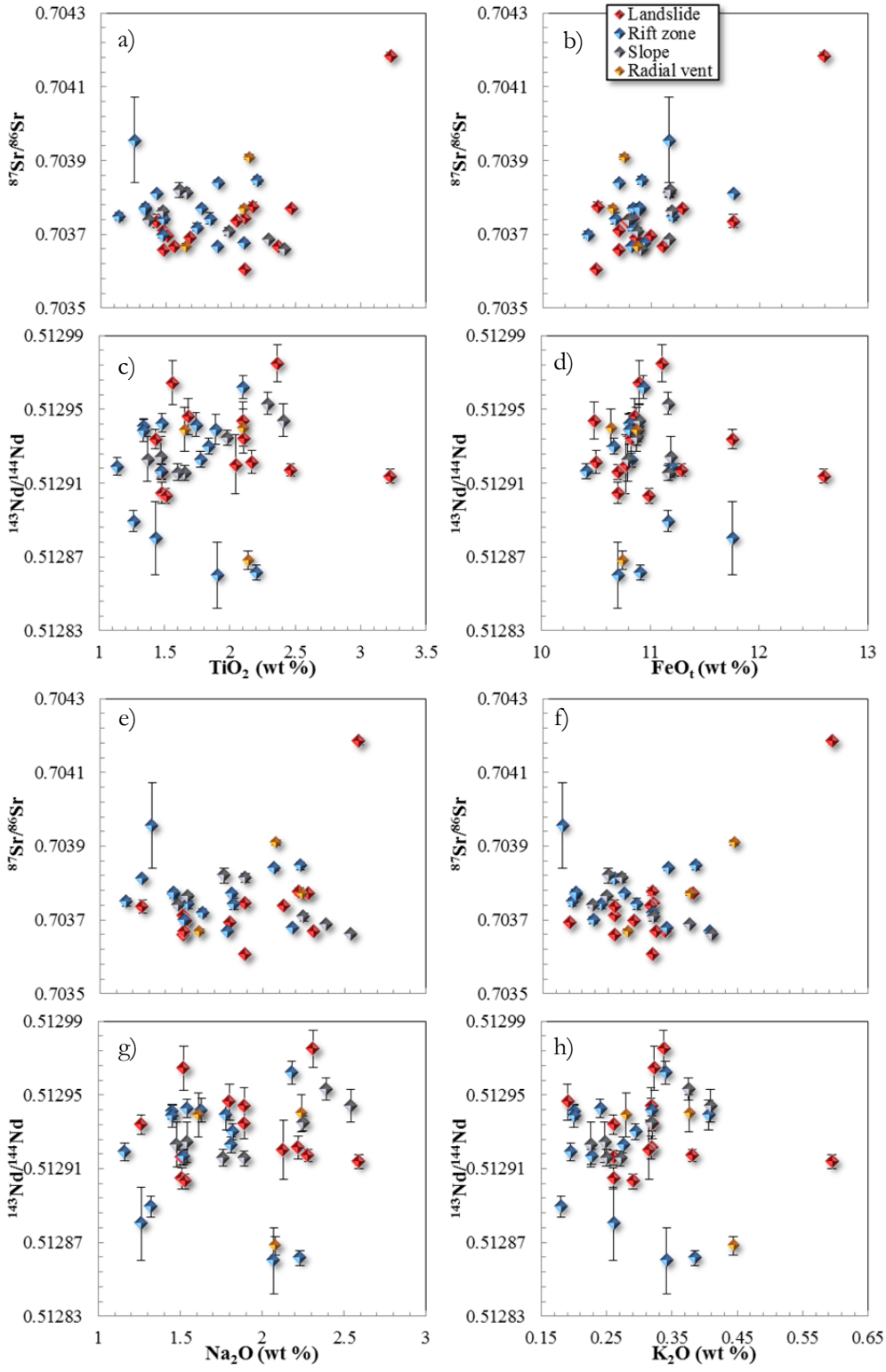

Figure 6.4 $^{87}Sr/^{86}Sr$ and $^{143}Nd/^{144}Nd$ versus major element oxides cont.

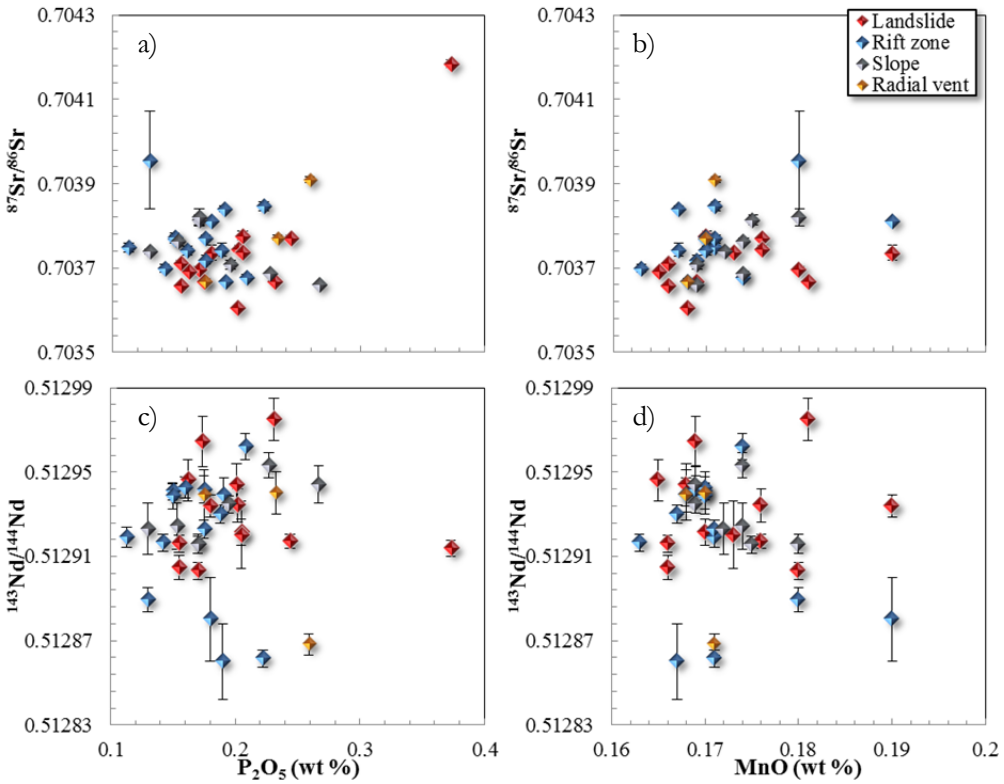

Figure 6.5 $^{87}Sr/^{86}Sr$ and $^{143}Nd/^{144}Nd$ versus major element oxides cont.

6.2 Isotopic composition with trace element variation

The isotopic data were also plotted against some representative trace elements e.g. Ni, Sc, Zr, Ln, La, and Yb (Figure 6.6Figure 6.7). Similarly to the major element oxides there is no relationship of trace element concentrations to isotopic compositions. The sample with anomalously high $^{87}Sr/^{86}Sr$ also has low MgO and high La, Rb, Zr, Nb, and Yb.

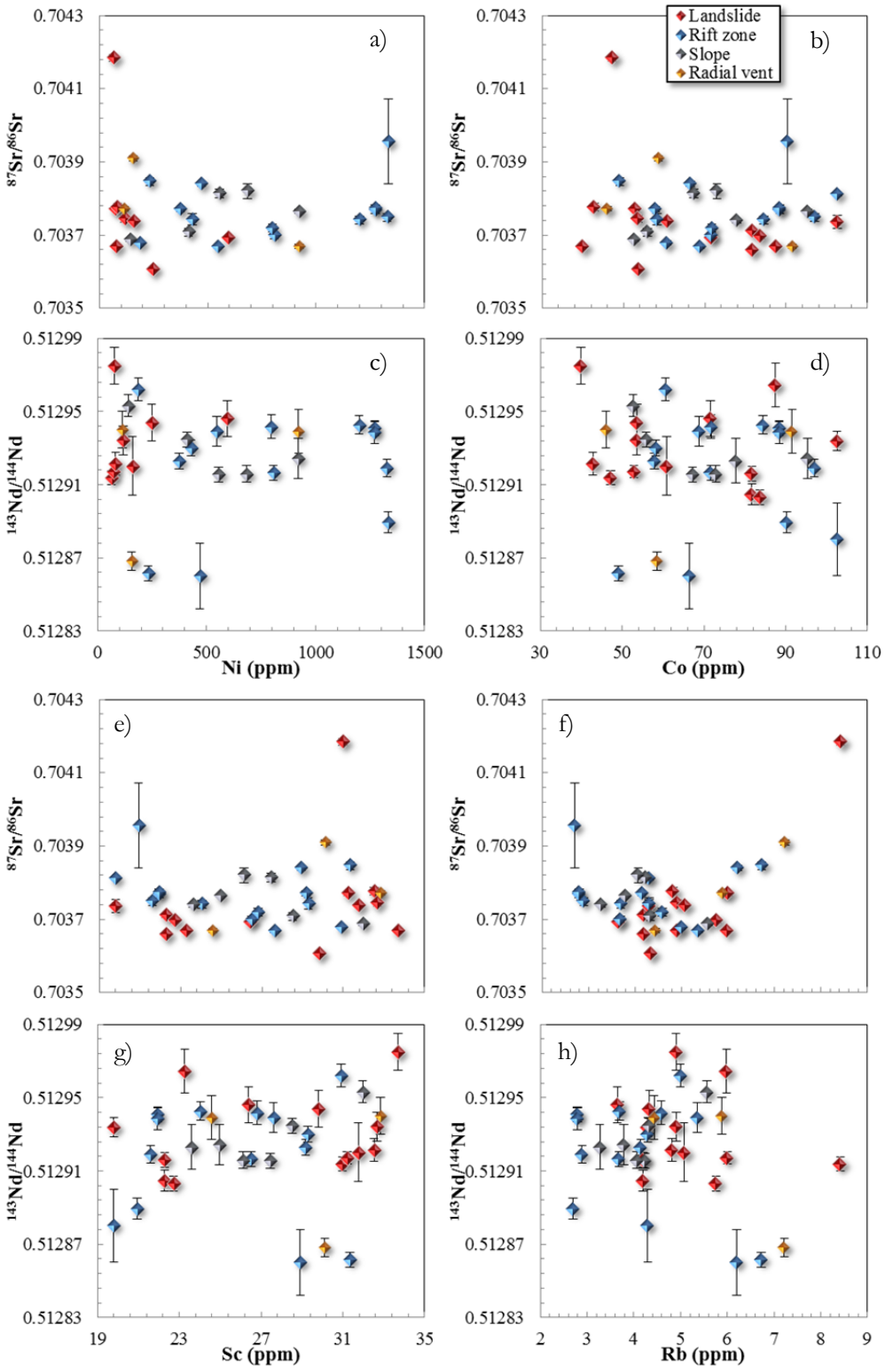

Figure 6.6 $^{87}Sr/^{86}Sr$ and $^{143}Nd/^{144}Nd$ versus some trace element concentrations.

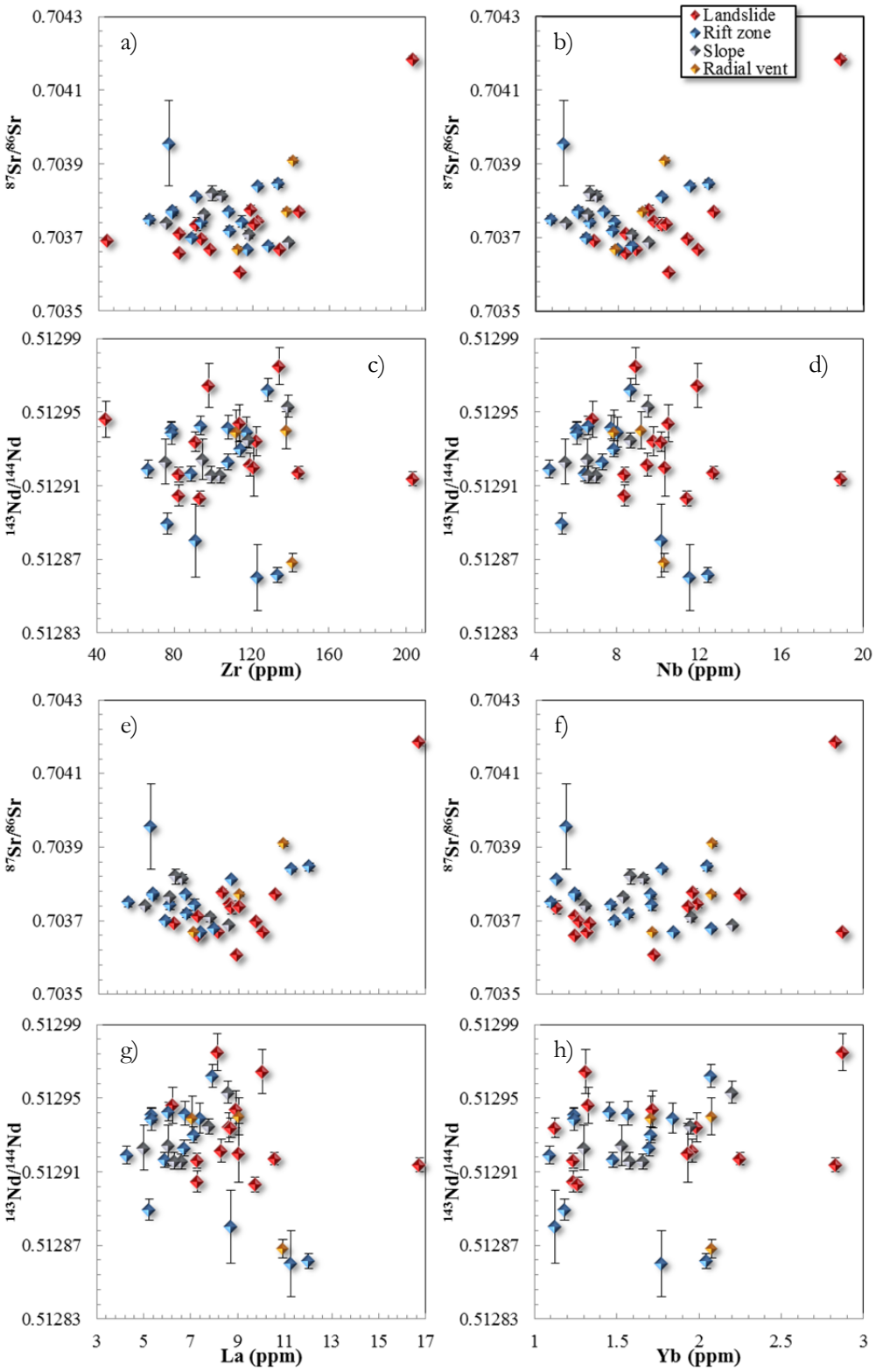

Figure 6.7 $^{87}Sr/^{86}Sr$ and $^{143}Nd/^{144}Nd$ versus some trace element concentrations cont.

In addition to trace element concentrations, Sr and Nd isotopic compositions were plotted against selected trace element ratios which should either remain constant throughout fractionation processes or vary with degree of melting (Figure 6.8Figure 6.9).

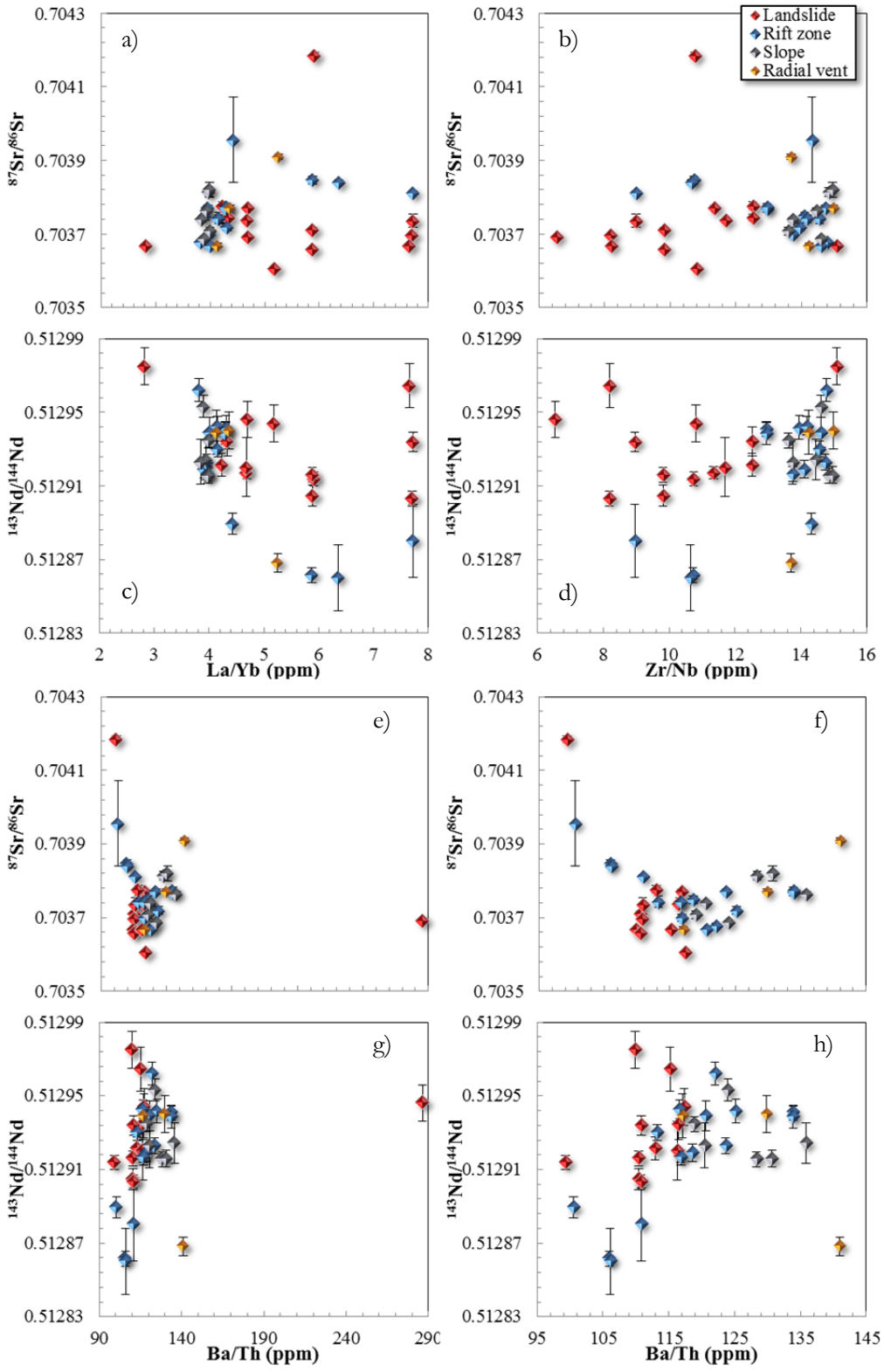

Figure 6.8 $^{87}Sr/^{86}Sr$ and $^{143}Nd/^{144}Nd$ versus some trace element concentrations cont. Note that f and h are enlargements of e and g.

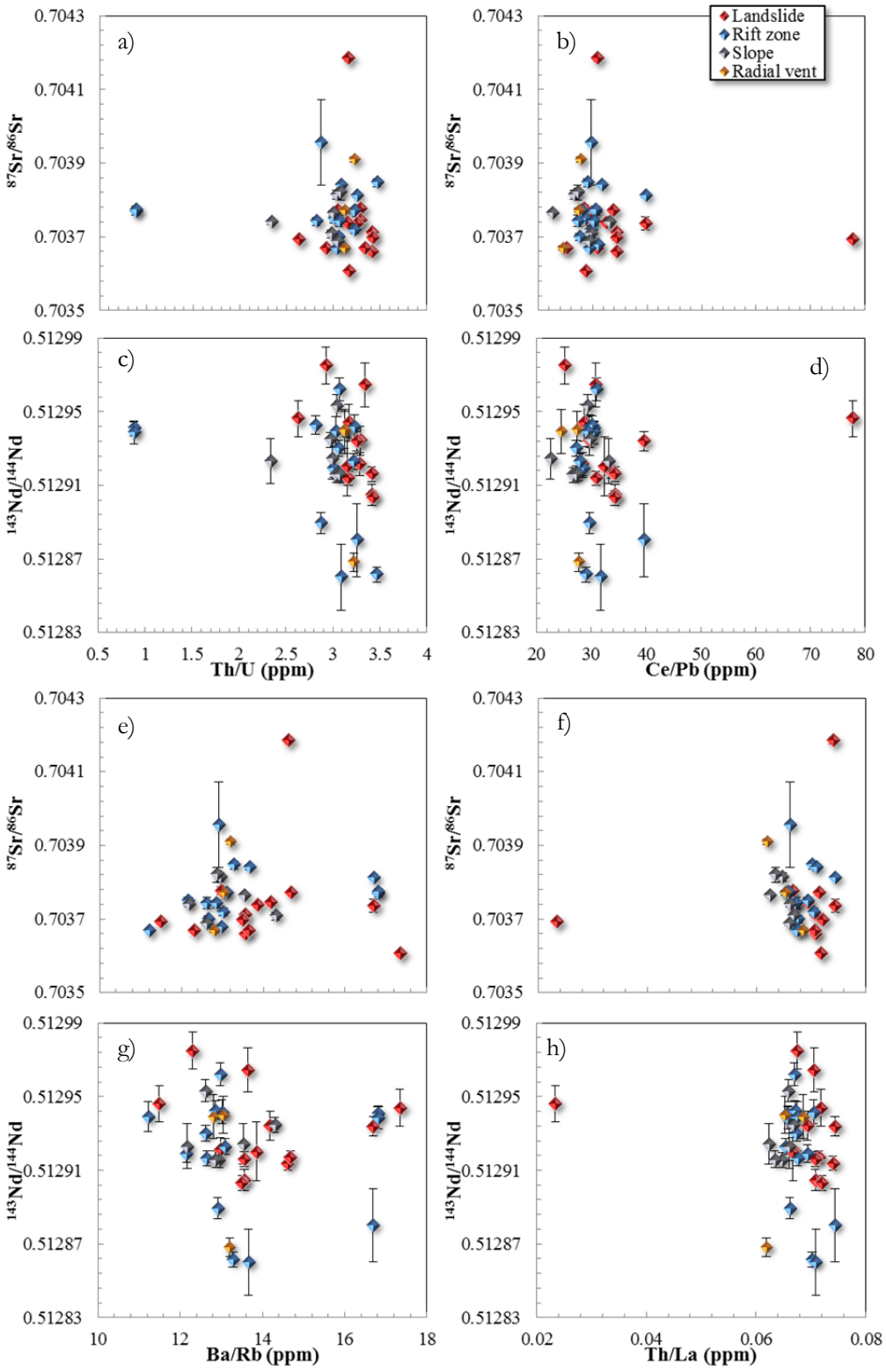

Figure 6.9 $^{87}Sr/^{86}Sr$ and $^{143}Nd/^{144}Nd$ versus some trace element concentrations cont.

There appears to be no significant correlation of the selected trace element ratios with isotopic composition, though La/Yb and Zr/Nb ratios clearly distinguish the landslide samples from the

other dredge types. Sample M14-32 has a very high Ba/Th ratio (Figure 6.8 e,g) caused by the low Th of that sample (0.15ppm), which also affects the Th/La ratio (Figure 6.9 f,h).

6.3 Isotopic composition in the global context

When ploted against other ocean floor basalts (OFB) (White and Hofmann, 1982), the samples from this study plot closer to the bulk silicate Earth (BSE) composition than many other OFB. This is also true when the data from this study are compared to a more recent compilation of OFB isotopic compositions by Hofmann (Hofmann, 2014), whereby most data from Hawaii and Iceland pot more towards the depleted MORB mantle (DMM) composition, though there are samples from the Cook-Austral Islands, Pitcairn-Gambier, Tristan da Cunha, as well as other Hawaiian samples which plot directly on the BSE composition in terms of Sr and Nd isotopes.

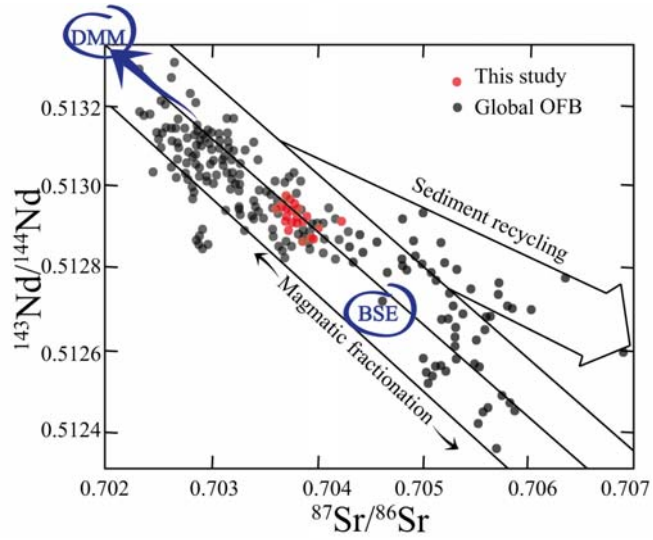

Figure 6.10 $^{143}Nd/^{144}Nd$ versus $^{87}Sr/^{86}Sr$ array of the some ocean floor basalts including data from the Mid-Atlantic Ridge, East Pacific Rise, Hawaiian Islands, Kerguelen, Easter Island, Guadalupe, Samoan Islands, Society Islands, St Helena, and Azores (grey circles). Modified from White and Hofmann (1982). Data from this study in red circles.

A compilation of literature isotopic data was collated in order to compare the data from this study to others from Mauna Loa and Kilauea (Figure 6.11). The data collected in this study all fall within the range of literature Mauna Loa data in terms of Sr and Nd isotopes, indicating that the samples from this study may be representative of Mauna Loa lavas in general. In addition, the Mauna Loa analyses are clearly separated from the Kilauea data. The data from Kilauea span to lower values of $^{87}Sr/^{86}Sr$, and are similar to the highest Mauna Loa εNd values though εNd remains more constant in the Kilauea data. The literature Mauna Loa data has low and constant $^{206}Pb/^{204}Pb$ and $^{208}Pb/^{204}Pb$ compared to Kilauea, with Kilauea spanning a much greater range in $^{206}Pb/^{204}Pb$ in particular.

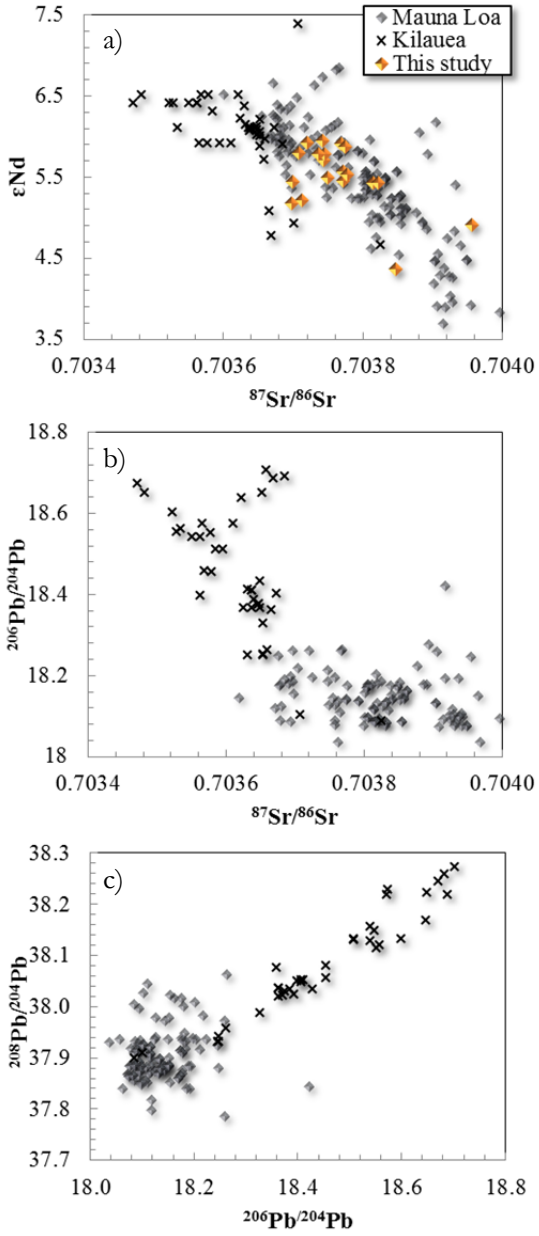

Figure 6.11 Literature isotopic compositions for Mauna Loa (grey diamonds) and Kilauea (grey crosses) with data from this study (yellow diamonds) overlaid (DePaolo et al., 2001, Kurz and Kammer, 1991, Wanless et al., 2005, Wanless et al., 2006, Rhodes and Hart, 1995, Cohen et al., 1996, Marske et al., 2007, Hauri and Kurz, 1997, Weis et al., 2011, Pietruszka and Garcia, 1999, Hanyu et al., 2010).

7 Discussion Part I – shallow magmatic petrogenesis

This chapter will be one of two discussion chapters that investigate the magmatic processes that control the chemistry of the Mauna Loa samples studied here. This chapter aims to determine the extent and nature of shallow magma chamber processes which occur in the upper ~8 km of the crust, and how these control the chemistry of Hawaiian lavas. Disentangling the shallow magma chamber processes will enable estimation of a probable parental magma composition from which Mauna Loa lavas were derived. The deep mantle (>100 km depth) melting processes and source assemblages that contributed to the parental magma composition can then be investigated by using this parental magma composition as a starting point and working backwards to a suitable mantle composition. The second chapter will also focus on the isotopic characteristics of the samples in this study and a geochemical comparison of Kilauea and Mauna Loa so that the differences in source chemistry and process between the two volcanoes can be explored.

This chapter will focus on the shallow magmatic processes that control the geochemistry of the Mauna Loa basalts presented in this study. It will cover olivine, cpx, and Cr spinel control trends using fractionation modelling software including MELTS (Ghiorso, 1983, Ghiorso and Sack, 1995), alphaMELTS (Smith and Asimow, 2005), and Petrolog (Danyushevsky and Plechov, 2011), and will then discuss the evidence that these olivine control trends may reflect olivine accumulation rather than fractional crystallisation. The use of fractionation-modelling software provides the ability to make conclusions about probable liquidus temperatures of the parental magma, as well as phase assemblages, the pressure and fO_2 range over which these magmas crystallized, and the effect of variable water content on the crystallization path. The chapter will then use whole rock data to calculate bulk partition coefficients for samples that should be unaffected by plagioclase and clinopyroxene fractionation. Errors on these partition coefficients will be evaluated and their validity will be critically assessed by comparison to literature values and to the default values used by the MELTS software. Finally, this chapter will present an estimated parental melt composition (or range of) by correcting to remove the effect of olivine fractionation to ~16 wt. % MgO (the MgO contents of a magma in equilibrium with $Fo_{90.5}$ olivine).

7.1 The dynamics of Hawaiian magma chambers

The processes that occur inside of a complex and dynamic magma chamber remain largely unknown even at well-studied volcanic systems such as Hawaii, as there is great difficulty in imaging shallow magma chambers tomographically. Establishing the dynamic processes that

occurred in the Mauna Loa magma chamber and related plumbing system is important in order to quantify the effect that these processes will have on the chemistry of the magmas so that a parental magma composition may be estimated.

The eruption history of Hawaii's volcanoes has been studied for a relatively long period of time compared to some volcanic systems, and important inferences can be made from these observations. According to a recent summary (Poland et al., 2014), magma supplied to volcanoes such as those at Hawaii is stored in reservoirs prior to intrusion via dykes and sills at the surface (Figure 7.1).

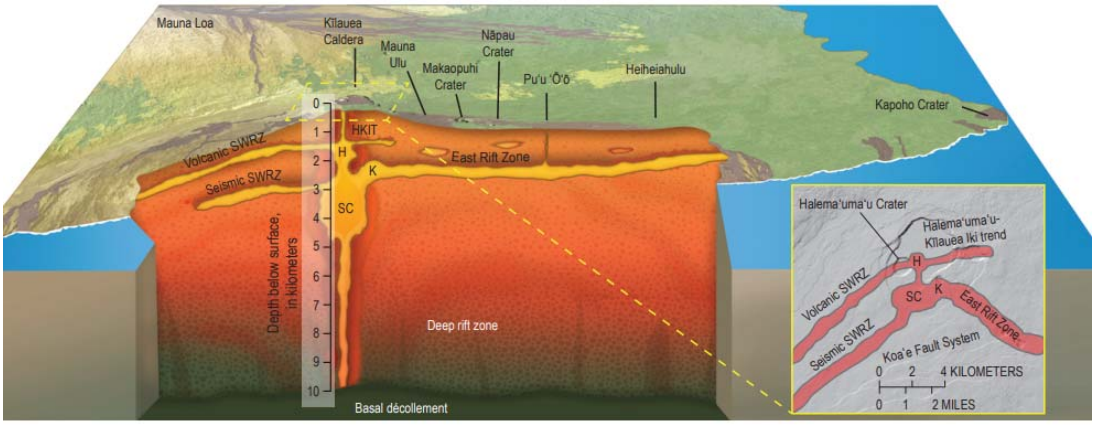

Figure 7.1 The internal structure of Kilauea's magmatic system as envisaged by Poland an co-authors (Poland et al., 2014). Here, HKIT = Halema'uma'u-Kilauea Iki Trend, H = Halema'uma'u reservoir, K = Keanakako'i reservoir, SC = south caldera reservoir, and SWRZ = south-west rift zone.

The lateral or vertical propagation of dykes is caused by overpressure from the build-up of magma within the source reservoir, with lateral propagation causing eruptions that can be kilometres from the source magma chamber. Mauna Loa is the perfect example of this, with its southwest rift-zone stretching for 60 km (Lipman, 1980). The eruption rate of magma into these 'reservoir complexes' and 'dense sills and feeder dykes' (Fiske and Kinoshita, 1969) can vary significantly over the life of the volcano, for example since the 1877 eruption of Mauna Loa the eruption rate has decreased (Lockwood and Lipman, 1987).

The eruption and supply rate has been recognised as an important factor in determining the lava chemistry (Garcia et al., 2003, Rhodes, 1988, Poland et al., 2014). Garcia and co-authors have shown that at Kilauea, high supply rates are correlated with high MgO contents (because magmas are not allowed sufficient time to differentiate before eruption), while during low supply where the volcano is erupting infrequently, the magmas are able to differentiate more

and become lower in MgO. Poland and co-authors have shown that for Kilauea, there is a correlation between MgO contents of the lavas and the eruption rate. The correlation may be because higher T lavas are higher in MgO, and the higher temperatures cause more melting and therefore higher supply to the volcano. Poland shows that at Kilauea when the eruption rate is at its peak the MgO contents are highest and the incompatible element concentrations are lowest. The effect of melt production on melt chemistry has been observed where small volumes of lower temperature magma recently erupted have stabilized at 7 wt. % MgO (Poland et al., 2014).

Poland (2014) also suggests that the Kilauea and Mauna Loa magma chambers are probably interconnected, and must be fed from the same plume based on evidence that they display both inverse and sympathetic patterns of eruption. In addition, CO_2 levels at Kilauea indicate that all the CO_2 from the magma that feeds Mauna Loa, Kilauea, and Loihi might escape from Kilauea indicating that these volcanoes must be connected at some level to enable the transfer of CO_2 to Kilauea.

The plumbing system of Kilauea has been used as an archetype for other basaltic shield volcanoes including Mauna Loa, and some findings have been summarised by Rhodes (Rhodes, 1988). Rhodes finds that at Kilauea, basaltic magma derived from the upper mantle is emplaced into a reservoir at 2-4 km depth below the summit caldera. Then, the magma accumulates and expands the chamber walls and surrounding crust, causing shallow seismic activity and eruptions either from the caldera or the injection of magma into the adjacent rift zones. This eruption of magma or injection into the rift-zones causes deflation in the summit region. Subsequently, differentiated magma may accumulate in the rift zones where it is able to mix with new pulses of magma. It was noted by Rhodes that unlike Kilauea, Mauna Loa's eruptions are more chemically uniform, possibly indicating that the build-up of magma in pockets may not have the chance to occur due to the much larger volumes of magma at Mauna Loa.

This approximate depth of crystallizing magma estimated by Rhodes is confirmed by a study on the CO_2 contents of olivine, which reveals that crystallization of olivine from Kilauea Iki began at depths of less than 6 km and the majority of olivine was crystallized at depths closer to 3 km, confirming a summit reservoir origin (Tuohy et al., 2016). However, olivines from the rift zone Kapoho indicate a wider range of crystallization depth (1-16 km) (Tuohy et al., 2016). Tuohy and co-authors suggest that deeply derived olivine crystals and their host magmas may mix with more evolved magma in the rift zone, and that the lava erupted at the surface is a mixture of primitive magma and evolved magma.

7.2 Olivine: an important determinant of basalt chemistry

It has been well documented that the primary control of the major element variability of Hawaiian tholeiitic lavas is olivine e.g. (Clague and Denlinger, 1994, Garcia, 1996, Rhodes, 1996, Norman and Garcia, 1999) as evidenced by strong olivine control trends. Many of these studies have used Fe/Mg ratios to calculate a parental magma composition in equilibrium with the most abundant Fo composition (Fo_{90} for samples in this study) or the highest Fo composition ($Fo_{90.8}$ in this study, but up to $Fo_{91.3}$ for Mauna Loa (Garcia et al., 1995)). Various studies have calculated the MgO contents of parental magma compositions finding that most are within the range of 12-17 wt. % (15 wt. % MgO (Eggins, 1991, Garcia, 1996, Norman and Garcia, 1999), 13% (Rhodes, 1995), 12-14 % (Wilkinson and Hensel, 1988), 17 % e.g. (Clague et al., 1991), up to 18.4% (Clague et al., 1995) between 13-17 % (Green et al., 2001), and 20 wt. % (Putirka, 2005). A review by Garcia however, has highlighted the wide range of suggested Mauna Loa parental magma compositions of 8-25 wt. % (Garcia et al., 1995).

Such parental magma compositions have then been used to calculate crystal fractionation paths to determine if a suite of basalts are genetically related via fractional crystallization by thermodynamically modelling mineral-melt equilibria. It has also been suggested that whole rock compositions from Mauna Loa with MgO contents higher than the parental magma composition may represent lava with variable amounts of accumulated olivine, that those with 12-17 wt. % MgO represent a parental melt, and that those with lower MgO contents represent an olivine fractionation trend e.g. (Wilkinson and Hensel, 1988, Norman and Garcia, 1999). A simple way to test what the bulk rock composition represents is to observe the modal proportions of olivine and the forsterite contents of those olivine crystals. If the bulk rock is a melt (100% liquid component) that has been then quenched or cooled quickly, then there should be no olivine crystals present. Alternatively if it represents the compositions of a magma (melt + crystals) with no crystal fractionation during crystallization then the MgO content of the bulk should remain constant regardless of modal olivine abundance, as any MgO lost from the melt is gained by the olivine in a closed system. In this case, the bulk rock composition still represents that of the initial parental melt. For this study, the effect of olivine crystallization on the SiO_2, MgO, and FeO_t compositions of a magma was tested using Petrolog melt modelling software (Petrolog and other melt modelling software will be discussed in more detail later). This software allows the user to vary the amount of olivine that is fractionated during crystallization so that the composition of a liquid (100% crystal fractionation) or a magma (0-99% fractionation) can be modelled. An example calculation is shown in Figure 7.2 assuming a starting composition of 16 wt. % MgO (this choice of parental magma composition lies within the 12 – 17 wt. % estimates mentioned above, and will be further discussed later in this chapter).

The path which best replicates the bulk major element oxide composition is the perfect fractionation model, where all olivine is removed from the remaining melt and therefore the trend represents the composition of the liquid only during fractionation. The high modal proportions of olivine phenocrysts in the bulk rock indicates that the bulk rock composition cannot represent a fractionating magma because the only path to fit the whole rock data would have no olivine present while the whole rocks contain large proportions of olivine (up to 33%).

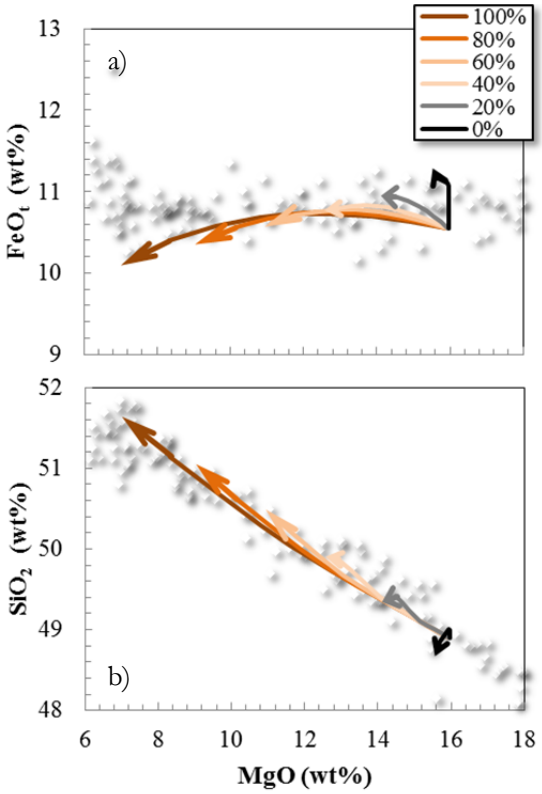

Figure 7.2 Mauna Loa major element compositions (grey; this study) and olivine fractionation paths with 0 to 100% of crystallised olivine removed from the magma (arrows) in terms of a) FeO_t and b) SiO_2.

In addition, if the whole rocks represented a fractionating magma then the forsterite contents of the olivine should decrease with increasing olivine fractionation. Analysis of forsterite contents of a large number of olivine crystals from samples in this study were obtained by Michael Davis and Michael Garcia at the University of Hawaii and published as part of a master's thesis (Davis, 2001) and Marc Norman at University of Tasmania and can be used to investigate the processes that formed Mauna Loa's lavas. Results reveal the most commonly occurring olivine is normally zoned with a high Fo core and lower Fo rim, which is caused by initial crystallization of an olivine in a primitive melt followed by crystallisation of the low Fo rim as the melt is progressively depleted in Mg and the existing olivines begin to re-equilibrate with the melt. The

presence of high Fo cores and low Fo rims supports the idea that the melt has evolved to a lower Mg# (= molar Mg/(Mg+Fe)) due to crystallization of olivine, and that olivine crystals are remaining suspended in the melt during crystallisation.

However, there are a wide variety of Fo contents in both cores and rims of the olivines (Figure 7.3), for example there is up to an 10 percentage point range in Fo content of the olivine rims in some samples. There is also no correlation of core or rim Fo content with the Mg # of the bulk rock composition, suggesting that most of the olivine present in the bulk rock is not in equilibrium with the bulk rock composition (Figure 4.8 major elements results section) and that the lavas may be well mixed.

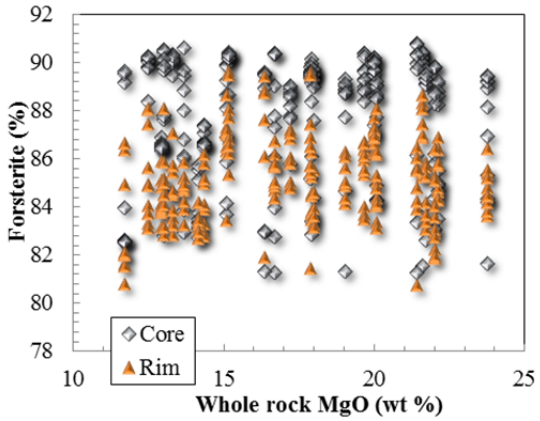

Figure 7.3 Forsterite content of cores (grey) and rims (yellow) of olivines versus whole rock MgO content.

In addition to the olivine chemistry, the modal abundance of olivine in the bulk rock can reveal how the lavas were formed. The high modal proportions of phenocrystic olivine (up to 33.3 vol. %) in the whole rock indicate that the bulk compositions of these lavas are not representative of melts (no crystals) produced by perfect fractional crystallization and quenched, as mentioned previously. Also, if the melt crystallises as a closed system, then the amount of olivine in the rock should increase with increasing fractionation while the amount of melt decreases. In fact, the opposite occurs and there is a positive correlation between modal olivine and MgO contents (R^2 = 0.63) (Figure 4.13b major element results section), i.e. olivine abundance decreases with decreasing MgO. The positive correlation of MgO with modal olivine indicates that that the modal abundance of olivine is the primary control of the MgO contents of the bulk rock, and contrary to representing a series of residual melt compositions produced by fractional crystallisation, the bulk rock trend may simply reflect mixing between an evolved melt and variable amounts of accumulated olivine.

In addition to looking at the modal olivine, a comparison of modal olivine to the CIPW normative abundance can provide further information about the bulk rock composition. Modal and normative mineral proportions were presented in the major elements results section previously of this thesis. A large fraction of the samples (39%) are silica over-saturated, containing normative quartz + hypersthene as major components and are free of normative olivine. The remaining samples contain varying amounts of normative olivine + hypersthene (1-39.6 vol. % olivine and 10-32 vol. % hypersthene) indicating that they are silica-saturated. This means that there is just enough silica to satisfy the silica requirements of all the silicate minerals in the samples, but not enough to produce any normative quartz. No samples are silica-undersaturated (not enough silica to produce hypersthene, only olivine + feldspathoids), as would be expected for basalts with tholeiitic composition.

Accepting that modal analysis can have large relative uncertainties (e.g. 11.7 – 32.3% 2xRSD for mineral proportion errors associated with point counts on granites (Neilson and Brockman, 1977), or 20% for major components (>10 vol. % of the rock) and 50% for minor components (<10 vol. % of the rock) (Laboratory and Yucca Mountain Project, 1990), Figure 4.13a in the major element results section shows that the modal olivine and normative olivine abundances are positively correlated beyond 10 wt. % MgO. In samples with <10 wt. % MgO the normative abundance is predicted to be silica over-saturated, so the reaction relationship between Si-rich melt and olivine to produce pyroxene should preclude high modal olivine abundances in these melts. However, modal olivine is found all throughout these samples (up to 9 vol. %), indicating that this olivine is out of equilibrium with those whole rock composition. Further to this, the Fo content of the olivines found in whole rock with <10 wt. % MgO are high (average of 86.4) while MELTS predicts the Fo content of olivines in equilibrium with <10 wt. % MgO to have Fo_{83}, decreasing to Fo_{78} during crystallization.

In addition, most of the normative olivine can be accounted for by modal olivine, i.e. all of the normative olivine is present as modal olivine. There is even 4-5% more modal olivine than can be accounted for normatively. This can be shown by fitting a linear regression when normative olivine was plotted against modal olivine. A line with the equation $y = 0.84x - 0.85$ is formed and it was found that regardless of the value of modal olivine (x value) substituted into this regression the returned value of normative olivine (y value) was always less than the modal value. For example when a modal value of 15 vol. % is substituted into the equation the returned normative value is 11.8 vol. %, and when a modal value of 25 vol. % is substituted the resulting normative value is 20.2 vol. %. If all of the normative olivine is present as actual olivine crystals, then the interstitial matrix material must be olivine-free, quartz-normative, and evolved (<10 wt. % MgO). This has been demonstrated to be correct through measurement of matrix

glass mentioned later. Comparison of normative versus modal olivine therefore supports the hypothesis that the bulk rock represents the accumulation of olivine crystals into a relatively evolved melt (at most 10 wt. % MgO). The whole rock compositions represent mixtures of an evolved melt with variable amounts of phenocrystic olivine. This olivine may have remained entrained after in-situ crystallisation in some cases, but the high forsterite content and high modal olivine proportion of many of the olivines suggests some have been added to the melt from other sources. The role of olivine accumulation in controlling the compositions of these Mauna Loa basalts is considered in greater detail in the following section.

7.3 Olivine accumulation

If the bulk composition of Hawaiian lavas is not controlled by olivine fractionation, then an alternative hypothesis is required. The control of the bulk composition by accumulation of olivine in Mauna Loa lavas has been documented previously (Rhodes, 1995, Garcia et al., 1995, Norman and Garcia, 1999, McCarter et al., 2006), with many authors agreeing that at least some of the olivine control trends must be the result of accumulation, particularly those with very high MgO contents (>20 wt. %). Here, I argue that the majority of the whole rock samples (MgO contents >8 wt. %) can be explained by olivine accumulation.

In order to test the effect of adding accumulated olivine to an evolved melt the progressive addition of Fo_{85}, and Fo_{90} olivine to a whole rock composition with 8 wt. % MgO was modelled (Figure 7.5). The analysis of multiple olivines within the one bulk rock sample reveals each whole rock sample contains olivines with a wide range in Fo contents (Fo_{81-91}, Figure 7.3), however Fo_{85} and Fo_{90} were chosen for this test because the forsterite contents of the olivines in the whole rock samples show two distinct peaks in the distribution (Figure 7.4): one sharp peak at Fo_{90} which is the most abundant olivine composition, and another more rounded peak centring at Fo_{85}. These peaks may occur because one core and one rim analysis was obtained for each olivine analysed and so the two peaks may be distinguishing the core compositions (higher Fo) and rim compositions (lower Fo) of the spectrum of olivines analysed (Figure 7.4). A starting melt composition with 8 wt. % MgO was chosen as this is the lowest MgO content for samples that lie on the olivine-only control line; those with less than 7 wt. % MgO may be affected by other phases such as pyroxene and plagioclase.

Mauna Loa submarine glasses analysed by (Davis et al., 2003) reveal maximum, minimum, and average MgO contents of 8.4, 5.2, and 6.5 wt. % respectively, suggesting that the selection of an 8 wt. % magma is probably a good estimate for the melt into which the olivine can be accumulated to form the whole rocks for the model (Figure 7.5).

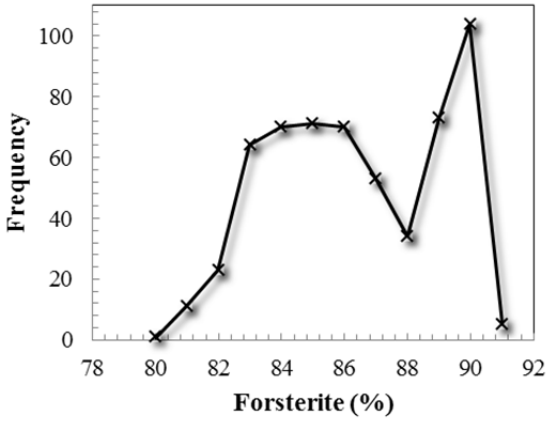

Figure 7.4 The distribution of forsterite contents in olivine phenocrysts found in the Mauna Loa lavas studied here (M.O. Garcia and M. D. Norman – unpublished data).

It was found that the MgO versus FeO_t Mauna Loa bulk rock trend falls in between the two modelled trends formed by the addition of Fo_{85} and Fo_{90}, while varying the Fo content of the added olivine does not appear to vary the SiO_2 contents to the same degree and both trends follow the bulk SiO_2 versus MgO pattern (Figure 7.5). The bulk rock composition may fall between the Fo_{85} and Fo_{90} addition trends because the average effect of olivine addition should be an intermediary between the Fo_{85} and Fo_{90} end-members. The average olivine composition in this data set is $Fo_{86.4}$, the average rim composition is Fo_{85}, and the average core composition is $Fo_{87.8}$. Despite the average olivine composition, the addition of $Fo_{86.4}$ does not fit the data as well as the addition of $Fo_{87.8}$ olivine (the average core analysis indicating the overall effect on the bulk rock may be controlled by addition of olivine with forsterite contents higher than the average forsterite analysis (Figure 7.5). This is could be because using the average olivine analysis of $Fo_{86.4}$ assumes an equal weighting of the core and rim analyses, i.e. it assumes the cores and rims each comprise 50% of the total olivine volume.

Analysis of olivines from Mauna Loa and Mauna Kea during the Hawaii Scientific Drilling Project (HSDP) confirms that they are also mostly normally zoned (higher Fo cores and lower Fo rims), with reversely zoned olivines making up only a small fraction of the phenocryst population (Garcia, 1996). A steep decline in Fo contents is often observed in the rims of olivine phenocrysts, which typically comprise only a minor portion of the olivine transects. Using the radii given from transects across olivines grains in Garcia (1996) and assuming a spherically shaped crystal, the core/rim proportions of four representative normally zoned olivines could be calculated. The rims comprised approximately 23%, 31%, 32%, and 61% respectively of the total volume of the olivine. This suggests that the core composition of many grains may need to be weighted more heavily than the rim when determining the average

composition to use in olivine addition models. It is also assumed that the analysed olivine was cut perfectly through the centre of the grain and parallel to a principle axis. If the cut was off-centre, then the core composition could be further under-represented and the grain size under-estimated. Similar patterns were found in lower Fo olivines from Garcia (1996), where the majority of the crystals have a high, constant Fo content in the core, while the narrow outer rim shows a dramatic drop in Fo contents with decreasing distance from the outer edge.

Furthermore, recent work by (Lynn et al., 2017) has shown that most of the olivine crystals found in lavas from the 1500-1820 tephra eruptions at Kilauea are normally zoned, grading from high Fo cores to lower Fo rims, and that the rims are narrow bands where re-equilibration of the Mg and Fe has started to occur while the olivine is in contact with melt. Cores often plateau at high and constant forsterite contents, which could explain why the peak at Fo_{90} is narrow compared to the more rounded peak showing the wide range of rim compositions.

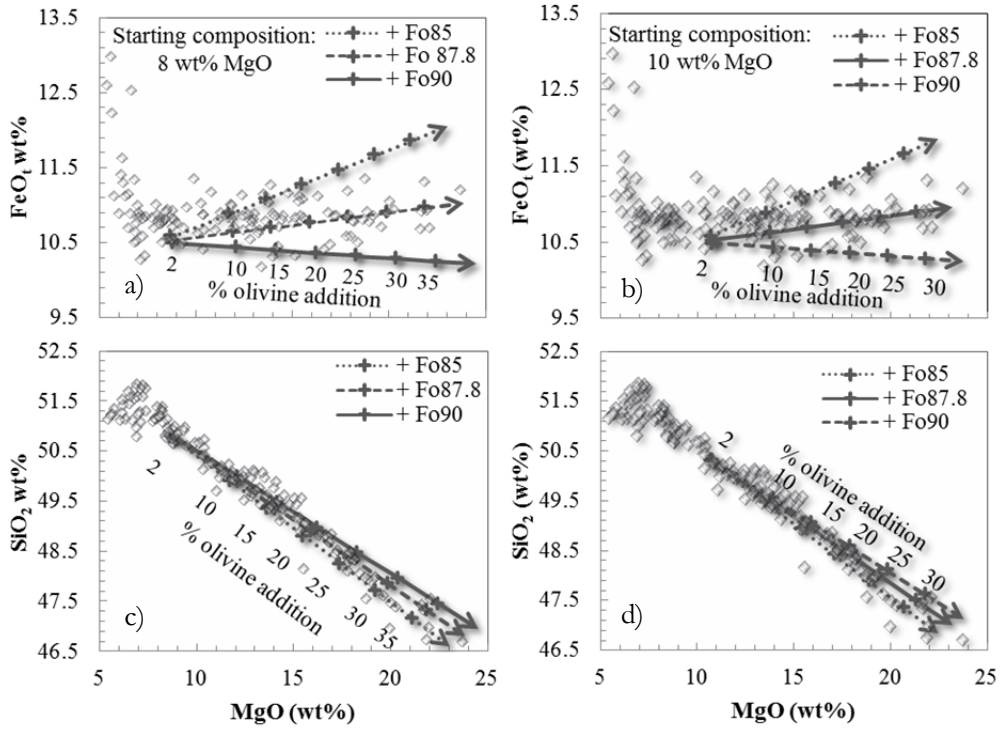

Figure 7.5 The effects of adding incremental proportions of Fo_{85}, $Fo_{87.8}$, and Fo_{90} olivine to a melt with 8 wt. % MgO (a & c) and 10 wt. % MgO (b & d). Additon of olivine with the average Fo analysis ($Fo_{86.4}$) creates a trend lying between the Fo_{85} and $Fo_{87.8}$ trends. Olivine addition here is in wt. %.

It can be seen that addition of olivine to a melt with 8 wt. % MgO would require up to 40 wt. % (35.2 vol. %) olivine addition to explain the highest MgO samples (Figure 7.5a,c), which is

slightly higher than the maximum 33 vol. % modal abundance determined by petrography. Therefore, a starting composition of 10 wt. % MgO was also tested to see if this could explain the high MgO samples. It was found that only 35 wt. % (30.8 vol. %) addition of olivine would be required to explain the highest MgO samples in the case of a 10 wt. % MgO starting composition (Figure 7.5b,d).

Further testing can be conducted to determine whether the modal proportions estimated via petrography match the predictions of the olivine addition models above. Figure 7.6 shows that the predictions match the modal estimated, with the maximum amount of olivine able to be added around 32%. Therefore, the addition of olivine with an average forsterite content of 87.8% into a melt or a range of melts with MgO 8-10% could account for the major element compositions of the samples in this study.

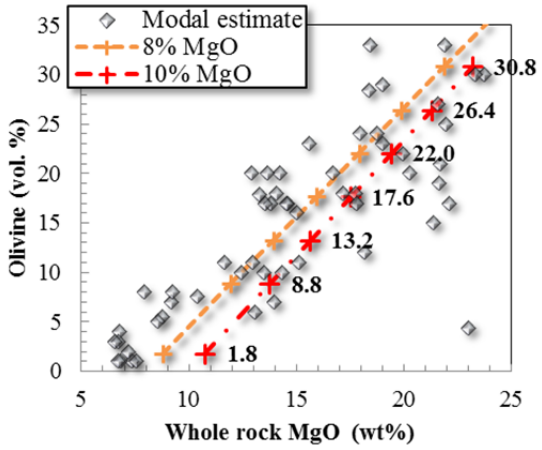

Figure 7.6 Correlation between modal olivine proportion and MgO (wt. %) (grey points) with predicted olivine content (vol. %) during addition of $Fo_{87.8}$ olivine into a melt with 8 wt. % MgO (orange) and 10 wt. % MgO (red). Labels on linear trend are vol. % olivine.

In addition to evidence of accumulation from the major elements, the Ni concentrations further support olivine accumulation over fractional crystallization. For example, Ni increases nearly linearly with increasing MgO in samples above 8 wt. % MgO (Figure 5.1b trace element results), whereas fractionation of olivine should vary according to a non-linear function because of the dependence of the partitioning of olivine with Ni concentration in the melt according to Henry's Law e.g. (Hart and Davis, 1978). Expected Petrolog-calculated Ni trends during olivine fractionation can also be seen in Figure 7.27e of this chapter, and will be discussed further later. The consequences of Henry's law mean that if the bulk rock composition represents the composition of a liquid during olivine fractionation, Ni will vary non-linearly with MgO, regardless of if a batch or fractional crystallization model is used. Hart and Davis show that the

use of a constant or variable D does not make a huge difference to the shape of the fractionation trend either. Conversely, an olivine accumulation trend will produce a linear trend. Hart and Davis also state that an accumulation trend can account for the Ni and MgO variability in whole rock samples from Kilauea tholeiites when variable amounts of olivine are added to a liquid with 9.5 wt. % MgO – a value consistent with the 8-10 wt. % MgO predicted in this study. The samples in this study with less than 8-10 wt. % MgO begin to diverge from the linear as other minerals such as plagioclase and clinopyroxene become the primary controls.

The composition of glasses from Mauna Loa support the hypothesis that the bulk compositions of the lavas studied here can be explained by accumulation of olivine into an evolved melt with ~8 wt. % MgO. Mauna Loa submarine glasses analysed by (Davis et al., 2003) reveal maximum, minimum, and average MgO contents of 8.4, 5.2, and 6.5 wt. % respectively, and olivine-hosted melt inclusions with maximum, minimum, and average MgO contents of 11.4, 2.6, and 7.3 wt. % respectively. Davis and co-authors note that the inclusions have a wider range in MgO than the submarine glasses; however most of the inclusions are comparable to the glasses. They also note that the high MgO inclusions also have low FeO, and so may have experienced post-entrapment crystallization and diffusion. Diffusion has been found to affect Fe, Mg, and Ca concentrations in olivines, particularly when cooling rates drop to below 1˚C/year (Norman et al., 2002). Norman and co-authors similarly found low MgO melt inclusions in olivines from Kilauea (6.35 – 7.69 wt. % MgO). Lynn and co-authors (Lynn et al., 2017) have noted the lack of glasses and melt inclusions that could be in equilibrium with a >Fo_{88} olivine in Keanakako'i Tephras, and have suggested that primitive magmas feeding Kilauea volcano have not reached the surface without the occurrence of significant crystal fractionation. Mauna Loa displays a similar lack of high MgO glasses and melt inclusions, with the highest reported by Wagner and co-authors (9.3-11.3 wt. % MgO) (Wagner et al. 1998- trace element abundances), although many of Mauna Loa's lavas have high modal olivine and high Mg# and may be revealing deep olivine crystallization (Garcia et al., 1995). In spite of the rarity of high MgO glasses, there have been some recorded in turbidite sands from Kilauea that have up to 15.0 wt. % MgO, providing direct evidence of at least some primitive melt at Kilauea (Clague et al., 1995).

7.4 Plagioclase and clinopyroxene control

Other phases have been documented in Mauna Loa picrites in samples of the 1852 and 1868 eruptions and of samples from below the 1868 flow, including plagioclase, clinopyroxene, orthopyroxene (phenocrysts and groundmass), and 'microphenocrysts' of Cr-spinel (Wilkinson and Hensel, 1988'Garcia, 1995 #630).

While olivine exerts the primary compositional control on magmas with >7 wt. % MgO, clinopyroxene and plagioclase are the expected primary controlling phases in magmas with <7 wt. % MgO (Frey and Rhodes, 1993, Norman et al., 2005, Helz and Wright, 1992). These phases are the next to crystallize and do so at lower temperatures from more evolved magmas. The elements that are most compatible in clinopyroxene and as such are most affected by clinopyroxene (cpx) control are Ca, Mg, Si, Fe, Sc, Ti, Cr, and V meaning that the CaO/Al_2O_3 ratios of the whole rock should decrease in the more evolved samples when clinopyroxene is the controlling phase. The low CaO/Al_2O_3 of samples with <7 wt. % MgO indicates that clinopyroxene crystallisation is occurring in these samples (Figure 4.13 major element results); although it should be noted that cpx is not mentioned in petrographic descriptions of these samples conducted by Garcia. This may be because the proportions were so minor they were not included, or because cpx crystals were all successfully fractionated.. Other trace element ratios that demonstrate control of clinopyroxene are Sc/Y, and Cr/Ni. Sc/Y decreases gradually with decreasing MgO, but decreases more sharply below 8 wt. % MgO consistent with Sc being partitioned into crystallizing cpx. Cr/Ni rises with decreasing MgO as Ni is preferentially partitioned into olivine, until 8 wt. % MgO where this ratio suddenly decreases as olivine ceases to be the controlling phase and clinopyroxene takes over (Figure 5.18a trace element results section).

Plagioclase phenocrysts are found in 18 of the more evolved samples (up to 3 vol. %) by Garcia in petrographic descriptions, and although cpx is absent from descriptions of these particular samples, between 1-4 vol. % of augite has been noted by Garcia in previous descriptions of southwest rift zone lavas (Garcia et al., 1995). Where whole rock analyses are available, plagioclase-containing samples have between 6.6 – 9.3 wt. % MgO. Plagioclase will preferentially partition the major elements Al, Ca, and Na as well as certain trace elements, for example, Eu and Sr. Fractionation of plagioclase may be demonstrated in the decrease of Al_2O_3 relative to TiO_2 at < 7 wt. % MgO, and in the removal of Sr relative to Nd, making the ratios of Al_2O_3/TiO_2 and Sr/Nd useful tools in demonstrating plagioclase control e.g. (West et al., 1992). The effect of relative Al and Sr removal can be seen in Figure 4.4e of the major elements results where a downturn in the average Al_2O_3/TiO_2 (relative excursion $\Delta 0.5$), and a slight downturn in the Sr/Nd ratio can be seen in Figure 5.15d of the trace element results section, however only very slightly and only affecting a small number of samples.

High water contents have been shown to supress the crystallization of plagioclase e.g. (Dolfi and Trigila, 1978, Gaetani et al., 1993). In contrast, the water contents of Mauna Loa glasses are typically quite low, varying from 0.09 to 0.87 % (Davis et al., 2003) with the average water contents of MORB ranging from approximately 1600-3500 ppm (Clog et al., 2013). In general,

low-K lavas contain the least water, with K-rich alkalic lavas containing the most - almost 1% - in a study of deep-sea pillow basalts erupted from Kilauea (Moore, 1970). In addition to decreases in Al_2O_3/TiO_2 and -Sr/Nd ratios, ~5 samples (M11-5, M17-43, M17-8, M18-35, and M6-26) also show a decrease in absolute Al_2O_3 contents at the point of plagioclase fractionation, whereas some continue to decrease in MgO with no decrease in Al_2O_3 potentially indicating that these samples may have had plagioclase fractionated out while others have not. It could be possible that these evolved lavas have more than one parental magma with variable water compositions.

Experiments from Dolfi and Trigila suggest that at 1025 ˚C, around 1.25 wt. % H_2O is required to supress the stability of plagioclase, however at 1100 ˚C only 0.25 wt. % H_2O is required and at temperatures of 1150 ˚C <0.1 wt. % would be required (Dolfi and Trigila, 1978).

Further evidence for plagioclase and cpx control over lavas with <7 wt. % MgO is the continued enrichment of incompatible trace elements even while MgO ceases to decrease. The samples with < 8 wt. % MgO appear to become progressively trace element enriched, showing a steeper slope against MgO than higher MgO samples (Figures 5.1-5.3 trace element results). This increase in incompatible trace elements in the evolved samples may suggest that while olivine ceases to crystallize, other phases (mostly clinopyroxene judging by trace element ratios) continue to crystallize and therefore the trace elements continue to be enriched in the melt. When the trace elements are plotted against CaO, however, a gap between the samples with enriched highly incompatible trace elements and high CaO exists (e.g. Figure 5.5h trace element results). This gap in the trace elements may be indicating that these enrichments are not a continuous fractional crystallization path but may distinguish a separate group of samples that mostly have low MgO and are enriched in the highly incompatible elements Nb, LREE, Sn, and Ba. Enrichment in trace element concentration at constant MgO can also be evidence of a periodically tapped and replenished magma chamber, as incompatible trace elements are left to accumulate in the melt while the compatible elements are fractionated into mineral phases. The counter argument for this is that these trace element-enriched samples mostly have low MgO contents and it remains unclear why enrichment would affect samples across the full range of MgO content uniformly unless situated in separate chambers; however this will be further discussed later in this chapter.

In addition to clinopyroxene and plagioclase, minor amounts of Cr-spinel have been noted previously in Hawaiian tholeiites, typically present as micro-phenocrysts within the matrix and as inclusions within the olivine phenocrysts (Wilkinson and Hensel, 1988, Norman and Garcia,

1999). Cr-spinel is likely the major control of Cr contents in samples with MgO contents between ~8-15 wt. %, as will be shown using MELTS modelling below.

7.5 Implications for magma chamber dynamics

The evidence from major element oxides and olivine chemistry and abundance implies olivine-controlled Mauna Loa lava is formed via accumulation processes while evolved lavas may have crystallized cpx and plagioclase, and experienced some trace element enrichment, indicating that Mauna Loa's magmatic plumbing system is dynamic and complex. This section will examine how the Mauna Loa submarine lavas from this study may have been formed, paying particular attention to magma density, viscosity, and crystal entrainment.

The terms 'olivine accumulation', 'cumulate', and 'picrite' should be discussed here briefly for clarity. It has been argued that the samples in this study may have formed by accumulation of olivine, here meaning that olivine has been added to an evolved melt, and therefore the olivine is no longer in equilibrium with the whole rock assemblage or the melt. These samples are not 'cumulates' as per the specific definition for a cumulate rock given by Irvine (Irvine, 1982) as they only contain up to 33.5% modal olivine (whereas many cumulate rocks contain >85% crystals), the phenocrysts do not touch one-another as they are surrounded by a micro-crystalline basaltic matrix, and there is no layering of crystal phases. They are high in MgO, which is why they can be referred to as 'picrites', though all samples in this study fall into the 'basalt' field and none fall in the 'picro-basalt' field according to LeMaitre's 1989 total alkalis and silica diagram (Figure 4.2 major element results section).

Garcia and co-authors suggested that the parts of the Mauna Loa plumbing system that lead to the submarine rift and vent eruptions may contain accumulated olivine phenocrysts which settled due to density differences between the phenocrysts and residual melt in the deeper parts of the volcano's plumbing system (Garcia et al., 1995). Garcia also suggests that picritic lavas may erupt selectively at distal parts of Mauna Loa volcano's submarine flanks, and that some samples may be representative of a parental magma composition, as they are in equilibrium with the highest Fo olivine and show no evidence of magma mixing. Rhodes (Rhodes, 1995) notes that high olivine basalts such as those found in this study are rare in Mauna Loa historical subaerial eruptions (1843-1984), comprising only 7% by volume of lavas erupted. Rhodes suggests that Mauna Loa picrites and their parental magmas could rise from the mantle into a compositionally stratified magma column which is organized by density, and that the picrites might originate from the deeper parts of this column than their more evolved and more common counterparts. Rhodes is also of the opinion that picrites erupted from Mauna Loa do not represent melt compositions, and are the result of accumulation of 10-27 vol. % olivine into

a magma with lower MgO content. In a study by (Lynn et al., 2017) evidence from olivine compositions, olivine-hosted melt inclusions, and glasses at Kilauea suggest that by the time a magma has reached the surface, the melt may have undergone sufficient crystal fractionation that any primitive signature is absent from erupted material.

The CO_2 contents of lava from Kilauea have been used to suggest that primitive olivine along with primitive partial melts are injected into, and mixed with a more evolved melt (Tuohy et al., 2016). The variable amounts of modal olivine may be due to density stratification of crystals such that if a magma conduit is left to settle for any given period of time, olivine will accumulate at the base and lava erupted may reflect a vertical gradient. A gradation in the modal proportions of olivine carried by lavas could also occur if eruptions along the distal rift zones were tapping into deeper parts of the plumbing system (Tuohy et al., 2016) and as such the lavas contained more accumulated olivine. Evidence from this study however, shows that the spatial distribution of erupted magmas does not correlate with modal olivine contents. Tuohy and co-authors have also suggested that primitive magmas may mix with evolved magmas to form the large variation in MgO contents. Alternatively, if a large amount of cumulate olivine was carried by a small amount of freshly injected primitive magma, and then thoroughly mixed and stratified, this could also provide an explanation for bulk major element chemistry.

The accumulation of olivine into an evolved, coexisting melt is supported by petrographic characteristics of the olivine crystals themselves. (Wilkinson and Hensel, 1988) described the olivine in some picrites from Mauna Loa and Kilauea petrographically, finding that lavas with greater than 14-15 wt. % MgO are olivine enriched and do not represent melt compositions. Wilkinson found that most of the olivine phenocrysts are euhedral and equant, with crystals up to 8 mm in diameter, suggesting that they are cognate with the host basalt (rather than xenocrysts). Most thin sections of the picrites described by Wilkinson and Hensel contained some evidence of magmatic resorption of olivine and some contain kink-banding in the olivine, however skeletal olivine is rare. Wilkinson and Hensel (1988) suggest that Mauna Loa picrites are formed by fractional crystallization of olivine from a parental melt with ~15 wt. % MgO and that the deformation seen in some if the olivines could have occurred during flow through narrow feeder conduits. Wilkinson further argues that the enrichment of olivine in these basalts is the result of post-eruptive flow differentiation of extruded mushes of intra-telluric (crystals formed at depth), genetically related olivine crystals. This hypothesis differs slightly from others in the literature where mixing of the olivine-melt mush occurs pre-eruption.

Garcia has analysed olivines from Mauna Loa and Kilauea in lavas collected during the Hawaii Scientific drilling project (Garcia, 1996). He concludes that the undeformed olivines with wide

compositional ranges (Figure 7.7) may be the result of 'delayed fractionation', and that these olivines may have remained entrained in the melt for up to 3 years. The olivines which are strongly deformed (Figure 7.7e, f) must be from disaggregated dunitic xenoliths (Garcia, 1996), which is counter to the arguments of Wilkinson and Hensel.

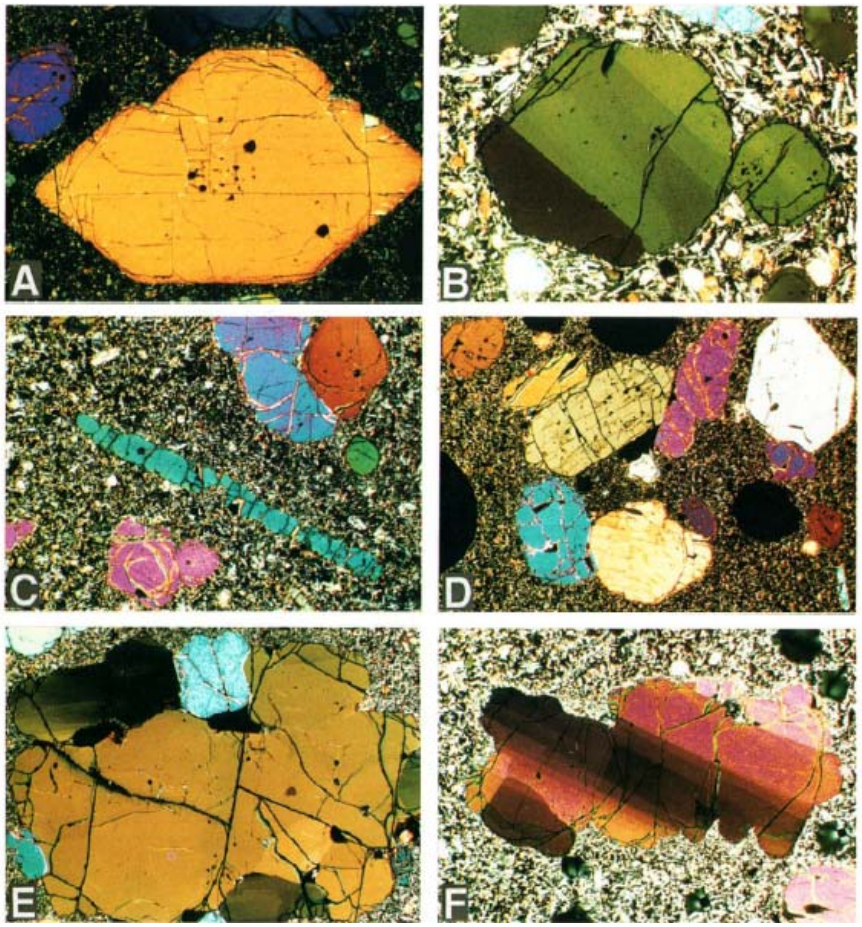

Figure 7.7 Petrographic images of olivine crystals from Mauna Loa collected during the Hawaii Scientific Drilling Project (Garcia, 1996). Shown are A) euhedral, undeformed, B) weakly kinked, C) elongate rod, D), euhedral aggregate, E) deformed dunitic xenolith, and F) strongly deformed xenocrystic olivines.

A study of dyke propagation at Mauna Loa reveals that the majority of magma from the mantle makes its way to the deep and intermediate parts of the south west or north east rift zones, with only a small fraction reaching the shallow magma chamber (Amelung et al., 2007). Amelung and co-authors measured ground deformation at Mauna Loa using an interferometric synthetic radar technique (InSAR) to determine the size, location, and geometry of inferred intrusive bodies beneath Mauna Loa. Their models suggest a spherical magma chamber with 1.1 km radius at 4.7 km below the summit (0.5km below sea level) (National Museum of Natural History, 2013).

Amelung and co-authors show that the intrusion of magma changes the stress field in the volcanic edifice resulting in dyke propagation into the rift zone (SW rift in the case of the 2002-2005 period), causing the sub-surface accumulation of magma in the rift zones. The accumulation of olivine into more evolved melt in the rift zones prior to eruption could provide the time for the magma to become well mixed in with phenocrystic and xenocrystic olivines, such that the olivine crystals are well entrained to the point that the forsterite content is no longer correlated with melt composition.

The large quantities of modal olivine (up to 33 vol. % in this study) may settle quickly in a primitive melt due to the relatively low viscosity of melt during the early stages of olivine ± chromite fractionation, forming a dunitic cumulate body at the base of the magmatic conduit (Clague et al., 1995). The higher T and lower SiO_2 content of the hypothetical parental magma will tend to lower the melt viscosity (Takeuchi, 2011). Conversely, highly evolved magmas will have a higher viscosity during the fractionation of clinopyroxene and plagioclase meaning that cpx and plagioclase may remain entrained (Clague et al., 1995). After the onset of plagioclase and cpx crystallization, the magma may penetrate the cumulate dunite body via dykes, breaking up the cumulate and entraining olivine into the magma. Clague and co-authors (1995) have used calculated melt viscosities to infer that the whole rock samples from Kilauea's Puna Ridge are mixtures of evolved liquid + entrained olivine + unfractionated plagioclase and augite.

In the previous section I have shown that entrainment of olivine into a melt with 8 – 10 wt. % MgO can explain the major element trends of the samples studied here (7.3 this chapter). There is also significant modal olivine present in samples with < 8 wt. % MgO (1-8 vol. %) and <7 wt. % MgO (1-4 vol. %).

In addition to melt viscosity, melt density may be an important determinant of eventual lava chemistry. Stolper and Walker have suggested that the reason most MORB basalts erupted on the ocean floor have a limited compositional range may be due to melt density (Stolper and Walker, 1980). They note that tholeiitic melts reach a minimum density just before the onset of plagioclase and cpx crystallization, at which point the magma is buoyant enough to overcome the density filter imposed by the crust and is erupted. By analogy, density constraints could be the reason that the glasses and inclusions found at Mauna Loa rarely have greater than 10% or less than 5% MgO (Davis, 2001), as these compositional ranges would be associated with minimums in magma density. The low density coupled with the high viscosity of melts near the pyroxene + plagioclase precipitation point could enable these melts to be selectively erupted whilst retaining significant proportions of entrained olivine. Entrainment and residence times of crystal in Mauna Loa's magmas are explored further in the next section.

In addition to melt viscosity and density, the concentration of olivine crystals in a melt will affect crystal settling rates. (Schwindinger, 1999) has shown that an important factor in the settling rate of crystals in a melt is the proportion of crystals to melt, and that high enough proportions (10-35%) will cause the settling velocity to fall to 1/10 - 1/2 of the average Stoke's settling velocity. This is because the particles will begin to be retarded by fluid streaming upwards at high crystal proportions. Schwindinger also states that at crystal concentrations higher than 35 wt. %, the crystals begin to interact with each other and the magma viscosity jumps to higher effective values. The critical point at which the magma begins to act as a solid due to entrained crystals is about 55 wt. % (Schwindinger, 1999). The dependence of magma viscosity on the crystal concentration in the magma may be a contributing factor to the proportions of olivine found in Mauna Loa basalts.

In summary, it appears plausible that influxes of parental magma from the mantle with ~16 wt. % MgO may enter Mauna Loa's rift zones via dyke propagation caused by the build-up of pressure by influxing magma. The >8 wt. % lavas may have formed via the settling of in rift zones, where olivine could be differentiated until the remaining melt was evolved (<10 wt. % MgO). Subsequent mixing and re-entrainment of the settled olivine could occur via pressure build up and release due to changing stress fields. Once the magma has reached critical viscosity and density parameters e.g. (Stolper and Walker, 1980), the lava may be erupted along with entrained olivine. The highly evolved samples contain small amounts of plagioclase and display cpx fractionation signatures, while not containing much olivine. The lavas containing plagioclase ± cpx may represent more evolved melts that have not been in contact with fractionated olivine, and may have experienced trace element enrichment via cpx + plagioclase fractionation or via continuous tapping and replenishment of the magma chamber.

Establishing the formation processes of Mauna Loa tholeiitic lavas is important, because it has implications for being able to accurately estimate the parental magma compositions of the erupted lavas. The significance of Mauna Loa picrites ($\geq$ 15 wt. % MgO (Garcia et al., 1995)) has been debated e.g. (Rhodes, 1995), with proponents of a primary magma origin arguing that these rock types could be evidence of primary mantle melts from which most other basaltic magmas are derived. If this were the case, the picritic compositions could be used directly to investigate the mantle source characteristics and mantle melting processes of the Hawaiian plume. I argue that despite advocating that Mauna Loa basalts with >8 wt. % MgO are the product of olivine accumulation, this does not mean they cannot also be used to infer a primitive magma composition for Mauna Loa.

One commonly used technique to infer a parental composition is to add or subtract olivine to a melt composition until an equilibrium composition (the MgO in equilibrium with the highest forsterite olivine) is reached. The evidence from bulk rock major elements, olivine forsterite contents, as well as olivine modal proportions suggests that the bulk rock samples may be mimicking the composition of a melt during crystallization of olivine, such that selecting one of the bulk rock samples with MgO contents in equilibrium with the highest forsterite olivine is identical to progressively adding olivine to one of the more evolved melts to reach a parental composition. This is supported by a previous study (Norman and Garcia, 1999) where it was suggested that some Mauna Loa bulk compositions may approximate primitive melts, despite containing abundant phenocrysts. This has also been shown in Figure 7.2 of this chapter, where the melt composition modelled using Petrolog assuming a starting composition of 16 wt. % MgO was a close fit to the bulk rock data with 8-16 wt. % MgO. Through its dynamic magma chamber processes, Mauna Loa Volcano and possibly other Hawaiian volcanoes, has 'recreated' the chemical composition of a melt during fractional crystallization of olivine by adding progressive amounts of olivine to an evolved melt before and/or during eruption.

7.6 Residence times of crystal phases in a magma chamber

If pre-eruption entrainment of olivine, and crystallization but not complete fractionation of plagioclase/cpx is required to explain the bulk rock petrography of these, it is therefore necessary to investigate how long olivine and other phases remain stored in a magma chamber and how long a crystal can remain suspended in a magma chamber melt.

Magma storage timescales have been estimated for olivine from Kilauea's 1959 eruption based on crystal size distributions (Mangan, 1990). For the crystal size distribution seen in the olivine-rich pumices produced by this fire-fountaining event of 0.01 – 6 mm in diameter and from assuming a growth rate of 10^{-10} cm/s, the average magma storage time was calculated to be 10.9 ± 3.6 years with a range of between 7.2 to 11.9 years. This means that for a crystal to remain entrained in the melt it must be able to be suspended for this period of time, or other forces must be at work to ensure the magma is churned to re-mobilize the crystals.

More recently, modelling of Fe-Mg and Ni zoning patterns in olivines from Kilauean lavas (specifically those from the 300+ year Keanakako 'I Tephra explosive eruption) was conducted by Lynn and co-authors to examine the rapid eruption versus prolonged storage hypotheses at Kilauea (Lynn et al., 2017). Their results reveal that the magmas were mixed and stored on timescales ranging from a few weeks to several years prior to eruption. The dominant type of olivine during this eruptive period was normally zoned, with cores containing $\geq Fo_{88}$, suggesting that these olivines may be analogous to those erupted by Mauna Loa.

In addition to crystal growth rates and diffusion modelling, residence times calculated from magma densities and viscosities can be used to estimate how long a crystal can remain suspended in a melt, and also therefore if crystallization is fractional or equilibrium in nature. The equation for the residence time of an olivine crystal in a magma chamber relates the height (h) in metres of a magma chamber to the settling velocity (Vs) in m/s and can be expressed:

$$\tau = \frac{\ln(2h)}{Vs}$$

The settling velocity is found using the equation: $Vs = \frac{g\Delta p a^2}{18pv}$ (Sparks et al., 1984)

Where g is the gravitational constant, Δp is the density difference between an olivine crystal and the melt, a is the size of the olivine crystal in m, p is the density of the fluid, and v is the kinematic viscosity in m^2/s. Here, we assume that an olivine crystal is 1 mm in diameter, the magma chamber is 1 km in height, the density of olivine is 3.32 g/cm^3, while the density of basaltic melt is 3.00 g/cm^3. In addition, the kinematic viscosity is approximately 0.1 m^2/s for basalt (Martin and Nokes, 1989). Results of this calculation give a residence time of around 150 days which is a similar order of magnitude to eruption timescales of three weeks during Mauna Loa's most recent eruption in 1984 (Crisp et al., 1994).

This analysis assumes homogeneous nucleation of crystals and quiescent setting. It is likely that actual residence times could be considerably longer considering the possibility that the magma chambers and conduits may be churned and disturbed as new pulses of magma are injected into the system. It is also possible that in addition to crystal settling, crystals may form on the sidewalls where magma is in contact with the cooler surrounding lithosphere and volcanic edifice. It has been envisaged by Pietruszka and Garcia that the side walls of Kilauea's magma chamber consist of an outer crystal-mush zone (Pietruszka and Garcia, 1999) (included in magma chamber volume estimates from geophysical studies) while the insides contain hot ductile magma.

Seismic P-wave travel time tomography of the regions below Kilauea and Mauna Loa paints a less stylized picture of the volcanoes' magma 'chambers' (Okubo et al., 1997). Okubo and co-authors have inferred that Mauna Loa and Kilauea's magma chambers may consist primarily of solidified, ultramafic cumulate, which causes upper-crustal deformation in the form of normal faulting and fracturing in response to magma injection within the volcanic edifice. In a setting where abundant olivine exists in the form of crystal mush at the sides and bottom of the magma chamber, or indeed comprising the majority of the chamber it is easy to see how crystals could

separate by flow differentiation upon the ascent of magma to the surface. In this case settling rates based on the assumption of a quiescent magma become less relevant.

Further to the simple crystal residence time calculation above, the density and viscosity of a magma that is fractionating olivine was obtained at increments of crystallisation using the MELTS geochemical modelling software (Table 7.1) (Ghiorso et al., 2002). A high MgO (wt. %) tholeiitic basalt composition was used as a starting melt, which was then cooled until olivine, cpx, plagioclase, plus minor spinel had fractionated leaving 15% remaining melt. This was set in a shallow magma chamber (0.4 kilobar) with an oxygen fugacity of QFM that was allowed to vary during crystallization. More information is given about the MELTS program and the justification for these parameters in later sections of this chapter; however the important aspect to observe here is how the viscosity and density of the melt changes during the crystallisation sequence. It can be seen that the density decreases during fractionation until the melt contains about 7 wt. % MgO, after which it begins to increase again due to the concentration and subsequent fractionation of a plagioclase component from the melt. Kinematic viscosity increases exponentially throughout crystallization.

Crystal residence times vary significantly with the degree of fractionation, increasing as the melt becomes more evolved. The residence times for olivine and cpx start at half a year in a primitive melt and increase to nearly two years at 6 wt. % MgO. When plagioclase begins to crystallize, residence time is high compared to olivine at 136 years at 6 wt. % MgO, after which the plagioclase briefly becomes positively buoyant again. This suggests that in melt compositions commonly found in glasses, plagioclase may never settle from the melt and so it might be expected that all of the plagioclase crystallized will remain entrained in the melt and be erupted. Theoretically, at 3 wt. % MgO the plagioclase eventually becomes denser than the surrounding melt again, yielding residence times of approximately 47 years.

Conclusions to be drawn from these calculations are that even assuming a perfectly quiescent magma chamber, and assuming magma storage rates in the order of weeks to years (Lynn et al., 2017), any crystallized olivine, cpx, or plagioclase could remain entrained in a melt until eruption. When the observation that the magma chamber is likely a turbulent, dynamic environment periodically disturbed by replenished magma, this seems even more likely. Furthermore, given the high modal proportions of olivine found in the high MgO samples (up to 33.5 vol. %) it is also feasible that the magma is able to sweep up extra olivine in addition to the amounts predicted to be produced from a crystallizing parental magma e.g. 17 % for estimates produced for Kilauea (Clague and Denlinger, 1994). The evidence from calculations above suggests that olivine, cpx, and plagioclase crystallization is likely to approximate an

equilibrium process, which could have important implications for the geochemical modelling of crystallization in systems similar to Hawaii.

Table 7.1 Calculated residence times for olivine, cpx, and plagioclase in a melt during fractional crystallization. ρ is the density, v is the kinematic viscosity, Δ ρ is the density difference between the crystal and the melt, Vs is the settling velocity, and τ is the residence time. A crystal size of 1 mm and a magma chamber height of 1 km was used, assuming constant densities of 3.32 g/cm^3 for olivine and cpx, and 2.7 g/cm^3 for plagioclase. The calculation assumed perfectly quiescent conditions during crystallization and homogeneous nucleation, i.e., no magma flow or sidewall crystallization.

				olivine & cpx							plagioclase					
(wt. %)	(wt. %)	(g/cm^3)	(m^2/s)			(m/s)	(s)	(d)	(y)	(y, h=200)	(y, h=5000)		(m/s)	(s)	(d)	(y)
Liquid	MgO	ρ	ν	Δρ		Vsx10^8	τx10^{-7}	τ	τ	τ	τ	Δρ	Vsx10^8	τx10^{-7}	τ	τ
100.0	18.26	2.71	0.28	0.608		43.0	1.8	204	0.56	0.44	0.68	-	-	-	-	-
100.0	17.74	2.71	0.32	0.607		38.5	2.0	229	0.63	0.49	0.76	-	-	-	-	-
96.8	16.67	2.71	0.36	0.609		33.6	2.3	262	0.72	0.57	0.87	-	-	-	-	-
93.7	15.64	2.71	0.41	0.611		29.7	2.6	296	0.81	0.64	0.98	-	-	-	-	-
90.9	14.65	2.71	0.46	0.613		26.6	2.9	331	0.91	0.71	1.10	-	-	-	-	-
88.4	13.70	2.70	0.52	0.616		24.0	3.2	366	1.00	0.79	1.22	-	-	-	-	-
86.0	12.78	2.70	0.57	0.618		21.9	3.5	402	1.10	0.87	1.34	-	-	-	-	-
83.8	11.91	2.70	0.63	0.621		20.0	3.8	439	1.20	0.95	1.46	-	-	-	-	-
81.8	11.07	2.70	0.68	0.624		18.5	4.1	476	1.30	1.03	1.58	-	-	-	-	-
79.9	10.28	2.69	0.74	0.626		17.1	4.4	514	1.41	1.11	1.71	-	-	-	-	-
78.1	9.51	2.69	0.80	0.629		15.9	4.8	553	1.52	1.19	1.84	-	-	-	-	-
76.5	8.79	2.69	0.86	0.632		14.9	5.1	592	1.62	1.28	1.97	-	-	-	-	-
74.9	8.10	2.69	0.92	0.635		13.9	5.5	632	1.73	1.37	2.10	-	-	-	-	-
73.5	7.46	2.68	0.98	0.636		13.1	5.8	670	1.84	1.45	2.23	-	-	-	-	-
67.0	6.34	2.69	1.03	0.629		12.4	6.2	712	1.95	1.54	2.36	0.009	0.18	430.2	49789	136.4
51.2	5.32	2.70	1.07	0.618		11.7	6.5	753	2.06	1.63	2.50	-0.002	-	-	-	-
41.4	4.46	2.71	1.10	0.606		11.1	6.8	793	2.17	1.71	2.63	-0.014	-	-	-	-
34.8	3.34	2.67	1.29	0.652		10.3	7.4	851	2.33	1.84	2.83	0.032	0.51	148.1	17138	47.0
25.1	2.36	2.59	1.61	0.734		9.6	7.9	918	2.52	1.98	3.05	0.114	1.48	51.2	5928	16.2
20.4	1.78	2.53	1.86	0.786		9.1	8.4	971	2.66	2.10	3.22	0.166	1.91	39.8	4607	12.6
17.7	1.38	2.50	2.08	0.824		8.7	8.8	1017	2.79	2.20	3.37	0.204	2.14	35.5	4113	11.3
15.8	1.09	2.47	2.26	0.853		8.3	9.1	1057	2.90	2.28	3.51	0.233	2.27	33.4	3869	10.6
14.4	0.87	2.44	2.43	0.877		8.0	9.5	1095	3.00	2.36	3.63	0.257	2.35	32.3	3736	10.2

7.7 Submarine versus subaerially erupted samples

A literature collation of 146 subaerial samples and 300 submarine samples (Moore and Clague, 1987, Rhodes, 1988, Garcia et al., 1989, Rhodes and Hart, 1995, Hofmann and Jochum, 1996,

Hauri and Kurz, 1997, Norman and Garcia, 1999, Garcia and Davis, 2001, Davis et al., 2003, Rhodes and Vollinger, 2004, Rhodes and Vollinger, 2005, Wanless et al., 2005, Wanless et al., 2006) including glasses and whole rocks was compiled to investigate differences in subaerially versus submarine erupted lavas from Mauna Loa. Samples from this study are from the rift, slope, and vents of the SW flank, samples from Wanless et al. (2006) are from radial vents on the western flank, those form Rhodes and Vollinger (2005) are from the 1984 eruption from the the Moku'aweoweo crater and also the upper SW rift and the NE rift zone, those from Hauri and Kurz (1997) include samples from subaerially-erupted SW rift, Rhodes and Hart (1995) include samples from the NE rift, the SW rift, the summit, and the north flank, those from Rhodes and Vollinger (2004) include drill core from the upper 245m of the HSDP drilling operation at Mauna Loa, Norman and Garcia include flow from subaerially-erupted SW rift zone, Rhodes (1988) focuses on the 1984 flow also, while Davis et al. (2003) have glasses from subaerial and submarine rift zone, flanks, and vents. The whole rock lavas are presented in Figure 7.8, while the glasses are presented in Figure 7.9. Accepting that sampling strategies can be biased for many reasons, it can be seen that the major elements of submarine and subaerial lavas from Mauna Loa are very similar (Figure 7.8). The majority of lavas from both submarine and subaerial settings contain low MgO (5-9 wt. %) with relatively fewer containing high bulk MgO. In fact, contrary to the hypothesis of (Garcia et al., 1995) that distal submarine portions of the rift zone contain denser lavas with higher MgO and higher olivine than their subaerial counterparts, submarine lavas have similar MgO contents to subaerial lavas (11.93 wt. % MgO average for submarine compared to 11.30 wt. % MgO for subaerial). The submarine glasses are also similar to the subaerial glasses in terms of average MgO (6.38 wt. % and 6.28 wt. % respectively).

Davis and co-authors have shown that much of Mauna Loa's flank is covered in pillow basalts which are similarly degassed to subaerially erupted lavas (Davis et al., 2003). It was therefore suggested that some volatile-poor lavas eventually erupted in a submarine environment may have originally risen through subaerial conduits, degassed, and then drained back down through more distal conduits via lavas tubes to be erupted via submarine vents. Un-degassed lavas were found mostly in Mauna Loa's submarine rift zones. The evidence from volatile contents could explain why submarine and subaerially erupted samples are broadly quite similar in terms of major element chemistry, and may indicate that there is a homogenization process at depth before the magma is either erupted subaerially, or filtered through subaerial conduits and then drained back out through more distal parts of the volcano.

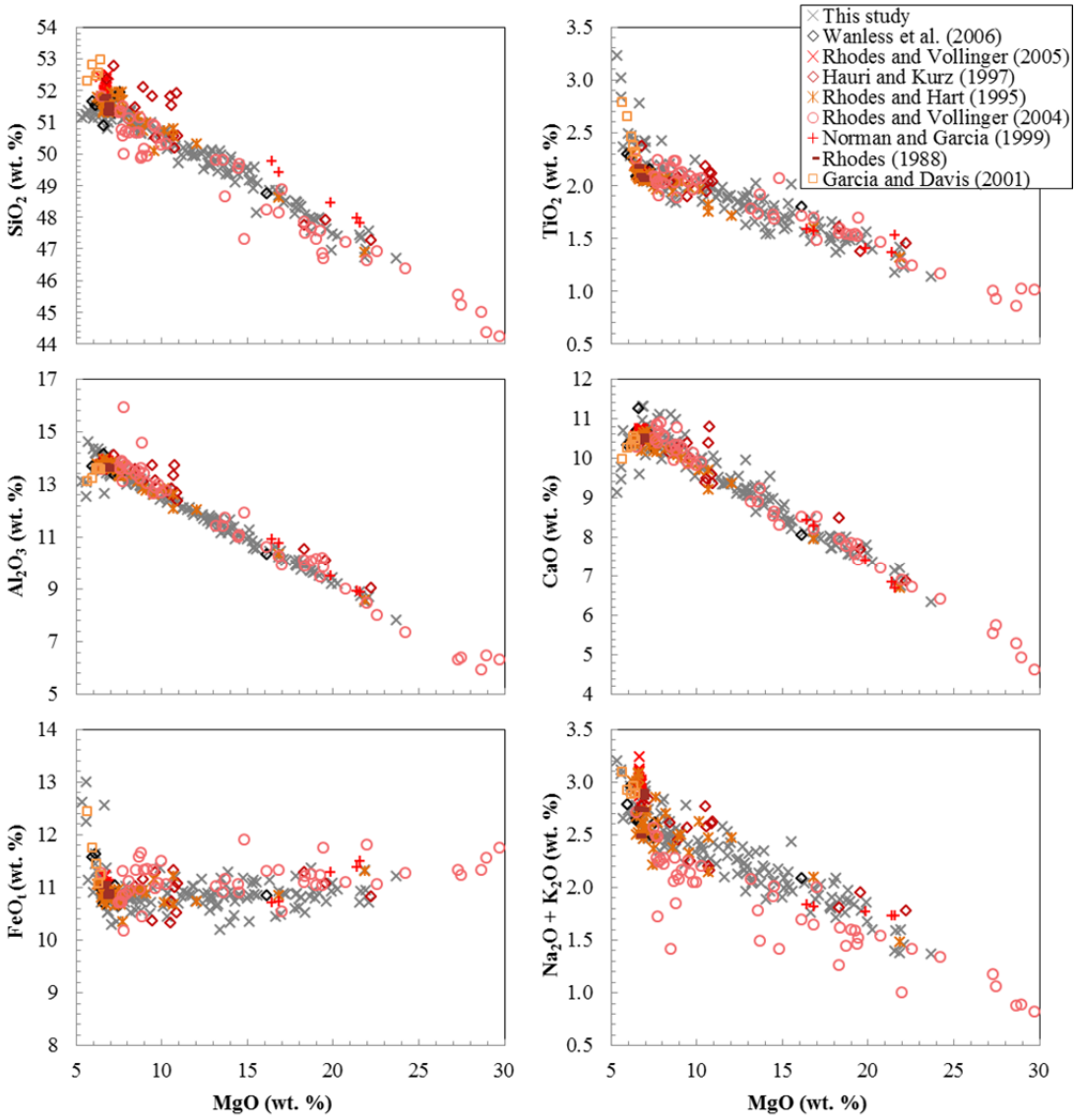

Figure 7.8 Literature Mauna Loa whole rock analyses divided by study (red/orange = subaerial, black/grey = submarine).

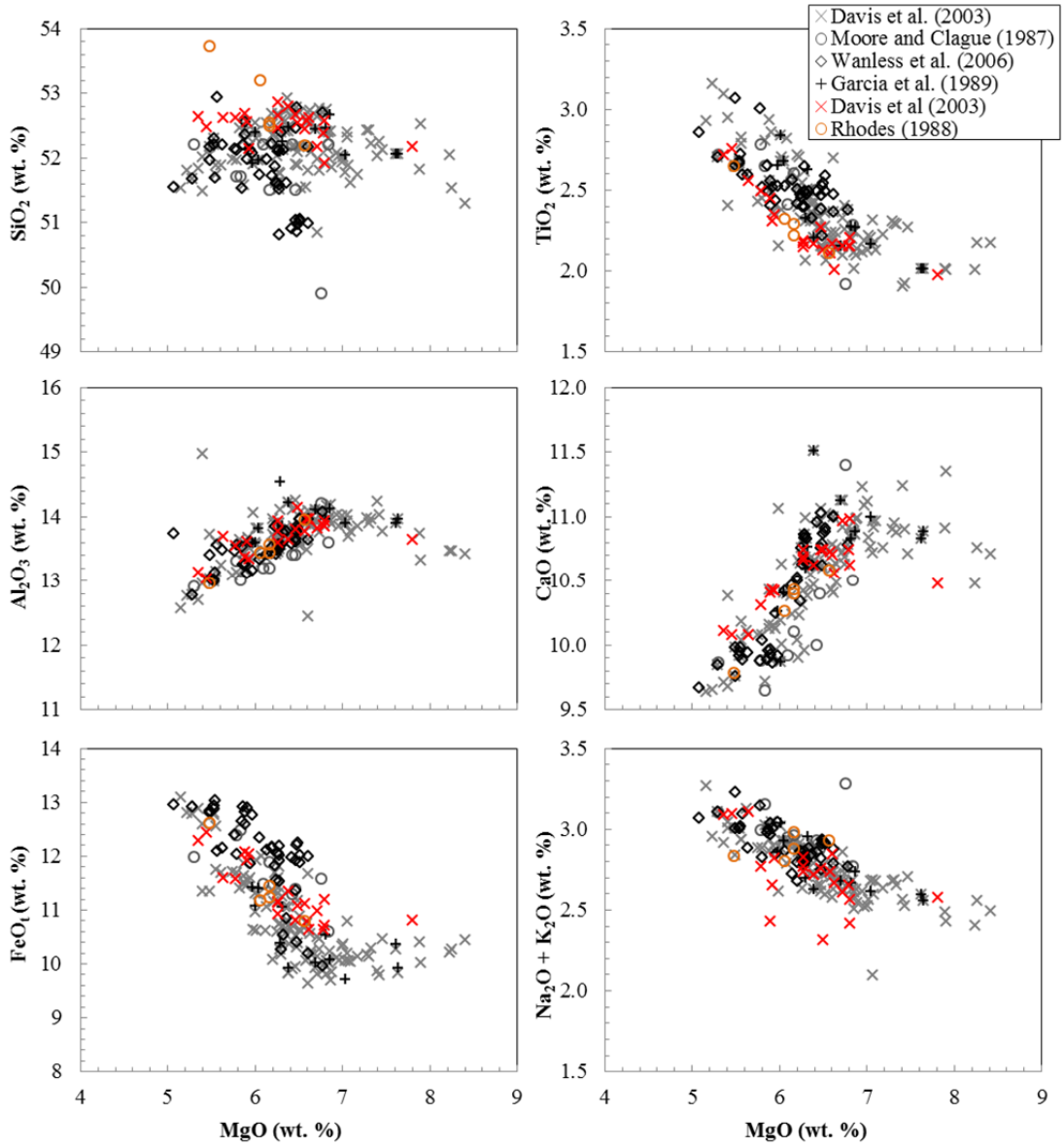

Figure 7.9 Literature Mauna Loa glass analyses divided by study (red/orange = subaerial, black/grey = submarine).

7.8 Other controls over chemistry

It can be concluded that the major control of the variation in major and trace elements within the samples studied here is due to the abundance of olivine (modal or normative) present in each sample. Element concentrations increase with increasing modal olivine if they are compatible in the olivine mineral structure e.g. Mg, Ni, and Co. Conversely, elements which make up less of the olivine crystal structure e.g. Si, Ca, Al, Ti, K, Na, and the majority of trace elements such as Zr, Nb, Sr, Ba, Th, REE, V, Sc etc. decrease in concentration with increasing modal olivine. In samples with <7 wt. % MgO it is clear that cpx and plagioclase also exert some control over major and trace element chemistry as discussed previously.

Despite modal olivine abundance and cpx/plagioclase crystallization being the major influences over geochemical variation in samples from this study, there is also a significant amount of variation in the major and trace element chemistry that cannot be accounted for olivine control.

The major and trace element data for all samples from this study were normalized to 15 wt. % MgO by adding or subtracting variable amounts of olivine (Figure 5.10, 5.11, 5.16, 5.22, 5.23 trace element results). The effect was to reduce the overall range somewhat, and considerably reduce the variation in the data between the first and third quartiles. The significant decrease in variability indicates that a large amount of the variation for the middle 50% of the data is controlled by the addition or subtraction of olivine. It also indicates that for a small number of samples (those in the outlying first and last quartiles), the addition and subtraction of olivine does not significantly change the value of the major elements and therefore their respective chemistries must have an alternative control. For the major elements, the samples with low Si, Al, and Ca, and high Ti, Fe, and Mn remain distinguishable from the majority of data after MgO normalization. Figure 4.9 in the major element results section shows the MgO-normalized major element arrays. It is clear that a slight positive correlation exists between CaO (15) and Al_2O_3 (15) with SiO_2 (15), and a slight negative correlation of FeO_t (15) with SiO_2 (15). This correlation suggests variation outside the effect of olivine control, and appears particularly to affect the more evolved samples with less than 8-9 wt. % MgO for the major elements, and is also the case for the trace elements. Trace element compositions show that some of the landslide samples are clearly distinguishable from the other samples in terms of their normalized Nb, Zr, and Y concentrations (Figure 5.16 trace element results), which may be an indicator that the compositions of those samples are affected by processes other than olivine fractionation, or that these samples may not be genetically related to rest of the Mauna Loa samples. Distinctions are also apparent in some TE ratios, e.g. Zr/Nb, La/Yb, and Sm/Nd; ratios which should not be fractionated by crystallization of any phase expected during crystallization of a tholeiitic melt. This could be an indicator that these samples have come from a chemically heterogeneous source, i.e. they may have origins from another nearby volcano, or they may represent variable degrees of melting from a similar source to the other

7.9 Modelling with Petrolog, MELTS, and alphaMELTS software

Major elements, trace elements, and the trace element ratios indicate strong control by olivine in most of the samples studied here, as well as clinopyroxene, plagioclase, and spinel control. To further investigate the crystallisation sequence of these Mauna Loa lavas, the sample compositions were modelled using the MELTS, alphaMELTS, and Petrolog magmatic modelling programs (Gualda et al., 2012, Ghiorso and Gualda, 2015, Ghiorso, 1983; Ghiorso and Sack, 1995, Smith and Asimow, 2005; Ghiorso et al 2002; Danyushevsky and Plechov,

2011). The aim of this exercise was to assess quantitatively how much the variation in the chemistry might represent the magmatic process of crystal fractionation, and how much, if any, of the compositional variation might require an alternative explanation. In general, the three programs produced very similar results in both major and trace elements for samples with >7 wt. % MgO, where the control of olivine is clear. Results were more variable between programs for the more evolved samples, which is discussed further below. This section will provide a brief overview of the software as well as present justification for a parental magma composition, prediction of crystallization sequence and temperatures, as well as the effects of varying parameters like oxygen fugacity and water content. In addition, bulk distribution coefficients have been calculated for all measured trace elements during crystal fractionation. This approach has yielded low relative uncertainty of the partition coefficient for the majority of elements (Table 7.5, section 7.10.1 of this chapter).

Various programs have been produced for the modelling of magma chamber processes such as crystallization and magma mixing, as well as assimilation. Typically the user inputs a melt starting composition and the liquid line of descent is calculated according to mineral-melt equilibria and thermodynamic parameters are derived from empirical and experimental studies. Such studies are generally relevant to a basaltic system like MORB, although recent updates to the MELTS program have widened the application to rhyolitic compositions and a greater range of possible pressure and temperature regimes.

These programs calculate the liquidus temperature of a melt and derive the compositions of fractionating minerals for a specified melt composition at a specified pressure, temperature, and oxygen fugacity. They combine empirical methods, specifically experimental data that have determined equilibrium phase stabilities when pressure, temperature, melt composition, and oxygen fugacity are known, and thermodynamic mineral-equilibrium models to determine an idealised magmatic fractionation compositional path. The MELTS program is probably the most well-known of these programs.

7.9.1 MELTS thermodynamic model

The MELTS software uses a method outlined in (Ghiorso, 1983) and (Ghiorso and Sack, 1995) that aims to minimize the Gibbs free energy of a system which comprises solid and liquid phases and ranges in many extrinsic variables such as pressure, temperature, volume, composition, entropy, enthalpy, and oxygen fugacity. The minimum Gibbs free energy (G) of a system can be solved uniquely by finding the derivative and then the second derivative of a Gibbs' energy surface. The $G^{(total)} = G^{(liquid)} + G^{(solid)}$. The $G^{(liquid)}$ is a term that is dominated by the chemical potentials of the components plus $G^{(mixing)}$, which needs to take into consideration

mixing of both ideal and regular solutions. For ideal solutions $\Delta U = 0$ and $\Delta H = 0$, the entropy has a positive value that is related to the activity of the components. It is assumed that the activity of each component in an ideal solution is equivalent to the mole fraction of each component in the system. In this scenario, mixing is always entropically favourable, and therefore mixing will always lower the total G of the system, meaning that mixing will always occur. The $G^{(ideal)}$ must be summed with the $G^{(regular)}$ in order to get the total $G^{(mixing)}$. $G^{(regular)}$ takes into account the fact that there are differences in the bonding and bond lengths in a system containing different components, and therefore mixing is not always favourable in non-ideal solution, as is the case for a heterogeneous and multi-component magma chamber. For the $G^{(regular)}$ to be calculated, some interaction parameters must be known to describe the mixing behaviour of each thermodynamic component in the system, which MELTS has obtained from a least squares minimization of an experimental database and then used as a base from which to extrapolate to end-member compositions. A specific algorithm in MELTS is employed to deal with 'rank deficient data' (data that are sparse for example experiments that do not cover complete ranges in P, T, or fO_2 or that do not well constrain mineral end-members). This database contains 2500 experimentally determined compositions of silicate liquids. Once this surface of G has been parameterised, taking the derivative and second derivative of this surface allows the program to minimise G for any given user-specified limitations in order to calculate the most energetically favourable arrangement. This is then provided in the output of MELTS.

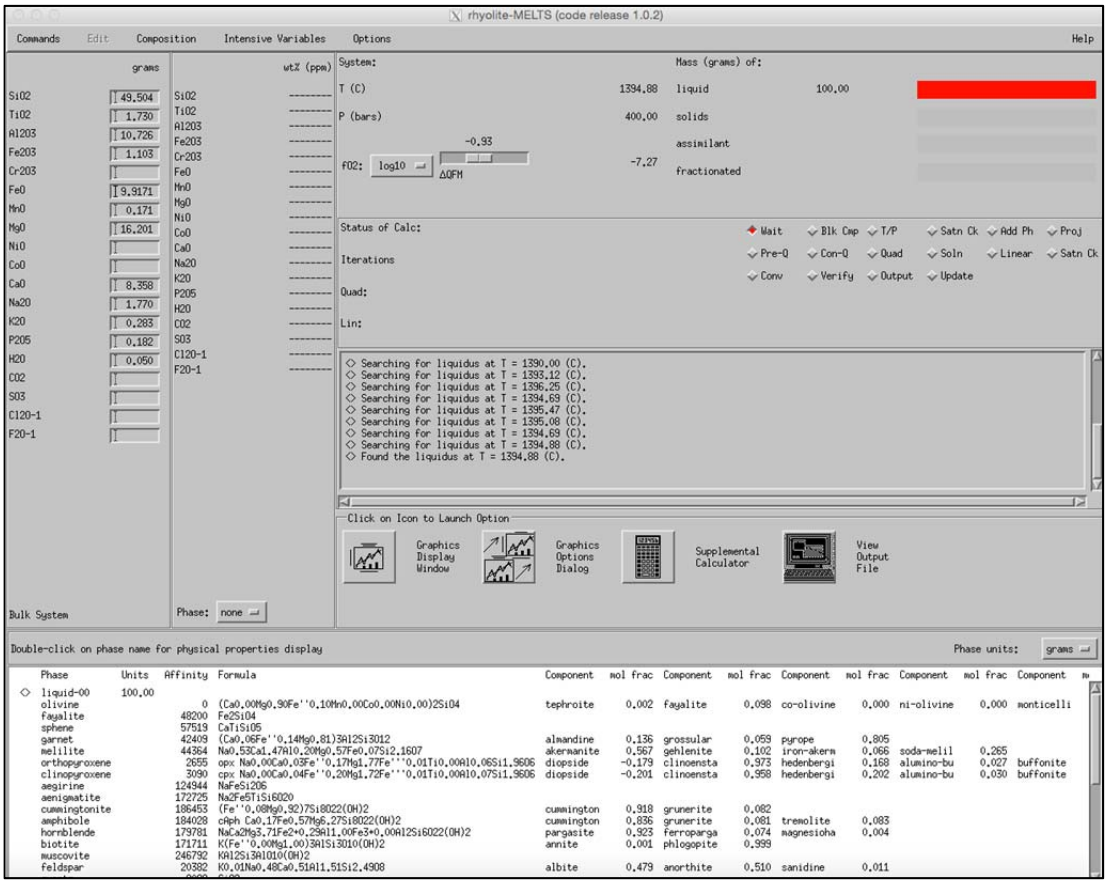

Figure 7.10 Graphical user interface of Rhyolite MELTS software (Gualda et al., 2012, Ghiorso and Gualda, 2015) showing input settings for major element composition, calculated liquidus temperatures, user-set pressure and fO_2 parameters, and output in the bottom panel of the screen showing example mineral formula that may be used during a calculation.

7.9.2 alphaMELTS software

alphaMELTS was developed using the MELTS algorithms as a basis, but has added sub-routines that can calculate equilibrium assemblages of a thermodynamic path set by the user (Smith and Asimow, 2005). alphaMELTS uses a command line interface as opposed to the graphical user interfaces of the MELTS and Petrolog packages. The use of a command line interface enables large amounts of information to be read into a calculation quickly and efficiently, for example trace element concentrations and partition coefficients. Unlike MELTS, alphaMELTS is able to include trace elements in its thermodynamic models using default partition coefficients from (McKenzie and O'Nions, 1991, Mckenzie and Onions, 1995), a lattice strain model using ionic radii and valence state as a guide, or the user can set their own. The benefits of using a command line interface which can call up input files is that any element can be looked at, so long as the element symbol, e.g., 'Sn' is used consistently throughout all files. In addition to the partition coefficients almost every other parameter can be varied to

some degree, e.g. setting min/max P, T, and fO_2 of the crystallization environment as well as setting the fractionation sequence to be isothermal, isentropic, isobaric, or isochoric. It is also possible to suppress particular phases and set the melting/fractionation type etc. A downside to both MELTS and alphaMELTS is that they are difficult to use on a Windows machine as Perl needs to be installed for alphaMELTS to work, while Mac OS generally come with Perl pre-installed.

Figure 7.11 Command line interface of alphaMELTS software (Smith and Asimow, 2005; Ghiorso et al, 2002) showing user input settings for an isentropic, adiabatic melt regime and menu options for all possible operations.

7.9.3 Petrolog software

The Petrolog software (Danyushevsky and Plechov, 2011) uses a compilation of computational approaches by various authors that have been derived in a similar way to the MELTS programs, in that they use empirical observations from collected experimental data. The user can choose which author's approach they want to use, unlike with the MELTS program. Of these various author models within Petrolog, only one has accounted for all of the four phases plagioclase, cpx, and opx in addition to olivine, which are most relevant to Hawaiian tholeiites (Ariskin et al., 1993). Ariskin and co-authors developed a computational program called COMAGMAT to model igneous processes up to 12 kilobar in a wide range of magmatic systems (primitive basalts to dacites) by using empirically calibrated mineral-melt equilibria for olivine, augite, pigeonite, plagioclase, ilmenite, and magnetite. This program was based on multiple empirical and experimental works e.g. (Nathan and Vankirk, 1978, Nielsen and Dungan, 1983, Frenkel and Ariskin, 1984, Ariskin et al., 1987, Ariskin et al., 1988, Ariskin et al., 1990a, Ariskin and Barmina, 1990, Ariskin et al., 1990b, Weaver and Langmuir, 1990). A further approach implemented by Petrolog has compared MORB glasses with 1 atmosphere crystallization experiments using MORB-like compositions to quantify the effect of H_2O on the crystallizing phases, and mineral-melt equilibria are used to calculate the pseudo-liquidus temperatures for all mineral phases involved, for a given composition. The phase with the highest T is the true liquidus phase and its composition is removed incrementally from the remaining melt. Studies by (Michael and Chase, 1987) and (Nielsen and Dungan, 1983) have applied these methods to natural systems to predict the compositions and abundances of phases that crystallised from basaltic magmas, and then assumed equivalent natural glasses were the parental magma of the respective basalt. (Michael and R., 1987, Nielsen and A., 1983)

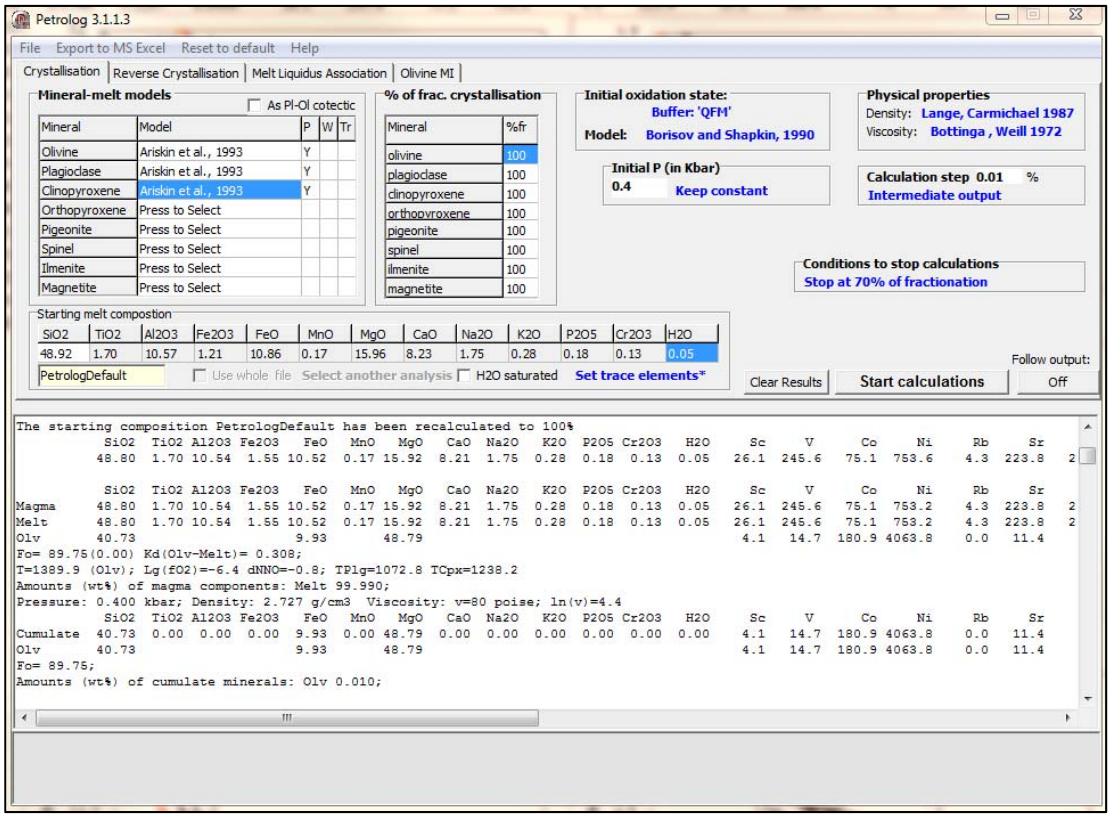

Figure 7.12 Graphical user interface of Petrolog software showing input settings for major element composition, preferred published fractionation model, oxidation state, pressure, % of crystallization, and output in the bottom panel of the screen.

7.9.4 Parental magma composition

In order to compare the predicted effects of melt composition to Mauna Loa's bulk rock chemistry, a parental magma must be estimated. As discussed in the previous sections, parental magma compositions range in MgO contents generally from between 12-18 wt. %, although some studies have suggested even higher values e.g. the estimate by (Budahn and Schmitt, 1985) of 24 wt. % from estimates from primary melts in equilibrium with a garnet peridotite. This latter estimate was one without consideration for the Fo contents of the olivine or the consideration of the other major element oxides.

The parental magmas selected for fractionation modelling in this study were chosen to reflect estimations determined by equilibrium olivine. An MgO content of approximately 14 wt. % is in equilibrium with the $Fo_{87.8}$ olivine determined to be the best fit in previous olivine addition models, assuming a Kd of about 0.3. Fo_{90} was the most common Fo proportion, and $Fo_{90.8}$ was the highest Fo olivine found in these samples. These would be in equilibrium with a melt closer to 16 wt. % MgO. The highest Fo olivines are produced from the most primitive magmas and are therefore good indicators that the equilibrium melt will represent the primitive parental

magma composition before any crystal fractionation takes place. The melts in equilibrium with the highest forsterite olivines also have the highest chance of being close to a deeper primary magma produced in the mantle.

The parental magma estimates were calculated assuming the methods outlined in (Eggins, 1991) and melt compositions were estimated using the partitioning of Fe/Mg between olivine and a mafic liquid (Roeder and Emslie, 1970). The Fe^{3+}/Fe^{2+} ratio can be estimated by assuming a particular oxygen fugacity e.g. QFM, and assuming an olivine-liquid distribution coefficient of $D^{Fe/Mg} = 0.30$. This provides an Mg number (= molar Mg/(Mg+Fe)) with an associated Fe content for the parental , and in the case of the Kilauea Iki eruption, the Mg number was 75, equating to a melt MgO content of 16 wt. % (Eggins, 1991). In order for Eggins to obtain the compositions of the other major element oxides, olivine was added to an evolved Kilauea melt composition until the MgO content reached 16 wt. %. As discussed previously, this has occurred naturally in the Mauna Loa magma chamber as actual olivine has been added to an evolved melt, providing an estimate of melt composition up to the desired MgO content of 16 wt. %, and as such it is possible to take an average of the samples with approximately 16 wt. % MgO in order to obtain the proportions of the other major element oxides. Olivine addition was also done computationally using the 'olivine addition' function on Petrolog to evaluate whether or not the outcome was the same as that of the natural effect. Below, the anhydrous estimate for the Mauna Loa parental magma is given (Table 7.2).

Table 7.2 Proposed anhydrous parental magma composition. Average major element oxide composition at ~ 16 wt. % MgO.

	wt. %		ppm		ppm		ppm
SiO_2	48.92	**Li**	5.0	**Zr**	101	**Eu**	1.32
TiO_2	1.70	**Be**	0.72	**Nb**	7.4	**Gd**	4.25
Al_2O_3	10.57	**Sc**	26.1	**Mo**	0.6	**Dy**	3.96
FeO_t	10.86	**V**	246	**Sn**	1.20	**Ho**	0.77
MnO	0.17	**Co**	75	**Sb**	0.024	**Er**	2.02
MgO	15.96	**Ni**	755	**Cs**	0.052	**Yb**	1.63
CaO	8.23	**Cu**	103	**Ba**	55	**Lu**	0.23
Na_2O	1.75	**Zn**	98	**La**	6.8	**Hf**	2.49
K_2O	0.28	**Ga**	15.5	**Ce**	18	**Ta**	0.50
P_2O_5	0.18	**Rb**	4.3	**Pr**	2.58	**Pb**	0.62
Cr_2O_3	0.13	**Sr**	224	**Nd**	13.1	**Th**	0.43
Sum	98.75	**Y**	21.2	**Sm**	3.77	**U**	0.15

7.9.5 MELTS and Petrolog modelling

Fractionation paths calculated by the Petrolog and MELTS software were compared to measured major element oxide concentrations in the Mauna Loa samples studied here. Identical starting composition, pressure, and oxygen fugacity were selected for comparison between the

two programs and the measured compositions. The pressure was set to a constant 0.4 kilobar, and the oxygen fugacity was initially set at the QFM buffer (though the effect of variable fO_2 is examined later). The fO_2 of basalts from Kilauea have been investigated previously by (Gerlach, 1993) where it was concluded that Kilauea basalt arrives in the crust with, or soon develops, an oxygen fugacity between the NNO and QFM buffers. The study by Gerlach demonstrated that oxygen fugacity of Kilauea melt varies as a function of temperature, and that at 1200 ˚C the fO_2 was ~ -8 log fO_2 units, comparable to the estimate of fO_2 at 1200 ˚C from Petrolog and MELTS when the fO_2 was set to QFM. Then assuming a QFM buffer, the initial Fe^{3+}/Fe^{2+} ratio was therefore calculated to be about 0.15. During initial modelling the system was set to contain 0.5 wt% H_2O, which is considered to be close to anhydrous. This minor fraction of water ensures that plagioclase was included as a fractionating phase, as plagioclase is found in small amounts (~ 3 vol. %) in the modal petrography. Estimates of water concentrations in Mauna Loa glasses range from 0.09 – 0.87 wt. % according to Davis and co-authors (2003) so the effect of variable H_2O contents is examined later. The starting MgO content was set to 14.3 wt. % MgO (Figure 7.12) and then run a second time under the same conditions using a starting composition of 15.96 wt. % MgO (Figure 7.14). The first is a bulk rock sample with an MgO contents close to a parental magma composition in equilibrium with $Fo_{87.8}$ olivine and the second is an average assemblage of the bulk rock samples with close to 16 wt. % MgO, in equilibrium with the highest Fo olivine ($Fo_{90.8}$). Subsequently, MgO values of between 10 - 20 wt. % were tested in order to determine the effects of variable starting composition and to establish possible lower and upper bounds on the possibilities of parental magma compositions; results of testing various starting compositions will be discussed later.

Other extrinsic variables that can be specified by the Petrolog user can include the density and viscosity of the magma. For this study, both of these parameters were left as the Petrolog defaults (Lange and Carmichael, 1987, Bottinga and Weill, 1972); while MELTS calculates density and viscosity as outputs. It is also possible to select whether fractionation occurs in equilibrium, whereby the fractionated phase remains in equilibrium with the melt, or if the melt and cumulates are separated from one another (fractional crystallization). These parameters can be varied within reasonable limits, for example, the user can specify that 50% of olivine cumulates are separated from the system. For the models reported here, 100% of the crystallizing phases were removed so that the changing composition of the liquid during crystallization could be observed.

The above parameters for starting composition, fO_2, viscosity, and density etc. were input to Petrolog and several published mineral-melt equilibria models were used to calculate fractional crystallization of mineral phases. Liquid lines of descent were calculated from the four model

options within Petrolog that account for crystallization of the three phases olivine, plagioclase, and clinopyroxene, and one that also includes orthopyroxene and spinel. These are shown below, with each tick on the curves representing 5% crystallisation (Figure 7.13).

The crystallization path of olivine for the four Petrolog model options are nearly identical; as is the one calculated by MELTS, and these paths have been plotted against bulk rock compositions of the samples in this study to evaluate how similar they are (Figure 7.13). During olivine control, the predicted melt compositions match the measured data well, indicating the chosen parental magma compositions can be successfully used to predict the olivine-controlled measured data. Differences can be seen in the composition and sequence of the other crystallizing phases, however. Using various solution models (Nielsen, 1985, Langmuir et al., 1992, Ariskin et al., 1993, Danyushevsky, 2001), the liquidus temperatures and the compositions, proportions, and sequence of each crystalizing phase can be compared and contrasted among the four model options. For the 14.3 wt. % MgO starting composition, the calculated liquidus temperature varies between 1354 – 1369 ºC for the Nielsen, Langmuir, and Ariskin models, whereas the one described by Danyushevsky (2001) returns a liquidus temperature of 1318 ºC. The calculated initial forsterite content of liquidus olivine predicted by these models is within one Fo-unit, ranging from $Fo_{87.8}$ – $Fo_{88.7}$, as would be expected given the $Fo_{87.8}$ content was used to calculate the starting MgO content of ~14 wt. %. All of the models predict that plagioclase followed by cpx crystallizes in melt compositions below 7 wt. % MgO. The range in An# in the plagioclase varies from $An_{69.7 - 75.6}$, while the range in Mg# of the crystallizing cpx is small (79.4 – 81). The MELTS results are comparable with an estimated liquidus temperature of 1351 ºC, with similar olivine, cpx, and plagioclase compositions to the Petrolog results, although plagioclase crystallizes out earlier. MELTS does not predict the crystallization of orthopyroxene at any stage in the crystallization process for the 14.3 wt. % MgO starting composition. The Ariskin model has the function to include opx in the crystallization sequence; in this case the liquidus temperature is the same as when opx is not included (1359 ºC), as is the olivine composition ($Fo_{88.7}$). Orthopyroxene begins to crystallize at 7 wt. % MgO and Mg# 80.9, followed by plagioclase ($An_{69.5}$) at 6.8 wt. % MgO, and clinopyroxene with Mg# 76.5 at 6 wt. % MgO. As the magma evolves, the crystallization of opx has the effect of reducing the Mg# of the crystallizing cpx and reducing the amount of SiO_2 in the melt early on as opposed to increasing it, and delaying the cpx crystallization-induced drop of CaO. This would suggest that opx crystallization may be necessary to account for the SiO_2 contents at low MgO in these samples (Figure 7.13a). The range of fO_2 during crystallization was -6.7 log fO_2 units at 1350 ºC and -9.5 log fO_2 at 1100 ºC according to both MELTS and Petrolog models, as would be expected when the fO_2 buffer was set to QFM.

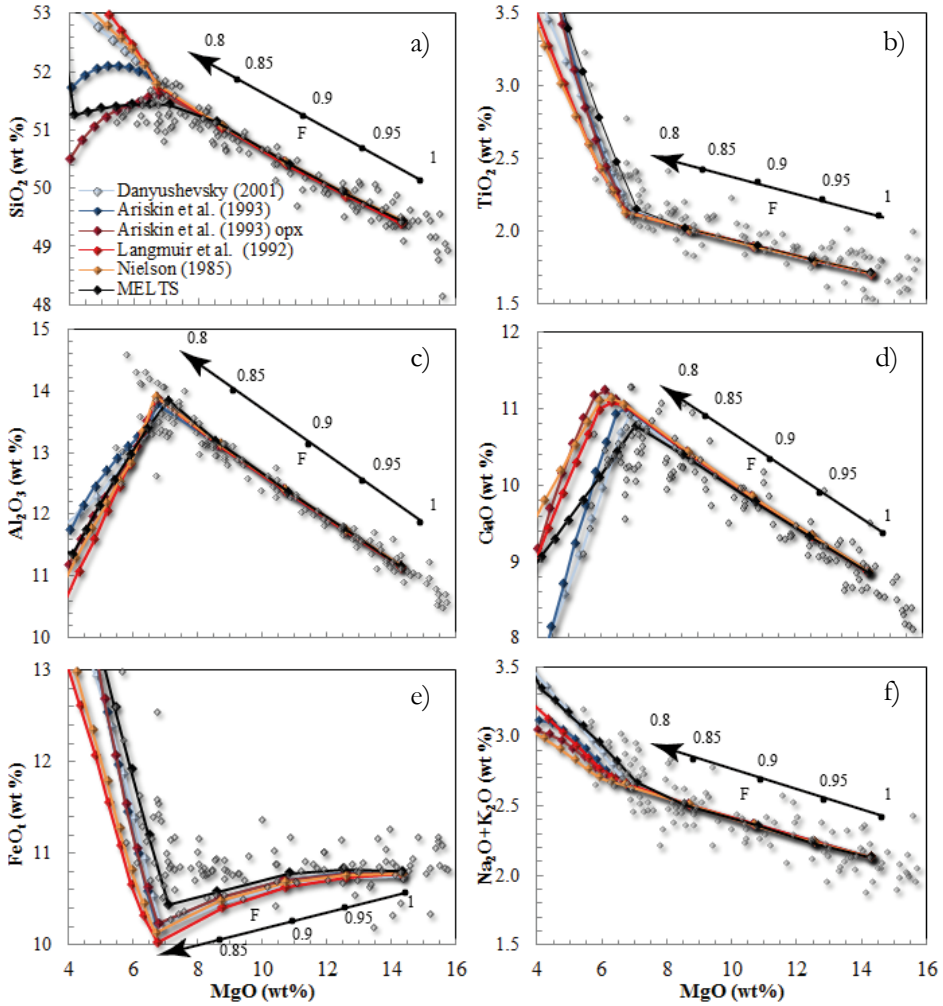

Figure 7.13 Calculated MELTS and Petrolog liquid composition paths during crystallization for starting composition 14.30 wt. % MgO. Arrows indicate direction of liquid composition during fractionation.

All calculated fractionation paths match the measured data for the olivine-dominated portion down to 6.5-7 wt. % MgO. The exception is FeO_t, which tends to be under-estimated by most of the models at a given MgO, though this may be related to the choice of parental melt which has FeO_t at the low end of the measured range at 16% MgO. The models also appear to predict a trend of decreasing FeO_t with decreasing MgO in the olivine-dominated portion, which is difficult to discern in the measured lava compositions. All models show that agreement between the lava compositions and the model predictions tend to be worse in the more evolved compositions with <7 wt. % MgO, with the exception of SiO_2 which fits better with the addition of an opx phase; however when opx is added the Ca trend no longer fits, and the drop in CaO contents requires a higher degree of fractionation to occur

The same process model parameters as those applied to the 14.3 wt. % MgO parental melt were applied to a starting melt composition with 15.96 wt. % to explore how a more primitive starting composition (and more likely parental composition) affects the liquid line of descent (Figure 7.14). Again, the same parameters for fO_2, H_2O content, and pressure were set as before.

The order of fractionating phases are similar (Table 7.3); however the value of F (fraction of melt remaining) is a few percent lower at a given MgO content for the 15.96 wt. % MgO starting composition compared to the 14.3 wt. % MgO starting composition as would be expected.

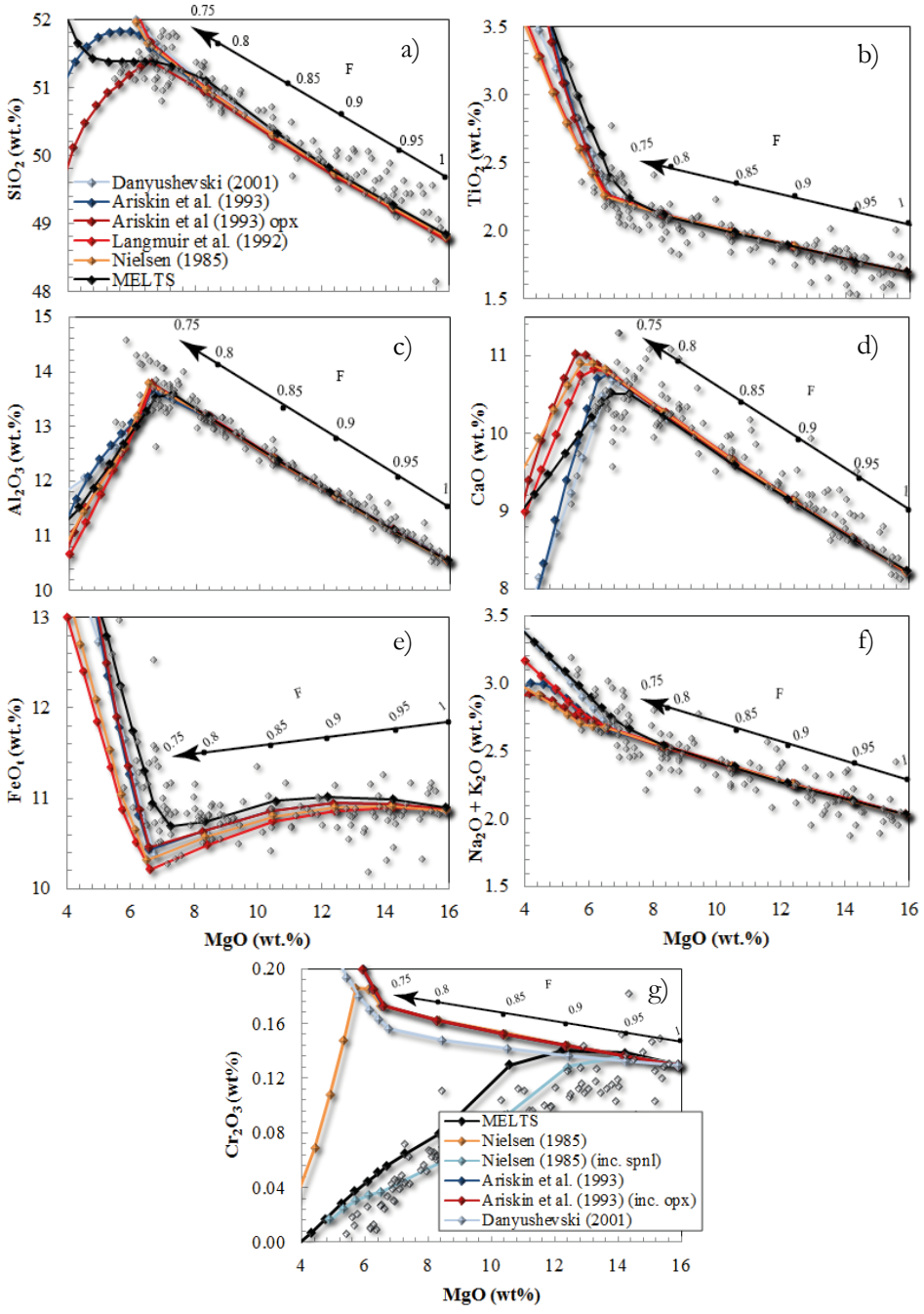

Figure 7.14 Application of published fractionation models to Mauna Loa for melts starting at 15.96 wt. % MgO with direction and percentage of fractionation given.

In addition to the seven major elements previously used, chromium was then added into the model as Cr_2O_3 (Figure 7.14g). A spinel phase was added to the Petrolog models because it is clear that spinel is needed to account for Cr during the crystallization process, as Cr_2O_3 in the bulk rock behaves compatibly throughout the crystallization sequence whereas Cr is moderately incompatible in olivine. The addition of a spinel phase does not affect the fractionation of the

other major elements greatly, and it ensures that Cr is depleted in the melt with decreasing MgO, consistent with the measured data. The Nielsen (1985) model produces a better fit to the Cr contents in the bulk rocks than other Petrolog models by beginning spinel fractionation from around 12 wt. % MgO with Cr# 60, and continuing fractionation until the spinel reaches a Cr# of 55.7 at around 6 wt. % MgO. The MELTS software also models the fractionation behaviour of Cr_2O_3 accurately as it automatically predicts the crystallization of Cr spinel.

7.9.6 Phase proportions

The liquidus phase proportions predicted by each of the four Petrolog models are within a few percent of each other. The Petrolog programs continue to fractionate olivine until the end of the simulation. This produces olivine with Fo_{80-83}, which is on the low end of the Fo spectrum observed in Mauna Loa lavas (Figure 7.4). MELTS fractionates olivine only down to 7.1 wt. % MgO (Fo_{79}) until cpx and plagioclase crystallization begins. At the end of the fractionation sequence (selected as 5 wt. % MgO because that is the composition of the lowest MgO Mauna Loa sample in this study) the Petrolog and MELTS models had fractionated between 18-28 wt. % olivine, 9-14% plagioclase, and between 2-16% clinopyroxene (Table 7.3). The model by Ariskin and co-authors (1993) produced 7% opx in addition when opx was selected to fractionate, while the MELTS programs only produced 1%. Very minor amounts of spinel are predicted to crystalize (<0.5%), with a composition varying between spinel, chromite, magnetite, and ulvospinel.

In addition, the MELTS models (Rhyolite MELTS as plotted in Figure 7.13 & Figure 7.14, and alphaMELTS – not plotted here as the paths are nearly identical to that produced by the Rhyolite MELTS model) also predict a higher proportion of plagioclase and cpx relative to olivine compared to the four models available in Petrolog. This means that for a given value of MgO, there was less melt remaining in the MELTS models. It must be noted that all of these model options predict a large amount of plagioclase (9-14%) and clinopyroxene (3-16%) fractionation, up to half the total amount of olivine. This is at odds with the petrographic observations, which shows up to 3% plagioclase in most samples, with the majority having up to 33.5% phenocrystic olivine suspended in a microcrystalline basalt matrix. The plagioclase may be explained by the low percentage of water included in these initial models, as water can suppress the onset of plagioclase fractionation and cause the amounts predicted here to be an overestimate of what would naturally crystallize in the system e.g. (Dolfi and Trigila, 1978, Gaetani et al., 1993).

Table 7.3 Crystallization progress at 5 wt. % MgO showing % of melt remaining at respective MgO content, and % of crystallized olivine, plagioclase, cpx, opx, and spinel for each

fractionation model. This is calculated for melts with a starting composition of 14.3 wt. % MgO (a) and repeated for melts with a starting composition of 15.96 wt. % MgO (b).

Initial MgO: 14.30 wt% *Final composition: 5 wt% MgO*						a)
	% melt remaining	***% Ol***	***%Plg***	***%Cpx***	***% Opx***	**-**
Langmuir et al. (1992)	63	24	10	3	-	-
Ariskin et al. (1993)	59	21	10	10	-	-
Nielsen (1985)	58	24	12	6	-	-
Danyushevsky (2001)	52	21	13	14	-	-
Ariskin et al. (1993) opx	60	19	11	3	7	-
MELTS	53	18	13	16	-	-

Initial MgO: 15.96 wt% MgO *Final composition: 5 wt% MgO*						b)
	% melt remaining	***% Ol***	***%Plg***	***%Cpx***	***% Opx***	***% Spl***
Langmuir et al. (1992)	61	28	9	2	-	-
Ariskin et al. (1993)	57	25	10	8	-	0.27
Nielsen (1985)	61	28	9	2	-	0.32
Danyushevsky (2001)	50	26	12	12	-	-
Ariskin et al. (1993) opx	58	23	10	2	7	-
alphaMELTS	48	21	14	16	1	0.41
MELTS	48	22	13	16	1	0.4

The relationship between temperature, MgO, and melt fraction can be observed from the computational models (Figure 7.15). It can be seen that melt fraction and temperature changes as plagioclase and cpx become the controlling phases, with a smaller decrease in temperature causing a larger percentage of crystallization compared to when olivine is the controlling phase. Similarly, a smaller decrease in MgO content is observed with each percentage of fractionation when cpx + plag are the controlling phases, as would be expected when low MgO phases begin to crystalize.

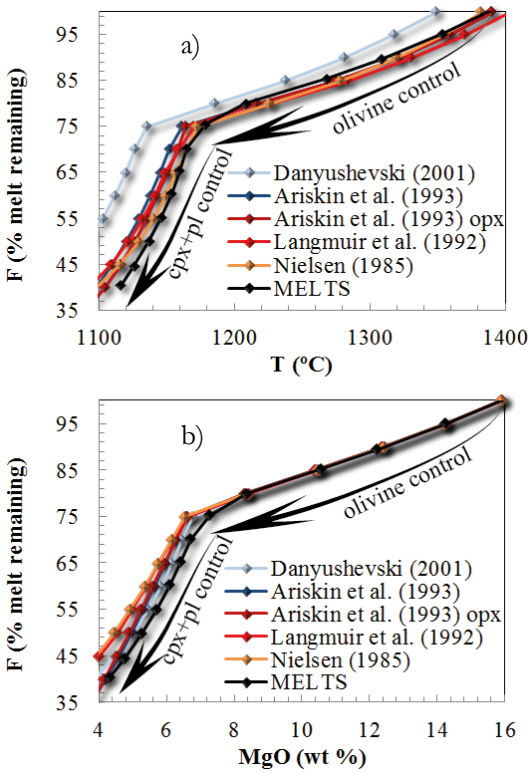

Figure 7.15 F (% melt remaining during fractional crystallization) versus temperature (a) and wt. % MgO (b) for the published fractionation models starting at 15.96 wt. % MgO.

In order to isolate the effect the various phases were having on the major element fractionation paths, a fractionation sequence was run in the Petrolog program by suppressing each evolved phase (plagioclase, cpx, opx, and spinel) one at a time (Figure 7.16). To ensure consistency, the variables P, X, fO_2, H_2O were kept the same as the previous runs and the model by Ariskin and co-authors (1993) was used in all cases.

It can be seen that opx crystallization may be necessary to produce the decrease in SiO_2 contents at low MgO (Figure 7.16a), and cpx crystallization is needed to account for the decrease in CaO at low MgO (Figure 7.16d) though the CaO path fits the evolved measured values closer when opx is suppressed. The effect of suppressing plagioclase is significant, leading to very different fractionation paths for TiO_2, Al_2O_3, FeO, and the alkalis. TiO_2 values are lower at low MgO when plagioclase is suppressed, as it FeO_t. Importantly, suppressing plagioclase can explain the high Al_2O_3 contents of some of the evolved samples, while crystallizing plagioclase can explain the low Al_2O_3 contents of some of the evolved samples (Figure 7.16c). It also appears that crystallizing plagioclase would be the only crystallization-related way to account for the evolved samples with high FeO contents (Figure 7.16e). The increase in the liquid of elements not compatible into plagioclase (Fe and Ti) can be explained by the fact that they will not be

incorporated into the plagioclase crystal structure and therefore will be concentrated in the melt. The opposite is true of elements compatible (alkalis and Al), as these will only be concentrated in the melt when plagioclase does not crystallize. Thus, the presence or absence of plagioclase as a crystallizing phase may be very important in determining liquid chemistry, while cpx, opx, and spinel may be less so.

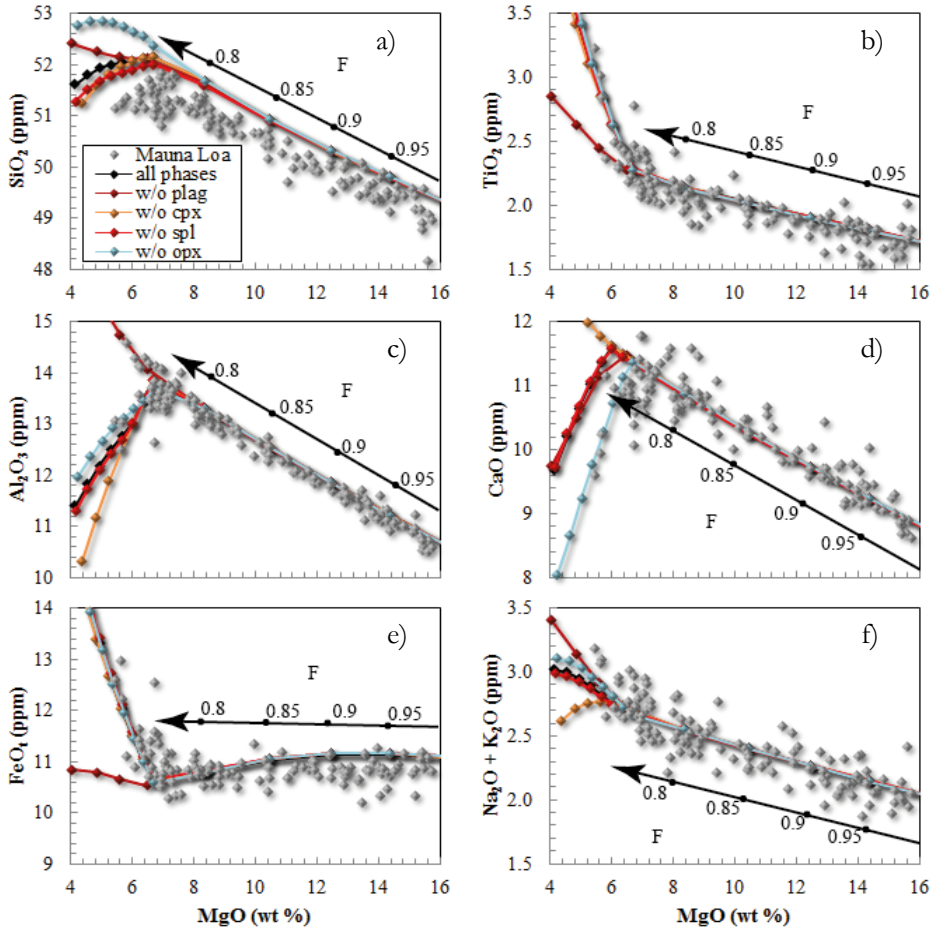

Figure 7.16 The effect on major elements of suppressing one phase during a crystallizing sequence.

The previous examples have used a nearly anhydrous system, though it is important to also look at the predicted phases proportions and crystallization sequence when water contents close to what is found in Mauna Loa glasses are used as input parameters for the model calculations. The same starting parameters as before were entered into alphaMELTS, though this time with 0.3 wt. % H_2O included. The major element data were then normalized to 99.7 wt. % and run as before (Table 7.4).

Results predict 23% olivine fractionation (1-2% more than the nearly anhydrous system), 12% cpx (4% less than anhydrous), 8% plagioclase (6% less than anhydrous), 0.4% opx, and 0.45%

spinel. Again, the first olivine to crystallize is Fo_{90}, and Fo_{78} when the melt reached 5 wt. % MgO. Two types of cpx crystallize out, which contain most of the major elements (Mg, Fe, Al, Ti, Na, Ca, Si) appearing to be varying types of omphacite and augite. The small amount of opx is high in MgO and so may be some type of enstatite, though again it contains small amounts of the other major elements. The plagioclase is essentially anorthite, though it contains small amounts of Na, and the spinel ranges in composition from a magnesio-chromite to a magnetite, while containing non-trivial amounts of Ti. The addition of 0.3 wt. % water delays the onset of cpx and plagioclase crystallization until the melt composition contains less than 6 wt. % MgO and allows the crystallization of olivine to continue longer.

Table 7.4 Phase proportions and stoichiometry predicted by alphaMELTS calculations assuming 0.3 wt. % H_2O and 15.9 wt. % MgO in starting melt set to QFM buffer. Mineral compositions in wt. % given at initial (first appearance of mineral) and final (5% MgO remaining in melt) points during the crystallization sequence.

T (°C)	liquid (%)	MgO liq (wt.%)	olivine (%)	orthopyroxene (%)	clinopyroxene (%)	clinopyroxene (%)	feldspar (%)	spinel (%)
1380	100.1	15.86	-	-	-	-	-	-
1370	98.6	15.36	1.50	-	-	-	-	-
1360	97.1	14.87	1.44	-	-	-	-	-
1350	95.7	14.38	1.38	-	-	-	-	-
1340	94.4	13.91	1.33	-	-	-	-	-
1330	93.1	13.45	1.28	-	-	-	-	-
1320	91.9	12.99	1.23	-	-	-	-	-
1310	90.7	12.55	1.18	-	-	-	-	-
1300	89.6	12.11	1.14	-	-	-	-	-
1290	88.5	11.69	1.10	-	-	-	-	-
1280	87.4	11.27	1.06	-	-	-	-	-
1270	86.4	10.86	1.02	-	-	-	-	-
1260	85.4	10.46	0.98	-	-	-	-	0.02
1250	84.4	10.07	0.95	-	-	-	-	0.02
1240	83.5	9.69	0.92	-	-	-	-	0.02
1230	82.6	9.32	0.89	-	-	-	-	0.02
1220	81.7	8.95	0.86	-	-	-	-	0.02
1210	80.8	8.60	0.83	-	-	-	-	0.02
1200	80.0	8.25	0.80	-	-	-	-	0.02
1190	79.2	7.92	0.78	-	-	-	-	0.02
1180	78.4	7.59	0.75	-	-	-	-	0.02
1170	77.7	7.27	0.73	-	-	-	-	0.02
1160	77.0	6.96	0.71	-	-	-	-	0.02
1150	76.1	6.66	0.43	0.39	-	-	-	0.02
1140	67.4	5.94	-	-	5.26	0.73	2.64	0.06
1130	61.1	5.46	-	-	1.61	1.79	2.92	0.05
1120	55.8	5.02	-	-	1.34	1.47	2.43	0.07
Total			23.27	0.39	8.21	3.99	7.98	0.45

	Initial	Final
Olivine formula:	$(Mg_{0.90}Fe^{2+}_{0.10})_2SiO_4$	$(Ca_{0.01}Mg_{0.78}Fe^{2+}_{0.21})_2SiO_4$
Orthopyroxene formula:	$Ca_{0.10}Fe^{2+}_{0.37}Mg_{1.48}Fe^{3+}_{0.02}Al_{0.08}Si_{1.95}O_6$	
Clinopyroxene formula:	$Na_{0.01}Ca_{0.70}Fe^{2+}_{0.24}Mg_{0.93}Fe^{3+}_{0.04}Ti_{0.02}Al_{0.17}Si_{1.88}O_6$	$Na_{0.01}Ca_{0.72}Fe^{2+}_{0.26}Mg_{0.88}Fe^{3+}_{0.05}Ti_{0.02}Al_{0.18}Si_{1.87}O_6$
Clinopyroxene formula:	$Ca_{0.26}Fe^{2+}_{0.41}Mg_{1.24}Fe^{3+}_{0.03}Ti_{0.01}Al_{0.13}Si_{1.92}O_6$	$Na_{0.01}Ca_{0.25}Fe^{2+}_{0.47}Mg_{1.19}Fe^{3+}_{0.03}Ti_{0.01}Al_{0.13}Si_{1.91}O_6$
Feldspar formula:	$Na_{0.28}Ca_{0.72}Al_{1.72}Si_{2.28}O_8$	$Na_{0.31}Ca_{0.68}Al_{1.68}Si_{2.32}O_8$
Spinel formula:	$Fe^{2+}_{0.40}Mg_{0.66}Fe^{3+}_{0.34}Al_{0.57}Cr_{0.97}Ti_{0.06}O_4$	$Fe^{2+}_{0.94}Mg_{0.40}Fe^{3+}_{0.66}Al_{0.33}Cr_{0.33}Ti_{0.34}O_4$

It is clear that the proportions of plagioclase crystallization predicted by Petrolog are too high compared to what is expected from modal petrography, and that plagioclase is a significant control of melt chemistry late in the crystallization sequence. Below, the measured Mauna Loa major element data is plotted again comparing plagioclase-present versus plagioclase-absent fractionation trends (Figure 7.17) produced using alphaMELTS software. The fits for CaO and the alkalis were improved somewhat in the alphaMELTS model, and the alkali and SiO_2 contents of the liquid do not differ greatly between the plagioclase-in versus plagioclase-free trend. The significant effects of suppressing plagioclase on Fe, Ti, and Al can again be seen in the alphaMELTS model. Similarly to Petrolog results, trends provide a possible explanation for the divergence of low Al_2O_3 and high Al_2O_3 in low MgO ML lavas. In terms of geological setting, the high Al_2O_3 samples are mostly 'landslide' type, while the low Al_2O_3 samples are mostly 'slope' type, though there are other dredge locality types mixed in.

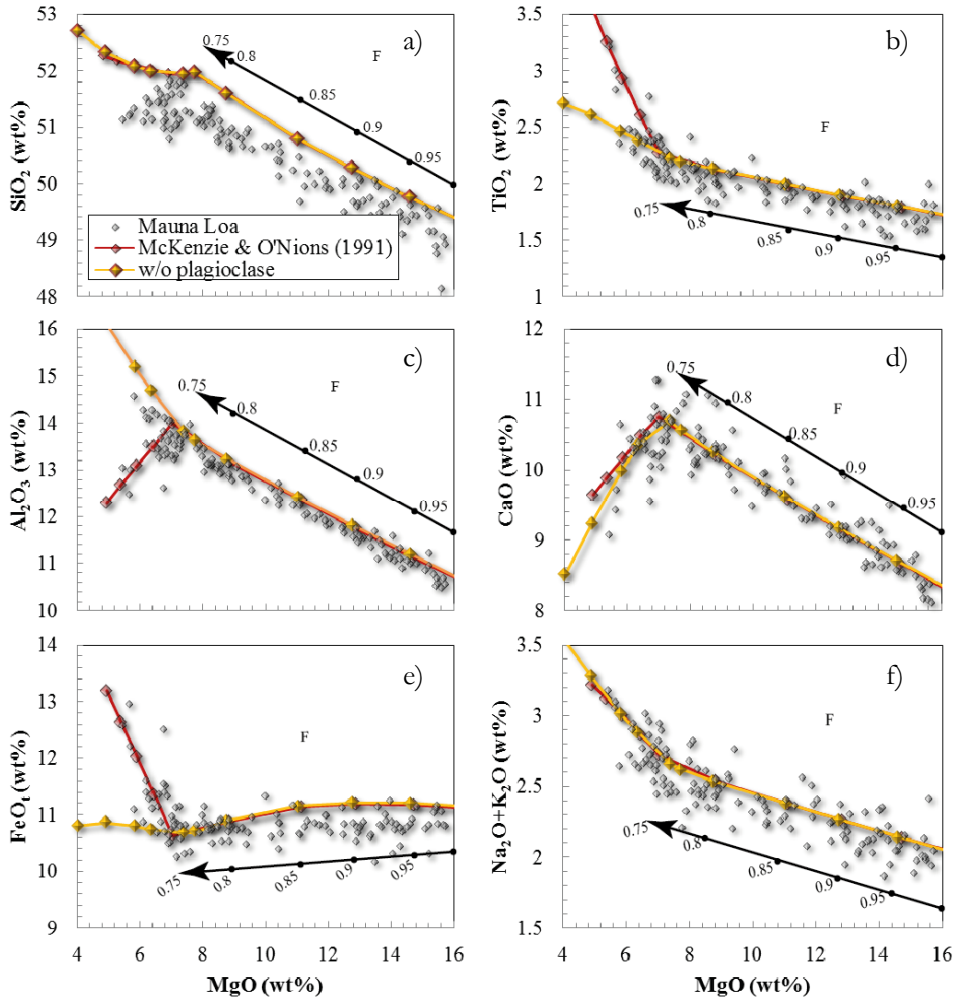

Figure 7.17 The effect of plagioclase-present (red) versus plagioclase-absent (yellow) fractionation on liquid composition.

Some of the bulk rock major element ratios (major element results Figure 4.4) were plotted against both the plagioclase-present and the plagioclase-absent fractionation paths (Figure 7.18). The drop in the CaO/Al_2O_3 ratio (Figure 7.18a) at low MgO can be explained with a crystallization sequence in which clinopyroxene crystallizes while plagioclase is absent. The samples that do not show this decrease in CaO/Al_2O_3 can be explained if plagioclase is included in the fractionating assemblage, because crystallisation of 5% of a gabbroic assemblage (cpx + plag) does not necessarily change the CaO/Al_2O_3 ratio greatly. Therefore, it could be that cpx and plag are both crystallizing while only cpx is crystallizing from others. The K_2O/P_2O_5 and SiO_2/CaO, ratios are not strongly affected regardless of the crystallization sequence used, and could therefore be reconciled by either model (Figure 7.18b, d), while the trend of SiO_2/Al_2O_3 in lavas with <7 wt. % MgO requires both a plagioclase-free and plagioclase-present crystallisation to account for the measured compositions (Figure 7.18e). The trends for SiO_2/TiO_2 and Al_2O_3/TiO_2 are better reproduced when plagioclase is included in the crystallising assemblage, but they do not preclude a separate plagioclase-free fractionation path because of the small amount of variation in SiO_2/TiO_2 and Al_2O_3/TiO_2 when plagioclase is absent. From this comparison of computational models with measured data, it can be concluded that the variation in major element oxide composition in the evolved samples is likely be due to fractionation of clinopyroxene and plagioclase.

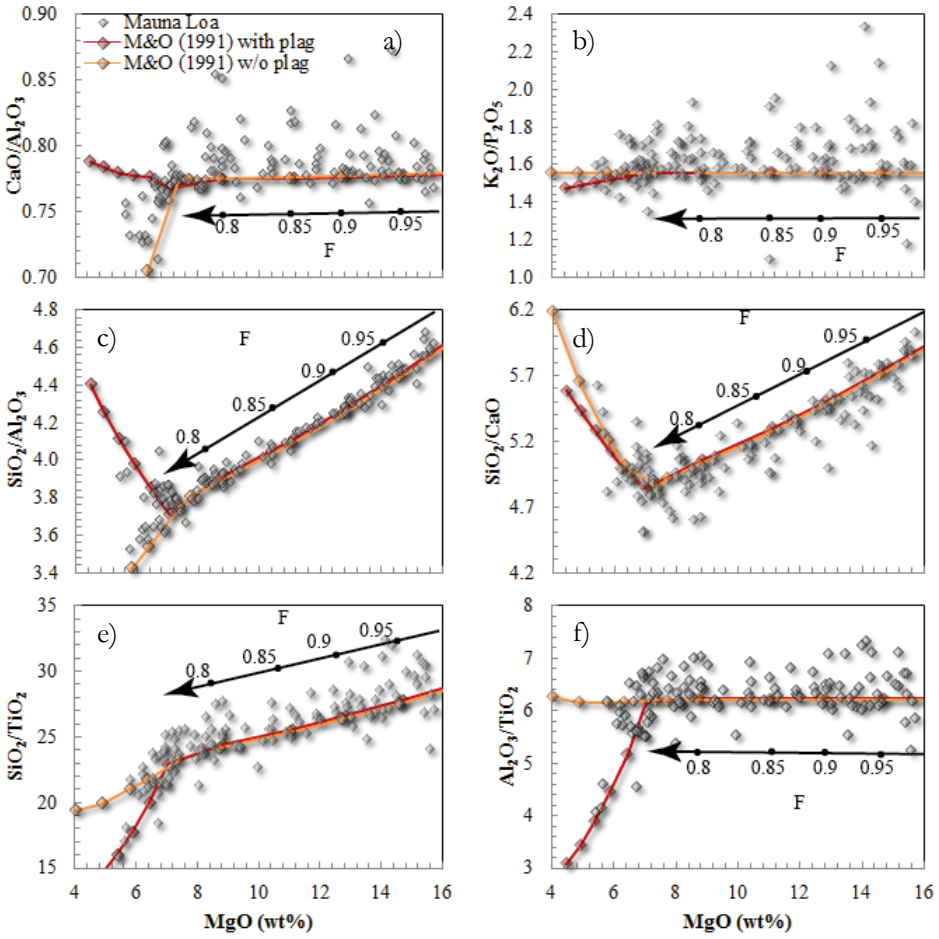

Figure 7.18 alphaMELTS fractionation paths including (red) and excluding (yellow) plagioclase fractionation. Plagioclase ± cpx crystallisation begins at 7 wt. % MgO. At higher MgO, the crystallization trajectory is controlled by olivine only. Tick marks are 5% fractionation increments.

7.9.7 Effects of varying starting composition, pressure, H_2O, and fO_2

The effect on major element oxide composition of the liquid by varying the starting composition, oxygen fugacity, and water concentration in the system was tested in MELTS. To see if changing the MgO content of the parental magma had any effect on the crystallization sequence, the starting compositions were varied from 10 to 20 wt. % MgO in order to establish upper and lower bounds on a possible parental magma composition. Other variables were kept the same except the major elements, which were taken at the given MgO from the olivine control trend. The water content was fixed at 0.3 wt. % to be close to Mauna Loa and Hawaiian published estimates e.g. (Byers et al., 1985, Garcia et al., 1989, Davis et al., 2003). The results for 12, 14, 18, and 20 wt. % MgO compositions are shown in Figure 7.19. The results of these calculations demonstrate that a range in starting composition of Δ8 wt. % MgO could account for some of the spread in the major element data. This is discussed in more detail below.

Changing the starting composition of the parental magma causes variation in the olivine-controlled segment of melt compositions, in particular for FeO_t and SiO_2. The iron content appears to increase initially during fractionation when a higher MgO starting composition is used, whereas total iron decreases continuously during fractionation. It also predicts greater variation in SiO_2 in the more evolved part of the sequence, with the crystallization paths varying when 18 and 20 wt. % starting compositions are used. This appears to reflect the variation in the average SiO_2 contents at respective values of MgO. The average SiO_2 appears to be slightly lower at 20 wt. % MgO compared to the other values, as the slope changes between 18 and 20 wt. % MgO, curving downward. This means that a parental magma composition with greater than 18 wt. % MgO would not be able to produce the entire range of evolved samples through a continuous process of crystal fractionation, and therefore is probably not a good estimate for a parental magma composition. The larger variation in SiO_2 and FeO_t for a given MgO may indicate that a range in these major element oxides could be expected in a parental magma, or could be the result of variation in the average forsterite content of the olivine contributing to the whole rock assemblage.

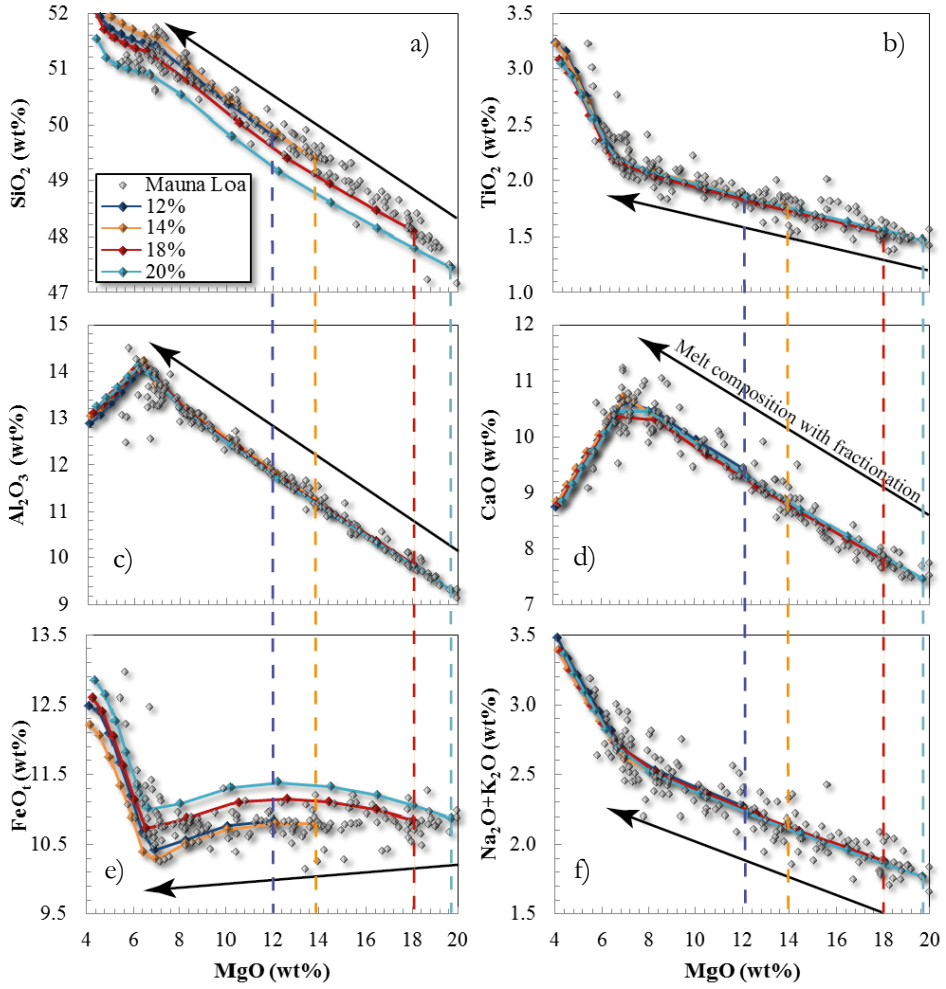

Figure 7.19 Fractionation paths for parental magmas with variable MgO starting compositions. 10 wt. % MgO starting composition (not shown here) behaves very similarly to the 12 wt. %.

The effect of varying the starting pressure of major elements in the fractionating system was small compared to the other extrinsic parameters. P-wave travel time tomography has revealed high velocity bodies in the upper 11 km of the crust below Hawaiian volcano rift zones, which are thought to represent solidified gabbro or dunite cumulates differentiated from magma injected into the Hawaiian crust. These cumulate regions provide spatial constraints on the size of magma storage areas beneath Kilauea and Mauna Loa (Okubo et al., 1997). Okubo and co-authors' observations along with other volumetric and geochemical constraints (4-8 km) (Garcia et al., 1995, Amelung et al., 2007) discussed previously, place a bounds on the depth of Mauna Loa's magma chambers. Changing the pressure from 3 to 0 kilobar, a change in depth of approximately 10 km, lead to no distinguishable difference in the fractionation pattern calculated by the Petrolog models and only a very small deviation calculated by MELTS.

The effect of variations in water concentration of the melt was then tested by adding different amounts of water to the parental magma ranging from anhydrous up to 1 wt. %, the upper limit of water concentrations found in Mauna Loa glasses (Davis et al., 2003). The result was that higher water contents in the parental melt made a significant impact on the fractionation sequence, and therefore the composition of the liquid during fractionation (Figure 7.21). By adding just 0.5 wt. % H_2O to the starting composition - a concentration typical of evolved Mauna Loa glasses - the predicted onset of plagioclase and cpx crystallization is delayed and opx crystallization is suppressed, causing differences in the fractionation trajectories of most of the major element oxides. The lower water contents decreased the calculated SiO_2 contents in the melt at <8 wt. % MgO due to the suppression of of opx crystallization, which could account for the triangular wedge-shape in the plot of SiO_2 v MgO at low values of MgO. When the water content is between 0 and 0.1 wt. % opx is the first phase to crystallize (producing 1.2-2.4% opx), with onset occurring when the melt contains ~7.45 wt. % MgO (Figure 7.20a). When the water content is greater than 0.1 wt. %, opx is not predicted to crystallize and the SiO_2 continues to increase with increasing MgO. Conversely, TiO_2 and FeO_t increase in concentration at lower MgO when the water concentration of the melt is lowest, which has been shown to relate to the earlier onset of plagioclase crystallization (Figure 7.17b,e). Significantly, a range of water contents could explain the divergence of the Al pattern in the samples with <7 wt. % MgO whereby some of the samples have lower Al_2O_3 and some higher. This may be evidence for a range of parental mama compositions with variable volatile contents. Variable water contents, therefore, could be responsible for producing these basalts, as a variability of 0.5 wt. % water is within the observed variability in glasses. A maximum of 0.5 wt. % H_2O in the parental magma would end up being 0.99 wt. % after crystal fractionation down to 4 wt. % MgO, which would fit within the range predicted from glass chemistry.

0.5 wt. % water was the amount predicted by Green (Green, 2015) whereby he suggests water enriched upper mantle could be the source of intraplate basalts, which may overlie a water-depleted part of the mantle from which MORB are sourced. The amount of water suggested for the MORB source by Green was 200 ppm (0.02 wt. % water), which is also well within the lower bounds for water content found in the glasses from Mauna Loa. Similar estimates of parental melt H_2O contents were found by Clague and co-authors of 0.35 wt. % (Clague et al., 1991), using offshore Kilauea picritic glasses, though modelling here shows that a range of 0 – 0.5% water may be required.

It is possible that variation in water in the ML magmas is the result of heterogeneous source components in the mantle. According to Green, the presence of old subducted oceanic crust could be a source of excess water, because redox reactions at the interface of old subducted slab

and ambient mantle can precipitate carbon and increase H_2O activity (Green, 2015). Alternatively, varying degrees of devolatilization of a magma with a small amount of water could also provide a mechanism for variable water contents in Hawaiian volcanoes. Estimations by Gerlach where a parental melt composition containing 0.3 wt. % H_2O was calculated, suggest that devolatilization occurs in Kilauea magmas over a pressure range of 84 to 0.2 MPa (Gerlach, 1986). In this scenario 0.19 wt. % H_2O can be lost from a parental magma originally containing 0.27 wt. % water, leaving 0.08 wt. % remaining upon eruption. Even with a conservative starting composition of 0.27 wt. % H_2O, this range is enough to make significant differences to major element-oxide compositions.

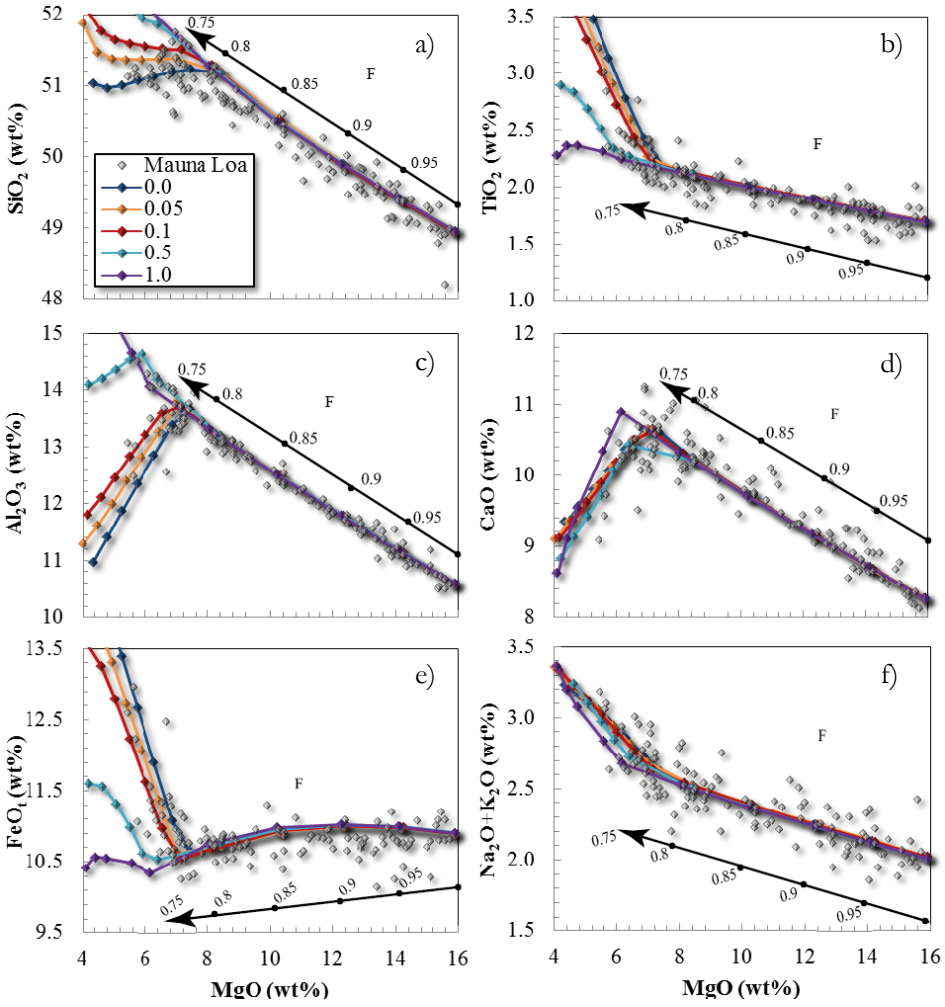

Figure 7.20 Melt compositions with variable parental magma water content (wt. %).

In addition to water contents, changing the oxygen fugacity of the system can change the fractionation trajectories of Si, Ca, and Fe to a significant degree (Figure 7.21a,d,e). Varying the oxygen fugacity of the melt changes the forsterite content of the liquidus olivine, which affects the Fe concentration in the melt during olivine-controlled crystallization. The melt is predicted

to be more Fe rich at a given value of MgO when fO_2 is higher, while it will be more Si rich at low MgO when fO_2 is lower. It can also be seen that at higher fO_2 (QFM+1), opx will begin to crystallize at 7.7 wt. % MgO, followed by cpx at 7.3 wt. % MgO. Comparatively at QFM-1, opx is not predicted to crystallize and cpx onset does not occur until the melt contains 6.3 wt. % MgO. Si and Ca are compatible into cpx and opx and therefore decreases at high fO_2 when opx and cpx crystallization occurs earlier, while FeO_t responds to the reduction in the proportion of olivine crystallized at high fO_2 and is enriched in the melt. Ti, Al, and the alkalis are not redox sensitive elements and therefore are not particularly sensitive to changes in fO_2 between QFM-1 and QFM+1.

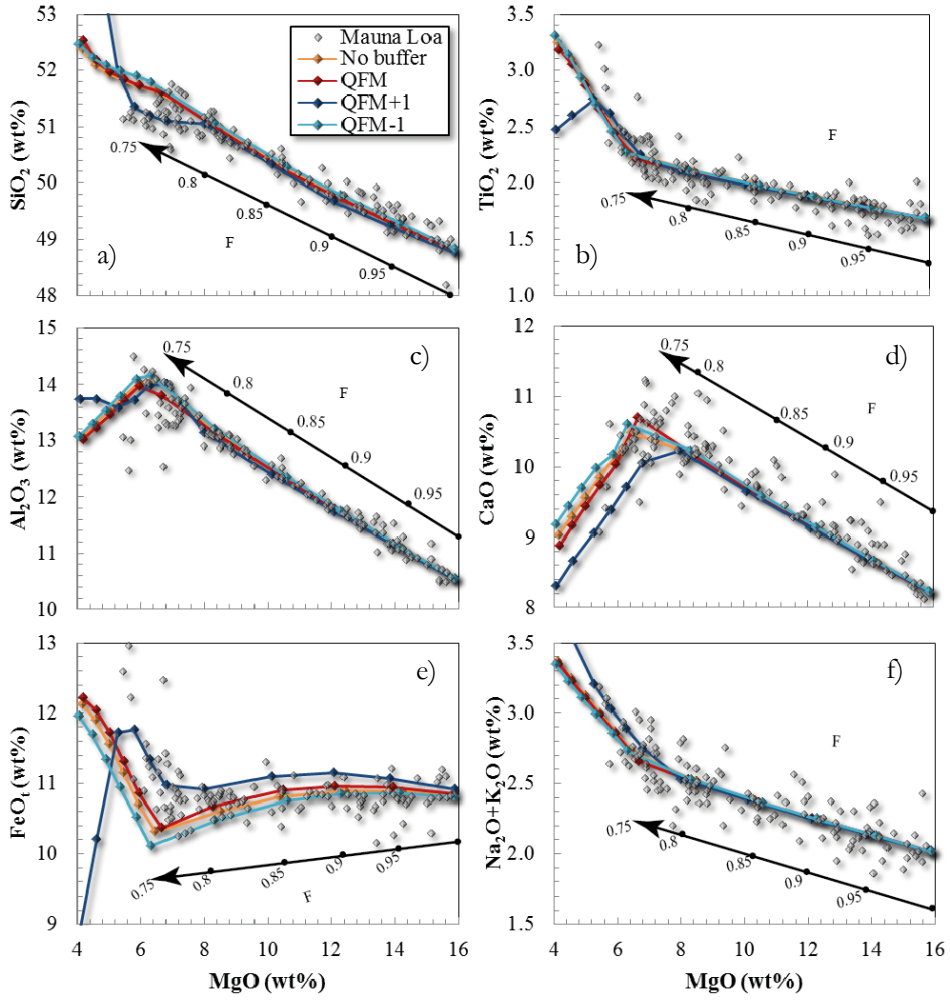

Figure 7.21 The effect of varying oxygen fugacity on fractionation trajectories calculated by MELTS.

This evidence from MELTS modelling suggests that for major elements, olivine, clinopyroxene, orthopyroxene, and spinel are compulsory phases to explain the range of bulk rock compositions observed in the ML basalts studied here. It is also clear that a plagioclase-absent,

in addition to a plagioclase-present fractionation sequence is necessary to explain the range of Al contents and divergent Al trends at low MgO, while an opx-present and opx-free sequence is needed to explain the range of SiO_2 contents at low MgO. The fractionation modelling of major elements presented here suggests that the major element data can be explained by two fractionation paths, one consisting of olivine + spinel + cpx + opx + plagioclase, and the other consisting of olivine + spinel + cpx +opx. The presence of ≤0.1 wt. % water to the parental magma would be the maximum H_2O that could produce the crystallisation assemblage ol + opx + cpx + plag + spinel, while the presence of 0.5 wt. % H_2O could produce the assemblage ol + cpx + spinel. A change of oxygen fugacity between QFM-1 to QFM+1 within the system would be consistent, given the measured range in the major element oxides. Thus, all major element variability within these samples can be explained through magmatic processes.

7.10 Trace elements

This section of the chapter will focus on how trace elements may behave in a shallow Mauna Loa magma chamber. Bulk distribution coefficients were calculated from samples for which olivine is the primary controlling mineral, and then as with the major elements, crystal fractionation models using MELTS and Petrolog will be presented.

7.10.1 Calculated trace element distribution coefficients

Hawaiian tholeiites display olivine control trends for most major and trace elements in samples with >7 wt. % MgO. Assuming the whole rock composition is representative of the melt composition and the percentage of the fractionated phase is known, mineral/melt distribution coefficients can be calculated. In general distribution coefficients are obtained experimentally using a known starting product, or by analysing natural samples where phenocryst–melt or phenocryst–phenocryst pairs are found to be in equilibrium.

For this study, mineral/melt distribution coefficients were calculated for olivine from whole rock data using Rayleigh fractional and equilibrium crystal fractionation models. These models equate the concentration of a trace element *i* in an initial melt composition (assumed here to be the whole rock composition), the concentration of *i* in the residual melt during fractionation, and the fraction of melt remaining to a distribution coefficient D (C_i in the solid/ C_i in the melt). Note that it will be assumed here that the bulk rock compositions were produced by crystallisation, either fractional or equilibrium, and not accumulation.

The equations can be rearranged to form:

Rayleigh fractionation: $\mathrm{D} = \frac{\log\left(\frac{\mathrm{CL}}{\mathrm{C0}}\right)}{\log(\mathrm{F})} + 1$

Equilibrium fractionation: $D = \frac{1}{1-F}\left(\frac{C0}{CL} - F\right)$

Where D is the bulk distribution coefficient, F is the fraction of melt remaining in values between zero and 1, C_0 is the concentration of element *i* in the starting melt composition, and C_L is the concentration of element i in the melt with progressive fractionation.

Here, Rayleigh fractionation expresses the change in the concentration of a trace element with crystallization as an exponential function, while equilibrium fractionation is an inverse power law function. They are very similar, and by eye the trends are difficult to distinguish when compared to the measured data; however an exponential function (fractional crystallisation) will increase the C_i more dramatically with decreasing F. Crystallization in nature is thought to be some combination of these two end members. While it is usually unlikely that pure equilibrium crystallization would occur in a highly viscous magma where crystals are impeded from settling, it is also unlikely that pure Rayleigh fractionation would occur due to the difficulty in extracting all melt from grain surfaces. Phenocrysts in OIB are from magma chambers that are continuously being replenished and mixed, and therefore may adhere more closely to an equilibrium-style regime, while crystals that are quickly removed from the melt and allowed to settle on the bottom of a magma chamber may adhere more closely to Rayleigh-style fractionation. From previous discussion about crystal setting rates above, it was predicted that an equilibrium crystallization environment will more accurately represent Mauna Loa's magma chambers.

Whole rock trace elements concentrations for 98 tholeiitic basalt samples were analysed using solution ICP MS, providing high precision trace element data for 36 elements. MELTS and Petrolog modelling of major or trace elements from 98 of the tholeiitic basalt samples from this study were conducted to test whether the whole-rock samples may represent crystal fractionation trends. As discussed in the previous sections, the whole rock chemistry appears to follow fractionation trends (although is not actually the liquid composition of a melt during progressive fractional crystallization). The compositional trends were found to be relatively insensitive to the precise starting composition, so a bulk rock composition with MgO contents between 14 – 18 wt. % could be safely assumed to be the parental composition. A starting composition of 15 wt. % MgO was used here as a parental magma to calculate bulk trace element partition coefficients.

The measured values of $\frac{CL}{C0}$ for whole rock trace element concentrations were plotted against values of F obtained from the major element MELTS modelling (Figure 7.22). The values of F obtained from the major element models used are close to those implied by the maximum and

minimum values of highly incompatible elements such as Ba and Pr, for which it is assumed that D=0 and therefore the range of F is simply the ratio of C_0/C_L. The range in F for samples with a range in MgO of 14.81 – 7.26 wt. % MgO was 1 – 0.782 for Ba and 1 - 0.763 for Pr. These elements were chosen as they are highly incompatible in olivine and have less scatter and therefore smaller uncertainties than some of the other highly incompatible elements such as Mo and Sb. An exponential Rayleigh curve and an inverse power equilibrium curve were fitted to each element plot of ITE versus MgO (thanks to Richard Skelton for writing a piece of code for this) using least squares minimization subject to the constraint $D \geq 0.0001$. This is because values lower than this are beyond the sensitivity of the model. An uncertainty on each fit was determined using a 1σ confidence interval, so that 68% of the data points lie between the fitted line and the bounding 1σ interval. The amount of scatter in the data for each element is highly variable and this is reflected in the estimation of error on calculated distribution coefficients (Table 7.5).

The value of C_0 was calculated from the average composition of n samples with MgO contents of ~15 wt. % MgO, where n = 1,2,5, or 10. This was done by varying the allowed range of MgO to include more or less samples, so for n = 10 the corresponding range in MgO was 14.35 – 15.42 wt. % and for n = 2 the corresponding range was 14.81 – 15.08 wt. %. Most trace elements obtained a lower uncertainty by using the average of n = 5 instead of n = 10 samples because the more samples used, the fewer had MgO contents close to 15 wt. %. The exceptions were Cu, V, Zn, Sr, Sb, Mo, and U, for which n = 10 provided a smaller uncertainty, probably as a result of some outlying measurements.

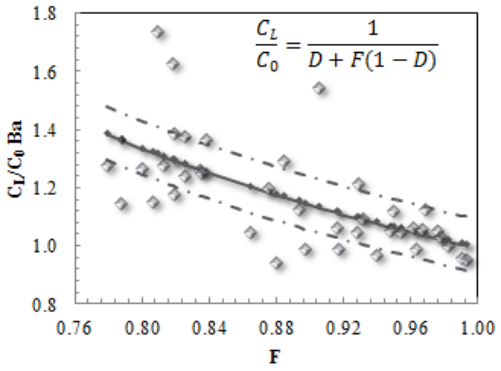

Figure 7.22 Example of an equilibrium fractionation curve fitted to measured Ba concentrations. The uncertainty (dashed lines) is ± one standard deviation.

The fitted curves were then used to calculate distribution coefficients for 35 trace elements, for both Rayleigh and equilibrium fractionation, assuming a constant D. The quoted uncertainties are derived from the 1σ standard deviation on the least squares regression. The error on the

individual measured concentrations is insignificant relative to the scatter in the data for all elements with the exception of Mo. The calculated D for Mo is indistinguishable from zero, and there may be less confidence in this value than some others.

Table 7.5 Calculated olivine-melt distribution coefficients for trace elements in Mauna Loa lavas assuming Rayleigh and equilibrium crystallization models, with ±1σ uncertainties.

	Li	*Sc*	*V*	*Co*	*Ni*	*Cu*	*Zn*	*Ga*	*Rb*	*Sr*	*Y*	*Zr*	*Nb*	*Mo*	*Sn*	*Sb*	*Cs*	*Ba*
Rayleigh D (melt/melt)	<0.001	0.219	0.102	1.873	5.511	0.350	0.750	0.229	0.004	0.068	0.260	0.117	<0.001	<0.001	0.038	0.035	<0.001	<0.001
±	0.171	0.035	0.046	0.114	0.344	0.139	0.049	0.039	0.150	0.057	0.078	0.068	0.122	0.152	0.095	0.231	0.213	0.130
Equilib. D (melt/melt)	<0.001	0.203	0.093	2.013	7.390	0.328	0.733	0.211	0.002	0.061	0.242	0.106	<0.001	<0.001	0.034	0.027	<0.001	<0.001
±	0.150	0.033	0.043	0.147	0.805	0.135	0.052	0.037	0.136	0.052	0.075	0.063	0.108	0.144	0.087	0.210	0.183	0.111

	-	*La*	*Ce*	*Pr*	*Nd*	*Sm*	*Eu*	*Gd*	*Dy*	*Ho*	*Er*	*Yb*	*Lu*	*Hf*	*Ta*	*Pb*	*Th*	*U*
Rayleigh D (melt/melt)	-	<0.001	<0.001	<0.001	<0.001	0.054	0.053	0.109	0.144	0.195	0.145	0.217	0.209	0.140	<0.001	0.117	<0.001	0.072
±	-	0.139	0.121	0.095	0.079	0.062	0.052	0.058	0.058	0.066	0.063	0.066	0.067	0.074	0.192	0.141	0.153	0.214
Equilib. D (melt/melt)	-	<0.001	<0.001	<0.001	<0.001	0.049	0.048	0.099	0.131	0.180	0.133	0.200	0.193	0.128	<0.001	0.108	<0.001	0.061
±	-	0.122	0.107	0.084	0.071	0.057	0.048	0.054	0.054	0.062	0.059	0.062	0.063	0.069	0.165	0.131	0.133	0.196

The partition coefficients obtained here represent apparent bulk distribution coefficients for the crystallizing assemblage. Because these partition coefficients are calculated for lavas with 7-15 wt. % MgO, they are assumed to be dominated by olivine with small a fraction of Cr-spinel. However, trapped melt that is sequestered with the crystals can also be considered as a cumulate phase with a D=1 (i.e., equivalent to the melt composition) such that apparent bulk D's represent upper limits to the true mineral-melt values (Shaw, 2003).

For Sc, V, Co, Ni, Zn, Ga, Y, Zr, Dy, Ho, Er, Yb, Lu, and Hf the uncertainties are an order of magnitude smaller than the calculated D, meaning that confidence in these values can be relatively high. In contrast, the bulk D's for Cu, Sr, Sn, Sm, Eu, Gd, and Pb have uncertainties that are the same order of magnitude as the inferred Ds, while Li, Rb, Nb, Mo, Sb, Cs, Ba, La, Ce, Pr, Nd, Ta, Th, and U have large relative uncertainties and the fitted D is 0.001 (i.e. the lower bound on the fit region), meaning that these elements have small but poorly constrained partition coefficients. For many of these elements, a value of D<0.001 is given because the models are insensitive at very small values of D and as such some predict negative values of D as an artefact of this insensitivity. Most of the elements show little sensitivity to whether an equilibration or fractionation model is used (Figure 7.23), though most have a slightly smaller error using an equilibrium model. This would be expected given previous discussions on residence times (part 6 of this chapter) where it was found that olivine could remain suspended in the melt during the eruption period. Ni is the exception however, with an error using the Rayleigh fractionation equation of 6 %, while the equilibrium equation has an 11% uncertainty.

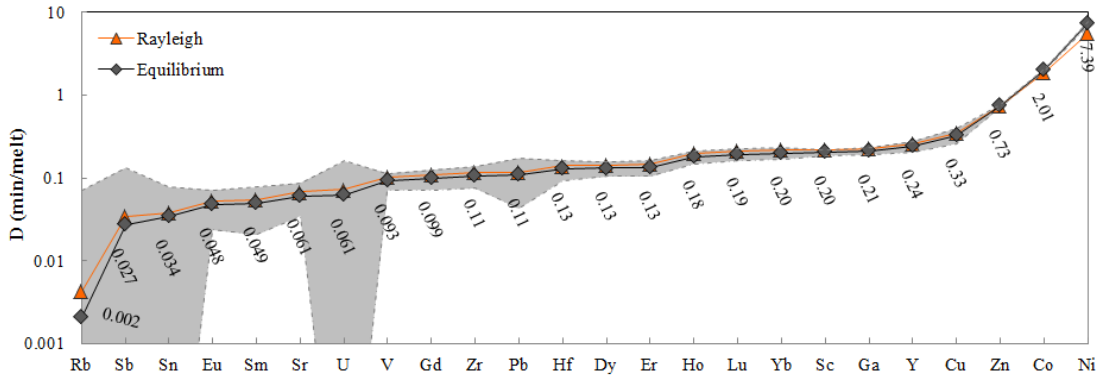

Figure 7.23 calculated Rayleigh (orange) and equilibrium (black) element apparent bulk partition coefficients, with labelled equilibrium D values and ±1σ error (grey shading). Partition coefficients are for Mauna Loa lavas with 7-15 wt. % MgO, for which it is assumed that olivine is the primary controlling phase.

There are, however, significant discrepancies in the D values calculated for the HREE compared to those reported in literature studies: $D^{min/melt}_{HREE}$ calculated here are routinely

showing values of ~0.2, which are an order of magnitude greater than that reported by (Beattie, 1993, Dunn and Sen, 1994, Fujimaki, 1984, Lemarchand, 1987b). This discrepancy may be due to incorporation of a small amount of chromite or orthopyroxene in the fractionating assemblage, which could be enough to affect the HREE concentrations of the bulk rock. Although studies are sparse, spinels have been observed to partition the HREE to a greater degree than olivine e.g. (Klemme et al., 2006, Nagasawa et al., 1980). D^{Y}, D^{Sr}, and D^{Zr} are also higher than in other published studies. The feasibility of this process can be evaluated by comparing the proportions of early-formed chromite and opx obtained from the major element models with their predicted effect on the trace element D's. According to Petrolog modelling, approximately 0.3% spinel fractionation and/or 5% opx fractionation can occur with olivine at the expected pressures and melt compositions. The D for any other phase that might be affecting the trace element concentration in the melt during crystallization can be calculated assuming a proportion of the other phase relative to olivine. The equation for bulk $Di=\Sigma W_A Di_A$ where W_A is the weight % of mineral A in the rock and Di_A is the partition coefficient if element i in mineral A. Assuming the crystallizing phases are 95% olivine and 5% 'other', the $D_{Yb}^{other/melt}$ would have to be 3.9 to be able to account for the bulk rock coefficient calculated. If the proportion of 'other' is increased to 10%, the necessary D would become 2, and if the proportion is decreased to 1% the necessary D would be 19.9. Given that petrographic studies have shown that only 1-2% of cpx and plagioclase are present in addition to olivine, high proportions of chromite and opx that would be necessary to account for the apparent D's calculated by this study seems unlikely. Another possibility could be that crustal material is assimilated into the lower-MgO magma (7-10 wt. % MgO), though Pacific MORB is enriched in HREE relative to LREE e.g. (Janney and Castillo, 1997). Alternatively pulses of magma that are depleted in HREE or enriched in the LREE could be fractionating the REE, or some magma chamber processes that enriches the moderately evolved magmas in LREE relative to HREE. It does not seem likely that there could be much variation in the HREE however, as Hawaiian tholeiites are known to have very constant HREE e.g. (Wagner et al., 1998).

In section 10.4, a compilation of literature partition coefficients for trace element extracted from default values MELTS (Table 7.6), which can be used for comparison to trace element partition coefficients calculated here. The D values calculated here were normalized to the expected olivine/melt literature value to reveal any systematic differences (Figure 7.24). Based on this comparison, it appears that the difference between the calculated Ds vs. literature values depend on the value of the literature partition coefficient. It is clear that the D's for the highly incompatible elements (literature $D < 0.01$) calculated from the data presented here are underestimated, while the moderately incompatible elements (literature $0.01 < D < 1$) are

overestimated aside from Eu. Compatible elements Co and Zn are also underestimated. This means that the moderately incompatible elements should be increasing more in concentration with decreasing MgO than they are, and the highly incompatibles should be increasing in concentration less with decreasing MgO than they are.

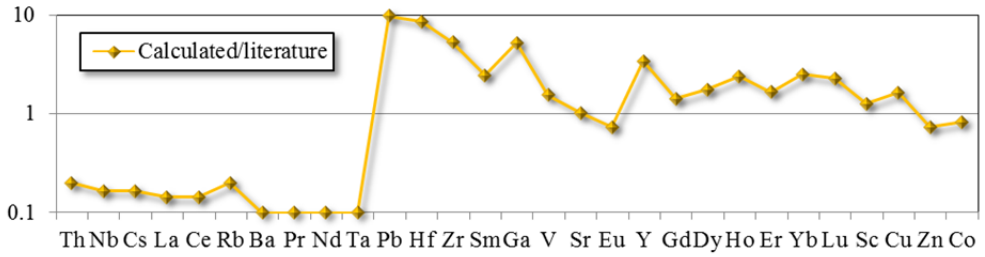

Figure 7.24 Calculated D/Literature D for trace elements. Elements are listed in order of compatibility according to literature collation, with least compatible on the left and most compatible on the right.

The trace element data in the range 7-15 wt. % MgO are plotted in Figure 7.25, showing that the highly incompatible elements have some outliers reaching to higher values (Figure 7.25a,c,e) than the moderately incompatible elements (Figure 7.25b,d,f) which have less spread in the data. This could be enough to skew the curve fit when C_L/C_0 was plotted against F such that the average concentration of the trace element in the range 7-9 wt. % MgO is higher than what it is in the range 10-15 wt. % MgO.

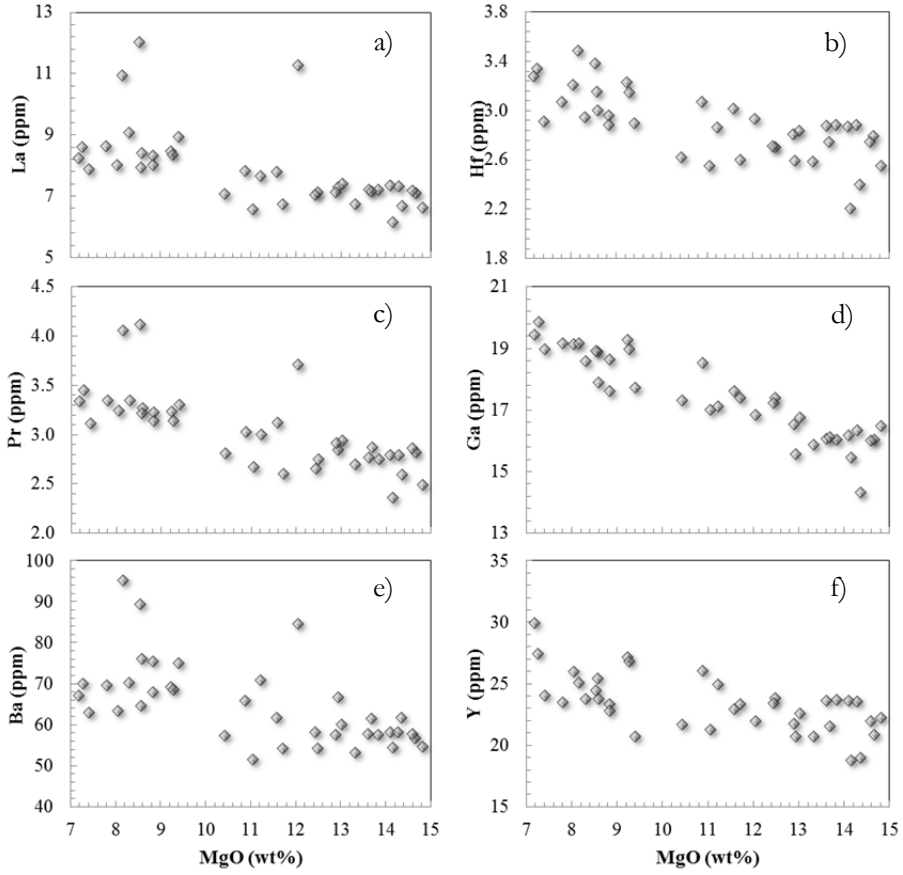

Figure 7.25 Highly incompatible trace elements (left) and moderately incompatible trace elements (right) versus MgO (wt. %).

Closer inspection of the trace element concentrations plotted against MgO reveal a gap in the data between 9-10 wt. % MgO, where a step in the slope appears for the highly incompatible TE. This could be revealing that the bulk rock data in the range 10-15 wt. % MgO are not a direct continuation of the more evolved data, and may represent variations in the formation processes of the bulk rock data. It can be seen that the concentrations between 7-9 wt. % MgO do not slope downwards and remain constant until a slight step downwards in concentration at 10 wt. % MgO.

In addition to variability in the measured data, the melt equations used are relatively sensitive to the value of F used, which can affect the calculated values of D. The value of F calculated above is from MELTS estimates of fractionation based on inputting major element information and fractionating olivine. The trace elements were also used to calculate an estimate of F by assuming D=0 for a perfectly incompatible element like Th. However, even making the possible range of F quite large (0.7-0.8) only changes the range in possible D values for Yb to between 0.411 - 0.12 respectively, which are still higher than would be expected for REE partitioning

into olivine. Aside from crystallizing garnet alongside olivine, which makes it hard to explain the high D_{Sr} and would require an unusual pressure regime, there are few other possibilities. Having said this, the partition coefficients used in Petrolog and alphaMELTS models are lower (by 1-2 orders of magnitude respectively) and these still produced curves that fit the HREE bulk assemblages very well, reaffirming that the expected value of C_L is fairly insensitive to variation in D at low values of D.

7.10.2 replenish, tap, fractionate?

In light of the discrepancy between calculated and literature partition coefficients, it is possible that the LREE are being fractionated from the HREE by a magma chamber process other than crystal fractionation. It has been proposed that the trace element chemistry of a magma chamber can be altered via constant replenishment with newly injected magma (O'Neill and Jenner, 2012). The concentration of trace elements, in particular the highly incompatible elements including the REE are enriched beyond the limits of fractional crystallization in MORB magma chambers globally. O'Neill and Jenner plotted REE concentrations from a global MORB array against MgO where the intercept at 10 wt. % MgO was taken to be the parental melt composition, and the slope and variability around the slope were calculated. These three have been used by O'Neill and Jenner to describe the behaviour of a trace element [M] with varying MgO, whereby d is the slope and d(log[M])/d[MgO] should approach a theoretical limit of -0.132 asymptotically as D_M goes to 0. The theoretical concentrations of certain trace elements were predicted by O'Neill and Jenner by combining partition coefficients for olivine, plagioclase, clinopyroxene, and selected minor phases, for whole rock samples ranging from 5-10 wt. % MgO with an assumed starting composition of 10 wt. % MgO. The LREE elements in MORB were all enriched well beyond the theoretical limits of crystal fractionation (La by nearly a factor of two), whereas the HREE were depleted comparatively (similar to the effect described above from Mauna Loa calculated partition coefficients but to a greater extent). The evidence from trace element fractionation in erupted MORB was used to suggest that the melt composition in mid-ocean ridge magma chambers is chemically modified by processes such as fluctuations in magma fluxes into and out of the chamber, in addition to chamber depth and differences in MORB source composition. Here, we have replicated this model using Mauna Loa samples with MgO contents 7-16 wt. % MgO, assuming a parental magma composition of 16 wt. % MgO. By using only MgO range 7-16 wt. %, then only the partition coefficients for olivine need to be considered as cpx and plagioclase fractionate from magmas with <7 wt. % MgO. These partition coefficients are the means from previous studies of experimentally determined olivine-melt partition coefficients (Beattie, 1993, Dunn and Sen, 1994, Shimizu et al., 1982, Nielsen and Gallahan, 1991). As all REE are highly incompatible in olivine, the limit of

fractional crystallization will be linear. All elements are enriched in the whole rock beyond that which can be explained by fractional crystallization, and the effect is greater with increasing ionic radius (Figure 7.26a). The same pattern can be seen between the MORB magmas and Mauna Loa magma, with the LREE enriched beyond fractional crystallization, although the effect is far less exaggerated in the Mauna Loa basalts compared to MORB by an order of magnitude (Figure 7.26b).

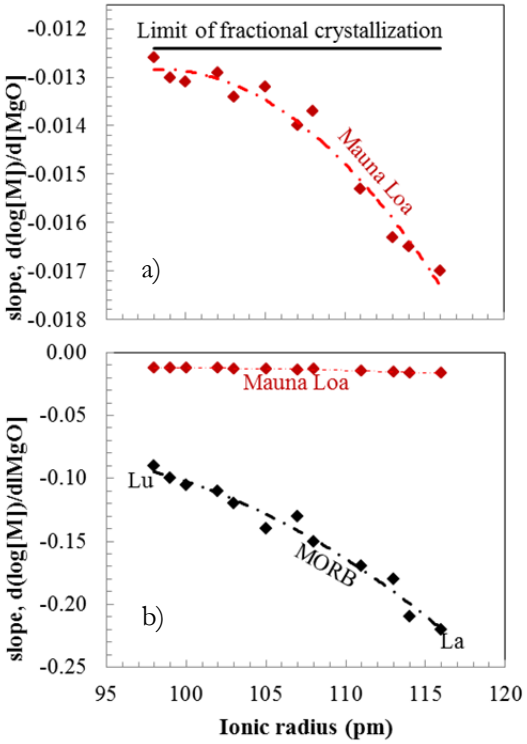

Figure 7.26 Slope of d(log[M])/d[MgO] versus ionic radii of REE for Mauna Loa (red) and MORB (black)(a), and then compared to MORB (b).

This suggests that Mauna Loa magmas and potentially Hawaiian magmas more broadly may be relatively free from compositional modification by replenishment of newly injected magma compared to MORB, and that Hawaiian magmas have a shorter residence time and may be more transient than MORB. The results here confirm the hypothesis by Rhodes (Rhodes, 1988) that lavas from Mauna Loa may not be subjected to the same magma chamber processes as other volcanoes such as Kilauea. Rhodes has suggested that the magma volume and influx rates may be so high that magma is not able to accumulate in pockets and be infiltrated by new pulses.

The slight discrepancy between the behaviour of the highly incompatible elements and the HREE may be due to processes of replenishment], tapping, and fractionation similar to those inferred for MORB but to a lesser degree. However, the slight effect would not be enough to

fractionate the REE in terms of ppm to a large degree, and all REE regardless of ionic radius have similar C^M_L/C^M_0 where C^M_L = the average concentration of the element M in the final liquid at 7 wt. % MgO and C^M_0 is the average concentration of element M in the initial parental magma at 16 wt. % MgO. The total range of C^M_L/C^M_0 is 1.34(La) – 1.22(Lu).

The method of O'Neill and Jenner applied to the Mauna Loa whole rock samples in this study may be further evidence that olivine control is the only major factor in major and trace element variation in samples with 7-16 wt. % MgO. Positively, the lack of disruption to the magmas while they are in the chamber as evidenced by the relatively insignificant fractionation of the REE means that the reversal of the fractional crystallization process on Hawaiian trace elements can be applied to an evolved melt to yield a good representation of a parental magma.

7.10.3 MELTS and Petrolog modelling of trace elements

One of the advantages of using the Petrolog and alphaMELTS software is that they enable the inclusion of trace elements in fractionation models, whereas the MELTS interface only allows major elements. The partition coefficients (D) for each trace element can be entered manually, or they can be imported from a limited number of literature studies. For example, in Petrolog the option exists to use the D values of (Beattie, 1993) for the elements Ni and Co during fractional crystallization of olivine, or to use the D values of (Blundy and Wood, 1991) for Sr and Ba during fractional crystallization of plagioclase. For this study, the trace elements Be, Ni, V, Sc, Co, Cu, Zn, Ga, Rb, Nb, Cs, Y, Zr, Ce, Eu, Ba, La, Pr, Nd, Gd, Sr, Sm, Eu, Dy, Ho, Er, Yb, Lu, Hf, Ta, Pb, Th, and U were able to be modelled during fractional crystallization of a shallow magma chamber in the Petrolog software using user input trace element concentrations and partition coefficients. A 16 wt. % MgO parental magma was used, fO_2 was set to QFM, pressure was kept constant at 0.4 kbar, and 0.05 wt. % H_2O was added (for initial run).

Petrolog and alphaMELTS modelling of trace elements does not allow bulk partition coefficients to be used and as such it is necessary to manually input Ds for each individual mineral. Literature mineral/melt partition coefficients from both experimental studies and naturally occurring basaltic samples were compiled for olivine, plagioclase, clinopyroxene, spinel, and orthopyroxene (Aigner-Torres et al., 2007, Beattie, 1993, Bennett et al., 2004, Bindeman and Davis, 2000, Bindeman et al., 1998, Chazot et al., 1996, Dunn and Sen, 1994, Elkins et al., 2007, Fujimaki, 1984, Green et al., 2000, Hart and Dunn, 1992, Hauri et al., 1994, Johnston et al., 2004, Klemme et al., 2002, Lemarchand, 1987a, Mckenzie and Onions, 1995, Nielsen and Gallahan, 1991, Rollinson, 1993, Shimizu et al., 1982, Tepley et al., 2010, Tuff and Gibson, 2006, Canil, 1999, Horn et al., 1994, Klemme et al., 2006, Mallmann and O'Neill, 2009, Nagasawa et al., 1980, Righter et al., 2006). These were consulted along with GERM partition

coefficient data base and a compilation by Rollinson in his book *Using Geochemical Data* (Rollinson, 1993) to estimate appropriate mineral/melt partition coefficients for use in the Petrolog geochemical modelling software. These studies were selected to be relevant to tholeiites and basalts, and instead of the average value being used often the most common value was selected due to the presence of many outliers in this large collection. The expected range and relative values was also narrowed down with consideration to lattice strain models. The adopted values can be found in Table 7.6.

Table 7.6 Mineral/melt partition coefficients used during trace element fractionation calculations.

	$D_i^{olv/melt}$	$D_i^{cpx/melt}$	$D_i^{opx/melt}$	$D_i^{plag/melt}$	$D_i^{spl/melt}$
Be	0.02	0.05	0.04	0.2	0.1
Sc	0.16	2.5	1.2	0.2	0.3
V	0.06	1.35	0.8	0.1	3
Co	2.41	2	3	0.2	4
Ni	Beattie *et al.* (1991)	4	5	0.1	14.41
Cu	0.2	0.18	0.2	0.04	2
Zn	1	0.5	0.6	0.13	4
Ga	0.04	0.7	0.1	0.7	3
Rb	0.01	0.03	0.01	0.05	0.01
Sr	0.06	0.17	0.01	1.8	0
Y	0.07	0.6	0.3	0.02	0.05
Zr	0.02	0.15	0.06	0.005	0.1
Nb	0.006	0.01	0.008	0.01	0.01
Cs	0.006	0.006	0.001	0.05	0
Ba	0.01	0.03	0.01	0.2	0.001
La	0.007	0.01	0.01	0.15	0.01
Ce	0.007	0.1	0.01	0.1	0.002
Pr	0.01	0.181	0.01	0.07	0.005
Nd	0.01	0.25	0.02	0.05	0.01
Sm	0.02	0.4	0.06	0.07	0.01
Eu	0.065	0.44	0.07	0.4	0.2
Gd	0.07	0.5	0.1	0.04	0.2
Dy	0.075	0.55	0.15	0.03	0.1
Ho	0.075	0.48	0.2	0.04	0.1
Er	0.08	0.5	0.25	0.02	0.01
Yb	0.08	0.48	0.28	0.02	0.01
Lu	0.085	0.4	0.3	0.02	0.01
Hf	0.015	0.26	0.05	0.008	0.2
Ta	0.01	0.01	0.01	0.01	0.02
Pb	0.011	0.05	0.1	0.5	0.001
Th	0.005	0.02	0.005	0.025	0.005
U	0.008	0.04	0.005	0.025	0.01

The Petrolog trace element fractionation paths including all phases, as well as suppressing one phase at a time were plotted (Figure 7.27, Figure 7.28, Figure 7.29). Once again, the effect of suppressing plagioclase has the most significant impact of all the phases, as many trace elements being less compatible in plagioclase than in cpx or opx. As expected, cpx crystallization is

necessary to account for the low Sc contents at low MgO (Figure 7.27b). Co is compatible in olivine and spinel (Figure 7.27d), and it has been suggested that the Co distribution coefficient in olivine and spinel depends strongly on the fO_2 of the crystallizing environment (Ehlers et al., 1992). The $D^{ol/melt}_{Co}$ has been shown to remain at a constant 2.8 over the log fO_2 range between -6.6 and -10.6, and decreases to 1.65 at log fO_2 = -12.2. Given that the calculated range in log fO_2 in this fractionating system is between -4.5 to -10.1 assuming buffers in the range of QFM+1 to QFM-1 and that fractionation occurs over an MgO range of 16 – 5 wt. % MgO, then it could be expected that the $D^{ol/melt}_{Co}$ should be close to 2.8. From Figure 7.27d, it can be seen that the input value of 2.41 for $D^{ol/melt}_{Co}$ produces a close fit for the measured concentrations of Co, indicating that the previously estimated range in log fO_2 of -4.5 to -10.1 (QFM+1 to QFM-1) is probably a good estimate for crystallization conditions within the magma chamber. The calculated Ni fractionation path for olivine-control is broadly consistent with the bulk rock data (Figure 7.27e), however the predicted fractionation path for all runs is more curved than the bulk data with >7 wt. % MgO. There are some samples that follow this curve, while others increase in Ni with MgO linearly. The linearity of the trend produced when Ni is plotted against MgO could be illustrating that most of the olivine in the bulk rock is the result of an olivine + evolved melt mixing trend, rather than a direct fractionation trend as discussed in detail earlier in this chapter (Part 3). (Hart and Davis, 1978) have shown that the partition coefficient of Ni between olivine and melt varies in a non-linear fashion according to the function $D = \frac{124.3}{MgO} - 0.897$ in the system Fo-Ab-An (1 Atm), demonstrating that the value of D will vary with MgO. Assuming an MgO content of 16%, the corresponding value of D would be 6.8 while at an MgO content of 8 wt. % the corresponding D would be 14.6. The equation used for the partitioning of Ni here (Beattie et al., 1991) has confirmed the findings by Hart and Davis (1978) and found that Ni partition coefficients in olivine-basalt systems depend linearly on the Mg partition coefficient. Beattie and co-authors agree with findings from Hart and Davis that the $D^{Ol/melt}_{Ni}$ can be approximated by the equation $D = \frac{a}{MgO} - b$ where a and b are empirical constants. This equation suggests that Henry's law is satisfied for the partitioning of Ni in olivine, meaning that D increases with decreasing concentration of Ni (Watson, 1985). Hart and Davis showed that when concentrations of Ni are plotted against MgO, the relationship will be curved regardless of whether a constant D is used (D=6 in their study) or if it is allowed to vary as a function of melt composition. A later study of olivine/melt partition coefficients in lavas from the 1955 Kilauea eruption predict much higher $D^{ol/melt}_{Ni}$ (25-38) as the melts used by Norman and co-authors were moderately evolved (5.4 and 6.6 wt. % MgO) (Norman et al., 2005). If melt MgO concentrations of 5.4 and 6.6 are input into the equation derived by Hart and Davis, the resulting partition coefficients to would be 22.1 and 17.9

respectively. Low Ni partition coefficients such (e.g. 5.5 calculated in this study) have been attributed to crystallization in a deep, reduced setting close to the magnetite-wustite buffer (Morse et al., 1991). This has been used by Rhodes to suggest that much of the olivine entrained by lavas erupted at Mauna Loa must have crystallised from a parental melt under reducing conditions deep within the volcano's magmatic plumbing system (Rhodes, 1995).

The bulk rock compositions of the Mauna Loa lavas studied here do not show an increase in copper concentration at low MgO, unlike the majority of other trace elements, and if anything the Cu concentrations decrease slightly with decreasing MgO (Figure 7.27f). The calculated Petrolog fractionation path does not match the trend for Cu in the bulk chemistry, indicating that the bulk partition coefficient for Cu could be higher than the one assumed here. Degassing of chalcophile elements might be one explanation for this apparent depletion in Cu, however, (Norman et al., 2004) on concentration or rhenium and chalcophile elements in basaltic glasses from Ko'olau and Moloka'i show that Cu concentrations do not appear to be altered by degassing events and may be related to the presence or absence of sulphide inclusions in the sample. In contrast, the Sr concentrations increase in some samples at low MgO, which can be reproduced by the plagioclase-free fractionation path (Figure 7.27j). The fractionation path in which plagioclase is present suggests that the fractionation of plagioclase would not alter the concentration of Sr significantly assuming $D_{Sr}^{plag/melt} = 1.8$. This is because it is the absence of plagioclase fractionation that will cause Sr to become enriched in the melt, while if plagioclase is allowed to crystallize the Sr concentration does not increase.

Other trace elements, e.g. Rb (Figure 7.27i), behave incompatibly throughout fractionation, increasing in concentration in the olivine-controlled samples, and then sharply increasing during fractionation of the other phases at MgO <7 wt. %. The elements incompatible in plagioclase and cpx increase in concentration when below 7 wt. % MgO, though not to the same extent when plagioclase is suppressed. This is probably due to the continued decrease in MgO concentration when only cpx/opx crystallize because only cpx and opx incorporate Mg into their structure, while plagioclase does not. Plagioclase fractionation means that incompatible trace elements continue to rise, while MgO decreases at a slower rate. Evolved samples with <8 wt. % MgO appear to follow the plagioclase-present fractionation path, indicating that the enrichment could be due to a further ~5-10% crystallization of solids after olivine fractionation.

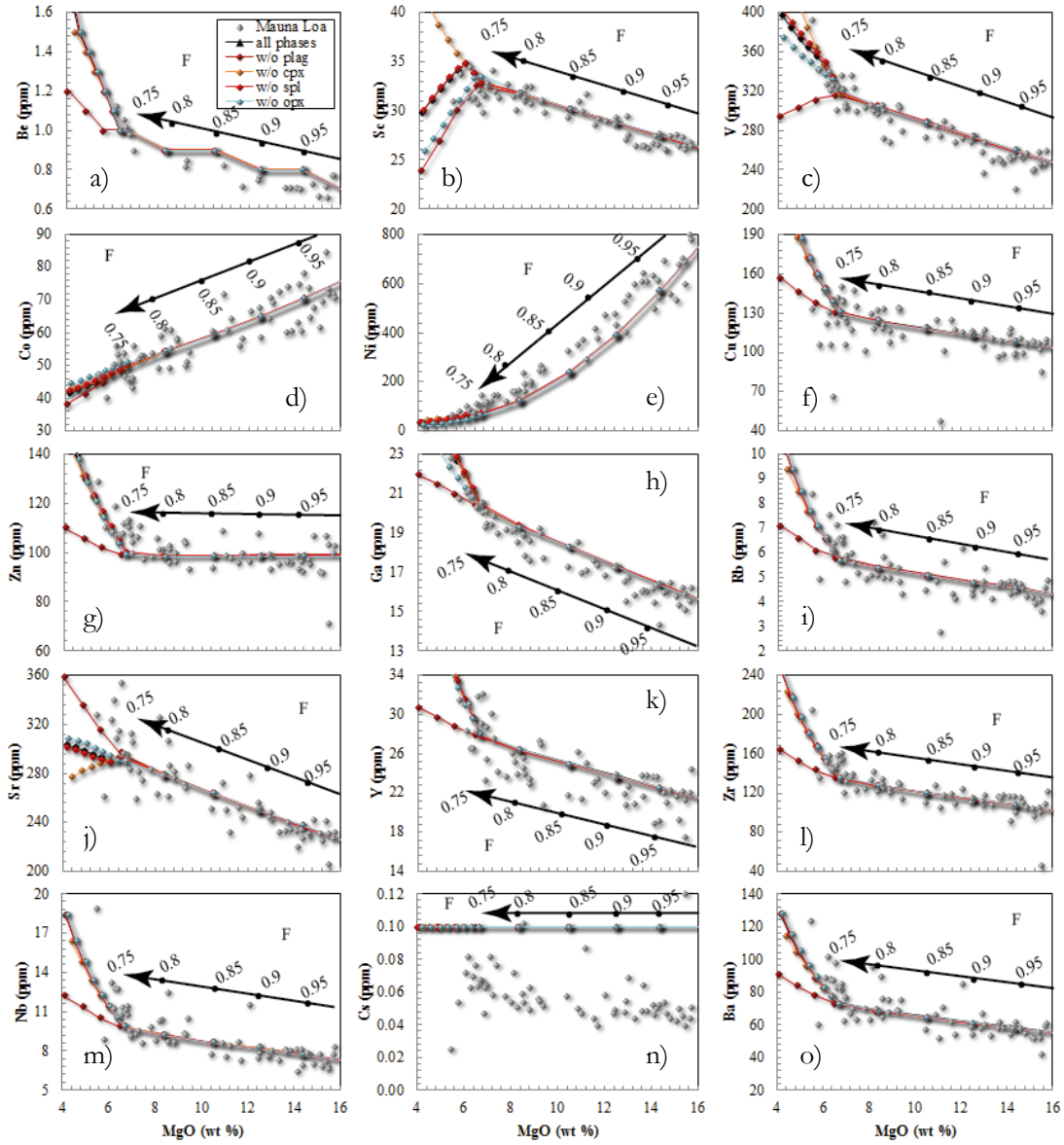

Figure 7.27 Petrolog trace element fractionation paths. Trajectories for all phases (black) are shown, as well as for suppressing plagioclase (maroon), cpx (yellow), spinel (red), and opx (light blue). Each tick mark represents 5% fractionation.

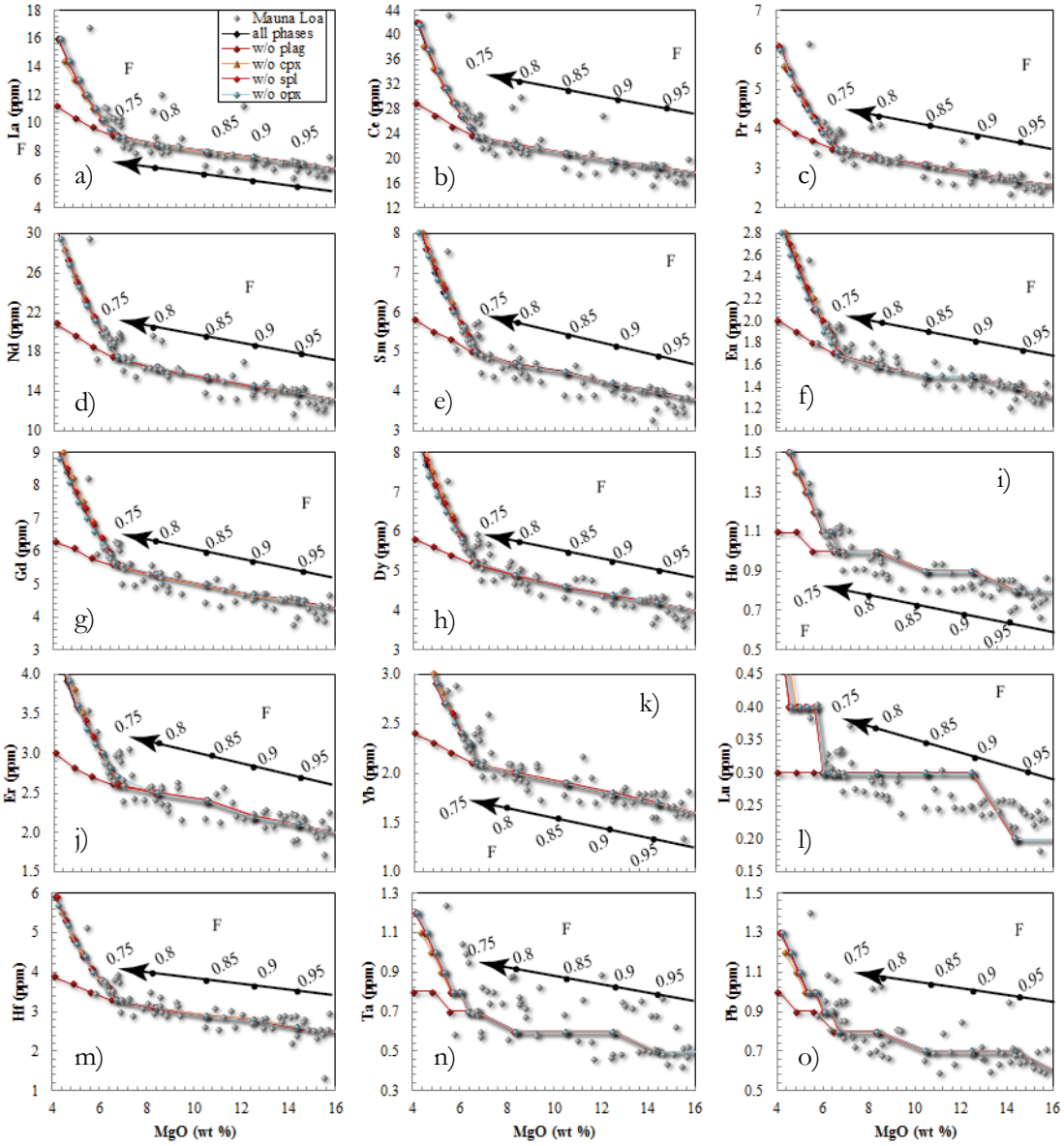

Figure 7.28 Trace element fractionation paths calculated by Petrolog. Trajectories for all phases (black) are shown, as well as for suppressing plagioclase (maroon), cpx (yellow), spinel (red), and opx (light blue). Each tick mark represents 5% crystallisation.

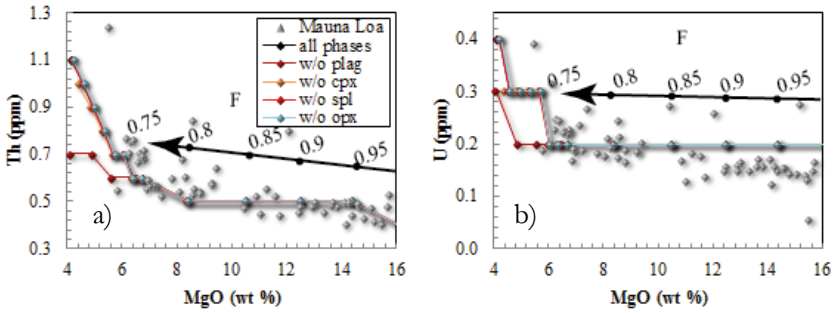

Figure 7.29 Trace element fractionation paths calculated by Petrolog. Trajectories for all phases (black) are shown, as well as for suppressing plagioclase (maroon), cpx (yellow), spinel (red), and opx (light blue). Each tick mark represents 5% crystallisation.

For comparison with the Petrolog results, the trace elements were also modelled using alphaMELTS using the default partition coefficients from (McKenzie and O'Nions, 1991, Mckenzie and Onions, 1995) (Table 7.7). In the alphaMELTS model for example, the default $D_{Zn}^{Ol/melt}$ is less than 1, however a $D_{Zn}^{Ol/melt}$ of about 1.2 is required to fit the olivine-controlled bulk data (Figure 7.30g). The same is true of Co, which requires a $D_{Co}^{Ol/melt}$ closer to 2.4 than 1 (Figure 7.30d). Sc and Cu do not increase in concentration at low MgO, and therefore compatibility into the other phases such as spinel (Sc) and sulphide (Cu) seems to be required. The $D_{Sc}^{Cpx/melt}$ was changed from 0.5 to 2.5 and the $D_{Cu}^{Cpx/melt}$ was changed from <1 to 2.5 also (Figure 7.30b,f). A D value of 2.5 of Cu into cpx is probably unrealistically high based on literature partition coefficients for Cu, and so it could be that another mechanism is depleting Cu in some samples e.g. sulphide inclusions as mentioned before. The partitioning of V into olivine has been used by (Canil, 1997) as an indicator of oxygen fugacity in Archaean komatiite magmas. The slopes of Sc/V, Ti/V and Zr/V for samples in this study (Figure 5.19 trace element results) suggest that $D_{Sc}^{Ol/melt} > D_{V}^{Ol/melt} = D_{Ti}^{Ol/melt} > D_{Zr}^{Ol/melt}$. Partition coefficients for V in alphaMELTS (0.06) and those calculated for equilibrium fractionation of olivine below (0.09) suggest an oxygen fugacity of ΔNNO-1, approximately equivalent to QFM. An oxygen fugacity of close to QFM for the samples in this study is also found using the $D_{V}^{Ol/melt}$ – fO_2 relationship of (Mallmann and O'Neill, 2009) when partition coefficients of 0.06-0.09 are assumed. Using this experimentally derived relationship between fO_2 and V partitioning Mallmann and O'Neill found that the oxygen fugacity of basalts globally including mid-ocean ridges, ocean islands, and island arcs is remarkably constant (QFM ±1).

Similarly to the Petrolog results, the suppression of plagioclase meant that the necessary enrichment in the highly incompatible elements at low MgO did not occur, and these fractionation paths fit the evolved bulk rock compositions very well e.g. Figure 7.30h.

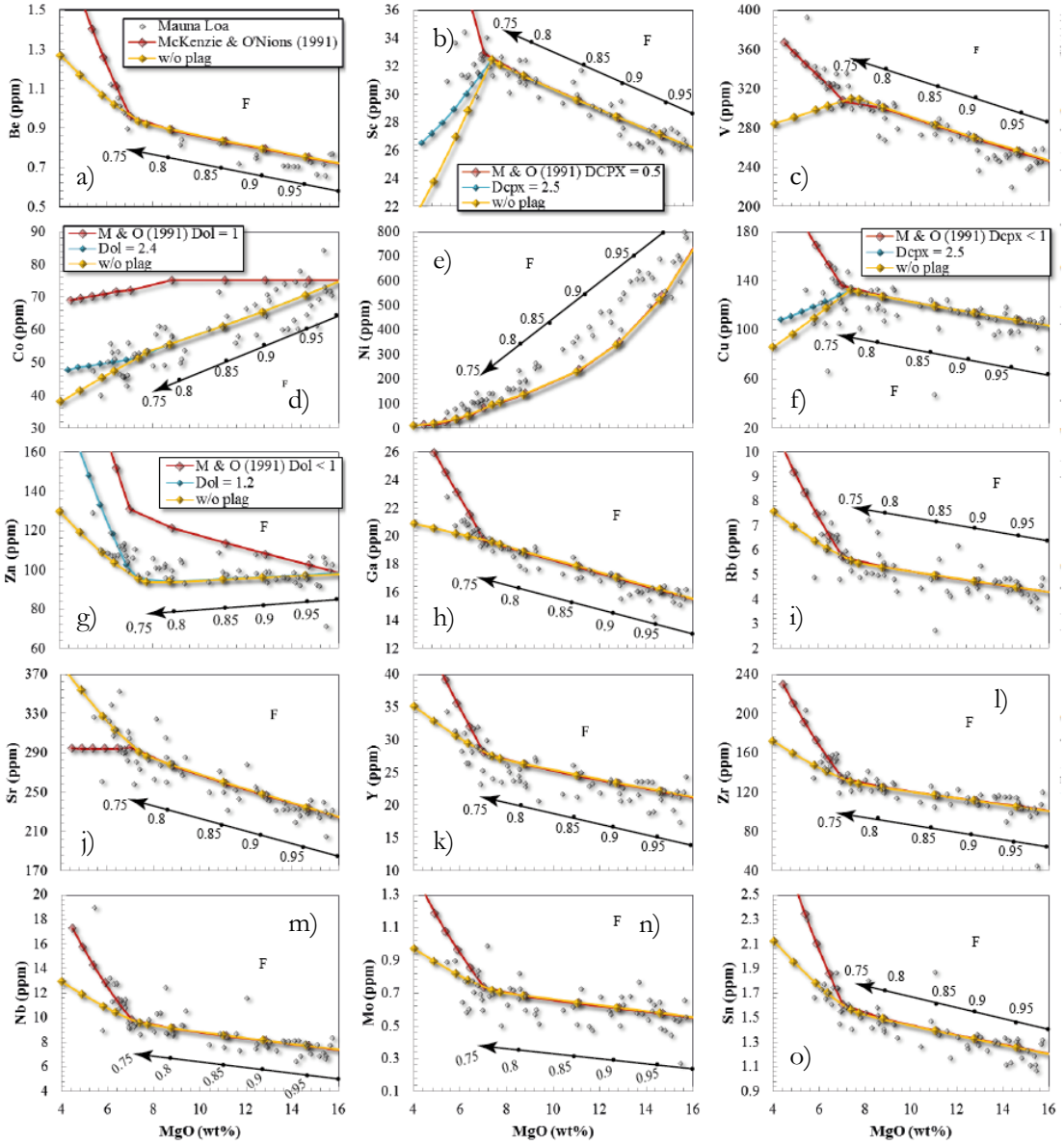

Figure 7.30 alphaMELTS modelling using default partition coefficients by Mackenzie and O'Nions (1991, 1995) (red), altered to fit (blue), and plagioclase suppressed (yellow).

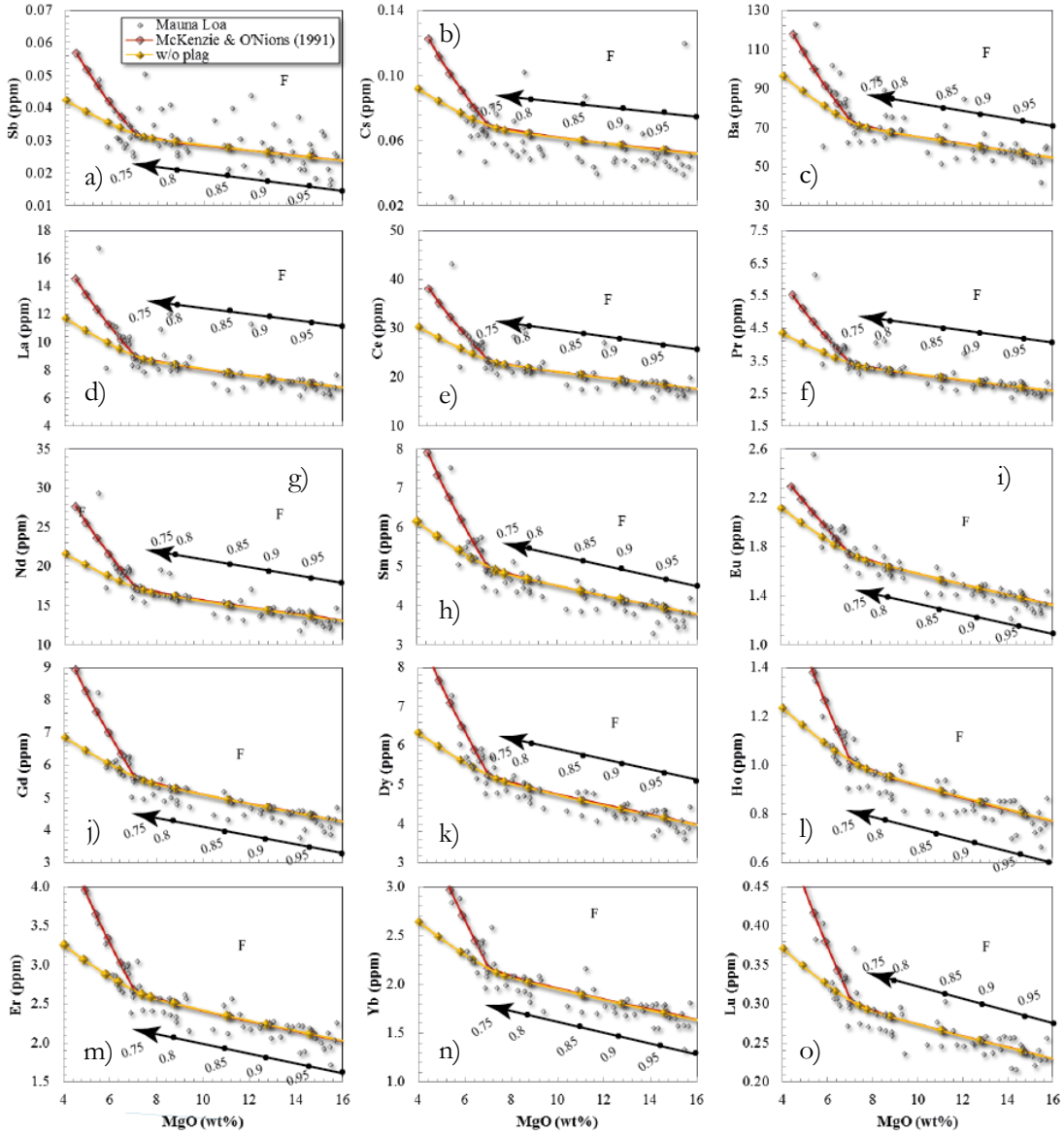

Figure 7.31 alphaMELTS modelling using default partition coefficients by Mackenzie and O'Nions (1991, 1995) (red), altered to fit (blue), and plagioclase suppressed (yellow).

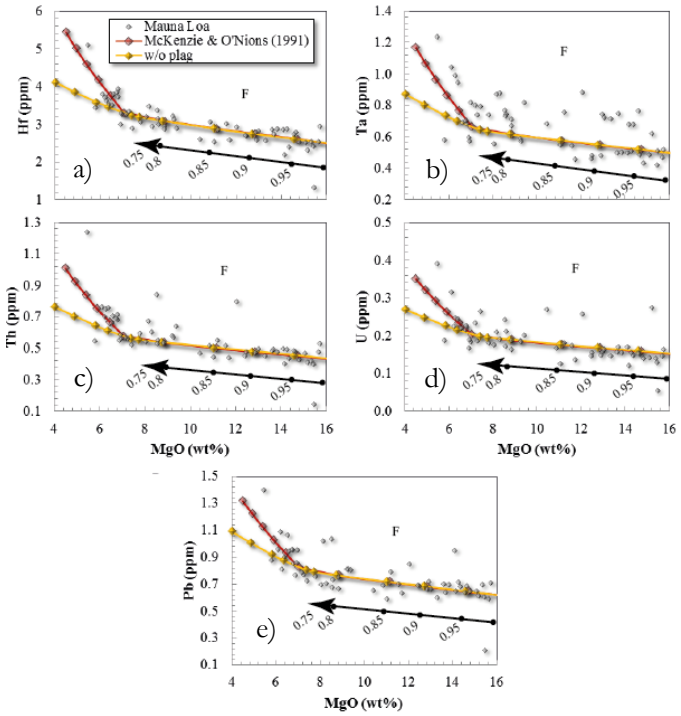

Figure 7.32 alphaMELTS modelling using default partition coefficients by Mackenzie and O'Nions (1991, 1995) (red), altered to fit (blue), and plagioclase suppressed (yellow).

The default mineral/melt partition coefficients used by alphaMELTS are tabulated below. These are a compilation of data from McKenzie and O'Nions (1991, 1995) (McKenzie and O'Nions, 1991, Mckenzie and Onions, 1995).

Table 7.7 Default partition coefficients from McKenzie and O'Nions (1991, 1995) used in alphaMELTS modelling of trace elements. Alternative values in brackets give a better fit to measured data.

	$D_i^{Cpx/melt}$	$D_i^{Plag/melt}$	$D_i^{Ol/melt}$	$D_i^{Opx/melt}$	$D_i^{Spl/melt}$
Sc	0.5(2.5)	0.02	0.16	0.33	-
Cu	-(2.5)	-	-	-(0.2)	-(2)
V	1.31	-	0.06	0.9	-
Zn	-	-	-(1.2)	-	-
Co	2	0.05	1(2.4)	3	4
Ni	9.4	-	9.4	9.4	-
Ga	0.74	-	0.04	0.2	5
Rb	0.001	0.03	0.00018	0.0006	0.0001
Sr	0.1283	2	0.00019	0.007	-
Y	0.2	0.03	0.005	0.005	-
Zr	0.1	0.01	0.01	0.03	-
Nb	0.02	0.01	0.005	0.005	-
Cs	0.0002	0.025	0.00005	0.0001	0.0001
Ba	0.0005	0.33	0.0003	0.0001	0.0001
La	0.054	0.27	0.0004	0.002	0.01
Ce	0.098	0.2	0.0005	0.003	0.01
Pr	0.15	0.17	0.0008	0.0048	0.01
Nd	0.21	0.14	0.001	0.0068	0.01
Sm	0.26	0.11	0.0013	0.01	0.01
Eu	0.31	0.73	0.0016	0.013	0.01
Gd	0.3	0.066	0.0015	0.016	0.01
Dy	0.33	0.055	0.0017	0.022	0.01
Ho	0.31	0.048	0.0016	0.026	0.01
Er	0.3	0.041	0.0015	0.03	0.01
Yb	0.28	0.031	0.0015	0.049	0.01
Lu	0.28	0.025	0.0015	0.06	0.01
Hf	0.22	0.01	-	0.01	-
Ta	0.02	-	0.005	0.005	-
Pb	0.01	0.36	0.0001	0.0013	-
Th	1.30E-03	0.05	0.00001	0.00001	-
U	9.00E-04	0.11	0.00001	0.00001	-

In addition to trace element concentrations, trace element ratios can be used to explore whether the trace elements have been fractionated beyond that expected for crystallization alone. The trace element ratios presented in the trace element results section (Figure 5.12, 5.13) were modelled using alphaMELTS (Figure 7.33). Results suggest that crystal fractionation (with or without plagioclase) cannot account for the significant variation in the ratios La/Yb, La/Sm, Nb/Y, Zr/Nb, or Sm/Nd (Figure 7.33a,b,c,d,e) that are observed in the lavas. This discrepancy suggests that the observed variations must have a control other than crystal fractionation, and will be discussed further in the next section of this thesis where source heterogeneity is addressed.

The ratio Sr/Nd varies at low MgO to a degree consistent with ~5% fractionation of non-olivine phases including plagioclase, but also does not preclude ~5% fractionation of other phases not including plagioclase for other samples (i.e. if plagioclase is suppressed, the Sr/Nd ratio remains relatively unchanged through cpx + opx fractionation) (Figure 7.33f). The decrease in Sc/Y and Cu/Zn appear to be reflecting cpx fractionation indicating that approximately 5-10% cpx + opx fractionation could account for the Sc/Y and Cu/Zn ratios in the bulk rock compositions. This would be assuming a $D_{Cu}^{Cpx/melt} > 1$, however, which is unlikely given evidence from partitioning studies e.g. (Hart and Dunn, 1992). Cu concentrations do not increase greatly at low MgO like the other highly incompatible elements, indicating Cu may be behaving only moderately incompatibly. On closer inspection, most of the samples with low Cu for a given MgO are landslide samples, indicating the variation in Cu bulk rock assemblage could be source related, meaning the landslide samples may have been transported from another volcano. This possibility will be explored further in the next section of this thesis.

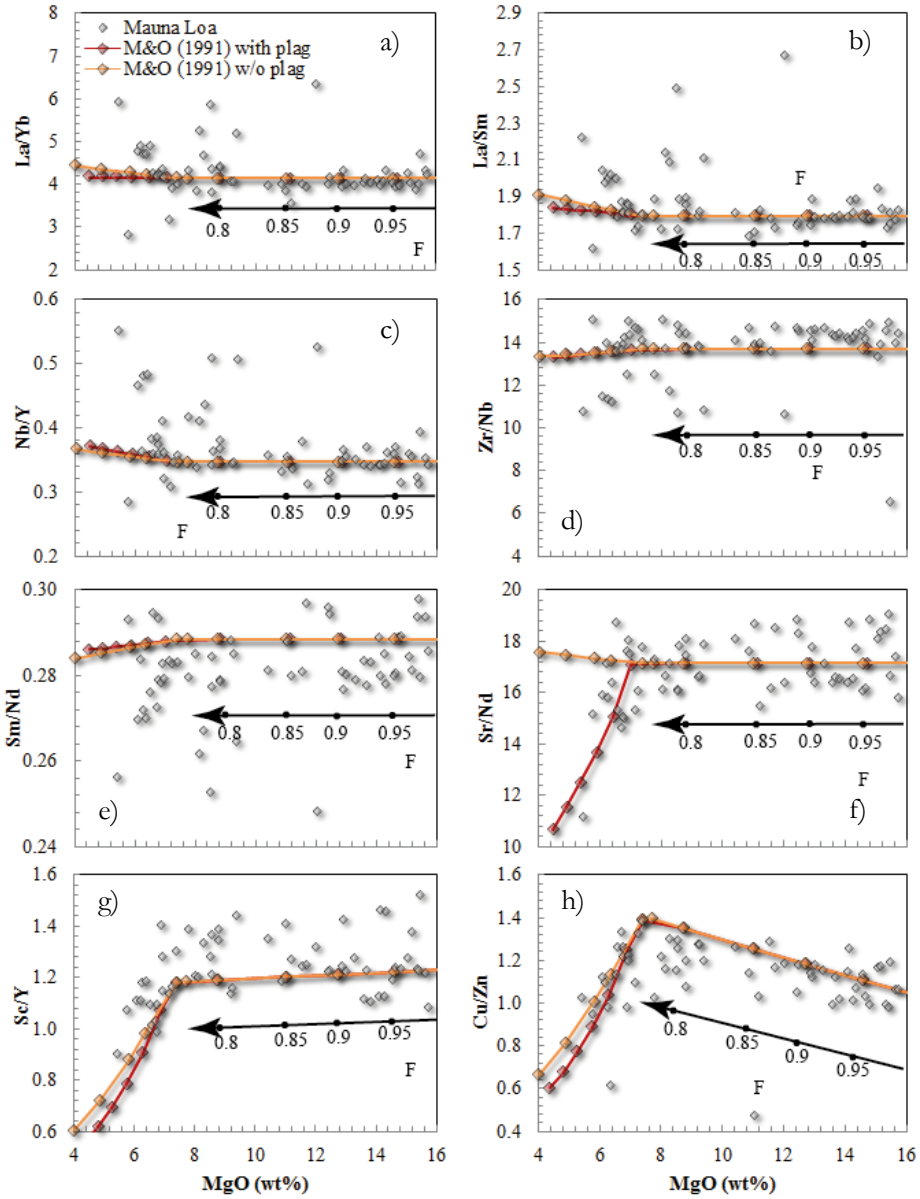

Figure 7.33 Results of alphaMELTS fractionation paths for showing plagioclase-present fractionation (red) and plagioclase-absent (yellow) trajectories.

The effect of varying the amount of water in the hypothetical parental melt was tested on the trace elements as it was with major elements (Figure 7.34). It can be seen that varying the water contents of the parental magma alters the MgO content at which the slope in the TE versus MgO trend changes. For the elements compatible in olivine, the proportion of water does not affect the evolved fractionation trend to a great degree e.g. Figure 7.34d. The trace elements incompatible in all phases will begin to increase in concentration at higher MgO when there is less water compared to when there is more water, where the slope change is delayed e.g. Figure 7.34e. This is because when more water is present, the crystallization of cpx and plagioclase are

delayed while olivine continues to crystallize, thereby continuing to deplete MgO contents and resulting in a flatter slope when trace elements versus MgO are plotted. It can also be seen that the highly incompatible elements e.g. Rb, Nb, La, and Ba (Figure 7.34e, h, i, j) are enriched in some samples beyond that which can be explained by the fractionation trends caused by variations in H_2O. Conversely, the HREE e.g. Y, Dy, and Ho (Figure 7.34g, k, l) can be explained simply by fractionation.

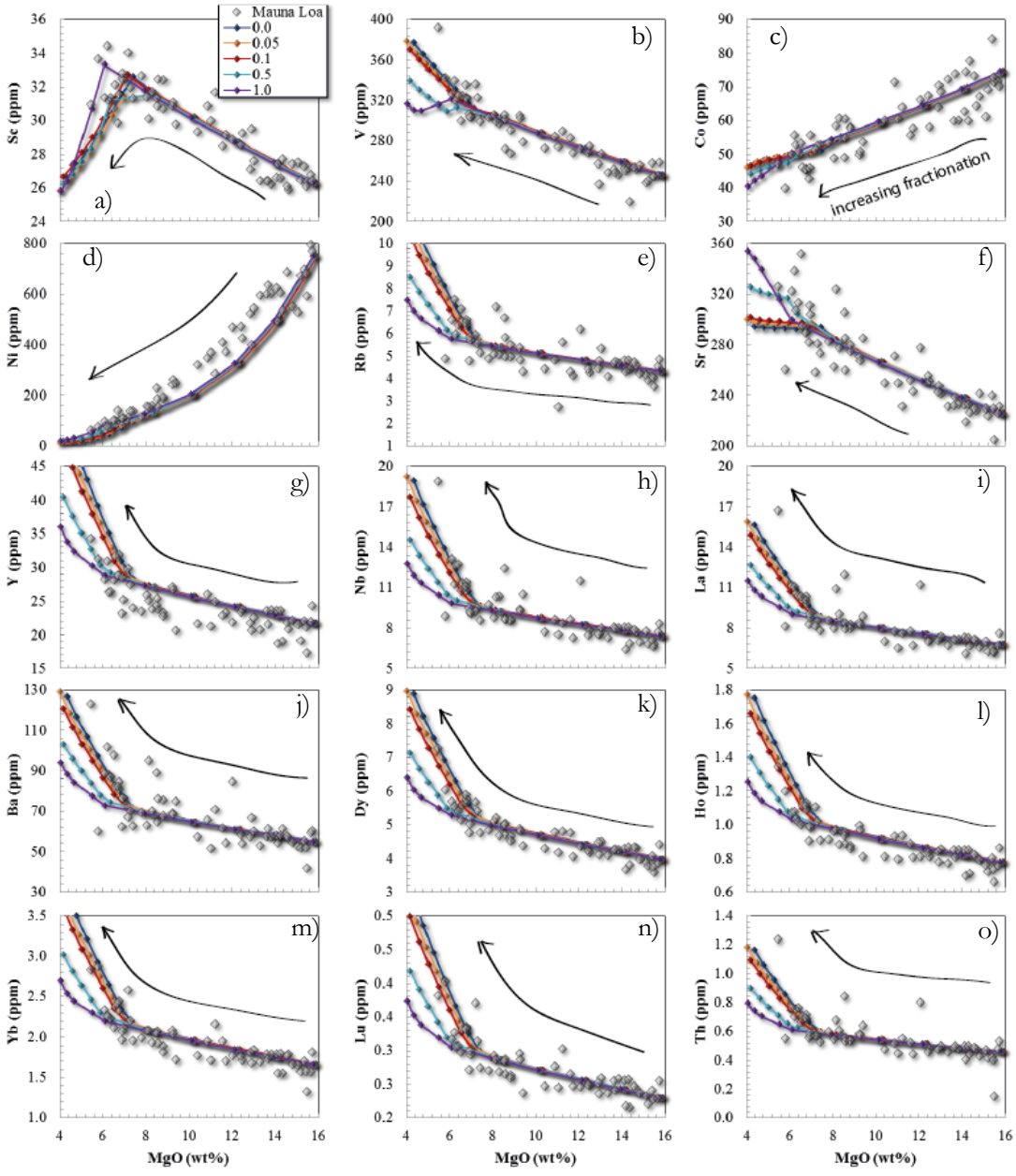

Figure 7.34 Trace element melt composition with variable parental magma water content (wt. %). Legend is showing wt. % water used for each calculation.

7.11 Conclusions

There is strong evidence to suggest that none of the whole rock samples are direct parental magmas. Evidence includes the high proportions of modal olivine in whole rock samples; Ni versus MgO does not form a polynomial curve as would be expected with a fractionation trend and is therefore more consistent with a mixing line, and glass compositions with low MgO contents. Furthermore, the forsterite content does not correlate with whole rock MgO contents, indicating that the core composition of the olivine is not in equilibrium with the whole rock composition and therefore the bulk assemblage is also unlikely to represent the composition of a cogenetic crystal + melt. More likely is that the melt has fractionated to an evolved composition (~8-10 wt. % MgO) and the olivine fractionated (average forsterite 87.5) was able to remain entrained until eruption due to the high viscosity of such magmas. This conclusion is supported by the 1:1 positive correlation between modal olivine and normative olivine proportions. In addition to retaining the olivine crystallized, some lavas must have accumulated additional olivine upon eruption, possibly scavenged from the sides of the magma chamber or vertical conduits for the whole rock samples with up to 33 vol. % modal olivine to result.

Despite evidence that the whole rock assemblage is not directly a parental magma, thermodynamic modelling suggests magmatic processes have recreated a parental magma composition via the retention of crystallized olivine in the melt until it has reached an evolved composition. This parental magma composition contains an MgO content of ~ 16 wt. % to be in equilibrium with the highest Fo olivine found in these samples, and the consequent major element oxide and trace element compositions for the proposed parental magma have been given.

Thermodynamic modelling suggests the estimated parental magma composition for all measured major and trace elements can reproduce the chemistry of the more evolved samples which are unaffected by olivine accumulation, further affirming its suitability for a parental magma estimate. The amount of MgO in the proposed composition is a minimum based on the maximum Fo contents of olivine found in samples from this study, however the higher Fo contents published in other studies suggests a more primitive composition with ~18 wt. % MgO may be equally suited to representing a Mauna Loa parental melt, and thermodynamic modelling has confirmed this. The proposed parental magma composition is therefore a good composition to use when investigating the melts produced in the deep mantle source below Hawaii.

Thermodynamic modelling using the estimated parental melt composition is consistent with fractionation of $Fo_{90.8\text{-}80.2}$ olivine (24.3% with 1 wt. % H_2O or 20.5% with no H_2O), cpx (7% with 1 wt. % H_2O or 12.6% with no H_2O), and spinel (~0.4%) in a melt which fractionates

down to 5 wt. % MgO. The fractionation of cpx can be seen in the ratios of CaO/Al_2O_3, Sc/Y, and Cr/Ni. The fractionation of some plagioclase (none with 1 wt. % H_2O or 11.6% with no H_2O) is also evident in some of the samples from the ratios of Al_2O_3/TiO_2 and Sr/Nd and a small amount of opx (0.4%) is predicted in low water models (<0.1 wt. % H_2O). Modelling suggests the occurrence of two distinct fractionation sequences: ol + sp + opx + cpx + plag and another with ol + sp + cpx, which could be achieved with minor variations in the water content (0 – 0.5 wt. %). The predicted proportions of fractionated cpx and plagioclase are higher than the amounts present in modal estimates, which are generally <5 wt. %, possibly reflecting that very few samples are fractionated to this extent.

From the literature collation of Mauna Loa data, it does not appear to matter whether the lava is erupted subaerially, or from submarine parts of the volcano as they are overall similar in terms of major elements. This vision of the Mauna Loa plumbing system contrasts with previous conceptual models in which more primitive submarine lavas erupt from feeder dikes that bypass the shallow summit reservoir. When samples are broken into dredge type locality, statistical tests reveal there are significant differences in the MgO-normalised trace element concentrations. The differences exist for 21 out of 27 of the trace elements tested, and the largest difference exists between the radial vent and rift zone pair, followed by the radial vent and slope pair. Some of the landslide samples may have an origin from a different volcano or different source according to trace element ratios, as they have variation beyond the effects of fractional crystallization (e.g. Zr/Nb, La/Yb, Sm/Nd). Trace element variation beyond fractional crystallization was further demonstrated when calculated mineral/melt partition coefficients showed fractionation between the moderately and highly incompatible elements.

So far, most discussion has related to the evolution of the shallow magma chamber. In the next section, the parental magma composition estimated in this study will be used to determine the possible range in source composition and degree of melting of the mantle to produce Mauna Loa primitive melts.

8 Discussion Part II: Deep magmatic process- melting of the source region below Hawaii.

The mantle source of Hawaii's volcanoes has been the subject of continued debate, and is often one of the first locations considered when models for the dynamics and chemistry of the mantle are considered. As discussed briefly in chapter 1, central arguments aim to reconcile the chemistry of the lavas with a possible mantle composition by varying pressure, temperature, and degree of melting, by varying the chemical composition through input of a crustal source, and/or by varying the phase proportions in the source that is melted. At present, the two most recurring proposals are that the Hawaiian plume has a greater potential temperature (the temperature equivalent at 1 bar) than surrounding mantle, which leads to thermal buoyancy and melting, possibly leading to thermal and therefore chemical zonation in the plume, and that there is some amount of recycled crustal component that is contributing geochemical heterogeneity to the lavas. Any model of the Hawaiian plume must take into account the existence of the Kea and Loa trends in terms of major element, trace element, and isotopic signatures, and the longer-term spatial and temporal trends of the Hawaiian-Emperor volcanism. The exact physical mechanisms and chemical contributions are still poorly understood e.g. (Jones et al., 2017).

This chapter will aim to reconcile the inferred parental magma composition with MgO contents of ~16-20 wt. % (Table 8.1) with melt compositions of various possible mantle sources including a range of peridotites and pyroxenites. This will be done by comparing the inferred parental magma with published experimental melt compositions and theoretical melt compositions calculated using the pMELTS software (Ghiorso et al., 2002). To address this goal, pMELTS calculations will be compared to experimental studies for the same parental compositions (spanning a range in olivine, pyroxene, and garnet assemblages) and pressures. The aim is to gain insight into the effects that the degree of melting, phase assemblages, and chemical proportions have on the consequent melt. Further to this, the experimental phase assemblages of a fertile peridotite will be used to calculate the trace element composition of the melt at each experimentally recorded fraction of melting. This will provide the opportunity to compare the possible processes, chemical compositions, and mineral assemblages that may have produced the chemical differences that are observed between the Kea and Loa track volcanoes.

8.1 Temperature and depth of melting of the Hawaiian plume

Many studies have focused on either chemical heterogeneities in the Hawaiian mantle plume, or variations in the thermal structure of the plume compared to that of ambient mantle to explain

the chemistry of erupted lavas. Sleep compiled data to investigate the volume, heat, and buoyancy flux for hotspots globally and found that Hawaii has the greatest buoyancy flux by far (8.7 Mg/s), an excess temperature of between 230-300 ˚C, and an erupted flux of 4 m^3s^{-1} (Sleep, 1990). Sleep also found that the average excess temperature of hotspots compared to that of the ambient asthenospheric mantle is approximately 200 ˚C. Watson and McKenzie modelled the Hawaiian plume using a fluid dynamical approach and suggested that a central potential temperature of 1558 ˚C can account for the volume and composition of the melt generated beneath Hawaii (Watson and Mckenzie, 1991). Watson and McKenzie also suggested that there is no temperature difference in the source region of Hawaiian tholeiites compared to that of MORB. Putirka has similarly argued that the primary driving force for the plume is thermal, rather than chemical in nature (Putirka, 2005). Putirka used olivine-liquid equilibria to infer that the temperature of the mantle where Hawaiian melts are generated must be significantly hotter compared to MORB mantle, finding that the Hawaiian plume could be as much as 250 ˚C hotter than the MORB source, at 1688 ˚C. This is consistent with a previous study (Liu and Chase, 1989) that suggested a temperature anomaly of 200-250 ˚C from numerical modelling simulations.

Falloon and co-authors have suggested that the minimum depth of melting below Hawaii is 60-90 km based on the occurrence earthquakes associated with historic Hawaiian volcanoes (Falloon et al., 1988). This is equivalent to a pressure of 1.7-2.7 GPa. Lee and co-authors have extended this from 60-180 km, or 2-5 GPa from solidi estimates based on thermobarometry using Si and Mg contents of lavas (Lee et al., 2009). Putirka has estimated a much greater depth of melting beneath Hawaii of 200-400 km (5.6-11.2 GPa) based on trace element ratios (Putirka, 1999).

Based on this brief review, it is evident that there are a wide range in the estimates of the temperatures and pressures of melting in the Hawaiian plume. By using a combination of experimental data, pMELTS modelling, and trace element modelling to compare to inferred parental magma compositions, we may be able to further constrain the pressure and temperature conditions of melting for Hawaiian volcanoes. In this section, experimental data from a variety of mantle source materials and a variety of depths is compiled, and the melts produced are compared to the parental melt composition determined in the previous section. The mantle source types encompass a variety of different peridotites and pyroxenites with variable amounts of garnet to encompass the range of imagined source compositions that have been suggested for Hawaii, and many of the source materials have been melted over a wide range of pressures.

8.2 Chemical heterogeneity within the Hawaiian plume

Further to the variables of pressure and temperature, there is considerable evidence for chemical heterogeneity within the Hawaiian plume based on the compositions of erupted lavas. Farnetani and Samuel have suggested that we should abandon the paradigms based on solely a thermal axisymmetric plume (i.e. thermal variation within the plume only, no chemical variation), and that fluid dynamical models are consistent with lateral filaments of chemical heterogeneity within the plume that present themselves in the erupted lavas (Farnetani and Samuel, 2005).

As described in chapter 1, the details as to the spatial arrangement of thermal or chemical heterogeneities within the plume have been debated e.g. (Hauri, 1996, Kurz et al., 1996). One argument proposes a concentrically zoned thermal and/or chemical structure with the plume being hotter in the centre and therefore the degree of melting may decrease toward the outer radius. Alternatively, it may entrain ambient mantle around the edges such that the plume core is enriched in Loa-type compositions and the outer margin contains a greater proportion of depleted mantle analogous to the MORB source. A second type of conceptual model is the idea that the plume may be bilaterally zoned, accounting for the parallel Kea and Loa volcanic tracks e.g. (Weis et al., 2011, Hofmann and Farnetani, 2013). In this scenario, the Loa and Kea volcanoes straddle a deep 'large low-shear-velocity province' (LLSVP), where the Loa trend volcanoes have the signature of the LLSVP while the Kea trend may reflect ambient upper mantle and as a result display a more MORB-like isotopic signature. Several recent studies have assumed a bilaterally zoned plume in which compositionally distinct components from the thermal boundary layer remain separated up to the surface e.g. (Weis et al., 2011, Hofmann and Farnetani, 2013, Farnetani et al., 2012). However, Jones and co-authors have countered the idea that deeply-sourced chemical heterogeneity could be the cause of the Kea and Loa tracks by showing that it is unlikely that any heterogeneous structure inherited from the lower-mantle could be mapped from geochemical observations at the surface (Jones et al., 2016), and that any memory of spatial distribution of lower-mantle heterogeneity will be lost during ascent. More recently, the Loa and Kea trends have been put into the context of the global plate tectonic environment (Jones et al., 2017), where the emergence of double track volcanoes at various hotspot tracks globally was found to coincide with a change in plate direction. This change in plate motion causes plume tilting, which allows varying depths of melting of chemical heterogeneities within the plume to be expressed laterally at the surface. Jones and co-authors suggest that the Kea track is the result of deep melting of peridotite, while the Loa track is the result of mantle pyroxenite formed through the melting of eclogite and subsequent reaction of those silicious melts with peridotite to form a secondary, low-Ca pyroxenite as imagined by Sobolev and co-authors (2005).

Chemical heterogeneity in the Hawaiian plume has been attributed to recycling of crustal materials into the mantle by many authors. One of the earliest papers suggesting that a recycled crustal component could explain the chemistry of Hawaiian volcanism was by Hofmann and White who suggested that altered oceanic crust is channelled into subduction zones whereby it enters the mantle with a composition that is essentially basaltic and sinks to the base of the mantle to form a layer of 'degenerate' crust (Hofmann and White, 1982). After this crust reaches a given thickness and age, radioactive heat production in the core heats this material until diapirs develop and rise into the upper mantle. Critically, Hofmann and White have suggested that the diapirs melt before the surrounding mantle, and then react with that mantle to form a secondary assemblage. They then suggest that this melt will inherit the major element compositions of the mantle, while the trace element assemblage remains fairly unchanged. Though there is not much further detail provided as to the physical mechanism of this process, their model does reconcile the high incompatible trace element concentrations of the lavas from Hawaii with the long-term depleted $^{87}Sr/^{86}Sr$ and $^{143}Nd/^{144}Nd$ isotopic values at relatively 'normal' degrees of melting (10-30%).

Hauri has further used correlations of Sr, Nd, Pb, and Os isotopic ratios with the abundances of SiO_2, TiO_2, Al_2O_3, CaO, and FeO to suggest the presence of a recycled crustal component in the Hawaiian plume. In particular, the high SiO_2 Ko'olau lavas must contain a significant fraction of SiO_2-rich melt derived by melting of mafic material in which olivine is not a stable phase (i.e. quartz-bearing garnet pyroxenite or eclogite) (Hauri, 1996).

Furthermore, Herzberg has suggested that the CaO and Ni contents of Hawaiian lavas are too low and too high respectively to be melts of a peridotite source (Herzberg, 2006). Herzberg explains the chemistry of Hawaiian lavas by invoking the presence of subducted oceanic crust in the plume, which has melted and reacted with mantle peridotite to produce a secondary garnet pyroxenite. Herzberg goes so far as to say there is no evidence for a peridotite source below Mauna Loa or Kilauea, using the narrow range in CaO contents expected for melts from a peridotite source as evidence. For example, Herzberg uses komatiites from Gorgona with 10 wt. % CaO along with experimental melts (Walter, 1998) from fertile peridotites with 10 wt. % CaO to infer a narrow range in CaO of peridotite melts.

Frey and co-authors have highlighted the trace element differences between the Kea and Loa trends by comparing the trace element compositions of various Kea and Loa trend volcanoes, including Mauna Kea, Kilauea, Mauna Loa, Lanai, and Ko'olau (Frey et al., 2016). They concluded that Kilauea tholeiites tend to be relatively enriched in LREE relative to HREE compared to those from Mauna Loa. Frey and co-authors also observe differences in some key

trace element ratios including higher Sr/Nd, Zr/Nb, and La/Nb for Loa-track lavas compared to Kea-track volcanoes. These ratios were used by Frey and co-authors to infer a higher proportion of recycled gabbro in the Loa-track volcanoes relative to the Kea track volcanoes. In contrast, a study by Hofmann and Jochum, which analysed the trace element concentration of six tholeiites from Mauna Loa and seven from Mauna Kea, emphasised the similarities in trace element compositions between Mauna Loa and Kilauea, and noted that Ba-Th-U-La data for Mauna Kea, Mauna Loa, Kilauea, Loihi, Haleakala, and Ko'olau all show characteristic depletion of Th and U relative to Ba and La. They suggest that this non-primitive fingerprint is a characteristic property of the Hawaiian source. They also confirm that the LREE abundances in tholeiites from Mauna Kea are about 50% higher in concentration than those from Mauna Loa, while the HREE are nearly identical in concentration, and that recycled oceanic gabbro mixed with ordinary mantle peridotite could contribute to the source of Hawaiian magmas.

Pietruszka and co-authors have also suggested that the Hawaiian plume contains significant proportions of recycled oceanic crust, with a factor of two variation in the proportion of this component from Loihi (8 – 11%) and Kilauea (9-16%) to Mauna Loa and Ko'olau (15-21%) (Pietruszka et al., 2012). They also found that tholeiitic lavas from Kilauea have higher Nb/La, Nb/Y, and Th/Ce compared to Mauna Loa, and they used these signatures to infer that the Kea trend contains mostly upper oceanic crust, which is gabbro-free and strongly dehydrated, while the Loa trend volcanoes are dominated by the lower-most portion of the subducted slab (gabbro rich).

Huang and co-authors outline the isotopic differences between Loa trend volcanoes (high $^{87}Sr/^{86}Sr$ and low $^{143}Nd/^{144}Nd$) and Kea trend volcanoes (low $^{87}Sr/^{86}Sr$ and high $^{143}Nd/^{144}Nd$), and show that these signatures are consistent with a greater abundance of recycled sediment-bearing oceanic crust in the Loa-trend volcanoes e.g. (Huang and Frey, 2005).

Trace element ratios in samples from this study do not correlate with Sr and Nd isotopes (Figures 6.8 and 6.9 isotope results section), indicating that the variation in the trace element ratios may be due to factors other than source chemistry. Given that incompatible trace elements are not fractionated greatly from one another by crystallization, a possible cause could be variation in degree of melting, a process which can greatly fractionate the highly incompatible elements from moderately incompatible elements. From previously mentioned studies, correlations between trace element ratios and isotopic signatures tend to occur over large spatial and temporal scales when comparing multiple volcanoes. From data acquired in this study, it appears that there may be variation in trace element ratios in the source of Hawaii's volcanoes, but only on the large scale. Some of the small scale variation in trace element ratios (as seen in

differences in Zr/Nb and Nb/Y of the landslide samples relative to other dredge locality types – figure 5.16 trace element results) may occur independently of source composition given lack of correlation with isotopes.

The addition of subducted oceanic crust was proposed by Falloon and co-authors who conducted experiments on the Hawaiian pyrolite composition (Falloon et al., 1988) originally by Green and Ringwood and later made synthetically for experiments by Jaques and Green (Green and Ringwood, 1963, Jaques and Green, 1979). Falloon and co-authors outline that in general, Hawaiian lavas have lower CaO and Al_2O_3 compared to MORB and higher FeO and TiO_2, and have found from their experiments that residual garnet is required in the source to explain the trace element composition of Hawaiian lavas, though major elements indicate equilibrium with harzburgite residua. Instead of melt from a recycled slab, they suggest that the presence of subducted slab in the mantle could oxidize CH_4 and H_2O-rich fluids, which could lead to volatile-fluxed melting and diapirism of the mantle, in turn leading to incipient melt-metasomatism of the asthenosphere below Hawaii. Importantly, Falloon and co-authors have outlined the 'garnet paradox' in their experimental study of Hawaiian pyrolite – this being that the major element composition of primitive Hawaiian lavas are in equilibrium with a harzburgite residue and not a lherzolite or garnet lherzolite, while the REE pattern requires residual garnet in order to fractionate the light from heavy REE.

The idea of a garnet paradox for Hawaiian volcanoes has evolved since then, with extensive later work by Yaxley and Sobolev. The fate of melt resulting from subducted oceanic crust was investigated (Yaxley and Green, 1998) in experiments that melted an eclogite composition assumed to represent subducted oceanic crust, followed by infiltration of the siliceous melt into the mantle peridotite. It was found that the eclogite melted at higher pressures than peridotites in an ascending plume, and that these melts may then react with the surrounding mantle to form an increasingly opx-rich mantle, while the residual eclogite becomes a bi-mineralic assemblage of cpx (mostly omphacite with jadeite and diopside components) and garnet. Yaxley and Green suggest that the opx-enriched mantle then melts and will retain the garnet trace element signature from the eclogite melt. The melts from the heterogeneous source will continue to react with the surrounding peridotite until the eventual mantle is a garnet lherzolite or garnet harzburgite, creating a source for OIB magmas. The final isotopic composition of the lavas produced will reflect the heterogeneous chemical history. Later, a study by Sobolev and co-authors went as far as to say there may not be any olivine present in the source of the Hawaiian plume, due to the difficulty in reconciling the high SiO_2 and Ni content and the low CaO/MgO ratio with melting of a peridotitic source (Sobolev et al., 2005). Sobolev and co-authors state that when even a relatively fertile peridotite melts, MgO contents are high in the melt with

correspondingly low SiO_2 contents, and Ni is buffered by olivine in the mantle such that Ni content cannot exceed ~500-600 ppm. The alternative offered by Sobolev and co-authors is a pyroxenite Hawaiian source formed from reaction of deep eclogite melts with peridotite until all olivine is reacted away. Under these conditions, Ni then becomes more incompatible in the olivine-free source.

Further to the major element composition of Hawaiian lavas, the high concentrations of Sr have been used to infer a pyroxenitic source for Hawaiian magmatism. The hypothesis by Yaxley and co-authors is that a subducted slab containing gabbro becomes entrained in the plume and is the first assemblage to melt producing a highly silicic melt. The silicic melt is dacitic in composition, will have a strong positive Sr anomaly, and will be out of equilibrium with the surrounding mantle causing it to react with peridotite to form a hybrid pyroxene + garnet lithology (Yaxley and Sobolev, 2007).

It is clear that for any explanation of the Hawaiian source, defining the phase assemblage of the source regions, mostly with respect to proportions of garnet and pyroxene, is fundamental to understanding the chemistry of Hawaiian magmatism. The major arguments have debated the degree to which olivine, pyroxene, and garnet control the chemistry of the erupted lavas, and many possible source variations have been suggested e.g. (Pietruszka et al., 2012).

The ratio of CaO/MgO is the basis of the software PRIMELTS2 model created by Herzberg and Asimow, which is used to distinguish melts derived from a peridotite source from those derived from a pyroxenite source (Herzberg and Asimow, 2008), and to therefore infer that Hawaii must have a pyroxenitic component e.g. (Rhodes et al., 2012). Rhodes and co-authors have presented the major element composition of melts which come from either a pyroxenite source or a peridotite source in terms of CaO and MgO content. They state that samples from a peridotite source will generally have higher CaO for a given value of MgO because CaO is compatible in the pyroxene phase whereas it is incompatible in olivine.

Rhodes and co-authors' method to distinguish pyroxene-derived from peridotite-derived lavas by CaO content at a given MgO was applied to samples from this study (Figure 8.1). It is clear that the CaO contents of samples in this study are low enough for a given MgO to fall into the possible pyroxenite source category, with the red line below defining the bounds between the two categories.

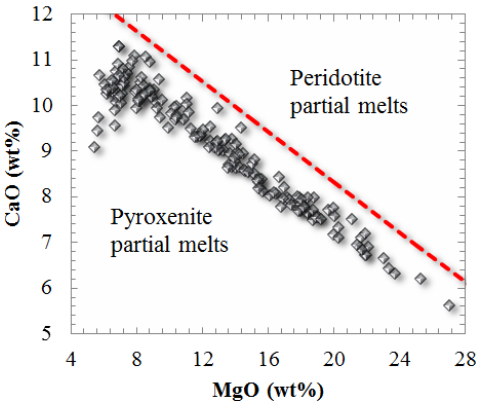

Figure 8.1 The line defining peridotite-derived from pyroxenite-derived lavas (Rhodes 2012-Compositional diversity of Mauna Kea).

Rhodes notes however, that the samples which lie below the line could also be peridotite partial melts that have had pyroxene removed if crystallization occurs during ascent. Significant augite fractionation only occurs when the magma has fractionated down to approximately 7.5 wt. % MgO e.g. (Herzberg, 2006) however, and the Mauna Loa magmas lie below the 'peridotite-pyroxene' line irrespective of MgO content.

A second method (Yang and Zhou, 2013) for determining pyroxenite versus peridotite source for basalts yielded similar results when applied to samples from this study. The method by Yang and Zhou uses the major element ratios FeO/CaO and MgO/SiO_2 of whole rock data from multiple experiments performed on peridotite and pyroxenite melts over the last 30 years up until the year 2013. They include 726 peridotite melts and 514 pyroxenite melts. This has allowed the authors to calculate a value based on whole rock major element data known as an FC3MS value (FeO/CaO-3*MgO/FeO), which is a pressure-independent value (the authors show that when FC3MS is plotted against pressure, there is no correlation – Yang and Zhou 2016 - Supplementary Information) that can separate pyroxenite-derived basalts from those that are derived from a peridotite source. The authors have confirmed two significant populations of data in the experiments studied using a T-test, and found that peridotite-derived melts have an average FC3MS value of -0.07 (σ = 0.254) and pyroxenite-derived melts will have an average FC3MS value of 0.46 (σ = 0.481) (Figure 8.2 a,b). In addition, the authors have determined FC3MS values for a representative MORB and continental OIB from China and Mongolia (Figure 8.2 c,d).

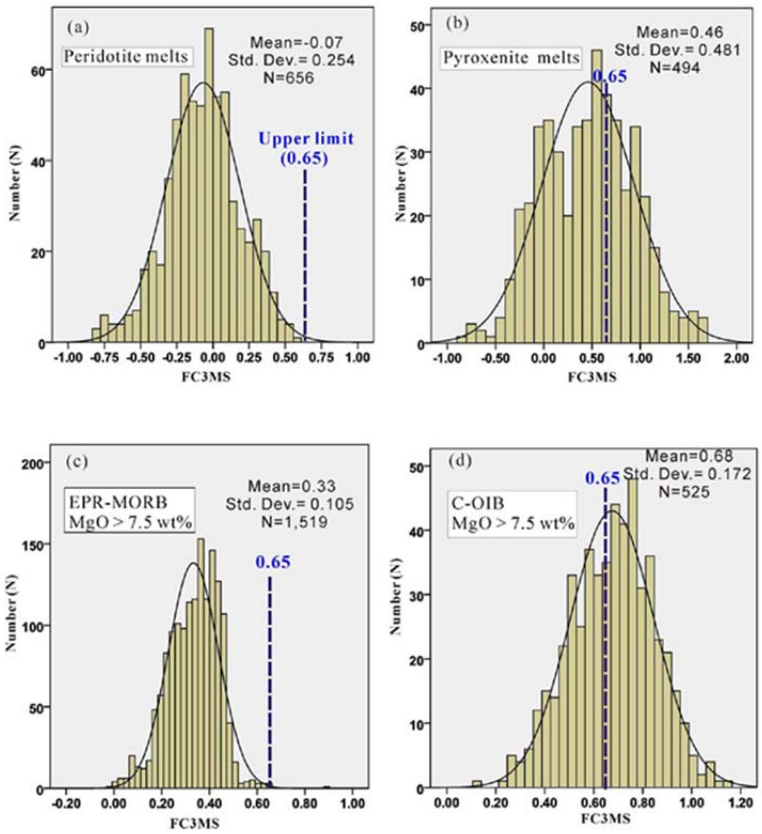

Figure 8.2 Distribution of peridotite and pyroxenite melts (a,b), and natural MORB and continental OIB (c,d) in terms of Fe, Ca, Mg, and Si (FC3MS) from Yang and Zhou (2013).

The FC3MS values were calculated for Mauna Loa samples, and the average was found to be 0.58 (σ = 0.17), as shown in (Figure 8.3). The data have been plotted in a histogram showing the probability density of FC3MS values, which was derived by counting the number of samples for a given FC3MS value. The histogram was fitted with a standard Gaussian distribution curve, which appears to fit the majority of data well, aside for a slight positive tail towards higher FC3MS values. The probability distributions (above) of peridotite and pyroxenite derived melts have been plotted for comparison. From the probability distributions, it can be said that the probability that the average Mauna Loa basalt is derived from a pyroxenite source is 10.21 times greater than the probability it is derived from a peridotite source.

For reference, Mauna Loa literature data has an average FC3MS value of 0.61 (σ = 0.24) from over 400 samples from nine studies, and Kilauea literature lavas have an average FC3MS value of 0.73 (σ = 0.26) from over 200 samples from nine studies. This would indicate that Kilauea lavas are even less likely to have evolved from a peridotitic source than the Mauna Loa lavas.

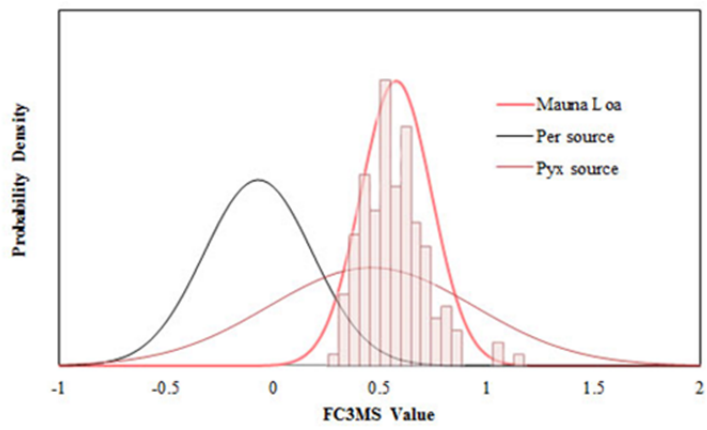

Figure 8.3 FC3MS distribution for Mauna Loa (pink) against peridotite sources (black) and pyroxenite sources (red).

When the FC3MS model as well as similar models by Herzberg and Asimow, which were later adapted by Rhodes 2012, are used to assess the differences between Mauna Loa and Kilauea, it is clear that Kilauea is no less likely to come from a pyroxenite source than Mauna Loa based on major element chemistry. It can be seen that Kilauea has generally the same CaO for a given MgO as Mauna Loa (Figure 8.3), and has an even higher FC3MS than Mauna Loa. This is in direct contrast with the most recent study by Jones and co-authors which suggests that Kea-track volcanoes are the result of melting of higher pressure ambient mantle, while Loa-track volcanoes are the result of melting of a pyroxenite source formed by the reaction of eclogite with mantle peridotite (Jones et al., 2017).

8.3 Sr, Nd, and Pb isotopes

In addition to the major and trace element compositions of the melts, the isotopic signatures are highly variable between Hawaiian volcanoes and must be accounted for in any model for the petrogenesis and structure of the Hawaiian plume. Sr and Nd isotopic compositions were obtained for several representative samples from this study, as well as a thorough literature compilation of Sr, Nd, and Pb isotopes for lavas from Mauna Loa and Kilauea (see isotope results section). A brief overview of the global mantle end members will be given in this section, followed by a review of isotopic characteristics of Hawaii and more specifically Mauna Loa and Kilauea.

8.3.1 Mantle end-members

The isotopic signature of Hawaiian volcanoes lies in the so called 'PREMA' (Prevalent Mantle) (Zindler and Hart, 1986) or later named 'FOZO' (Focal Zone) (Hart et al., 1992) region of the global isotopic array (figure 1.4 chapter 1). The FOZO composition is thought to be

represented to some degree in many oceanic basalts, and is therefore thought to represent a relatively primitive region of Earth and to possibly contain material from the lower mantle (Hart et al., 1992). The evidence for this is that many OIB samples appear to form binary mixing arrays that radiate from 'FOZO' (Hofmann, 2014). It is neither particularly enriched or contaminated with oceanic crust, continental crust, or pelagic sediment, and nor is it depleted due to continuous melting in the same way that depleted MORB mantle (DMM) is. It is thought that all mantle types are derived in some way from this isotopic composition. Stracke and co-authors have since changed the composition of FOZO to make is much higher in $^{206}Pb/^{204}Pb$ and closer to the HIMU field compared to previous estimates such that lavas from Kilauea and Mauna Loa no longer reside within the FOZO field (Stracke et al., 2005). The study by Stracke and co-authors demonstrated that the samples collated here from literature Kilauea and Mauna Loa studies (figure 6.11 isotopic results section) sit well within the field of Atlantic, Pacific, and Indian MORB in terms of $^{143}Nd/^{144}Nd$ and $^{206}Pb/^{204}Pb$ (Figure 8.4) as well as $^{87}Sr/^{86}Sr$ and $^{208}Pb/^{204}Pb$.

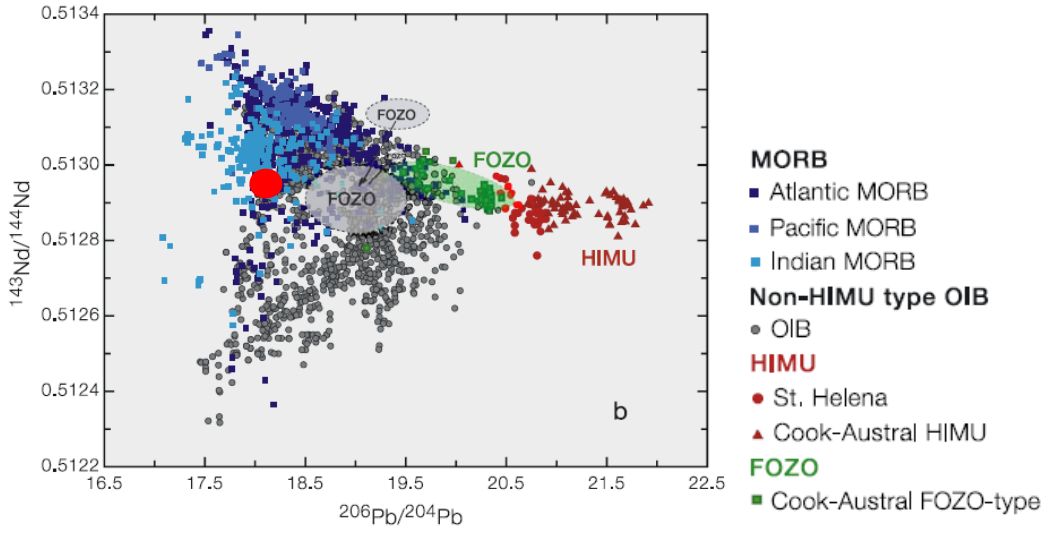

Figure 8.4 $^{206}Pb/^{204}Pb$ vs. $^{143}Nd/^{144}Nd$ isotopic array from Stracke et al (2005). Samples from this study plot approximately where the red circle is.

As documented originally by Tatsumoto, there is great isotopic variability between the Hawaiian volcanoes (Tatsumoto, 1978). Various possibilities for the differences in OIB and specifically Hawaii compared to other ocean floor basalts have been suggested over a number of decades. Staudigel and co-authors summarized the total range in $^{87}Sr/^{86}Sr$ and $^{143}Nd/^{144}Nd$ of ocean floor basalts globally and have shown that the Hawaiian Islands span a large proportion of this total range, with significant overlap with mid-ocean ridges. The Hawaiian isotopic signature overlaps with the Mid-Atlantic ridge at high $^{143}Nd/^{144}Nd$ and low $^{87}Sr/^{86}Sr$ and Kerguelen -

another archetypal hotspot – with low relative $^{143}Nd/^{144}Nd$ and high $^{87}Sr/^{86}Sr$ (Staudigel et al., 1984). Staudigel and co-authors suggest that the Hawaiian source must consist of at least three isotopically distinct materials, which are best represented in the volcanoes Ko'olau, Kilauea, and Honolulu series volcanics. It was suggested that the Kilauea component represents a deep plume signature while the Ko'olau and Honolulu components may be derived from the lithosphere. Staudigel and co-authors also show that the range of $^{206}Pb/^{204}Pb$ for the Hawaiian Islands is on the low end of the spectrum compared to other OIB, lying within the field of Indian MORB and overlapping with the lowest $^{206}Pb/^{204}Pb$ Mid-Atlantic Ridge samples.

Kurz and Kammer analysed He, Sr, and Pb isotopes of Mauna Loa lavas and found the three isotopic systems to be coupled, and therefore not a consequence of degassing but representative of the source region (Kurz and Kammer, 1991). They also found there to be a minimum of three sources involved in Mauna Loa lavas; a plume source (Loihi end-member) mixed with a MORB source was able to explain the majority of the variance according to Kurz and Kammer, though the distinct isotopic signature of the historical lavas required lithospheric involvement.

Frey and Rhodes have shown that Kilauea has systematically higher incompatible major and trace elements than Mauna Loa and have found this to be the result of differences in degree of melting because there is little correlation between major elements and trace element ratios with isotopic composition (Frey and Rhodes, 1993). Specifically, the decoupling of Rb/Sr with $^{87}Sr/^{86}Sr$ and Sm/Nd with $^{143}Nd/^{144}Nd$ suggests that the parent/daughter ratios have been modified recently by processes such as degree of melting or metasomatism, while variation in SiO_2 within the spinel field is associated with variation in melting depth. The attribution of major element variation to variable depth of melting is consistent with the findings of Klein and Langmuir who showed that geochemical variation in MORB, in particular Na and Fe contents, was dependent on depth of melting (Klein and Langmuir, 1987). Contamination with oceanic lithosphere was ruled out as a potential cause for isotopic variation at Hawaii based on Sr and Pb isotopes. The most important conclusion from Frey and Rhodes is that the trace element and isotopic signatures appear to be decoupled from each other, indicating that the process causing the trace element signature is not necessarily the same as that causing the isotopic signature.

A later study by Bennett and co-authors has described the isotopic signature of Loa trend volcanoes using Os and Pb isotopes from seven volcanic centres including Ko'olau, Kahoolawe, Kohala, Hualalai, Mauna Loa, Loihi, and Kilauea (Bennett et al., 1996). Bennett and co-authors found that binary mixing arrays are formed in Os versus Pb isotopic ratios, with Kilauea comprising the low $^{187}Os/^{188}Os$ and high $^{206}Pb/^{204}Pb$, $^{206}Pb/^{204}Pb$, and $^{208}Pb/^{204}Pb$, and Ko'olau

comprising the high $^{187}Os/^{188}Os$ and low $^{206}Pb/^{204}Pb$, $^{206}Pb/^{204}Pb$, and $^{208}Pb/^{204}Pb$ end-members. It was suggested that the addition of recycled oceanic crust into a depleted mantle could be the source of the Ko'olau component, while the Kilauea component represents a depleted source similar to DMM.

More recently, the isotopic heterogeneity in the plume has been investigated in terms of plume structure (DePaolo et al., 2001). Nd and He isotopic maps were created through analysis of lavas from Mauna Kea and Mauna Loa and were found to be 'broadly consistent' with axisymmetric geochemical structure rather than north-east south-west bilateral symmetry. Bryce and co-authors have suggested a radially-zoned plume structure through comparisons of Nd, Sr, Pb, Hf, and Os isotopes between Mauna Loa and Mauna Kea volcanoes, also discounting a bilateral asymmetry (Bryce et al., 2005). Lower εNd of Mauna Loa compared to Kea trend may be due to Mauna Loa being closer to the plume core, and that the differences between the two volcanoes can be explained by an 'anomalous blob' in the Mauna Loa source. They suggest that the axial part of the plume may contain recycled oceanic crust mixed with lower mantle while the rest of the plume may consist of a more depleted mantle source similar to DMM, and that a significant amount of vertical heterogeneity must exist in the plume to account for the temporal isotopic variation.

Juxtaposed to the idea of a radially zoned plume is a bilaterally zoned plume. Hofmann and Farnetani show that evidence from Pb isotopes suggests that a 'plum pudding model' where there are heterogeneous blobs of material within the plume cannot explain the bilateral differences in Pb isotopes or trace element ratios between the Kea and Loa trends. Pb isotopes are the clearest discriminant between the Kea and Loa tracks, and Hofmann and Farnetani show that this occurs independently of melt fraction as there is no correlation between the trace element ratio La/Yb with Pb isotopic signature (Hofmann and Farnetani, 2013). They suggest that the plume may be split into two parallel conduits surrounded by a peripheral rim of relatively depleted material, which starts at the buoyant thermal boundary layer and remains separated upon ascent to the surface.

In contrast, Frey and co-authors have shown that there *are* correlations between $^{143}Nd/^{144}Nd$ and $^{206}Pb/^{204}Pb$ isotopes with the trace element ratios Sr/Nd, Zr/Nb, La/Nb, and Th/La (Frey et al., 2016), perhaps because they selected relatively fewer volcanoes (5 compared to 16 in the Hofmann and Farnetani study). The study used samples from a range of volcanoes on both the Kea and Loa trends including Kilauea, Mauna Kea, Mauna Loa, Lanai, and Ko'olau. They attributed this to input of a Loa component, possibly a delaminated lower continental crust component with a large proportion of plagioclase. The high Sr/Nd and La/Nb ratios and high

$^{208}Pb/^{206}Pb$ alongside low $^{143}Nd/^{144}Nd$ and $^{206}Pb/^{204}Pb$ were used to infer that gabbro was the major component of the Loa source, though the inverse trend between Sr/Nd and $^{143}Nd/^{144}Nd$ discounted oceanic gabbro and implicated lower continental crustal gabbro was a potential candidate for the Loa component. Frey and co-authors have suggested a complex geological history to account for the chemistry of the Kea and Loa volcanic trends. They suggest that there are three parts to the Loa component signature, involving gabbroic cumulate added to the mantle through subduction or delamination, an ancient pelagic sediment to account for the $^{176}Hf/^{177}Hf$ and $^{143}Nd/^{144}Nd$ ratios, and a third component which needs to be high in $^{87}Sr/^{86}Sr$ which must have undergone a relatively recent event (<1 Ga) to lower the Rb/Sr as the $^{87}Sr/^{86}Sr$ has been decoupled from the Rb/Sr ratios. Frey and co-authors also note that variable degree of melting cannot be the cause for the enriched LREE and buffered HREE abundances, as melt degrees ≤ 5% would be required to explain the trace element patterns, but not produce large enough volumes of magma for Hawaii.

8.3.2 Kilauea and Mauna Loa

The isotopic compositions of Hawaii suggest that there is a range in source composition from volcano to volcano and also within volcanoes. Mauna Loa typically displays a more isotopically enriched signature compared to Kilauea, with higher $^{87}Sr/^{86}Sr$ and lower $^{143}Nd/^{144}Nd$ in comparison e.g. Frey and Rhodes (1993). The difference in isotopic signature has been interpreted to mean that there is a significant source difference between Kilauea and Mauna Loa, with Kilauea having a more depleted isotopic signature than Mauna Loa, and Mauna Loa displaying evidence of a recycled component, the nature of which was discussed above.

This is interesting however, because Kilauea is less depleted in its trace element signature than Mauna Loa, and many studies have shown that the slope of Kilauea trace element REE pattern is much steeper, because the LREE are much more enriched than Mauna Loa's, while the HREE remain constant. There are many possible answers for this, one being that while Kilauea may have a more depleted source it could be that it has also undergone a smaller degree of partial melting. This would be consistent with the overall melt flux calculations and volumetric estimates of Kilauea's lava production, with one study showing the total volume of Kilauea to be 31.6 x 10^3 km^3 while Mauna Loa has a total volume of 74.0 x 10^3 km^3 (Robinson and Eakins, 2006).

In this study, there are two main clusters that can be seen in the isotopic data (figure 6.2 isotope results). The majority fall in one slightly more depleted group (high $^{143}Nd/^{144}Nd$ and low $^{87}Sr/^{86}Sr$) while there are six samples which fall in a slightly more enriched group (low $^{143}Nd/^{144}Nd$ and high $^{87}Sr/^{86}Sr$). There is no obvious correlation between isotopic signature and

dredge type locality or with dredge number, indicating that the isotopic heterogeneity in the source is not spatially differentiated in the erupted lavas. The samples from this study span a large part of the range of historical Mauna Loa lavas in terms of Sr and Nd isotopes (figure 6.11 isotope results) indicating they are probably a representative sub-sample of Mauna Loa lavas in general. There is also no correlation between parent daughter abundance ratios with isotopic ratios for example Rb/Sr and $^{87}Sr/^{86}Sr$ or Sm/Nd and $^{143}Nd/^{144}Nd$. Lack of correlation indicates that the parent – daughter ratios have been affected by a partial melting process which has differentiated them beyond the original source composition (Frey and Rhodes, 1993).

Similarly to trace element ratios, there is no correlation between major element oxides and the Sr and Nd isotopes (figures 6.3-6.5 isotope results). Major element and isotopic correlations are generally inferred on larger scale comparisons, for example when comparing overall averages of multiple volcanoes. It therefore appears that on the small scale of Mauna Loa the major elements do not vary significantly due to source variation, as was the case with trace element ratios.

8.4 Comparison of experimental data with pMELTS results and Mauna parental magma

Possible mantle source compositions were investigated using literature experimental data and pMELTS software through the alphaMELTS interface in order to determine if the estimated parental magma composition could be produced by melting of any of those sources. This approach enabled the comparison of inferred Mauna Loa parental melts to experimental melt compositions from a variety of sources, as well as the opportunity to investigate the application of pMELTS software to a mantle melting problem. The parental magma compositions used here are the same as those used as the 16 – 20 wt. % starting composition in the shallow crystallization modelling from chapter 7. For the purposes of this exercise it is assumed that the parental melts are also a primary melt that was effectively in equilibrium with mantle residue. This approach has previously been investigated by Eggins, who calculated a primary magma composition for Kilauea by adding olivine to an evolved melt with 9.5 wt. % MgO until the melt was in equilibrium with an olivine with $Fo_{90.5}$ producing a melt with 15.98 wt. % MgO (Eggins, 1991). Eggins' primary melt composition was melted in experiments over a pressure range of 1 – 3.5 GPa. It was found that olivine was the liquidus phase for pressures near to 2 GPa, then between 2 – 2.5 GPa opx becomes the liquidus phase, followed by cpx at pressures up to 3.5 GPa. Above 3.5 GPa garnet becomes the liquidus phase. Eggins' melting experiments suggest that primary Kilauea melts are in equilibrium with harzburgite residues at 2 GPa and ~1450 °C, where importantly garnet is not stable.

Here, we have used not only the 16 wt. % MgO magma composition in equilibrium with the highest forsterite olivine found at Mauna Loa, but an 18 and 20 wt. % composition (found to be in equilibrium with Fo_{90} olivine at 2.68 GPa in melting experiments of Hawaiian tholeiite (Maaloe, 2004)). Further to this, the highest Fo olivine observed from Hawaii has Fo # 91.3 (Garcia et al., 1995), which the MELTS program suggests would be in equilibrium with a melt containing approximately 20 wt. % MgO. It is also important to provide a higher estimate for a possible parental magma because the MgO content of lavas sampled after a volcanic eruption will be a minimum estimate of a mantle primary magma, as some olivine may have fractionated upon ascent to the surface.

It has been shown that high MgO magmas will contain large proportions of olivine phenocrysts after ascent to the magma chamber due to the associated high flow rates (Huppert and Sparks, 1985), while lower MgO basalts will contain fewer because of their higher viscosities. Huppert and Sparks show however, that any crystals formed during ascent should remain suspended in the magma with no loss of crystals occurring. Parental magmas can differ from their primary magmas due to reaction of the melt with the mantle during ascent, whereby reaction with mantle pyroxenite may alter the SiO_2 content (Hauri, 1996). Hauri has shown that the correlation of SiO_2 with higher $^{87}Sr/^{86}Sr$ and lower $^{143}Nd/^{144}Nd$ as well as elevated Os isotope ratios, indicates there is minimal mantle contamination of the Hawaiian plume. Furthermore, the possibility of contamination of magmas by local, seawater-altered Pacific crust has been discounted (Lassiter and Hauri, 1998) because the Os and Pb isotope composition of the lower Pacific crust precludes its generation of the Kea end-member by assimilation. Generation of the Kea end-member by local Pacific lithospheric mantle was also discounted by Lassiter and Hauri. Assuming minimal loss of olivine phenocrysts and minimal mantle contamination during ascent, it is valid to say that the inferred Mauna Loa parental magmas may remain relatively unchanged from their original primary mantle melts.

The melting behaviour of some peridotites and pyroxenites was investigated by comparing literature experimental melt compositions and pMELTS outputs while varying the pressure, temperature, and style of melting i.e. fractional versus batch (Figure 8.5-Figure 8.19). The mantle compositions were chosen to be from both sides of the thermal divide that separates rock types in which either olivine (silica-undersaturated) or quartz/coesite is stable (silica-saturated), but never both at the same time. The two sides of the thermal divide have been expressed as hypersthene (Hy) – (diopside (Di) + jadeite (Jd))$_{ss}$ projected from garnet (Ga) onto the face (Di+Jd)$_{ss}$ – Quartz (Qz) – Olivine (Ol) (Yaxley and Green, 1998). The thermal divide separates high SiO_2 eclogite-sourced liquids from the nepheline-normative picritic liquids from a lherzolitic source.

Theoretical melting using the pMELTS software was modelled using the same pressures and starting compositions as those used in the respective experimental study (

Table 8.4), with variable temperatures and solidus phase stabilities. Trace elements were also modelled using the software assuming the partition coefficients of McKenzie and O'Nions (1991, 1995). Near-perfect fractional, adiabatic, isentropic melting was tested first, in an attempt to investigate melting of a material in an upwelling plume. Each melt fraction was removed from the source and kept separate, and melting occurred over a range of pressures from the starting pressure to the surface. Temperature gradually decreased as pressure decreased. The output for the fractional melt model was then used to estimate an accumulated fractional melt composition where each melt fraction is added to the total melt and the melt composition becomes an average of the accumulated melt fractions. In addition, isobaric equilibrium melting was modelled in an attempt to recreate conditions in a melting experiment where pressure is kept constant, the melt is produced by increasing temperature, and the melt remains in contact with the starting material.

Sources considered include various fertile peridotites and pyroxenites within either the olivine or coesite stability fields, including:

MORB pyrolite (MPY)- This is a theoretical composition originally determined to be the source of MORB magmas by Green and Ringwood from experimental studies (Green and Ringwood, 1967). It was suggested that the melt was saturated in olivine + aluminous pyroxene at 1.35 GPa, which was the criteria for a melt segregated from a mantle lherzolite. They produced this by adding together one part primitive MORB to 3 parts refractory harzburgites (Green and Falloon, 1998).

Hawaiian pyrolite (HPY)- A theoretical composition similar to MPY but made from a combination of refractory harzburgite and Kilauea Iki olivine tholeiite. At 2 GPa this yields a phase assemblage of 54.5% olivine, 15% opx, 0.5% spinel, and 30% melt (by weight) (Green and Falloon, 1998). HPY has a slightly lower olivine/orthopyroxene ratio than MPY. The Green 2015 estimate for the sub-solidus mineralogy of HPY is olivine > orthopyroxene > clinopyroxene, with a pressure-dependent phase which is plagioclase at low pressure, spinel at intermediate pressure and garnet at higher pressure (Green, 2015).

Peridotite KLB-1- Originally described by Takahashi, KLB-1 was chosen in their study to investigate mantle melting because it represents an undepleted, primitive mantle composition in the form of a natural spinel lherzolite and was available in large quantities (Takahashi, 1986).

Primitive mantle (PM)- Originally described by (Sun and McDonough, 1989) this is another primitive mantle composition which was derived from the behaviour of trace and major elements during depletion of the mantle, and represents an estimated composition of the bulk silicate Earth before differentiation of the continental crust. A peridotite (KR4003) with similar composition was later used in melting experiments by Walter (1998).

HZ1- an experimental peridotite (Grove et al., 2006) which was produced from an approximated undeleted primitive mantle composition (Hart and Zindler, 1986). This composition is very similar to MPY, except it contains 0.03 wt. % K_2O compared to 0% in MPY. This is a mantle lherzolite, which was originally derived from measured major and REE abundances of natural mantle lherzolites. The experiments by Grove and co-authors allowed for 14.5 wt. % water to be added, and so these experiments were designed to investigate flux melting of the mantle wedge above the subducted oceanic slab, although the anhydrous version was used in the pMELTS work.

MIX1G- The composition was derived from a mix of two natural pyroxenites from the Balmuccia massif (Shervais and Mukasa, 1991), and was later synthesized for an experimental study on garnet pyroxenites (Hirschmann et al., 2003). This composition was also used in a study (Lambart et al., 2016) as a starting composition for a representative pyroxenite because it is close to the average composition of 431 literature pyroxenite compositions, and pMELTS can reproduce its solidus and super-solidus phase relations, according to Lambart and co-authors.

KG2- A pyroxenite composition made by mixing peridotite and MORB in a mixture of 2:1 (Kogiso et al., 1998) to investigate basalt genesis through the mixing of peridotite and basalt. This mixture was melted during experiments at 1.5 – 3 GPa to investigate possible sources of OIB.

G2- This composition is a quartz eclogite that is a good approximation for subducted oceanic crust (Pertermann and Hirschmann, 2003). This composition was melted at 2-3 GPa in order to investigate the effects of melting recycled oceanic crust in the mantle.

GA2- Produced by Spandler and co-authors, this composition represents altered MORB, with slightly higher TiO_2 contents to promote rutile saturation (Spandler et al., 2017). This was melted experimentally at 3-5 GPa by Spandler and co-authors.

Out of these, Hawaiian pyrolite, primitive mantle (KR4004 and KLB-1), MIX-1G, KG2, and GA2 are elaborated on more fully below as these represent a diverse suite of potential mantle sources including fertile peridotite, common mantle pyroxenite, pyroxenite as a by-product of mixing recycled oceanic crust with peridotite, as well as the recycled slab component itself.

Table 8.1 Inferred Mauna Loa parental magma at 16, 18, and 20 wt. % MgO. (Trace elements in PPM, major element oxides in wt. %).

	Mauna Loa parental magma							
at 16% MgO	SiO_2	48.92	Be	0.72	Nb	7.37		
	TiO_2	1.70	Sc	26.12	Mo	0.550	Gd	4.25
	Al_2O_3	10.57	V	246	Sn	1.20	Dy	3.96
	FeO_t	10.86	Co	75.26	Sb	0.024	Ho	0.768
	MnO	0.169	Ni	755	Cs	0.052	Er	2.02
	MgO	15.96	Cu	103	Ba	54.65	Yb	1.63
	CaO	8.23	Zn	98.13	La	6.76	Lu	0.229
	Na_2O	1.749	Ga	15.51	Ce	17.64	Hf	2.49
	K_2O	0.275	Rb	4.29	Pr	2.58	Ta	0.498
	P_2O_5	0.177	Sr	224	Nd	13.07	Pb	0.619
	Cr	878	Y	21.21	Sm	3.77	Th	0.434
	Li	4.99	Zr	101	Eu	1.32	U	0.153
at 18% MgO	SiO_2	48.30	Be	0.66	Nb	6.67		
	TiO_2	1.52	Sc	24.75	Mo	0.515	Gd	3.89
	Al_2O_3	9.92	V	228	Sn	1.08	Dy	3.65
	FeO_t	10.78	Co	79.97	Sb	0.022	Ho	0.710
	MnO	0.17	Ni	912	Cs	0.042	Er	1.88
	MgO	18.04	Cu	96	Ba	49.05	Yb	1.51
	CaO	7.81	Zn	96.63	La	6.07	Lu	0.214
	Na_2O	1.65	Ga	14.43	Ce	16.02	Hf	2.36
	K_2O	0.25	Rb	3.90	Pr	2.36	Ta	0.413
	P_2O_5	0.15	Sr	207	Nd	11.90	Pb	0.571
	Cr	998	Y	19.43	Sm	3.41	Th	0.407
	Li	4.45	Zr	95	Eu	1.22	U	0.140
at 20% MgO	SiO_2	47.48	Be	0.59	Nb	8.32		
	TiO_2	1.47	Sc	23.07	Mo	0.470	Gd	3.67
	Al_2O_3	9.26	V	210	Sn	1.02	Dy	3.29
	FeO_t	10.88	Co	83.82	Sb	0.029	Ho	0.632
	MnO	0.169	Ni	1142	Cs	0.048	Er	1.68
	MgO	19.95	Cu	88	Ba	58.43	Yb	1.33
	CaO	7.45	Zn	93.56	La	7.23	Lu	0.186
	Na_2O	1.494	Ga	13.26	Ce	18.27	Hf	2.23
	K_2O	0.249	Rb	4.59	Pr	2.58	Ta	0.562
	P_2O_5	0.155	Sr	211	Nd	12.38	Pb	0.574
	Cr	1020	Y	17.03	Sm	3.31	Th	0.505
	Li	4.14	Zr	91	Eu	1.18	U	0.161

Table 8.2 Major element starting compositions of mantle melting models (wt. %).

	KR4003	PM	MIX1G	KLB-1	KG2	HPY	GA2
SiO_2	44.9	44.9	45.6	44.59	46.22	45.1	49.68
Al_2O_3	4.26	4.44	15.2	3.59	7.69	3.6	16.94
FeO_t	8.02	8.03	7.8	8.1	9.22	9.54	9.71
MnO	0.13	0.13	0.15	0.12	-	0.1	-
MgO	37.3	37.71	16.67	39.22	28.83	36.6	8.08
CaO	3.45	3.54	11.48	3.44	6.05	3.3	9.28
Na_2O	0.22	0.36	1.4	0.3	1.11	0.5	3.34
Cr_2O_3	0.41	0.38	0.11	-	-	-	-
TiO_2	0.16	0.2	0.9	0.16	0.57	0.7	1.82
NiO	0.24	0.25	-	0.25	0.17	0.3	-
K_2O	0.09	0.03	0.04	0.02	0.09	0.13	0.37

Table 8.3 Trace element starting compositions for mantle melting models (ppm).

	KR4003	PM	MIX1G	KLB-1	KG2	HPY	GA2
P	-	91.7	44	-	-	262	-
Ni	-	1965	609	-	-	-	92
Co	-	-	-	-	-	-	43
Sc	-	-	82	-	-	-	39.8
V	-	-	245	-	-	-	309
Cr	-	2600	-	-	-	-	249
Ga	-	-	-	-	-	-	17.5
Mn	-	822	-	-	-	-	-
Cs	-	0.032	-	-	-	-	0.034
Tl	-	0.005	-	-	-	-	0.02
Rb	-	0.635	-	0.06	1	-	2.88
Ba	-	6.989	-	4.1	-	-	-
W	-	0.02	-	-	-	-	0.12
Th	-	0.085	-	0.004	0.14	-	0.404
U	-	0.021	-	0.008	0.045	-	0.119
Nb	-	0.713	-	0.15	1.85	-	5.24
Ta	-	0.041	-	-	-	-	0.34
La	-	0.687	-	0.064	1.78	-	5.21
Ce	-	1.775	-	0.41	5.23	-	14.86
Pb	-	0.185	-	0.12	0.27	-	0.57
Pr	-	0.276	-	0.11	0.82	-	2.24
Mo	-	0.063	-	-	-	-	0.46
Sr	-	21.1	182	11.5	50.67	-	129
Nd	-	1.354	-	0.8	4.54	-	12.03
Sm	-	0.444	-	0.38	1.53	-	3.82
Zr	-	11.2	51	6.3	43.17	-	116.9
Hf	-	0.309	-	-	-	-	2.79
Eu	-	0.168	-	0.152	0.55	-	1.36
Gd	-	0.596	-	0.66	2.1	-	4.99
Tb	-	0.108	-	0.122	0.38	-	0.9
Dy	-	0.737	-	0.86	2.6	-	6.08
Li	-	1.6	-	-	-	-	6.5
Y	-	4.55	-	4.7	15.4	-	36.8
Ho	-	0.164	-	0.19	0.55	-	1.28
Er	-	0.48	-	0.62	1.68	-	3.79
Tm	-	0.074	-	-	-	-	-
Yb	-	0.493	-	0.62	1.62	-	3.63
Lu	-	0.074	-	0.098	0.24	-	0.53

Table 8.4 Literature melt compositions from experimental studies (cited in the text) on a range of mantle compositions. Ol = olivine, o = orthopyroxene, c = clinopyroxene, g = garnet, s = spinel, k = potassium feldspar, q = quartz, co = coesite, and r = rutile.

	KR4003	KR4003	KR4003	KR4003	KR4003	KR4003	KR4003	KR4003	HPY	HPY	HPY
% melt	14	19	24	37	53	9	13	39	10	14	12
P (Gpa)	3	3	3	3	3	4	4	4	2	2	2
Temp C	1515	1530	1540	1580	1630	1590	1610	1660	1400	1450	1500
SiO_2	46.17	46.66	46.91	48.98	47.96	46.38	45.52	46.17	46.67	46.09	48.15
TiO_2	0.91	0.7	0.64	0.48	0.39	1.45	1.27	0.46	5	2.56	2.35
Al_2O_3	13.32	13.06	12.46	11.06	9.5	9.81	10.35	10.28	14.66	14.71	10.76
FeO_t	9.55	8.75	8.86	9.45	9.19	10.65	10.65	9.67	9.5	10.34	10.16
MnO	0.18	0.18	0.17	0.18	0.17	0.2	0.19	0.19	-	-	-
MgO	16.9	17.58	18.22	19.71	23.89	18.58	19.89	22.31	10.6	13.9	16.21
CaO	10.69	10.92	10.92	8.78	7.7	10.31	9.31	8.96	7.84	10.24	9.38
Na_2O	0.96	0.93	0.82	0.77	0.52	0.93	1.08	0.4	4.1	1.29	1.87
Cr_2O_3	0.31	0.35	0.43	0.55	0.51	0.33	0.25	0.48	-	0.31	0.6
K_2O	0.56	0.41	0.34	0.22	0.22	0.83	0.7	0.22	1.63	0.55	0.39
res. phase	ol,o,c,	ol,o,c	ol,o	ol,o	ol	ol,c,g	ol,o,c,g	ol,o	ol,o,c	ol,o	ol,o

	HPY	HPY	HPY	HPY	HPY	KLB-1(1%H_2O)	KLB-1	KLB-1	KLB-1	MIX1G	MIX1G
% melt	-	-	-	24	-	15.8	24	47	-	26	14
P (Gpa)	2	2	2	3	3	1	1.5	1.5	3	2	2
Temp C	1500	1530	1600	1600	1600	1050	1450	1550	1550	1400	1375
SiO_2	49.33	50.18	49.16	46.6	47.79	54.35	48.8	50.1	47	45.1	44.4
TiO_2	2	1.74	1.4	2.67	1.81	0.7	0.5	0.4	0.9	2	2.3
Al_2O_3	9.48	8.61	6.83	10.81	8.55	21.7	14.7	11.5	11	16.2	16.4
FeO_t	9.43	9.34	9.19	8.52	9.55	4.66	7.6	7.8	7.8	10.9	12.81
MnO	0.22	0.19	0.15	-	0.21	0.23	-	-	-	0.16	0.1
MgO	18.21	19.96	24.96	18.78	21.39	6	15	20.4	19.2	11.1	10.6
CaO	8.34	7.4	6.11	9.56	7.6	9.99	11.3	7.9	12.2	9.98	9.3
Na_2O	1.61	1.4	1.13	2.23	1.52	1.87	1.5	1.2	1.2	2.6	3.78
Cr_2O_3	1.01	0.85	0.8	0.4	0.83	-	-	-	-	0.03	-
K_2O	0.37	0.32	0.26	0.43	0.35	0.46	-	-	-	0.08	0.12
H2O	-	-	-	-	-	6.3	-	-	-	-	-
res. phase	ol,o	ol,o	ol	ol,o	ol,o	-	ol,o	ol	ol,c	c,s	c,g,s

	MIX1G	MIX1G	MIX1G	KG2	KG2	KG2	KG2	KG2	KG2	KG2	GA2
% melt	67	28	21	9	35	47	4	25	12	22	4
P (Gpa)	2.5	2.5	2.5	1.5	1.5	1.5	2	2	3	3	3
Temp C	1500	1475	1455	1300	1350	1400	1350	1400	1500	1525	1240
SiO_2	45.2	42.7	43.1	50.55	48.3	49.08	49.03	46.53	43.32	46.63	63.6
TiO_2	1.3	1.87	2.58	1.96	1.29	1.1	1.82	1.72	2.94	1.97	2.56
Al_2O_3	15.2	14.54	14.2	19.86	15.81	14.37	19.08	17.26	14.88	12.68	15.69
FeO_t	9.1	12	13.6	6.37	8.82	8.17	8.05	9.28	11.54	10.5	3.64
MgO	15	13.54	12.5	7.12	12.76	14.16	7.99	12.17	14.99	15.57	1.22
CaO	11.2	10.3	10.2	5.79	10.15	10.35	5.51	9.09	6.64	9.4	3.45
Na_2O	1.91	3.04	3.72	7.29	2.51	2.49	5.91	3.53	4.84	2.75	4.31
Cr_2O_3	0.05	-	-	0.03	0.11	0.08	0.05	0.05	0.04	0.08	-
K_2O	0.05	0.09	0.08	1.04	0.26	0.2	2.56	0.37	0.8	0.42	4.36
res. phase	c,g	c,g	c,g	ol,o,c,s	ol,o,c	ol,o	ol,o,c,s	ol,o,c	ol,c,g	ol,c,g	c,g,q,k,r

	GA2	GA2	GA2	GA2	GA2	GA2	GA2	GA2	GA2	GA2	GA2
% melt	10	21	24	36	61	85	7	10	19	23	53
P (Gpa)	3	3	3	3	3	3	4	4	4	4	4
Temp C	1260	1280	1320	1360	1400	1440	1280	1320	1360	1400	1450
SiO_2	63.23	63.99	61.57	57.86	53.64	52	66.08	62.68	60.34	58.4	53.69
TiO_2	2.99	2.77	2.83	2.94	2.25	2	2.67	3.72	4.09	4.13	2.9
Al_2O_3	15.41	15.25	15.68	16.32	16.72	16.42	13.92	14.45	14.18	14.3	15.67
FeO_t	4.28	4.66	5.96	7.54	9.08	9.1	4.13	5.07	6.83	7.81	9.79
MgO	1.42	1.67	1.96	3.02	5.38	7.04	1.02	1.32	2.36	2.9	4.77
CaO	3.47	4.34	5.09	6.54	8.32	9.19	2.75	3.61	5.98	6.53	8.41
Na_2O	5.03	5.21	4.91	4.53	4.02	3.5	3.2	3.35	3.76	3.7	3.65
Cr_2O_3	-	-	-	-	-	-	-	-	-	-	-
K_2O	3.27	1.75	1.62	1.05	0.58	0.46	5.59	4.83	1.96	1.65	0.77
res. phase	c,g,q,k,r	c,g	c,g	c,g	c,g	g	c,g,co,r	c,g,co	c,g	c,g	c,g

8.5 Comparative study results

8.5.1 PM

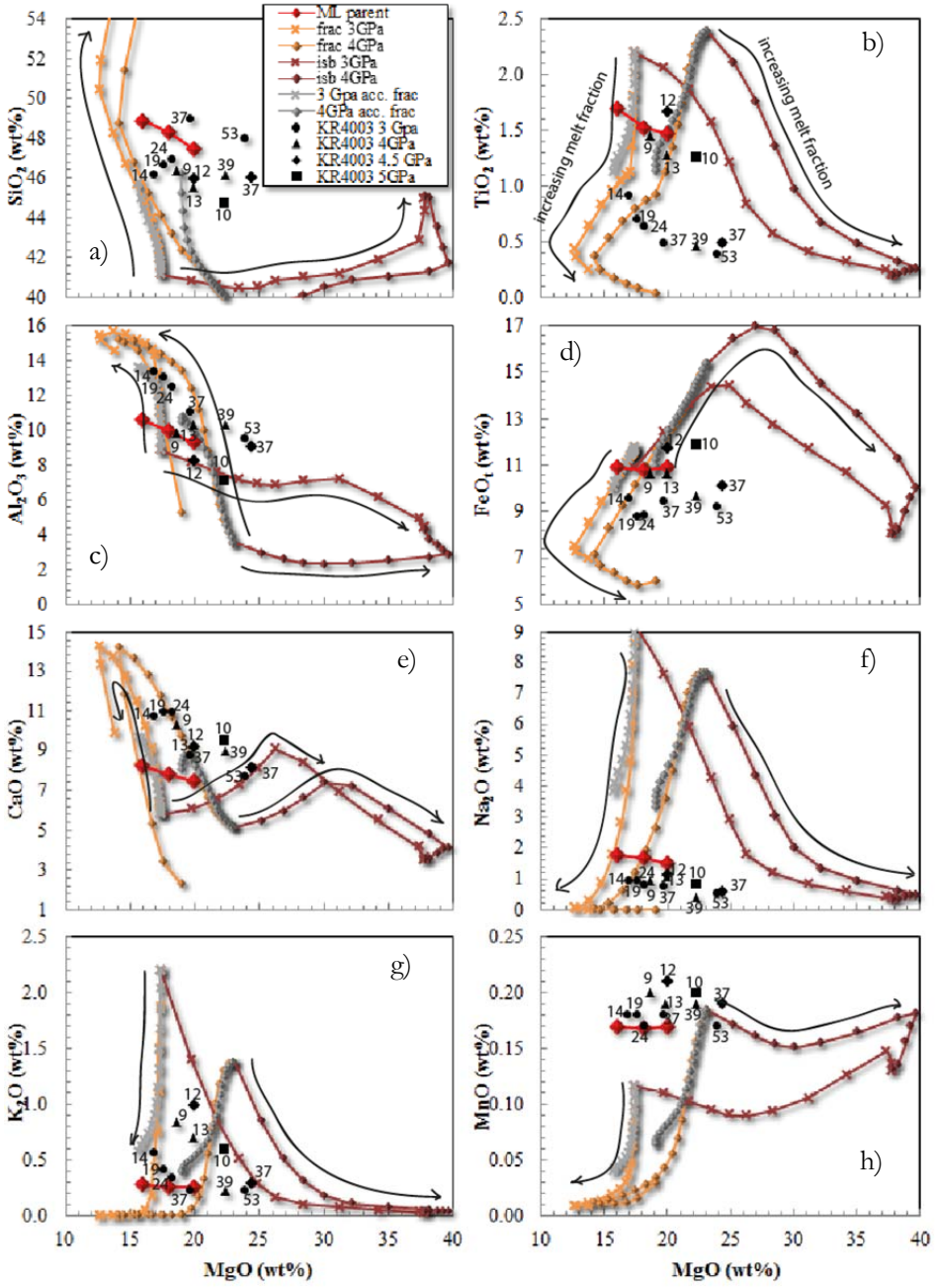

Figure 8.5 pMELTS fractional melting of Sun and McDonough (1989) primitive mantle composition (yellow), accumulated fractional (grey), isobaric (dark red), with Mauna Loa parental magma compositions (red diamonds). Black markers are melting of primitive mantle-like peridotite KR4003 at 3 GPa (circles), 4 GPa (triangles), 4.5 GPa (diamonds), and 5 GPa (square) with % of melt marked (Walter, 1998). Each marker on the yellow pMELTS curve

represents a decrease of 2000 bars in pressure, while each marker on the red curve represents an increase of 20 ˚C.

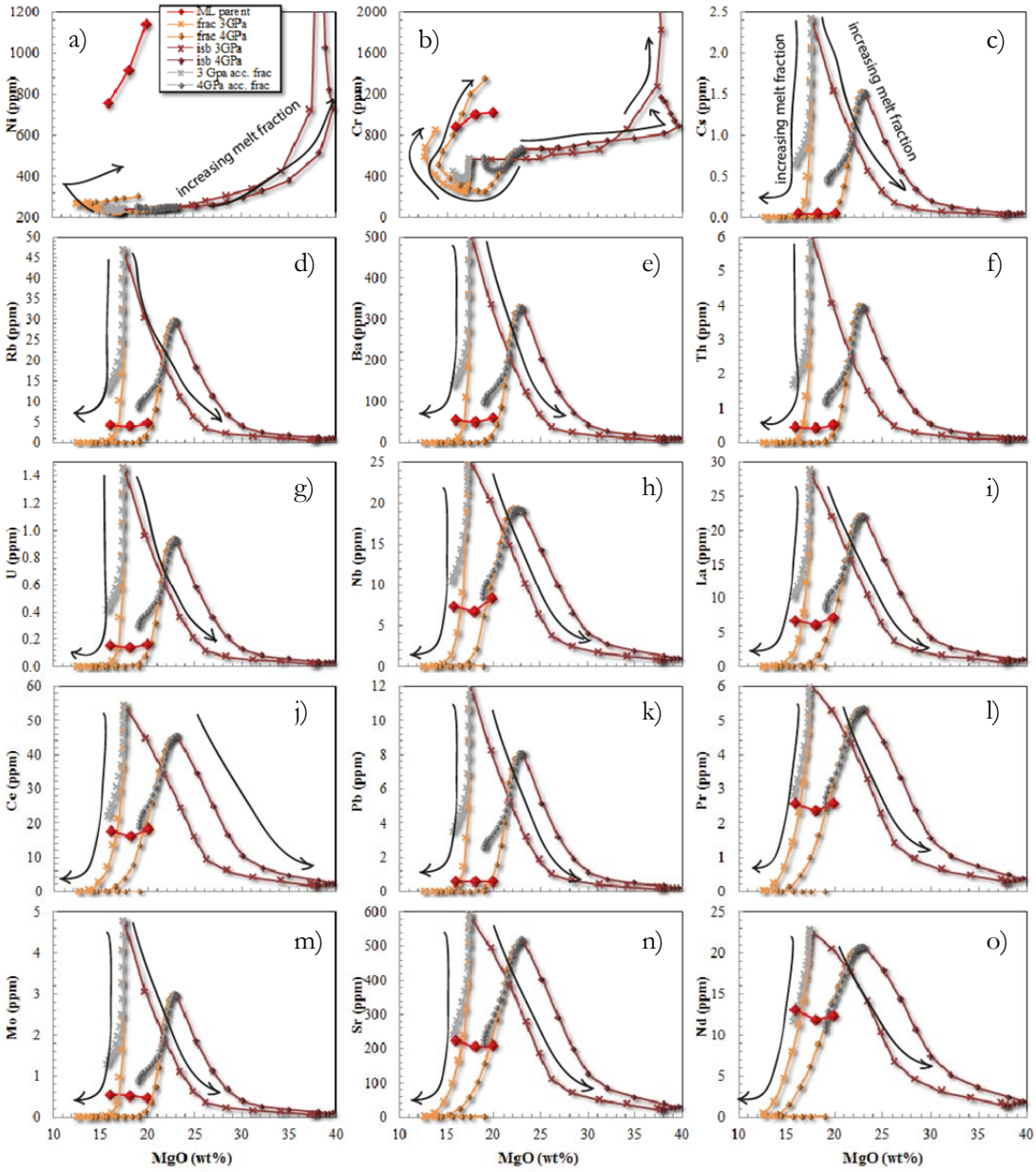

Figure 8.6 pMELTS fractional melting of Sun and McDonough (1989) primitive mantle composition (yellow), accumulated fractional (grey), isobaric (dark red), with Mauna Loa parental magma compositions (red diamonds). Each marker on the yellow pMELTS curve represents a decrease of 2000 bars in pressure, while each marker on the red curve represents an increase of 20 ˚C.

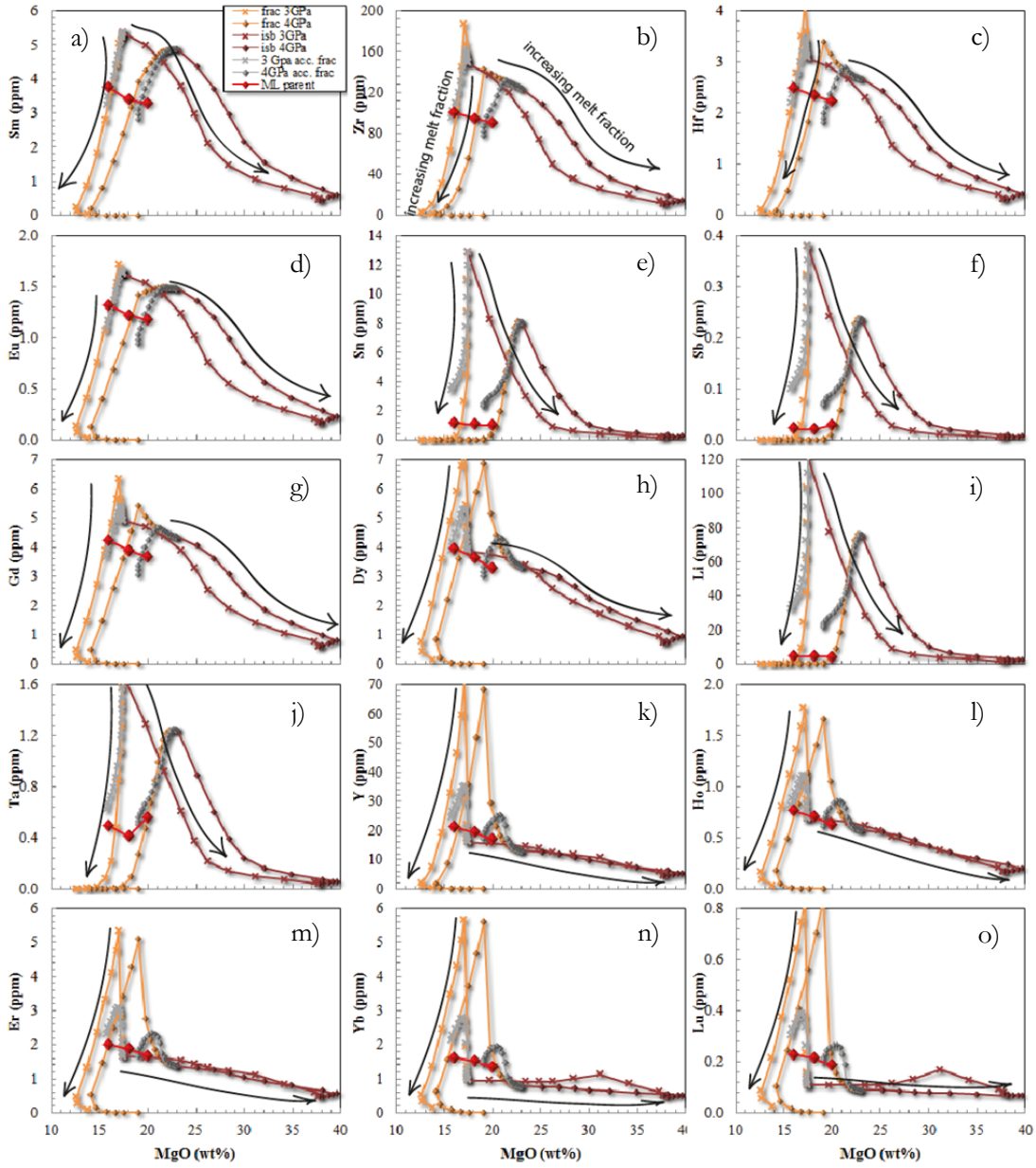

Figure 8.7 pMELTS fractional melting of Sun and McDonough (1989) primitive mantle composition (yellow), accumulated fractional (grey), isobaric (dark red), with Mauna Loa parental magma compositions (red diamonds). Each marker on the yellow pMELTS curve represents a decrease of 2000 bars in pressure, while each marker on the red curve represents an increase of 20 ˚C.

Walter melted a fertile peridotite which represents a composition similar to that of primitive mantle at pressures between 3 and 7 GPa (Walter, 1998). Results of melt Walter's melt compositions compared to Mauna Loa inferred parental magma are shown in Figure 8.5Figure 8.6Figure 8.7

The near-solidus phase proportions of KR4003 in the experimental study at 3 GPa were 53% olivine, 17% opx, 27% cpx, and nearly 2% garnet. At 4 GPa the near-solidus material contained less opx and more garnet, this time with 54% olivine, 6% opx, 28% cpx, and 13% garnet.

The experimental study yielded SiO_2 contents between 46.17 and 48.98 wt. % SiO_2 at 3 GPa while total SiO_2 contents were lower at 4 GPa (45.52 – 46.67 wt. %), and MgO contents are higher for a given melt fraction, as is temperature (1580 ˚C is enough to produce 37 % melt at 3 GPa, however at 4 GPa the temperature needs to be 1660 ˚C to produce a similar melt fraction). Al_2O_3 contents were also higher at lower pressure; however TiO_2, FeO, and K_2O were higher in the melts at 4 GPa.

Increased degree of melting in the experimental data had the effect of slightly increasing the SiO_2 contents at 3 GPa, while decreasing the TiO_2, K_2O, Al_2O_3, and CaO contents at both 3 and 4 GPa. FeO, Na_2O, and MnO remained fairly constant with increasing melt fraction.

pMELTS modelling fails to recreate the experimental melt compositions as well as the experimentally predicted near-solidus assemblage. Rather, it indicates that at 3 GPa the near-solidus phase assemblage is 55% olivine, 11% garnet, 15% opx, 17% cpx, and 1% spinel. At 4 GPa the assemblage is 54% olivine, 14% garnet, 14% opx, 14% cpx, and 0.8% spinel. At 3 GPa the pMELTS prediction differs from the experimental data, which suggests 10% more cpx is stable, while pMELTS suggests 10% more garnet is stable. At 3 GPa the garnet proportions are more similar between the experimental data and pMELTS model, however pMELTS predicts the proportions of opx and cpx should be approximately equal when the experimental data predicts 6% opx and 28% cpx.

The pMELTS modelling shows a wider range in major element oxide compositions in the melt than the experimental data. In addition, pMELTS melt compositions vary greatly depending on the style of melt model used. pMELTS isobaric melting increases the MgO contents of the melt with increasing temperature while SiO_2, Al_2O_3, and MnO remain fairly constant. TiO_2, Na_2O, and K_2O decrease with increasing T and melt fraction, and CaO and FeO increase initially up to 10-15% melting and then decrease, correlating with an increase in olivine melting and/or being near to the cpx-out point.

In contrast for adiabatic fractional melting, MgO decreases in the melt with increasing melt fraction. This is because the temperature calculated by pMELTS decreases with decreasing pressure according to the geotherm. Here, the dependence of MgO content on temperature is demonstrated e.g. (Nisbet et al., 1993). The accumulated fractional adiabatic melt trajectory is similar to the fractional melt path, but the range is much smaller because the high degree melts

are accumulated into the low degree melts, making the average intermediate to initial and final melt fractions.

The melt fraction was allowed to increase up to 100% for isobaric melting, which occurred over a temperature range of 1480 – 1700 ˚C at 3 GPa and 1540 – 1780 ˚C at 4 GPa. The fractional adiabatic melting only reached 26 and 27 wt. % at 3 GPa and 4 GPa respectively until the system reaches 0 GPa, equivalent to the surface. The melting was allowed to occur from the solidus up until the melting reached 0 GPa. The temperature range for fractional melting during adiabatic ascent was 1480 ˚C at the source at 3 GPa to 1327 ˚C at 0 GPa and 1540 ˚C at the source at 4 GPa to 1317 ˚C at 0 GPa.

In comparison to the Mauna Loa inferred parental magma compositions, the experimental melts from Walter (1998) of a primitive mantle composition have higher Al_2O_3 and CaO contents, and lower TiO_2, FeO, and Na_2O for a given MgO. Although 16-20 wt. % MgO represent minimum values for a primitive Mauna Loa melt, the assumed parental melt composition could not be produced via addition olivine to parental melts, as doing so would decrease Al_2O_3 and CaO relative to MgO, moving the melt further away from the experimental melt compositions. If melting was occurring similarly to the adiabatic melting model shown, MgO contents would decrease during melting while SiO_2 increased to reach a composition closer to Mauna Loa inferred parental magmas, however this would not work for TiO_2 which decreases during adiabatic mantle melting. The fact that both SiO_2 and TiO_2 are both slightly too high in the Mauna Loa parental composition indicates that increasing or decreasing the pressure would also not be able to reproduce this composition, because of the inverse relationship between SiO_2 and TiO_2 contents with pressure change. Thus, the only option is to slightly change the source composition from PM in terms of the major elements to be able to reproduce melts that are higher in both SiO_2 and TiO_2.

Important relationships can be seen between the major element oxide compositions, degree of melting, and pressure across both the experimental data and the isobaric pMELTS models. TiO_2, Al_2O_3, CaO, MnO, and K_2O all decrease with increasing melt fraction in the experimental data as well as the pMELTS model, although Na_2O is much lower and more constant in the experimental melts. SiO_2 increases greatly with increasing melt fraction in the fractional melting models, and can be seen to increase slightly in the experimental data at 3 GPa. Increasing pressure increases the TiO_2, FeO, and MgO contents, while it decreases the SiO_2 and Al_2O_3 content. This effect is exaggeratedly mimicked by the isobaric pMELTS model. Importantly, the experimental melts form trends closer to the isobaric pMELTS model than the adiabatic melting model, as would be expected given that the melting experiments are similarly isobaric. Figure

8.5d,f shows that the pMELTS modelling produces unnatural melt compositions, especially for FeO and Na_2O.

The trace elements were modelled with pMELTS using isobaric, fractional, and accumulated fractional melting models. As near-solidus phase assemblage was incorrectly estimated, the trace element concentrations will also be incorrect, though they are shown here anyway (Figure 8.6Figure 8.7). Partition coefficients for garnet, spinel, olivine, cpx, and opx are those of McKenzie and O'Nions (1991,1995). All of the incompatible trace elements decrease with increasing melt fraction, across the three models, while Ni increases gradually with increasing temperature, behaving similarly to MgO. The Ni content also increases slightly in the adiabatic melting model, but neither can reproduce the very high Ni content of the inferred Mauna Loa parental composition. Of note is the fact that the HREE behave differently during adiabatic melting to the LREE. The concentrations of HREE remain almost constant throughout melting, probably because of buffering by the 11-14% garnet predicted.

In summary, the 4 GPa experimental melts are close in composition to the 18 and 20 wt. % MgO parental magmas, with the exception of CaO which is slightly too high. There are large differences in the pMELTS predicted results and the experimental melt compositions, showing that pMELTS does not correctly predict experimentally determined near-solidus phase assemblages of primitive mantle at 3 and 4 GPa. A high pressure assemblage appears to produce higher MgO melt which matches fairly closely the Mauna Loa parental melt in terms of most other major element oxides. If the Rhodes parental magma composition (Rhodes, 1995) was used, then this would be even harder to match via melting of a primitive mantle composition, given that this estimation contains 13 wt. % MgO and 50.29 wt. % SiO_2. None of the melts produced in the experiments between 3 and 7 GPa produce melts with MgO contents as low as 13 wt. %. The 20 wt. % MgO parental magma appears to be closest to the 9 and 13% melts at 4 GPa in terms of most of the major element oxides with the exception of K_2O. 9 – 13% melting is higher than one estimate of the melt fraction for the Hawaiian source, at no greater than 6.6 % for a melt extent region of ~55 km and a maximum radial extent of ~132 km (Watson and Mckenzie, 1991).

8.5.2 HPY

Experimental results from melting of HPY by Falloon et al. (1988) yield magma compositions that are the closest to the inferred ML parental magma of any experimental melts examined here (Figure 8.8). The experimental melts are a good fit for the Mauna Loa parental magmas, with both the 2 and 3 GPa melts closely resembling the 20 wt. % MgO sample in terms of most

major element oxides. For SiO_2 however, the 2 GPa melts are closer to the 16 wt. % MgO parental magma, while the 3 GPa melts are closer to the 20 wt. % MgO parental magma.

The residual phases were olivine and opx but the residual phase proportions were not given in the study. Although garnet was not a residual phase in HPY at 1500 ºC and 2 GPa in the experiment by Falloon and co-authors, it was noted that garnet is stable in a Hawaiian pyrolite at pressures as low as 2 GPa when a small amount of water is present (0.3 wt. %). In addition, the near-solidus phase proportions of HPY at 2 GPa are not provided by Falloon and co-authors, however Norman and Garcia have estimated the composition HPY to be composed of 86.5% ol+opx, 10% cpx, 3.5% garnet (Norman and Garcia, 1999). It can be assumed that about 55% of the ol+opx is olivine from previously mentioned estimates (Green and Falloon, 1998), leaving the remaining 31.5% as opx. This proportion of opx is relatively high for estimates of the mantle, with average mantle xenoliths containing 21.5% opx, 63.7% olivine, 11.7% cpx, and 9.6% garnet (off-craton) or 20.8% opx, 71.9% olivine, 3.3% cpx, and 6.2% garnet (on-craton) according to a recent compilation (Pearson et al., 2003). The major difference between this composition and the experimentally determined phase proportions of primitive mantle by Walter is the higher proportion of opx to cpx in HPY, as the proportion of olivine and garnet is approximately similar.

Near solidus phase proportions estimated by pMELTS are 55% olivine, 1% garnet, 23% opx, and 19% cpx at 2GPa, and 55% olivine, 6% garnet, 20% opx, and 18% cpx at 3 GPa. The pMELTS trends do not change greatly with the increase in pressure and proportion of garnet; they are just translated to lower SiO_2, Al_2O_3, and CaO and higher TiO_2, FeO, Na_2O, and K_2O.

The lowest temperatures where melt occurs in the experiments are 1350 ºC at 2 GPa (<10% melt) and 1500 ºC at 3GPa (<24% melt). pMELTs predicts a solidus temperature of 1350 ºC at 2 GPa and 1430 ºC at 3 GPa. The HPY composition produced melts that were overall similar in SiO_2, FeO, MgO, and CaO to PM experimental melts (HPY melts were most similar to 25-35 % PM melts), however the HPY melts were overall higher in TiO_2 and Na_2O.

Experimentally, SiO_2 behaved the same in the PM experiments as the HPY experiments, as the concentrations increase with increasing melt fraction, and decrease with increasing pressure. TiO_2 also behaved similarly between the HPY and PM starting compositions, decreasing with increasing melt fraction, but increasing with increasing pressure. CaO and Al_2O_3 in PM and HPY melts behave similarly, decreasing with increasing melt fraction with no clear relationship with pressure, and FeO and Na_2O remain fairly constant with increasing melt fraction and pressure for HPY melts, as is seen for the PM starting composition. K_2O decreased with

increasing melt fraction as with the PM starting material; however no clear relationship with pressure is seen.

Like the pMELTS-calculated melt compositions for PM, the pMELTS-calculated melts from the HPY source have unnatural concentrations of K_2O, TiO_2, FeO_t, and Na_2O, and do not match experimentally-determined melt compositions.

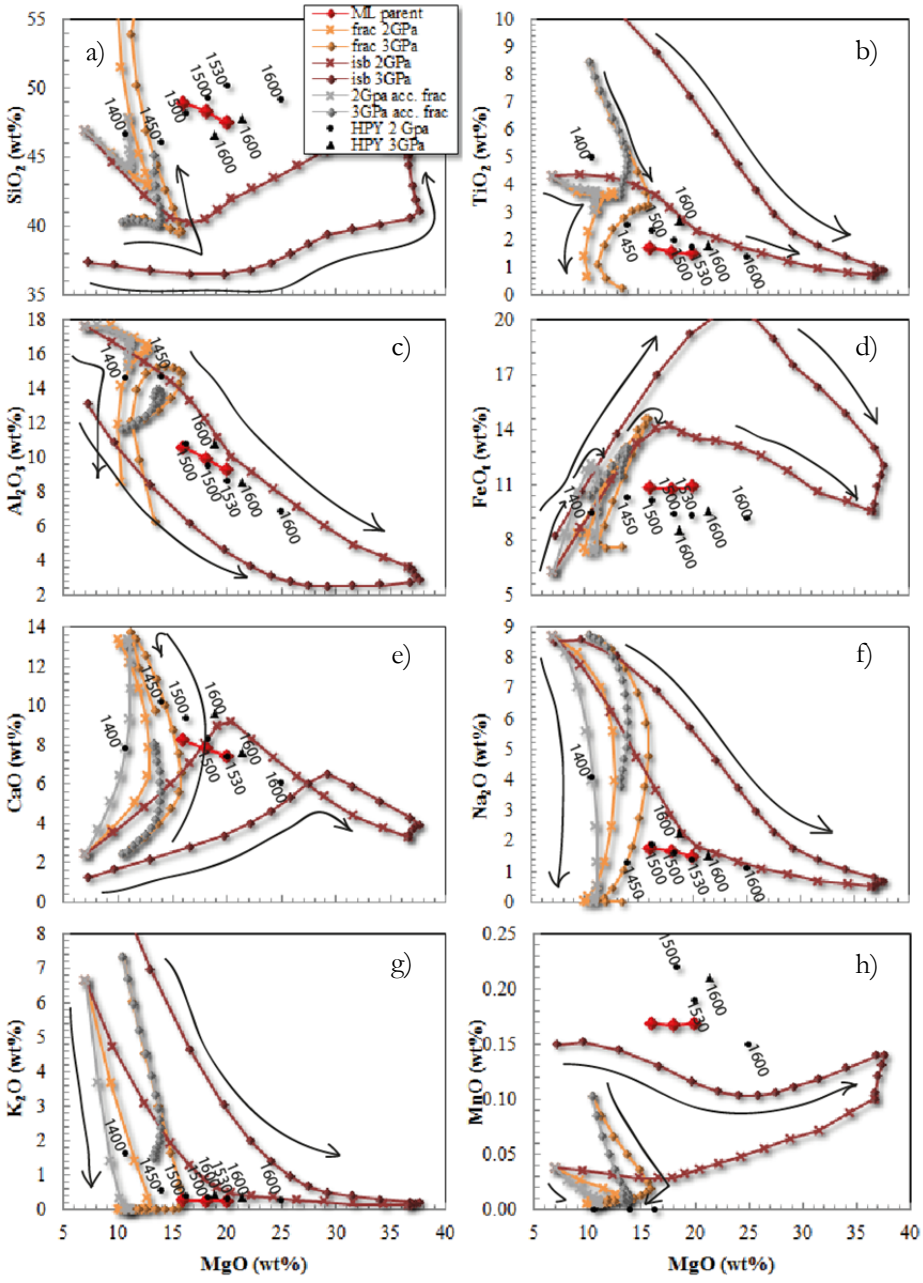

Figure 8.8 Green and Falloon (1998) pMELTS fractional melting of Hawaiian pyrolite composition (yellow), accumulated fractional (grey), isobaric (dark red), with Mauna Loa parental magma compositions (red diamonds). Black markers are melting of HPY composition

at 2 (circle) and 3 (triangle) GPa (Falloon et al., 1988) with temperature of experiment given. Each marker on the yellow pMELTS curve represents a decrease of 2000 bars in pressure, while each marker on the red curve represents an increase of 20 ˚C.

8.5.3 KLB-1

Takahashi melted a dry peridotite (KLB-1) in pressures up to 14 GPa to investigate the peridotitic upper mantle (Takahashi, 1986). The sub-solidus phase assemblage changed from olivine + opx + cpx + spinel at pressures less than 2.5 GPa to olivine + opx + cpx + spinel + garnet to pressures up to 7 GPa. At greater than 7 GPa opx is no longer a stable phase. The solidus temperature is between 1250 ˚C and 1275 ˚C at 1 GPa, between 1500 ˚C and 1550 ˚C at 3 GPa, and is over 1600 ˚C at 5 GPa. pMELTS predicts 60 (wt.) % olivine, 37% cpx, and 3% spinel at 1.5 GPa and 1300 ˚C, and 62% olivine, 10% garnet, 9% opx, and 17% cpx at 3 GPa and 1500 ˚C.

KLB-1 produces melts that have similar SiO_2 compared to the inferred ML parental magma composition, and MgO ranging from 15-20 wt. %. Experimental melt compositions are too low in TiO_2 (0.9 wt. % at 3 GPa) and FeOt (~7% at 1.5 and 3 GPa) and too high in CaO (~12 wt. % at 3 GPa) compared to the ML parental composition except for at low pressure and high degrees of melting, though the Al_2O_3 contents are fairly close to the ML parent.

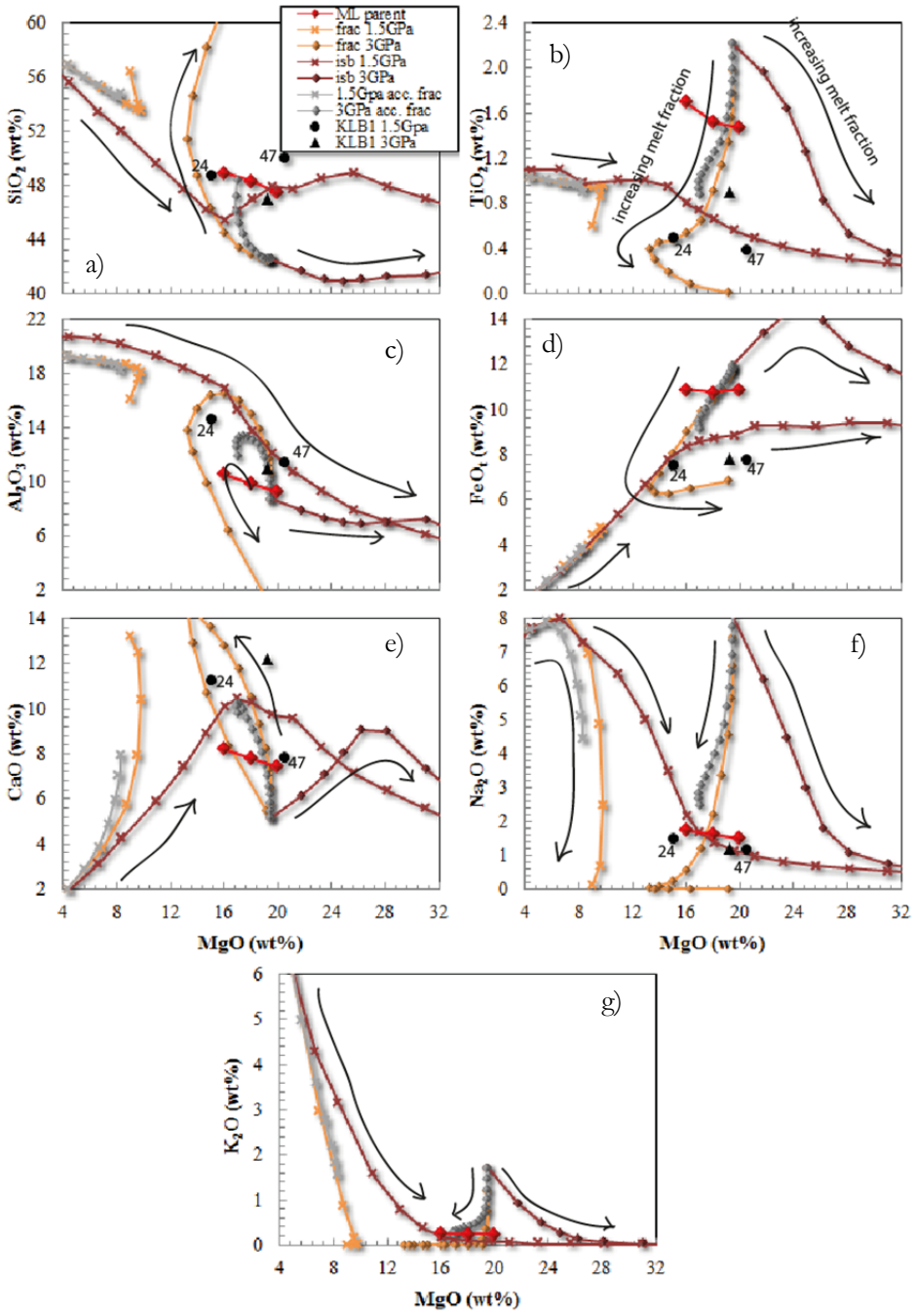

Figure 8.9 pMELTS fractional melting of spinel lherzolite composition (Takahashi, 1986) (yellow), accumulated fractional (grey), isobaric (dark red), with Mauna Loa parental magma compositions (red diamonds). Black markers are experimental melting of KLB-1 composition at 1.5 (circles) and 3 (triangle) GPa (Takahashi et al., 1993) with experimental melt fraction given. Each marker on the yellow pMELTS curve represents a decrease of 2000 bars in pressure, while each marker on the red curve represents an increase of 20 ˚C.

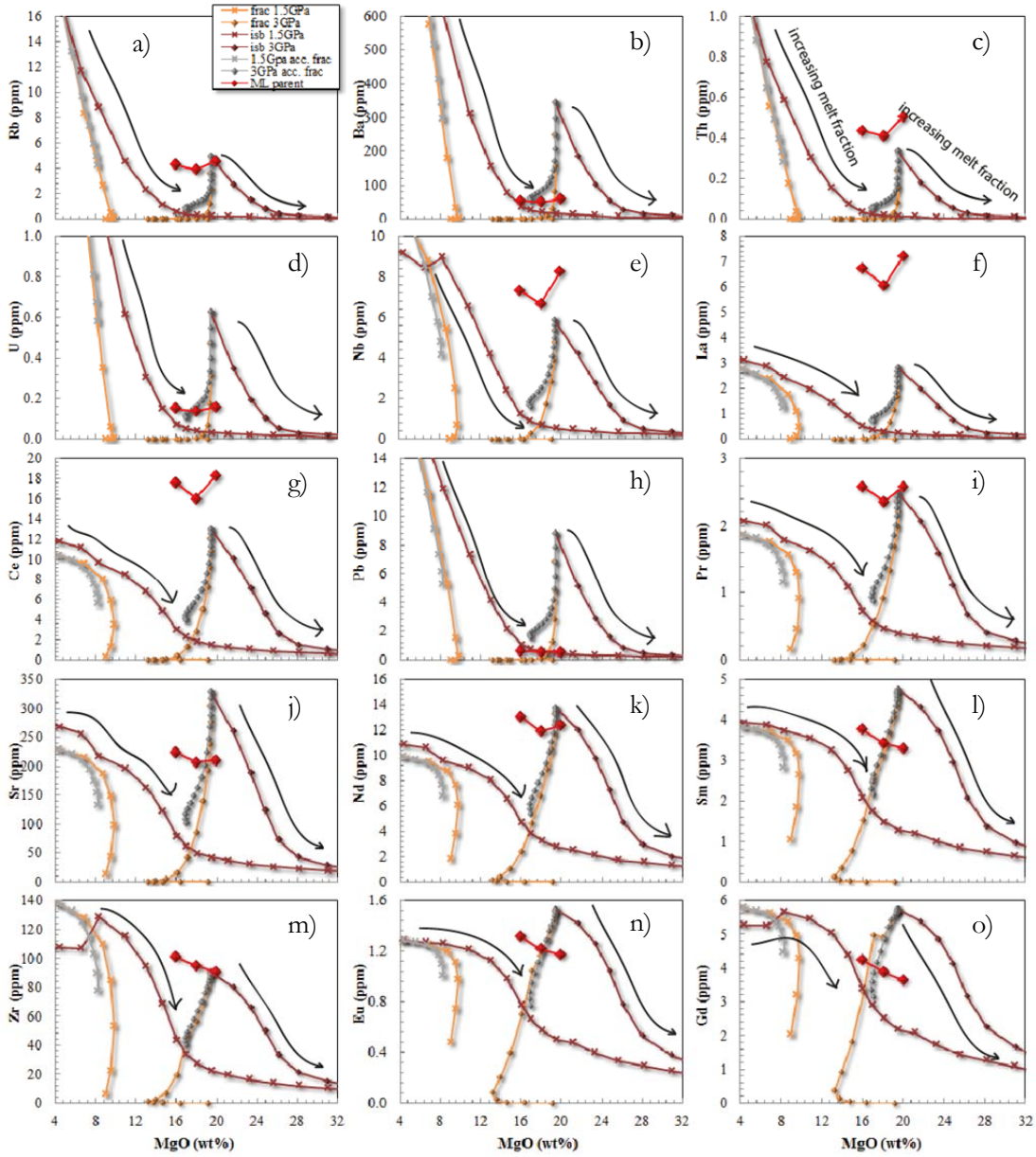

Figure 8.10 pMELTS fractional melting of spinel lherzolite composition (Takahashi, 1986) (yellow), accumulated fractional (grey), isobaric (dark red), with Mauna Loa parental magma composition (reds diamonds). Each marker on the yellow pMELTS curve represents a decrease of 2000 bars in pressure, while each marker on the red curve represents an increase of 20 ˚C.

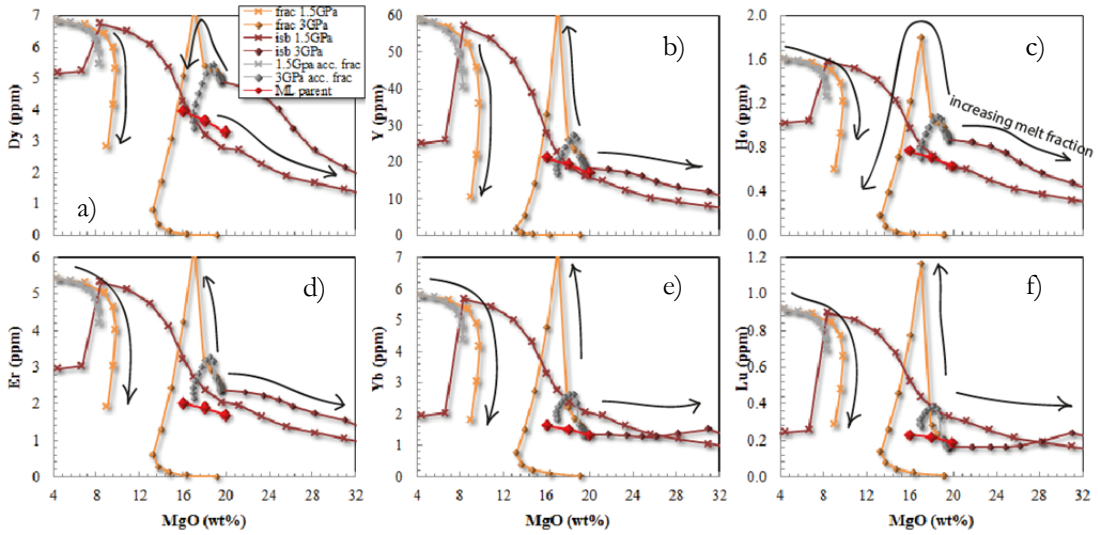

Figure 8.11 pMELTS fractional melting of spinel lherzolite composition (Takahashi, 1986) (yellow), accumulated fractional (grey), isobaric (dark red), with Mauna Loa parental magma compositions (red diamonds). Each marker on the yellow pMELTS curve represents a decrease of 2000 bars in pressure, while each marker on the red curve represents an increase of 20 ˚C.

8.5.4 MIX1G

The partial melts of MIX1G are silica poor (42.7 – 45.2 wt. % SiO_2) (Figure 8.12), and the sub-solidus assemblage is cpx + garnet + spinel + olivine + melt at 2.5 GPa and cpx + garnet + spinel + melt at 2 GPa, although no quantitative near-solidus modal proportions could be found (Hirschmann et al., 2003). At 2.5 GPa the solidus temperature is between 1375 ºC and 1400 ºC. The solidus phases at 2.5 GPa are predicted to be cpx + garnet + spinel + olivine according to Hirschmann and co-authors, although precise near-solidus modes are not given. In one experiment at 2 GPa and 1375 ˚C the modal proportions were 73% cpx, 7% garnet, 6% spinel, and 14% melt. At 2.5 GPa and 1455 ˚C the modal proportions were 47% cpx, 32% garnet, and 21% melt. In another study by Kogiso and co-authors, the phase relations at 5 GPa and 1650 ˚C were 53% garnet, 28% cpx, and 19% melt (Kogiso et al., 2003). This trend clearly indicates that the proportions of garnet increase with increasing pressure at the expense of cpx.

pMELTS predicts 4% olivine, 41% garnet, 51% cpx, and 1% spinel as a near solidus assemblage at 2 GPa and 5% olivine, 45% garnet, 47% cpx, and 0.5% spinel at 2.5 GPa, both at approximately 1300 ºC.

MIX1G contains a higher proportion of pyroxene than a mantle peridotite, but yields lower SiO_2 for a given MgO than a peridotite melt (Hirschmann et al., 2003). This relationship indicates that to obtain the high SiO_2 contents of the Mauna Loa parental magma, a peridotite source composition is more suitable. Significantly, the experimental melt MgO contents are too

low to produce the ML parental magmas, and CaO and Al_2O_3 contents are too high at all degrees of melting. Na_2O, K_2O, and TiO_2 are approximately equivalent to the ML composition.

SiO_2, K_2O, Na_2O, MnO, CaO, and Al_2O_3 remain more constant with increasing melt fraction compared melts from the peridotite sources, although TiO_2 still decreases with increasing melt fraction. For this source composition to produce melt close to the ML parent, the degree of melting would have to be very high (>70%) and also probably occur at high pressures. The predicted pMELT melt concentrations for Na_2O, FeO_t, and MnO are again far too high to be considered natural melt compositions. The overestimation of the incompatible major element oxides in the melt compositions predicted by pMELTS appears to be a systematic. Trace elements would similarly be consistent with very high degree melts of this lithology during isobaric melting (Figure 8.13).

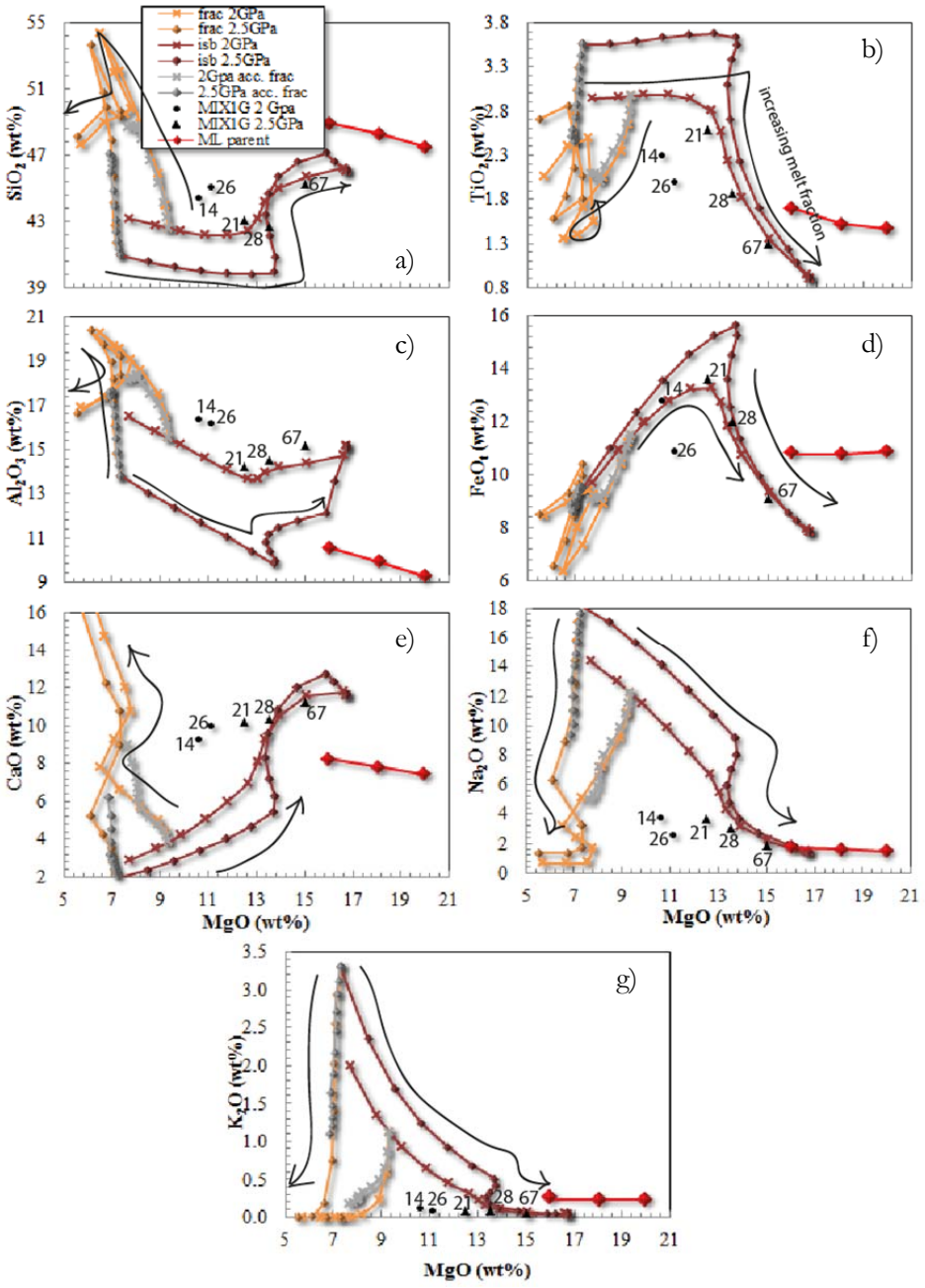

Figure 8.12 pMELTS fractional melting of pyroxenite composition (yellow), accumulated fractional (grey), isobaric (dark red), with Mauna Loa parental magma compositions (red diamonds). Black markers are experimental melting of MIX-1G composition at 2 (circles) and 2.5 (triangles) GPa (Hirschmann et al., 2003) with temperature of experiment given. Each marker on the yellow pMELTS curve represents a decrease of 2000 bars in pressure, while each marker on the red curve represents an increase of 20 °C.

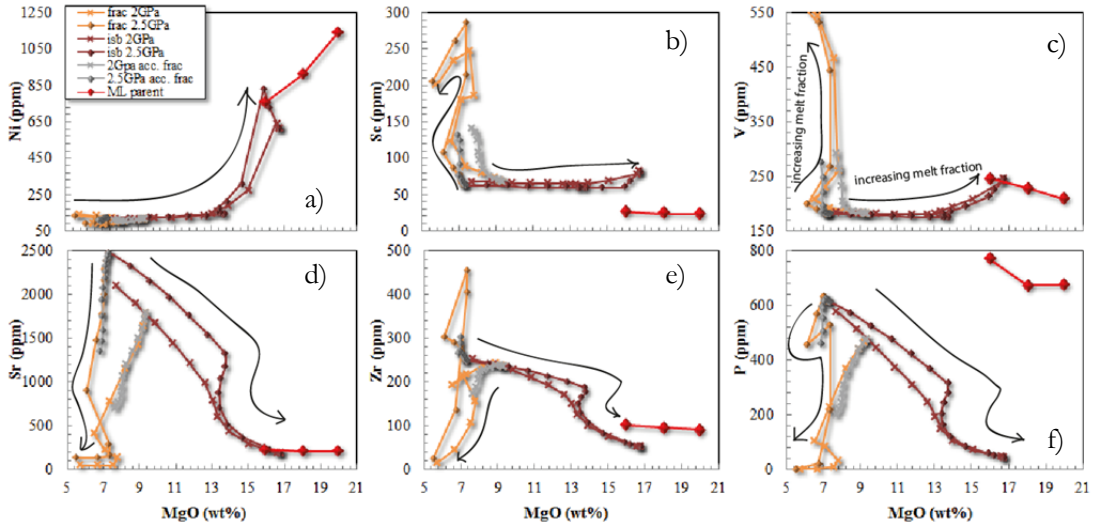

Figure 8.13 pMELTS fractional melting of pyroxenite composition (yellow), accumulated fractional (grey), isobaric (dark red), with Mauna Loa parental magma compositions (red diamonds). Each marker on the yellow pMELTS curve represents a decrease of 2000 bars in pressure, while each marker on the red curve represents an increase of 20 ˚C.

8.5.5 KG2

KG2 behaved similarly to MIX1G in that SiO_2 contents were too low for a given MgO (14.99 and 15.57 wt. % at 1500 ˚C and 1525 ˚C respectively) during partial melting compared to the estimated Mauna Loa parental magma composition. At 3 GPa, the partial melts of the pyroxenite contained 43.32 and 46.63 wt. % SiO_2 at 1500 and 1525 ˚C respectively (Kogiso et al., 1998).

The TiO_2, CaO, and FeO_t contents were approximately equivalent to the ML parental composition, though the Al_2O_3 contents were high (12-20 wt. %), as were the Na_2O and K_2O contents. The residual phases at 3 GPa were olivine + cpx + garnet, whereas at lower pressures garnet was absent and spinel + opx were present. At lower pressures (1.5 and 2 GPa) where opx is the dominant pyroxene and garnet is absent, low degree melts (<10%) only contain 7 wt. % MgO at 1.5 GPa and 8 wt. % MgO at 2 GPa. The MgO in the melt at these pressures only increases to 14 wt. % at 47% partial melting at 1.5 GPa and 12 wt. % at 25% partial melting at 2 GPa. The low MgO content of the low pressure KG2 melts indicates ol + opx + cpx melts could not produce the ML parental magma composition. The 3 GPa melt at 22% melting is closest to the proposed ML parental magma (Figure 8.14), though for all other melt compositions this lithology produces melts that are too low in MgO. Greater pressures and melt fractions would be required to reach the ML parent composition.

The solidus temperature of these olivine-normative pyroxenites conflicts with ideas that secondary pyroxenite formed by the reaction of eclogite-derived melt with peridotite may begin melting at lower pressures than surrounding peridotite e.g. (Yaxley and Green, 1998, Jones et al., 2017). The solidus temperatures from studies that have melted MIX1G and KG2 are equivalent that of PM or KLB-1 peridotites, and therefore it appears that if a pyroxenite is olivine normative, then the melting point will not be significantly lower than a peridotite.

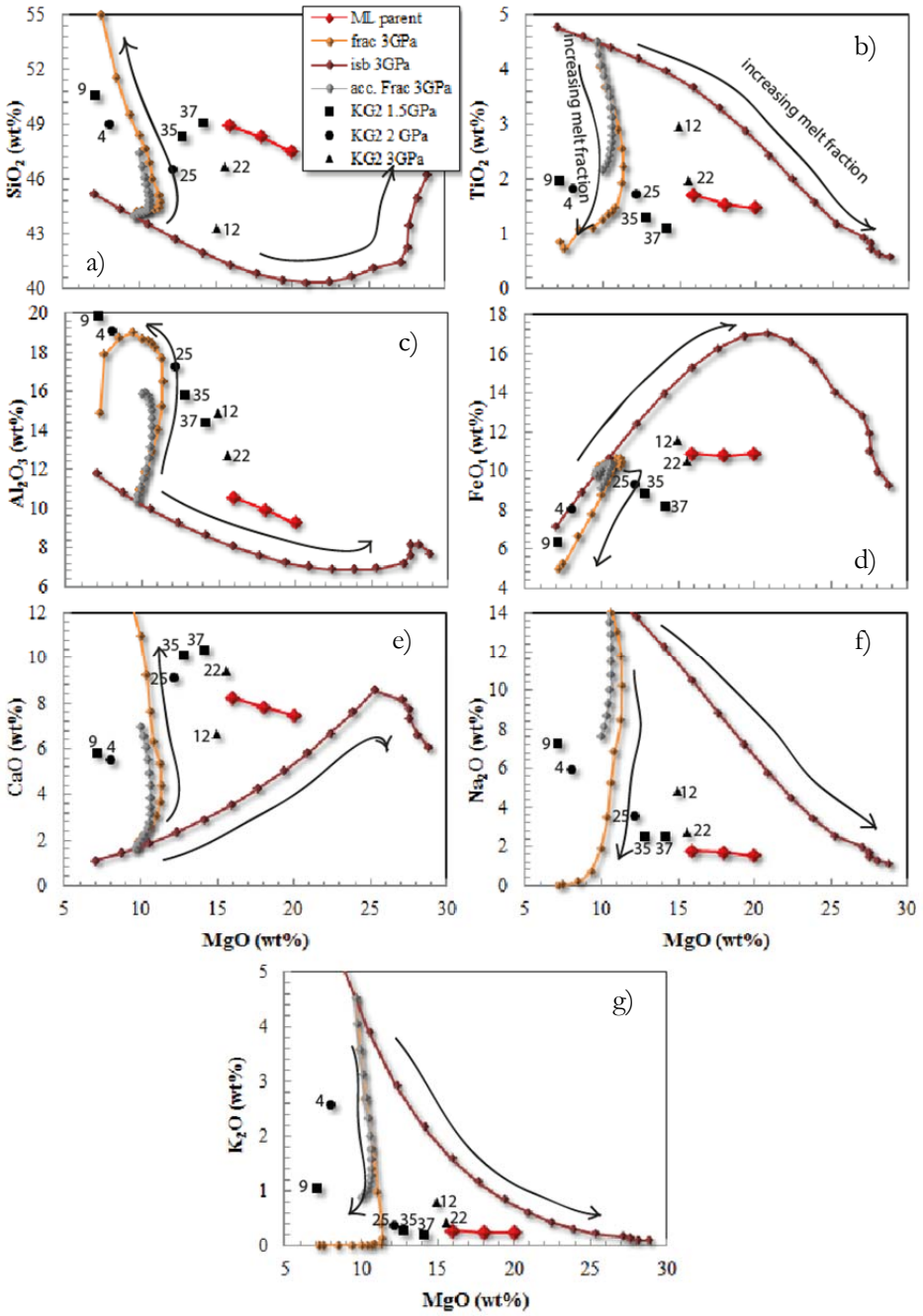

Figure 8.14 pMELTS fractional melting of pyroxenite (2:1 peridotite:MORB) composition (yellow), accumulated fractional (grey), isobaric (dark red), with Mauna Loa parental magma

compositions (red diamonds). Black markers are experimental melting of KG2 composition at 3 GPa (Kogiso et al., 1998) with temperature of experiment given. Each marker on the yellow pMELTS curve represents a decrease of 2000 bars in pressure, while each marker on the red curve represents an increase of 20 ˚C.

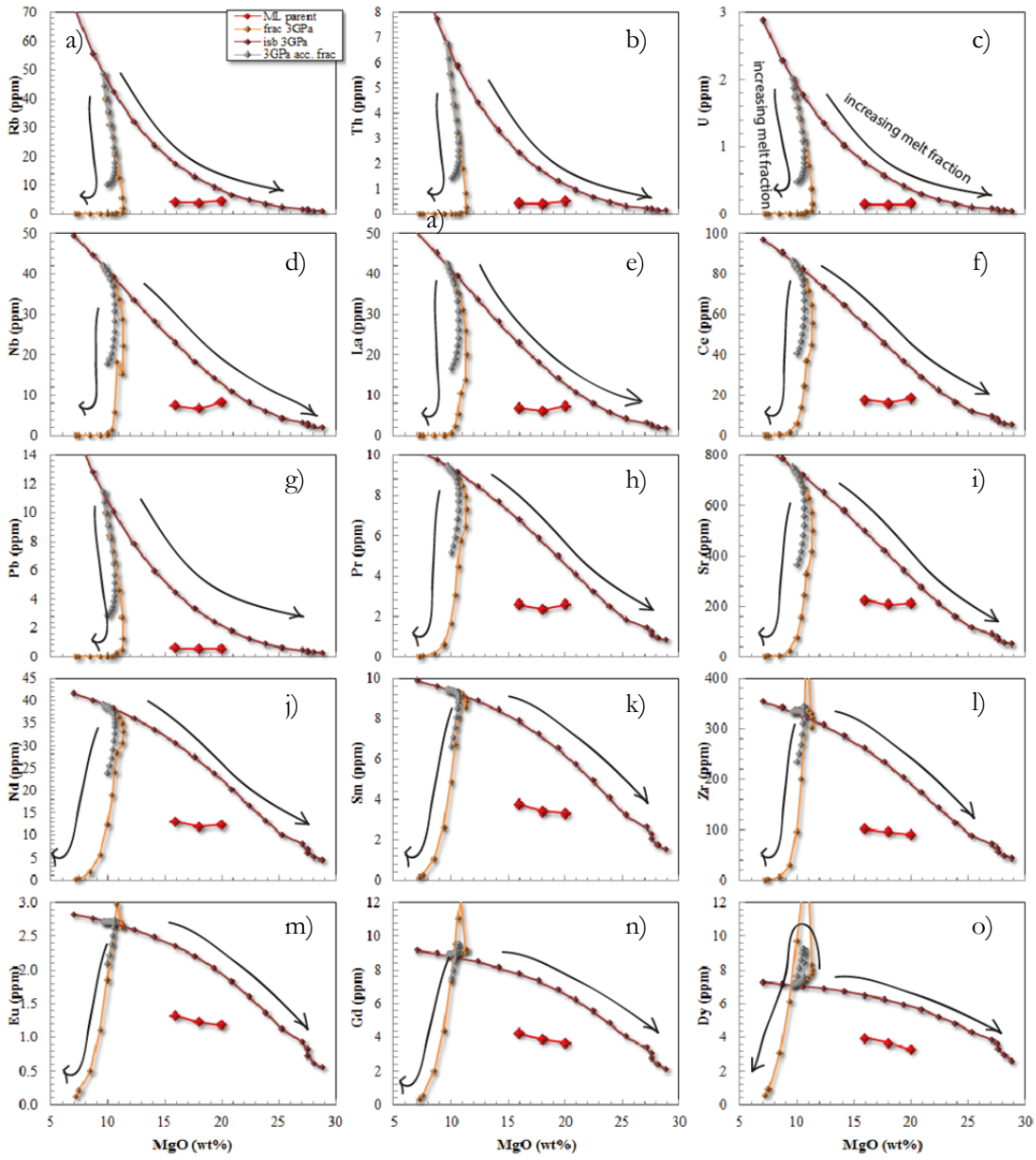

Figure 8.15 pMELTS fractional melting of pyroxenite (2:1 peridotite:MORB) composition (yellow), accumulated fractional (grey), isobaric (dark red), with Mauna Loa parental magma compositions (red diamonds). Each marker on the yellow pMELTS curve represents a decrease of 2000 bars in pressure, while each marker on the red curve represents an increase of 20 ˚C.

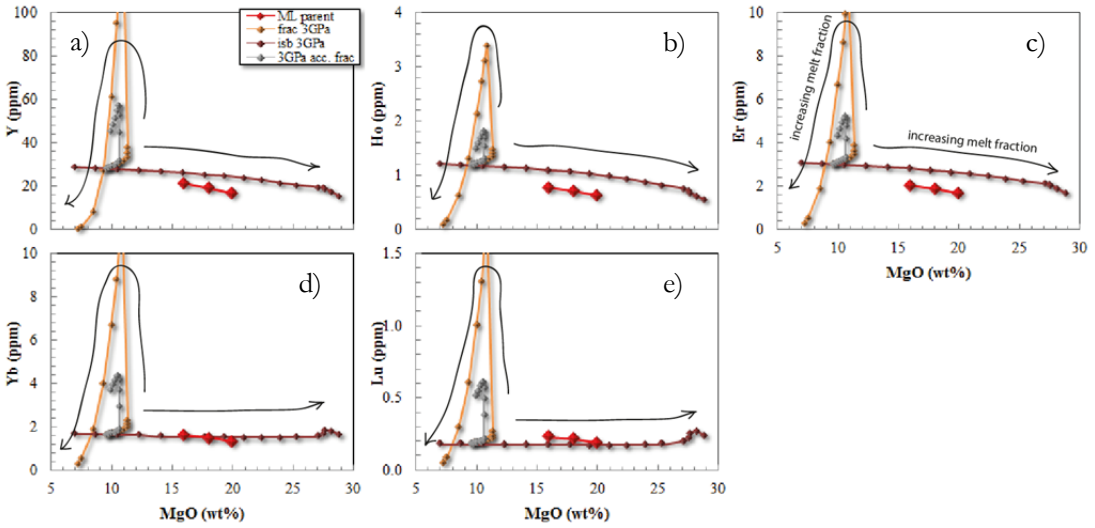

Figure 8.16 pMELTS fractional melting of pyroxenite (2:1 peridotite:MORB) composition (yellow), accumulated fractional (grey), isobaric (dark red), with Mauna Loa parental magma compositions (red diamonds). Each marker on the yellow pMELTS curve represents a decrease of 2000 bars in pressure, while each marker on the red curve represents an increase of 20 ˚C.

8.5.6 GA2

GA2 is a K-bearing eclogite which represents a sea-floor-altered MORB composition except with slightly higher TiO_2 contents to promote rutile saturation (Spandler et al., 2008). This was melted under temperature conditions ranging from 1200-1600 ˚C and pressure conditions ranging from 3 to 5 GPa by Spandler and co-authors (Spandler et al., 2008). The sub-solidus mineralogy was found to be garnet and clinopyroxene with minor amounts of quartz-coesite, rutile, and potassium feldspar. Solidus temperatures are noticeably lower than peridotite and olivine-pyroxenites (just 1230 ˚C a 3 GPa and 1300 ˚C at 5 GPa) because quartz, K-feldsapr, and rutile are minerals with lower melting points than olivine and pyroxene. This agrees with evidence that if recycled crust is present in an upwelling plume the recycled eclogite will be the first to melt (Yaxley and Green, 1998, Jones et al., 2017), though when the eclogite-derived melt reacts with peridotite to form a secondary pyroxenite, the melting point of that pyroxenite may not be any lower than that of a peridotite as discussed previously.

Melting of this eclogitic material at 3 GPa produces melts that are strongly SiO_2 rich (66 wt. % at 4% partial melting and 4 GPa, down to 52 wt. % at 85% partial melting at 3 GPa), and are very low in MgO (1-7 wt. %) (Figure 8.17). Importantly, the behaviour of the major element oxides differs with increasing melt degree compared to when a peridotite source is melted. SiO_2 and K_2O behave similarly and decrease with increasing melt fraction, while TiO_2 initially increases before it begins to decrease after about 30% melting. This is opposite to the anti-

correlation between SiO_2 and K_2O + TiO_2 seen in the Mauna Loa and Kilauea literature data. Also, CaO, FeO, and Al_2O_3 increase with increasing melt fraction, opposite to the melting of peridotite. Na_2O behaves similarly to TiO_2.

Trace element concentrations are in general too high in the GA2 melt for the ML parental composition except for Ni, Co, Ga, Cu, and Sc (Figure 8.18).

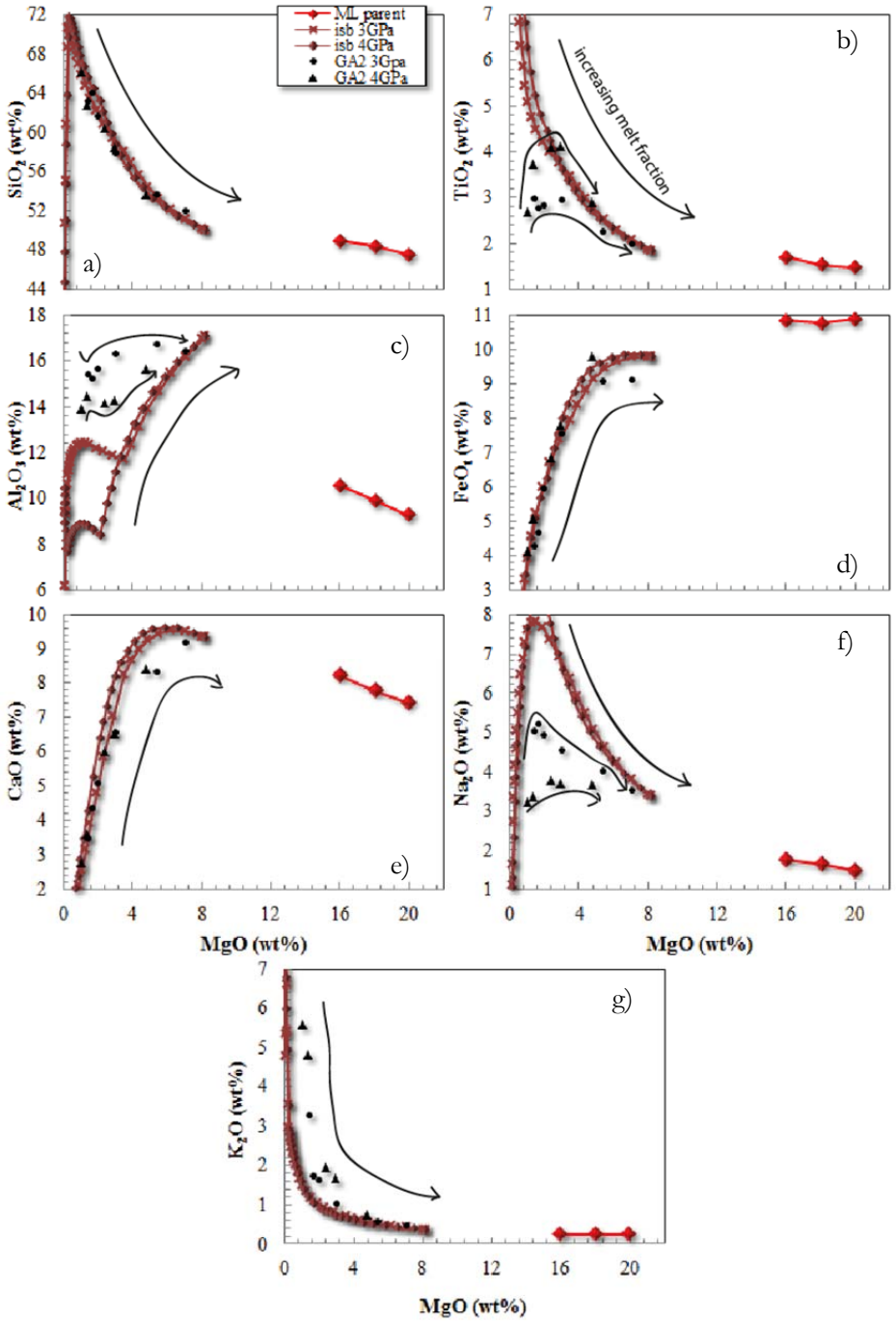

Figure 8.17 pMELTS isobaric melting of sea-floor-altered MORB composition (dark red), with Mauna Loa parental magma compositions (red diamonds). Black markers are experimental melting of GA2 composition at 3 (circles) and 4 (triangles) GPa (Spandler et al., 2008). Experimental melt percentages at 3 GPa, in order of lowest MgO to highest MgO are 4, 10, 21, 24, 36, 61, and 85 %. Melt pertentages at 4 GPa are 7, 10, 19, 23, and 53 %. Each marker on the yellow pMELTS curve represents a decrease of 2000 bars in pressure, while each marker on the red curve represents an increase of 20 °C.

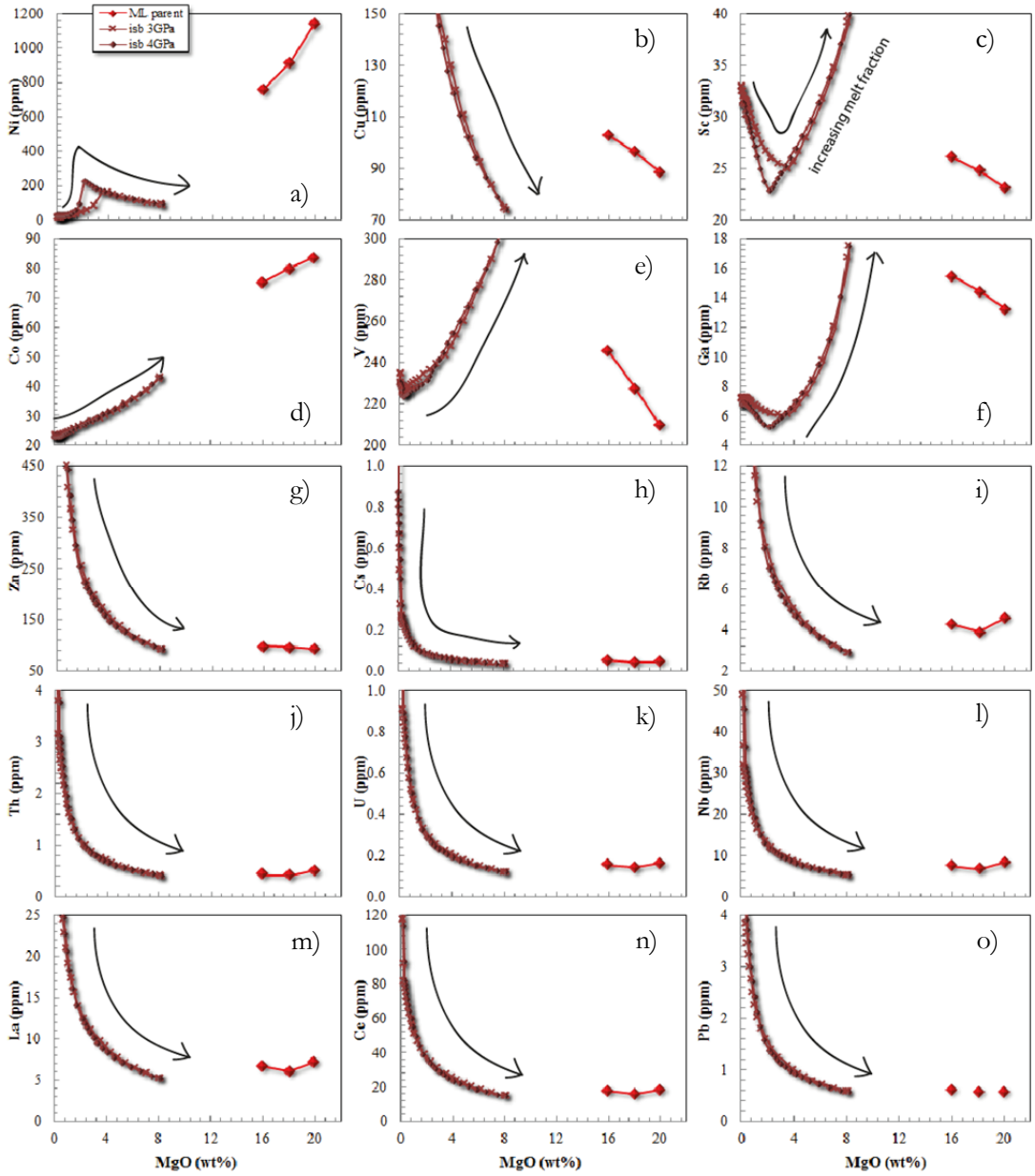

Figure 8.18 pMELTS isobaric melting of sea-floor-altered MORB composition (dark red), with Mauna Loa parental magma compositions (red diamonds). Each marker on the yellow pMELTS curve represents a decrease of 2000 bars in pressure, while each marker on the red curve represents an increase of 20 °C.

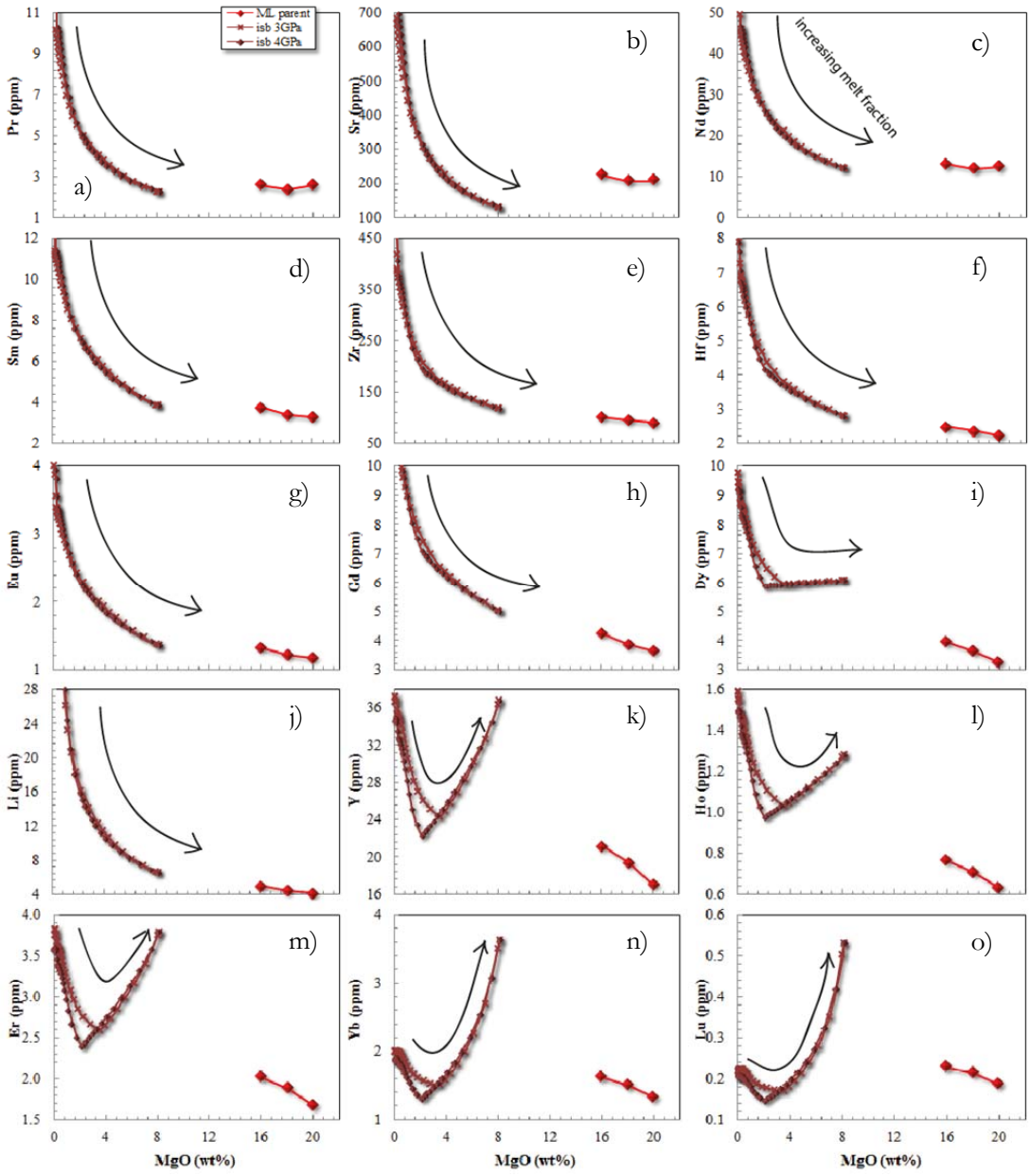

Figure 8.19 pMELTS isobaric melting of sea-floor-altered MORB composition (dark red), with Mauna Loa parental magma compositions (red diamonds). Each marker on the yellow pMELTS curve represents a decrease of 2000 bars in pressure, while each marker on the red curve represents an increase of 20 °C.

8.6 Mauna Loa versus Kilauea

The only obvious differences in the major element compositions between Kilauea and Mauna Loa from the literature data compilation in this study is the inverse relationship between SiO_2 and TiO_2 + K_2O (Figure 8.20a, b, c), and the very slightly lower Al_2O_3 content of Kilauea compared to Mauna Loa. P_2O_5 (not pictured) behaves the same as K_2O and TiO_2, with slightly

higher P_2O_5 in Kilauea lavas than Mauna Loa lavas. The relationship of the major element oxides between Mauna Loa and Kilauea found here are consistent with those found by Frey and Rhodes, though they found a greater difference in the CaO contents between the two volcanoes, with Kilauea containing higher CaO than Mauna Loa (Frey and Rhodes, 1993). If the melts below Kilauea came from deeper in the mantle and from a smaller melt fraction, the effect when melting an assemblage on the silica-undersaturated side of the thermal divide would be that the melt has higher TiO_2 and K_2O and lower SiO_2 than melts produced at shallower depths and higher melt fractions, which may be how lavas from Mauna Loa are produced.

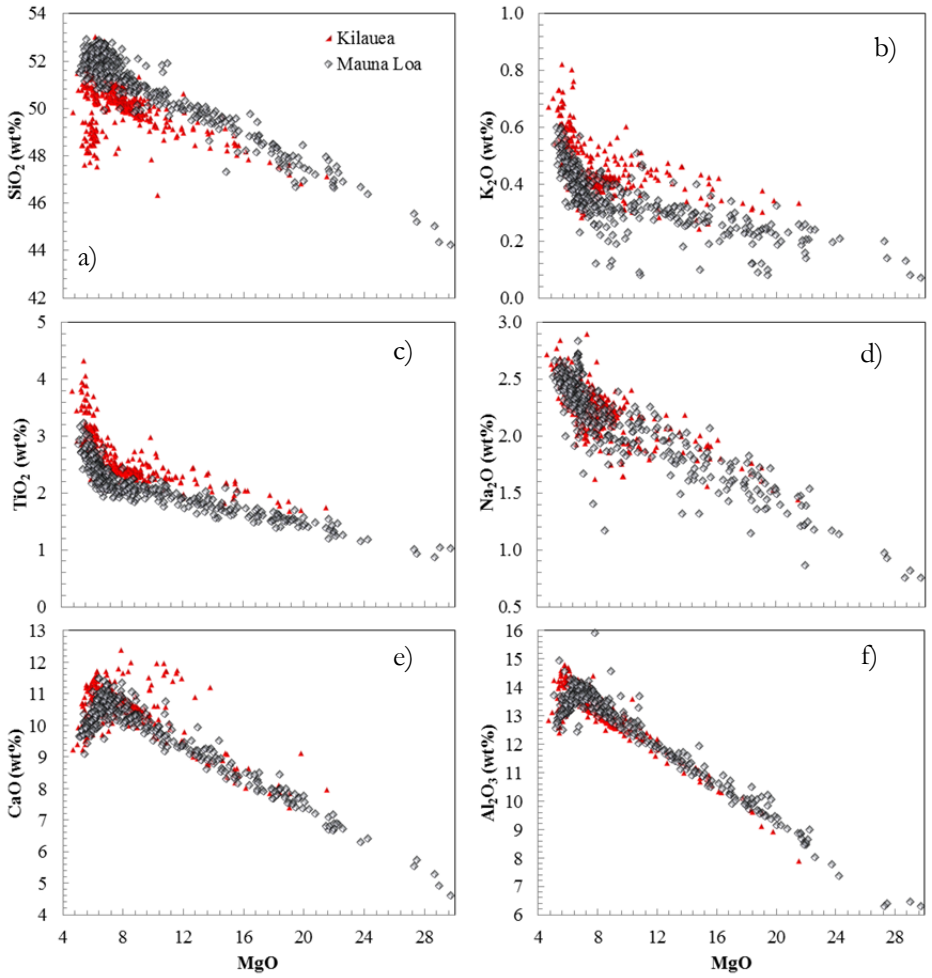

Figure 8.20 Literature compilation of Mauna Loa and Kilauea tholeiites (Moore and Clague, 1987, Rhodes and Hart, 1995, Hofmann and Jochum, 1996, Hauri and Kurz, 1997, Norman and Garcia, 1999, Davis et al., 2003, Rhodes and Vollinger, 2004, Rhodes and Vollinger, 2005, Wanless et al., 2005, Wanless et al., 2006).

The relationship between the major element oxides SiO_2, TiO_2, and K_2O may be of significance during melting. Studies have shown that changing the composition of the source to be silica-

saturated will produce different chemistry of the melt compared to variable degrees or pressure of melting of a constant composition source. Klemme and co-authors experimentally melted a composition representing subducted oceanic slab (a silica-saturated assemblage) at 3 GPa and found that the SiO_2 content decreased with increasing melt fraction while TiO_2 content increased (Klemme et al., 2002). Green and Pearson conducted melting experiments on various mafic, intermediate, and felsic compositions, and found that when the melt is saturated with a Ti-bearing phase (like rutile as is the case with oceanic crust), the Ti contents increases with increasing temperature, while the SiO_2 and K_2O contents decrease with increasing temperature (Green and Pearson, 1986). This is the opposite effect of what is seen during melting of peridotite, where TiO_2 and K_2O behave similarly and opposite to SiO_2, and is also the opposite of what is seen in the Kilauea and Mauna Loa literature data, where SiO_2 is higher and K_2O is lower in Mauna Loa lavas relative to Kilauea lavas. The relationship between SiO_2 and K_2O means that the difference between Mauna Loa and Kilauea must be due to variable degrees or pressure of melting of a peridotite source or a silica-undersaturated pyroxenite, and rules out the differences in the major elements between Kilauea and Mauna Loa being directly due to varying contributions of melted subducted slab material.

In addition to the relationship between melt fraction and major element content, the relationship between depth of melting and composition may be controlling the CaO/Al_2O_3 ratio of the Kilauea and Mauna Loa melts (Figure 8.21). There is a lower Al_2O_3 contents of the low degree PM melt at 4 GPa, which increases with increasing melt degree compared to 3 GPa where Al_2O_3 starts high in the low degree melt and decreases with increasing melt fraction (Figure 8.5c). Conversely, the CaO contents appears to be less dependent on pressure with CaO contents of peridotite decreasing with increasing melt degree irrespective of pressure. The relationship of CaO/Al_2O_3 between Kilauea and Mauna Loa suggests the source must be melting at a higher pressure where Al_2O_3 contents are lower at low degrees of melting, as it appears to be variation in Al_2O_3 rather than CaO controlling the CaO/Al_2O_3 differences (Figure 8.20f). The opposite behaviour of Al_2O_3 to the other incompatible major elements TiO_2 and K_2O indicates melting may be occurring closer to 4 GPa than 3 GPa. If Kilauea melts are the product of lower degree melting at high pressure, the compounding effect of the low degree melting and increase in pressure could drive the SiO_2 contents lower while the TiO_2 and K_2O contents are driven higher.

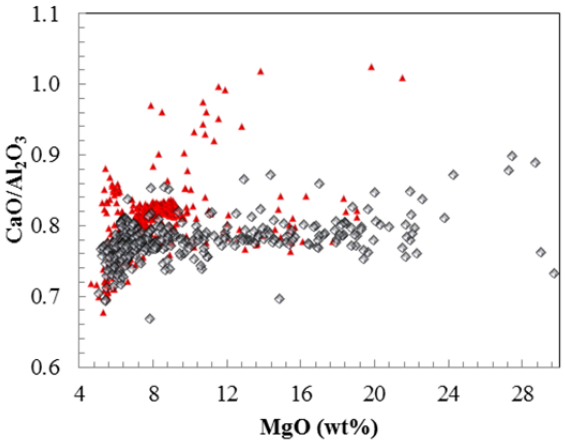

Figure 8.21 CaO/Al_2O_3 for Kilauea and Mauna Loa tholeiite literature data.

8.7 Peridotites as source for Hawaiian plume

When experimental melt data was compared to the Mauna Loa inferred parental magma composition earlier in this chapter, it was shown that peridotitic compositions such as primitive mantle (KR4003 and KLB-1) and Hawaiian pyrolite (HPY) best fitted the parental magmas. The closest of the pyroxenite melts were from the experimental composition formed by mixing of peridotite with a MORB-like composition - 'KG2'.

These mantle peridotite melts have been compiled (Figure 8.22) and again compared to three possible Mauna Loa parental magma compositions from the olivine control line established in Discussion chapter part I. As mentioned earlier, the parental magma compositions represent a minimum (16 wt. % MgO) estimate – in equilibrium with the highest Fo olivine from this study (~$Fo_{90.5}$), an intermediate (18 wt. % MgO) – in equilibrium with the highest Fo olivines found at Kilauea (~Fo_{91}), and a higher MgO composition (20 wt. % MgO), which would be approximately in equilibrium with an Fo_{92} olivine. The total range in major elements of the experimental melt compositions is large, and many are within the range of the Mauna Loa parental magma composition.

First of all, it can be noted that the melts from KG2 (made from peridotite + MORB in a 2:1 ratio) would require a higher degree of melting than primitive mantle or Hawaiian pyrolite in order to produce anything close to the parental magma composition. The highest MgO melt only reaches 15.57% MgO at 22 % melting, while the majority of melt compositions contain between 5 and 15 wt. % MgO. Given the Hawaiian primary magma probably contain at least 18 wt. % MgO it is unlikely this pyroxenite is a suitable candidate, though it appears that MgO increases with increasing pressure so it could be that melting at pressures higher than 3 GPa could increase melt MgO.

Secondly, the primitive mantle composition represented by experimental whole rock samples KR4003 and KLB-1 produces melts with a more appropriate MgO and SiO_2 range; however the TiO_2, FeO_t, and Na_2O in most melts are too low except for at very high pressures (4 GPa). Conversely, the Al_2O_3, CaO, and K_2O are mostly too high.

Finally, the Hawaiian pyrolite melts appear to lie closest to the Mauna Loa parental compositions, with melts matching in terms of SiO_2, TiO_2, Al_2O_3, CaO, Na_2O, and K_2O. The FeO_t contents of experimental HPY melts are significantly lower than the proposed ML parent, particularly at 18 and 20 wt. % MgO. Most of the major element oxides fit closest with the melts at 2 GPa which are garnet-free in their near-solidus assemblages, though SiO_2 appears closest to the 3 GPa melts. While the 2 GPa melts fit closest for most major element oxides, the 2 GPa SiO_2 contents only fit at low MgO, and that the 3 GPa melts are closest to the 20 wt. % MgO parental magma.

The scatter in the data show clearly which major elements are most strongly affected by variations in pressure, and those which are more sensitive to composition. It can be seen that the concentration of Al_2O_3 remains relatively constant at a given MgO over a large pressure range (between 1.5 - 4 GPa), for example when the primitive mantle composition is melted between 1.5 and 3 GPa a relatively tight linear array is formed with a negative correlation to MgO content. It is only the Hawaiian pyrolite composition that veers away from this array, as it contains a lower starting proportion of Al_2O_3 relative to PM (3.6% compared to 4.4%). The relatively fixed Al_2O_3 concentration could explain the small range in Al_2O_3 for a given MgO observed in Hawaii's lavas e.g. (Frey and Rhodes, 1993). Rhodes has also noted the narrow range in Al_2O_3 at a given MgO for Hawaiian shield lavas, and used this as evidence that the source of Hawaiian melts must contain garnet, which may buffer the Al_2O_3 content of the melt (Rhodes, 2016). The exception is that the 4 GPa melts are lower in Al_2O_3 at lower melt degree, which differs from melts of other pressures, indicating Al_2O_3 may be buffered when high proportions of garnet are present (12%).

Conversely, it can be seen that SiO_2 contents are most sensitive to pressure. It has been shown that the SiO_2 contents of partial melts decrease with increasing pressure e.g. (Klein and Langmuir, 1987), due to the variable stability of opx with pressure e.g. (Walter, 1998). Figure 8.22a shows that when primitive mantle compositions are melted, SiO_2 contents can vary from 50.1 wt. % at 20 wt. % MgO for melts at 1.5 GPa, to 45.5 wt. % at the same MgO for melts at 4 GPa. This is significant considering the high SiO_2 contents of Mauna Loa lavas relative to Kilauea lavas is used as evidence for recycled subducted slab in Mauna Loa's source (Hauri, 1996, Frey et al., 2016). The high SiO_2 contents of Mauna Loa lavas may be the result of melting

at lower pressures than Kilauea (at least 3 GPa if the 20 wt. % parental magma composition is used).

Similarly, total FeO appears to be sensitive to pressure, with a pressure dependent range of the iron between 7.8 and 10.65 wt. % FeO_t at a given MgO for the primitive mantle compositions, showing thatin general, Fe content increases with increasing pressure of melting. The high iron content of the Mauna Loa parental magmas appears to suggest a minimum pressure of 4 GPa. MgO appears to be most sensitive to degree of melting, but also to a large extent pressure. The effect of pressure on MgO can be most clearly seen in the MIX1G and KG2 melts where a significant difference can be seen over a pressure range of just 0.5 GPa. The other major element oxides (CaO, TiO_2, Na_2O, and K_2O) appear to be dependent on both starting composition and melt fraction, and to a smaller extent pressure. It can be seen that the CaO composition can span a wide range just with the variation in melt degree (Figure 8.22e). The range in CaO by melting one starting composition e.g. KR4003 at one pressure e.g. 3 GPa is 7.7-10.9 wt. %. The maximum is reached at about 10-20% melting depending on the pressure, though low CaO contents can be reached at low or high degrees of melting, the pattern of which can be seen in Figure 8.26e. MELTS modelling pattern of CaO in melts from HPY, appears to be reflected in experimental melts from HPY, suggests that at higher pressures, these low CaO, low degree melts can be formed at high MgO, placing them closer to the predicted parental magma compositions. Unfortunately, there are very few data points for the higher pressure melts from PM and HPY, so it is not possible to be certain how CaO will behave at pressures above ~3 GPa.

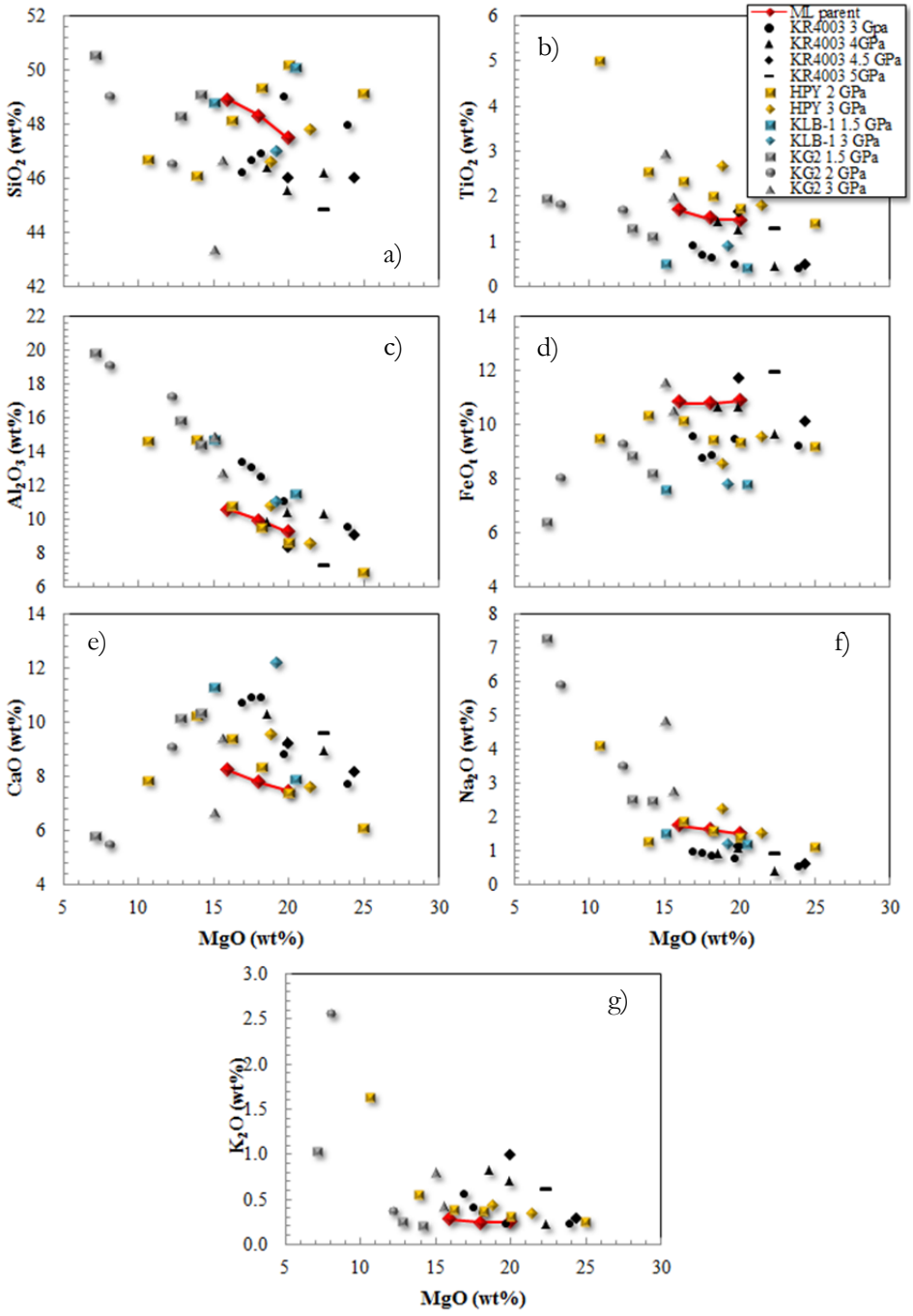

Figure 8.22 Experimental melt compositions of the peridotites KR4003, HPY, and KLB, and pyroxenite KG2,

8.7.1 Primitive mantle

A further attempt at reproducing primitive mantle melt compositions was made using the pMELTS program; however this time using different pressures to those used in the experiments. By lowering the pressure input into MELTS, the experimental melt major element

compositions from melting of bulk composition KR4003 at 3 GPa were able to be recreated using the pMELTS software (

Figure 8.23). The pMELTS program was able to recreate the experimental melt when the input pressure was set to 1.4 GPa, a significant total offset of 1.6 GPa. The solidus phases predicted by pMELTS were 51.2% olivine, 27.5% opx, 16.3% cpx, and 3.4% spinel. pMELTS in this case has failed to correctly predict garnet (1.9% predicted experimentally), has over-predicted the proportion of opx (27.5% compared to 17.7% experimentally), and under-predicted the proportion of cpx (16.3% compared to 27.3% experimentally). The large discrepancy in the predicted phase assemblages means that attempting to use pMELTS to model trace elements will not yield meaningful results.

As shown in section 8.6.1, the Mauna Loa parental magmas span a range of 16 – 20 wt. % MgO, which coincides with melt percentages ranging from 9 to 37% for the primitive mantle composition. pMELTS predicts a range of 11 – 30% melting over the same MgO interval. The higher pressure melts (4 GPa) have lower melt degrees over the MgO interval (9-13%) than the 3 GPa melts (14-37%). The 3 GPa melts are closer to the 20 wt. % MgO parental magma than the 4 GPa melts for SiO_2, but the 4 GPa melts are closer in terms of TiO_2, FeO, and Al_2O_3.

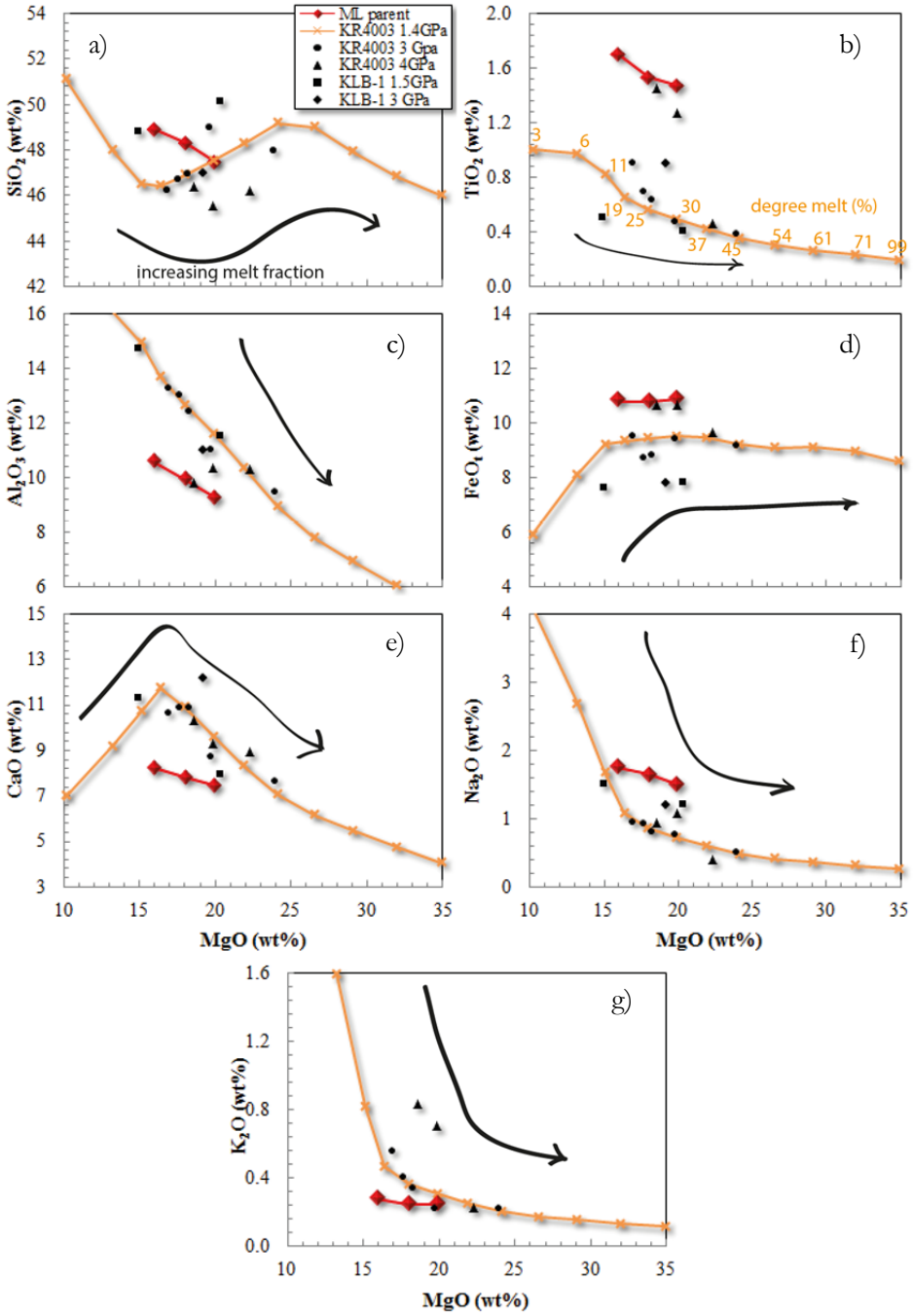

Figure 8.23 MELTS calculated fractionation path of PM at 1.4GPa

Instead of using pMELTS to model trace element paths during melting of the mantle, trace element melting paths were calculated using trace element melting equations (Rollinson, 1993Zou, 2007 #2095) and plotted against La in Figure 8.24. Primitive mantle was melted at 3 and 4 GPa using a non-modal batch melting equation:

$$\frac{CL}{C0} = \frac{1}{D0 + F(1-P)}$$

Where C_L is the concentration of the trace element in the liquid, C_0 is the concentration of the trace element in the source, F is the melt fraction between 0 and 1, D_0 is the bulk distribution coefficient, and P is the bulk distribution coefficient of the minerals which make up the melt. Phase assemblages for primitive mantle used to calculate D_0 were from 3 and 4 GPa (garnet stable) experiments from Walter (1998) and partition coefficients used were those of McKenzie and O'Nions (1991;1995) which are those used in by the pMELTS software and as given in discussion chapter I. Given that the melt reaction coefficient (which is later multiplied by each mineral/melt partition coefficient to calculate the coefficient 'P' in the melting equation) changes with each degree of melting, each value of C_L was calculated individually for every melt fraction given in the experimental data. The melt reaction coefficients were determined by taking the sum of the normative fraction of each mineral making up the melt (based on the changing mineral assemblage given in the experimental data) and can be found in Table 8.5. Because the experimental data don't contain estimates for very low degree melting and near-solidus phase assemblages appear anomalous (i.e. the phase assemblage at with 9% melt in the Walter 1998 4 GPa experimental data), the concentrations at 4 and 7 % melt were inferred by taking a mid-way point between the starting compositions and the first melt fraction given.

Notably, there is significant variation in the garnet content of the compositions, with the 3 GPa PM assemblage containing 1.9% garnet, and the 4 GPa assemblage containing 12.9% garnet, which has a significant impact on calculate HREE concentrations. Results are plotted in Figure 8.24 against La as an indicator of melt degree.

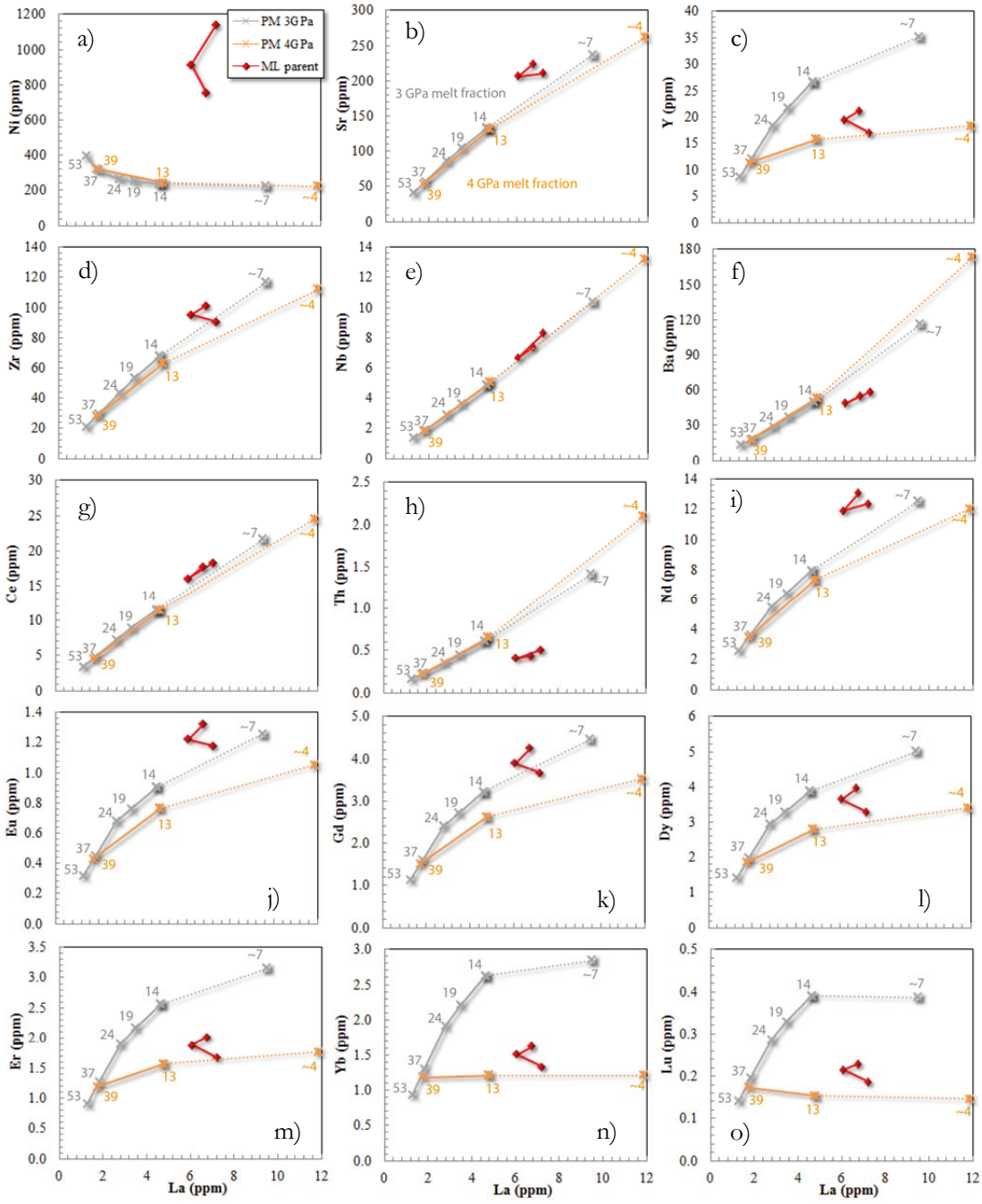
a)
PM 3GPa
PM 4GPa
ML parent
Ni (ppm)
b)
3 GPa melt fraction
4 GPa melt fraction
Sr (ppm)
c)
Y (ppm)
d)
Zr (ppm)
e)
Nb (ppm)
f)
Ba (ppm)
g)
Ce (ppm)
h)
Th (ppm)
i)
Nd (ppm)
j)
Eu (ppm)
k)
Gd (ppm)
l)
Dy (ppm)
m)
Er (ppm)
n)
Yb (ppm)
o)
Lu (ppm)
La (ppm)
~7
~4

Figure 8.24 Calculated melting curves for primitive mantle at 3 and 4 GPa.

Table 8.5 Melt reaction coefficients used in trace element melt models assuming batch melting. The melt reaction coefficients were determined using the sum of the normative fraction of each mineral making up the melt (based on the changing mineral assemblage given in the experimental data)

	Solidus assemblage %		Melt reaction coefficients								
	3 Gpa	4 Gpa	3 Gpa					4 GPa			
Melt (%)			7	14	19	24	37	53	4	13	39
olivine	53.1	53.6	0.04	0.04	0.09	0.11	0.01	0.11	0.41	0.16	0.16
opx	17.7	5.6	-0.15	-0.14	-0.16	-0.30	0.21	0.34	-0.13	-0.12	-0.21
cpx	27.3	27.9	0.97	0.96	0.97	1.12	0.73	0.52	-0.81	0.36	0.73
garnet	1.9	12.9	0.13	0.14	0.10	0.08	0.05	0.04	1.53	0.60	0.32

The highly incompatible elements are insensitive to changes in pressure (Nb, Ba, Sr, Th, and Ce) while the moderately incompatible and HREE are strongly dependent of pressure, in particular Er, Yb, and Lu due to their compatibility in garnet. At no pressure is the calculated concentration of Ni high enough in the melt to produce the Mauna Loa parental magma concentration, while some of the highly incompatible elements are close to the ML parent at ~ 10% melting (Zr, Nb, Ce). Th and Ba appear to be slightly overestimated in the models for a given value of La, while Nd, Eu, and Sr are slightly underestimated. Additionally, the heavy and middle REE are not fractionated from one-another enough, with the calculated HREE composition being higher than that of the 3 GPa melt, while the heavy REE are very close to the 4 GPa melt. The predicted 4 GPa melts are systematically too low in almost all trace elements with the exception of Ba and Th, reflecting the increased compatibility of the trace elements with increasing proportion of garnet relative to opx in the solidus assemblage. In conclusion, a large amount of garnet is needed to fractionate the HREE sufficiently from the LREE, indicating that melting must occur at a relatively high pressure (between 3-4 GPa) where a significant proportion of garnet is stable.

Out of interest, the trace element fractionation paths for melting of primitive mantle with pMELTS at 1 and 2 GPa (equivalent to between 1.5 and 4 GPa experimentally) is shown in Figure 8.25 below, against ML parental magma trace element estimates. It can be seen that pressure has the opposite on melt composition compared to the above calculations as higher pressure melts are increasingly enriched in trace elements, and that pressure has a much smaller effect on trace element concentrations than in the above calculations. This difference to the non-modal melting model above, along with the fact that solidus assemblage is incorrectly calculated for primitive mantle at high pressures, may indicate that pMELTS is misrepresenting trace element behaviour during melting of a peridotite at pressures > 1 GPa.

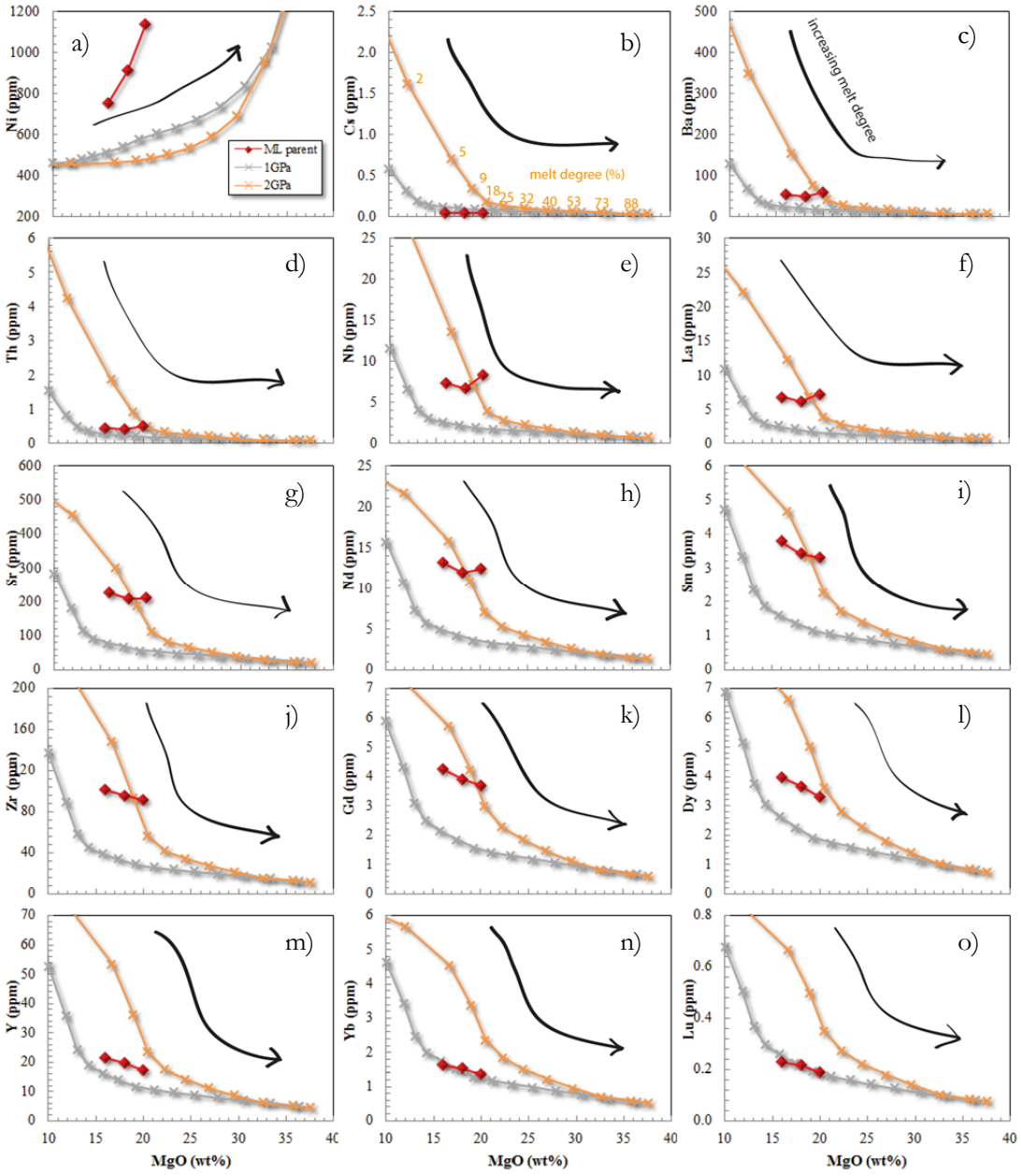

Figure 8.25 pMELTS calculated trace element melt paths

8.7.2 Hawaiian Pyrolite

It was shown that in terms of matching the experimental melts with the proposed Mauna Loa parental magma composition, the Hawaiian pyrolite composition (initially calculated by Green and Ringwood (1963) and later the experimental composition was formulated by Falloon and co-authors (1988)) matches the inferred parental magma composition of Mauna Loa relatively closely compared to other experimental melt composition considered here. The 2 GPa melt curve created from the experimental data intersects the range in the Mauna Loa parental magma

composition for all major elements except TiO_2 and K_2O which are too high, and FeO_t which is too low in the experimental melts compared to the parental magma (Figure 8.22). The 3 GPa curve comes close to the major element oxide composition of the parental magma for most oxides at a high melt degree except FeO_t, which is again too low in the experimental data. If the 3 GPa curve was continued to higher melt degrees it appears as though it would intersect the parental magma composition at a high MgO (>20 wt. %). The discrepancy may reflect that the Hawaiian pyrolite composition was created as the source of Kilauea (high TiO_2 and K_2O compared to Mauna Loa) by adding the composition of a Kilauea tholeiite to a harzburgite/dunite composition. Also, the experimental 2 GPa melts have higher SiO_2 for a given MgO than the estimated parental magma composition for example 49.33 wt. % SiO_2 at 18.21 wt. % MgO which is higher than Mauna Loa values. The 2 GPa HPY melts containing higher SiO_2 compared to Mauna Loa lavas when it has been documented that Kilauea lavas have significantly lower SiO_2 than Mauna Loa (Hauri, 1996, Frey and Rhodes, 1993) may further indicate that the pyrolite composition is more suited to be the source of Hawaii's lavas at higher pressures closer to 3 GPa.

pMELTS was used to recreate the HPY melt compositions from experiments (Figure 8.26). It was possible to recreate the melting path of the 2 GPa melt by inputting the pressure to 1.1 GPa, an 0.9 GPa offset. The pMELTS-predicted phase assemblage at the solidus was 55% olivine, 40% cpx, and 0.4% spinel however after a small amount of melting it was 56% olivine, 25% opx, and 15% cpx, indicating that pMELTS struggles to predict the phase assemblage for Hawaiian pyrolite in addition to primitive mantle, and even more so very close to the solidus.

The melt compositions of the Kilauea-derived Hawaiian pyrolite relative to those of Mauna Loa allow some inferences to be made about the mechanisms by which Mauna Loa is differentiated from Kilauea in terms of major element chemistry. The two parameters which can easily change the melt compositions of the two volcanoes without altering the source chemistry are degree of melting and pressure of melting. SiO_2 is noticeably different between the two volcanoes with Mauna Loa melts containing higher SiO_2 at a given MgO. In order to achieve this, Kilauea would need to be either melted at a higher pressure than Mauna Loa, by a smaller melt degree, or both. The difference in SiO_2 at a given MgO between Mauna Lo and Kilauea from the compilation in this study (Figure 8.20) is about 1 wt. %, which could be accounted for with a difference of >10% melting in the higher melt degrees at 3 GPa (assuming PM starting composition) or >4% at the lower melt degrees of the 4 GPa melts. Alternatively, an increase in pressure of 1 GPa can cause a 3.5 wt. % decrease in SiO_2 at a given MgO.

TiO_2 is also a distinguishing component with Kilauea containing higher TiO_2 than Mauna Loa at a given MgO. This can also be affected by pressure somewhat but to a lesser degree than SiO_2. It can be seen in Figure 8.26 that TiO_2 (and to a smaller extent K_2O) would need to be lower than the 2 GPa HPY source can produce, which may indicate a decrease in pressure is necessary (in the range of 0.5-1 GPa). Unfortunately, doing so would then drive the SiO_2 too high and FeO_t too low to fit the ML parental composition. A 0.3% difference in TiO_2 is seen between Kilauea and Mauna Loa at a given MgO, which could be driven by a 10% difference in melting at 3 GPa or a >4% difference in melting at 4 GPa.

A 0.4 wt. % increase in K_2O is seen in Kilauea compared to Mauna Loa. This difference would again require a >23% difference in melt degree at 3 GPa but only a >4% difference at 4 GPa. These differences are probably because the 4 GPa PM melts reached lower overall melt fractions than those at 3 GPa. Therefore, these differences in major elements can be accounted for with a feasible variation in melt degree, so long as the overall melt degrees are small. It is unclear if 4 GPa melting is required because low degree melts are missing at 3 GPa from the Walter (1998) study.

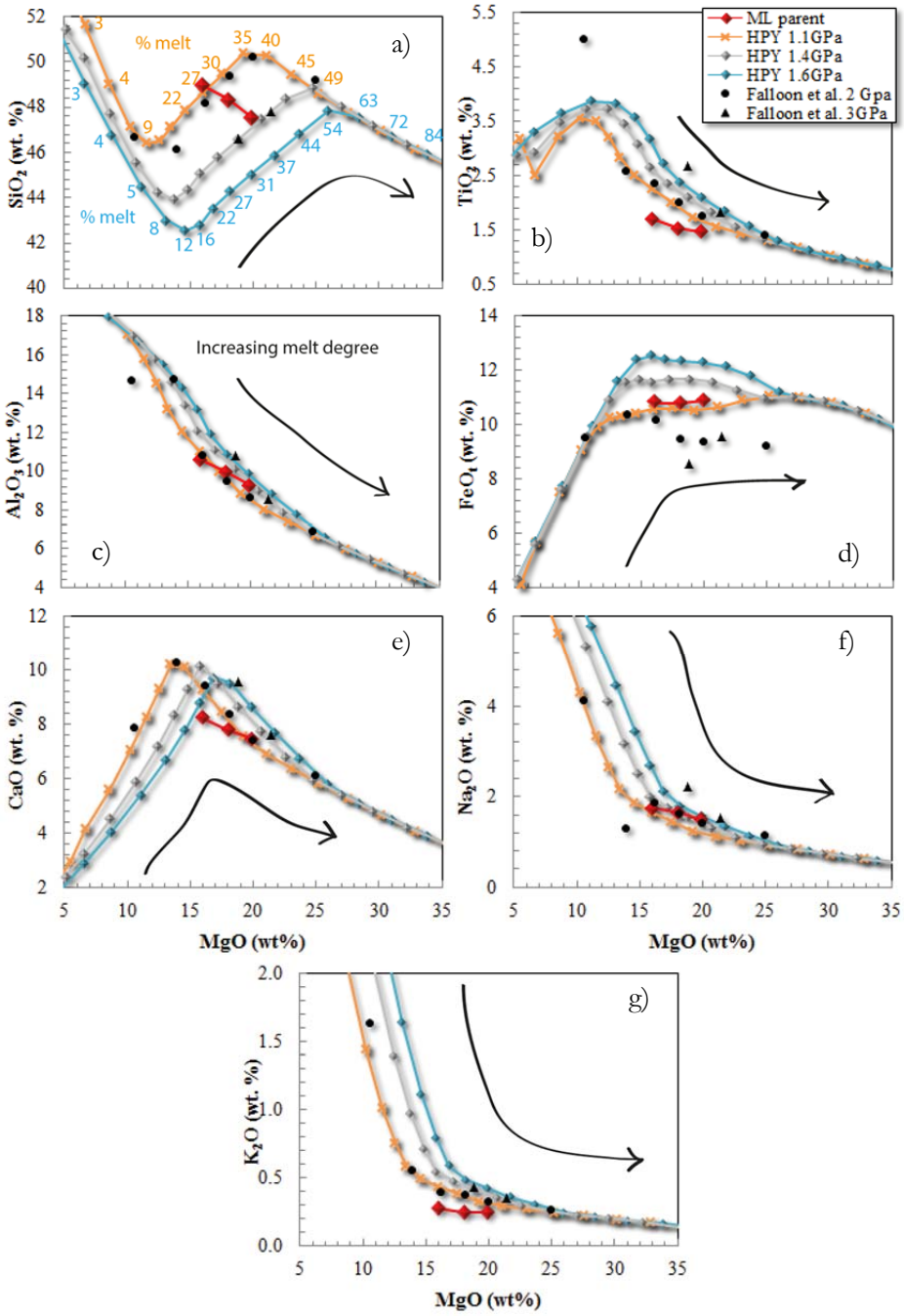

Figure 8.26 pMELTS-calculated melt compositions for melting Hawaiian pyrolite within the range of 2 and 3 GPa experimental melts.

8.7.3 Isotopes weigh in

A compilation of Mauna Loa and Kilauea isotopes (figure 6.11 isotope results section) shows that Mauna Loa and Kilauea have $^{87}Sr/^{86}Sr$ and $^{143}Nd/^{144}Nd$ signatures that lie between bulk silicate Earth (BSE) and DMM. Lavas from Kilauea are characterised by higher $^{143}Nd/^{144}Nd$ and lower $^{87}Sr/^{86}Sr$.

Isotopic compositions have been used to infer that the Hawaiian plume must contain recycled oceanic crust, for example it has been suggested that the low $^{143}Nd/^{144}Nd$ of the Ko'olau component (and by extension other Loa-track volcanoes) as evidence of sediment-containing oceanic crust (Huang and Frey, 2005). Similarly, Frey and co-authors have suggested that the low $^{143}Nd/^{144}Nd$ and $^{206}Pb/^{204}Pb$ of Loa-track volcanoes might indicate the presence of delaminated lower continental crust with a large proportion of plagioclase in the Loa-track volcano (Frey et al., 2016). The compilation of Kilauea and Mauna Loa lavas from this study was plotted in three dimensional space in terms of $^{87}Sr/^{86}Sr$, $^{143}Nd/^{144}Nd$ and $^{206}Pb/^{204}Pb$ (Figure 8.27Figure 8.28Figure 8.29) with the compositions of BSE, DMM, Enriched DMM (E-DMM), and Depleted DMM (D-DMM) (Workman and Hart, 2005). The E-DMM composition can be found in MORB including Indian MORB and the high $^{87}Sr/^{86}Sr$, low $^{143}Nd/^{144}Nd$ end-member of the Mid-Atlantic Ridge basalts, while D-DMM is closer to the low $^{87}Sr/^{86}Sr$, high $^{143}Nd/^{144}Nd$ end-member of the Mid-Atlantic Ridge, as well as the East Pacific Rise, and Juan De Fuca Ridge. Workman and Hart demonstrate that $^{206}Pb/^{204}Pb$ is the isotopic ratio with the greatest variance in MORB (47%) compared to 18% for $^{87}Sr/^{86}Sr$ and 35% for $^{143}Nd/^{144}Nd$. They also show that BSE and D-DMM have very similar $^{206}Pb/^{204}Pb$ signatures (both with $^{206}Pb/^{204}Pb = 17.5$), while E-DMM lavas have the high $^{206}Pb/^{204}Pb$ end-member ($^{206}Pb/^{204}Pb = 19$). It can be seen that the lavas mostly lie within a plane, varying predominantly in $^{143}Nd/^{144}Nd$ and $^{206}Pb/^{204}Pb$ with a relatively narrow range in $^{87}Sr/^{86}Sr$ (Figure 8.29). The Mauna Loa lavas form an 'L' shape with some lavas trending towards BSE and some trending towards Kilauea lavas and overlapping with them. Kilauea lavas form a near-linear trend between the Mauna Loa lavas at one extreme, and the composition of E-DMM at the other extreme. It is clear that the average DMM (and therefore average MORB) signature is too low in $^{206}Pb/^{204}Pb$ and $^{87}Sr/^{86}Sr$ while being too high in $^{143}Nd/^{144}Nd$ to be an end-member of the Hawaiian lavas; however an enriched type E-MORB or E-DMM component could be a potential Kilauea end-member. Given the major discriminant between the Kea and Loa tracks is Pb isotopic signatures (Abouchami et al., 2005), it is significant that Kilauea trends towards the 'enriched' high $^{206}Pb/^{204}Pb$ E-DMM signature.

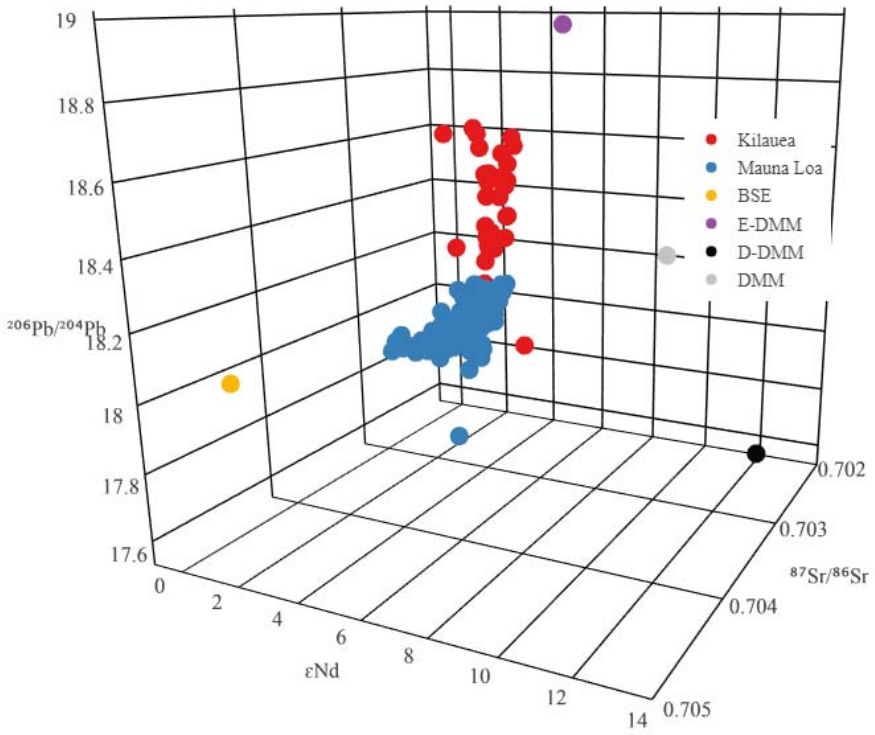

Figure 8.27 Isotopic composition of Mauna Loa (blue) and Kilauea (red) lavas.

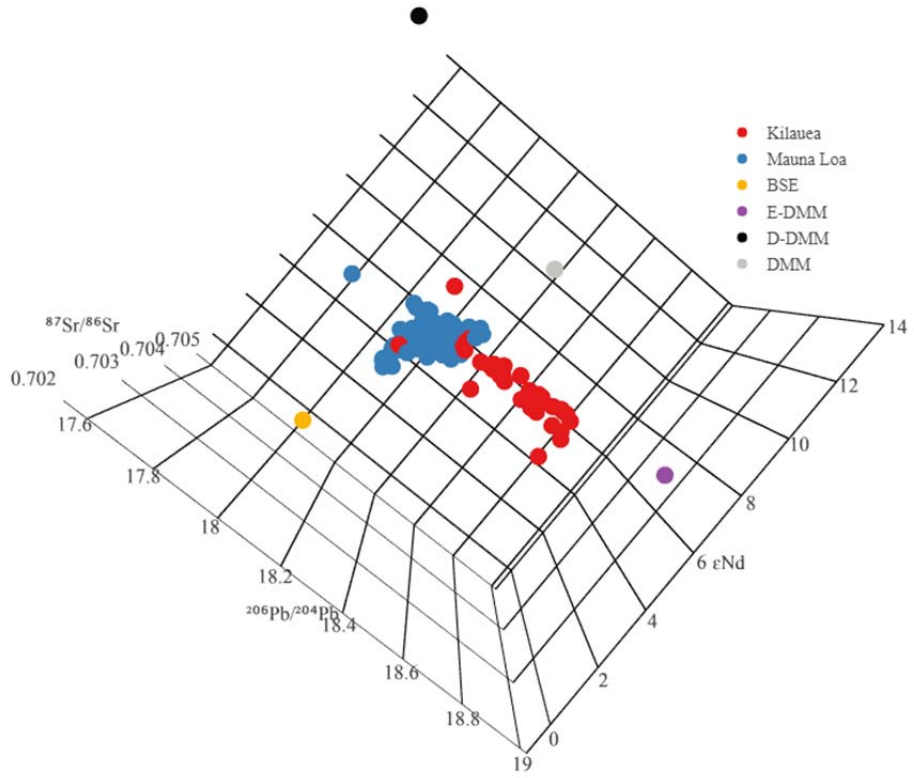

Figure 8.28 Isotopic composition of Mauna Loa (blue) and Kilauea (red) lavas cont.

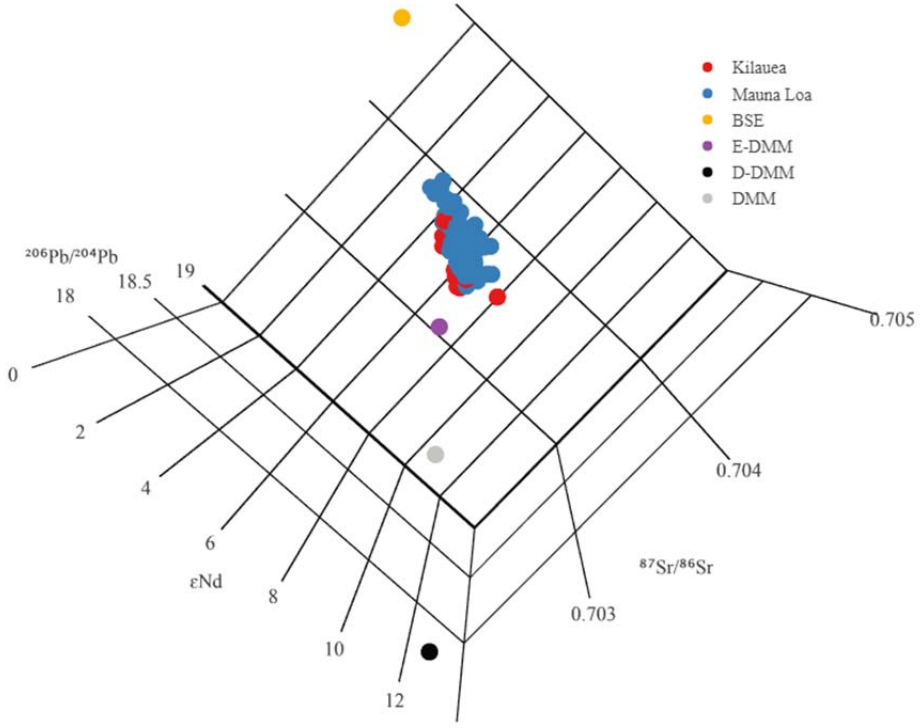

Figure 8.29 Isotopic composition of Mauna Loa (blue) and Kilauea (red) lavas.

8.7.4 Reconciling the trace elements

The trace element compositions of various mantle sources and basalts are plotted below (Figure 8.30) normalized to the Mauna Loa parental magma composition at 20 wt. % MgO in order to establish which sources may provide the best fit to the trace element pattern of Mauna Loa tholeiites. It is clear that the Mauna Loa pattern is very close to that of Sun & McDonough's E-MORB composition (Sun and McDonough, 1989), which has slightly lower HREE and higher highly incompatible and LREE than N-type MORB, lying between N-type and alkali basalts. The difference between N-Type and E-Type MORB here is that E-Type is more enriched in highly incompatibles Rb, Nb, Cs, Ta, Th, and U compared to N-Type while N-type is slightly higher in the HREE and moderately incompatibles Gd, Dy, Ho, Er, Yb, and Lu. The Mauna Loa parent is similar to the E-MORB in terms of the highly incompatibles though slightly lower in Ho, Er, Yb, and Lu, suggesting slightly more fractionation of the LREE from the HREE, most likely due to the presence of residual garnet in the Mauna Loa source compared to that of N-MORB. .

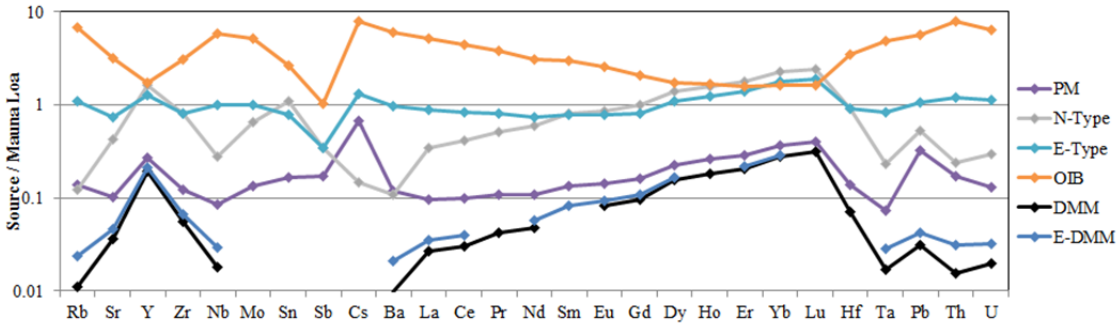

Figure 8.30 Trace element compositions of primitive mantle (Sun and McDonough, 1989), depleted and enriched-depleted mantle (Workman and Hart, 2005), and normal, enriched, and ocean island basalt (Sun and McDonough, 1989) compositions normalized to Mauna Loa 20% MgO parental magma.

In addition to melting the primitive mantle composition, mixtures of MORB components with depleted mantle components were tested to see if a suitable source for Mauna Loa tholeiites could be produced. It was found that melting a DMM or E-DMM source could not account for the high concentrations of trace elements in the Mauna Loa parent at any degree of melting, because the trace element concentrations of either MORB source were far too low. In order to increase the concentrations of trace elements in the source, 10% E-MORB was added to 90% DMM and melted using the same method as described earlier, as well as a source with 10% ML parent added to 90% DMM. Results are shown below in Figure 8.31, where it can be seen that the results of the 10% ML + 90% DMM fit the Mauna Loa parental magma the closest, with approximately 10% melting at pressures between 3 and 4 GPa. The 10% E-MORB + 90% DMM fit the next closest, while the primitive mantle melt matches the least closely of the three.

The trace element composition of Kilauea lavas at the equivalent MgO content of 20 wt. % was calculated by applying an enrichment factor from the trace element comparison of Kilauea and Mauna Loa lava by Frey and co-authors (2016) to the 16, 18, and 20% MgO Mauna Loa lavas. The results were plotted below in Figure 8.31. The Kilauea lavas are consistent with a lower degree of melting (~6%) compared to Mauna Loa (~12%) and possibly at a slightly higher pressure, or from a source further differentiated from PM composition (particularly in terms of U).

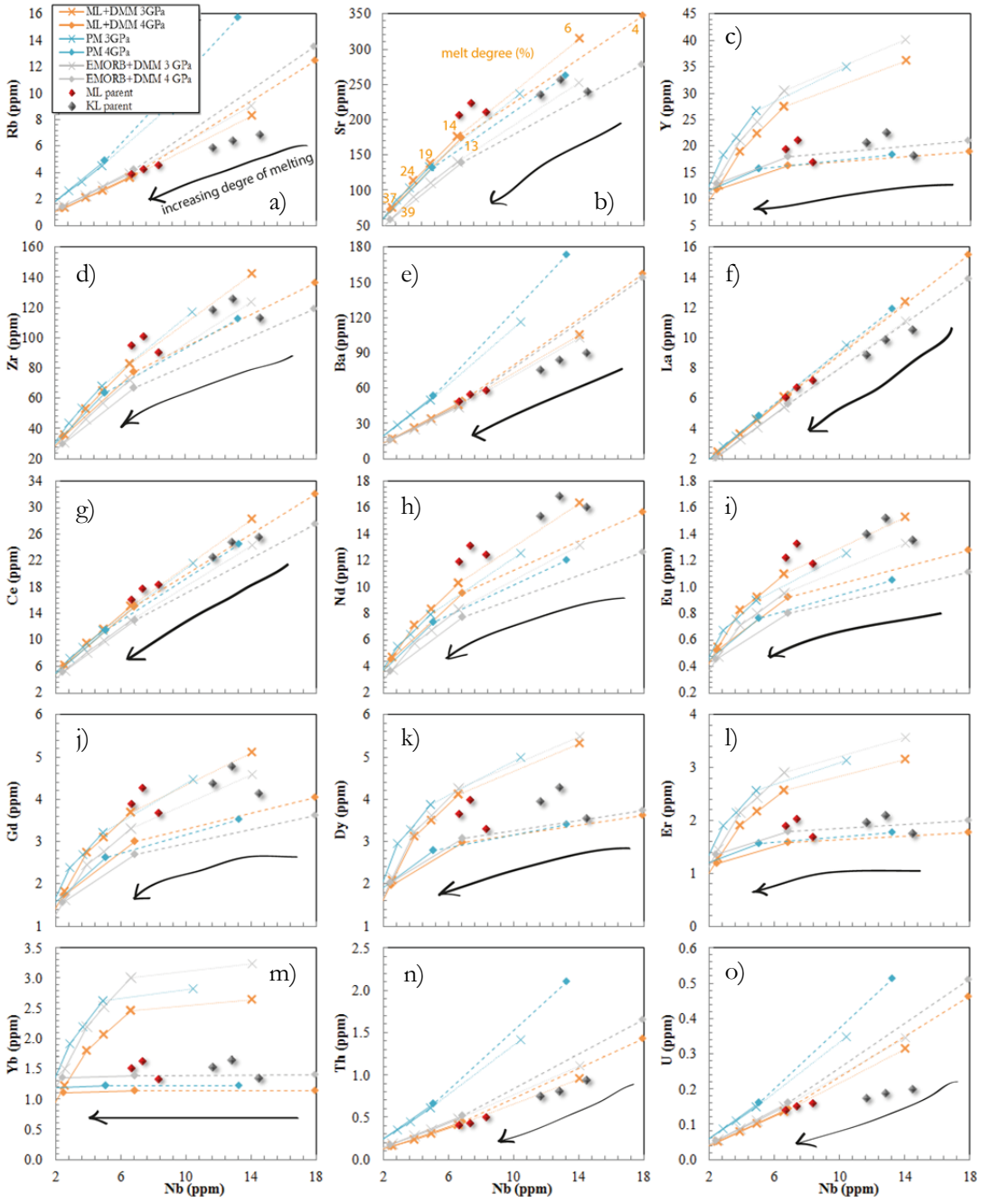

Figure 8.31 Trace element melt modelling of a DMM + E-MORB source and a DMM + ML source. Mauna Loa parental magma composition shown in red at 16, 18, and 20 wt. % MgO and the same for the equivalent Kilauea parental trace element composition shown in grey.

The calculated ML + DM (10/90) source trace element composition was plotted against the DMM and E-DMM compositions of Workman and Hart (2005) (Figure 8.32). When comparing source compositions, the Mauna Loa parental magma source formed by the addition of 10% Mauna Loa and 90% DMM is closest to primitive mantle, in terms of the ratio of the LREE relative to the HREE (Figure 8.32). It is slightly lower in the highly incompatible elements Ba,

Th, and Rb but higher in most of the incompatible elements, while being lower in Yb and Lu than primitive mantle.

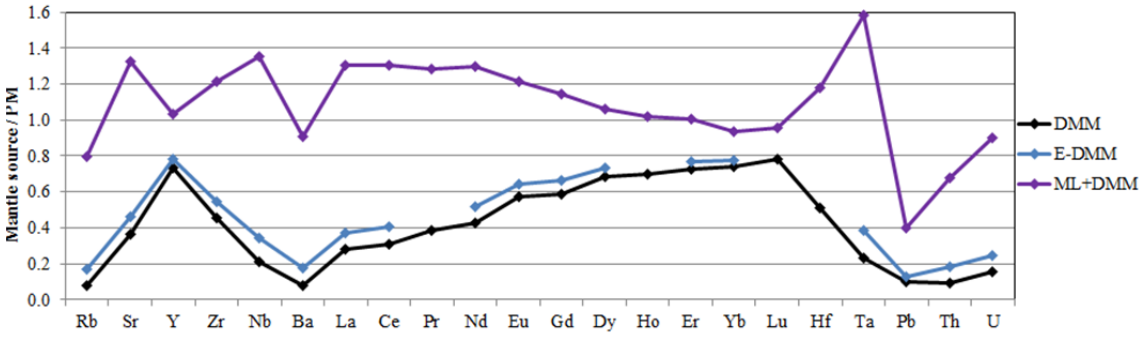

Figure 8.32 Mantle compositions DMM, E-DMM, and ML + DMM (10/90) normalized to primitive mantle.

When the major element composition of the ML + DM (10/90) is compared to that of primitive mantle there is a remarkably close match, with the exception of perhaps Na_2O and Cr_2O_3. The close match of the major elements to primitive mantle may be evidence that Mauna Loa volcano is the result of ~10% melting of a relatively fertile mantle composition. Although the trace element concentrations are also close to that of primitive mantle, the key features of the pattern illustrates strong fractionations that are inconsistent with a true primitive mantle, e.g., Nb/U and Th/U ratios are strongly fractionated relative to PM. though may have been altered slightly by removal of some highly incompatible elements and HREE, and addition or relative enrichment of some highly-to-moderately incompatible elements. Alternatively, 10% of subducted E-MORB or equivalent enriched MORB may be a component in the Mauna Loa source. For this to be the case, the subducted crust would have to melt to a large degree if not completely, which could be possible based on experimentally-determined temperatures of melting eclogite compared to peridotite (

Table 8.4). The differences in trace elements between Kilauea and Mauna Loa appear to be able to be explained mostly by a smaller degree of melting of the Kilauea source (~6% compared to ~12%) at slightly higher pressure than Mauna Loa, though some of the highly incompatibles (Rb, Ba, U) may need to be slightly lower in the Kilauea source relative to the highly-moderately (La, Ce, Nd, Eu etc.).

Table 8.6 ML + DMM (10/90) major element composition compared with primitive mantle of Sun and McDonough (1989).

	ML+DMM	PM
SiO_2	44.99	44.90
TiO_2	0.26	0.20
Al_2O_3	4.51	4.44
FeO_t	8.45	8.03
MnO	0.13	0.13
MgO	36.85	37.71
CaO	3.60	3.54
Na_2O	0.27	0.36
K_2O	0.03	0.03
P_2O_5	0.03	0.02
Cr_2O_3	0.53	0.38

Roden and co-authors have shown that the Ko'olau (Loa) component lavas have higher La/Nb and Sr/Nd than other Hawaiian tholeiites (including those from Kilauea), which they have suggested are inconsistent with origins from primitive mantle, recycled material, or metasomatized source (Roden et al 1994- New He, Nd, Pb). Below (Figure 8.33) it can be seen that the Kilauea lavas are furthest away from a primitive mantle melt than Mauna Loa. If the relationships between Kilauea and Mauna Loa melts (from Frey et al., 2006) are accurate, then in the fine detail Mauna Loa and Kilauea cannot be simply related through variable degrees of melting of a primitive mantle source. High La/Nb and Sr/Nd have been used to infer gabbro in the source for ML (Frey et al., 2016), though it appears that the high La/Nb and Sr/Nd are closer to a fertile mantle composition than the Kilauea source is.

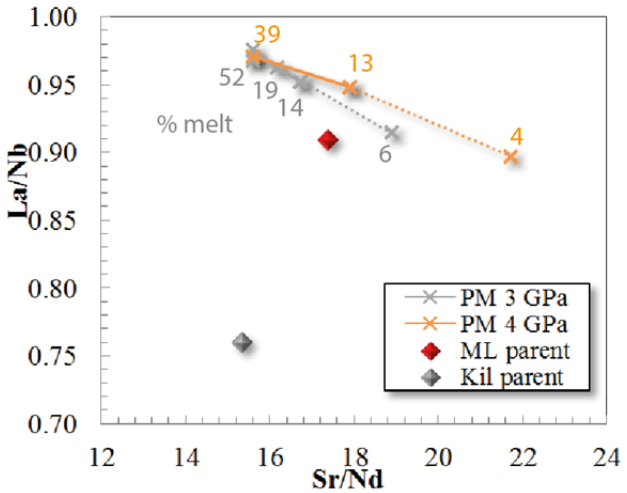

Figure 8.33 estimated variation in La/Nb and Sr/Nd with degree of melting, with Mauna Loa (red) and Kilauea (grey) parental magmas at 18 wt. % MgO.

8.7.5 Water

The water content expected for Mauna Loa magmas through variable degrees of melting of a primitive mantle was modelled. A primitive mantle water estimate (C_0) (Kovalenko et al., 2006) range of 93-420 ppm was assumed, while the trace element partition coefficients of Ce were used, as it has been shown that for $D_{H_2O}^{min/melt}$, La>H_2O≈Ce>Nd (Michael, 1995). The Kovalenko range in water composition is consistent with another primitive mantle estimate of 245-290 ppm (Bell and Rossman, 1992). C_0=93 yielded a range in melt water contents of 0.11-0.02 wt. % over a melting interval of 6-53% at a pressure of 3 GPa (Figure 8.34). The upper estimate by Kovalenko and co-authors (C_0=420) yielded a range in melt water contents of 0.51-0.08 wt. % over the same melting range and pressure. Pressure was not a large factor in the variation of water contents expected in the melt.

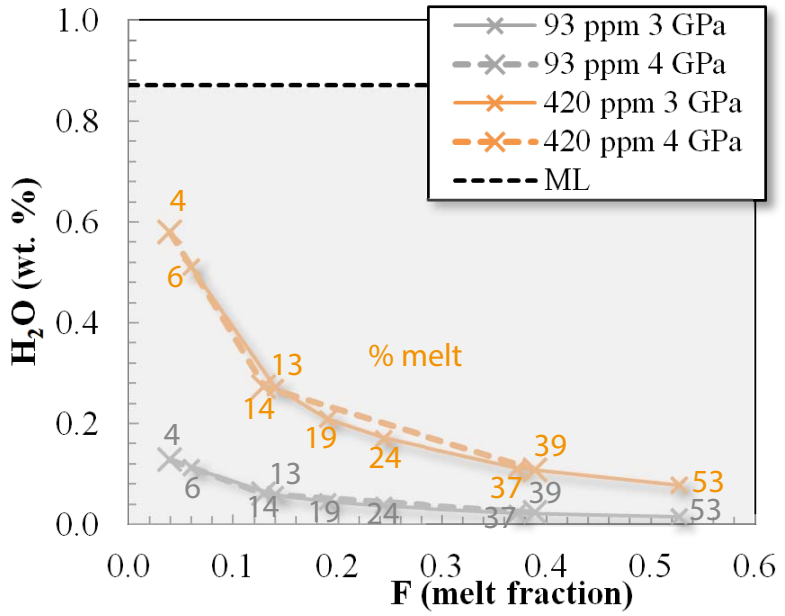

Figure 8.34 Predicted water content of melt at variable degrees of melting of a primitive mantle at 3 and 4 GPa assuming 93 ppm starting H_2O (orange) or 420 ppm starting H_2O (grey) according to a likely range for PM H_2O (Kovalenko et al., 2006). Area shaded in grey is the range of H_2O found in Mauna Loa glasses (up to 0.87 wt. %) (Davis et al., 2003).

The water content in Mauna Loa glasses has been shown to range from nearly zero to 0.87 wt. % (Davis et al., 2003), which is well above the estimates produced in the melt calculation above, even at low degrees of melting (Figure 8.34). The parental magma estimate used in chapter 7 (0.3 wt. % H_2O) can be produced with ~13 % melting of a source containing 420 ppm H_2O at

3-4 GPa. The most depleted value (93 ppm) is less than Kovalenko and co-author's estimate of depleted MORB mantle (100-200 ppm H_2O), and therefore cannot reproduce the parental magma estimate of 0.3 wt. % H_2O at any of the melt fractions or pressures tested here. Water content in the melt is highly dependent on the H_2O content of the mantle source, and there are a wide range of mantle water estimates that can vary the outcome when modelling water content during melting of the mantle (Kovalenko et al., 2006).

8.7.6 Nickel

One of the arguments made for a pyroxenitic mantle is that the nickel contents of Hawaiian lavas are too high to be explained by melting of a peridotite (Sobolev et al., 2005). Although the concentration of most trace elements in Mauna Loa and Kilauea lavas can broadly be explained by melting of a garnet peridotite to varying degrees, the problem remains that the nickel contents of a melt produced from a primitive mantle (1965 ppm) are far too low (<400 ppm - Figure 8.24) by comparison with the Mauna Loa basalts studied here (755 – 1141 ppm). The high Ni contents of Hawaiian lavas have been used as evidence of an olivine-free source for the Hawaiian volcanoes (Sobolev et al., 2005) and so it is important to establish why this may be the case for nickel, particularly considering the other trace elements are broadly consistent with melting of a fertile peridotite.

The predicted composition of Ni was modelled during melting of a garnet-pyroxenite representing the composition of recycled slab assuming the same method as above, but with reaction coefficients calculated using reported phase assemblages from Spandler et al. (2008). It was found that the Ni concentration did not exceed 60 ppm even after 85% melting, because despite the low partition coefficients for Ni in cpx and garnet, the starting Ni concentration in MORB is only approximately 360 ppm at 11 wt. % MgO (Elthon, 1989). Even when a PM composition of 1965 ppm Ni is used, the maximum Ni in the melt after 85% of it has been melted is 620 ppm.

As seen in Figure 8.24a, a melt of a garnet peridotite cannot exceed ~400 ppm nickel assuming the partition coefficients as used in MELTS modelling and a starting composition of 1965 ppm Ni. The only other ways to produce the ~800 ppm Ni in the Mauna Loa melts from a fertile peridotite are to start off with a very high mantle nickel contents (over 6000 ppm would be required to reach the minimum Ni at a reasonable degree of melting), or to vary the mineral/melt partition coefficients.

It has been shown that nickel olivine/melt partitioning is highly sensitive to temperature (Hirschmann and Ghiorso, 1994). At 1550 ºC the $D_{Ni}^{ol/melt}$ asymptotically reaches a limit of ~2.5. The effect of diminishing $D_{Ni}^{ol/melt}$ is magnified when the melt is particularly high in MgO,

as is assumed here to be the case for Hawaii. The effect of bulk D=2.5 is plotted in Figure 8.35, showing a Ni content of >800 ppm can be achieved at relatively low degrees of melting of a fertile peridotite. Here, $D_{Ni}^{opx,cpx,garnet/melt}$ must also not exceed about 2.5 or the melt will not be high enough in Ni at low degrees of melting. Low $D_{Ni}^{opx,cpx/melt}$ at mantle-melting conditions may be valid to assume because it has been shown that D_{Ni}^{cpx} is highly pressure dependent in the same way it is for olivine, with partition coefficients reaching as low as 1.5 at high temperatures (>1300 ˚C) (Lindstrom and Weill, 1978), and that D_{Ni}^{opx} is highly dependent on the D_{Mg}^{opx} and can reach a value as low as 1.6 (Beattie et al., 1991). The variation in Ni possible (Figure 8.35) shows that the partition coefficients selected when modelling Ni during mantle melting can make a significant difference to the resulting melt nickel content, and that it is very important to be deliberate with the partition coefficient chosen and the inferences that are made from melt modelling.

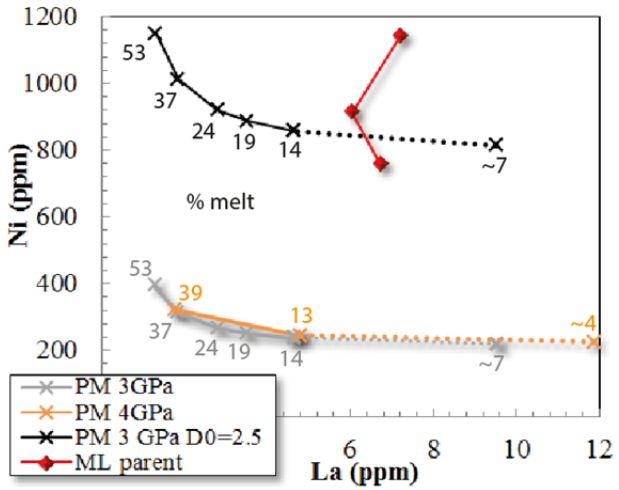

Figure 8.35 The predicted Ni concentration for a melt where the bulk $D_{Ni}^{ol/melt}$ = 2.5.

8.8 Conclusions

Through a comparison of the inferred Mauna Loa parental magma range with experimental melt compositions, it was shown that the Mauna Loa source composition is most likely to be a fertile garnet peridotite. Melts of a fertile peridotite provide a good fit to the major element compositions of Mauna Loa basalt, with Hawaiian Pyrolite slightly better. High pressures of ~4 GPa where garnet is stable appear to fit Mauna Loa compositions better than garnet-free assemblages. None of the pyroxenites tested here can produce melts with MgO content high enough to be in equilibrium with the highest forsterite olivines found at Hawaii, and this is especially the case at reasonable melt fractions (<20% melting). The highest MgO melt from a pyroxenite is 15.57% at 3 GPa and 22 % melting, which is lower than a melt in equilibrium with the highest forsterite olivine, and at higher degrees of melting than have previously been

considered feasible for Mauna Loa. The average degree of melting is thought to be <10% for the Hawaiian plume (Watson and Mckenzie, 1991), or 7-10% for Mauna Loa (Norman and Garcia, 1999). MgO contents of the melt change significantly with pressure and degree of melting, and the high MgO contents of Mauna Loa primitive lavas require a peridotitic source at relatively high pressure, due to the relationship of increasing MgO in the melt with increasing pressure. It is clear that the MgO content is equally important to SiO_2 and CaO, for distinguishing peridotite- from pyroxenite-source melts.

It was shown that SiO_2 contents of the melt is strongly dependent on pressure and melt fraction, therefore SiO_2 differences between Mauna Loa and Kilauea should not be used as a reflection of source composition, i.e. it should not be used to suggest subducted crust in the source of Mauna Loa, e.g. (Hauri, 1996, Sobolev et al., 2005). The higher SiO_2 contents of Mauna Loa relative to Kilauea could be because Mauna Loa magmas are melted at shallower depths than Kilauea magmas, or that Mauna Loa represents a higher melt fraction than Kilauea – consistent with relationships found between SiO_2, pressure, and melt fraction by Walter (Walter, 1998). The variation in TiO_2 is a further constraint, suggesting degree of melting is the primary variation because TiO_2 content is not significantly pressure dependent, but is highly dependent of melt fraction particularly at low melt fractions (Walter, 1998).

Furthermore, garnet-present melts of HPY fit just as well as the garnet-absent melts in terms of major elements, and the higher pressure garnet-rich sources of the PM compositions fit the major elements better than the lower pressure equivalents, particularly at high-MgO. It is therefore not possible to exclude a garnet-bearing source based on the major element composition e.g. (Falloon et al., 1988), arguments outlined in (Eggins, 1991).

Variation in CaO appears to have more to do with starting CaO composition than pressure. A low CaO melt can still come from a peridotite if the starting CaO content is low e.g. in Hawaiian pyrolite, and does not require there to be a pyroxenitic source. Low CaO can occur at low or high degrees of melting, with a maximum in CaO contents in between. It appears that a shift in MgO occurs with pressure, and so the low CaO part of the melting line may move towards the higher MgO of the ML parental magmas at high pressure, but there are too few data points for the high pressure melts in the studies used here.

Similarly, Al_2O_3 is highly dependent on melt fraction and pressure. The Al_2O_3 content is too high in melts from primitive mantle at lower pressure (1.5 – 3 GPa), though at pressures between 4-5 GPa, the relationship of Al_2O_3 with melt fraction changes, and low Al_2O_3 can be found in low degree melts. FeO_t appears to also favour the high pressure PM melts (≥4 GPa). TiO_2 concentrations in melts also suggest a high pressure, with melts from 4-5 GPa producing

high enough Ti, though K_2O is low in the ML parental magma, and only melts coming from high melt fractions at all pressures can produce K_2O low enough. A pressure of 4 GPa would correlate with a depth of approximately 135 km depth: in line with the Hawaiian plume depth of melting estimates of Li and co-authors (Li et al., 2000).

Melts of HPY fit the ML parental magma composition well for most major element oxides (except FeO_t) at both 2 and 3 GPa, though the 3 GPa melts are in equilibrium with the 20 wt. % parental melt in terms of SiO_2 while the 2 GPa melt is in equilibrium with the 16 wt. % MgO parental melt.

pMELTS does not produce meaningful results when modelling the melting of a peridotite or pyroxenite at high pressures (1.5 – 5 GPa), and it cannot predict experimentally determined solidus phase assemblages, and therefore trace element models should not be trusted.

Trace element modelling reveals the differences between Mauna Lo and Kilauea can broadly be explained by variable degrees of melting of a fertile, garnet peridotite, with Mauna Loa resulting from ~12% melting and Kilauea resulting from ~6%. A better fit for the Mauna Loa melts is achieved when using a source created by the addition of 10% Mauna Loa parental magma with 90% DMM composition, but this is a somewhat circular approach. Such a source would have major and trace element concentrations that are close to the composition of primitive mantle, but with lower highly incompatibles (Rb, Ba, U) and HREE (Yb, Lu) and higher highly-moderately incompatibles (La, Ce, Nd, Eu etc.). Irrespective, there are anomalously low U contents and high Ni contents in the ML parent which are difficult to reconcile with melting of a primitive mantle composition.

It was shown that low-olivine pyroxenites cannot produce the required high Ni content of Mauna Loa lavas, and that the Ni may be better explained by the high temperatures and high MgO contents associated with the Hawaiian plume which cause an associated decrease in the bulk D_{Ni}. This negates the need for a low-olivine pyroxenite as the source.

The estimated ~12% melting of primitive mantle to produce the Mauna Loa trace element composition is consistent with the major elements, providing it occurs at high pressures. All ML parental magma major elements except K_2O are closest to the 9 and 13% melts at 4 GPa and the 12% melt at 4.5 GPa. This confirms that even if the source of Mauna Loa magmas is not technically a primitive, undifferentiated mantle, it is likely to be a fertile peridotite that is close.

The estimated parental magma water content in Mauna Loa lavas (~0.3 wt. %) can be produced if the source mantle water composition is high (420 ppm), however when the primitive mantle estimate is lower (93 ppm) the ML parental magma water concentrations cannot be reached via

mantle melting. It is highly possible that the increased water content of Kilauea relative to Mauna Loa may be the result of lower melt degree, as this can cause a range in water contents of 1-4 wt. % depending on the source water content used.

A compilation of isotope data from Mauna Loa and Kilauea confirms the trace element ratios in demonstrating that Mauna Loa is closest to a primitive mantle composition, while Kilauea may contain some other component with higher radiogenic lead and $^{143}Nd/^{144}Nd$, and lower $^{87}Sr/^{86}Sr$. In $^{87}Sr/^{86}Sr$, $^{143}Nd/^{144}Nd$, and $^{206}Pb/^{204}Pb$ space, the Mauna Loa and Kilauea trend forms mostly a linear array between the enriched-DMM end member, and an end-member that is part way between DMM and BSE. There is a slight tick in the DMM-BSE end of the trend towards BSE. The array is mostly planar rather than 3-dimensional, with the majority of variation occurring in the $^{143}Nd/^{144}Nd$ and $^{206}Pb/^{204}Pb$ rather than in the $^{87}Sr/^{86}Sr$ plane. It is clear that there must be long-term enrichment in U or depletion in Pb, though it is not clear what could cause this variation. The incorporation of a small amount of E-DMM crust may be possible, or simply whatever the process is in MORB which alters the lead isotopes may be happening also to Kilauea's lavas.

If the main difference between Kilauea and Mauna Loa is variation in melt degree, it follows that the variation in melt degree may be the result of slight variation in pressure, which would agree with Jones and co-author's vison of lateral separation of melting areas due to a tilted plume. Therefore neither a concentrically zoned plume, nor a plume which rises in two conduits form the core-mantle boundary are necessary to explain the emergence of the Kea and Loa tracks. Instead, most of the variation may occur at the melt region of a fertile garnet peridotite.

9 Conclusion

There is strong evidence to suggest that none of the whole rock samples are direct parental magmas. Evidence includes: 1) the high proportions of modal olivine in whole rock samples; 2) that Ni versus MgO does not form a polynomial curve as would be expected with a fractionation trend and is therefore more consistent with a mixing line; 3) that glass compositions contain low MgO contents (typically 5-6 wt. % MgO); and 4) that forsterite contents of olivine cores and rims are out of equilibrium with the whole rock composition. More likely is that the melt has fractionated to an evolved composition (~8-10 wt. % MgO) and that fractionated olivine (average forsterite 87.5) was able to remain entrained until eruption due to the high viscosity of such magmas, and that additional olivine must have become entrained in some cases to account for the high modal olivine in some samples.

Despite evidence that the whole rock assemblage is not directly a parental magma, thermodynamic modelling suggests magmatic processes have recreated a parental magma composition and what appears as a fractionation trend via the retention of crystallized olivine in the melt until it has reached an evolved composition. This parental magma composition contains an MgO content of ~ 16 wt. % to be in equilibrium with the highest Fo olivine found in these samples, and the consequent major element oxide and trace element compositions for the proposed parental magma could then be determined by constraining to MgO = 16 wt. %. The amount of MgO in the proposed composition is a minimum based on the maximum Fo contents of olivine found in samples from this study, however the higher Fo contents published in other studies suggests a more primitive composition with ~18 wt. % MgO may be equally suited to representing a Mauna Loa parental melt.

Thermodynamic modelling using the estimated parental melt composition is consistent with fractionation of $Fo_{90.8\text{-}80.2}$ olivine (24.3% with 1 wt. % H_2O or 20.5% with no H_2O), cpx (7% with 1 wt. % H_2O or 12.6% with no H_2O), and spinel (~0.4%) in a melt which fractionates down to 5 wt. % MgO. The fractionation of some plagioclase (predicted by MELTS to be none with 1 wt. % H_2O or 11.6% with no H_2O) is also evident in some of the samples. Modelling suggests the occurrence of two distinct fractionation sequences: ol + sp + opx + cpx + plag and another with ol + sp + cpx, which could be achieved with minor variations in the water content (0 – 0.5 wt. %). The 0.5 wt. % estimate is consistent with the Hirschmann 'wetspot' model estimate of 300-1000 ppm, and is also consistent with upper estimates for water content in the Sun and McDonough 'Primitive Mantle' of up to 420 ppm

The question of Hawaii having a peridotite or pyroxenite source was answered through a comparison of the inferred Mauna Loa parental magma range with experimental melt compositions, and it was shown that the Mauna Loa source composition is most likely to be a fertile garnet peridotite. Melts of a fertile peridotite provide a good fit to the major element compositions of Mauna Loa basalt, and Hawaiian Pyrolite slightly better. High pressure sources (~4 GPa) where garnet is stable appear to explain Mauna Loa compositions better than garnet-free assemblages. None of the pyroxenites tested here can produce melts with MgO content high enough to be in equilibrium with the highest forsterite olivines found at Hawaii, and this is especially the case at reasonable melt fractions (<20% melting). It is clear that the MgO content is equally important as SiO_2 and CaO, for distinguishing peridotite- from pyroxenite-source melts.

It was shown that SiO_2 contents of the melt is strongly dependent on pressure and melt fraction, therefore SiO_2 differences between Mauna Loa and Kilauea should not be used as a reflection of source composition, i.e. it should not be used to suggest subducted crust in the source of Mauna Loa, e.g. (Hauri, 1996, Sobolev et al., 2005).

Furthermore, garnet-present melts of HPY fit just as well as the garnet-absent melts in terms of major elements, and the higher pressure garnet-rich sources of the PM compositions fit the major elements better than the lower pressure equivalents, particularly at high-MgO. It is therefore not possible to exclude a garnet-bearing source based on the major element composition e.g. (Falloon et al., 1988), arguments outlined in (Eggins, 1991).

Trace element modelling reveals a the differences between Mauna Lo and Kilauea can be explained by variable degrees of melting of a fertile, garnet peridotite, with Mauna Loa resulting from ~12% melting and Kilauea resulting from ~6%. It was shown that low-olivine pyroxenites cannot produce the required high Ni content of Mauna Loa lavas, and that the Ni may be better explained by the high temperatures and high MgO contents associated with the Hawaiian plume which cause an associated decrease in the bulk D_{Ni}. This negates the need for a olivine-free pyroxenite as the source.

The estimated ~12% melting of primitive mantle to produce the Mauna Loa trace element composition is consistent with the major elements, providing it occurs at high pressures. All ML parental magma major elements except K_2O are closest to the 9 and 13% melts at 4 GPa and the 12% melt at 4.5 GPa.

A compilation of isotope data from Mauna Loa and Kilauea confirms the trace element ratios in demonstrating that Mauna Loa is closest to a primitive mantle composition, while Kilauea may

contain some other component with higher radiogenic lead and $^{143}Nd/^{144}Nd$, and lower $^{87}Sr/^{86}Sr$. In $^{87}Sr/^{86}Sr$, $^{143}Nd/^{144}Nd$, and $^{206}Pb/^{204}Pb$ space, the Mauna Loa and Kilauea trend forms mostly a linear array between the enriched-DMM end member, and an end-member that is part way between DMM and BSE.

If the main difference between Kilauea and Mauna Loa is variation in melt degree, it follows that the variation in melt degree may be the result of slight variation in pressure, which would agree with Jones and co-author's vison of lateral separation of melting areas in a tilted plume. Therefore neither a concentrically zoned plume, nor a plume which rises in two conduits form the core-mantle boundary are necessary to explain the emergence of the Kea and Loa tracks.

Where this model differs to the Jones model however, is that Mauna Loa does not require a recycled crustal component to explain high Si and Ni contents compared to Kilauea, or any form of eclogite melt reacting with mantle peridotite, and instead may be the result of a slightly higher degree of melting in the shallower part of a tilted plume. In contrast to most studies, isotopic signatures suggest additional components may be actually be required in the *Kilauea* source rather than the Mauna Loa source, as Mauna Loa signatures are overall closer to primitive mantle.

Given that Mauna Loa and Kilauea are good representatives of the 'Loa' and 'Kea'-track volcanoes of Hawaii in general, the majority of geochemical variation between the 'Loa' and 'Kea'-trends may occur due to variable degrees of melting of a fertile garnet peridotite, with plume-tilting resulting in their lateral separation.

Appendix

Trace elements obtained during XRF analysis by Prof. J. Michael Rhodes and Mr. Michael Vollinger at the University of Massachusetts. The results were not used in trace element discussion to reduce discontinuity problems arising from the different analysis techniques and because of the extensive nature of the ICP-MS work; however the results of the XRF analysis are displayed below.

Table 1 XRF trace element results (Ti in wt. %, others in ppm).

	Ti	Nb	Zr	Y	Sr	U	Rb	Th
M1-1	1.05	4.6	66	12.7	153	0	3.1	0
M1-2	1.66	8.1	118	21.8	272	0	5.4	0
M1-6	1.46	7.1	103	19.2	238	0	4.7	1
M1-8	1.54	7.1	96	18.1	216	0	4.2	0
M1-9	1.76	8.1	119	21.8	277	0	5.7	1
M1-13	1.04	4.5	64	12.9	160	0	3	0
M1-14	1.37	6.6	98	18.3	225	0	4.6	1
M1-16	1.33	6	84	16.3	203	0	3.7	1
M1-20	1.46	6.4	91	17.5	216	0	4.1	0
M1-26	1.16	5	68	13.2	167	0	2.7	0
M1-27	1.78	7.4	106	20.4	248	0	4.5	0
M1-30	1.94	8.3	117	22.5	268	0	5.3	1
M2-3	1.49	7	100	18.2	210	0	4.2	0
M2-10	1.68	6.8	103	20.2	236	0	3.9	1
M2-12	1.6	7	105	19.6	228	0	4.2	0
M2-18	1.73	7.3	109	20.5	245	0	4.5	0
M2-26	1.61	7.3	105	19.1	220	0	4.5	0
M3-7	1.71	7.4	110	20.2	224	0	4.8	1
M3-13	1.32	5.4	81	15.3	177	0	2.6	0
M4-3	1.67	7.7	112	20.1	236	0	4.7	0
M4-14	1.84	7.6	113	21	238	0	5.5	1
M11-5	3.17	18.2	209	33.6	327	0	8.4	1
M12-3	2.07	10.3	118	20.8	295	0	4.3	0
M12-4	2.31	12	145	25.8	305	0	5.6	1
M12-14	2.34	11.9	143	25.6	312	0	6.2	1
M12-19	1.94	8.5	114	22.1	281	0	4.5	1
M12-42	2.03	9	120	22.5	280	0	5	1
M13-2	2.15	8.8	138	30.9	257	0	4.9	0
M13-5	2.03	8.6	129	27.4	252	0	5.6	0
M13-12	1.36	8.8	90	15.6	214	0	4.4	0
M13-14	1.42	6.2	88	17.7	214	0	4.2	0
M13-15	2.04	8.7	128	27.6	253	0	5.7	1
M13-21	1.42	11.3	98	15.5	242	0	5.9	0
M13-29	1.73	8	114	23.4	227	0	5.4	0
M13-35	2.25	12.4	149	26.7	316	0	6.2	1
M22-4	1.5	7.1	104	18.6	204	0	4.1	1
M22-11	1.63	7.3	108	19.7	216	0	4.2	1
M26-1	1.52	6.1	94	18	220	0	3.6	0
M26-10	2.04	9.5	137	23.7	336	0	6.4	0
M26-14	1.36	5.7	86	16.4	200	0	3.3	1
M26-16	1.48	6.1	92	17.5	213	0	3.4	0
M26-18	1.62	6.8	103	19.4	239	0	4	1
M26-43	1.55	6.5	97	18.6	226	0	3.7	1
M27-2	1.99	8.7	132	24.6	301	0	5.5	1
M27-11	1.97	8.4	131	24.3	302	0	5.3	1
M27-32	1.86	7.8	118	21.9	254	0	4.4	1
M28-2	2.13	10.1	146	25.9	322	0	6.8	1

Table 1 XRF trace element results (Ti in wt. %, others in ppm) cont.

	Pb	Ga	Zn	Ni	Cr	V	Ce	Ba	La
M1-1	1	11	101	1232	1489	143	11	35	6
M1-2	1	17	102	174	388	216	23	67	8
M1-6	1	14	101	421	986	194	17	57	7
M1-8	1	15	100	659	1004	200	18	47	6
M1-9	1	17	100	167	422	227	24	67	8
M1-13	1	11	96	1100	1337	145	10	29	5
M1-14	2	14	101	520	1245	184	16	56	9
M1-16	1	14	98	821	987	181	14	39	5
M1-20	1	14	97	779	707	195	16	44	6
M1-26	1	12	95	1094	1599	154	13	41	5
M1-27	1	17	102	322	604	233	20	53	8
M1-30	1	19	101	128	434	251	21	55	6
M2-3	1	14	102	839	924	181	16	50	5
M2-10	1	16	105	350	687	223	18	46	8
M2-12	1	15	102	604	810	206	18	44	7
M2-18	2	17	100	419	727	223	20	53	9
M2-26	1	15	104	747	896	198	17	56	9
M3-7	2	15	103	682	643	213	19	54	7
M3-13	1	12	95	1090	1150	164	17	32	8
M4-3	2	15	104	622	771	205	18	52	7
M4-14	1	17	104	544	583	228	20	58	6
M11-5	1	23	136	59	45	356	42	117	15
M12-3	1	19	102	244	599	251	25	75	7
M12-4	1	20	109	65	90	275	27	81	10
M12-14	1	21	108	60	64	281	29	83	13
M12-19	1	19	95	123	388	249	21	66	8
M12-42	2	19	101	107	363	250	24	65	8
M13-2	1	21	119	66	145	294	23	55	12
M13-5	2	19	111	107	305	277	21	63	6
M13-12	2	13	103	1061	1017	182	20	51	7
M13-14	1	15	102	470	1043	207	16	49	6
M13-15	1	19	109	105	294	277	21	62	6
M13-21	1	13	104	1052	1026	182	24	72	11
M13-29	2	16	104	274	661	235	19	65	7
M13-35	1	21	109	82	181	258	28	76	9
M22-4	1	14	103	886	1023	190	18	46	6
M22-11	1	14	103	744	899	203	18	53	10
M26-1	1	15	104	614	1024	201	18	45	5
M26-10	1	19	109	87	186	249	26	83	8
M26-14	1	13	105	800	1100	183	13	41	8
M26-16	2	15	105	686	1035	194	16	46	8
M26-18	1	16	107	400	860	213	16	51	5
M26-43	1	15	105	550	956	205	18	43	6
M27-2	2	19	107	98	206	252	22	71	10
M27-11	2	19	105	98	213	252	22	69	7
M27-32	2	17	108	295	773	226	20	57	8
M28-2	2	20	116	62	78	273	24	89	8

References

Abouchami, W., Hofmann, A. W., Galer, S. J. G., Frey, F. A., Eisele, J., & Feigenson, M. (2005). Lead isotopes reveal bilateral asymmetry and vertical continuity in the Hawaiian mantle plume. *Nature, 434*(7035), 851-856. doi: Doi 10.1038/Nature03402

Aigner-Torres, M., Blundy, J. U. P., & Pettke, T. (2007). Laser ablation ICP MS study of trace element partitioning between plagioclase and basaltic melts; an experimental approach.

Alard, O., Luguet, A., Pearson, N. J., Griffin, W. L., Lorand, J. P., Gannoun, A., . . . O'Reilly, S. Y. (2005). In situ Os isotopes in abyssal peridotites bridge the isotopic gap between MORBs and their source mantle. *Nature, 436*, 1005-1008.

Amelung, F., Yun, S. H., Walter, T. R., Segall, P., & Kim, S. W. (2007). Stress control of deep rift intrusion at Mauna Loa volcano, Hawaii. *Science, 316*(5827), 1026-1030. doi: 10.1126/science.1140035

Anderson, D. L. (1981). Hotspots, basalts, and the evolution of the mantle. *Science*.

Anderson, D. L. (1995). Lithosphere, Asthenosphere, and Perisphere. *Reviews of Geophysics, 33*(1), 125-149. doi: Doi 10.1029/94rg02785

Anderson, D. L. (2001). Top-down tectonics? *Science, 293*(5537), 2016-2018. doi: 10.1126/science.1065448

Ariskin, A. A., & Barmina, G. S. (1990). Thermometry of equilibria of plagioclases with melts of basalts and andesites. *Geokhimiya*(3), 441-447.

Ariskin, A. A., Barmina, G. S., & Frenkel, M. Y. (1988). A crystallization mechanism of formation of tholeitic series. *Izvestiya Akademii Nauk Sssr Seriya Geologicheskaya*(4), 11-19.

Ariskin, A. A., Barmina, G. S., & Frenkel, M. Y. (1990). Thermodynamic modeling of lunar basaltic melt crystallization. *Geokhimiya*(10), 1476-1485.

Ariskin, A. A., Barminga, G. S., Frenkel, M. Y., & Yaroshevsky, A. A. (1987). Computer-simulation of fractional crystallization of tholeiitic magmas at Low-pressures. *Geokhimiya*(9), 1240-1259.

Ariskin, A. A., Frenkel, M. Y., Barmina, G. S., & Nielsen, R. L. (1993). COMAGMAT; a Fortran program to model magma differentiation processes. *Computers & Geosciences, 19*(8), 1155-1170.

Ariskin, A. A., Frenkel, M. Y., & Tsekhonya, T. I. (1990). fractional crystallization of tholeiite magmas at elevated Pressures. *Geokhimiya*(2), 172-183.

Ballmer, M. D., Ito, G., van Hunen, J., & Tackley, P. J. (2011). Spatial and temporal variability in Hawaiian hotspot volcanism induced by small-scale convection. *Nature Geoscience, 4*(7), 457-460. doi: 10.1038/NGEO1187

Bargar, K. E., & Jackson, E. D. (1974). Calculated volumes of individual shield volcanoes along the Hawaiian-Emperor chain. *J. Res. US Geol. Survey*.

Barnard, W. M. (1995). Mauna Loa Volcano: Historical eruptions, explorations, and observations (1779-1910) *Mauna Loa revealed: Structure, composition, history, and hazards* (Vol. 92): American Geophysical Union.

Beattie, P. (1993). Olivine-melt and ortho-pyroxene-melt equilibria. *Contributions to Mineralogy and Petrology, 115*(1), 103-111. doi: 10.1007/Bf00712982

Beattie, P., Ford, C., & Russell, D. (1991). Partition-coefficients for olivine-melt and ortho-pyroxene-melt systems. *Contributions to Mineralogy and Petrology, 109*(2), 212-224. doi: 10.1007/Bf00306480

Bell, D. R., & Rossman, G. R. (1992). Water in Earth's mantle: The role of nominally anhydrous minerals. *Science, 255*(5050), 1391-1397. doi: 10.1126/science.255.5050.1391

Bennett, S., Blundy, J., & Elliott, T. (2004). The effect of sodium and titanium on crystal-melt partitioning of trace elements. *Geochimica Et Cosmochimica Acta*.

Bennett, V. C., Esat, T. M., & Norman, M. D. (1996). Two mantle-plume components in Hawaiian picrites inferred from correlated Os-Pb isotopes. *Nature, 381*(6579), 221-224. doi: 10.1038/381221a0

Bennett, V. C., Nutman, A. P., & Esat, T. M. (2002). Constraints on mantle evolution from 187Os/188Os isotopic compositions of Archean ultramafic rocks from southern West Greenland (3.8 Ga) and Western Australia (3.46 Ga). *Geochimica Et Cosmochimica Acta, 66*(14), 2615-2630.

Bindeman, I. N., & Davis, A. M. (2000). Trace element partitioning between plagioclase and melt; investigation of dopant influence on partition behavior. *Geochimica Et Cosmochimica Acta.*

Bindeman, I. N., Davis, A. M., & Drake, M. J. (1998). Ion microprobe study of plagioclase-basalt partition experiments at natural concentration levels of trace elements. *Geochimica Et Cosmochimica Acta.*

Blichert-Toft, J., Frey, F. A., & Albarede, F. (1999). Hf isotope evidence for pelagic sediments in the source of Hawaiian basalts. *Science, 285*(5429), 879-882. doi: 10.1126/science.285.5429.879

Blundy, J. D., & Wood, B. J. (1991). Crystal-chemical controls on the partitioning of Sr and Ba between plagioclase feldspar, silicate melts, and hydrothermal solutions. *Geochimica Et Cosmochimica Acta.*

Bottinga, Y., & Weill, D. F. (1972). Viscosity of magmatic silicate liquids - Model for calculation. *American Journal of Science, 272*(5), 438-475. doi: 10.2475/ajs.272.5.438

Brandon, A. D., & Walker, R. J. (2005). The debate over core-mantle interaction. *Earth and Planetary Science Letters, 232*(3-4), 211-225. doi: 10.1016/j.epsl.2005.01.034

Bryce, J. G., DePaolo, D. J., & Lassiter, J. C. (2005). Geochemical structure of the Hawaiian plume: Sr, Nd, and Os isotopes in the 2.8 km HSDP-2 section of Mauna Kea volcano. *Geochemistry Geophysics Geosystems, 6*. doi:10.1029/2004gc000809

Budahn, J. R., & Schmitt, R. A. (1985). Petrogenetic Modeling of Hawaiian Tholeiitic Basalts - a Geochemical Approach. *Geochimica Et Cosmochimica Acta, 49*(1), 67-87. doi: 10.1016/0016-7037(85)90192-9

Byers, C. D., Garcia, M. O., & Muenow, D. W. (1985). Volatiles in pillow rim glasses from Loihi and Kilauea volcanos, Hawaii. *Geochimica Et Cosmochimica Acta, 49*(9), 1887-1896. doi: 10.1016/0016-7037(85)90083-3

Campbell, I. H. (2007). Testing the plume theory. *Chemical Geology, 241*(3-4), 153-176. doi: 10.1016/j.chemgeo.2007.01.024

Campbell, I. H., & Griffiths, R. W. (1990). Implications of mantle plume structure for the evolution of flood basalts. *Earth and Planetary Science Letters, 99*(1-2), 79-93. doi: 10.1016/0012-821x(90)90072-6

Canil, D. (1997). Vanadium partitioning and the oxidation state of Archaean komatiite magmas. *Nature, 389*(6653), 842-845. doi: 10.1038/39860

Canil, D. (1999). Vanadium partitioning between orthopyroxene, spinel and silicate melt and the redox states of mantle source regions for primary magmas. *Geochimica Et Cosmochimica Acta, 63*(3-4), 557-572. doi: 10.1016/S0016-7037(98)00287-7

Chazot, G. M., Martin, A., & Harte, B. (1996). Determination of partition coefficients between apatite, clinopyroxene, amphibole, and melt in natural spinel lherzolites from Yemen; implications for wet melting of the lithospheric mantle. *Geochimica Et Cosmochimica Acta.*

Christensen, U. R., & Hofmann, A. W. (1994). Segregation of subducted oceanic-crust in the convecting mantle. *Journal of Geophysical Research-Solid Earth, 99*(B10), 19867-19884. doi: 10.1029/93jb03403

Clague, A., & Denlinger, R. (1994). Role of olivine cumulates in destabilizing the flanks of Hawaiian volcanoes. *Bulletin of Volcanology, 56*(6-7), 425-434.

Clague, D. A., & Dalrymple, G. (1989). Tectonics, geochronology, and origin of the Hawaiian-Emperor volcanic chain. *Geological Society of America, N.*

Clague, D. A., & Dalrymple, G. B. (1987). The Hawaiian-Emperor volcanic chain. *U.S. Geological Survey Professional Paper 1350*, 5-54.

Clague, D. A., Moore, J. G., Dixon, J. E., & Friesen, W. B. (1995). Petrology of submarine lavas from Kilaueas Puna Ridge, Hawaii. *Journal of Petrology, 36*(2), 299-349. doi: 10.1093/petrology/36.2.299

Clague, D. A., & Sherrod, D. R. (2014). Growth and degradation of Hawaiian volcanoes: Chapter 3 in Characteristics of Hawaiian volcanoes (V. S. Center, Trans.) *Professional Paper*. Reston, VA.

Clague, D. A., Weber, W. S., & Dixon, J. E. (1991). Picritic glasses from Hawaii. *Nature*(353), 553-556.

Clog, M., Aubaud, C., Cartigny, P., & Dosso, L. (2013). The hydrogen isotopic composition and water content of southern Pacific MORB: A reassessment of the D/H ratio of the depleted mantle reservoir. *Earth and Planetary Science Letters, 381*, 156-165. doi: 10.1016/j.epsl.2013.08.043

Cohen, A. S., O'Nions, R., & Keith, K. M. D. (1996). Chemical and isotopic variations in Mauna Loa tholeiites. *Earth and Planetary Science Letters*.

Courtillot, V., Davaille, A., Besse, J., & Stock, J. (2003). Three distinct types of hotspots in the Earth's mantle. *Earth and Planetary Science Letters, 205*(3-4), 295-308. doi: 10.1016/S0012-821x(02)01048-8

Crisp, J., Cashman, K. V., Bonini, J. A., Hougen, S. B., & Pieri, D. C. (1994). Crystallization history of the 1984 Mauna-Loa lava flow. *Journal of Geophysical Research-Solid Earth, 99*(B4), 7177-7198. doi: 10.1029/93jb02973

Cross, W., Iddings, J. P., Pirsson, L. V., & Washington, H. S. (1902). A quantitative chemico-mineralogical classification and nomenclature of igneous rocks. *Journal of Geology, 10*(6), 555-U510. doi: Doi 10.1086/621030

Danyushevsky, L. V. (2001). The effect of small amounts of H2O on crystallisation of mid-ocean ridge and backarc basin magmas. *Journal of Volcanology and Geothermal Research, 110*(3-4), 265-280.

Danyushevsky, L. V., & Plechov, P. (2011). Petrolog3: Integrated software for modeling crystallization processes. *Geochemistry Geophysics Geosystems, 12*. doi: 10.1029/2011gc003516

Davies, D. R., Goes, S., Davies, J. H., Schuberth, B. S. A., Bunge, H. P., & Ritsema, J. (2012). Reconciling dynamic and seismic models of Earth's lower mantle: The dominant role of thermal heterogeneity. *Earth and Planetary Science Letters, 353*, 253-269. doi: 10.1016/j.epsl.2012.08.016

Davies, D. R., Goes, S., & Lau, H. C. P. (2015). Thermally dominated deep mantle LLSVPs: A review. *Earth's Heterogeneous Mantle: A Geophysical, Geodynamical, and Geochemical Perspective*, 441-477. doi: 10.1007/978-3-319-15627-9_14

Davies, G. F. (2005). A case for mantle plumes. *Chinese Science Bulletin, 50*(15), 1541-1554. doi: 10.1360/982005-918

Davis, M. G. (2001). *Volatiles in glasses from Mauna Loa Volcano, Hawaii:Implications for degassing, contamination, and growth.* (Master of Science), University of Hawai'i.

Davis, M. G., Garcia, M. O., & Wallace, P. (2003). Volatiles in glasses from Mauna Loa Volcano, Hawai'i: implications for magma degassing and contamination, and growth of Hawaiian volcanoes. *Contributions to Mineralogy and Petrology, 144*(5), 570-591. doi: DOI 10.1007/s00410-002-0416-z

DePaolo, D. J., Bryce, J. G., Dodson, A., Shuster, D. L., & Kennedy, B. M. (2001). Isotopic evolution of Mauna Loa and the chemical structure of the Hawaiian plume. *Geochemistry Geophysics Geosystems, 2*.

DePaolo, D. J., Stolper, E. M., & Thomas, D. M. (2003, October 21 2003). Hawaii Scientific Drilling Project (1991-2008). Retrieved 14/10/2018, from https://dosecc.com/hawaii-scientific-drilling-project/

Dixon, J. E., & Clague, D. A. (2001). Volatiles in basaltic glasses from Loihi seamount, Hawaii: Evidence for a relatively dry plume component. *Journal of Petrology, 42*(3), 627-654. doi: 10.1093/petrology/42.3.627

Dixon, J. E., Clague, D. A., & Stolper, E. M. (1991). Degassing history of water, sulfur, and carbon in submarine lavas from Kilauea volcano, Hawaii. *Journal of Geology, 99*(3), 371-394. doi: 10.1086/629501

Dolfi, D., & Trigila, R. (1978). Role of water in the 1944 Vesuvius eruption. *Contributions to Mineralogy and Petrology, 67*(3), 297-304. doi: 10.1007/Bf00381457

Dunn, T., & Sen, C. (1994). Mineral/matrix partition-coefficients for ortho-pyroxene, plagioclase, and olivine in basaltic to andesitic systems - a combined analytical and experimental-study. *Geochimica Et Cosmochimica Acta, 58*(2), 717-733. doi: 10.1016/0016-7037(94)90501-0

Eaton, J. P., & Murata, K. J. (1960). How volcanoes grow. *Science, 132*(3432), 925-938. doi: 10.1126/science.132.3432.925

Eggins, S. M. (1991). Petrogenesis of Hawaiian tholeiites - .1. phase-equilibria constraints. *Contributions to Mineralogy and Petrology, 110*(2-3), 387-397. doi: 10.1007/Bf00310752

Eggins, S. M., Woodhead, J. D., Kinsley, L. P. J., Mortimer, G. E., Sylvester, P., McCulloch, M. T., . . . Handler, M. R. (1997). A simple method for the precise determination of >=40 trace elements in geological samples by ICPMS using enriched isotope internal standardisation. *Chemical Geology, 134*(4), 311-326. doi: 10.1016/S0009-2541(96)00100-3

Ehlers, K., Grove, T. L., Sisson, T. W., Recca, S. I., & Zervas, D. A. (1992). The effect of oxygen fugacity on the partitioning of nickel and cobalt between olivine, silicate melt, and metal. *Geochimica Et Cosmochimica Acta, 56*(10), 3733-3743. doi: 10.1016/0016-7037(92)90166-G

Elkins, L., Gaetani, G., & Sims, K. (2007). Partitioning of U and Th during garnet pyroxenite partial melting; constraints on the source of alkaline ocean island basalts. *Earth and Planetary Science Letters, 265*(1-2), 270-286.

Elthon, D. (1989). Pressure and origin of primary mid-ocean ridge basalts. *Geological Society of London Special Publications, 42*, 125-136.

Falloon, T. J., Green, D. H., Hatton, C. J., & Harris, K. L. (1988). Anhydrous partial melting of a fertile and depleted peridotite from 2-Kb to 30-Kb and application to basalt petrogenesis. *Journal of Petrology, 29*(6), 1257-1282. doi: 10.1093/petrology/29.6.1257

Farnetani, C. G. (1997). Excess temperature of mantle plumes: The role of chemical stratification across D". *Geophysical Research Letters, 24*(13), 1583-1586. doi: 10.1029/97gl01548

Farnetani, C. G., & Hofmann, A. W. (2010). Dynamics and internal structure of the Hawaiian plume. *Earth and Planetary Science Letters, 295*(1-2), 231-240. doi: 10.1016/j.epsl.2010.04.005

Farnetani, C. G., Hofmann, A. W., & Class, C. (2012). How double volcanic chains sample geochemical anomalies from the lowermost mantle. *Earth and Planetary Science Letters, 359*, 240-247. doi: 10.1016/j.epsl.2012.09.057

Farnetani, C. G., & Samuel, H. (2005). Beyond the thermal plume paradigm. *Geophysical Research Letters, 32*(7). doi: Artn L07311

10.1029/2005gl022360

Fiske, R. S., & Kinoshita, W. T. (1969). Inflation of Kilauea Volcano prior to its 1967-1968 eruption. *Science, 165*(3891), 341. doi: 10.1126/science.165.3891.341

Fitton, J. G. (2007). The OIB Paradox. In G. R. Foulger & D. M. Jurdy (Eds.), *Plates, plumes, and planetary processes* (Vol. 430, pp. 387-412). Boulder, CO: The Geological Society of America.

Foulger, G. R. (2007). The "plate" model for the genesis of melting anomalies. *GSA special papers, 430*, 1-28.

Frenkel, M. Y., & Ariskin, A. A. (1984). Computer-simulation of equilibrium and fractional crystallization of basaltic melts. *Geokhimiya*(10), 1419-1431.

Frey, F. A., Huang, S. C., Xu, G. P., & Jochum, K. P. (2016). The geochemical components that distinguish Loa- and Kea-trend Hawaiian shield lavas. *Geochimica Et Cosmochimica Acta, 185*, 160-181. doi: 10.1016/j.gca.2016.04.010

Frey, F. A., & Rhodes, J. M. (1993). Intershield geochemical differences among Hawaiian volcanos - implications for source compositions, melting process and magma ascent paths. *Philosophical Transactions of the Royal Society a-Mathematical Physical and Engineering Sciences, 342*(1663), 121-136. doi: 10.1098/rsta.1993.0009

Frey, F. A., Wise, W. S., Garcia, M. O., West, H., Kwon, S. T., & Kennedy, A. (1990). Evolution of Mauna-Kea Volcano, Hawaii - Petrologic and Geochemical Constraints on Postshield Volcanism. *Journal of Geophysical Research-Solid Earth and Planets, 95*(B2), 1271-1300. doi: 10.1029/Jb095ib02p01271

Fujimaki, H. T., Mitsunobu Aoki, Ken-ichiro. (1984). Partition coefficients of Hf, Zr, and REE between phenocrysts and groundmasses. *Journal of Geophysical Research, 89*(S02).

Gaetani, G. A., Grove, T. L., & Bryan, W. B. (1993). The Influence of water on the petrogenesis of subduction-related igneous rocks. *Nature, 365*(6444), 332-334. doi: 10.1038/365332a0

Gao, S., Liu, X. M., Yuan, H. L., Hattendorf, B., Gunther, D., Chen, L., & Hu, S. H. (2002). Determination of forty two major and trace elements in USGS and NIST SRM glasses by laser ablation-inductively coupled plasma-mass spectrometry. *Geostandards Newsletter-the Journal of Geostandards and Geoanalysis, 26*(2), 181-196. doi: 10.1111/j.1751-908X.2002.tb00886.x

Garcia, M. O. (1996). Petrography and olivine and glass chemistry of lavas from the Hawaii Scientific Drilling Project. *Journal of Geophysical Research-Solid Earth, 101*(B5), 11701-11713. doi: 10.1029/95jb03846

Garcia, M. O., Caplan-Auerbach, J., De Carlo, E. H., Kurz, M. D., & Becker, N. (2006). Geology, geochemistry and earthquake history of Lo'ihi Seamount, Hawai'i's youngest volcano. *Chemie Der Erde-Geochemistry, 66*(2), 81-108. doi: 10.1016/j.chemer.2005.09.002

Garcia, M. O., & Davis, M. G. (2001). Submarine growth and internal structure of ocean island volcanoes based on submarine observations of Mauna Loa volcano, Hawaii. *Geology, 29*(2), 163-166. doi: 10.1130/0091-7613(2001)029<0163:Sgaiso>2.0.Co;2

Garcia, M. O., Foss, D. J. P., West, H. B., & Mahoney, J. J. (1995). Geochemical and isotopic evolution of Loihi Volcano, Hawaii. *Journal of Petrology, 36*(6), 1647-1674.

Garcia, M. O., & Hulsebosch, T. P. (1995). Olivine-rich submarine basalts from the southwest rift zone of Mauna Loa Volcano; implications for magmatic processes and geochemical evolution. *Mauna Loa Revealed.*

Garcia, M. O., Hulsebosch, T. P., & Rhodes, J. M. (1995). Olivine-rich submarine basalts from the southwest rift zone of Mauna Loa volcano: Implications for magmatic processes and geochmical evolution *Mauna Loa revealed: Structure, composition, history, and hazards*. Geophysical monography 92: American Geophysical Union.

Garcia, M. O., Muenow, D. W., Aggrey, K. E., & Oneil, J. R. (1989). Major element, volatile, and stable isotope geochemistry of Hawaiian submarine tholeiitic glasses. *Journal of Geophysical Research-Solid Earth and Planets, 94*(B8), 10525-10538. doi: 10.1029/Jb094ib08p10525

Garcia, M. O., Pietruszka, A., & Rhodes, J. M. (2003). A petrologic perspective of Kilauea volcano's summit magma reservoir. *Journal of Petrology, 44*(12), 2313-2339. doi: 10.1093/petrology/egg079

Garnero, E. J., & McNamara, A. K. (2008). Structure and dynamics of Earth's lower mantle. *Science, 320*(5876), 626-628. doi: 10.1126/science.1148028

Gerlach, T. M. (1986). Exsolution of H2O, CO2, and S during eruptive episodes at Kilauea volcano, Hawaii. *Journal of Geophysical Research-Solid Earth and Planets, 91*(B12), 2177-2185. doi: 10.1029/Jb091ib12p12177

Gerlach, T. M. (1993). Oxygen buffering of Kilauea volcanic gases and the oxygen fugacity of Kilauea basalt. *Geochimica Et Cosmochimica Acta, 57*(4), 795-814. doi: Doi 10.1016/0016-7037(93)90169-W

Ghiorso, M. S. (1983). Lseqieq - a Fortran-IV subroutine package for the analysis of multiple linear-regression problems with possibly deficient pseudorank and linear equality and inequality constraints. *Computers & Geosciences, 9*(3), 391-416. doi: 10.1016/0098-3004(83)90008-0

Ghiorso, M. S., & Gualda, G. A. R. (2015). An H2O-CO2 mixed fluid saturation model compatible with rhyolite-MELTS. *Contributions to Mineralogy and Petrology, 169*(6). doi: 10.1007/s00410-015-1141-8

Ghiorso, M. S., Hirschmann, M. M., Reiners, P. W., & Kress, V. C. (2002). The pMELTS: A revision of MELTS for improved calculation of phase relations and major element partitioning related to partial melting of the mantle to 3 GPa. *Geochemistry Geophysics Geosystems, 3*. doi: 10.1029/2001gc000217

Ghiorso, M. S., & Sack, R. O. (1995). Chemical mass-transfer in magmatic processes .4. A revised and internally consistent thermodynamic model for the interpolation and extrapolation of liquid-solid equilibria in magmatic systems at elevated-temperatures and pressures. *Contributions to Mineralogy and Petrology, 119*(2-3), 197-212. doi: 10.1007/Bf00307281

Green, D. H. (2015). Experimental petrology of peridotites, including effects of water and carbon on melting in the Earth's upper mantle. *Physics and Chemistry of Minerals, 42*(2), 95-122. doi: 10.1007/s00269-014-0729-2

Green, D. H., & Falloon, T. J. (1998). Pyrolite: a Ringwood concept and its current expression. In I. Jackson (Ed.), *The Earth's Mantle: Composition, Structure, and Evolution*. Cambridge: Cambridge University Press.

Green, D. H., & Falloon, T. J. (2005). Primary magmas at mid-ocean ridges, "hotspots," and other intraplate settings: Constraints on mantle potential temperature. *Plates, Plumes and Paradigms, 388*. doi: 10.1130/2005.2388(14)

Green, D. H., Falloon, T. J., Eggins, S. M., & Yaxley, G. M. (2001). Primary magmas and mantle temperatures. *European Journal of Mineralogy, 13*(3), 437-451. doi: 10.1127/0935-1221/2001/0013-0437

Green, D. H., & Ringwood, A. E. (1963). Mineral assemblages in a model mantle composition. *Journal of Geophysical Research, 68*(3), 937-945. doi: 10.1029/Jz068i003p00937

Green, D. H., & Ringwood, A. E. (1967). Stability fields of aluminous pyroxene peridotite and garnet peridotite and their relevance in upper mantle structure. *Earth and Planetary Science Letters, 3*(2), 151-160. doi: 10.1016/0012-821x(67)90027-1

Green, T. H., Blundy, J. D., Adam, J., & Yaxley, G. M. (2000). SIMS determination of trace element partition coefficients between garnet, clinopyroxene and hydrous basaltic liquids at 2-7.5 GPa and 1080-1200 degrees C. *Lithos, 53*(3-4), 165-187. doi: 10.1016/S0024-4937(00)00023-2

Green, T. H., & Pearson, N. J. (1986). Ti-Rich accessory phase saturation in hydrous mafic-felsic compositions at high P,T. *Chemical Geology, 54*(3-4), 185-201. doi: 10.1016/0009-2541(86)90136-1

Grove, T. L., Chatterjee, N., Parman, S. W., & Medard, E. (2006). The influence of H2O on mantle wedge melting. *Earth and Planetary Science Letters, 249*(1-2), 74-89. doi: 10.1016/j.epsl.2006.06.043

Gualda, G. A. R., Ghiorso, M. S., Lemons, R. V., & Carley, T. L. (2012). Rhyolite-MELTS: a modified calibration of MELTS optimized for silica-rich, fluid-bearing magmatic systems. *Journal of Petrology, 53*(5), 875-890. doi: 10.1093/petrology/egr080

Gubbins, D., Alfe, D., Masters, G., Price, G. D., & Gillan, M. J. (2003). Can the Earth's dynamo run on heat alone? *Geophysical Journal International, 155*(2), 609-622. doi: 10.1046/j.1365-246X.2003.02064.x

Hahm, D., Castillo, P. R., & Hilton, D. R. (2009). A deep mantle source for high 3He/4He ocean island basalts (OIB) inferred from Pacific near-ridge seamount lavas. *Geophysical Research Letters, 36*(20).

Hanyu, T., Kimura, J. I., Katakuse, M., Calvert, A. T., Sisson, T. W., & Nakai, S. (2010). Source materials for inception stage Hawaiian magmas: Pb-He isotope variations for early Kilauea. *Geochemistry Geophysics Geosystems, 11*. doi: 10.1029/2009gc002760

Hart, S., & Dunn, T. (1992). Experimental cpx/melt partitioning of 24 trace elements. *Contributions to Mineralogy and Petrology*.

Hart, S. R., & Davis, K. E. (1978). Nickel partitioning between olivine and silicate melt. *Earth and Planetary Science Letters, 40*(2), 203-219. doi: 10.1016/0012-821x(78)90091-2

Hart, S. R., Hauri, E. H., Oschmann, L. A., & Whitehead, J. A. (1992). Mantle plumes and entrainment - isotopic evidence. *Science, 256*(5056), 517-520. doi: 10.1126/science.256.5056.517

Hart, S. R., & Zindler, A. (1986). In search of a bulk-Earth composition. *Chemical Geology, 57*(3-4), 247-267. doi: 10.1016/0009-2541(86)90053-7

Harvey, J., Gannoun, A., Burton, K., Rogers, N. W., Alard, O., & Parkinson, I. J. (2006). Ancient melt extraction from the oceanic upper mantle revealed by Re–Os isotopes in abyssal peridotites from the Mid-Atlantic ridge. *Earth and Planetary Science Letters, 244*(3-4), 606-621.

Hauri, E. H. (1996). Major-element variability in the Hawaiian mantle plume. *Nature, 382*(6590), 415-419. doi: 10.1038/382415a0

Hauri, E. H., & Kurz, M. D. (1997). Melt migration and mantle chromatography, 2: a time-series Os isotope study of Mauna Loa Volcano, Hawaii. *Earth and Planetary Science Letters, 153*(1-2), 21-36. doi: 10.1016/S0012-821x(97)00158-1

Hauri, E. H., Wagner, T. P., & Grove, T. L. (1994). Experimental and Natural Partitioning of Th, U, Pb and Other Trace-Elements between Garnet, Clinopyroxene and Basaltic Melts. *Chemical Geology, 117*(1-4), 149-166. doi: Doi 10.1016/0009-2541(94)90126-0

Helz, R. T., & Wright, T. L. (1992). Differentiation and magma mixing on Kilauea east rift-zone - a further look at the eruptions of 1955 and 1960. Part I. The Late 1955 Lavas. *Bulletin of Volcanology, 54*(5), 361-384. doi: 10.1007/Bf00312319

Herzberg, C. (2006). Petrology and thermal structure of the Hawaiian plume from Mauna Kea volcano. *Nature, 444*(7119), 605-609. doi: 10.1038/Nature05254

Herzberg, C., & Asimow, P. D. (2008). Petrology of some oceanic island basalts: PRIMELT2.XLS software for primary magma calculation. *Geochemistry Geophysics Geosystems, 9*. doi: 10.1029/2008gc002057

Hieronymus, C. F., & Bercovici, D. (1999). Discrete alternating hotspot islands formed by interaction of magma transport and lithospheric flexure. *Nature, 397*(6720), 604-607.

Hirschmann, M. M. (2006). Water, melting, and the deep Earth H2O cycle. *Annual Review of Earth and Planetary Sciences, 34*, 629-653. doi: 10.1146/annurev.earth.34.031405.125211

Hirschmann, M. M., & Ghiorso, M. S. (1994). Activities of nickel, cobalt, and manganese silicates in magmatic liquids and applications to olivine liquid and to silicate metal partitioning. *Geochimica Et Cosmochimica Acta, 58*(19), 4109-4126. doi: 10.1016/0016-7037(94)90268-2

Hirschmann, M. M., Kogiso, T., Baker, M. B., & Stolper, E. M. (2003). Alkalic magmas generated by partial melting of garnet pyroxenite. *Geology, 31*(6), 481-484. doi: 10.1130/0091-7613(2003)031<0481:Amgbpm>2.0.Co;2

Hofmann, A. (2014). Sampling mantle heterogeneity through oceanic basalts: Isotopes and trace elements. *Treatise on Geochemistry, 2*.

Hofmann, A. W. (1988). Chemical differentiation of the Earth - the relationship between mantle, continental-crust, and oceanic-crust. *Earth and Planetary Science Letters, 90*(3), 297-314. doi: Doi 10.1016/0012-821x(88)90132-X

Hofmann, A. W. (1997). Mantle geochemistry: The message from oceanic volcanism. *Nature, 385*(6613), 219-229. doi: Doi 10.1038/385219a0

Hofmann, A. W., & Farnetani, C. G. (2013). Two views of Hawaiian plume structure. *Geochemistry, Geophysics, Geosystems, 14*(12), 5308-5322. doi: 10.1002/2013GC004942

Hofmann, A. W., & Jochum, K. P. (1996). Source characteristics derived from very incompatible trace elements in Mauna Loa and Mauna Kea basalts, Hawaii Scientific Drilling Project. *Journal of Geophysical Research-Solid Earth, 101*(B5), 11831-11839. doi: 10.1029/95jb03701

Hofmann, A. W., & White, W. M. (1982). Mantle plumes from ancient oceanic crust. *Earth and Planetary Science Letters, 57*(2), 421-436. doi: http://dx.doi.org/10.1016/0012-821X(82)90161-3

Holcomb, R. T. (1987). Eruptive history and long-term behavior of Kilauea Volcano. *USGS Professional Paper*.

Horn, I., Foley, S. F., Jackson, S. E., & Jenner, G. A. (1994). Experimentally determined partitioning of high-field strength-elements and selected transition-elements between spinel and basaltic melt. *Chemical Geology, 117*(1-4), 193-218. doi: 10.1016/0009-2541(94)90128-7

Huang, S. C., & Frey, F. A. (2005). Recycled oceanic crust in the Hawaiian plume: evidence from temporal geochemical variations within the Koolau shield. *Contributions to Mineralogy and Petrology, 149*(5), 556-575. doi: 10.1007/s00410-005-0664-9

Humayun, M., Qin, L. P., & Norman, M. D. (2004). Geochemical evidence for excess iron in the mantle beneath Hawaii. *Science, 306*(5693), 91-94. doi: 10.1126/science.1101050

Huppert, H. E., & Sparks, R. S. J. (1985). Cooling and contamination of mafic and ultramafic magmas during ascent through continental-crust. *Earth and Planetary Science Letters, 74*(4), 371-386. doi: 10.1016/S0012-821x(85)80009-1

International Union of Geological Sciences. (1989). *A classification of igneous rocks and glossary of terms: Recommendations of the international union of geological sciences subcommission on the systematics of igneous rocks* (R. W. Le Maitre Ed. Vol. 3): Blackwell.

Ireland, T. J., Walker, R. J., & Brandon, A. D. (2011). 186Os–187Os systematics of Hawaiian picrites revisited: New insights into Os isotopic variations in ocean island basalts. *Geochimica Et Cosmochimica Acta, 75*(16), 4456-4475.

Irvine, T. N., & Baragar, W. R. A. (1971). Guide to chemical classification of common volcanic rocks. *Canadian Journal of Earth Sciences, 8*(5), 523-+. doi: 10.1139/e71-055

Jackson, M. G., Weis, D., & Huang, S. C. (2012). Major element variations in Hawaiian shield lavas: Source features and perspectives from global ocean island basalt (OIB) systematics. *Geochemistry Geophysics Geosystems, 13*. doi: 10.1029/2012gc004268

Janney, P. E., & Castillo, P. R. (1997). Geochemistry of Mesozoic Pacific mid-ocean ridge basalt: Constraints on melt generation and the evolution of the Pacific upper mantle. *Journal of Geophysical Research-Solid Earth, 102*(B3), 5207-5229. doi: 10.1029/96jb03810

Jaques, A. L., & Green, D. H. (1979). Determination of liquid compositions in high-pressure melting of peridotite. *American Mineralogist, 64*(11-1), 1312-1321.

Jenner, G. A., Longerich, H. P., Jackson, S. E., & Fryer, B. J. (1990). ICP-MS - a powerful tool for high-precision trace-element analysis in Earth sciences - Evidence from analysis of selected USGS reference samples. *Chemical Geology, 83*(1-2), 133-148. doi: 10.1016/0009-2541(90)90145-W

Ji, Y., & Nataf, H. C. (1998). Detection of mantle plumes in the lower mantle by diffraction tomography: Hawaii. *Earth and Planetary Science Letters, 159*(3-4), 99-115. doi: 10.1016/S0012-821x(98)00060-0

Jochum, K. P., Hofmann, A. W., Ito, E., Seufert, H. M., & White, W. M. (1983). K, U and Th in mid-ocean ridge basalt glasses and heat-production, K/U and K/Rb in the mantle. *Nature, 306*(5942), 431-436. doi: 10.1038/306431a0

Johnston, A., Schwab, B., & Mercer, C. (2004). Partitioning of trace elements between clinopyroxene and peridotitic partial melts; implications for the mechanism(s) by which piston-cylinder partial melting experiments equilibrate. *Chemical Geology, 136*(1-2).

Jones, T. D., Davies, D. R., Campbell, I. H., Iaffaldano, G., Yaxley, G., Kramer, S. C., & Wilson, C. R. (2017). The concurrent emergence and causes of double volcanic hotspot tracks on the Pacific plate. *Nature, 545*(7655), 472-+. doi: 10.1038/nature22054

Jones, T. D., Davies, D. R., Campbell, I. H., Wilson, C. R., & Kramer, S. C. (2016). Do mantle plumes preserve the heterogeneous structure of their deep-mantle source? *Earth and Planetary Science Letters, 434*, 10-17. doi: 10.1016/j.epsl.2015.11.016

Julian, B. R. (2004). Seismology: the hunt for plumes. 2017, from http://www.mantleplumes.org/WebpagePDFs/Seismology.pdf

Klein, E. M., & Langmuir, C. H. (1987). Global correlations of ocean ridge basalt chemistry with axial depth and crustal thickness. *Journal of Geophysical Research-Solid Earth and Planets, 92*(B8), 8089-8115. doi: 10.1029/Jb092ib08p08089

Klein, F. W. (1982). Patterns of historical eruptions at Hawaiian volcanoes. *Journal of Volcanology and Geothermal Research, 12*(1-2).

Klemme, S., Blundy, J. D., & Wood, B. J. (2002). Some experimental constraints on major and trace element partitioning during partial melting of eclogite. *Geochimica Et Cosmochimica Acta, 66*(17).

Klemme, S., Gunther, D., Hametner, K., Prowatke, S., & Zack, T. (2006). The partitioning of trace elements between ilmenite, ulvospinel, annalcolite and silicate melts with implications for the early differentiation of the moon. *Chemical Geology, 234*(3-4), 251-263. doi: 10.1016/j.chemgeo.2006.05.005

Kogiso, T., Hirose, K., & Takahashi, E. (1998). Melting experiments on homogeneous mixtures of peridotite and basalt: application to the genesis of ocean island basalts. *Earth and Planetary Science Letters, 162*(1-4), 45-61. doi: 10.1016/S0012-821x(98)00156-3

Kogiso, T., Hirschmann, M. M., & Frost, D. J. (2003). High-pressure partial melting of garnet pyroxenite: possible mafic lithologies in the source of ocean island basalts. *Earth and Planetary Science Letters, 216*(4), 603-617. doi: 10.1016/S0012-821x(03)00538-7

Kovalenko, V. I., Naumov, V. B., Girnis, A. V., Dorofeeva, V. A., & Yarmolyuk, V. V. (2006). Estimation of the average contents of H2O, Cl, F, and S in the depleted mantle on the basis of the compositions of melt inclusions and quenched glasses of mid-ocean ridge basalts. *Geochemistry International, 44*(3), 209-231. doi: 10.1134/S0016702906030013

Kurz, M. D., & Kammer, D. P. (1991). Isotopic evolution of Mauna Loa Volcano. *Earth and Planetary Science Letters, 103*(1-4), 257-269.

Kurz, M. D., Kenna, T. C., Lassiter, J. C., & DePaolo, D. J. (1996). Helium isotopic evolution of Mauna Kea Volcano: First results from the 1-km drill core. *Journal of Geophysical Research-Solid Earth, 101*(B5), 11781-11791. doi: 10.1029/95jb03345

Laboratory, L. A. N., & Yucca Mountain Project. (1990). Procedure for determination of volume constituents in thin sections of rocks: Los Alamos National Laboratory.

Lambart, S., Baker, M. B., & Stolper, E. M. (2016). The role of pyroxenite in basalt genesis: Melt-PX, a melting parameterization for mantle pyroxenites between 0.9 and 5 GPa. *Journal of Geophysical Research-Solid Earth, 121*(8), 5708-5735. doi: 10.1002/2015JB012762

Lambart, S., Laporte, D., & Schiano, P. (2013). Markers of the pyroxenite contribution in the major-element compositions of oceanic basalts: Review of the experimental constraints. *Lithos, 160*, 14-36. doi: 10.1016/j.lithos.2012.11.018

Lange, R. A., & Carmichael, I. S. E. (1987). Densities of Na2o-K2o-Cao-Mgo-Feo-Fe2o3-Al2o3-Tio2-Sio2 Liquids - New Measurements and Derived Partial Molar Properties. *Geochimica Et Cosmochimica Acta, 51*(11), 2931-2946. doi: 10.1016/0016-7037(87)90368-1

Langmuir, C. H., Klein, E. M., & Plank, T. (1992). Petrological systematics of mid-ocean ridge basalts - Constraints on melt generation beneath ocean ridges. *Mantle Flow and Melt Generation at Mid-Ocean Ridges, 71*, 183-280.

Lassiter, J. C., & Hauri, E. H. (1998). Osmium-isotope variations in Hawaiian lavas: evidence for recycled oceanic lithosphere in the Hawaiian plume. *Earth and Planetary Science Letters, 164*(3-4), 483-496. doi: 10.1016/S0012-821x(98)00240-4

Lemarchand, F. (1987a). Trace element distribution coefficients in alkaline series. *Geochimica Et Cosmochimica Acta, 51*(5).

Lemarchand, F. (1987b). Trace element distribution coefficients in alkaline series.

Li, X., Kind, R., Priestley, K., Sobolev, S. V., Tilmann, F., Yuan, X., & Weber, M. (2000). Mapping the Hawaiian plume conduit with converted seismic waves. *Nature, 405*(6789), 938-941.

Lindstrom, D. J., & Weill, D. F. (1978). Partitioning of transition-metals between diopside and coexisting silicate liquids .1. Nickel, cobalt, and manganese. *Geochimica Et Cosmochimica Acta, 42*(Na6), 817-831. doi: 10.1016/0016-7037(78)90095-9

Lipman, P. W. (1980). The southwest rift-zone of Mauna-Loa - Implications for structural evolution of Hawaiian volcanos. *American Journal of Science, 280*, 752-776.

Lipman, P. W., & Coombs, M. L. (2006). North Kona slump: Submarine flank failure during the early(?) tholeiitic shield stage of Hualalai volcano. *Journal of Volcanology and Geothermal Research, 151*(1-3), 189-216. doi: 10.1016/j.jvolgeores.2005.07.029

Liu, M. A., & Chase, C. G. (1989). Evolution of midplate hotspot swells - Numerical solutions. *Journal of Geophysical Research-Solid Earth and Planets, 94*(B5), 5571-5584. doi: 10.1029/Jb094ib05p05571

Lockwood, J. P., & Lipman, P. W. (1987). Holocene eruptive history of Mauna Loa volcano. *U.S. Geological Survey Professional Paper 1350*, 509-535.

Lynn, K. J., Garcia, M. O., Shea, T., Costa, F., & Swanson, D. A. (2017). Timescales of mixing and storage for Keanakako` i Tephra magmas (1500-1820 CE), Kilauea volcano, Hawai'i. *Contributions to Mineralogy and Petrology, 172*(9). doi: 10.1007/s00410-017-1395-4

Maaloe, S. (2004). The PT-phase relations of an MgO-rich Hawaiian tholeiite: the compositions of primary Hawaiian tholeiites. *Contributions to Mineralogy and Petrology, 148*(2), 236-246. doi: 10.1007/s00410-004-0601-3

Macdonald, G. A., Abbott, A. T., & Peterson, F. L. (1970). *Volcanoes in the sea: The geology of Hawaii* (2nd ed.). USA: University of Hawaii Press.

Macpherson, C. G., Hilton, D. R., Sinton, J. M., Poreda, R. J., & Craig, H. (1998). High He-3/He-4 ratios in the Manus backarc basin: Implications for mantle mixing and the origin of plumes in the western Pacific Ocean. *Geology, 26*(11), 1007-1010. doi: 10.1130/0091-7613(1998)026<1007:Hhhrit>2.3.Co;2

Mallmann, G., & O'Neill, H. S. C. (2009). The Crystal/Melt Partitioning of V during Mantle Melting as a Function of Oxygen Fugacity Compared with some other Elements (Al, P, Ca, Sc, Ti, Cr, Fe, Ga, Y, Zr and Nb). *Journal of Petrology, 50*(9), 1765-1794. doi: 10.1093/petrology/egp053

Mangan, M. T. (1990). Crystal size distribution systematics and the determination of magma storage times - the 1959 eruption of Kilauea volcano, Hawaii. *Journal of Volcanology and Geothermal Research, 44*(3-4), 295-302. doi: 10.1016/0377-0273(90)90023-9

Marske, J. P., Pietruszka, A. J., Weis, D., Garcia, M. O., & Rhodes, J. M. (2007). Rapid passage of a small-scale mantle heterogeneity through the melting regions of Kilauea and Mauna Loa Volcanoes. *Earth and Planetary Science Letters, 259*(1-2), 34-50. doi: 10.1016/j.epsl.2007.04.026

Martin, D., & Nokes, R. (1989). A fluid-dynamic study of crystal settling in convecting magmas. *Journal of Petrology, 30*(6), 1471-1500. doi: 10.1093/petrology/30.6.1471

Matzen, A. K., Wood, B. J., Baker, M. B., & Stolper, E. M. (2017). The roles of pyroxenite and peridotite in the mantle sources of oceanic basalts. *Nature Geoscience, 10*(7), 530-+. doi: 10.1038/NGEO2968

McCarter, R. L., Fodor, R. V., & Trusdell, F. (2006). Perspectives on basaltic magma crystallization and differentiation: Lava-lake blocks erupted at Mauna Loa volcano summit, Hawaii. *Lithos, 90*(3-4), 187-213. doi: 10.1016/j.lithos.2006.03.005

McDonough, W. F., & Sun, S. S. (1995). The Composition of the Earth. *Chemical Geology, 120*(3-4), 223-253. doi: 10.1016/0009-2541(94)00140-4

McDougall, I. (1979). Age of shield-building volcanism of Kauai and linear migration of volcanism in the Hawaiian island chain. *Earth and Planetary Science Letters, 46*(1), 31-42.

Mckenzie, D., & Bickle, M. J. (1988). The volume and composition of melt generated by extension of the lithosphere. *Journal of Petrology, 29*(3), 625-679.

McKenzie, D., & O'Nions, R. (1991). Partial melt distributions from inversion of rare earth element concentrations. *Journal of Petrology, 32*(5).

Mckenzie, D., & Onions, R. K. (1995). The source regions of ocean island basalts. *Journal of Petrology, 36*(1), 133-159. doi: 10.1093/petrology/36.1.133

McNamara, A. K., Garnero, E. J., & Rost, S. (2010). Tracking deep mantle reservoirs with ultra-low velocity zones. *Earth and Planetary Science Letters, 299*(1-2), 1-9. doi: 10.1016/j.epsl.2010.07.042

McNamara, A. K., & Zhong, S. J. (2004). Thermochemical structures within a spherical mantle: Superplumes or piles? *Journal of Geophysical Research-Solid Earth, 109*(B7). doi: 10.1029/2003jb002847

McNamara, A. K., & Zhong, S. J. (2005). Thermochemical structures beneath Africa and the Pacific Ocean. *Nature, 437*(7062), 1136-1139. doi: 10.1038/nature04066

Michael, P. (1995). Regionally distinctive sources of depleted MORB - Evidence from trace-elements and H2O. *Earth and Planetary Science Letters, 131*(3-4), 301-320. doi: 10.1016/0012-821x(95)00023-6

Michael, P. J., & Chase, R. L. (1987). The Influence of primary magma composition, H2O and pressure on mid-ocean ridge basalt differentiation. *Contributions to Mineralogy and Petrology, 96*(2), 245-263. doi: 10.1007/Bf00375237

Miklius, A., & Cervelli, P. (2003). Volcanology: Interaction between Kilauea and Mauna Loa - Last year witnessed an unexpected communication between this pair of volcanoes. *Nature, 421*(6920), 229-229. doi: 10.1038/421229a

Montelli, R., Nolet, G., Dahlen, F. A., & Masters, G. (2006). A catalogue of deep mantle plumes: New results from finite-frequency tomography. *Geochemistry Geophysics Geosystems, 7*. doi: 10.1029/2006gc001248

Montelli, R., Nolet, G., Dahlen, F. A., Masters, G., Engdahl, E. R., & Hung, S. H. (2004). Finite-frequency tomography reveals a variety of plumes in the mantle. *Science, 303*(5656), 338-343. doi: 10.1126/science.1092485

Moore, J., & Clague, D. (1987). Coastal lava flows from Mauna Loa and Hualalai volcanoes, Kona, Hawaii. *Bulletin of Volcanology, 49*(6), 752-764.

Moore, J. G. (1970). Water content of basalt erupted on the ocean floor. *Contributions to Mineralogy and Petrology, 28*(4), 272-279.

Moore, J. G., Bryan, W. B., Beeson, M. H., & Normark, W. R. (1995). Giant blocks in the south Kona landslide, Hawaii. *Geology, 23*(2), 125-128. doi: 10.1130/0091-7613(1995)023<0125:Gbitsk>2.3.Co;2

Moore, J. G., & Chadwick, W. W. (1995). Offshore geology of Mauna Loa and adjacent areas, Hawaii. In J. M. Rhodes & J. Lockwood, P. (Eds.), *Mauna Loa Revealed: Structure, composition, history, and hazards*. Washington DC: American Geophysical Union.

Moore, J. G., & Clague, D. A. (1992). Volcano growth and evolution of the island of Hawaii. *Geological Society of America, 104*(11), 1471-1484.

Moore, J. G., Clague, D. A., Holcomb, R. T., Lipman, P. W., Normark, W. R., & Torresan, M. E. (1989). Prodigious submarine landslides on the Hawaiian ridge. *Journal of Geophysical Research-Solid Earth and Planets, 94*(B12), 17465-17484. doi: 10.1029/Jb094ib12p17465

Moore, R. B., Clague, D. A., Rubin, M., & Bohrson, W. A. (1987). Hualalai Volcano; a preliminary summary of geologic, petrologic, and geophysical data. *U.S. Geological Survey Professional Paper 1350, 571-585*.

Morgan, W. (1971). Convection plumes in the lower mantle. *Nature, 230*, 42-43.

Mulyukova, E., Steinberger, B., Dabrowski, M., & Sobolev, S. V. (2015). Survival of LLSVPs for billions of years in a vigorously convecting mantle: Replenishment and destruction of chemical anomaly. *Journal of Geophysical Research-Solid Earth, 120*(5), 3824-3847. doi: 10.1002/2014JB011688

Nagasawa, H., Schreiber, H. D., & Morris, R. V. (1980). Experimental mineral-liquid partition-coefficients of the rare-Earth elements (REE), Sc and Sr for perovskite, spinel and melilite. *Earth and Planetary Science Letters, 46*(3), 431-437. doi: 10.1016/0012-821x(80)90056-4

Nathan, H. D., & Vankirk, C. K. (1978). Model of magmatic crystallization. *Journal of Petrology, 19*(1), 66-94. doi: 10.1093/petrology/19.1.66

National Museum of Natural History. (2013). Mauna Loa. *Global volcanism program*. 2018, from https://volcano.si.edu/volcano.cfm?vn=332020

Neilson, M. J., & Brockman, G. F. (1977). Error associated with point-counting. *American Mineralogist, 62*(11-1), 1238-1244.

Nielsen, R., & Gallahan, W. (1991). Experimentally determined mineral-melt partition coefficients for Sc, Y and REE for olivine, orthopyroxene, pigeonite, magnetite and ilmenite. *Contributions to Mineralogy and Petrology, 110*(4), 488-499.

Nielsen, R. L. (1985). EQUIL - A program for the modeling of low-pressure differentiation processes in natural mafic magma bodies. *Computers & Geosciences, 11*(5), 531-546. doi: 10.1016/0098-3004(85)90084-6

Nielsen, R. L., & Dungan, M. A. (1983). Low-pressure mineral-melt equilibria in natural anhydrous mafic systems. *Contributions to Mineralogy and Petrology, 84*(4), 310-326. doi: 10.1007/Bf01160284

Nisbet, E. G., Cheadle, M. J., Arndt, N. T., & Bickle, M. J. (1993). Constraining the potential temperature of the Archean mantle - A review of the evidence from Komatiites. *Lithos, 30*(3-4), 291-307. doi: 10.1016/0024-4937(93)90042-B

NOAA. (2004). Multibeam Bathymetry Database (MBBDB). Retrieved 7/6/2017

Nolet, G., Karato, S. I., & Montelli, R. (2006). Plume fluxes from seismic tomography. *Earth and Planetary Science Letters, 248*(3-4), 685-699. doi: 10.1016/j.epsl.2006.06.011

Norman, M., Garcia, M. O., & Pietruszka, A. J. (2005). Trace-element distribution coefficients for pyroxenes, plagioclase, and olivine in evolved tholefites from the 1955 eruption of Kilauea Volcano, Hawai'i, and petrogenesis of differentiated rift-zone lavas. *American Mineralogist, 90*(5-6), 888-899. doi: 10.2138/am.2005.1780

Norman, M. D., & Garcia, M. O. (1999). Primitive magmas and source characteristics of the Hawaiian plume: petrology and geochemistry of shield picrites. *Earth and Planetary Science Letters, 168*(1-2), 27-44. doi: 10.1016/S0012-821x(99)00043-6

Norman, M. D., Garcia, M. O., & Bennett, V. C. (2004). Rhenium and chalcophile elements in basaltic glasses from Ko'olau and Moloka'i volcanoes: Magmatic outgassing and composition of the Hawaiian plume. *Geochimica Et Cosmochimica Acta, 68*(18), 3761-3777. doi: 10.1016/j.gca.2004.02.025

Norman, M. D., Garcia, M. O., Kamenetsky, V. S., & Nielsen, R. L. (2002). Olivine-hosted melt inclusions in Hawaiian picrites: Equilibration, melting, and plume source characteristics. *Chemical Geology, 183*(1-4), 143-168. doi: 10.1016/S0009-2541(01)00376-X

Norman, M. D., Pearson, N. J., Sharma, A., & Griffin, W. L. (1996). Quantitative analysis of trace elements in geological materials by laser ablation ICPMS: Instrumental operating conditions and calibration values of NIST glasses. *Geostandards Newsletter-the Journal of Geostandards and Geoanalysis, 20*(2), 247-261. doi: 10.1111/j.1751-908X.1996.tb00186.x

O'Neill, H. S., & Jenner, F. E. (2012). The global pattern of trace-element distributions in ocean floor basalts. *Nature, 491*(7426), 698-+. doi: 10.1038/Nature11678

Okubo, P. G., Benz, H. M., & Chouet, B. A. (1997). Imaging the crustal magma sources beneath Mauna Loa and Kilauea volcanoes, Hawaii. *Geology, 25*(10), 867-870. doi: 10.1130/0091-7613(1997)025<0867:Itcmsb>2.3.Co;2

Pearson, D. G., Canil, D., & Shirey, S. B. (2003). Mantle samples included in volcanic rocks: Xenoliths and diamonds. *Treatise on Geochemistry, 2*, 568. doi: 10.1016/B0-08-043751-6/02005-3

Pertermann, M., & Hirschmann, M. M. (2003). Partial melting experiments on a MORB-like pyroxenite between 2 and 3 GPa: Constraints on the presence of pyroxenite in basalt source regions from solidus location and melting rate. *Journal of Geophysical Research-Solid Earth, 108*(B2). doi: 10.1029/2000jb000118

Peterson, D. W., & Moore, R. B. (1987). Geologic history and evolution of geologic concepts, Island of Hawaii. *USGS Professional Paper 1350, 1*, Chapter 7.

Phipps Morgan, J., & Morgan, W. J. (1999). Two-stage melting and the geochemical evolution of the mantle; a recipe for mantle plum-pudding. *Earth and Planetary Science Letters, 170*(3), 215-239.

Pietruszka, A. J., & Garcia, M. O. (1999a). A rapid fluctuation in the mantle source and melting history of Kilauea Volcano inferred from the geochemistry of its historical summit lavas (1790-1982). *Journal of Petrology, 40*(8), 1321-1342. doi: 10.1093/petrology/40.8.1321

Pietruszka, A. J., & Garcia, M. O. (1999b). The size and shape of Kilauea Volcano's summit magma storage reservoir: a geochemical probe. *Earth and Planetary Science Letters, 167*(3-4), 311-320. doi: 10.1016/S0012-821x(99)00036-9

Pietruszka, A. J., Norman, M. D., Garcia, M. O., Marske, J. P., & Burns, D. H. (2012). Chemical heterogeneity in the Hawaiian mantle plume from the alteration and dehydration of recycled oceanic crust. *Earth and Planetary Science Letters, 361*, 298-309. doi: 10.1016/j.epsl.2012.10.030

Poland, M. P., Miklius, A., & Montgomery-Brown, E. K. (2014). Magma supply, storage, and transport at shield-stage Hawaiian volcanoes. In M. P. Poland, T. J. Takahashi & C. M. Landowski (Eds.), *Characteristics of Hawaiian Volcanoes* (Vol. 1801). USGS Geological Survey Professional Paper USGS Geological Survey.

Putirka, K. (1999). Melting depths and mantle heterogeneity beneath Hawaii and the East Pacific Rise: Constraints from Na/Ti and rare earth element ratios. *Journal of Geophysical Research-Solid Earth, 104*(B2), 2817-2829. doi: 10.1029/1998jb900048

Putirka, K. D. (2005). Mantle potential temperatures at Hawaii, Iceland, and the mid-ocean ridge system, as inferred from olivine phenocrysts: Evidence for thermally driven mantle plumes. *Geochemistry Geophysics Geosystems, 6*. doi: 10.1029/2005gc000915

Putirka, K. D., Perfit, M., Ryerson, F. J., & Jackson, M. G. (2007). Ambient and excess mantle temperatures, olivine thermometry, and active vs. passive upwelling. *Chemical Geology, 241*(3-4), 177-206. doi: 10.1016/j.chemgeo.2007.01.014

Regelous, M., Hofmann, A. W., Abouchami, W., & Galer, S. J. G. (2003). Geochemistry of lavas from the Emperor Seamounts, and the geochemical evolution of Hawaiian magmatism from 85 to 42 Ma. *Journal of Petrology, 44*(1), 113-140. doi: 10.1093/petrology/44.1.113

Rhodes, J., & Hart, S. (1995). Episodic trace element and isotopic variations in historical Mauna Loa lavas; implications for magma and plume dynamics *Mauna Loa rvealed: Structure, composition, history, and hazards* (Vol. 92). Hawaii: American Geophysical Union.

Rhodes, J. M. (1988). Geochemistry of the 1984 Mauna Loa eruption - Implications for magma storage and supply. *Journal of Geophysical Research-Solid Earth and Planets, 93*(B5), 4453-4466. doi: 10.1029/Jb093ib05p04453

Rhodes, J. M. (1995). The 1852 and 1868 Mauna Loa picrite eruptions: Clues to parental magma composiitons and the magmatic plumbing system *Mauna Loa revealed: Structure, compositoin, history, and hazards* (Vol. 92). Hawaii: American Geophysical Union.

Rhodes, J. M. (1996). Geochemical stratigraphy of lava flows sampled by the Hawaii Scientific Drilling Project. *Journal of Geophysical Research-Solid Earth, 101*(B5), 11729-11746. doi: 10.1029/95jb03704

Rhodes, J. M. (2015). Major-element and isotopic variations in Mauna Loa magmas over 600 ka: Implications for magma generation and source lithology as Mauna Loa transits the Hawaiian plume. *Hawaiian Volcanoes: From Source to Surface, 208*, 59-78.

Rhodes, J. M. (2016). The aluminum conundrum in Hawaiian shield-building lavas: An argument for a deep, garnet-bearing, mantle source. *Geochimica Et Cosmochimica Acta, 185*, 216-231. doi: 10.1016/j.gca.2016.04.008

Rhodes, J. M., Huang, S. C., Frey, F. A., Pringle, M., & Xu, G. P. (2012). Compositional diversity of Mauna Kea shield lavas recovered by the Hawaii Scientific Drilling Project: Inferences on source lithology, magma supply, and the role of multiple volcanoes. *Geochemistry Geophysics Geosystems, 13*. doi: 10.1029/2011gc003812

Rhodes, J. M., & Vollinger, M. J. (2004). Composition of basaltic lavas sampled by phase-2 of the Hawaii Scientific Drilling Project: Geochemical stratigraphy and magma types. *Geochemistry Geophysics Geosystems, 5*. doi: Doi 10.1029/2002gc000434

Rhodes, J. M., & Vollinger, M. J. (2005). Ferric/ferrous ratios in 1984 Mauna Loa lavas: a contribution to understanding the oxidation state of Hawaiian magmas. *Contributions to Mineralogy and Petrology, 149*(6), 666-674. doi: 10.1007/s00410-005-0662-y

Rhodes, J. M., Wenz, K. P., Neal, C. A., Sparks, J. W., & Lockwood, J. P. (1989). Geochemical evidence for invasion of Kilaueas plumbing system by Mauna-Loa magma. *Nature, 337*(6204), 257-260. doi: 10.1038/337257a0

Righter, K., Leeman, W. P., & Hervig, R. L. (2006). Partitioning of Ni, Co and V between spinel-structured oxides and silicate melts: Importance of spinel composition. *Chemical Geology, 227*(1-2), 1-25. doi: 10.1016/j.chemgeo.2005.05.011

Ringwood, A. E. (1994). Role of the transition zone and 660 km discontinuity in mantle dynamics. *Physics of the Earth and Planetary Interiors, 86*(1-3), 5-24. doi: 10.1016/0031-9201(94)05058-9

Robinson, J. E., & Eakins, B. W. (2006). Calculated volumes of individual shield volcanoes at the young end of the Hawaiian Ridge. *Journal of Volcanology and Geothermal Research, 151*(1-3), 309-317. doi: 10.1016/j.jvolgeores.2005.07.033

Roden, M. F., Trull, T., Hart, S. R., & Frey, F. A. (1994). New He, Nd, Pb, and Sr isotopic constraints on the constitution of the Hawaiian plume - Results from Koolau volcano, Oahu, Hawaii, USA. *Geochimica Et Cosmochimica Acta, 58*(5), 1431-1440. doi: 10.1016/0016-7037(94)90547-9

Roeder, P., & Emslie, R. (1970). Olivine-liquid equilibrium. *Contributions to Mineralogy and Petrology, 29*(4), 275-789.

Rollinson, H. R. (1993). *Using geochemical data: evaluation, presentation, interpretation*. Essex, England: Longman Group UK Ltd. .

Romanowicz, B., & Gung, Y. C. (2002). Superplumes from the core-mantle boundary to the lithosphere: Implications for heat flux. *Science, 296*(5567), 513-516. doi: 10.1126/science.1069404

Rosenthal, A., Yaxley, G. M., Green, D. H., Hermann, J., Kovacs, I., & Spandler, C. (2014). Continuous eclogite melting and variable refertilisation in upwelling heterogeneous mantle. *Scientific Reports, 4*. doi: 10.1038/Srep06099

Roser, B., Kimura, J. I., & Sifeta, K. (2003). Tantalum and niobium contamination from tungsten carbide ring mills - much ado about nothing. *Geoscience Rept. Shimane University, 22*, 107-110.

Ruben, K. (2018a). Hualalai Volcano. Retrieved 7/6/2017, from http://www.soest.hawaii.edu/GG/HCV/hualalai.html

Ruben, K. (2018b). Mauna Loa Volcano: Eruption history. Retrieved 7/6/2017, from http://www.soest.hawaii.edu/GG/HCV/mloa-eruptions.html

Schilling, J. G. (1991). Fluxes and excess temperatures of mantle plumes inferred from their interaction with migrating mid-ocean ridges. *Nature, 352*(6334), 397-403. doi: 10.1038/352397a0

Schwindinger, K. R. (1999). Particle dynamics and aggregation of crystals in a magma chamber with application to Kilauea Iki olivines. *Journal of Volcanology and Geothermal Research, 88*(4), 209-238. doi: 10.1016/S0377-0273(99)00009-8

Sharp, W. D., & Clague, D. A. (2006). 50-Ma initiation of Hawaiian-Emperor bend records major change in Pacific plate motion. *Science, 313*(5791), 1281-1284. doi: 10.1126/science.1128489

Shaw, D. M. (2003). *Trace elements in magmas: A theoretical treatment*: Cambridge University Press.

Shervais, J. W., & Mukasa, S. B. (1991). The Balmuccia Orogenic Lherzolite Massif, Italy. *Journal of Petrology*, 155-174.

Shimizu, H., Sangen, K., & Masuda, A. (1982). Experimental study on rare-earth element partitioning in olivine and clinopyroxene formed at 10 and 20 kb for basaltic systems. *Geochemical Journal, 16*.

Shirey, S. B., & Walker, R. J. (1998). The Re-Os isotope system in cosmochemistry and high-temperature geochemistry. *Annual Review of Earth and Planetary Sciences, 26*, 423-500. doi: 10.1146/annurev.earth.26.1.423

Sleep, N. H. (1990). Hotspots and mantle plumes - Some phenomenology. *Journal of Geophysical Research-Solid Earth and Planets, 95*(B5), 6715-6736. doi: 10.1029/Jb095ib05p06715

Smith, P. M., & Asimow, P. D. (2005). Adiabat_1ph: A new public front-end to the MELTS, pMELTS, and pHMELTS models. *Geochemistry Geophysics Geosystems, 6*. doi: 10.1029/2004gc000816

Sobolev, A. V., Hofmann, A. W., Kuzmin, D. V., Yaxley, G. M., Arndt, N. T., Chung, S. L., . . . Teklay, M. (2007). The amount of recycled crust in sources of mantle-derived melts. *Science, 316*(5823), 412-417. doi: 10.1126/science.1138113

Sobolev, A. V., Hofmann, A. W., & Nikogosian, I. K. (2000). Recycled oceanic crust observed in 'ghost plagioclase' within the source of Mauna Loa lavas. *Nature, 404*(6781), 986-990. doi: 10.1038/35010098

Sobolev, A. V., Hofmann, A. W., Sobolev, S. V., & Nikogosian, I. K. (2005). An olivine-free mantle source of Hawaiian shield basalts. *Nature, 434*(7033), 590-597. doi: 10.1038/Nature03411

Spandler, C., Hammerli, J., & Yaxley, G. M. (2017). An experimental study of trace element distribution during partial melting of mantle heterogeneities. *Chemical Geology, 462*, 74-87. doi: 10.1016/j.chemgeo.2017.05.002

Spandler, C., Yaxley, G., Green, D. H., & Rosenthal, A. (2008). Phase relations and melting of anhydrous k-bearing eclogite from 1200 to 1600 degrees C and 3 to 5 GPa. *Journal of Petrology, 49*(4), 771-795. doi: 10.1093/petrology/egm039

Staudigel, H., Zindler, A., Hart, S. R., Leslie, T., Chen, C. Y., & Clague, D. (1984). The isotope systematics of a juvenile intraplate volcano - Pb, Nd, and Sr isotope ratios of basalts from Loihi seamount, Hawaii. *Earth and Planetary Science Letters, 69*(1), 13-29. doi: 10.1016/0012-821x(84)90071-2

Steiger, R. H., & Jager, E. (1977). Subcommission on geochronology - convention on use of decay constants in geochronology and cosmochronology. *Earth and Planetary Science Letters, 36*(3), 359-362. doi: 10.1016/0012-821x(77)90060-7

Stolper, E., & Walker, D. (1980). Melt density and the average composition of basalt. *Contributions to Mineralogy and Petrology, 74*(1), 7-12. doi: 10.1007/Bf00375484

Stracke, A., Hofmann, A. W., & Hart, S. R. (2005). FOZO, HIMU, and the rest of the mantle zoo. *Geochemistry Geophysics Geosystems, 6*. doi: 10.1029/2004gc000824

Strnad, L., Mihaljevic, M., & Sebek, O. (2005). Laser ablation and solution ICP-MS determination of rare earth elements in USGS BIR-1G, BHVO-2G and BCR-2G glass reference materials. *Geostandards and Geoanalytical Research, 29*(3), 303-314. doi: 10.1111/j.1751-908X.2005.tb00902.x

Stuart, F. M., Lass-Evans, S., Fitton, J. G., & Ellam, R. M. (2003). High 3He/4He ratios in prcritic basalts from Baffin Island and the role of a mixed reservoir in mantle plumes. *Nature, 424*.

Sun, S., & McDonough, W. (1989). Chemical and isotopic systematics of oceanic basalts; implications for mantle composition and processes. *Geological Society, London, Special Publications, 42*, 313-345.

Takahashi, E. (1986). Melting of a dry peridotite KLB-1 up to 14 GPa - Implications on the origin of peridotitic upper mantle. *Journal of Geophysical Research-Solid Earth and Planets, 91*(B9), 9367-9382. doi: 10.1029/Jb091ib09p09367

Takahashi, E., Shimazaki, T., Tsuzaki, Y., & Yoshida, H. (1993). Melting study of a peridotite KLB-1 to 6.5 GPa, and the origin of basaltic magmas. *Philosophical Transactions of the Royal Society of London Series a-Mathematical Physical and Engineering Sciences, 342*(1663), 105-120. doi: 10.1098/rsta.1993.0008

Takeuchi, S. (2011). Preeruptive magma viscosity: An important measure of magma eruptibility. *Journal of Geophysical Research-Solid Earth, 116*. doi: 10.1029/2011jb008243

Tatsumoto, M. (1978). Isotopic composition of lead in oceanic basalt and its implication to mantle evolution. *Earth and Planetary Science Letters, 38*(1), 63-87. doi: 10.1016/0012-821x(78)90126-7

Tepley, F. J., Lundstrom, C., McDonough, W., & Thompson, A. (2010). Trace element partitioning between high An plagioclase and basaltic to basaltic andesite melt at 1 atmosphere pressure. *Lithos, 118*(1-2), 82-94.

Thorne, M. S., Garnero, E. J., & Grand, S. P. (2004). Geographic correlation between hot spots and deep mantle lateral shear-wave velocity gradients. *Physics of the Earth and Planetary Interiors, 146*(1-2), 47-63. doi: 10.1016/j.pepi.2003.09.026

Torsvik, T. H., Smethurst, M. A., Burke, K., & Steinberger, B. (2006). Large igneous provinces generated from the margins of the large low-velocity provinces in the deep mantle. *Geophysical Journal International, 167*(3), 1447-1460. doi: 10.1111/j.1365-246X.2006.03158.x

Tuff, J., & Gibson, S. (2006). 3-7 GPa trace-element partitioning in Fe-rich picrites. *Geochimica Et Cosmochimica Acta, 70*.

Tuohy, R. M., Wallace, P. J., Loewen, M. W., Swanson, D. A., & Kent, A. J. R. (2016). Magma transport and olivine crystallization depths in Kilauea's east rift zone inferred from experimentally rehomogenized melt inclusions. *Geochimica Et Cosmochimica Acta, 185*, 232-250. doi: 10.1016/j.gca.2016.04.020

USGS (Producer). (2015, 7th May 2017). Hualalai - Hawaii's third active volcano. Retrieved from http://hvo.wr.usgs.gov/volcanoes/hualalai/

USGS. (2018). Active volcanoes of Hawaii: Mauna Kea. Retrieved 7/6/2017, from https://volcanoes.usgs.gov/observatories/hvo/hvo_volcanoes.html

van der Hilst, R. D., de Hoop, M. V., Wang, P., Shim, S. H., Ma, P., & Tenorio, L. (2007). Seismostratigraphy and thermal structure of Earth's core-mantle boundary region. *Science, 315*(5820), 1813-1817. doi: 10.1126/science.1137867

Wagner, T. P., Clague, D. A., Hauri, E. H., & Grove, T. L. (1998). Trace element abundances of high-MgO glasses from Kilauea, Mauna Loa and Haleakala volcanoes, Hawaii. *Contributions to Mineralogy and Petrology, 131*(1), 13-21. doi: 10.1007/s004100050375

Wallace, P. J. (1998). Water and partial melting in mantle plumes: Inferences from the dissolved H2O concentrations of Hawaiian basaltic magmas. *Geophysical Research Letters, 25*(19), 3639-3642. doi: 10.1029/98gl02805

Wallace, P. J., & Anderson, A. T. (1998). Effects of eruption and lava drainback on the H2O contents of basaltic magmas at Kilauea Volcano. *Bulletin of Volcanology, 59*(5), 327-344. doi: 10.1007/s004450050195

Walter, M. J. (1998). Melting of garnet peridotite and the origin of komatiite and depleted lithosphere. *Journal of Petrology, 39*(1), 29-60. doi: 10.1093/petrology/39.1.29

Wang, Z. R., & Gaetani, G. A. (2008). Partitioning of Ni between olivine and siliceous eclogite partial melt: experimental constraints on the mantle source of Hawaiian basalts. *Contributions to Mineralogy and Petrology, 156*(5), 661-678. doi: 10.1007/s00410-008-0308-y

Wanless, V. D., Garcia, M. O., Rhodes, J. M., Weis, D., & Norman, M. D. (2005). Shield-stage alkalic volcanism on Mauna Loa Volcano, Hawaii. *Journal of Volcanology and Geothermal Research, 151*(1-3), 141-155. doi: 10.1016/j.jvolgeores.2005.07.027

Wanless, V. D., Garcia, M. O., Trusdell, F. A., Rhodes, J. M., Norman, M. D., Weis, D., . . . Guillou, H. (2006). Submarine radial vents on Mauna Loa Volcano, Hawai'i. *Geochemistry Geophysics Geosystems, 7*. doi: 10.1029/2005gc001086

Wasserburg, G. J., & Depaolo, D. J. (1979). Models of Earth structure inferred from neodymium and strontium isotopic abundances. *Proceedings of the National Academy of Sciences of the United States of America, 76*(8), 3594-3598. doi: 10.1073/pnas.76.8.3594

Watson, E. B. (1985). Henry's law behavior in simple systems and in magmas - Criteria for discerning concentration-dependent partition-coefficients in nature. *Geochimica Et Cosmochimica Acta, 49*(4), 917-923. doi: 10.1016/0016-7037(85)90307-2

Watson, S., & Mckenzie, D. (1991). Melt generation by plumes - a study of Hawaiian Volcanism. *Journal of Petrology, 32*(3), 501-537. doi: 10.1093/petrology/32.3.501

Weaver, J. S., & Langmuir, C. H. (1990). Calculation of Phase-Equilibrium in Mineral Melt Systems. *Computers & Geosciences, 16*(1), 1-19.

Weis, D., Garcia, M. O., Rhodes, J. M., Jellinek, M., & Scoates, J. S. (2011). Role of the deep mantle in generating the compositional asymmetry of the Hawaiian mantle plume. *Nature Geoscience, 4*(12), 831-838. doi: 10.1038/Ngeo1328

Weis, D., Kieffer, B., Maerschalk, C., Pretorius, W., & Barling, J. (2005). High-precision Pb-Sr-Nd-Hf isotopic characterization of USGS BHVO-1 and BHVO-2 reference materials. *Geochemistry Geophysics Geosystems, 6*. doi: 10.1029/2004gc000852

West, H. B., Garcia, M. O., Gerlach, D. C., & Romano, J. (1992). Geochemistry of Tholeiites from Lanai, Hawaii. *Contributions to Mineralogy and Petrology, 112*(4), 520-542. doi: 10.1007/Bf00310782

Whitehead, J. A., & Luther, D. S. (1975). Dynamics of Laboratory Diapir and Plume Models. *Journal of Geophysical Research, 80*(5), 705-717.

Wilkinson, J. F. G., & Hensel, H. D. (1988). The Petrology of Some Picrites from Mauna-Loa and Kilauea Volcanos, Hawaii. *Contributions to Mineralogy and Petrology, 98*(3), 326-345. doi: 10.1007/Bf00375183

Wilson, J. T. (1963). A Possible Origin of Hawaiian Islands. *Canadian Journal of Physics, 41*(6), 863-&.

Winter, J. D. (2010). Principles of igneous and metamorphic petrology. *Pearson Prentice Hall.*

Workman, R. K., & Hart, S. R. (2005). Major and trace element composition of the depleted MORB mantle (DMM). *Earth and Planetary Science Letters, 231*(1-2), 53-72. doi: 10.1016/j.epsl.2004.12.005

Xu, G. P., Huang, S., Frey, F. A., Blichert-Toft, J., Abouchami, W., Clague, D. A., . . . Beeson, M. H. (2014). The distribution of geochemical heterogeneities in the source of Hawaiian shield lavas as revealed by a transect across the strike of the Loa and Kea spatial trends: East Molokai to West Molokai to Penguin Bank. *Geochimica Et Cosmochimica Acta, 132*, 214-237. doi: 10.1016/j.gca.2014.02.002

Yamasaki, S., Kani, T., Hanan, B. B., & Tagami, T. (2009). Isotopic geochemistry of Hualalai shield-stage tholeiitic basalts from submarine North Kona region, Hawaii. *Journal of Volcanology and Geothermal Research, 185*(3), 223-230. doi: 10.1016/j.jvolgeores.2009.06.006

Yang, Z. F., & Zhou, J. H. (2013). Can we identify source lithology of basalt? *Scientific Reports, 3*. doi: 10.1038/Srep01856

Yaxley, G. M., & Green, D. H. (1998). Reactions between eclogite and peridotite: Mantle refertilisation by subduction of oceanic crust. *Schweizerische Mineralogische Und Petrographische Mitteilungen, 78*(2), 243-255.

Yaxley, G. M., & Sobolev, A. V. (2007). High-pressure partial melting of gabbro and its role in the Hawaiian magma source. *Contributions to Mineralogy and Petrology, 154*(4), 371-383. doi: 10.1007/s00410-007-0198-4

Zhao, D. P. (2007). Seismic images under 60 hotspots: Search for mantle plumes. *Gondwana Research, 12*(4), 335-355. doi: 10.1016/J.Gr.2007.03.001

Zhao, D. P. (2009). Multiscale seismic tomography and mantle dynamics. *Gondwana Research, 15*(3-4), 297-323. doi: 10.1016/j.gr.2008.07.003

Zindler, A., & Hart, S. (1986). Chemical Geodynamics. *Annual Review of Earth and Planetary Sciences, 14*, 493-571. doi: 10.1146/annurev.earth.14.1.493

Zindler, A., Jagoutz, E., & Goldstein, S. (1982). Nd, Sr and Pb Isotopic Systematics in a 3-Component Mantle - a New Perspective. *Nature, 298*(5874), 519-523. doi: 10.1038/298519a0